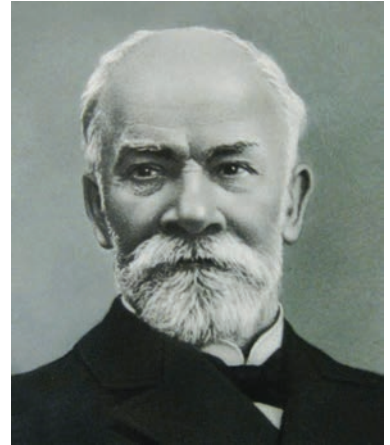


*Dedicated to the 180<sup>th</sup> anniversary of the famous  
Russian scientist Dmitry CHERNOV*

---



# **26th IFHTSE CONGRESS 2019**

## **International Congress on Metal Science and Heat Treatment**

*Proceedings*

**2019 / SEPTEMBER 17-19**

**Moscow, Russia**

---

UDC

**26th IFHTSE CONGRESS 2019.**  
**International Congress on Metal Science and Heat Treatment,**  
**dedicated to the 180th Anniversary of Dmitry CHERNOV.**  
Moscow : Metallurgizdat, 2019. 340 p.

26th IFHTSE Congress of 2019 in Moscow is dedicated to the 180th anniversary of the famous Russian scientist Dmitry CHERNOV known worldwide as the father of metallography.

The history of Russian metallurgists' communities dates back to the very end of the 19th century, and it is strongly associated with the name of Dmitry CHERNOV. In 1899, D. K. CHERNOV established an official department of Metal Science in the Imperial Russian Technical Society, and in 1910, the Russian Metallurgic Society was formed.

Today the Russian Society of Metal Science and Heat Treatment (ROMIT) inherits the tradition of uniting metal scientists that dates back to Dmitry CHERNOV.

We hope that the IFHTSE Congress of 2019 in Moscow will contribute to the networking on the latest techniques in heat treatment of metals and surface engineering.

© IFHTSE, 2019

© The Russian Society of Metal Science and Heat Treatment ROMiT, 2019

© FSUE I.P. Bardin Central Research Institute for Ferrous Metallurgy, 2019

© Metallurgizdat, 2019

## International Advisory Committee

Prof. Dr. **Arkadiy Tikhonov** [Russia], I.P. Bardin Central Research Institute for Ferrous Metallurgy, President of the Russian Society for Metal Science and Heat Treatment ROMIT

Dr. **Scott Mackenzie** [USA], Houghton International Inc., President of IFHTSE

Dr. **Eva Troell** [Sweden], Swerea IVF, Vice-President of IFHTSE

Prof. Dr. **Larisa Petrova** [Russia], MADI University, IFHTSE Executive Committee

Dr. **Patrick Jacquot** [France], Bodycote, IFHTSE Past-President

Prof. Dr. **Hans-Werner Zoch** [Germany], IWT Bremen, IFHTSE Past-President

Dr. **Stefan Hock** [Italy], IFHTSE General Secretary

Dr. **Imre Felde** [Hungary], Óbuda University, IFHTSE Executive Committee

Dr. **Massimo Pellizzari** [Italy], University of Trento, IFHTSE Executive Committee

Prof. **Reinhold Schneider** [Austria], TU Upper Austria Wels, IFHTSE Past-President

Prof. Dr. **Xu Kewei** [China], Xi'an University, IFHTSE Past-President

**Simon Blantern** [UK], Bodycote, IFHTSE Executive Committee

Prof. **Masahiro Okumiya** [Japan], Toyota Technological Institute, IFHTSE Executive Committee

## National Organizing Committee

**Sergey Tsyb** [Russia], Deputy Minister of the Ministry of Industry and Trade of the RF – Chairman

Prof. Dr. **Arkadiy Tikhonov** [Russia], Chairman of ROMIT

**Viktor Semenov** [Russia], General Director of FSUE I.P. Bardin Central Research Institute for Ferrous Metallurgy

Prof. Dr. **Andrey Rudskoy** [Russia], Academician of the RAS, Rector of the Peter the Great St. Petersburg Polytechnic University

**Pavel Servatinskiy** [Russia], Director of the Department of the MIT RF

**Aleksey Gospodarev** [Russia], Director of the Department of the MIT RF

Prof. Dr. **Aleksey Dub** [Russia], First Deputy General Director of the “Science and Innovations”

Prof. Dr. **Leopold Leontyev** [Russia], Academician of the RAS, Director of the Institute of Metallurgy, Ural Division of the RAS

Prof. Dr. **Fedor Grechnikov** [Russia], Academician of the RAS, Samara State Aerospace University

Prof. Dr. **Vyatcheslav Prikhodko** [Russia], RAS Corresponding Member, the President of the Russian Association of Engineering Technologists

**Vladimir Bannikov** [Russia], General Director of Exhibition Company “Mir-Expo”

**Mikhail Podvyaznikov** [Russia], General Director of GOZ

**Boris Gusev** [Russia], RAS Corresponding member, the President of the Russian Engineering Academy

Prof. Dr. **Aleksander Gulyaev** [Russia], Moscow Region State University.

## Academic Committee

Prof. Dr. **Oleg Bannykh** [Russia], Academician of the RAS, IFHTSE Past-President – Chairman

Prof. Dr. **Larisa Petrova** [Russia], MADI University – Vice-Chairman

Dr. **Tatiana Moskvina** [Russia], Deputy General Director of FSUE I.P. Bardin Central Research Institute for Ferrous Metallurgy – Vice-Chairman

Prof. Dr. **Alexander Glezer** [Russia], I.P. Bardin Central Research Institute for Ferrous Metallurgy – Vice-Chairman

Prof. Dr. **Georgy Filippov** [Russia], I.P. Bardin Central Research Institute for Ferrous Metallurgy

Prof. **Marcel A.J. Somers** [Denmark], Technical University of Denmark

Dr. **George Totten** [USA], Portland State University

Prof. **Massimo Pellizzari** [Italy], The University of Trento

Prof. **Reinhold Schneider** [Austria], The University of Applied Sciences FH Upper Austria

Prof. **Hans-Werner Zoch** [Germany], Foundation Institute of Materials Engineering IWT

Prof. **Zoltan Kolozsvary** [Romania], Technical Sciences Academy of Romania

Prof. Dr. **Tomasz Babul** [Poland], Director of the Institute of Precision Mechanics

Dr. **Thomas Waldenmaier** [Germany], Material Development and Heat Treatment Metals (CR/APM4) Robert Bosch GmbH

**Aleksey Ushakov** [Russia], Deputy Director of the Department of the MIT RF

Dr. **Irina Rodionova** [Russia], I.P. Bardin Central Research Institute for Ferrous Metallurgy

Prof. Dr. **Lydmila Botvina** [Russia], Baikov Institute of Metallurgy and Materials Science

Prof. Dr. **Vyatcheslav Matunin** [Russia], National Research University “Moscow Power Engineering Institute”

**Lydmila Skoromnikova** [Russia], MITOM Scientific Journal

Dr. **Vladimir Skorobogatych** [Russia], State Research Center JSC “RPA “CNIITMASH”

Dr. **Sergey Tsih** [Russia], State Research Center JSC “RPA “CNIITMASH”

Prof. Dr. **Lydmila Kaputkina** [Russia], MISIS National Research University

Dr. **N. Bogdanova** [Russia], Peter the Great St. Petersburg Polytechnic University

Prof. Dr. **Sergey Prokoshkin** [Russia], MISIS National Research University

Prof. Dr. **Yuriy Tsvetkov** [Russia], Academician of the RAS

Prof. Dr. **Valentin Levlev** [Russia], Academician of the RAS

Prof. Dr. **Evgeniy Gulihandanov** [Russia], SPbSTU

Dr. **Vladimir Aleksandrov** [Russia], MADI University

## CONTENTS

Foreword .....	9
<b><u>Plenary Lectures</u></b>	
<b>A.K.Tikhonov</b>	
The 180th Birth Anniversary of D.K.Chernov and influence of his discovery of iron polymorphism on global development of metal heat treatment processes.....	10
<b>Stefan Hock</b>	
Case hardening steels: Challenging the invisible and outsmarting the unavoidable. An approach integrated along the process chain to new potentials in a mature technology.....	18
<b>Marcel A.J. Somers, Thomas L. Christiansen</b>	
Thermochemical surface engineering of stainless steels with interstitials: symbiosis of science, technology and innovation.....	22
<b>Rolf Zenker, Anja Buchwalder</b>	
The Electron Beam Can Do More than Surface Hardening.....	30
<b><u>In Memory of D.K. Chernov</u></b>	
<b>L.I. Leontiev, V.V. Tsukanov</b>	
D.K. Chernov – scientist, pioneer and teacher – the founder of modern metallurgy and metal science theory .....	34
<b>A.I. Gnevko, O.E. Zubov, S.N. Solovov, M.V. Mukomela, A.I. Chmihalo, V.A. Yanushkevich</b>	
Prediction of the durability of metal structures based on the analysis of their microstructure .....	39
<b>I.G. Rodionova, O.N. Baklanova, A.A. Pavlov, N.A. Karamysheva, A.S. Melnychenko, S.V. Denisov, V.E. Telegin, S.G. Andreev, A.V. Mastyaev</b>	
Controlling the structure and properties of cold-rolled mill products made of light alloyed steel (HSLA type) subjected to continuous annealing .....	42
<b>V. Nikitin, K. Nikitin</b>	
Application of genetic engineering technologies to reduce the hold time under heat treatment of Al-Si cast aluminum alloys.....	47
<b><u>Structure and Properties</u></b>	
<b>Massimo Pellizzari, Vasco Menegante, Matteo Villa, Marcel A. J. Somers</b>	
On the influence of deep cryogenic treatment on tempering transformations in AISI D2 steels.....	52
<b>A.I. Zaitsev, S.V. Denisov, V.E. Telegin, A.V. Koldaev, I.G. Rodionova, A.B. Stepanov</b>	
Development of the complex technologies basis for production of a new cold-rolled low-carbon and ultra-low-carbon steels generation with improved complex properties .....	58
<b>Patricia Jovičević Klug, Bojan Podgornik</b>	
Deep Cryogenic Treatment of High Speed Steels.....	62
<b>A.V. Levina, V.P. Levin, L.R. Botvina</b>	
Correlation between mechanical and acoustic properties of low-carbon steel after static test .....	64

**A.A. Kholodnyi, Yu.I. Matrosov, G.A. Filippov, M.Yu. Matrosov**  
Pipeline steels for sour service: chemical composition, thermomechanical treatment, microstructure and properties .....68

**A. Chastukhin, D. Ringinen, L. Efron**  
Control of austenite structure evolution during TMCP in microalloyed steels .....75

### **Heat Treatment**

**D. Scott MacKenzie, Pedro Luiz Pioli, John Kim**  
Effect of temperature and catalyst on the oxidation of oil used for the Mar-tempering of Gears.....81

**A.S. Chaus, M. Bračik, M. Sahul, M. Dománková**  
Vacuum heat treatment of as cast high-speed steel of M2 type .....86

**Piotr Nawrocki, Karolina Lukasik, Kamil Wasiluk, Dawid Myszka**  
Heat treatment with intercritical heating of ductile iron.....92

**Jakub Kotous, Jaromír Dlouhý, Daniela Nacházelová**  
Influence of accelerated spheroidisation on quenching process and resultant mechanical properties in spring steel 54SiCr6 .....97

### **Thermo-Chemical Treatment**

**A. Dreano, P. Arnaud, E. Héripree, V. Aubin, J. Laporte, S. Fouvry, O. Skiba, G. Michel, C. Dannoux, V. Branger, R. Guiheux**  
“Bespoke” compound layers for fretting response optimization.....103

**Tomasz Babul, Zdzisław Obuchowicz, Piotr Nawrocki**  
Head treatment in active fluidized bed.....109

**Undrakh Mishigdorzhyn, Nikolay Ulakhanov**  
Boron-based composite diffusion layers for operational improvement of dies.....113

**Naohide Kamiya, Yuuki Tanaka, Keisuke Inoue**  
Effect of AlN Particle Size on Abnormal Grain Growth During Carburization .....117

**S.G. Tsikh, A.A. Krasulya, K.D. Polinovsky, V.N. Skorobogatykh, A.S. Pomelnikova**  
Low-temperature liquid boronizing of structural steels .....122

**Thomas Müller, Andreas Gebeshuber, Martin Aigner**  
Ecological and practical process comparison of plasma and gas nitriding-nitrocarburizing for users .....126

**Simon Thibault, Vincent Argoud, Stéphane Gourdin**  
Nitrided gears engineering: bending fatigue strength prediction from process parameters.....131

**Tsuyoshi Sugimoto, Dong-Ying Ju**  
Research for heat treatment simulation on hyper carburizing process considering with segmentation of alloy elements .....137

**M.S. Tsikh, A.A. Krasulya, A.A. Mironova, A.D. Metlyakov**  
Features of boronized layers formation on pre-carburized steels.....142

### **Additive Manufacturing**

**T. Tarasova, R. Ableyeva, G. Gvozdeva**  
Investigation of structure and properties from aluminum matrix composite materials produced by selective laser melting .....146

<b>D.S. Fatyukhin, R.I. Nigmatzianov, A.V. Sukhov</b>	
Ways of ultrasonic additive manufacturing development .....	151
<b>A.V. Gusarov, R.S. Khmyrov, P.A. Podrabinnik, T.V. Tarasova</b>	
Submicron structure formation at selective laser melting of WC-Co .....	153
<b><u>Quality Control</u></b>	
<b>Frerichs Friedhelm, Lübben Thomas</b>	
Application of different measuring techniques for characterization of quenching processes in water based polymer solutions .....	157
<b>V.M. Matyunin, A.Yu. Marchenkov, A.L. Goncharov, A.P. Sliva, Nuha Abusaif</b>	
Instrumented indentation application for express control of materials surface layers mechanical properties after various treatment. ....	163
<b>Hideo Kanamori, Tsuyoshi Sugimoto, Riki Homma, Dong-Ying Ju</b>	
Measurement of cooling curves and visualization of boiling phenomenon on disk probe .....	168
<b>L.R Botvina</b>	
Fractodiagnostics: tasks and methods .....	173
<b><u>Combined Processes</u></b>	
<b>M.Yu. Semenov, A.E. Smirnov, A.S. Mokhova, A.P. Alekhin</b>	
The tribological properties of the heat resistant steel after a complex thermo-chemical treatment .....	176
<b>David Hradil, Michal Duchek, Miroslav Šugár, Piotr Nawrocki</b>	
Effect of combined gas nitriding and deep cryogenic treatment on wear behaviour of AISI D2 steel .....	180
<b>V.M. Prikhodko, D.S. Simonov, T.D. Dmitriev, Lotof Yassin Qeblawi</b>	
Combination of thermochemical treatment methods with ultrasound. ....	186
<b>O.V. Chudina, P. Bringulis</b>	
Electroplating on the surface of steels after ultrasonic treatment .....	189
<b><u>Processes Modeling and Simulation</u></b>	
<b>Thomas Waldenmaier, Hermann Autenrieth</b>	
Simulation of low-pressure carburizing with acetylene for industrial applications .....	193
<b>E. Vyazmina, G. Mougín, J. Sheng, S. Jallais, L. Coudurier, F. Januard</b>	
Acetylene decomposition during low pressure carburization treatment: modelling and optimisation of the process .....	197
<b>Hannes Birkhofer, Ben Taylor, Thomas Lübben</b>	
Distortion of a fixture hardened planet gear blank – a finite element simulation study .....	202
<b>Sándor Szénási, Zoltán Fried, Károly Széll, Imre Felde</b>	
Application of universal function approximator to predict HTC during quenching .....	207
<b>Hideo Kanamori, Dong-Ying Ju</b>	
Identification of heat transfer coefficients and simulation of quenching distortions on disk probe .....	211
<b><u>Plasma, Laser, and Electron Beam Processes</u></b>	
<b>Youichi Watanabe, Nobuhiko Satomi, Haruna Ishizuka, Kosuke Takamura, Weibo Li, Nobuyuki Kanayama</b>	
Microstructure and tribological properties of expanded austenite formed in austenitic stainless steels by low-temperature active screen direct current plasma carburising. ....	217

<b>O.V. Chudina, A.V. Eletsy, E.V. Terentyev</b>	
Surface hardening of steel nanocarbon materials during laser and electron-beam treatment .....	224
<b>Liu Ming-xia, Chang Geng-rong, Duan Kai Liang, Fu Fu-xing, Xie Yan-xiang, Dai Jun, Yu Li-jun, Xu Ke-wei</b>	
Effect of laser remelting on surface microstructure and corrosion resistance of ultra-high speed laser cladding coating. ....	229
<b>L.G. Petrova, V.A. Aleksandrov, A.S. Sergeeva, V.M. Vdovin</b>	
Effects of different types of discharge on thermo-chemical processes of structural and tool steels .....	235
<b>Němeček Stanislav, Černý Ivo, Kec Jan, Ganev Nikola, Čapek Jiří</b>	
Benefits and properties of laser-hardening. ....	240
<b><u>Coatings and Films</u></b>	
<b>Kazuki Kawata, Toru Kidachi</b>	
Characterization of Al <sub>2</sub> O <sub>3</sub> /TiAlN/TiN multilayer coatings prepared by pulsed DC plasma-enhanced chemical vapor deposition .....	244
<b>V.A. Alexandrov, I.Yu. Isayeva, I.V. Odinokova, G.Yu. Ostaeva</b>	
The formation composite coatings of structural steel by the copper-containing nanoparticles .....	250
<b>Beibei Han, Dongying Ju, Susumu Sato, Maorong Chai</b>	
Microstructure and corrosion behavior of DLC films deposited on SUS316L and titanium substrate for bipolar plates. ....	253
<b><u>Poster Session</u></b>	
<b>S.K. Sundukov, D.S. Fatyukhin, A.A. Volkov</b>	
Ultrasonic surface treatment of components produced by additive manufacturing technologies .....	259
<b>R.I. Nigmatzianov, S.K. Sundukov, V.A. Perekrestova</b>	
The combination of ultrasonic hardening and nitriding .....	262
<b>E.A. Kosenko, V.A. Zorin, N.I. Baurova</b>	
Recognition of subfilm corrosion of metal surfaces of machines parts with various coatings by infrared thermography. ....	265
<b>L.G. Petrova, P.E. Demin, A.V. Kosachev, G.Yu. Timofeeva</b>	
Combined surface modification of steel by zinc coating and nitriding .....	268
<b>A. Neverov, O. Seliverstova, I. Sergeev</b>	
Influence of contact surfaces on the properties of the two-pivotal systems .....	272
<b>A.Yu. Malakhov, T.E. Likhachova, V.A. Perekrestova, A.E. Perekrestov</b>	
Research of surface strengthened automobile parts during automobile-technical expertise .....	277
<b>Doryun Lee, Dongjun Mun</b>	
Effect of forging on creep properties of cast Cr based steel. ....	283
<b>Tsuyoshi Saito, Kento Kurihara, Ryota Gemma</b>	
Possibility of nitriding treatment of Si under N <sub>2</sub> atmosphere purified by CaSi <sub>2</sub> .....	287
<b>T.M. Pugacheva</b>	
History of aviation bearing steels development and its heat treatment .....	291
<b>L.G. Petrova, P.E. Demin</b>	
Nitriding of steels in electrolytic plasma: specifics of combined processes .....	296

<b>A.A. Chervyakov, A.V. Chikurov, A.K. Tihonov</b>	
The new technology of strengthening the large-scale stamp working surfaces for sheet steel products through hard chrome plating . . . . .	<b>301</b>
<b>A.I. Zaitsev, A.V. Koldaev, A.B. Stepanov, N.A. Arutyunyan, S.F. Dunaev</b>	
The principles of creating new economically alloyed ferritic steels with a unique complex of difficult to combine properties . . . . .	<b>306</b>
<b>Hideo Kanamori, Tsuyoshi Sugimoto, Riki Homma, Msayuki Kato, Dong-Ying Ju</b>	
Measurement of cooling curves and visualization of boiling phenomenon on cylinder probe . . . . .	<b>310</b>
<b>A.A. Sorokin</b>	
Heat treatment of fasteners at AO Belebeevsky plant “Avtonormal” . . . . .	<b>316</b>
<b>I.G. Rodionova, O.N. Baklanova, A.A.Pavlov, N.A. Karamysheva, A.S. Melnichenko, S.V. Denisov, V.E.Telegin, S.G.Andreev, A.V.Mastyayev</b>	
Control of the structure and properties of cold rolled steel of two-phase ferrite and martensitic steel (of DFMS type) subjected to continuous annealing . . . . .	<b>318</b>
<b>M.O. Smirnov, T.A. Chizhik, I.N. Tsybulina, A.M. Zolotov</b>	
Investigation of the steel structure 15Kh11MF-Sh depending in the thermo-deformation parameters of treatment, investigation of the characteristics of large-sized stamped blanks of turbine blades . . . . .	<b>322</b>
<b>E. N. Beletskiy, M. R. Tyutin, L. R. Botvina, U.S. Perminova</b>	
Fracture toughness and fracture microrelief of stainless steel with ultrafine-grained structure . . . . .	<b>327</b>
<b>I.M. Sosnin, A.A. Vikarchuk, A.E. Romanov</b>	
Influence of thermo treatment on the dislocation substructure and photocatalytic properties of ZnO . . . . .	<b>330</b>
<b>A.U. Petrov, A.E. Shestovskikh, V.N. Timofeev, V.I. Luzgin , A.S. Koptyakov, I.V. Kostin, S.G. Bocvar</b>	
Ultrasonic treatment of aluminum alloys in the technology of casting products with enhanced resource characteristics . . . . .	<b>333</b>
<b>Božidar Matijević</b>	
Properties of the quenchant measured with Liščić/QRC and ISO 9950 or ASTM D6200 probes . . . . .	<b>337</b>

## FOREWORD

The 26th IFHTSE CONGRESS 2019 • International Congress on Metal Science and Heat Treatment is dedicated to the 180th birth anniversary of Dmitry K. Chernov, an outstanding Russian engineer and scientist, to whom several articles by Russian and foreign scientists in this collection are devoted.

Today's International Congress of IFHTSE is held in Russia after a long break: last time such event took place in the USSR in 1989 in Moscow, with Tom Bell taking part in it, on the celebration of the 150th birth anniversary of D.Chernov. I was also lucky to participate in that Congress and to give a talk.

Great changes have happened over these 30 years: in 1999 the city of Yalta, Crimea, where D.K.Chernov spent last years of his life on health reasons, hosted Chernov's Readings on celebration of his 160th birth anniversary. Russian community of metal scientists organized an opening ceremony of Memorial on his grave in Polykurovskoye cemetery where he was buried in 1921.

During this period of time, International Federation for Heat Treatment and Surface Engineering (IFHTSE) held its Congresses in many countries of the world: USA, United Kingdom, Germany, France, Italy, Japan, China and other countries. IFHTSE unites 46 developed countries, including Russia, which has actively participated the Congresses held.

Congress on global development of nitriding process was held in 1998 in Florence (Italy). Professor Tom Bell dedicated his talk to Professor Yu. M.Lakhtin, the founder of the Russian scientific nitriding school.

It should be mentioned that in late 20th and early 21st centuries extensive researches were carried out on saturation of metal surfaces with carbon and nitrogen, both individually and in combination with oxygen and other elements (aluminum, molybdenum, etc.). For instance, application of plasma processes with obtaining of nano-structural particles in metal surface layers results in several-times increase of wear resistance compared to initial heat treatment.

Thermal and thermochemical treatment in vacuum furnaces under low pressure have become commonly used. Application of vacuum furnaces for heat treatment is one of the main global trends, as in addition to high quality of parts it also ensures reduced energy consumption with much less emissions and, therefore, better environment. A lot of attention is paid in this collection of articles to thermochemical treatment as the main type of heat treatment at automotive factories. The amount of heat treated steel is 1.5 times more than melted, therefore, metallurgist and heat treatment experts of the world are facing the challenge of technology digitalization for more successful process control and production process engineering. Thermal and thermochemical treatment of metals is the main way of their strengthening, therefore it should be a separate dedicated area in preparation of future experts and young scientists in the field of metal science and heat treatment.

*The President of ROMiT,  
Academician of the Russian Engineering Academy,*



*Professor ARKADIY TIKHONOV*

## THE 180th BIRTH ANNIVERSARY OF D.K.CHERNOV AND INFLUENCE OF HIS DISCOVERY OF IRON POLYMORPHISM ON GLOBAL DEVELOPMENT OF METAL HEAT TREATMENT PROCESSES



**A.K. Tikhonov**

Chairman of ROMiT (Russian Society of Metal Science and Heat Treatment)

arkadiy.tikhonov@vaz.ru

D.K.Chernov is the author of discovery of critical points  $a$  ( $Ac_1$ ) and  $b$  ( $Ac_3$ ), which became a basis for iron-carbon diagram. He discovered metal slide curves named Chernov-Luders lines. He is the author of technology with heat treatment, rather than forging, being final strengthening operation.

**Keywords:** critical points; diagram; physical metallurgy; pellets; process strength; Chernov-Luders lines.

In November 2019 we are celebrating the 180th birth anniversary of D.K. Chernov, an outstanding Russian engineer and metallurgy scientist. This year also marks the 151st anniversary of his famous speech on internal transformations of steel. In 1868, when working at Obukhov's Plant in St.Petersburg, Chernov completed his research and made a talk at the Russian Technical Society meeting on results of his work. In the same year his reports were published in the *Society Transactions* in the articles *Critical Review of Articles by Messrs Lavrov and Kalakutsky on Steels and Steel Tools* and *D.K. Chernov's own researches on the same subject* (July 1868) and *Materials to study Steels and Steel Tools* (Nov–Dec 1868). And discovery of critical points corresponding to certain temperatures of steel structural transformations. Critical temperatures defined according to colors of steel heat were called by Chernov as  $a$ -point (deep cherry-color heat) and  $b$ -point (red non-shiny heat) (Fig. 1a, b).



Discovery of this phenomenon and its actually immediate application at the Obukhov's Plant for steel improvement are the merits of the scientist and engineer. Discovery of critical points served as the main condition for application of hardening process

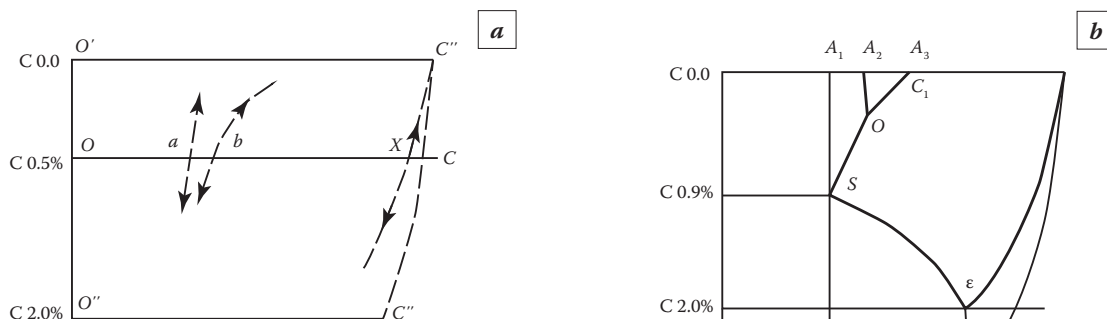


Fig. 1.  $a$  – diagram drawn by Chernov;  $b$  – diagram drawn by Roberts-Austen

for components made of various steel grades and became the basis of iron-carbon diagram.

French scientist Ph.Osmonde, in further development of Chernov's work, defined numerical values of  $\alpha$  and b points with a thermoelectric pyrometer in 1885. According to designation introduced by Ph.Osmonde,  $\alpha$ -point is shown as letter A with index 1, while b-point is shown as letter A with index 3. D.Chernov considered designation proposed by Osmonde to be not very appropriate, though he did recognize it as a "solid foundation for modern metal science". The works by the above-mentioned European scientists performed during 80s–90s years of the 19th century, completely confirmed these, both in qualitative and quantitative terms, and today they represent a foundation for modern theory of steel transformations and ensuing methods of steel heat treatment. The essence of these transformations refers to phenomena of iron polymorphism, Fe- $\alpha$  and Fe- $\gamma$  polymorphic types being most important along with dissociation of solid solutions (austenite) into Fe- $\alpha$  and Fe<sub>3</sub>C cementite.

Later on, a new d-point was added by Chernov, the point which should be reached by quick cooling-down after pre-heating above  $\alpha$ -point, in order to achieve maximum hardening effect.

Chernov established a connection between steel treatment and its structure and properties. He said: "Steel properties are changing along with its structure. That is why studying effect of heat on steel properties makes basis for familiarization with steel as a material for making ordnance, shells, or similar objects" Chernov's work provided the materials which became a basis for scientific substantiation of the main task of the new area of knowledge - physical metallurgy, this task being establishment of regular dependences connecting metal structures with treatment methods on the one hand and properties on the other hand.

d-point, like  $\alpha$  -point, did not raise any disputes or interpretations other than those given by Chernov. The meaning of martensite point, discovered for the second time in XX, completely coincided with Chernov's d-point notion, and there were no disagreements on that. Destiny of b-point happened to be different, as there was a hot discussion around it.

In each of his points, D.Chernov mainly saw a certain temperature, which, if reached in heating or cooling-down process, might lead to changes in structure of properties controllable through varying heat-treatment parameters (examples), used for practical purposes.

As regards the Nature of the changes in properties observed and importance of  $\alpha$  and d points, there were no disagreements both before and after

appearance of constitutional diagram. As for treatment above b-point, remarkable modifications in structure and properties were observed and applied by Chernov not only in hardening process but also in getting equilibrium structures, despite their return to the same phase state after heating as existed in initial steel casting or forging. According to a single constitutional diagram built based on thermal analysis curves (i.e. without consideration of micro and macro structures), heating and slow colling-down do not result in residual changes in phase states. While admitting actually full numeric coincidence of b and Ac<sub>3</sub> points, Chernov yet considered the essence and practical application of b-point as not purely a transition to a certain transformation, but also as its certain consequences, i.e. physical structural changes accompanying such transition, even if phase content was the same as the one of the initial steel. In fact, Chernov stated already that time that properties were defined not only by alloy composition and its position in the constitutional diagram, but also by its structure, which, in its turn, is defined by kinetics and mechanism of transformation, which became quite obvious today. Currently, S-shaped curves characterize steel properties after reaching various temperature and speed Fig. 2.

Thus, admitting that Chernov's  $\alpha$ -point and b-point are phase transformation points, we have a full right to say that Chernov was the one who first determined steel critical points and thus put foundation of the theory of phase transformations, that means he was the founder of modern physical metallurgy. Steel represents a crystalline solid, which is subject to all physical laws applied to crystals. Metallurgist S.S.Steinberg said: "This was Chernov who raised metallurgy from the state of descriptive practical art up to the level of theoretical science".

But could it be that only we, Russians so highly appreciate achievements of our outstanding compatriot and the rest of the world attributes foundation of scientific physical metallurgy to other later scientists?

Let us look how Chernov and his work are evaluated by scientists from various countries. American Professor Henry M.Howe in his book *Iron, Steel and Other Alloys*, 1908, dedicated to Chernov called him "Father of metallography".

Professor A.Sover wrote in 1902: "The younger generation of metallurgists dealing with steel fairly look at professor Chernov as a founder of scientific research of steel properties and structure. His works describing the results of his great achievements published back in 1868 will remain classic for a long time to serve as a model of clarity and consistency for metallurgy researchers..."

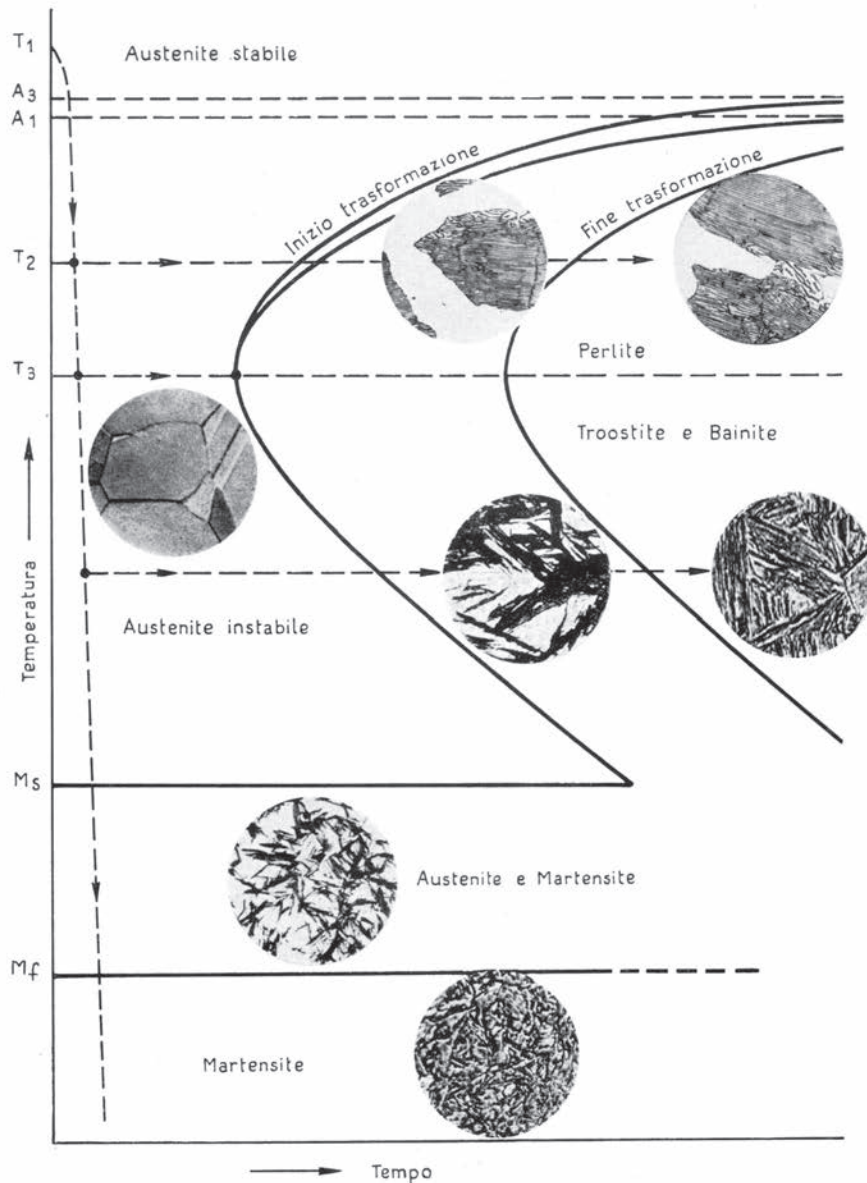


Fig. 2. S-shaped curve and main micro-structures [4]

Ph. Osmonde, direct follower of Chernov's work, wrote: "Researches in the area, which is called "physics of steel" in America, started by professor Chernov and actively continued during the last fifteen years resulted in late 1896 in the meeting of two streams which used to develop in parallel in the past – scientific metallurgy and physical chemistry", and then he states that the merge was fruitful.

As for importance of Chernov's works for the industry, it was best expressed by P. Montgolfier, director of one of the largest plants in France, at metallurgists' meeting during the 1900 World Exhibition in Paris: "I deem it my duty to say openly and publicly, in front of so many experts and connoisseurs, that our plants and the whole steel foundry business owe to a great extent their current development and success to works and researches done by a Russian engi-

neer mister Chernov, and I invite you to express our sincere gratitude and appreciation to him on behalf of the entire foundry industry".

A.Porthaven wrote in D.Chernov obituary in 1922: "His name will stay connected with two fundamental discoveries which became a starting point for almost all new researches of steel: they are the notion of steel critical points and the notion of structural changes in steel during heat treatment... Chernov was a forerunner and a school leader, his early works demonstrate the origin of remarkable development of our knowledge with regard to steel: he managed to change ferrous metallurgy completely, to turn it into a field of industry where a real revolution became a result of science integration".

Chernov was mentioned in *The 500 Million of the Begum* (1879) by Jules Verne as a famous theorist of steel foundry business.

One of the steel crystal types – dendrite – was named after him.

In 1960 C. Smith published his History of Metallography, where the name of D.K. Chernov was mentioned 20 times.

French metal scientist Delbard wrote in *La Revue de Metallurgie* Journal in 1967: “Starting from the ancient times people could increase steel hardness by water quenching, without understanding of the hardening mechanism. Chernov defined that such hardness increase was not happening gradually with temperature rise to certain level. He gave designations a, c, d, e and f to temperatures which he considered remarkable. It became known later that some of these designations correspond to allotropic modifications...”

d and e points were defined by Chernov around 200 and 450 °C, they correspond to martensite and bainite transformations. Based on the above statements, it is not possible nowadays to speak of metal science development without a reference to D. Chernov’s works.

Academician A.A. Baikov mentioned in his article dedicated to the 100th Birth Anniversary of D.K. Chernov that the works by the mentioned scientists of the world performed during 80s–90s years of the 19th century, “fully confirmed Chernov’s discoveries both in qualitative and quantitative terms, and make nowadays a basis for modern theory of steel transformations and ensuing methods of steel heat treatment. Chernov taught us how to take objects for research from our life or day-to-day production environment. One could not find a better example of efficient and fruitful implementation of the idea of theory and practice unity than D. Chernov’s work. The entire further course of development of the metal and alloy science completely proved the correctness of D. Chernov’s views. This confirms up-to-date importance of his research for physical metallurgy history and for modern stage of metal science.

Since 1889 he was a Professor in Mikhailovskaya Artillery Academy.

D. Chernov’s merits in the global science were totally recognized. He was a Honored Professor of the Mikhailovskaya Artillery Academy, a Honorary Member and laureate of the Russian Technical Society, honorable Chairman of the Russian Metallurgy Society, a honorable member of Petrograd Technological Institute, Petrograd Polytechnic Institute, General Ship-Building Department of Maritime Ministry, Honorable Vice-President of British Institute of Iron and Steel, honorable corresponding member of the Royal Society in London, honorable member of American Institute of Mining Engineers

and the Board of Institute of International Experts. In 1901 D. Chernov was awarded with French Order of the Legion of Honour [1–3, 6].

Thus, in terms of contents and results of his work and also in terms of their purposefulness, Dmitry K. Chernov was very close to the present time, as a person who established continuously developing metal science and physical metallurgy.

Professor S.V. Kolpakov, Minister of Ferrous Metallurgy of the USSR wrote on opening of D. Chernov’s Memorial on Polikurov Hill in Yalta: “The work of the great Russian metallurgist allowed for major improvements in converter process. Before Chernov, only high-silicon iron was used, as silicon was considered to be the main heat carrier. D.K. Chernov at Obukhov’s Plant, and simultaneously K.P. Polenov at Nizhny Saldinsk Plant, suggested application of low-silicon iron pre-heated in cupola furnace. They proved advisability of using oxygen-enriched air to intensify converter process. D.K. Chernov is a universally recognized creator of the theory of crystal structure of cast steel. Nowadays, new foundry processes have been developed to allow for steel deoxidization, vacuum smelting, etc. All these substantially reduce number and size of gas cavities in cast metal, and continuous pouring of liquid steel makes it possible to obtain castings without shrinkage holes. However, consumer properties of metal products are provided by thermal or thermo-mechanical treatment”.

We could quote more statements by famous scientists, but the above ones sufficiently describe him as a metallurgist of genius.

Global practices demonstrate that modification of melting technology, off-furnace treatment and teeming can often have more material effect on steel structure and properties than changing its chemical composition. In the process of refining our technology of micro-alloying calcium steel in open-hearth furnace and electric furnace with pellets at our plants, minor changes in quantitative proportions of deoxidizers and modifiers resulted in radical change in composition and morphology of non-metal inclusions, therefore various process properties and their anisotropism were obtained. Difference in cutting machinability for various heats reached 2 folds. Fig. 4. Table 1 shows influence of different smelting processes on mechanical and technological properties of steel, including chip appearance at various cutting speeds, and micro-structure, see Fig. 5–9.

Fig. 3 demonstrates that, having the same hardness, steel smelted in electric furnace with pellets has higher tensile strength, while steel smelted in open-hearth furnace with conditional charge mixture has lower tensile strength. Such dependence can be ex-

Table 1. Steel properties for various smelting processes

Grade of steel	Mechanical properties						
	$\sigma_T$ , MPa	$\sigma_B$ , MPa	$\delta_5$ , %	KCU, J/cm <sup>2</sup>	Score of austenitic grain	change in size mm	Coefficient of increase of tool durability
8620AISI* (20CrMnNiMo)	950	1200	6	60	3–5	>4	0.9
AC20CrMnNiMo**	1060	1300	13	120	7–9	2.6	1.3

\*\*High and low limits of aluminum and sulfur; calcium introduced into the process; defined contents of sulfur before alloying is maximum 0.008%. Size of austenitic grain should be no higher than 5, anisomeric grains should be within 3 neighboring points, hardenability should be within 32–41HRC at 6 mm distance from butt end, as per Jominy test method [6].

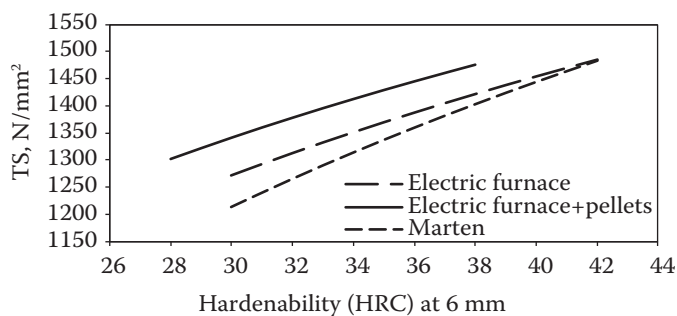


Fig. 3. Correlative dependence of tensile strength on hardenability at 6 mm point for 20CrMnNiMo steel in various smelting conditions [7]

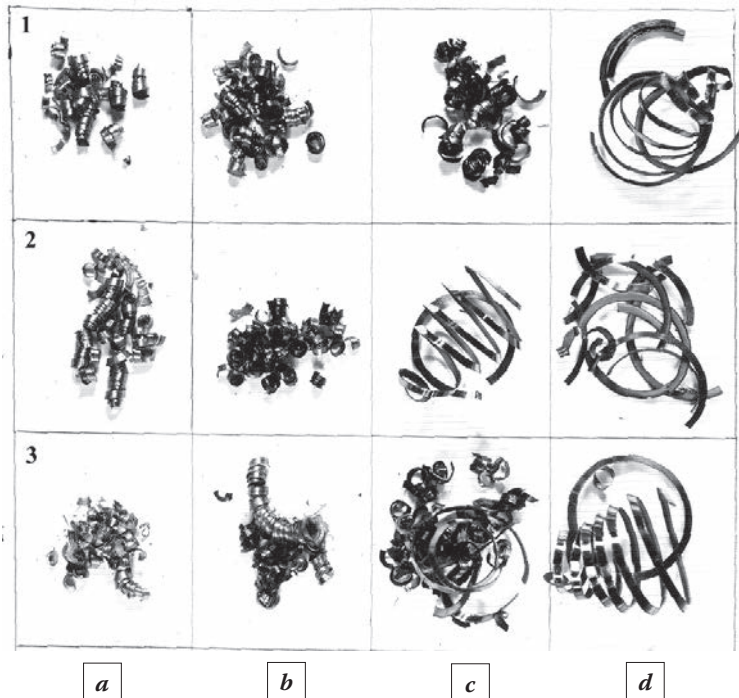


Fig. 4. Appearance of chips formed in free turning process with P6M5 high-speed tool, at different speed:

1 – ACa20CrMn steel; 2 – ACa20CrMnB steel;  
3 – ACa20CrMnV steel.

a –  $V_{\text{cutting}} = 15$  m/min; b –  $V_{\text{cutting}} = 30$  m/min;  
c –  $V_{\text{cutting}} = 45$  m/min; d –  $V_{\text{cutting}} = 60$  m/min

plained by globular shape of oxisulfides located inside the grains and not on the grain boundaries, with micro-structure shown in Fig. 5 and 6.

Fig. 4 shows that modification of micro-structure of non-metal inclusions formation, with micro-alloying elements added, changes chip shape, i.e. cutting speed.

Fig. 6 shows pictures of characteristic non-metal inclusions in steels made in electric furnace and open-hearth furnace.

Fig. 7 shows X-ray spectral micro-analysis of a complex non-metal inclusion in

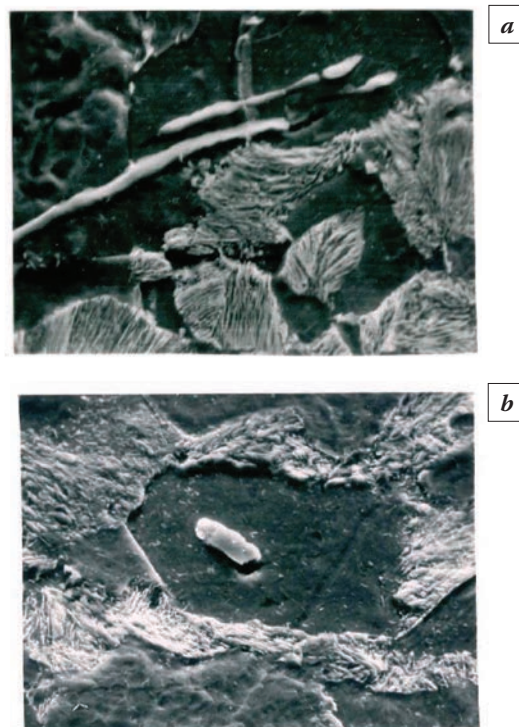


Fig. 5. Manganese sulfides in 20CrMnNiMo steel: a – alloyed with sulfur under standard technology (S = 0.039%); b – alloyed with sulfur and modified with calcium under the new technology (S = 0.04%)

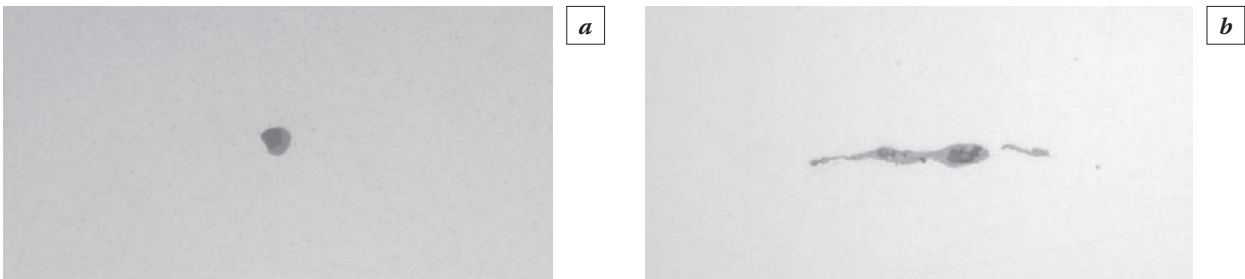


Fig. 6. Oxisulfides in 20CrMnNiMo steel: *a* – smelting in electric furnace with pellets (×500); *b* – open-hearth furnace smelting (×500)

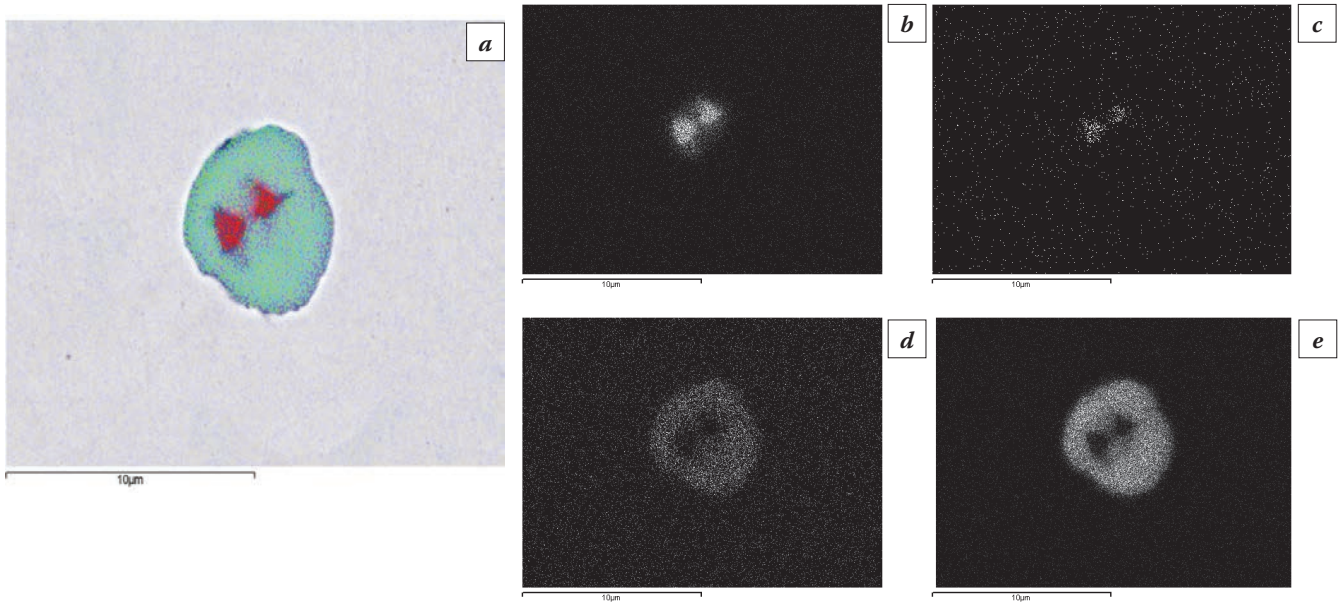


Fig. 7. X-ray spectral micro-analysis of a complex non-metal inclusion in samples of 20CrMnNiMo steel grades made in electric furnace with pellets: *a* – Al – red, S – green, Ca – blue; *b* – Al distribution; *c* – O distribution; *d* – Ca distribution; *e* – S distribution

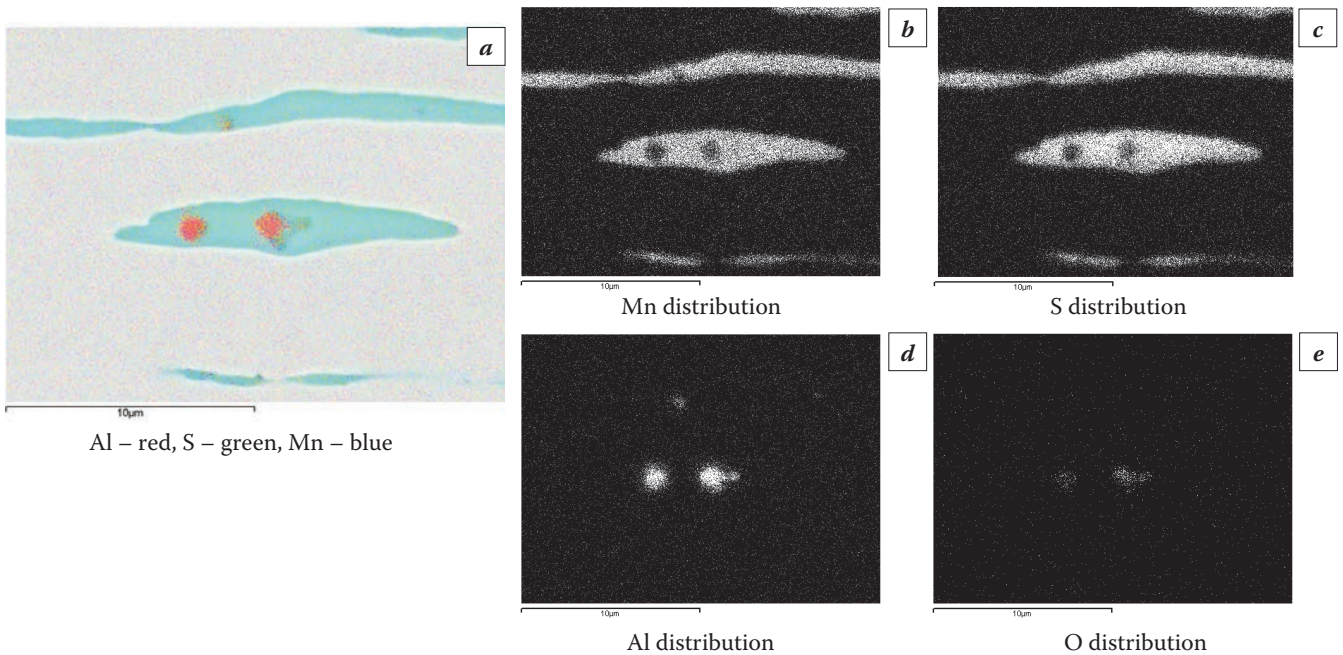


Fig. 8. X-ray spectral micro-analysis of a complex non-metal inclusion in sample of 20CrMnNiMo steel made in open-hearth furnace: *a* – color scheme for distribution of major elements; *b*–*e* – distribution of individual elements in inclusions

ACa20CrMnNiMo steel grades made with electric furnace and open-hearth furnace processes.

Inclusions size: sulfides 75 microns, oxisulfides 12 microns, they have a globular shape; and manganese is there in the solid solution to increase hardenability of a finished part after its final heat treatment.

Size of inclusions: sulfides 290 microns, oxisulfides – 150 microns.

Manganese exists in sulfide form, thus depleting steel solid solution.

Thus, the above micro-structures confirm the influence on all properties of metals.

Micro-structure changed with the change of smelting technology and micro-alloying, which resulted in 30–40% increase of cutting speed, tool consumption decrease by 1.5 to 4 times, decreased hardening deformation and 1.5 times higher parts service life. Higher tensile strength and impact ductility allowed design engineers to modify gear tooth module from 2.5 to 2.1, which resulted in significant decrease of tooth deformation and, finally, in lower noise of gear box and higher speed in car operation. Such combination of strength and ductility, as well as process durability will make it further possible to reduce the module even more in order to switch to tooth knurling instead of cutting, which will raise metal utilization rate from 0.40 up to 0.85, exclude application of expensive hob cutters and other cutting tools and make gear manufacturing more environmentally-friendly, as no bactericide coolants will be used.

Strength depending on production specifics and metal treatment, taking into account capabilities and life cycle of components is called process durability compared to design durability ( $K_{1c}$ ) defined by physical and mechanical properties of metal, part design and dimensions. This is reached by special pre-treatment of metal to be machined, purposeful standardization of its composition, structure and properties to fit with all further process operations.

Let us take an example of influence of micro-structure in process steps on properties of low-carbon high-ductility steel sheet.

The supposition that a preset strength of cold-rolled steel sheet, the same as of hot-rolled one, could only be ensured at reeling temperature of 560 °C turned out to be wrong, as for cold-rolled products there it is already possible to control release of excessive phases in the course of recrystallization annealing. Cementite is dissolved during the annealing process leading to less amount of complex release, bigger lots of products with reeling temperature below 560 °C. The particles are formed during annealing and not during a roll colling-down, their number is growing with longer heating and holding, thus

decreasing strength and increasing ductility. This allows for getting a steady complex of properties and higher ductility – up to 26%, with shorter annealing time, especially when slow cooling-down is used after annealing, resulting in deposition of cementite onto nanoparticles of niobium carbonitride making them larger from 10 to 30–50 nanometers.

We can see sometimes various color waves on a cold-rolled sheet, which we call flow lines. Chernov has a priority here as well.

Chernov's *Summarized Report on Certain Observations of Steel Machining* was published in *Imperial Russian Technical Society Transaction* in 1885, in which the author stated that cast steel behaved like all elastic solids transferring external forces in undulatory manner until these forces exceed elastic limit. In such case deformation happens and a pattern of this waves is fixed on polished steel plates in form of matt lines.

This way tension lines were first discovered in plastically deformed metal, which are presently known as Chernov-Luders lines.

D.Chernov's ideas of distribution of deformation in metals were so much ahead of his time, that French metal scientist Ph.Osmonde attached the following note to French translation of this book in 1902: "Author of the book Professor Chernov, whose steel treatment researches had such a great influence on steel metallurgy evolution, once again became a real forerunner in this work of him".

The work done by D.Chernov has a huge scientific and practical importance, as he gave a theoretical substantiation and experimental proofs of the fact that decisive influence on steel structure and properties formation is provided by heat treatment, and not by forging, as people used to think before. It is called now thermo-mechanical treatment. Possibility and advisability of purely thermal treatment of steel, without any mechanical effect, arose from the nature of the discovery made by D.Chernov. In the modern world this is induction hardening. All construction structures undergo heat treatment after rolling: angle bars, T-beams, H-beams, etc. to be used in building construction.

Chemicothermal treatment, i.e. saturation with carbon, nitrogen, oxygen and other elements, takes its special place. Triple diagrams are drawn-up to perform heat treatment after saturation using polymorphic transformations of micro-structures on steel surface at different speeds of cooling-down in water, oil and various atmospheres, getting hardness from 500 to above 1000 HV [9, 10].

Polymorphic transformations are used in various non-ferrous alloys with mandatory drawing-up of the diagrams. For instance, multiple metastable

and interim phases are formed in titanium alloys in form of intermetallic compounds, carbides, hydrides, etc. However, main phases in industrial titanium alloys are  $\alpha$  and  $\beta$ , so polymorphic  $\alpha=\beta$  is also the most important one. Thermal cycling effect is largely provided by phase hardening in this transformation [11].

The importance of critical points discovery and building of lower corner of the iron-carbon diagram could be compared with importance of construction of periodic table by Dmitry Mendeleev. Thousands of diagrams have been created in the world today which are followed to perform heat treatment. In this respect Chernov's achievements are priceless for the industry.

Heat treatment represents the main, most common and most economically efficient method to improve metal properties to fit with particular conditions of product operation. In 2018, above 1.8 billion tonnes of steel were smelted in the world, while 1.5 times more metals were heat-treated. 60 million tonnes of aluminum, 20 million tonnes of copper. Such a leap forward happened in the 20th century thanks to discovery of iron polymorphism by D.Chernov. In early 20th century, a car having weight of 1 tonne could accelerate to 20 km per hour, and in early 21st century it is over 300 km per hour, thanks to scientific developments and practical implementation of heat treatment for metallic materials. Therefore, the 20th century can be called the century of heat treatment. This is the merit of scientists of the world.

Dmitry Chernov wrote: "It was a good luck that the start of my practical activities coincided with the birth of the Russian Technical Society, it provided all technical people with the chance to have free networking and exchange of their opinions at technical discussions on various areas of applied science and technical practice, which they had never had before..." Today we are united in the International Federation for Heat Treatment and Surface Engineering. It is a great achievement. It is an example of a real Congress, where scientists share their ideas, and they are the ones who move the progress forward.

Joliot-Curie wrote: "Art masterpiece is undoubtedly more timeless, yet I am sure that an artist and a scientist are moved by the same inspirations, which require thoughts and actions of the same nature. Thus, an artist and a scientist meet to create beauty and happiness in all their forms, without which our life would be just a too doleful journey".

This can be proved. In early 1911, the Society of Friends of Music held a violin competition participated by Dmitry Chernov. This event was a real triumph of Dmitry Chernov, as the members of the reputable jury couldn't tell which violin the violinist was playing: the one made by ancient Italian master



in Cremona (Straivari) or the one made in the 20th century in Saint-Petersburg by Professor of Metallurgy Dmitry Chernov.

## REFERENCES

1. **Bochvar A.A.** Works by D.K. Chernov on physical metallurgy and their importance for modern science // *MiTOM*. 1989. № 11. P. 44–47.
2. **Golovin A.F.** On life and work of Dmitry Konstantinovich Chernov. (1839–1921) // *MiTOM*. № 11. P. 47–51.
3. **Grigoryn G.G., Kozhina L.B., Morozova S.G., Danilina V.N.** Dmitry Konstantinovich Chernov, an outstanding metallurgy engineer. History of Engineering Ideas Project. Moscow Polytechnic Museum. 1999. P. 86.
4. **Natale T., Verdiccio P., Dassano G.B.** *Necnologia del trattamento termico della acciai*. Torino, 1963. 363 c.
5. **Krishtal M.A.** Technological Strength and Non-Destructive Control Methods in Heat Treatment // *MiTOM*. 1977. № 8. P. 33–35.
6. **Gnevko A.I.** On the 160th Birth Anniversary of D.K. Chernov // *MiTOM*. 2000. № 4. P. 7–13.
7. **Palagin Yu.M., Tikhonov A.K., Mashkin V.A.** Influence of Steel Smelting Methods on Strength of Components / *Mat. of the 2nd International Conf. Materials in Automotive Industry, Togliatti*. 2004, Vol. 1. P. 84–91.
8. **Tikhonov A.K.** Polymorphism of Iron and Practices of Heat Treatment of Iron-Carbon Alloys // *MiTOM*. 2000. № 4. P. 13–14.
9. **Kozlovsky I.S.** *Chemicothermal Treatment of Gears*. M. : Machine Building, 1970. P. 232.
10. **Lakhtin Yu.M., Kogan Ya.D.** *Steel Nitriding*. M.: Machine Building, 1976. P. 256.
11. **Lyasotskaya V.S., Knyazeva S.I.** Polymorphic transformation as a Basis for Thermal Cycling of Titanium Alloys // *MiTOM*. 2000. № 4. P. 20–23.

**CASE HARDENING STEELS:  
CHALLENGING THE INVISIBLE AND OUTSMARTING  
THE UNAVOIDABLE  
AN APPROACH INTEGRATED ALONG THE PROCESS CHAIN  
TO NEW POTENTIALS IN A MATURE TECHNOLOGY**



**Stefan Hock**

IFHTSE Secretary General, Italy  
stefan.hock@ifhtse.org

*With gratefully acknowledged contributions  
from Thomas Blum, Jörg Kleff, Martin Schulz, Alfred Sollich, and Dieter Wiedmann,  
and with the kind permission of ZF Friedrichshafen AG*

---

**Keywords:** Grain Size; Nonmetallic inclusions; Fatigue; rare events; Probability of failure.

---

In case hardening, both the processes and the steels used have been successfully applied and improved for decades, to the point where nowadays millions of case-hardened components perform to full satisfaction in vehicles, machines and plants of all kinds. And yet, in spite of the tremendous amount of research done, there remain structures and effects which are still scarcely explored and explained. Two examples treated here are coarse prior austenite grains in the hardened structure, and non-metallic inclusions.

### **HARD TO FIND: FEW SPOTS IN A BULK OF MATERIAL**

These features are sometimes found by chance during investigations with other aims, and only in very rare cases they show up as problems or failures. Safe and sound mass production in spite of their presence just shows that our current design and production, based on experience with the materials and processes commonly used, applies sufficient safety margins. On the other hand, an enhanced knowledge *about* and a smart management *of* these items can allow higher performance and higher reliability for

specifically selected components, and, on the other side, lower cost for others.

Both structures are hard to study.

– one, for the sophisticated and costly techniques to apply, then,

– two, because there are very few of them dispersed in a huge bulk of material, so that very large amounts of samples or material have to be scanned to find them, and

– last, but perhaps most important, because the laboratory in one company is not enough to do it. Rather, a cooperation is needed along the whole process and delivery chain, both in research projects and in series production. This means that beyond the materials laboratory and the heat treatment shop many other company functions are called to join in, and this makes it a management job rather than a mere technical one.

### **COARSE GRAIN TO BLAME FOR DISTORTION AND POOR STRENGTH**

Austenite grain size has a considerable effect on hardenability, and so inhomogeneous grain size can

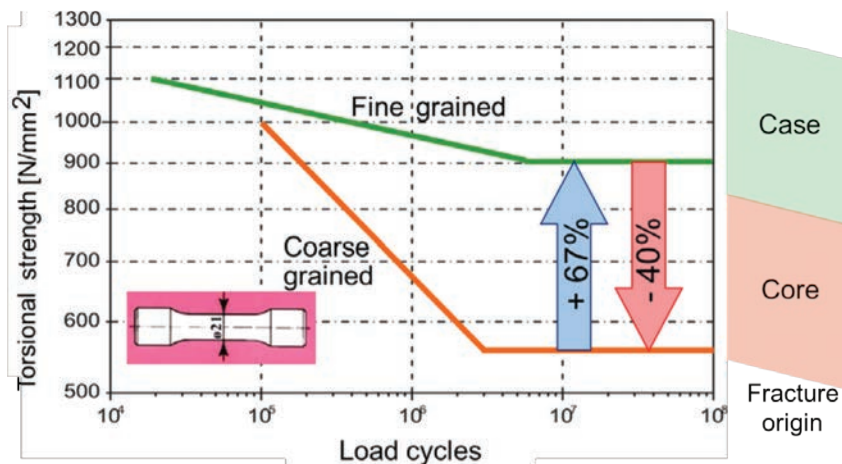


Fig. 1. Effect of grain size on torsion fatigue. Note that the fractures due to coarse grain originated not at the point of maximum stress on the surface but below in the core

Table 1. More (right) and less (left) critical components to have their strength or reliability compromised by coarse grain

Small parts		big parts
Strongly notched shape		smooth surface
High load, short life cycle		low load, high cycle
Linear bending	rotating bending, torsion	push/pull

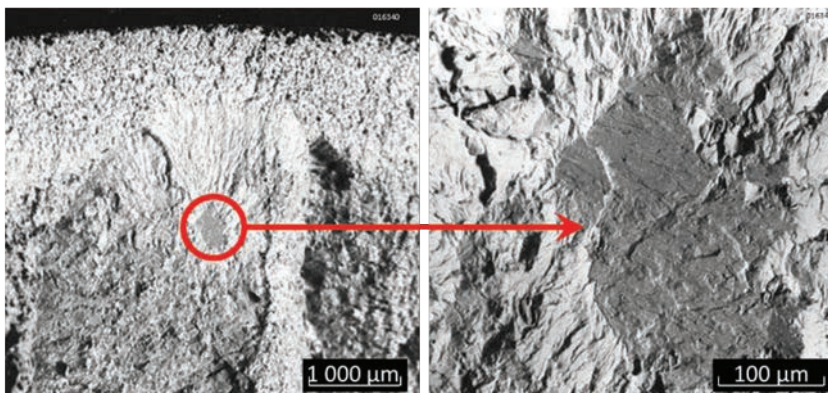


Fig. 2. Origin of a fatigue fracture from one large grain

cause inconsistent distortion. Distortion problems in the industrial practice are probably often grain size problems gone undetected because hard to identify.

Strength, especially fatigue strength, may be severely compromised by the presence of coarse grain (Fig. 1). Not all components, however, are equally critical: Much depends on the probability that a coarse grain is located in a highly loaded area (Table 1).

## INHOMOGENEOUS GRAIN STRUCTURE

Coarse prior austenite grains can be revealed in metallographic sections by etching with a picric acid

solution, to the Béchet-beaujard method from ISO 643. They form during prolonged exposure to the carburising temperature, but this is anything but a uniform process. Instead, the first grain larger than its neighbours tends to consume those, the more the bigger it becomes, and thus a large grain can persist for a long time in an environment of fine grains. Because this is a local effect, it can easily go undetected in one random sample. Instead, sampling must be aimed at components and regions which to experience are particularly prone to form them, and allow for a search in a considerable area.

Unfortunately, such an individual grain may be enough to start a failure (Fig. 2) – the chain breaks at the weakest link. For the same reason,

the grain size must be assessed not to average, but to the total size distribution, and special attention given to the coarse side of the size spectrum.

## FINE GRAIN STABILITY: A MEMORY ACQUIRED THROUGHOUT THE PROCESS CHAIN

Grain growth in the austenite structure during carburisation is impeded by fine precipitates on the grain boundaries. During the whole production chain prior to carburisation (commonly deformation and annealing steps), the microstructure undergoes processes like recrystallisation, dissolution, precipitation, and

coarsening of particles. The resulting composition, size, and distribution of precipitates with which the material comes to the final heat treatment constitute a kind of memory of all the prior production steps.

This memory is hard to account for.

It is obvious that the chemical composition of the steel must bring the elements required to form the precipitates, and this can be determined by chemical analysis. On the other hand, because of the very small size of the particles, their structural status is practically impossible to determine on a given part waiting to be case hardened. To challenge this „invisible memory“, each and every process between steel casting and carburising must be strictly defined, based on successful tests, and subsequently monitored in series production.

To identify procedures which rather stabilize grain stability, and those which rather put it as risk, many variants of deformation/annealing sequences have been tried out. Some findings are:

- Short heating to forging temperature can reconstitute fair grain stability to material previously found prone to grain growth.
- Dwelling at forging temperature for long (many minutes) does the opposite.
- Shapes with strongly varying degrees of deformation from section to section may undergo inhomogeneous recrystallisation, resulting in areas with coarse grain after carburising.
- Ferrite/pearlite annealing tends to decrease grain stability. If applied repeatedly, e.g. in combination with cold forming, it can result in coarse grain formation.
- In these cases, spheroidising without austenitisation is safer, although more costly.
- For the transition from austenitisation to the isothermal ferrite/pearlite transformation temperature, slow cooling is better than fast cooling.
- Quenching and tempering before carburising, however costly, can create very stable grain structures.

## INDISPENSABLE FOR HIGH-TEMPERATURE CARBURISING

Among the many projects currently undertaken to increase the carburising temperature in order to cut time and costs, apart from furnace enhancements much attention goes to various steel alloys which should provide sufficient grain stability at elevated temperature. To bring these efforts to completion and success, the grain stability, the „invisible memory“ acquired in the process chain must absolutely be accounted for, too.

## NON-METALLIC INCLUSIONS: ALWAYS PRESENT BUT RARELY DETECTED

Non-metallic inclusions, primarily oxides, can come in case-hardening steels in a size spectrum from sub-micron to many millimeters. While the very small ones are frequent but innocuous or even desired, those in multi-millimeter-size have a devastating effect on properties. However, luckily these are extremely rare since they are avoided by numerous metallurgical measures in the steel plant, and still, should they occur, they are normally detected by online ultrasonic inspection of the billets. But inclusions too small for this online inspection can still be very detrimental.

In recent years, ultrasonic inspection has been successfully applied to samples immersed in liquid, and thus been able to detect inclusions down to the mm order of magnitude. The volume of material so tested is about 50000 times more than what is normally tested by micrographs, and so the material can be characterised even with respect to these very rare, dispersed features (Fig. 3). Still, there remains a part of the size spectrum (question mark in Fig. 3) where potentially detrimental inclusions cannot be detected with the presently available techniques.

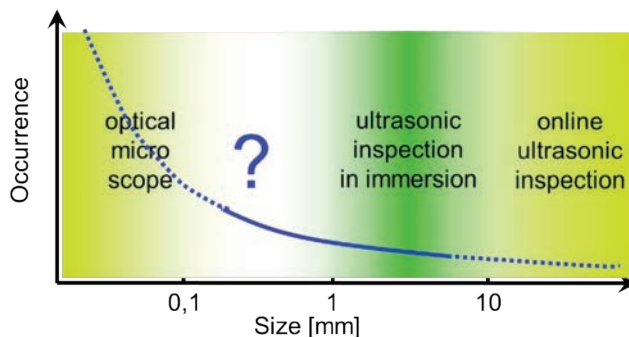


Fig. 3. Frequency of occurrence and detection techniques for non-metallic inclusions

## HIGH PURITY GREATLY ENHANCES PERFORMANCE OF CRITICAL COMPONENTS

Inspection of many samples with this method shows that the steel heats commonly used in series production can differ widely in purity (Fig. 4). Since both samples represent the common series production, an extensive test programme has been carried out to investigate the influence of these inclusions on the fatigue life of samples, again in rotating bending as was done above for the influence of coarse grain. The effect shown in Fig. 5 is too strong to be ignored.



Fig. 4. Ultrasonic scan of billets from two heats. The results are quantified (to Stahl-Eisen-Prüfblatt 1927) in terms of the sum of the total length of all inclusion indications per volume. The value of the upper sample is 0, the lower is 596 mm/dm<sup>3</sup>. Note that both heats are to specification, and are normal series quality

Again, not all components are equally sensitive to these inclusions, and what counts is again the probability that they are present in a highly loaded zone. So Table 1 is valid here, too. An addition to that table should be made here: surface hardened components

are more sensitive to these effects because right underneath the case, where the local strength decreases, the local stress can be high enough for an additional flaw in the material to cause a crack.

### SELECTED MATERIALS FOR SELECTED COMPONENTS

While the current series production copes with the whole (im-)purity spectrum represented in Fig. 4 and 5, it is most interesting to see whether there is a way to choose proven high-purity steel for selected critical components, without recurring to the expensive method of vacuum arc remelting. To further explore how the beginning of the cast strand suffers from a higher impurity level, samples for scans like those of Fig. 4 were taken all along the strand length of three heats.

The results in Fig. 6 show that there is indeed a way to select material to purity. However, we see also

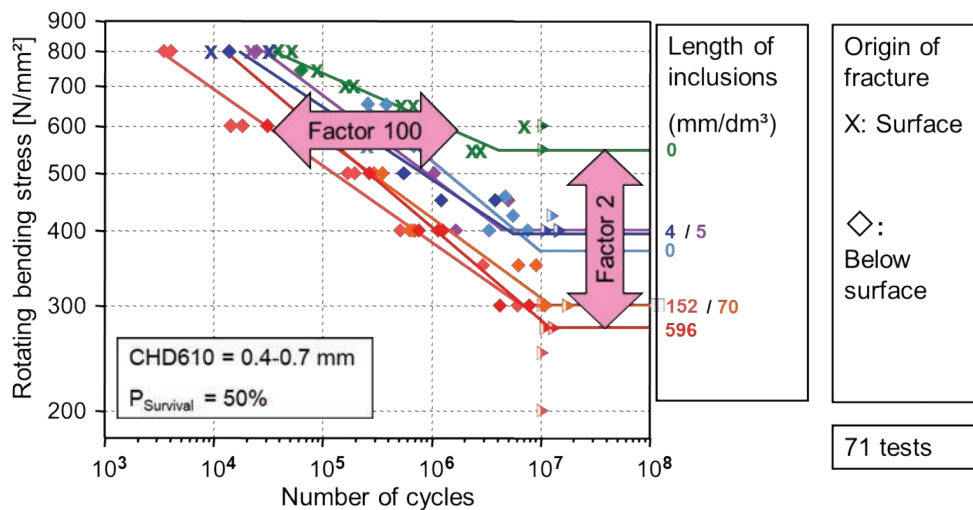


Fig. 5. Effect of inclusions detected by ultrasonic inspection in immersion on fatigue. The substantial difference between the two sample sets with 0 detectable inclusions show that also particles below the threshold of detectability can be detrimental

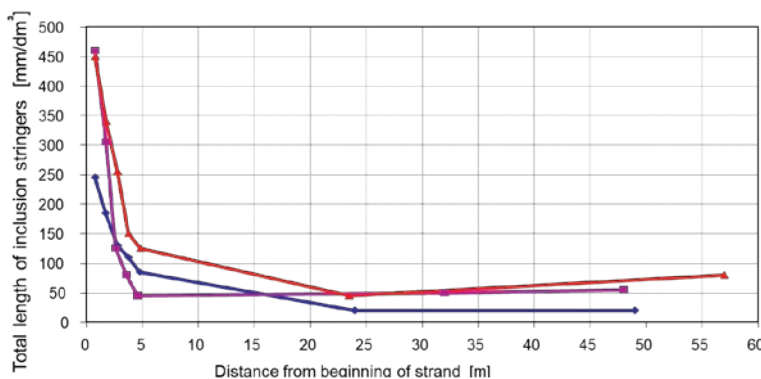


Fig. 6. Purity of cast strands vs. distance from beginning (three different heats)

that the commonly applied cropping of only a short part of the strand head, a metre or less, is insufficient to do away with all the material that falls in the category of „beginning of strand“.

The inclusions in this part of the strand must be regarded as unavoidable to the present state of the art in the steel mills. But these findings show a way how carefully selected material for carefully selected components can largely enhance performance, lifetime, and cut risk of failure.

# THERMOCHEMICAL SURFACE ENGINEERING OF STAINLESS STEELS WITH INTERSTITIALS: SYMBIOSIS OF SCIENCE, TECHNOLOGY AND INNOVATION



Marcel A.J. Somers, Thomas L. Christiansen

Technical University of Denmark, Department of Mechanical Engineering,

Lyngby, Denmark

somers@mek.dtu.dk, tch@mek.dtu.dk

Thermochemical surface engineering of stainless steels with carbon and nitrogen atoms was originally considered bad practice, because these elements would readily bind to chromium and thereby compromise the stainless character of the steel. The 80-ies and 90-ies of the previous century saw the introduction of low and high temperature routes for thermochemical surface engineering of stainless steels, without the formation of chromium carbides/nitrides. These routes are currently known as low temperature surface hardening (LTSH) and high temperature solution nitriding (HTSN), respectively. The present contribution addresses the scientific understanding, the technological feasibility and the innovative materials solutions related to dissolving interstitials in stainless steels. This is illustrated with examples from our own research group and combines experimental and numerical approaches.

**Keywords:** stainless steel; thermochemical; surface engineering; expanded austenite; nitriding; carburizing.

## INTRODUCTION

Surface hardening of stainless steel by gaseous processes has long been considered bad practice and was already in the late 1940s commercially known as Malcomizing. Good practice thermochemical surface engineering of austenitic stainless steels emerged in the mid-80ies as a surface engineering technology to mitigate wear and galling, while retaining, or even improving, the (pitting and crevice) corrosion performance of this class of metals. Carburizing in carbon-enriched liquid alkali baths (today known as Kolsterizing®) [1] and plasma-assisted nitriding [2] were among the first processes. As compared to conventional carburizing/nitriding processing occurs at relatively low temperature to prevent the nucleation of chromium-based carbides/nitrides during treatment (cf. Fig. 1) and the resulting loss of corrosion resistance. Scientifically, the microstructural features responsible for surface hardening of austenitic stainless steels were poorly understood. For many years, and sometimes even today, the surface-adjacent region affected by carbon/nitrogen was referred to as S-phase [3], suggesting that a new phase develops at the surface. Later, it became apparent that, essentially, the case developing during low temperature surface hardening (LTSH) consists of a supersaturated solid solution of interstitials in an f.c.c. parent lattice. The supersaturation is enabled by chromium's affini-

ty for C/N and the slow diffusion of substitutionally dissolved elements at the process temperature, which effectively retards carbide/nitride precipitation. Throughout the 90-ies, all published scientific studies on LTSH dealt with plasma-based treatment of stainless steels. The plasma treatment was considered essential for the removal of the passive layer from stainless steels. Unfortunately, the plasma-

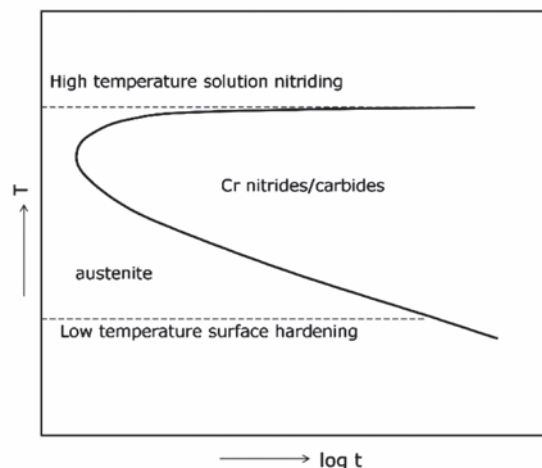


Fig. 1. Schematic TTT diagram showing high temperature solution nitriding (HTSN) is performed at a temperature where no nitrides/carbides are stable; low temperature surface hardening (LTSH) is performed at a temperature where it takes a long time before nitrides/carbides nucleate

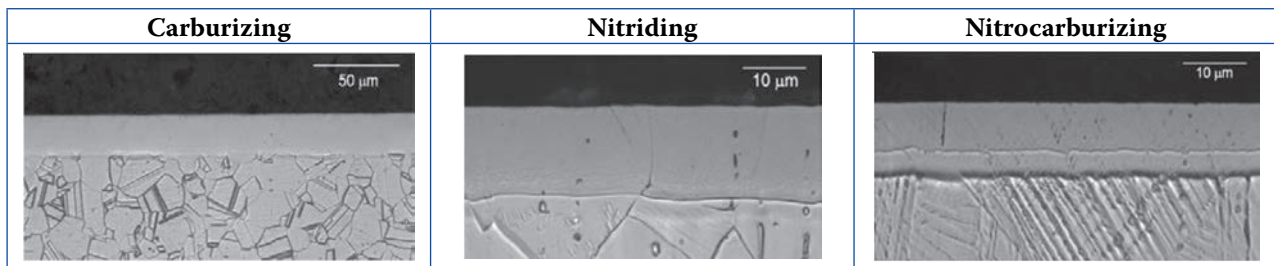


Fig. 2. Micrographs of cross sections of carburized, nitrided and nitrocarburized AISI 316 (304 for the nitrocarburized specimen). Conditions were as follows: carburizing in  $C_2H_2-H_2-N_2$  at 783 K for 3 h [12]; nitriding at 718 K for 22 h in 60%  $NH_3-40\% H_2$  [13]; nitrocarburizing at 693 K for 19h in 14%  $C_3H_8-54\% NH_3-22\% H_2-10\% Ar$  [12]

*Правильно?* assisted investigations only allowed the synthesis of graded systems with steep gradients in composition and associated residual stresses. This obscured an actual interpretation of the nature of the case. The 00-s saw the emergence of gas-based processes for carburizing [4], nitriding and nitrocarburizing [5], where the passive film was removed or transformed during a pre-treatment or, preferably, as an integrated part of the treatment. This enabled precise control of the temperature and composition of the C/N-providing medium, thus opening up for targeted surface engineering.

Another development is the surface engineering of austenitic, ferritic, martensitic and duplex stainless steels, which was initiated by Berns [6, 7] in the 90-ies and is currently known as high temperature solid solution nitriding (HTSN). Here, the treatment temperature is in a range where Cr-based nitrides and carbides are not stable (cf. Fig. 1) and an appreciable amount of nitrogen can be dissolved in austenite at high temperature, typically above 1050 °C. The HTSN treatment can be applied to austenitic, martensitic, ferritic and duplex stainless steels [7] and should be followed by fast cooling to prevent the development of chromium nitrides (cf. Fig. 1) that would compromise the corrosion performance.

The present contribution highlights some of the scientific, technological and innovative aspects of LTSH and HTSN, as obtained in our research group.

## LOW TEMPERATURE SURFACE HARDENING OF AUSTENITIC STAINLESS STEEL

The identity of the supersaturated solid solution of interstitials (nitrogen and carbon) in austenitic stainless steels has been under discussion for 35 years, since the first publications by Kolster [1] and Zhang and Bell [2]. It appears now widely accepted that this supersaturated solid solution is not a separate phase, but that the lattice of metal atoms

remains f.c.c., while nitrogen and carbon atoms are dissolved in the octahedrally coordinated interstices. As compared to the major alloying elements Fe and Ni, Cr has a stronger affinity to C and particularly N. Therefore, in the supersaturated solid solution short range ordering (SRO) occurs between Cr and N/C [8, 9]. For very high interstitial contents, as for N, long-range ordering (LRO) of the interstitials can occur in addition to the aforementioned SRO [10]. Recent research indicates that the LRO is commensurate with LRO in  $\gamma'-Fe_4N$ , albeit that combined SRO and LRO leads to over-stoichiometry as compared to the ratio  $M:N=4:1$  (where M represents all metallic elements in the f.c.c. lattice of the alloy, i.e. Fe,Cr,Ni,Mo), implying that the N content exceeds 20 at.%; this LRO has been dubbed  $\gamma'_N$  [12]. Typical examples of micrographs of expanded austenite cases stabilized by carbon, nitrogen or nitrogen and carbon are given in Fig. 2.

The micrographs show an almost featureless case, because the electrochemical properties of expanded austenite are improved as compared to the initial stainless steel. Grain boundaries from the steel are observed to continue in the case, consistent with the interpretation that no new phase develops. Orientation image maps (OIMs) as determined with electron back-scatter diffraction (EBSD) for a nitride sample indicate that the expanded austenite case is characterized by a rotation of the original lattice, which is evidence that plastic deformation has occurred under the dissolution of a high content of interstitial elements (Fig. 3) [14].

Such plastic deformation as a response to a mere change in composition, can be understood as follows. The dissolution of interstitials in an f.c.c. lattice leads to a lattice expansion. For low interstitial contents this lattice expansion can be accommodated by compressive elastic strains (residual stress) in the case. Along with the dissolution of interstitials, solid solution strengthening occurs leading to an increase of the yield strength. With increasing interstitial content the residual stresses can become so high that

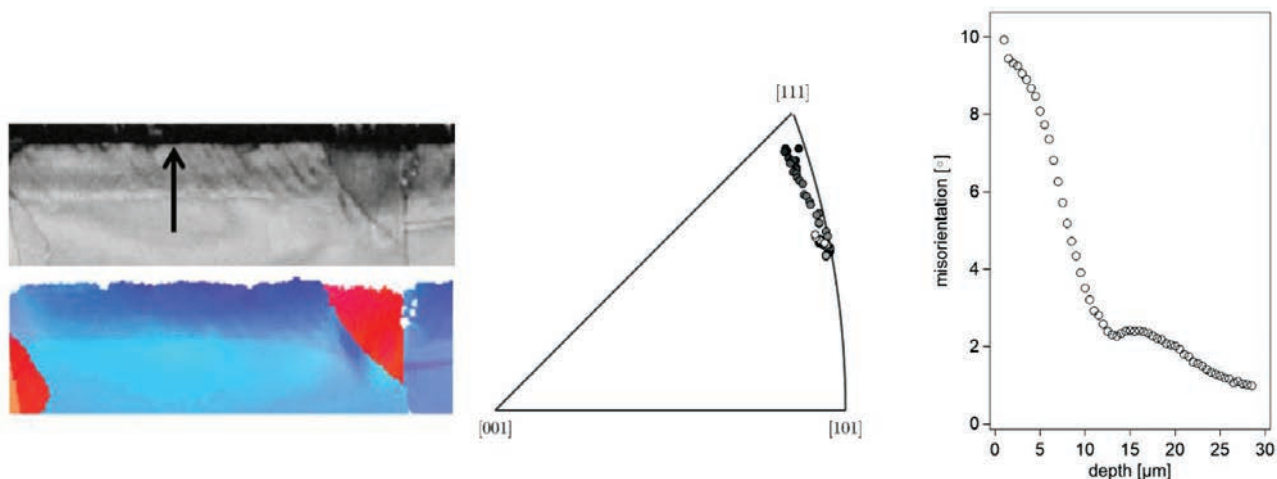


Fig. 3. Image quality maps (top left) and orientation image maps (bottom left) as obtained from EBSD investigation of AISI 316 nitrided at 713 K for 8 h in  $\text{NH}_3$ . The dots on the orientation triangle (middle) show the lattice rotation from substrate (white dots) to surface (black dots) along the arrow indicated in the top row; corresponding quantitative misorientation (right) [14]

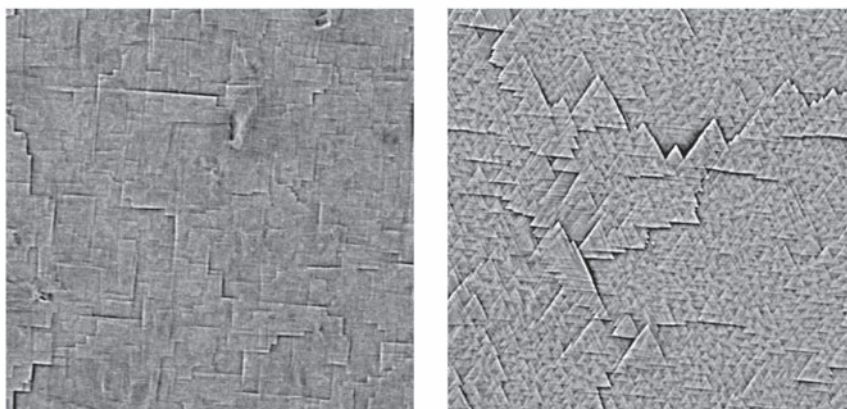


Fig. 4. Surface of single crystals of AISI 316L after nitriding at 693 K in a gas mixture of 80%  $\text{NH}_3$  and 20%  $\text{H}_2$ ; left  $\langle 001 \rangle$ , right  $\langle 111 \rangle$ . Quadratic (left) and triangular (right) patterns are the result of dislocation slip along  $\{111\}$  intersection with the surface. Note that no lattice rotation occurs for  $\langle 001 \rangle$  and  $\langle 111 \rangle$  [17]

they locally exceed the increase of the yield strength and, accordingly, plastic deformation occurs. Such plastic deformation has been observed in polycrystalline materials by the appearance of slip lines at the surface [15, 16] and is most clearly illustrated on the surface of initially polished single crystals of stainless steel 316 (Fig. 4) [17]. For a crystal with  $\langle 001 \rangle$  perpendicular to the surface quadratic patterns emerge, because four  $\{111\}$  slip planes intersect with the  $\{001\}$  surface; for a  $\langle 111 \rangle$  oriented single crystal (or grain) triangular patterns emerge, as three  $\{111\}$  slip planes intersect with the surface.

The residual stresses in expanded austenite have been determined with X-ray diffraction analysis. As a consequence of the occurrence of gradients in both stress and composition as well as strong elastic and plastic anisotropy, it is not a straightforward task

to accurately determine residual stresses. An overview of the various procedures to deal with these conditions was provided in [14] and references therein. Residual stresses in nitrogen stabilized expanded austenite ( $g_N$ ) on AISI 316 are maximally (in compression)  $-5$  GPa, while for carburized AISI 316 about  $-2.7$  GPa [18] was determined. These huge elastic stresses are far beyond the yield stress of stainless steel and indicate that considerable strengthening has been achieved by dissolving interstitials.

Numerical simulation of the development of composition and

stress profiles during nitriding (or carburizing) requires consideration of concentration-dependent diffusion of nitrogen in the f.c.c. lattice and the incorporation of elasto-plastic accommodation, including strengthening, of the volume expansion. A numerical model, incorporating thermal, chemical and mechanical coupling was developed [19, 20], which allows the prediction of nitrogen concentration as well as elasto-plastic and thermal strain distributions from thermodynamic, crystallographic, diffusion and thermal expansion (and magnetic properties) data for expanded austenite. By means of example the composition, residual stress and elastic, plastic and thermal strains calculated for 3 different nitriding times in pure  $\text{NH}_3$  are shown in Fig. 5 [14].

Comparison of the plastic strains in Fig. 5 (red lines) with the misorientation profile by plastic de-

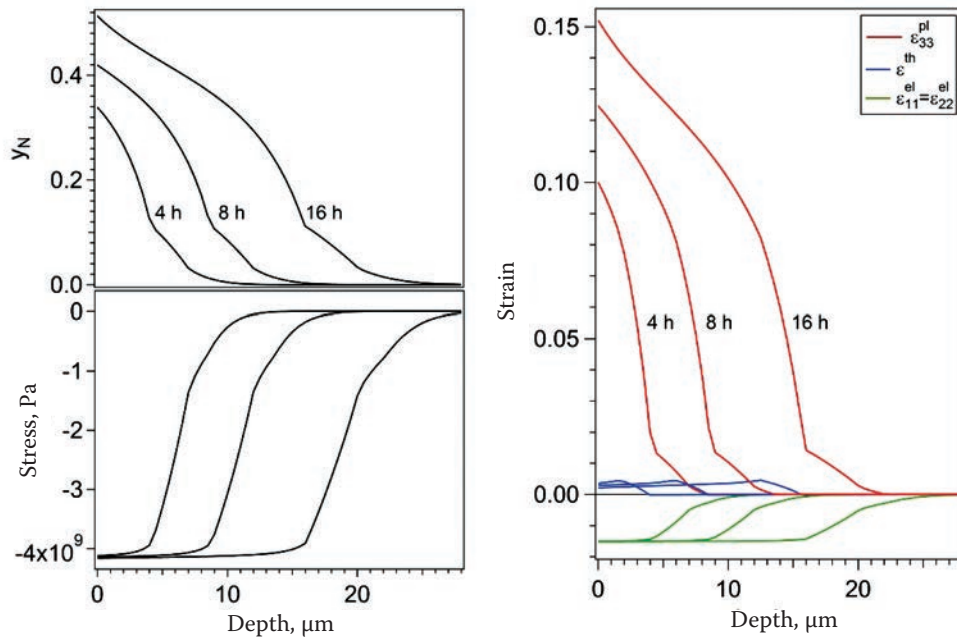


Fig. 5. Calculated evolutions of nitrogen content (expressed as the number of N atoms per 100 metal atoms,  $\gamma_N$ ), residual stress as well as elastic, plastic and thermal strains in AISI 316 for 3 different nitriding times at 713 K in pure  $\text{NH}_3$  [14]

formation in Fig. 3, shows an encouraging qualitative agreement between the experimental and predicted profiles. It was demonstrated recently that there is a quantitative discrepancy between the predicted and experimental evolutions of the composition (and associated strain) profiles, which can be attributed to the role of the surface reaction (ammonia dissociation) in controlling the nitrogen transfer from the gas to the solid state [20]. In this sense, the developed multi-physics numerical model can be used to further explore the role of the surface reaction and optimize the gaseous treatment such that shorter treatment times can be realized under practical conditions.

The model can also be applied to plasma nitriding [20] and gaseous carburizing [21]. An example of the latter is shown in Fig. 6. Here, X-ray diffraction was used to determine both the carbon content in solid solution and the associated residual stress. The carbon concentration profile was fitted with a diffusion model, as accurate diffusion coefficients for carbon in expanded austenite are unavailable. From the carbon concentration profile, which essentially is the strain-free volume expansion of the austenite lattice, the residual stresses were calculated assuming elasto-plastic accommodation of the expansion. To this end, elastic (Young's modulus) and plastic (yield strength and work hardening coefficient) properties were assessed from nano-indentation. An excellent quantitative correspondence was obtained between thus calculated and measured residual stresses [21].

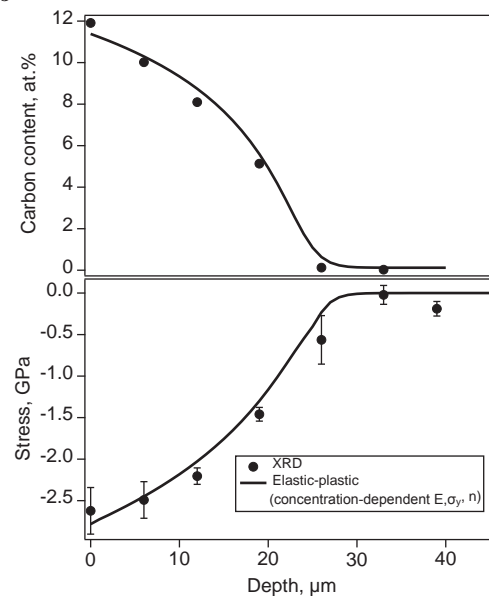


Fig. 6. Carbon content and residual stress determined with X-ray diffraction on expanded austenite in AISI 316L carburized for 30 h at 743 K in a  $\text{CO-H}_2$  gas mixture [21]

## HIGH TEMPERATURE SOLUTION NITRIDING OF STAINLESS STEEL

In contrast to LTSN in a gaseous environment, where it was necessary to activate the surface by stripping the passive layer prior to treatment, dissolving nitrogen during HTSN is straightforward as Cr-oxide evaporates as  $\text{CrO}_3$  in this temperature regime [22]. Moreover,  $\text{N}_2$  gas dissociates at the stainless steel surface, hence nitrogen can directly be dissolved. The

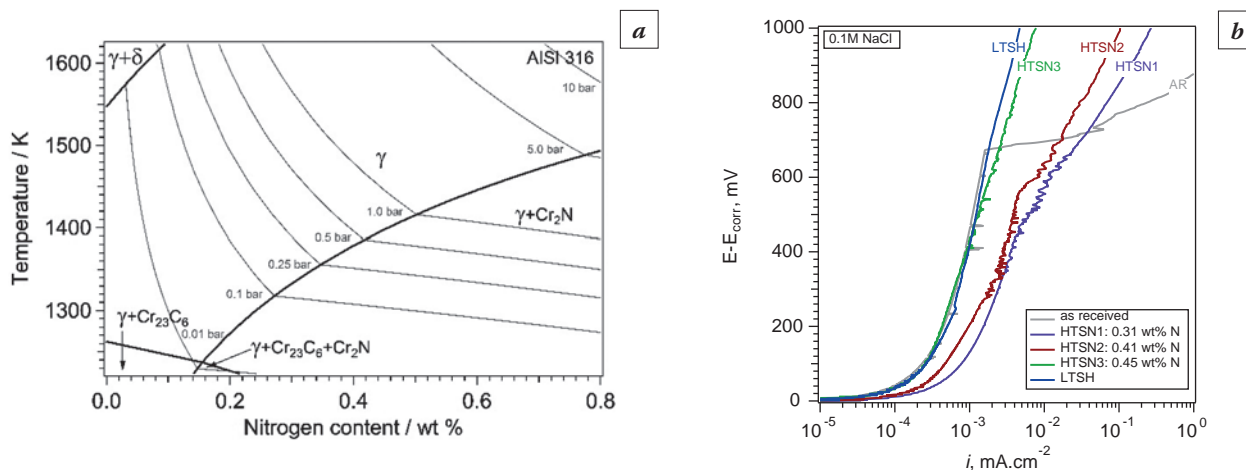


Fig. 7. *a.* (left) Isopleth (black lines) of AISI 316 in the high temperature range for increasing nitrogen content; isobars (grey lines) of  $\text{N}_2$  pressure are superimposed [23]; *b.* (right) polarization diagrams with respect to the corrosion potential ( $E_{\text{corr}}$ ) for AISI 316 in as-received, HTSN (for 3  $\text{N}_2$  pressures) and LTSH condition [25]

equilibrium nitrogen content that can be dissolved is determined by the alloy composition, the applied temperature and the (total or partial)  $\text{N}_2$  pressure in the gas [7]. An example of the relation between temperature and gas pressure is shown in the isopleth for AISI 316 in Fig. 7a [23]. HTSN at 1400 K in 0.25 bar  $\text{N}_2$  yields an equilibrium solubility of 0.30 wt% N. The case depth that is achieved can be several hundreds of microns deep. This allows the development of a thick austenite case on stainless steels, or for components made from sheet, an enhanced nitrogen content throughout the thickness. As a matter of fact HTSN is an attractive alternative means to synthesize high-nitrogen steels. The motivation for applying an HTSN treatment could be the enhanced corrosion resistance that is achieved, because N has an important influence on the PREN or MARC number of stainless steels [24]. Fig. 7b illustrates that in particular the pitting potential is importantly improved after HTSN of AISI 316 for different  $\text{N}_2$  pressures, giving the N contents provided in the legend to Fig. 7b.

Another motivation for HTSN is an increase of the hardness and yield strength. An example of the change of the mechanical properties is given in Fig. 8 [23]. The combination of alloy composition, nitrogen content and degree of deformation can establish a wide range of hardness values (Fig. 8a). Clearly, the yield strength and the work hardening coefficient of AISI 316 and AISI 304L are drastically changed, while ductility is maintained (Fig. 8b).

An important effect of nitrogen on austenite is a modification of the stacking fault energy (SFE). Although the exact relation between N content and SFE is not accurately known, the considerable stabilization of austenite against strain-induced martensite formation upon deformation widens the application potential of these alloys. This is the main reason for the difference in the tensile curves for AISI 316/ 304L on the one hand side and EN 1.4369 on the other (Fig. 8b). The former two alloys develop strain-induced martensite upon tensile straining, while the latter already contains 0.23 wt% N

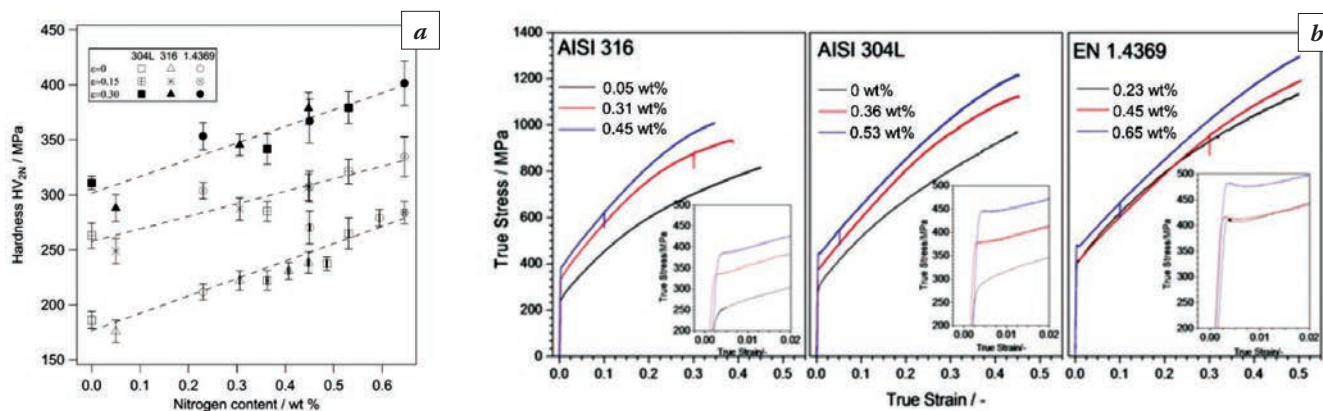


Fig. 8. *a.* (left) hardness at 2N load measured in AISI 316/304L and EN 1.4369 for different combinations of nitrogen content obtained by HTSN and tensile straining (see legend); *b.* (right) tensile testing curves for as received (black lines) and HTSN treated (red and blue lines) AISI 316/304L and EN 1.4369 [23]

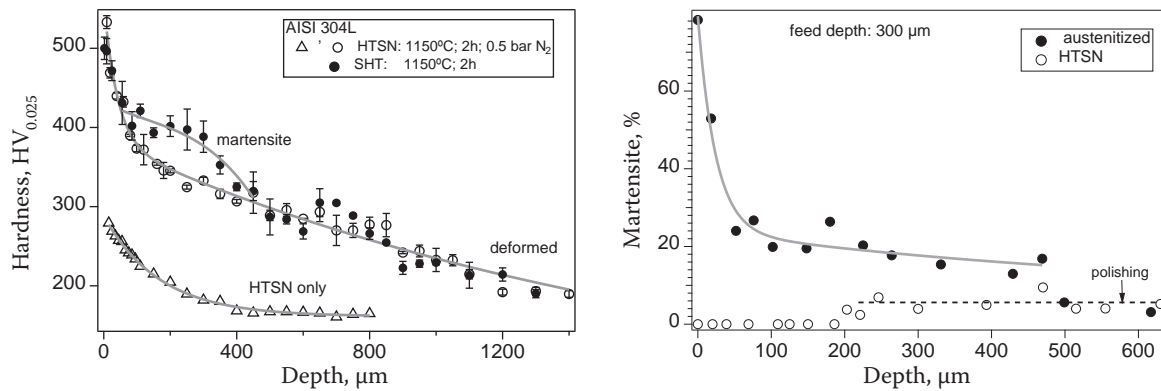


Fig. 9. Hardness (load 25g), measured in cross section, and martensite content (determined with XRD and successive layer removal) as a function of depth for solution heat treated (SHT), i.e. austenitized, and HTSN treated AISI 304L after surface roller burnishing. The martensite in the roller burnished HTSN treated sample is a result of mechanical polishing necessary to enable XRD as a function of depth [27]

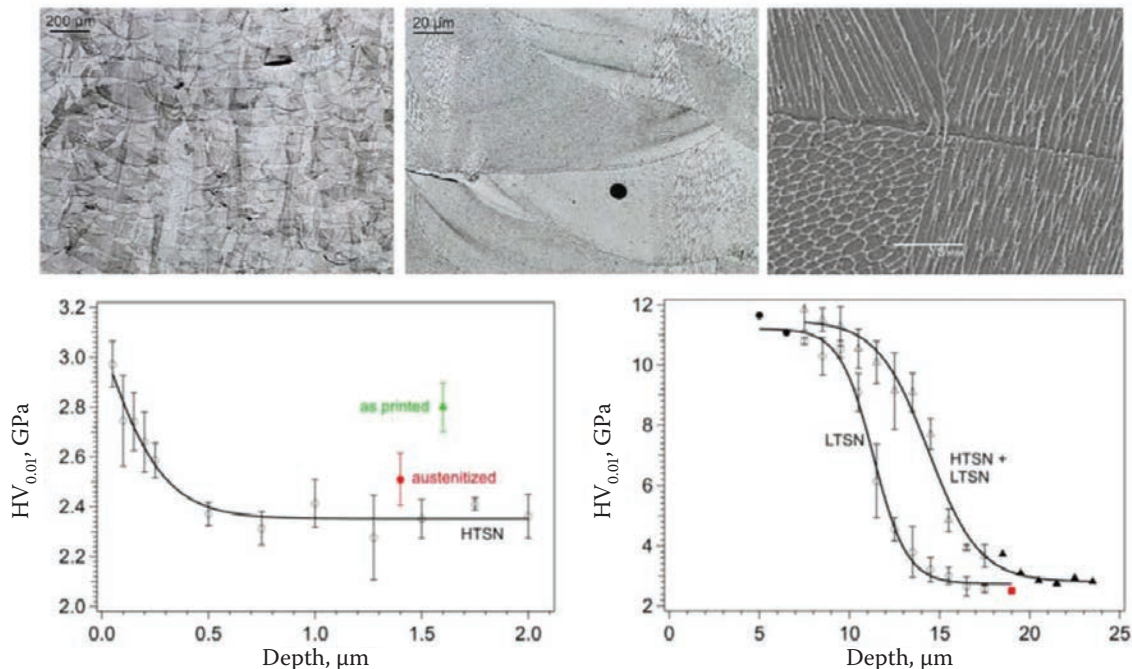


Fig. 10. Hierarchical microstructure (top row) of selective laser melted AISI 316L, showing, from left to right, elongated grains, weld lines and cell structure. The cell structure is dissolved upon austenitizing, leading to a hardness decrease, which for HTSN is counteracted in the surface region. Low temperature surface nitriding (LTSN), provides a hardened case, with a surface hardness (load 10g) of 11 GPa [29]

and is stable in the as-received state. Thus, HTSN of EN 1.4369 does not change the tensile behavior as pronouncedly as for AISI 304L/316. The enhanced stability of austenite and the prevention of strain-induced martensite on plastic deformation opens up for innovative forming applications. Strain-induced martensite negatively influences the corrosion performance of stainless steel and is particularly harmful during LTSH, where it promotes CrN precipitation. Stabilizing austenite by a prior HTSN treatment, allows deformation by plastic forming (bending or embossing) or shot peening to promote high strength (cf. Fig 8b) or compressive residual stresses to improve fatigue performance, while re-

taining the corrosion performance. An example of extreme deformation by surface roller burnishing is given in Fig. 9 [27].

In the surface near region, the material is nanocrystalline, while at larger depth twinning and/or martensite (both  $\alpha'$  and  $\epsilon$ ) formation occurs depending on the nitrogen content and corresponding SFE [27].

HTSN can also be a very effective treatment prior to deformation and subsequent LTSH by nitriding, carburizing or nitrocarburizing [27]. Here, the HTSN case has several advantages:

- it provides enhanced load-bearing capacity for the expanded austenite zone (cf. Fig. 8 or, after deformation, Fig. 9);

– it provides a gradual change in the electrochemical properties (cf. Fig. 7b) and consequently, excellent, corrosion performance;

– it avoids formation of strain-induced martensite and associated CrN development on LTSH, which was demonstrated to yield excellent uniformity of LTSH independent of the degree of deformation [23].

Finally, the rapid evolution of additive manufacturing, in particular 3D printing of stainless steels, requires targeted heat and surface treatment to mitigate the unconventional and hierarchical microstructure (Fig. 10), which has poor corrosion resistance. Here, the combination of HTSN and LTSH has been demonstrated to provide excellent improvement of wear performance and restoration of the corrosion performance [29].

As is clear from the examples given in this article, the LTSH and HTSN treatments are currently applied to the most widely applied austenitic stainless steels. Certainly, process variants for other types of stainless steels are also available. What all stainless steels have in common is that they were never intended to be surface treated by LTSH or HTSN, but they derive their application from a combination of corrosion performance, deformability, strength, and for the case of martensitic qualities, wear resistance. In the last 30 years the metallurgical understanding of the interplay between LTSH/ HTSN and the stainless steel microstructure has reached a level that allows the design of stainless alloy compositions that are targeted to exploit the many beneficial aspects of these treatments [30]. These alloys could be considered pendants to special carburizing and nitriding steels. In particular, the enormous scientific attention that high-entropy alloys currently receive, may contribute to inspire in which direction these stainless nitriding and carburizing steels should be developed.

## CONCLUSION

Thermochemical surface engineering of stainless steels with interstitials has evolved into high temperature and low temperature variants. The various processing technologies allow dissolution of controlled quantities of carbon and nitrogen into stainless steels. The scientific understanding has reached maturity and shows that in particular the nitrided case formed at low temperatures is extremely complex. Thus formed expanded austenite contains (steep) gradients in composition, residual stress, texture, and degrees of deformation and magnetization. The complexity is reflected in a thermochemi-

cal/mechanical multi-physics numerical model that enables simulation of composition and stress profiles from the treatment parameters temperature, time and gas composition, and takes all the elasto-plastic straining into account. Interstitials in stainless steels have a large influence on the mechanical properties (hardness and yield strength) and improve the localized corrosion performance. Combinations of high and low temperature treatments, including (intermediate) plastic deformation enable innovative materials solutions, where strength, load bearing capacity, wear performance and corrosion performance are improved. The metallurgical understanding of the processing is ready for the post-treatment of innovative AM (3D print) components and the development of stainless carburizing and nitriding steels.

## ACKNOWLEDGEMENT

Over the years several PhDs and Postdocs and numerous MSc students have contributed importantly to various aspects of the work presented. We are grateful to Thomas S. Hummelshøj, Jette Oddershede, Bastian K. Brink, Federico Bottoli, Frederico A.P. Fernandes, Freja N. Jespersen, Ömer C. Kücüküydiz, Yawei Peng, Emilie H. Valente and Bo Wang for their valuable research contributions. Also, the collaborations with our (former) colleagues Kenny Ståhl, Grethe Winther, Hossein Alimadadi, Jesper H. Hattel, Kristian V. Dahl, Morten S. Jellesen, Steffen S. Munch and Flemming B. Grumsen are highly appreciated.

## REFERENCES

1. **Kolster B.H.** Verschleiß- und korrosionsfeste Schichten auf austenitischen Stählen. VDI-Berichte. 1983; 503: 107–113.
2. **Zhang Z.L., Bell T.** Structure and corrosion resistance of plasma-nitrided stainless steel // Surf Eng. 1985; 1: 131–136.
3. **Dong H.** S-phase surface engineering of Fe–Cr, Co–Cr and Ni–Cr alloys // Int Mater Rev. 2010; 55: 65–98.
4. **Collins S., Williams P.** // Adv Mater Proc. 2006; 164: 32–33.
5. **Christiansen T., Somers M.A.J.** Low temperature gaseous nitriding and carburizing of stainless steel // Surf Eng. 2005; 21: 445–455.
6. **Berns H.** Patents DE 403 3706 A1 1990 and DE 433 3917 A1, 1994.
7. **Berns H.** Stainless steels suited for solution nitriding // Mat-wiss u Werkstofftech. 2002; 33: 5–11.

8. **Oddershede J., Christiansen T.L., Ståhl K., Somers M.A.J.** Extended X-ray absorption fine structure investigation of nitrogen stabilized expanded austenite // *Scripta Mater.* 2010; 62: 290–293.
9. **Oddershede J., Christiansen T.L., Ståhl K., Somers M.A.J.** Extended X-Ray Absorption Fine Structure Investigation of Carbon Stabilized Expanded Austenite and Carbides in Stainless Steel AISI 316 // *Steel Res Int.* 2011; 82: 1248–1254.
10. **Brink B., Christiansen T.L., Hansen M.F., Frandsen C., Somers M.A.J.** Composition-dependent variation of magnetic properties and interstitial ordering in homogeneous expanded austenite // *Acta Mater.* 2016; 106: 32–38.
11. **Che H.L., Tong S., Wang K.S., Lei M.K., Somers M.A.J.** Co-existence of  $g'_N$  phase and  $g_N$  phases on nitrided austenitic Fe-Cr-Ni alloys- I. Experiment // *Acta Mater.* submitted.
12. **Christiansen T., Hummelshøj T.S., Somers M.A.J.** Gaseous Carburising of self-passivating Fe-Cr-Ni alloys in acetylene-hydrogen mixtures // *Surf Eng.* 2011; 27: 602–608.
13. **Christiansen T., Somers M.A.J.** Controlled dissolution of colossal quantities of nitrogen in stainless steel // *Metall Mater Trans A.* 2006; 37: 675–682.
14. **Somers M.A.J., Kücükyildiz O.C., Ormstrup C., Alimadadi H., Christiansen T.L., Winther G.** Residual stress in expanded austenite on stainless steel; origin, measurement and prediction// *Mater Perf Char.* 2018; 7: 693–716.
15. **Fewell M.P., Mitchell D.R.G., Priest J.M., Short K.T., Collins G.A.** The nature of expanded austenite // *Surf Coatings Techn.* 2000;131: 300–306.
16. **Templier C., Stinville J.C., Villechaise P., Renault P.O., Abrasonis G., Rivière J.P., Martinavičius A., Drouet M.** On lattice plane rotation and crystallographic structure of the expanded austenite in plasma nitrided AISI 316L steel // *Scripta Mater.* 2010; 63: 496–499.
17. **Kücükyildiz O.C., Grumsen F.B., Christiansen T.L., Winther G., Somers M.A.J.** Low temperature gaseous nitriding of single crystals of stainless steel; the role of elastic and plastic anisotropy-I. Experimental. in preparation.
18. **Christiansen T.L., Somers M.A.J.** Stress and composition of carbon stabilized expanded austenite on stainless steel // *Metall Mater Trans A.* 2009; 40: 1791–1798.
19. **Jespersen F.N., Hattel J.H., Somers M.A.J.** Modelling the evolution of composition- and stress-depth profiles in austenitic stainless steels during low-temperature nitriding // *Mod Sim Mater Sci Eng* 2016; 25: 025003 (31 pages).
20. **Kücükyildiz O.C., Sonne M.R., Thorborg J., Somers M.A.J., Hattel J.H.** Thermo-chemical mechanical simulation of low temperature gas and plasma nitriding of austenitic stainless steel; inverse modelling of surface reaction rates // *Mod Sim Mater Sci Eng.* submitted.
21. **Peng Y., Liu Z., Jiang Y., Wang B., Gong J.M., Somers M.A.J.** Experimental and numerical analysis of residual stress in carbon-stabilized expanded austenite // *Scripta Mater.* 2018; 157: 106–109.
22. **Caplan D., Cohen M.** The volatilization of chromium oxide // *J Electrochem Soc.* 1961; 108: 438–442.
23. **Bottoli F., Winther G., Christiansen T.L., Dahl K.V., Somers M.A.J.** Low-temperature nitriding of deformed austenitic stainless steels with various nitrogen contents obtained by prior high-temperature nitriding // *Metall Mater Trans A.* 2016; 47: 4146–4159.
24. **Speidel M.O.** Nitrogen containing austenitic stainless steels // *Mat-wiss u Werkstofftech.* 2006; 37: 875–880.
25. **Bottoli F., Jellesen M.S., Christiansen T.L., Winther G., Somers M.A.J.** High temperature solution-nitriding and low-temperature nitriding of AISI 316: Effect on pitting potential and crevice corrosion performance // *Appl Surf Sci.* 2018; 431: 24–31.
26. **Bottoli F., Winther G., Christiansen T.L., Somers M.A.J.** Influence of plastic deformation on low-temperature surface hardening of austenitic stainless steel by gaseous nitriding // *Metall Mater Trans A.* 2016; 46: 2579–2590.
27. **Wang B., Hong C.S., Christiansen T.L., Somers M.A.J.** (in preparation).
28. **Christiansen T.L., Hummelshøj T.S., Somers M.A.J.** Patents WO 2012 146254-A1 and WO. 2013 159781-A1.
29. **Valente E.H., Christiansen T.L., Somers M.A.J.** High-temperature solution nitriding and low-temperature surface nitriding of 3D printed austenitic stainless steel. *Proc. European Conference on Heat Treatment (ECHT) Nitriding and Nitrocarburizing.* 2018: 71–80.
30. **Christiansen T.L., Dahl K.V., Somers M.A.J.** New Stainless Steel Alloys for Low Temperature Surface Hardening // *Berg- und Hüttenmännische Monatshefte.* 2015; 160: 406–412.

## THE ELECTRON BEAM CAN DO MORE THAN SURFACE HARDENING



Rolf Zenker<sup>1,2</sup>, Anja Buchwalder<sup>1</sup>

<sup>1</sup> TU Bergakademie Freiberg, Institute of Materials Engineering, Germany

<sup>2</sup> Zenker Consult, Mittweida, Germany

**Keywords:** electron beam; surface treatment; joining; ablating; additive manufacturing.

High energy electron beam (power density up to  $10^6$  W/cm<sup>2</sup>) is advantageously useable for thermal processes like surface treatment, ablating, joining or additive manufacturing of metallic materials (Fig. 1) [1]. In particular, EB welding and EB hardening are well industrial established. But due to the permanently new and more complex demands in applications there exist great challenges regarding new materials and increased load behavior. Furthermore, new solutions for flexible and/or geometry adapted beam deflection techniques, enhanced process control, and raised productivity are urgently required.

For other technologies such as liquid phase surface treatments, combined surface treatments, brazing or profiling, a broad basic knowledge is available and will be extended by further investigations. Currently the transfer of know-how from research to industrial applications is being promoted.

In case of additive manufacturing a rapid development is to be observed. First successful applications are

known, especially in the field of aerospace. For other industrial branches different scientific development programs started up.

The present contribution is a summary of the work of the authors of more than 20 years, demonstrating the state of the art in R&D for selected EB technologies and gives examples for different applications, especially for actual new solutions.

The **EB surface treatments** can be performed as solid phase process or liquid phase process with or without additive (see Fig. 1). The main aim of all these surface technologies is the improvement of the local load behavior of functional surfaces by means of the increase of hardness, wear and/or corrosion resistance [1].

Modern **EB surface hardening (EBH)** technologies are carried out using temperature-controlled power control systems. This technique guarantees a constant surface temperature around the running surface of the cam by adaption of the beam current

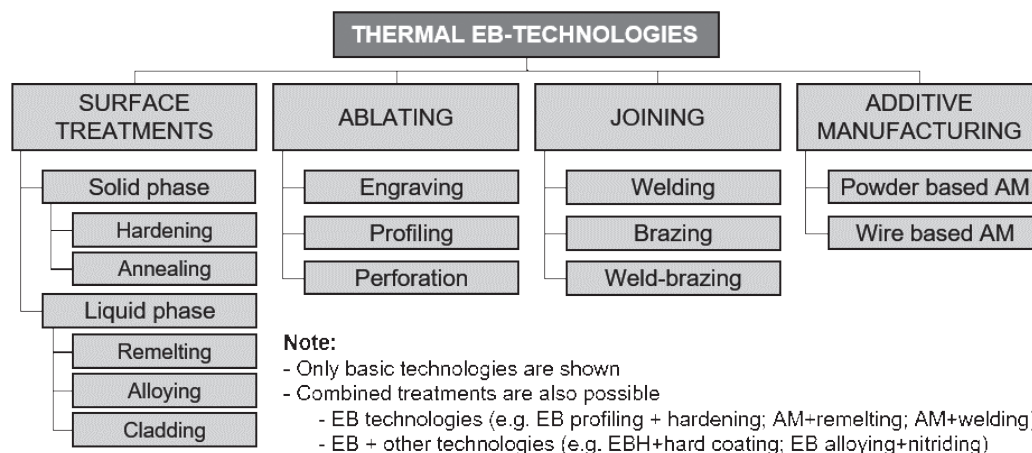


Fig. 1. Thermal EB technologies (overview)

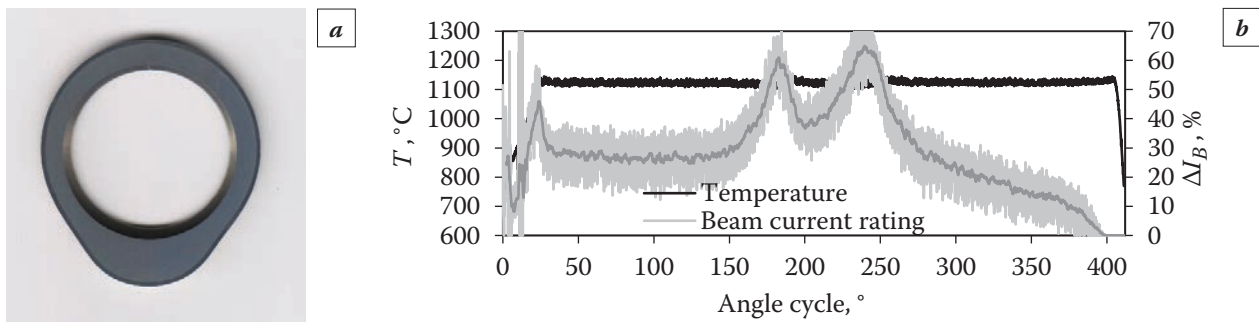


Fig. 2. EBH of (a) cam with (b) geometry adapted temperature/beam current cycles [2]

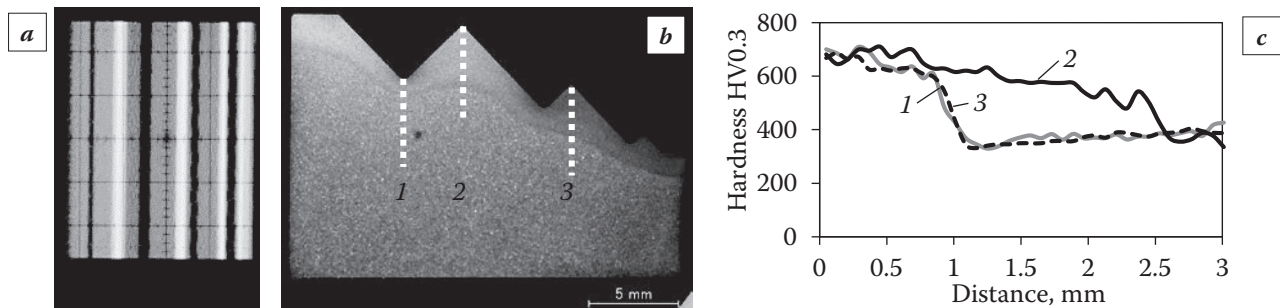


Fig. 3. EBH of tooth contour with flash technique using (a) divided energy transfer field for generating (b) homogeneous EBH layer (cross section) and (c) hardness-depth profiles

(Fig. 2b). As a result, a constant hardening depth is achieved (Fig. 2a).

A further strong challenge is the surface hardening of tooth profiles (Fig. 3b). In this case the EBH is carried out by flash technique. Because of the tooth geometry, e.g. different angle of incidence and difficult energy transport conditions in the surface near area, the local energy transfer is very complex. The energy transfer field must exactly programmed (Fig. 3a). Considering all these aspects, the desired EBH profile is realized (Fig. 3a) and the hardness depth profiles fulfill the demands, in both the teeth tip and space (Fig. 3c).

Furthermore, the EB surface treatments are used in **combination** with **thermochemical treatment** or **hard coating** for optimizing the local load behavior. In case of these combined or duplex treatments, EB surface hardening or remelting provide the basis for both the subsequent treatability or/and a supporting effect for the hard thermochemical layers or hard coatings [3], [4].

The industrial application of **surface remelting** and **surface alloying** has reached different levels. The EB surface remelting of camshafts for power fueled engines is in industrial use since 1990s. The local surface alloying of valve seats in cylinder heads was developed in 2005 (see [1], [8], [14]).

**EB ablating** processes are divided into engraving, ablating or profiling (Fig. 1)[5]. These exposing technologies are used for inserts in cast components

or for generation of small dimples for improved lubrication in bearings.

EB profiling (EBP) generates lateral pattern indentations for improving the mechanical interlocking of sprayed layers with the base material. This is depending on the substrate surface among many other factors. This process is used to improve the load-bearing capacity of layer-matrix-compounds [6], [7]. For example due to the flash/multi-spot technique 3600 defined indentations are simultaneously generated within a process time of 0.15 s [1], [8], [13]. The indentations can programmed as point patterns (Fig. 4a) [1], [8], [13], but also as line patterns with variable design (Fig. 4b–d) [1], [3], [5], [9]. During high-energy EB interaction some material is vaporized (indentions) and partially liquidized (bulges) (Fig. 5a). The latter was processed mechanically before depositing thermal sprayed layer (Fig. 5b).

As a result of the EBH with combined patterns (Fig. 4d) a 320% higher shear strength was achieved because of the good mechanical interlocking in the profile indentations and the positive influence of the edgewise bulges against shear forces. Both adhesive and cohesive forces came into effect [5], [9].

Typical **EB joining** technologies are welding (EBW), brazing (EBS) or weld-brazing (Fig. 1). EBW is industrial used in a wide scale and is characterized by its narrow weld seams with extremely high depths. Mostly the welding process is carried out without filler material. Furthermore, the process specific fea-

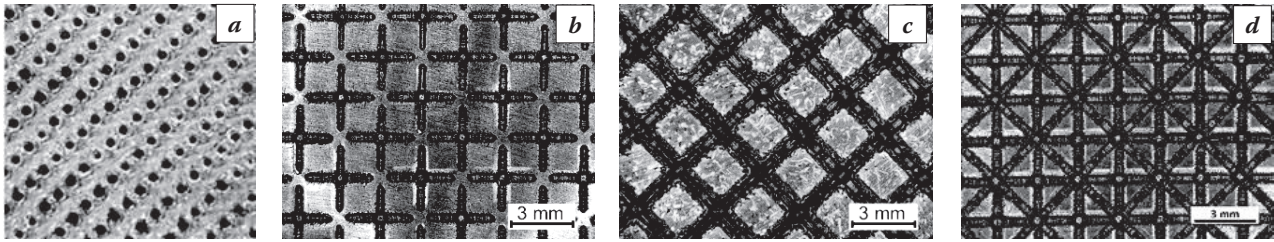


Fig. 4. EB patterns with (a) point-shaped, (b) “plus”-shaped, (c) cross-shaped oscillation figures, and (d) the combination of both patterns [9]

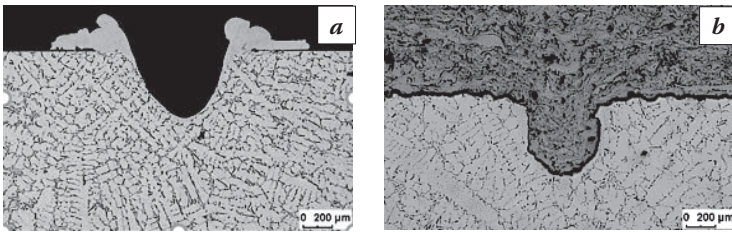


Fig. 5. Profiled surface before (a) and (b) after thermal spraying [5], [9]

tures, regarding high energy density and various possibilities of high speed beam deflection techniques are beneficial characteristics, useable for joining of challenging materials like cast iron [10] or particle-reinforced TRIP/TWIP cast steels [11].

For **welding** of dissimilar materials, such as cast iron (A) and low alloyed steel (B) (Fig. 6a), the conventional welding techniques or the on-spot EB

welding are not suitable due to the massive crack formation. Therefore, special 3-spot EB technique was developed (Fig. 6a). Each spot fulfill specific task: first spot (I in Fig. 6a): local pre-heating of the material, second spot II in Fig. 6a): welding, and third spot (III in Fig. 6a): post heating and smoothing. Due to this function sharing, the excessive hardening increase in both the welding seam (WS) and the heat affected zone caused (HAZ) (cf. 1-spot and 3-spot in Fig. 6c) by the high C content of the cast iron was prevented.

**EB additive manufacturing** can be carried out as powder bed or as wire-based technology (see Fig. 1). By powder bed technology very complex structures of components (e.g. internal cooling channels) can be generated but because of the small powder particle

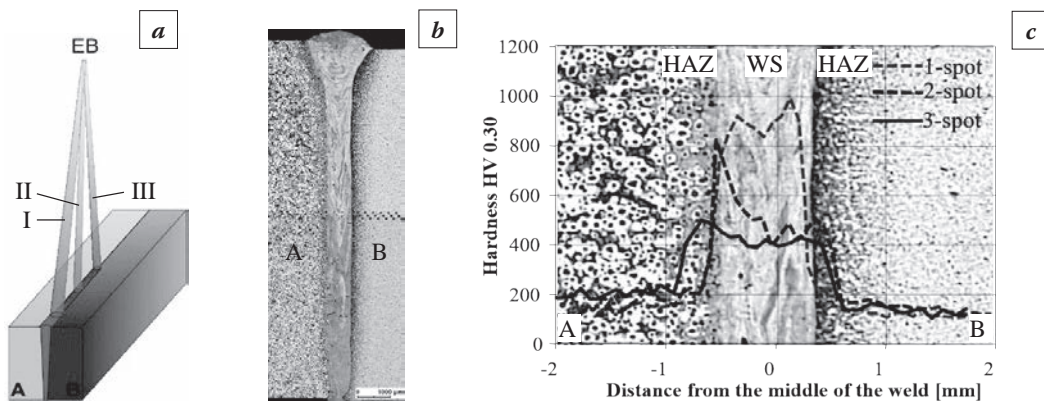


Fig. 6. Dissimilar EB welding with (a) 3-spot technique, (b) weld seam and (c) hardness profiles across de weld seam [7], [8]

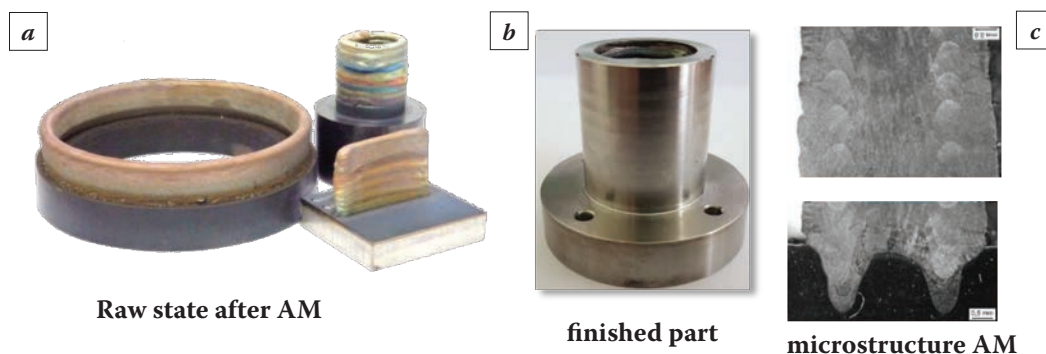


Fig. 7. Wire-based additive manufacturing (a), different bodies after deposition (b), component past to machining and microstructure (c) [13]

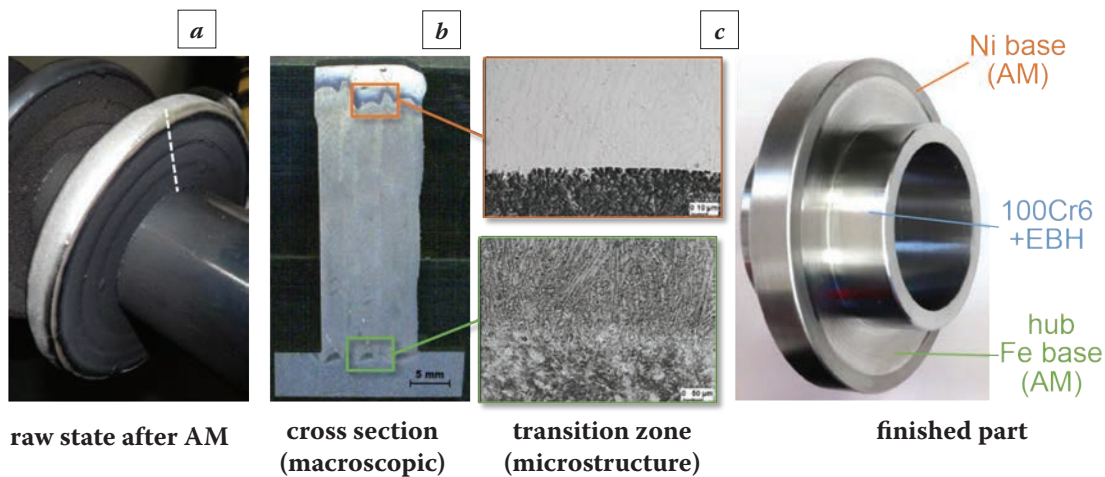


Fig. 8. Generation of a multi material mixed component by AM

size (50...150  $\mu\text{m}$ ) the layer by layer deposition takes a long process time. In case of wire-based technology the deposited layer thickness is considerably larger (wire diameter 0.5...2.0 mm), so this technology is much more efficient but it is useable only for more simple constructive structures. Fig. 7 shows examples of wire-based additive manufactured components before (Fig. 7a) and after subsequent machining (Fig. 7b). The challenges are as well as the heat balance during additive processing and the development of the microstructure, which changes with the successive generation of layers (Fig. 7c) [13]. This results in local different properties.

Current investigations are focused on the generation of a **multi-material mix** AM components [13]. In the present case a component, consisting of three different materials: shaft: 100Cr6, wheel hub: 42CrMo4, wear-stressed outer ring contour: Ni-based alloy, was produced by wire-based AM (Fig. 8). The running surface for a roller bearing is additional hardened by EB. The most important challenges are the connection between different metals at the transition zone (Fig. 8b and c) and the porosity. Both challenges are solved very successfully. The metallurgical connection is free from defects: no pores, cracks or other imperfections.

## ACKNOWLEDGMENT

The contribution contains partial results, which are funded by the Federal Ministry for Economic Affairs and Energy within the project EB-Profil (KF2211903CK3).

Furthermore, the authors would like to thank all industrial R&D partners and the EB team of the Institute of Materials Engineering at the TU Bergakademie Freiberg for the the excellent cooperation and support.

## REFERENCES

1. **Zenker R., Buchwalder A.** Elektronenstrahl-Randschichtbehandlung, Innovative Technologie für höchste industrielle Ansprüche, pro-beam AG & Co. KGaA, 2010.
2. **Halbauer L., Hofner M., Zenker R., Löwer T.** Strahltechnische Tagung Halle. 2015.
3. **Zenker R.** // Journal of Microstructure and Materials Properties. 2015, 10. 1. P. 47–63.
4. **Grumbt G., Zenker R., Biermann H., Weigel K., Bewilogua K., Bräuer G.** // Surf. Coat. Technol. 2015, 283. P. 201–209.
5. **Hengst P., Zenker R., Süß T., Hoffmann K.** // Electrotechnica & Electronica (E+E). 5-6/2016, 51. P. 189–194.
6. **Rüthrich K., Zenker R., Buchwalder A., Frenkler N.** / 9<sup>th</sup> Intern. Conf. on Electron Beam Technologies. 2009. Varna, 1.–4.6.2009.
7. **Rüthrich K., Zenker R., Buchwalder A., Frenkler N.** / Proc. of the 22<sup>nd</sup> Intern. Conf. on Heat Treatment 2008. Brno, 25.–27.11.2008.
8. **Zenker R., Buchwalder A., Frenkler N., Thieme S.** Vakuuum in Forschung und Praxis. 17(2005) 2. P. 66–72.
9. **Hengst P., Zenker R., Süß T., Hoffmann K.** // HTM 71(2016) 6. S. 265–271.
10. **Rüthrich K.** Beitrag zur Entwicklung des Elektronenstrahl-Mehrspot/Mehrprozess-Schweißens von Gusseisen/Gusseisen- und Gusseisen/Stahl-Verbindungen ohne Schweißzusatzstoffe. PhD thesis. Freiberg, 2014.
11. **Halbauer L., Zenker R., Buchwalder A., Biermann H.** Welding in the World. 2016, 60. 4. P. 645–652.
12. **Zenker R., Buchwalder A.** Steel Heat Treating Fundamentals and Processes // J. Dossett, G.E. Totten, ASM International, 2013.
13. **Buchwalder A., Zenker R.** The Application of Modern High-Energy Electron Beam Technologies. In: Int. J. Microstructure and Materials Properties 12(2017), 3/4, S. 288–300.

## D.K. CHERNOV – SCIENTIST, PIONEER AND TEACHER – THE FOUNDER OF MODERN METALLURGY AND METAL SCIENCE THEORY

L.I. Leontiev<sup>1a</sup>, V.V. Tsukanov<sup>2b</sup>

<sup>1</sup>Academician of the Russian Academy of Sciences. Russia

<sup>2</sup>NRC “Kurchatov Institute” – CRISM “Prometey”. Russia

<sup>a</sup> leo@presidium.ras.ru, <sup>b</sup> mail@crism.ru

The paper contains the informational material about the essence of the discoveries made by D.K. Chernov in the field of metal science, theory and practice of heat treatment, new types of tests and investigations. The significance of the discoveries, and D.K. Chernov was the real pioneer of extremely important phenomena in the field of phase and structural transformations, casting structure, study of strength of steel products, undoubtedly, puts D.K. Chernov's name on the first place in a row of world scientists – metallurgists and metal scientists.

Later his discoveries allowed one to develop the science of metals and its subdisciplines – metallurgy, steel deformability, theory of phase and structural transformations, tests and research of metals, theory and technology of heat treatment.

**Keywords:** D.K. Chernov; metals; metallurgy; metallurgical scientists; history of metallurgy; metal science; metallography.

The name of Dmitry Konstantinovich Chernov (1839–1921) is widely known to our contemporaries, especially those who are interested in metal science history and working in this sphere of knowledge.

In the mid-19th century the transition from bronze and cast-iron cannons to steel forged cannon barrels began worldwide. This mostly enabled an increase in cannon calibre, its range and wear resistance. Such a transition was observed both for field cannons and coast battery and ship cannons, including a new class of ships, i.e. battleships.

In Russia this process of new manufacture formation was thorny, difficult and with no stable positive results. The cannons by the Zlatoust Factory, the only plant of this kind in Russia, were manufactured at that time in limited sizes and, in modern language, with no strict scientific approach.

Thus, with the insufficient domestic experience, attempts to loan data from skilled western manufacturers were made. The factory of a well-known German manufacturer Krupp had the greatest experience and large-scale commercial production, but in view of no admittance to his plant for visitors and strict know-how secrecy, production information was completely closed. Chernov who worked at that time at the Obukhov Steel Foundry paid attention to this seemingly unsolvable issue. No one could tell that there were no works of our scientists on the de-

velopment of iron and steel production and attempts to obtain sound forgings in Russian publications. However, these works were not systematized; were of empirical nature without supporting on any scientifically substantiated statements.

In 1868 Chernov noted an important and useful contribution of papers by Lavrov and Kalakutsky to iron and steel production in Russia that had been published in 1866 and 1867. His critical remarks, proposals and recommendations from his own experience Chernov stated in his paper titled “Critical review of articles by Lavrov and Kalakutskii on steel and steel cannons, and investigations by D.K. Chernov on the same subject” (1868). The analysis of these proceedings with the account of his own research results allowed him to come to very important and fundamental conclusions on the structure of cast pigs (the term of that time), gas formation inside them, possible hollows, and also to practical recommendations on melting and metal pouring in a mould.

The analysis of steel ingot structure and discovery of a new phenomenon such as precipitation of tree-like areas (dendrites) led to a very important conclusion about the necessity to obtain a more ductile and tough structure by forging.

The main provisions of this work are as follows (in modern language and shorter terms):

– forging changes cast metal structure with increasing its density;

- forging initiates the welding-up of internal defects;
- uncontrollable heating cycles of already forged metal eliminate forging effects. (Now it is interpreted so that high-temperature heating of already forged metal can lead to grain growth and fracture deterioration);
- forging should be performed till brown-reddish metal as “rearrangement phase” lies close to this temperature.

Based on the analysis of the above proceedings, Chernov noted that “our literature should be proud of the papers by Lavrov and Kalakutsky; they were the first to point to the distribution of hollows in cast steel pigs and their dependence on melting and casting conditions”, and it is not their fault that it was also necessary to familiarize readers with a great number of errors in this matter. In his conclusion Chernov stated that “till now our views and prejudices concerning steel treatment are extremely false in their main basics” [1].

Further let us outline the main provision of Chernov’s theory on steel. The basis of many radically new discoveries made by Chernov is the determination of temperature effect of metal (carbon steel) heating on its properties, in particular, on the obtained ductile disperse fracture of a broken sample. The whole system of dependences of fracture structure change and fracture appearance on heating temperature of Fe–C alloy (mainly with a 0.4 and 0.8% carbon content) was established.

The above major discoveries and developments were the first to be made by Chernov, verified experimentally many times and given relevant scientific explanation at the level of scientific knowledge of the time. They include the following provisions:

**1. Discovery of critical “a” and “b” points by 1868.** The position of “a” point was determined at around 700 °C for iron-carbon alloys (0.4 and 0.8% C) and was interpreted as the temperature at heating below which the steel was not sensitive to quenching. Now it is the PSK line on the Fe-C diagram or a critical point (the line  $A_{c1}$ ).

The description of this highly important diagram of phase transitions (in modern terms) was given by Chernov (Fig. 1) and consists in the following: “0” point determines a thermometric scale zero point, “a” point means dark-cherry heat, “b” point stands for red non-shiny heat, and “c” point is melting temperature for the given steel. “a”, “b” and “c” points have no constant place on the scale and vary with steel composition (in particular, with the carbon content). Chernov notes that the limits of such transitions are relatively small, but with no special devices for pre-

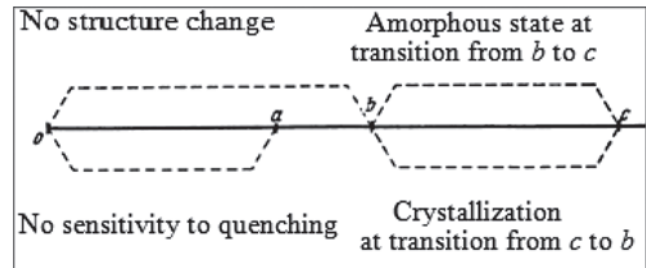


Fig. 1. Position diagram for critical “a”, “b” and “c” points according to Chernov

cise temperature measurements, he had to be guided by the temperature heat colours. He noted, however, that with a low carbon content the temperature corresponding to “b” point sharply increased and matched “white heat”.

**2. The value of “b” point.** “b” point has a more difficult and a multiple-factor nature of influence on the technology of hot deformation, heat treatment, fracture, and mechanical properties. Here are the basic provisions:

- “Steel, being heated below “b” point, does not change its structure, no matter how slowly or rapidly it is cooled after heating. ... As soon as the temperature of steel reaches “b” point, the mass of steel quickly turns from granular (or generally speaking, crystal) into amorphous waxy state. Such a transition has much in common with an aggregate state change,” as Chernov described in 1914;

- the more is the carbon content of steel (up to 0.8% C), the lower heating temperature can be (i.e. the temperature of “b” point decreases);

- it is highly reasonable to heat slightly above “b” point to get a ductile state at thermal heating, as well as to forge with heating above “b” point for ductile fracture and higher strength to be obtained;

- forging below “b” point is hardly possible, but in small cross sections there will be a one-sided elongation (it is feasible for damask steel manufacturing, but when heating at the region of “b” point and above, there will be no pattern that is typical for damask steel);

- the best way to forge is by heating above “b” point. During the process one should lower the temperature within the range of “b” point with structure heterogeneity being observed, then heat up to “b” point and cool rapidly beyond its limits, with subsequent slow cooling in sand or ash. After that a ductile fracture in steel is obtained. To summarize, such heat treatment needs to be made for all large steel products (in reality, it is “isothermal annealing” in the range  $A_{r3} \div A_{r1}$  range).

A series of micrographs (7 pcs.) for martensitic alloyed steel with c 0.2% C content illustrates well the current concept of Chernov’s point “b” (Fig. 2).

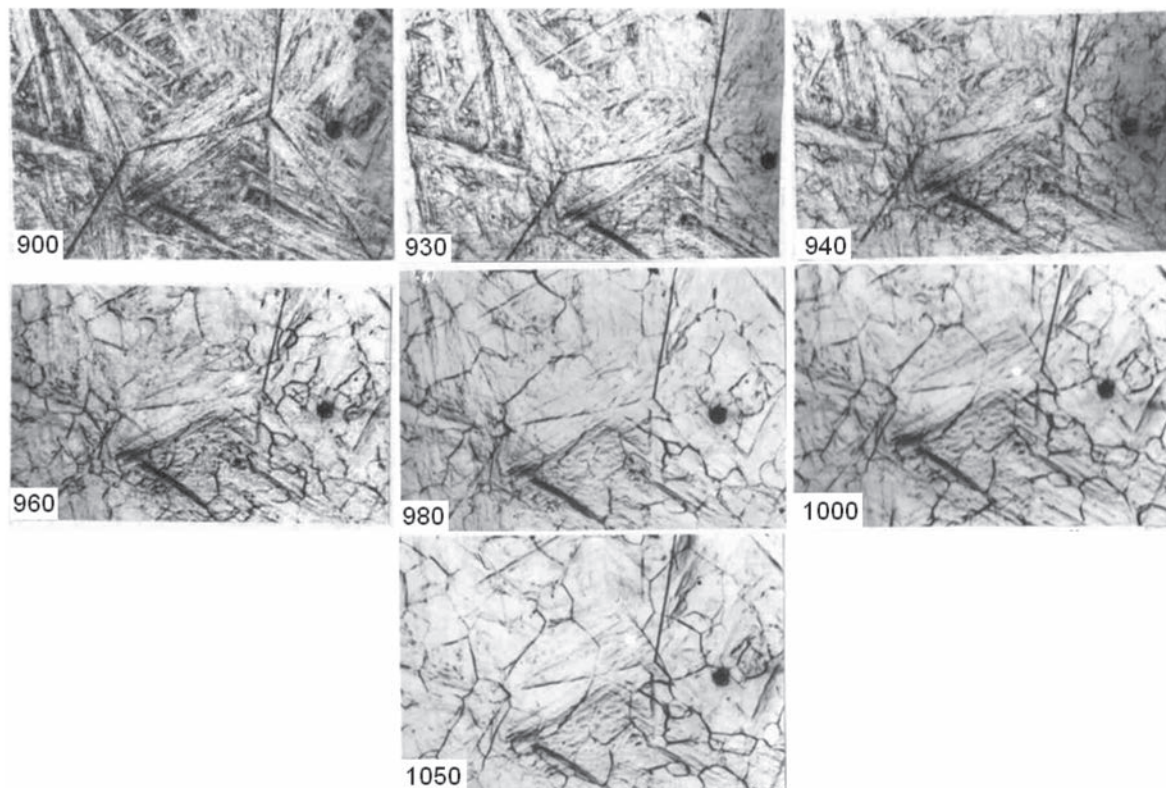


Fig. 2. Kinetics of recrystallized austenitic grain change with 0.2% C ( $\times 100$ )

It is shown that heating to temperatures in the range of  $900\div 1050^\circ\text{C}$  as applied to preliminarily overheated steel up to  $1200^\circ\text{C}$  leads to a multiple grain refinement. Therewith, the following overheated structure change peculiarities are observed:

- nucleation of new grains within the coarse austenitic grain;
- formation of new fine grains with increasing temperature and slow growth start of grains formed before;
- elimination of primary overheated grain boundaries in case of straight-line borders;
- grain refinement occurs at some temperature range, in this example this range is from  $920$  to  $\sim 1050^\circ\text{C}$  (in the region about  $60\div 100^\circ\text{C}$ ) followed by intensive grain growth, the grain boundaries being not straight but winding;
- the analysis of carbide precipitate [2] has shown its considerable dilution ratio in solid solution.

Thus, it can be concluded that nucleation of new grains at the previous austenitic grain boundaries with the blurring of old boundaries needs to be related to recrystallization processes in the temperature “band” range (instead of point “b”), further growth of grains occurs with the natural process of collective recrystallization and elimination of barriers in the form of fine-dispersed carbides of cementite type and special carbides, though VC type carbide traces still remain in solid solution.

To sum up, one can say with certainty that the fundamental innovative discoveries by Chernov are becoming increasingly meaningful.

**3. Development and justification of production methodology of steel cannon barrels.** This helped to apply and introduce in practice some important provisions further developed by scientists of subsequent generations.

Heat treatment of steel barrels of cannons. Forging of barrels made of medium-carbon steel ( $\sim 0.4\% \text{C}$ ) was carried out keeping in mind “b” point temperature and the necessity to obtain a fine-dispersed structure after forging. Heating of barrel and its cooling in oil tank is shown in Fig. 3. In such experiments Chernov used forged barrels and believed that forged billets had a better structure than cast ones with possibly more foundry defects.

Chernov described the proposed technology of heat treatment as follows:

- a billet of barrel, previously heated up to  $\sim 300^\circ\text{C}$  outside the furnace, was charged vertically into the furnace for further heating up to red heat (close to the point “b” temperature).

- then the heated billet was placed into a linseed oil tank for a short ageing for  $\sim 1/2$  minutes to avoid tempering (!). After being cooled slightly below “b” point, the billet was then removed from the tank, filled up with sand and slowly cooled, because “steel no longer changes its structure below “b” point”.

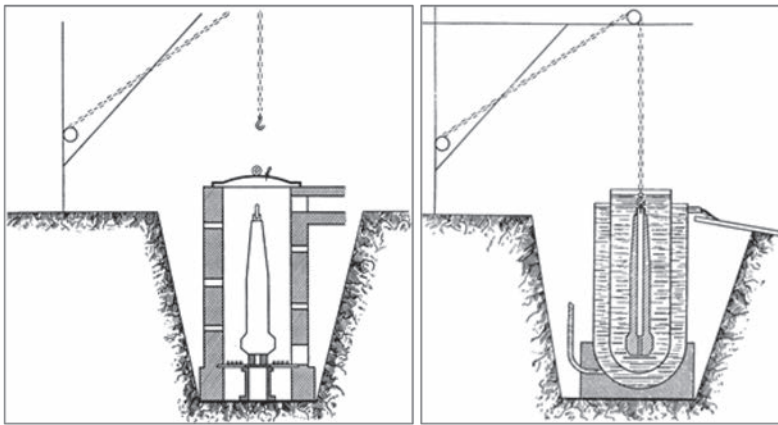


Fig. 3. Barrel heating and cooling in oil tank

In modern language, cooling was carried out slightly below the recrystallisation temperature followed by ferrite-pearlitic structure formation at slow cooling within grain boundaries formed at “b” point during heating. For oil circulation the barrel had a  $\sim\text{Ø}60$  mm bore drilled along the axis in its bolt area, which was then locked with a screw.

**4. Technology development of armor-piercing shells.** The production technology of large-calibre shells made by Krupp was studied for this purpose and the advanced production technology of shells and cannon barrels of up to 12-inch calibre was created in the Obukhov Steel Foundry.

By the 80s of the 19<sup>th</sup> century there was an issue of armor-piercing shells, especially of large-calibre of 10÷12 inches. Krupp shells appeared to be the best by the time and no other company could excel it in piercing thick steel plates. The competition announced in Russia with many public and private enterprises as participants revealed no one who could beat the quality of Krupp’s shells.

In 1885 Chernov addressed the Russian technical society as saying, “You see, my dear Sirs, what kind of material I had to set to work on shells: no leading thoughts, no openly expressed assumptions of shells production, everything is shrouded in mystery. It’s all the same when it comes to foreign publications: no research was done to combine conditions of steel shells production. Therefore, I had to start all over again” [3].

The numerous experiments further conducted by Chernov to determine the chemical composition of steel for high-strength shells of large-calibre, billet technology (cast and forged), hardness distributions and the most effective distribution along cross-section of shells enabled him to develop an optimized production technology of armor-piercing shells in Russia.

The basic provisions of production technology of large-calibre armor-piercing shells developed by Chernov are as follows:

- manufacture of an individual billet of any type of shells obtained by casting and forging. Besides, it was necessary to avoid internal flaws (defects in steel billets);
- creating a special hard layer located in specific zones, both external and internal;
- getting the minimum level of residual stresses in metal volume.

It has been possible to meet these conditions by using special heaters and a spray cooling system shown in Fig. 4.

**Development of a manufacturing technology of large-calibre shells.** A new scientific knowledge was gained while developing a technology of manufacturing large-calibre shells and their testing when firing at thick steel plates. This knowledge has been developed at a later time and generally accepted as terms:

- it was determined that the process of quenching practically came to an end when cooling down to 200 °C and below, i.e. the martensite finish temperature  $M_F$  was found as a critical point. Low-temperature tempering at 200 °C was considered to be the most efficient process to follow quenching. It was found that the possibility of quenching with self-tempering due to supplementary heat release from the central zones;

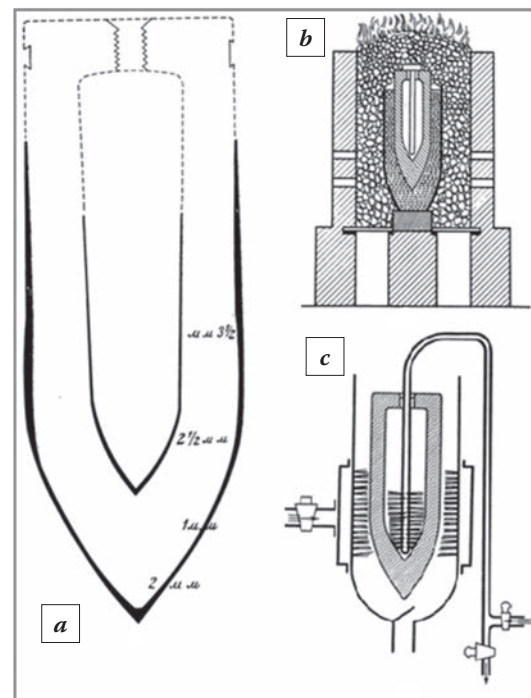


Fig. 4. *a* – Hardness distribution over the shell inside and outside; *b* – diagram of heating the shell case for quenching; *c* – diagram of cooling when quenching the shell case

- a superplasticity phenomenon when quenching in medium at  $\geq 220$  °C was determined for the first time and the possibility of hammer straightening of curved steel billets was shown;

- steel temper colours were identified depending on the tempering temperature of steel products;

- the definitions of “full hardening” and “critical quenching rate” were given for the first time. These phenomena contributed to a deeper understanding of heat treatment processes and phase transformations;

- it was the first time that the concept of transfer of the carbon from as-quenched steel to the carbide  $Fe_3C$  during tempering had been formulated;

- the deformability and fracture were evaluated at slow and rapid loading of armor-piercing shell cases that could practically be considered as the fundamentals of fracture mechanics emerging at that time.

Chernov also proved himself to be a pioneer in other fields of metal science. Their main lines are briefly listed below:

- development of the advanced flow chart of manufacturing cannon barrels and shells and development of scientific methodology at main stages;

- for the basic technology of manufacturing cannon barrels and shells to be developed Chernov studied the processes of ingot crystallization, structure of cast billets, effect of strains on macro- and micro-structural changes;

- he extensively used tensile tests of metals, formulated almost modern concepts of yield strength, ultimate strength, true strength, such plasticity characteristics as elongation and reduction in area. The study of metal elongation when heating and graphic construction of these dependences laid the foundation of dilatometry dealing with phase and structural transformations;

- Chernov evaluated the importance of using alloying elements for changes in steel properties. One might say that the scientist laid the foundation for the doctrine of alloyed steels.

These developments and in-depth conducted studies expanded the understanding of metal science and allowed the essence of processes occurring in metal to be interpreted more deeply. Through these processes the properties of steels can be affected and controlled, and new steels and alloys for industrial needs and development of science and technology to be engineered.

A very important chapter of Chernov's life is his more than 25-year period of teaching activity.

“In 1889 Chernov was invited as head and professor of the department of metallurgy at the Mikhailovskaya Artillery Academy in St. Petersburg. From this time onward, his teaching activity having lasted more than a quarter of a century begins. His lectures were

listened to with exciting interest. He was an outstanding teacher knowing how to impart his deep theoretical knowledge and enormous production experience to his listeners. The courses on steelmaking and iron-making developed by Chernov show a high scientific level, clear and accurate statement of material on theoretical and practical issues of artillery production. Several generations of Russian artillerymen got systematic training under Chernov's leadership. Later on, many of them became prominent scientists in the field of iron and steel production.

In 1914 during the celebration of Chernov's 75<sup>th</sup> anniversary and the 25<sup>th</sup> anniversary of its teaching activity, the Artillery Academy conference addressed him an official greeting. It stated, “A quarter of a century ago, equipped with a vast scientific and practical knowledge, you joined the Grand Duke Mikhail Mikhailovskaya Artillery Academy professorship and having headed the department of steel metallurgy being of prime importance and responsible for the engineering training of artillery officers, you brought it to the adequate level from the very beginning of your activity and then kept it scientifically updated by untiring efforts and with great talent for twenty five years.

Yours ever fascinating lectures opening a wide scientific vista before your listeners not only in the practice of metallurgy but also in other allied areas of technology and natural science left an indelible lifelong impression on them and pointed to the proper ways for further development and improvement of metallurgical practice. Your listeners made of wide use of it in their practical activity than your listeners widely used at their practical activities on artillery service” [4].

This brief overview of some Chernov's developments allows one to consider him by right the founder of scientific and physical metallurgy, academic adviser and inspirer of new ideas for the development of these fields for many generations of his followers.

## REFERENCES

1. **Chernov D.K.** Critical review of articles by Lavrov and Kalakutskii on steel and steel cannons, and investigations by D. K. Chernov on the same subject: *Zapiski Russkogo Tekhnicheskogo Obshchestva*. 1868, No. 7. 399–400.

2. **Tsukanov V.V.** Modern steel and technology engineering. St. Petersburg, 2014.

3. **Chernov D.K.** Report to the Russian Technical Society, 1885.

4. **Golovin A.F.** Chernov's work contribution to the development of the domestic artillery materiel / Proc. on the history of technology, Is. 2. M. : Ed. by Academy of Sciences of the USSR, 1953. P. 60.

## PREDICTION OF THE DURABILITY OF METAL STRUCTURES BASED ON THE ANALYSIS OF THEIR MICROSTRUCTURE

**A.I. Gnevko, O.E. Zubov, S.N. Solovov, M.V. Mukomela,  
A.I. Chmihalo, V.A. Yanushkevich**

The Military Academy of Strategic Rocket Troops after Peter the Great. Russia  
a\_gnevko@mail.ru, zubov13rak@yandex.ru, ssolovov@mail.ru, myka123@yandex.ru,  
himoff2012@rambler.ru, v\_yanushkevich@mail.ru

The development of modern materials science involves a number of activities, including ensuring the reliability of the structures, which implies a forecast of durability. One of the main processes limiting the service life of metal structures is the propagation of cracks. Corrosive cracking is particularly dangerous. Therefore, the purpose of the study was to develop a method to identify dangerous from the point of view of cracking steel structures. Studies have shown that delayed fracture can occur when the relatively hard structural components of the alloy are surrounded by a continuous layer of the soft component. According to the results of the studies, a method has been developed for evaluating the tendency to corrosion cracking of alloys, a method for simulating structural failure, and special materials for fracture modeling. The developed methods have been introduced and have shown quite high efficiency in assessing the durability of metal structures operating under conditions of tensile stresses, as well as designs of unique monuments of Russian foundry art. also designs of unique monuments of foundry art of Russia.

**Keywords:** durability; slamming; slowly destruction; microstructure; microharmovity.

The works of Dmitry Konstantinovich Chernov allow us to distinguish three directions of material science development and heat treatment that are important for theory and practice. The first direction is to improve the quality of metal structures by improving the traditional properties of materials (strength, corrosion resistance, creep resistance, susceptibility to aging, wear resistance, and others). An example is the discovery of iron polymorphism and the scientific foundations of heat treatment. The second direction is to ensure the reliability of the structures, including the performance and durability of materials. For example, the work «On the burnout channels in steel tools.» The third direction is the improvement of the quality of structures by using materials with fundamentally new properties (according to Chernov, using the restructuring of the structure of steel to reveal the nature of the transformation of world energy during hardening). For example, metals with amorphous structure, materials with shape memory, metamaterials and others.

The most common direction, the results of which are in demand in each design, is the prediction of durability. In connection with the above, we carried out studies on the effect of the microstructure characteristics of metallic materials, determined by heat treatment regimes, on their tendency to delayed

destruction (stress corrosion cracking). It is known that the spread of cracks is one of the main processes limiting the service life of metal structures that are exposed to tensile stresses. Of particular danger is corrosion cracking, which develops covertly under constant or slowly changing loads. There is reason to believe that the death of the US submarine «Tresher» and the Russian submarine «Komsomolets» (in fire conditions) were caused by the slow cracking of their titanium hull in seawater. To predict the durability, taking into account the propagation of cracks, information is needed on the critical values of the stress intensity factors (crack resistance) of materials under operating conditions. The quantitative assessment of the crack resistance of materials is a relatively time-consuming process, requiring testing of samples with pre-applied cracks. In addition, each of the structures in the operating conditions may have separate elements that have an increased tendency to delayed destruction. Therefore, the aim of the study was to develop a method for analyzing the microstructure, which allows to identify dangerous areas directly on the operated metalwork. The goal was achieved by evaluating the microhardness by scratching with a constant load on the indenter, which provided a consistent indirect measurement of the strength of all structural components of the alloy. The tests were

carried out on a specially designed setup using a cantilever microscope. Studies have shown that delayed fracture occurs when the relatively solid structural components of the alloy are surrounded by a continuous layer of the soft component. Another important condition for the implementation of delayed fracture is the possibility of unimpeded propagation of cracks along the soft interlayer under conditions of plane-deformed stress state, which is realized with a sufficiently large thickness of the material sheets (for example, more than 30 mm for low carbon steels).

According to the results of the studies, a method has been developed that allows one to estimate the tendency of a material to delayed fracture [1] based on the results of microhardness measurements [1] and can be carried out under operating conditions on a real structure.

Ideas about the nature of slow crack growth have allowed the development of special materials [2], which become prone to delayed fracture when heated to certain critical temperatures. The structure of the material consists, for example, of lead grains surrounded by a continuous layer of Wood alloy. When heated to a temperature close to the melting point of the Wood alloy, cracks propagate in the material.

On the basis of the material developed, a method for testing the crack resistance of metal structures under given constant loads, simulating operational loads, was proposed [3]. A distinctive feature of the method is that it does not change the magnitude of the load (it remains constant, for example, loading on its own weight), but the crack resistance of the material changes as the temperature rises. Cracks begin to develop in the most dangerous places of the structure,

which allows to identify and produce timely strengthening of weakened areas. The proposed method was implemented in the simulation of the destruction of the Tsar Bell. From the developed material, which consisted of a Wood alloy filled with lead shot, the Tsar-Bell 1: 50 model was cast. The model was slowly heated to a temperature slightly lower than the melting temperature of the Wood alloy. The model began to collapse under its own weight, almost the same as the destruction of the real Tsar Bell (Fig. 1)

The results of physical modeling coincided with the calculated assessment of the crack resistance of the Tsar Bell, made using the finite element method. Thus, the stated version of the destruction of the Tsar Bell, according to which it cracked under the influence of cold water falling on a hot surface, is not true. The bell cracked when heated, caused by a fire, to a temperature at which the eutectoid softened (the structural component of bronze).

The developed methods have been introduced and have shown quite high efficiency in assessing the durability of metal structures operating under conditions of tensile stresses and the designs of unique monuments of the Russian foundry art. Elements of cast-iron structures that showed a tendency to slow crack growth were investigated. The critical values of the stress intensity factors for delayed fracture were approximately two times less than for brittle fracture. Evaluation of the real bearing capacity of monuments was carried out by trial loading with control of acoustic emission.

In the middle of the nineteenth century, a number of monuments of Russia were made of gray cast iron, which had good casting properties, but was prone to delayed destruction. The most significant



Fig. 1. Destruction of the Tsar Bell (a) and model (b)



Fig.2. Monument-column to Dmitry Donskoy on Kulikovo field (a), the carriage of Tsar-cannon (b), Triumphal Arch in Moscow (c)

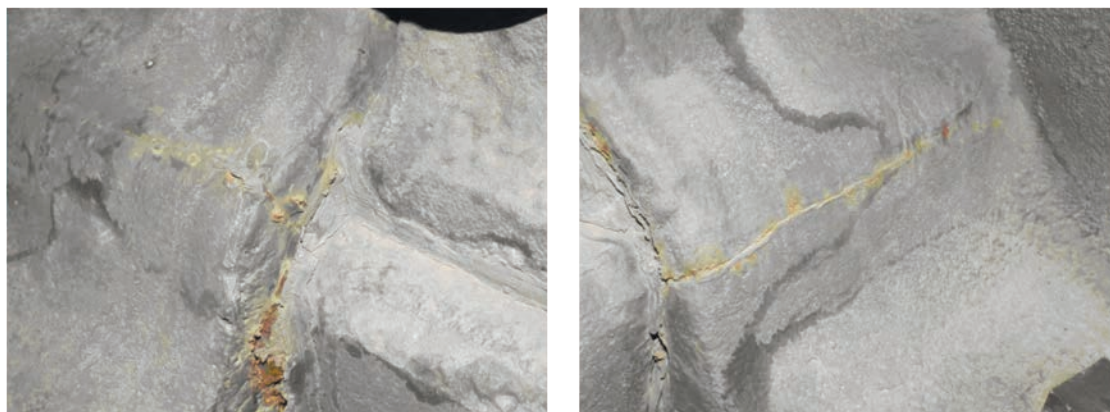


Fig. 3. Development of cracks in the gun carriage Tsar-cannon

are the 30-meter monument-column Dmitry Donskoy on Kulikovo field, the carriage Tsar-cannon, the Triumphal Arch in Moscow (Fig. 2) and others.

Monument to Dmitry Donskoy was on the verge of complete destruction. For the restoration of the monument-column received the State Prize of Russia.

Similarly, elements of the sculptures of the Arc de Triomphe were destroyed and restored.

In the tsar gun cannon, the development of cracks began (reached 50 mm) in the most stretched zone (Fig. 3), which also requires monitoring the strength of the unique monument.

Thus, for a sufficiently reliable confirmation of the durability of metal structures, it is necessary to control the quality of heat treatment (control of the microstructure) of the material, based on the assessment of crack resistance, using, among other things, the proposed methods for analyzing the hardness of the microstructural components.

## REFERENCES

1. **Pat. 2354957** Rossiyskaya Federatsiya, MPK7 G01N 17/00. Sposob otsenki sklonnosti k korrozionnomu rastreskivaniyu splavov / Gnevko A.I., Lazarev D.V., Solovov S.N.; zayavitel' i patentoobladatel' GOU VPO Voyennaya akademiya RVSN imeni Petra Velikogo. – № 2007140554/28; zayavl. 02.11.07; opubl. 10.05.09, Byul. № 13. 5 s.
2. Material dlya modelirovaniya razrusheniya konstruktsiy : **a. s. 1357762** Ros. Federatsiya : MPK51 G 01 N 3/00 / A.I. Gnevko, V.V. Golubev-Il'in, P.I. Logvinyuk, S.N. Solovov; – № 4006522/25–28; zayavl. 13.01.1986; opubl. 07.12.1987, Byul. № 45.
3. Sposob modelirovaniya razrusheniya konstruktsiy: **a. s. 2269312** Ros. Federatsiya: MPK51 G 01 N 3/00 / A.I. Gnevko, P.I. Logvinyuk, D.N. Kochkin, A.A. Yedomskikh; – № 3846318/25–28; zayavl. 28.01.1985; opubl. 23.05.1986, Byul. № 19.

## CONTROLLING THE STRUCTURE AND PROPERTIES OF COLD-ROLLED MILL PRODUCTS MADE OF LIGHT ALLOYED STEEL (HSLA TYPE) SUBJECTED TO CONTINUOUS ANNEALING

I.G. Rodionova<sup>1a</sup>, O.N. Baklanova<sup>1</sup>, A.A. Pavlov<sup>1</sup>, N.A. Karamysheva<sup>1</sup>, A.S. Melnychenko<sup>2</sup>,  
S.V. Denisov<sup>3</sup>, V.E. Telegin<sup>3</sup>, S.G. Andreev<sup>3</sup>, A.V. Mastyaev<sup>3</sup>

<sup>1</sup> FSUE "I.P. Bardin Central Research Institute for Ferrous Metallurgy". Moscow, Russia

<sup>2</sup> National University of Science and Technology "MISIS". Moscow, Russia

<sup>3</sup> PJSC "Magnitogorsk Iron & Steel Works". Magnitogorsk, Russia

<sup>a</sup> igrodi@mail.ru

Using the methods of statistical analysis to assess the influence of the chemical composition and technological parameters on the properties of cold-rolled HSLA steels after processing in a continuous annealing unit (CAU), key technological parameters have been identified, optimizing of which allow improving the complex of mechanical characteristics. The formulated hypotheses about the mechanisms of influence of technological parameters on the processes occurring at different stages of the production of cold-rolled steel have been tested experimentally. The possibility of influencing the steels properties of not only traditional hardening mechanisms (grinding grain structure, solid solution hardening and dispersion hardening), but also processes occurring at the low-temperature processing stage at the CAU have been shown.

**Keywords:** high-strength steels, cold-rolled steels, low-alloy steels, HSLA steels, thermal treatment, continuous annealing unit, technological parameters, mechanical properties, statistical analysis

At present high-strength cold-rolled light alloyed (micro alloyed) steels (HSLA type) are becoming more commonly used in global and domestic car manufacturing. Their use enables to reduce vehicle weight, ensure compliance with legislative requirements for decrease of fuel consumption, improve environmental situation and increase safety of operation. The foregoing defines relevance of the works aimed to improve a property package of such steels – improve plasticity, stability of strength properties with reduction of expenses for production by optimizing the chemical composition of steel and parameters of cross-cutting technology.

Using the methods of statistical analysis [1] to assess impact of chemical composition and technological parameters on properties of the cold-rolled mill products made of HSLA steels with 260–380 MPa strength grades after processing in a continuous an-

nealing line (CAL), the key technological parameters, optimization whereof can improve the package of obtained mechanical characteristics, were revealed. Hypotheses about effect mechanisms for technological parameters on processes occurring for various stages of cold-rolled mill products manufacture were formulated. Further above hypothesis were checked experimentally and among other factors it was with laboratory simulation of annealing cycles in CAL in complex «Gleebl» for processing in CAL across various modes of cold-rolled hammer-hardened mill products made in steels grades HC300LA and HC340LA of current manufacture with variation of annealing temperature and temperature intervals of overageing. Steels chemical composition for laboratory simulation is shown in Table 1.

It is confirmed the basic parameters of cold-rolled mill products processing in CAL that determine the

Table 1. Steels chemical composition for laboratory simulation, % mass

Grade	Reference number	C	Si	Mn	S	P	Cr	Ni	Cu	N	Al	Nb
CR300	1	0.05	0.06	0.5	0.004	0.008	0.04	0.02	0.03	0.005	0.052	0.033
CR340	2	0.06	0.02	0.69	0.004	0.005	0.02	0.01	0.03	0.006	0.05	0.048

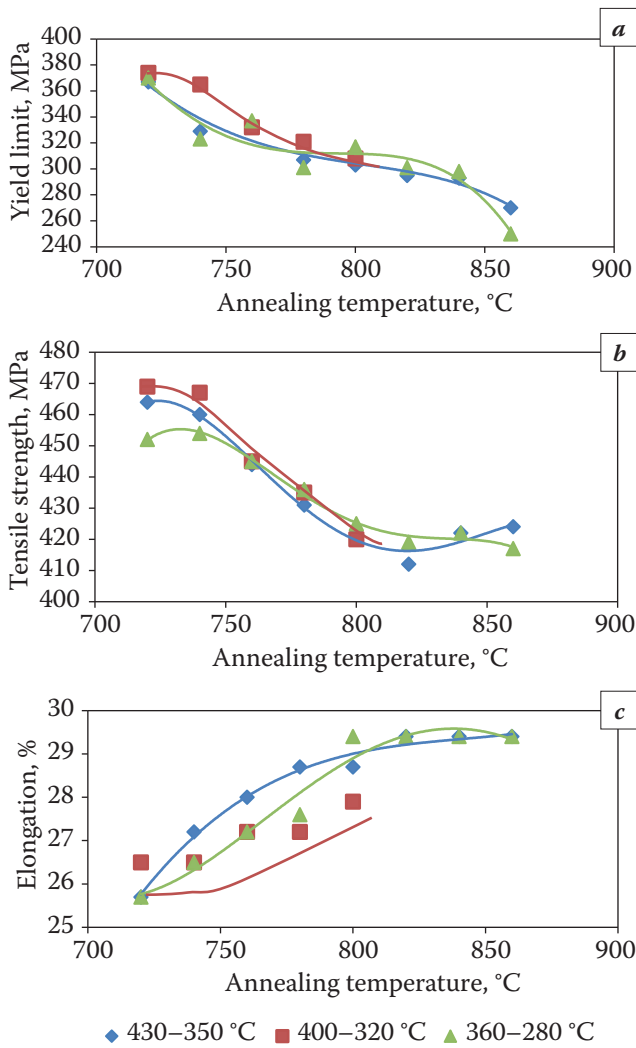


Fig. 1. Mechanical properties dependence on annealing temperature for steel used to produce mill product of strength class 300: *a* – yield limit, *b* – tensile strength, *c* – relative elongation with variation of overageing temperature intervals (430–350 °C, 400–320 °C, 360–280 °C)

level of its strength properties are the annealing temperature P5. When reducing the temperature P5 for mill products with strength 300 specifically between 800 and 720 °C the strength properties are increased (especially yield limit) ensuring the step from one class of strength to another one (300, 340 и 380). At that ductile property is decreased slightly (see Fig. 1). The overageing mode has great impact on indicators of strength properties only in zone of annealing low temperatures (720–740 °C). The highest values of strength properties may be obtained when overageing begins at temperature between 405–420 °C. The usage of higher overageing temperatures is an important condition to produce cold-rolled mill products with higher strength class – 340 and especially – 380 made of steel used for cold-rolled products with strength 300 now, if necessary.

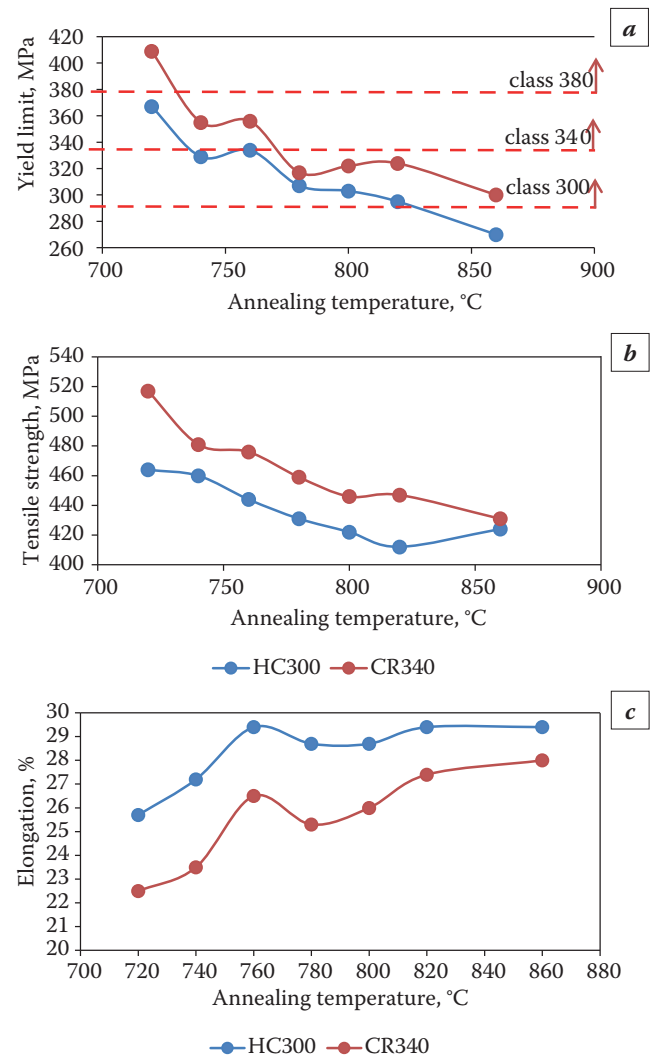


Fig. 2. Dependence of strength properties (*a*, *b*) and relative elongation (*c*) of steels HC300 and CR340 on heating temperatures with annealing simulation in CAL

It's clear that a band strain reducing with annealing in CAL at stages of heating, holding and retarded cooling relative to rated value delays diffusive and thus recrystallization processes. This leads to production of more fine structure with annealing up to 760 °C, as well as it delays concretion of nanosized extraction of niobium carbide. The highest values of strength properties are found after annealing at 720 °C with rated and decreased strain. By this means annealing low temperatures and strain use are not above rated value and it's mandatory condition to receive the high strength properties at stages of heating and holding.

Based on the results of annealing simulation in CAL for steel CR340 mill product samples it's seen that production of mill product is possible only with the same strength classes that of less alloy steel of grade HC300LA – 260–380. It is evident that pro-

duction of the mill product with strength class 260 and 300 from more expensive steel is economically impractical than steel used for these classes now. At that the loss of strength occurs faster with temperature increase in range 720–800 °C of steel grade CR340 than for mill product of steel grade HC300LA and after annealing at 780 °C class 340 is not ensured of this steel.

Main influence patterns for chemical composition parameters on mill product properties annealed in continuous lines are formulated based on statistical analysis and laboratory simulation results. These main influence patterns are as follows. Carbon content increase leads to higher strength properties, primarily it's about the tensile strength involving increase of cementite phase percentage (in fact, cementite or perlite) and increase of nanosized niobium carbide extractions number that causes a dispersion hardening as well as the carbon content involves the aging processes. Increase of manganese content starts to results in an increase of yield limit and tensile strength for classes 340 and 380 when it grows more than 0.6–0.7%. Reason of manganese holding in hardening is retardation of diffusion processes in its presence except small solid solution strengthening. It results to slow down both grain growth and coagulating of nanosized niobium carbide extractions. That is the strength is increased for the account of the grain refinement and enhance the effectiveness of dispersion hardening with its increase especially more than 0.7%. The strength properties increase and ductility reduction together with niobium content growth related to increase of dispersion hardening holding. Increase of silicium content causes solid solution hardening.

Hot rolling parameters influence on cold-rolled mill products properties for steels HSLA relates primarily with their influence on number and sizes of nanosized niobium carbide extractions and grain size in finished mill products. The temperature rise of rolling end reduces the hardening through the grain refinement due to quantity reduction of sub-micron releases of niobium carbonitride forming while hot rolling and retarding the recrystallization processes. At that the carbon and niobium content in solid solution is increased upon hot rolling end which contributes to forming of wound hot-rolled coil with cooling or large quantity of nanosized niobium carbide extractions while following annealing of cold rolled mill products. It improves efficiency of dispersion hardening. Other condition of implementation for dispersion hardening mechanism in finished mill product is optimal temperature use of coiling for mill products with strength class 300 and

more at level 560–580 °C. Diffusion mobility of atoms is not enough for forming of nanosized niobium carbide extractions at lower temperatures of coiling. The sizes of forming particles are increased at higher temperatures of coiling that also reduces the dispersion hardening effectiveness.

The influence on properties of annealing high-temperature parameters in the continuous lines is connected with their influence on recrystallization processes, formation of nanosized extraction of excess phases, their number and morphology. Both the ferrite grain size and sizes of nanosized niobium carbide extractions are increased with rise of annealing temperature and reduction in speed of the band motion within finished mill product. And quantity of niobium carbide extractions is reduced. Strength properties reduction is connected herewith as well as raise of ductility with increase of annealing temperature and speed reduction of the band motion in CAL and CGL (continuous galvanizing line). By varying the above parameters it's possible to change the steel strength and ductility. It's possible to further accelerate the processes of the grain increase and the nanosized extractions with raising the band tension at stages of heating and holding which is related to acceleration the diffusion processes.

The influence on parameters at low-temperature stage of processing in continuous lines are related to the processes of carbon redistribution due to its solubility reduction in ferrite with the temperature can drop. Aging processes resulting in hardening for most cases refer to the such processes as well as the cementite precipitation processes onto nanoparticles of niobium carbide. This has led to loss of strength and ductility increase due to reduction in the efficiency of dispersion hardening

Transmission electron microscope examination (TEM) of structural condition characteristics including nanostructural component (type, quantity, sizes, morphology of nanosized extractions of excess phases) indicates that the density of niobium carbide nanosized extractions is reduced essentially with annealing temperature raise (particles content per 1  $\mu\text{m}^2$  of micro slice area) and share of smaller particles with size 1–2 nm is decreased too, their middle and maximum diameter is increased (see Tables 2 and 3).

A great many of the smallest particles formed in steels of strength classes 300 and 340 upon annealing at 720 °C is an important reason to provide the highest strength of such steels.

Matching coefficients of correlation for mechanical properties values with parameters of particles for investigated mill product are shown in the Table 4.

Table 2. Design parameters of niobium carbide nanosized extractions upon annealing simulating in CAL for steel mill product HC300LA

Temperature, °C	Particles density, $\mu\text{m}^{-2}$	Middle diameter, nm	Maximum diameter, nm	Deviation	Share of particles with size 1–2 nm, %
720	1165	1.68	6.11	0.018	85
760	843	1.53	8.68	0.021	88
800	269	1.80	6.14	0.054	73
840	304	1.79	7.37	0.053	62

Table 3. Design parameters of niobium carbide nanosized extractions upon annealing simulating in CAL for steel mill product CR340

Temperature, °C	Particles density, $\mu\text{m}^{-2}$	Middle diameter, nm	Maximum diameter, nm	Deviation	Share of particles with size 1–2 nm, %
720	2094	1.40	5.83	0.012	92
760	1541	1.44	5.47	0.015	82
800	503	1.70	4.46	0.035	67

Table 4. Matching coefficients of correlation for mechanical properties values with parameters of particles

	$\sigma_T$ , MPa	$\sigma_B$ , MPa	$\sigma_T/\sigma_B$	$\delta_4$ , %
Density of particles, $\mu\text{m}^{-2}$	<b>0.946</b>	<b>0.972</b>	<b>0.726</b>	<b>-0.792</b>
Middle diameter, nm	<b>-0.684</b>	<b>-0.789</b>	<b>-0.444</b>	<b>0.536</b>
Share of particles with size 1–2 nm, %	<b>0.799</b>	<b>0.693</b>	<b>0.802</b>	<b>-0.569</b>

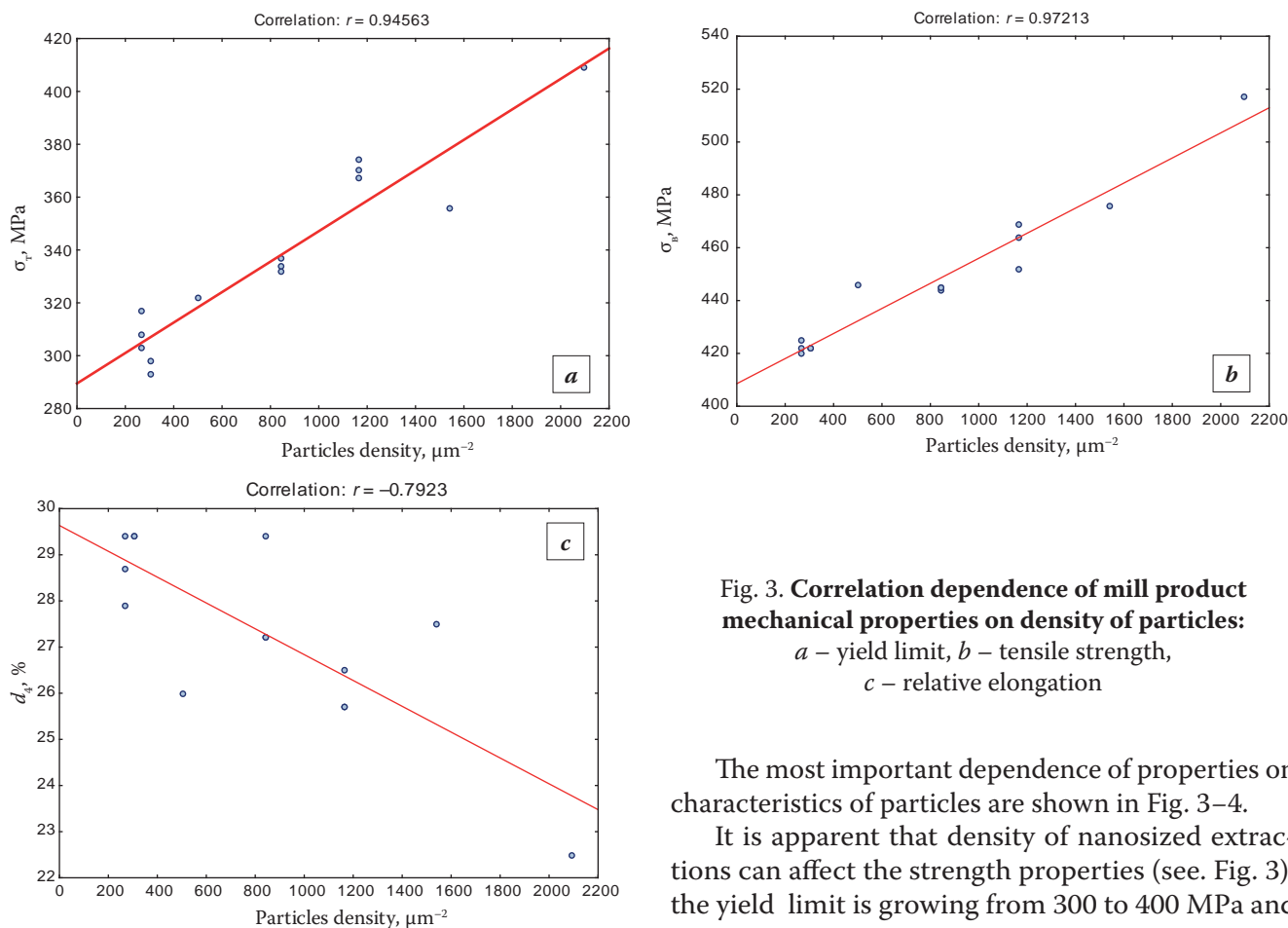


Fig. 3. Correlation dependence of mill product mechanical properties on density of particles:  
*a* – yield limit, *b* – tensile strength,  
*c* – relative elongation

The most important dependence of properties on characteristics of particles are shown in Fig. 3–4.

It is apparent that density of nanosized extractions can affect the strength properties (see. Fig. 3), the yield limit is growing from 300 to 400 MPa and

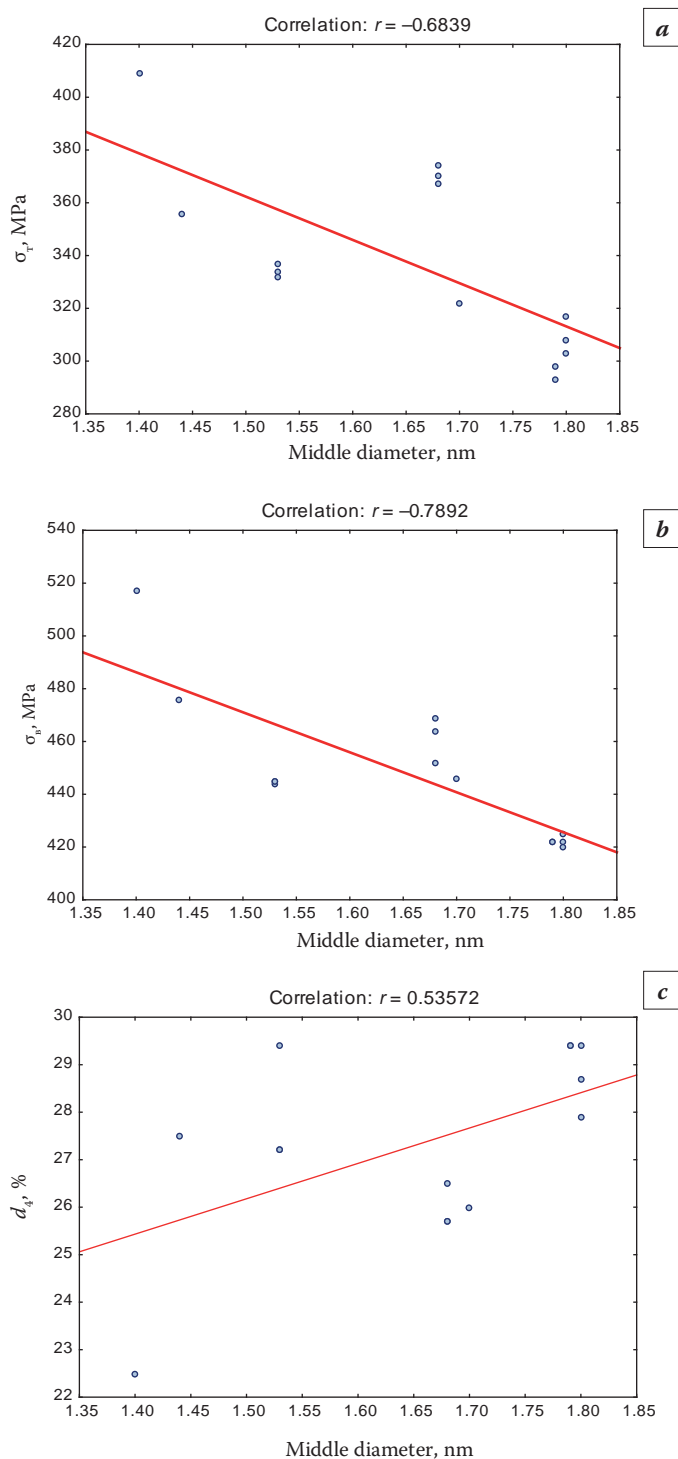


Fig. 4. Correlation dependence of mill product mechanical properties on middle diameter of particles: *a* – yield limit, *b* – tensile strength, *c* – relative elongation

more with density increase from 300 up to 2000  $\mu\text{m}^{-2}$ . The middle diameter of particles has less influence on properties, it has changed within relatively close lim-

its (see Fig. 4). Nevertheless it is seen that the middle diameter increase up to 1.8 nm results in considerable reduction of strength properties.

Thus quantity and sizes of niobium carbide nanosized extractions are key factors for structure and properties formation. To increase the steel strength properties of same chemical composition it should be to make higher number of smaller the niobium carbide extractions in mill products. It's evident that the key parameters are annealing temperature and the band motion speed – the strength is increased with annealing temperature reduction and enhancing the speed of band motion through the quantity increase and reduction of the particles sizes and thus at the expense of dispersion hardening holding increase. In order to raise the holding of dispersion hardening additionally it's possible to form a part of above extractions as early as in hot-rolled mill product. The rise of temperature of rolling end and optimization of coiling temperature lead to increase of above extraction share with middle size about 1.5 nm. The temperature of coiling is optimum in range 560–580 °C for mill products with strength class 300 and above. It's possible to restrict or even to reduce the band tension in the CAL in order to additionally reduce the effectiveness of strength loss related to particles coarsening

It's possible to settle the specified modes of overageing primarily, the start of overageing (P10) between 405–420 °C for additional strength properties increase as to ageing treatment mechanism for mill product to be annealed in CAL. It ensures the implementation of ageing processes resulting in hardening.

## REFERENCES

1. Rodionova I.G., Baklanova O.N., Pavlov A.A., Karamysheva N.A., Melnychenko A.S., Denisov S.V., Telegin V.E., Andreev S.G., Mastyaev A.V. Investigation of chemical composition and process parameters influence on cold-rolled mill product properties of low-alloy steel (HSLA type) after continuous annealing process with use of statistical methods // Problems of iron and steel industry and material science. 2019. № 1. P. 79 – 91.

# APPLICATION OF GENETIC ENGINEERING TECHNOLOGIES TO REDUCE THE HOLD TIME UNDER HEAT TREATMENT OF Al-Si CAST ALUMINUM ALLOYS

V. Nikitin, K. Nikitin

Samara state technical University, Samara, Russian Federation  
kvn-6411@mail.ru

The fraction of the consumption of aluminum in transport engineering amounts on the average to 30–40% of the total consumption of aluminum articles by all branches of industry. The main consumer is the automotive industry. Manufacturing of cast articles from metallic alloys requires much power not only in the stage of preparation of the alloys but also during heat treatment of ready castings. This makes the development of power-saving processes in the production of aluminum castings an important direction of research.

The known heat treatment modes are mainly aimed at refinement of eutectic silicon and provision of conditions for growth of spherical crystals. Consequently, the main effect of the heat treatment of silumins is exerted on the size and morphology of eutectic silicon.

The paper shows that the application of the basic laws of the phenomenon of structural heredity in practice (technology of genetic engineering in alloys) provides a reduction in the holding time during heat treatment of silumins. The evaluation criterion to reduce the holding time at the heat treatment depending on the parameters of the cast structure was proposed.

**Keywords:** aluminum alloy; microstructure; chill casting; heat treatment; quenching and aging.

## INTRODUCTION

At present we witness continuous growth of the consumption of cast articles from aluminum alloys in machine building. By the data of analytical review [1] the fraction of the consumption of aluminum in transport engineering amounts on the average to 30–40% of the total consumption of aluminum articles by all branches of industry. The main consumer is the automotive industry. Manufacturing of cast articles from metallic alloys requires much power not only in the stage of preparation of the alloys but also during heat treatment of ready castings. This makes the development of power-saving processes in the production of aluminum castings an important direction of research.

It is known that inoculation of alloys in the stage of their manufacturing is the main operation providing a fine-crystal structure in the cast article and formation of the required level of mechanical, process, and operating properties [2, 3]. However, the relation between the inoculation parameters and the parameters of the heat treatment for obtaining the needed characteristics in the cast structure of silumins has not been studied enough.

The heat treatment modes standardized by GOST 1583–93 are mainly aimed at refinement of eutectic silicon and provision of conditions for growth

of spherical crystals [4–8]. For example, in the process of isothermal holding for hardening the crystals of eutectic silicon undergo fragmentation and then coagulation. As a result of the hardening, clusters of compact crystals with spherical morphology form in the place of former colonies of eutectic silicon. In eutectic silumins the crystals of primary silicon usually preserve their size after the heat treatment and become somewhat spheroidized. This is accompanied by dissolution of secondary phases of the casting origin ( $\text{CuAl}_2$ ,  $\text{MgSi}_2$ , etc.). The iron-containing phases (especially  $\text{FeSiAl}_2$ ) do not virtually change their sizes and morphology as a result of heat treatment. Consequently, the main effect of the heat treatment of silumins is exerted on the size and morphology of eutectic silicon.

Results of a study of the effect of hardening and aging modes on the structure and phase composition of alloy AK7ch inoculated jointly with Sr and Sc are presented in [9]. Optimum parameters of such heat treatment are developed. However, the work does not give the characteristics of alloy AK7ch and does not analyze the effect of the inoculation on its microstructure. It is mentioned that it is possible to shorten the time of heat treatment without distorting the fine cast structure of the metal by special treatment of the melt. For example, an electrohydropulse action on the melt of AK9ch refines the structural components

*Правильно?*

in the cast condition and makes it possible to reduce the time of the aging process from 16 to 5 h [10].

## THEORETICAL SUBSTANTIATION

done a theoretical analysis of the relation between the refinement of crystals of eutectic silicon due to inoculation and the rate of their dissolution during heat treatment as compared to the not inoculated condition at the same temperature modes. In accordance with [11], the rate of dissolution of crystals of eutectic silicon during a hold of the alloy at temperature  $T$  may be described as

$$\frac{dn}{dt} = n_b e^{-Q/kT}, \quad (1)$$

where  $n$  is the number of atoms,  $t$  is the time,  $Q$  is the activation energy of diffusion,  $n_b$  is the number of atoms on the boundary, and  $k$  is the Boltzmann constant.

Since the number of atoms of a crystal boundary is proportional to its area, we may write

$$n_b \approx R^2. \quad (2)$$

Let us assume that the crystals have a spherical shape. Then the volume of a crystal prior to inoculation is

$$V_1 = \frac{4}{3} \pi R^3, \quad (3)$$

where  $R$  is the radius of the crystal.

The volume of the crystal after inoculation is

$$V_2 = \frac{4}{3} \pi r^3, \quad (4)$$

where  $r$  is the radius of the crystal after inoculation.

We assume that as a result of the inoculation the volume of one crystal decreases by a factor of  $N$ , i.e.,

$$V_1 = N V_2. \quad (5)$$

Then

$$R^3 = N r^3, \quad (6)$$

$$r = R / \sqrt[3]{N}. \quad (7)$$

Consequently, expression (1) for the not inoculated metal acquires the form

$$\frac{dn}{dt} = R^2 e^{-Q/kT}. \quad (8)$$

For the inoculated condition we obtain by analogy

$$\frac{dn}{dt} \approx r^2 e^{-Q/kT} \approx N^{-2/3} R^2 e^{-Q/kT}. \quad (9)$$

Thus, the decrease in the size of a crystal under inoculation reduces its volume by one-two orders of magnitude as compared to the volume in the not inoculated metal. The number of crystals in the inoculated alloy also increases by the same value. This means that factor  $N$  in formula (5) reflects the factor of growth in the number of spherical crystals with radius  $r$ . Since the decrease in the crystal size by a factor of  $N$  increases their number by about a factor of  $N$  and thus increases the total area of their surface, we may write

$$\frac{dn}{dt} \approx N^{1/3} R^2 e^{-Q/kT}. \quad (10)$$

With allowance for (7) we find that the rate of dissolution  $N$  of particles of radius  $r$  at temperature  $T$  is equal to

$$\frac{dn}{dt} \approx \frac{R}{r} R^2 e^{-Q/kT}. \quad (11)$$

Comparing Eqs. (8) and (11) we infer that the refinement of crystals in cast condition due to inoculation should promote growth of the rate of their dissolution under heat treatment by a factor of about  $(R/r)$  as compared to the not inoculated condition at the same temperature modes. The aim of the present work was to study the possibility of shortening the hold, and hence the consumed power, in heat treatment of silumins of the Al–Si–Cu system due to inoculation of the alloy with microcrystalline blend.

## STUDY

Правильно?

It was studied aluminum alloys AK6M2 and AK8M3ch. Alloy AK6M2 in inoculated and not inoculated conditions was chill cast at the Center for Casting Technologies of the Samara State Technical University. Ingots of alloy AK6M2 (GOST 1583–93) were melted in a graphite crucible in an induction furnace, refined with flux FNK-A (TU 2149-008-43884713, Russia) in an amount of 0.22%, and degassed with a “Degazer” preparation (TU 2458-002-79162668, Russia) in an amount of 0.06% of the mass of the melt. The melt of AK6M2 was inoculated by adding an AlTi5 microcrystalline alloy of the own production in an amount of 0.02% with respect to titanium. The inoculated and not inoculated melts of AK6M2 were chill cast to obtain plate-type test castings. The castings were hardened in a SShOL resistance furnace. The GOST 1583–93 Standard prescribes casting of alloy AK6M2 at a temperature of the cooling medium 20–100 °C after 3–5 h of heating at 525±5 °C. In our

experiment the heating for hardening was conducted at  $525 \pm 5$  °C for 2 and 4 h with water cooling (20 °C). We measured the *HB* hardness and the electric resistivity of the ingots in the initial condition and after the hardening. The hardness was measured with the help of a TSh-2 hardness meter with a steel ball diameter of 5 mm at a load of 250 kgf applied for 30 sec. We determined the average values of *HB* measured at five points at a distance of at least 10 mm from each other. The resistivity was determined using a VS-30N eddy current device accurate to  $\pm 0.1 \times 10^{-8}$  Ω·m using an average value after ten measurements.

Specimens of alloy AK8M3ch (GOST 1583–93) were obtained in the foundry shop of the Volsk Mechanical Works (Volsk, Russia). Frame-type chill castings were fabricated by the active and experimental processes. In the active process an ingot of alloy AK8M3ch was melted, degassed with “Degazer” preparation in an amount of 0.1%, and inoculated with a mixture of salts (62.5% NaCl + 25% NaF + 2.5% KCl) in an amount of 0.4% of the mass of the melt. In the experimental process the composition of the melt was enriched with 20% remelted microcrystals (RMC) obtained from elements of gate runners and rejected castings of alloy AK8M3ch. The inoculation was performed with a composite “Evtektika” flux (Belarus, Minsk, TU RB 100196035.005–2000) in an amount of 0.2%, K2ZrF6 salt (TU 95-1833–89, Russia) in an amount of 0.1% with additions of a microcrystalline blend (1% of the mass of the melt) before casting. The castings of alloy AK8M3ch were heat treated by mode T5 of GOST 1583–93, i.e., hardening from  $510 \pm 5$  °C (6 h) with water cooling at 20 °C + aging at  $160 \pm 5$  °C (12 h). The specimens for mechanical tests and metallographic studies were cut

from the ingots in cast and heat treated conditions. The ultimate strength and the ductility were determined according to GOST 1497–84 for specimens of type 3, No. 8 cut from the walls of a casting using a 20SZBDA testing machine. We used the average values of the characteristics after three tests per point. The metallographic analysis was performed using the SIAMS-700 software and hardware set (SHS) (the SIAMS Company, Ekaterinburg) for at least 10 fields; the results were averaged.

## RESULTS

The results of the estimation of the macrohardness and resistivity of alloy AK6M2 are presented in Fig. 1. It can be seen that when the hold time in heating for hardening is increased, the hardness and the resistivity of the specimens of AK6M2 grow. The not inoculated alloy AK6M2 has a maximum hardness (*HB* = 920 MPa) after the following hardening mode: 4-h hold at 510 °C, water cooling. When the ingot is held for hardening for 2 h, the hardness of the alloy in the not inoculated condition amounts to about 800 MPa. The resistivity increases with growth in the hardness.

In the inoculated condition alloy AK6M2 exhibits its maximum macrohardness already after a hold for 2 h. Prolongation of the hold does not virtually change the hardness. Measurement of the resistivity of specimens of alloy AK6M2 in the inoculated condition as a function of the time of holding for hardening shows the same dependence.

The study of the microstructure of alloy AK6M2 has shown that water hardening after a 2-h hold at

510 °C virtually does not change the characteristic size of the crystals of eutectic silicon in the not inoculated alloy. As a result of inoculation of the alloy, the transverse size of the secondary arms of the  $\alpha$ -Al dendrites decreases from 42 to 21  $\mu\text{m}$ ; that of the crystals of eutectic silicon decreases from 24 to 18  $\mu\text{m}$  as compared to the same characteristics in the not inoculated condition. In accordance with relation (11) the factor  $(R/r) \sim 1.33$ –2.0. Spheroidization of the crystals of eutectic silicon occurs after a 4-h hold of the alloy for hardening. The mean size of the crystals decreases by about 25% (to about 18  $\mu\text{m}$ ). In the case of heat treatment of the inoculated alloy AK6M2 spheroidization and refinement of the crystals of eutectic silicon develop after

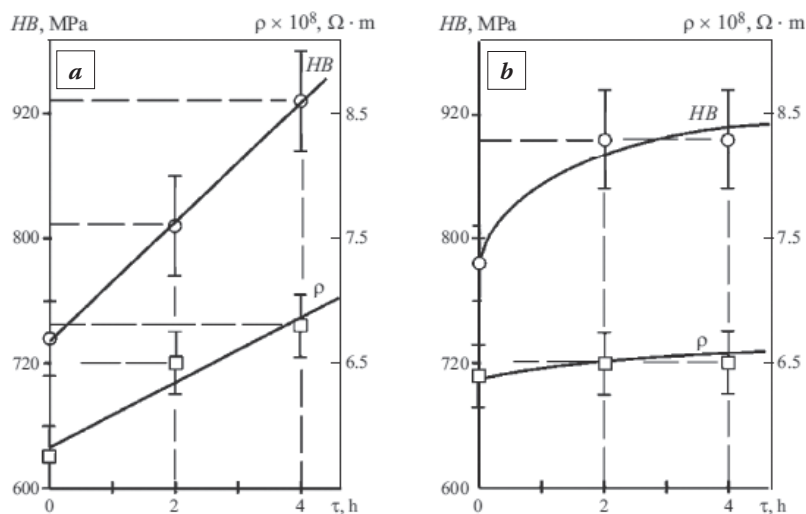


Fig. 1. Dependence of the hardness *HB* and electric resistivity on the duration of the hold of alloy AK6M2 for hardening in not inoculated (a) and inoculated (b) conditions.

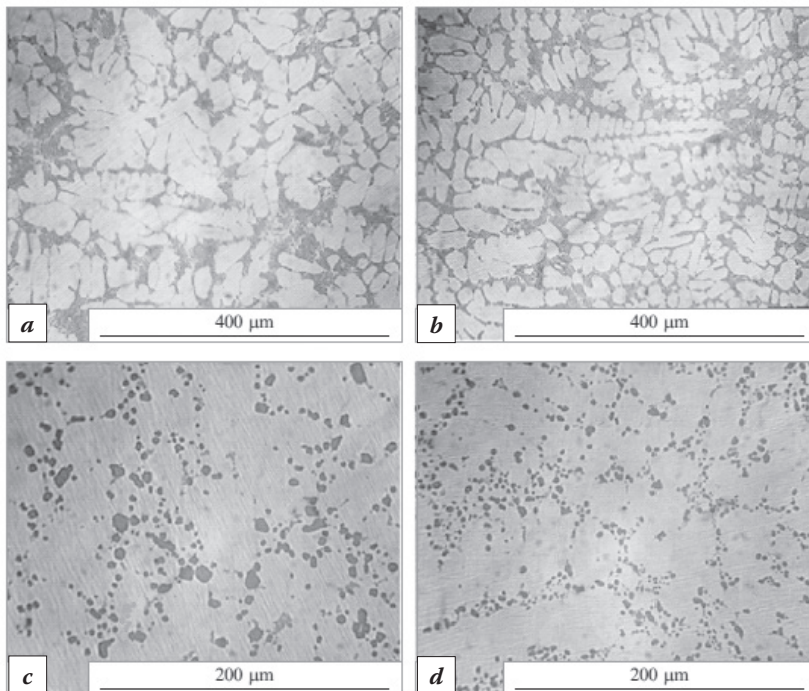


Fig. 2. Microstructure of alloy AK8M3ch obtained by the active (*a, c*) and novel (*b, d*) production processes: *a, b* – after casting; *c, d* – after heat treatment (hardening and aging)

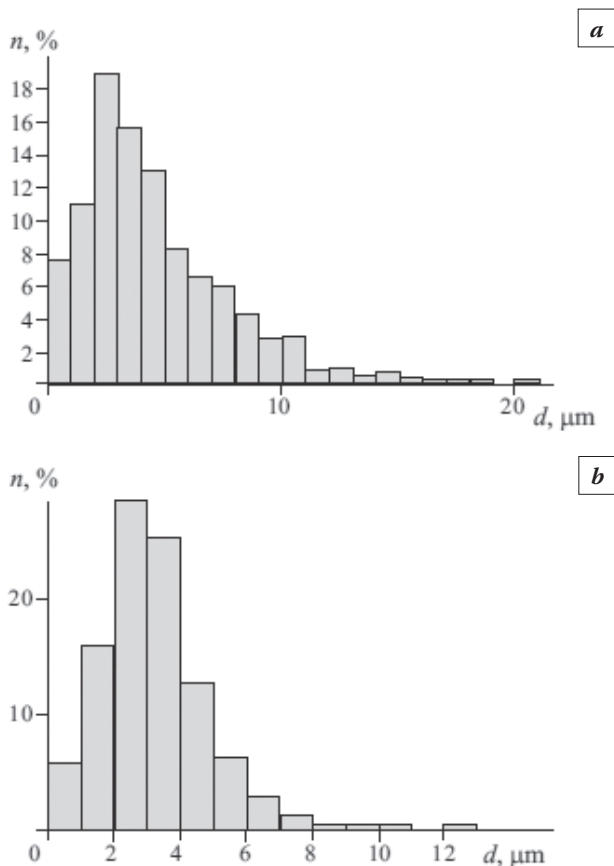


Fig. 3. Size distribution of silicon particles ( $n$  is the number of cases) in heat treated alloy AK8M2ch produced by the active (*a*) and novel (*b*) processes

a 2-h hold for hardening. Note that after the 4-h hold for hardening the mean size of the crystals of eutectic silicon in the inoculated alloy is 1.2 times smaller than in the not inoculated alloy.

The results of the metallographic study of alloy AK8M3ch in the cast and heat treated conditions are presented in Figs. 2 and 3. The specimens have been taken from chill castings of a frame type produced by the active and experimental processes. The experimental process differs from the active one by the presence of 20% remelted microcrystals (RMC) obtained from elements of gate runners and rejected castings of alloy AK8M3ch. Application of the experimental process at the Volsk Mechanical Works gave alloy AK8M3ch with an average ultimate strength  $\sigma_r$  increased by 35% in the cast condition and by 23% in the heat treated condition. The transverse size of the secondary arms of the  $\alpha$ -Al dendrites in the structure of the

cast alloy obtained by the active process is 60–70  $\mu\text{m}$ . The mean size of the spheroidized crystals of eutectic silicon after the heat treatment is 5–8  $\mu\text{m}$  (Fig. 3a). Introduction of the novel process has provided decrease in the transverse size of the secondary arms of the  $\alpha$ -Al dendrites to 30–35  $\mu\text{m}$  in the cast condition and that of the spheroidized crystals of eutectic silicon after the heat treatment to 3–4  $\mu\text{m}$  (Fig. 3b). Thus, the change in the production process of alloy AK8M3ch has refined the structural components of ingots by a factor of 2.0–2.5. After theoretical evaluation of the time of heat treatment by Eq. (11) for the conditions of the Volsk Mechanical Works the aging time of the experimental castings was reduced from 12 to 6 h (see Table 1). After the aging for 6 h the values of the ultimate strength of the alloy exceeded the minimum level required by the GOST 1583–93 Standard. To determine rapidly the readiness of the melt for casting we suggest to estimate the microstructure and the ultimate strength of the alloy in cast condition with the help of a special nomogram (Fig. 4). To plot the nomogram, we prepared specimens for comparing the microstructures of alloy AK8M3ch and used statistical analysis to plot the dependence of the ultimate strength of the alloy in heat treated condition on the values of  $\sigma_r$  in cast condition (Fig. 4).

When the value of the ultimate strength of the alloy matches region I of the nomogram, the melt requires additional treatment. The kind of the additional treatment is determined by comparison of the

Table 1. Effect of the Hold Time in Aging on the Ultimate Strength of Alloy AK8M3ch Obtained by Different Processes

Melting process	Heating for hardening	Aging mode	$\sigma_r$ , MPa
Active	510 °C, 6 h (conventional)	160 °C, 12 h (conventional)	285–350
Novel*	510 °C, 6 h (conventional)	160 °C, 12 h (conventional)	410–430
	510 °C, 6 h (conventional)	160 °C, 6 h (shortened)	405–410

\* The melt was enriched with 20% remelted microcrystals.

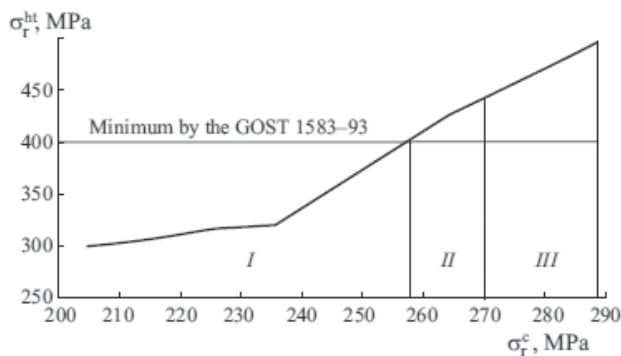


Fig. 4. Nomogram for rapid analysis of readiness of a melt of AK8M3ch for casting: *I*) the melt requires additional treatment; *II*, *III*) the melt is ready for casting;  $\sigma_r^c$  and  $\sigma_r^{ht}$  – ultimate strength of the alloy in cast and heat treated conditions respectively

actual microstructure of the alloy with the developed comparison specimens. In the case of the presence of gas or interdendrite shrinkage porosity on three analyzed areas of the lap, the melt should be subjected to additional degassing. If the transverse size of the secondary arms of the  $\alpha$ -Al dendrites exceeds 35  $\mu\text{m}$ , additional inoculation is required. If the values of  $\sigma_r$  in cast condition match region *II* of the nomogram, the melt does not require additional treatment and may be cast. The heat treatment of ready castings should be conducted according to the active specification. If the values of  $\sigma_r$  match region *III*, the melt is ready for casting, and the heat treatment of the ready castings may be conducted with a shorter aging hold.

## CONCLUSIONS

Theoretical and experimental studies have shown that the time of the hold of in some kinds of heat treatment of ready castings may be reduced depending on the parameters of the cast structure of copper silumins. The criterion for the estimation may be the ratio ( $R/r$ ), where  $R$  and  $r$  are the sizes of the crystals prior to and after the inoculation, respectively. The criterion is applicable for replacing a low-efficiency inoculant by an inoculant with elevated capacity for crystal refinement.

Castings produced from silumins of other groups or by other casting techniques require an additional study.

## REFERENCES

1. Nappi C. The Global Aluminum Industry 40 Years from 1972. World Aluminum, 2013. 27 p.
2. Napalkov V. I., Makhov S.V. Alloying and Inoculation of Aluminum and Magnesium [in Russian]. Moscow: MISiS, 2002. 37 p.
3. Brodova I.G., Popel P.S., Barbin N.M., Vatin N.A. Initial Melts as a Base for Formation of Structure and Properties of Aluminum Alloys [in Russian]. Ekaterinburg: UrORAN, 2005. 369 p.
4. Prigunova A.G. et al., in: Yu. N. Taran and V. S. Zolotarevskii (eds.), Silumins: an Atlas of Microstructures and Fractograms [in Russian]. Moscow: MISiS, 1996. 175 p.
5. Zolotarevskii V.S., Belov N.A. The Physical Metallurgy of Castable Aluminum Alloys [in Russian]. Moscow: MISiS, 2005. 376 p.
6. Belov N.A. Phase Composition of Commercial and Perspective Aluminum Alloys [in Russian]. Moscow: MISiS, 2005. 511 p.
7. Belov N.A., Savchenko S.V., Khvan A.V. Phase Composition and Structure of Silumins [in Russian]. Moscow: MISiS, 2008. 283 p.
8. Belov N.A., Savchenko S.V., Belov V.D. An Atlas of Microstructures of Commercial Silumins [in Russian]. Moscow: MISiS, 2009. 204 p.
9. Kutsova V.Z., Ayupova T.A. Effect of heat treatment on the structure and phase composition of inoculated alloy AK7ch, in: Construction Engineering, Materials Science, Machine Building [in Russian] // PGASiA, Dnepropetrovsk, 2008. Issue 42, Part 1. P. 10–17.
10. Volkov G.V. Effect of electrohydropulse treatment on structure formation of alloys and adaptability of subsequent operations to manufacturing // Liteinoe Proizvod. 2012, No. 9. P. 16–17.
11. Umanskii Ya.S., Skakov Yu.S. The Physics of Metals. Atomic Structure of Metals and Alloys [in Russian]. Moscow: Atomizdat, 1978. 352 p.

## ON THE INFLUENCE OF DEEP CRYOGENIC TREATMENT ON TEMPERING TRANSFORMATIONS IN AISI D2 STEELS

Massimo Pellizzari<sup>1</sup>, Vasco Menegante<sup>1</sup>, Matteo Villa<sup>2</sup>, Marcel A. J. Somers<sup>2</sup>

<sup>1</sup> University of Trento, Department of Industrial Engineering, Trento, Italy

<sup>2</sup> Technical University of Denmark, Department of Mechanical Engineering, Kongens Lyngby, Denmark  
massimo.pellizzari@unitn.it, vasco.menegante@studenti.unitn.it, matv@mek.dtu.dk, somers@mek.dtu.dk

The aim of this paper is to investigate the effect of deep cryogenic treatment (DCT) on the tempering behaviour of AISI D2 steel. Dilatometry samples were austenitized at 1030 °C for 30 min and thereafter quenched at 120 °C/min. One set of samples was isochronally tempered at a rate of 6 °C/min until 800 °C to distinguish four tempering stages: i. precipitation of transition carbides (RT–220 °C), ii. precipitation of cementite (220–350 °C), iii. decomposition of retained austenite (600–650 °C) and iv. precipitation of secondary alloy carbides (450–700 °C). In-situ Synchrotron X-Ray Diffraction (S-XRD) investigation of the same tempering cycle shows a reduction of the martensite tetragonality in stage i. In stage ii., retained austenite experiences a marked lattice expansion, which can be ascribed to relaxation of phase-specific compressive stresses (stresses of type II) that had built-up during quenching. Stages iii. and iv. start at approx. 450 °C with C depletion of retained austenite, as revealed by an anomalously low thermal expansion of the austenite lattice at  $T > 450$  °C, and continues with a further relaxation of the martensite structure starting at 540 °C. Simultaneously, austenite decomposes into ferrite and secondary alloy carbides, which is completed at 650 °C. The effect of DCT, carried out by immersion in boiling nitrogen and soaking at –196 °C for various times, can be summarized in a) a shift of transition carbide precipitation to higher temperature, b) a more pronounced volume reduction associated with precipitation of cementite and c) a less pronounced volume expansion associated with (partial) decomposition of RA. Very limited effects (if any) of storage time in boiling nitrogen (i.e. 5 min vs 29 h or 72 h) could be observed on dilatometry curves and on the structural parameters of austenite and martensite.

**Keywords:** tool steel; cryogenic treatment; retained austenite; dilatometry; differential scanning calorimetry; XRD; synchrotron.

### INTRODUCTION

Deep Cryogenic Treatment (DCT) of tool steel is considered an effective way to improve the life of tools and dies. The literature documents many application studies that report a dramatic improvement in wear resistance and mechanical properties after introducing low temperature soaking at boiling nitrogen temperature (–196 °C) of steels, in particular ledeburitic cold work tool steels like AISI D2 [1–3]. DCT has the largest impact when the steel microstructure comprises freshly formed (untempered) martensite, retained austenite and undissolved eutectic carbides. It should therefore be carried out immediately after quenching from the austenitization temperature. Then, the most evident and directly measurable effect of DCT is the transformation of (most of) retained austenite into martensite, causing a hardness increase [4]. Nevertheless, martensite formation alone cannot account for the positive effect of DCT on the performance. Consequently, less evident and controversial effects, challenging metallurgical principles, have been reported for the effect of DCT. It is the authors' opinion that a deeper metallurgical

understanding of the influence of DCT on the steel microstructure is of primary importance to enable targeted and reproducible performance.

The phase transformations occurring during tempering in plain carbon steel and in low- and medium alloyed steels have been described in the literature and comprise i) the precipitation of transition carbides from martensite, ii) the decomposition of retained austenite into ferrite and cementite and iii) the precipitation of cementite from transition carbides and segregated carbon [5]. Furthermore, pre-precipitation stages including C atom redistribution by segregation and clustering at low temperature (<100 °C) were reported. Segregation of C atoms to lattice defects and grain boundaries reduces the C content in solid solution in martensite. Clustering is a local enrichment of C atoms, which may act as a preferential nucleation site for transition carbide precipitation.

For highly alloyed steels, like ledeburitic cold work tool steels, the three classical stages are slightly modified, mostly because substitutional alloy elements (Cr, Mo and V) shift all transformations to higher temperature and lead to secondary carbide

precipitation at about 500–550 °C. Hence, cementite becomes a transition carbide that, after precipitation at low temperature, is replaced by secondary alloy carbides. The tempering sequence in these tool steels involves i) the precipitation of transition  $\epsilon$ -carbides from martensite [6], ii) the precipitation of cementite from transition carbides and segregated carbon, iii) the decomposition of retained austenite into ferrite and cementite [7] and iv) the precipitation of secondary carbides like  $M_7C_3$ ,  $M_{23}C_6$ , MC and  $M_2C$ , from Cr, V and Mo, respectively [6, 8]. All the above phase transformations can be conveniently, albeit indirectly, studied by combining differential scanning calorimetry and dilatometry [5, 9], considering that events accompanied by large enthalpy changes may correspond to small volume changes and vice versa. DCT has been shown to enhance the pre-precipitation step which leads to increased carbide precipitation from martensite during tempering [10, 11]. According to [11] it has been shown that longer DCT soaking times lead to a higher degree of transformation of RA into martensite, as well as more clustering and segregation of carbon, which promotes carbide precipitation.

The aim of this paper is to investigate the effect of DCT on the tempering behaviour of AISI D2 steel. Dilatometry, differential scanning calorimetry and in situ synchrotron X-Ray diffraction (S-XRD) were applied to study the influence of storage in liquid nitrogen for different times on the stages of tempering.

## MATERIALS AND EXPERIMENTAL PROCEDURES

A commercial AISI D2 cold work tool steel (1.55%C, 0.3%Si, 0.4%Mn, 11.3%Cr, 0.8%Mo, 0.8%V) was used for this research work.

Cylindrical samples ( $\varnothing 4$  mm, length 10 mm), were extracted by electro-discharge machining from a cylindrical bar ( $\varnothing 12$  mm) with main axis along the rolling direction. All heat treatments were carried out using a Bähr 805A/D dilatometer. Samples were austenitized at 1030 °C for 30 min followed by quenching (Q) at 120 °C/min. One set of samples was isochronally tempered at a rate of 6 °C/min until 800 °C to distinguish the four tempering stages. Three sets of samples were deep cryogenically treated immediately after quenching by immersion in boiling nitrogen (–196 °C) and soaked for 5 min (0 h), 29 h and 72 h (DCT0, DCT29 and DCT72). Final (rapid) heating to RT

was achieved by immersion of the samples in a beaker containing ethanol. Analogous to the Q samples, the DCT samples were isochronally tempered at a rate of 6 °C/min until 800 °C. Tempering started within 15 min after reaching RT, to avoid retained austenite stabilization. For all conditions, additional samples were isochronally tempered using a differential scanning calorimeter (model Perkin Elmer DSC7). Discs ( $\varnothing 4$  mm, 50–80 mg) were cut from quenched dilatometry samples with a precision micro-cutting machine with a mounted diamond blade. Lubrication and a very low feed rate were used to avoid any possible stress/strain-induced transformation of austenite. In view of the limited enthalpy change associated with phase transformations, two scans were carried out on each sample. Assuming that all phase transformations were completed after the first scan, the second curve was used for background subtraction from the first scan. The complete list of samples (dilatometry, DSC and S-XRD) and related symbols is reported in Table 1.

The fractions of retained austenite in the untempered Q and DCT samples was determined by XRD analysis using Co K $\alpha$  radiation. The measurements were performed in the  $2\theta$  range of 40°–110°, using a step size of 0.1° $2\theta$ , with a counting time per step of 5 s. The volume fraction of retained austenite was calculated by the Rietveld method using MAUD (Materials Analysis Using Diffraction) software. For microstructural analysis of these conditions scanning electron microscopy (SEM) was used after standard metallographic preparation, using emery papers and diamond paste. The 0.1 kg Vickers hardness was measured according to ASTM-E92.

Energy dispersive in situ Synchrotron X-Ray Diffraction (S-XRD) investigation of the same isochronal tempering cycle was performed several weeks after hardening at the synchrotron facility HZB-BESSY II at the experimental station EDDI [12]. Samples were 0.3 mm thick disks  $\varnothing 12$  mm. Austenitization (1030 °C, 30 min) was performed in a horizontal Kanthal tube furnace under a continuous Ar flow and was followed by quenching (average rate of ~25 °C/min,

*Правильно?*

Table 1. Heat and cryo treatments for the investigated samples

Sample code	HEAT and CRYO treatment			Hardness HV 0.1
	Quenching – Q		Deep Cryogenic Treatment – DCT	
Q	1030 °C	0.5 h	–	905±20
Q+DCT0	1030 °C	0.5 h	–196 °C for 5 min	911±5
Q+DCT29	1030 °C	0.5 h	–196 °C for 29 h	945±10
Q+DCT72	1030 °C	0.5 h	–196 °C for 72 h	952±13

~120 °C/min in the interval 550 °C–1030 °C). DCT consisted of immersion of the samples in boiling nitrogen, soaking at –196 °C for 72 h and re-heating to room temperature by immersion in water. DCT was performed immediately after quenching. Tempering was performed in an Anton Paar DHS 1100 Domed Hot Stage under Ar atmosphere (continuous flow, 1.4 bar). The samples were placed on the heating element (alumina plate) onto which they were secured by mild clamping. The temperature was measured with a Pt-Pt10Rh thermocouple fixed to the stage. Diffraction lines were fitted with pseudo-Voigt profile functions. The evolution of the fraction of retained austenite during tempering was evaluated from the relative intensity of the  $200_{\gamma}$ ,  $311_{\gamma}$  and the  $200_{\alpha}$ ,  $211_{\alpha}$  reflections for austenite and martensite, respectively. The relaxation of the martensite structure was evaluated based on the Integral breath  $\beta$  (and on the asymmetry, not presented here) of the  $200_{\alpha}$  reflection. The lattice parameter of austenite was evaluated from the positions of the  $200_{\gamma}$  and  $311_{\gamma}$  reflections on the energy scale. A gold reference standard was used for calibration of the absolute value of the lattice parameters.

## RESULTS AND DISCUSSION

### As quenched (Q) and cryo-treated (Q+DCT) samples

The microstructures of Q, Q+DCT0 and Q+DCT72 samples show a martensitic matrix containing a high fraction of Cr rich  $M_{7}C_{3}$  eutectic carbides (Figure 1). Due to the limited resolution, scanning electron microscopy cannot resolve the finest microstructural details regarding the influence of DCT. These are currently under investigation with transmission electron microscopy. According to thermodynamic calculations, the C content in austenite is 0.55 wt%, which would correspond to a mixture of  $\{557\}_{\gamma}$  lath and  $\{225\}_{\gamma}$  plate martensite forming below  $M_s$  (145 °C). Also, the formation of a very small

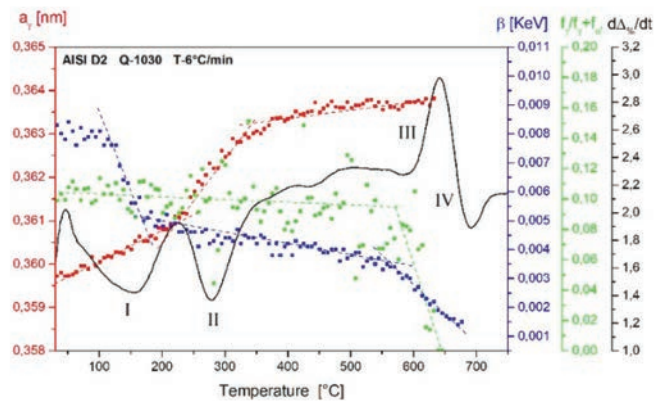


Fig. 2. Isochronal tempering diagram of Q sample: first derivative of dilatometry strain (black), integral breath of the  $200_{\alpha}$  martensite peak in S-XRD (blue), austenite fraction (green) and austenite lattice parameter (red)

amount of bainite was detected on the dilatometry diagram. Moreover, S-XRD revealed the presence of MC and  $M_{23}C_6$  carbides after hardening. The austenite content, determined by XRD, is about 12 vol.% in Q and decreases to about 4–5 vol.% after DCT. The hardness increases from 905 to a maximum of 952 HV 0.1 (Table 1).

*Проньск?*

### Tempered samples

The isochronal tempering behavior of Q is described in Fig. 2. The first derivative of the dilatometry strain (black curve) highlights four peaks that, consistent with literature, can be ascribed to the following transformations:

- precipitation of transition carbides (RT–220 °C)
- precipitation of cementite (220–350 °C)
- decomposition of retained austenite (600–650 °C) and
- precipitation of secondary alloy carbides (450–700 °C).

All precipitation reactions are accompanied by a volume contraction, while the decomposition of

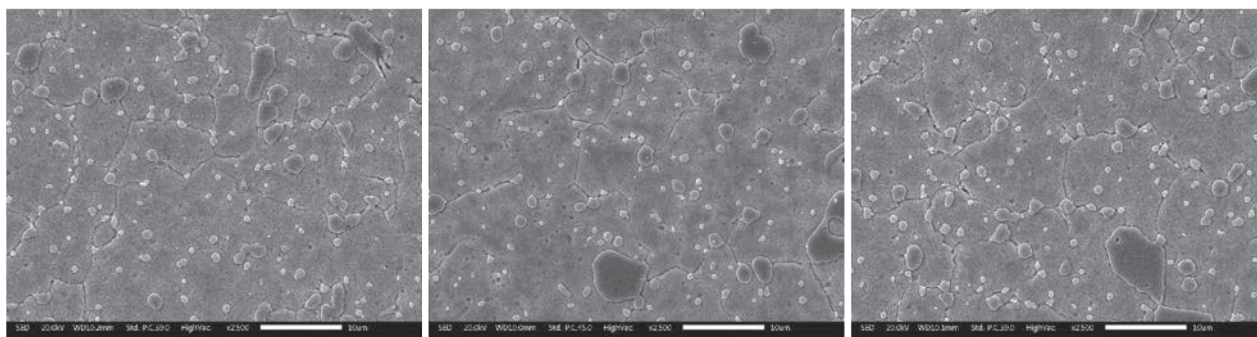


Fig. 1. Secondary electron images of the microstructure of Q, Q+DCT0 and Q+DCT72 (left to right)

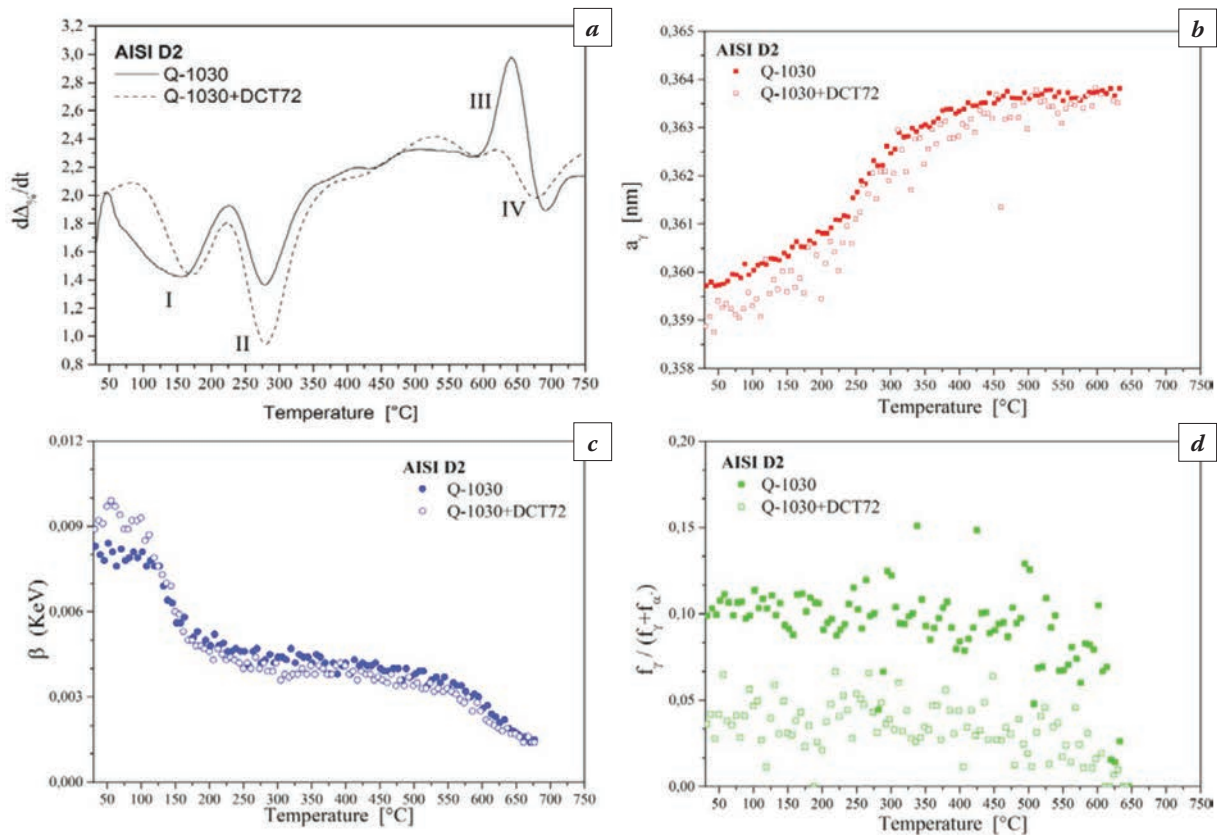


Fig. 3. Isochronal tempering diagram of Q-1030 and Q-1030+DCT72: *a* – first derivative of dilatometric strain, *b* – austenite lattice parameter, *c* – integral breath of the  $(200)\alpha'$  martensite peak and *d* – austenite fraction

retained austenite into ferrite and alloy element carbides leads to an expansion. In-situ S-XRD investigation of the same tempering cycle shows a relaxation of the martensite structure from tetragonal to cubic in stage I, as demonstrated by (not shown here) asymmetric-to-symmetric evolution of the martensite peaks, reflected by a marked reduction of the Integral breath of the  $200_{\alpha'}$  reflection (blue dots in Fig. 2). In stage II, retained austenite experiences a marked lattice expansion (red dots in Fig. 2), which can be ascribed to relaxation of phase specific compressive stresses in austenite (stresses of type II) that had built-up during martensite formation [13]. Conversely, in the temperature range 450 °C–650 °C, the austenite lattice (red dots in Fig. 2) shows an anomalously low coefficient of thermal expansion (CTE), which indicates that, concurrent with thermal expansion, a volume reduction occurs; perhaps by gradually reducing the C content. Note in this respect the small peaks on the dilatometry curve in-between II and III, suggesting precipitation reactions. Finally, on continuous heating, retained austenite (green dots in Fig. 2) decomposes into ferrite and secondary alloy carbides (stage III) at a slightly higher temperature and the reaction is completed at 650 °C. Eventually, a further relaxation

of the tempered martensite structure commences at 540 °C along with the precipitation of alloy carbides and the decomposition of retained austenite (stages III and IV).

Based on dilatometry, the following observations are made comparing Q and DCT72 (Fig. 3a):

CTE is slightly reduced after DCT72 as compared to Q, because more martensite is present;

– the onset of transition carbide precipitation in stage I is shifted to higher temperature after DCT72;

– the volume reduction associated with precipitation of cementite (stage II) from martensite is more pronounced;

– the volume expansion associated with (partial) decomposition of RA (stage III) is less pronounced.

Moreover, S-XRD on Q and DCT72 appears to evidence a systematically, albeit slightly, lower lattice parameter of retained austenite (indicating higher compressive stress) up to its decomposition temperature (Fig. 3b), a higher tetragonality of martensite (larger  $\beta$ ) before the completion of transition carbides precipitation (up to 120 °C, Fig. 3c) and a lower amount of austenite (Fig. 3d) for Q-DCT72 vs. Q.

Apart from the anticipated effects associated with a lower retained austenite fraction, the most striking

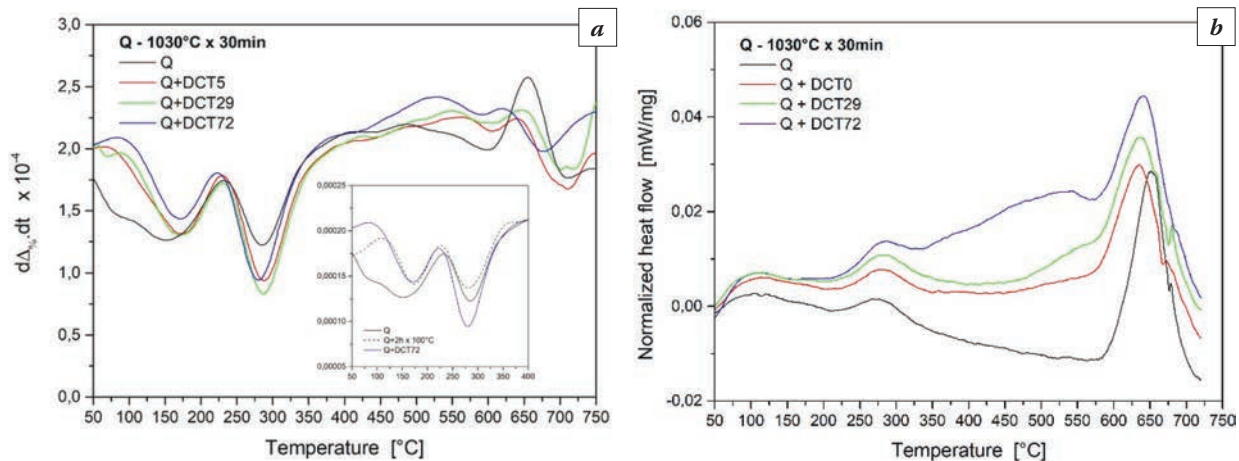


Fig. 4. Isochronal tempering diagram of Q and Q+DCTx samples: a) first derivative of dilatometric strain, b) DSC heat flow. Inset in Fig. 4a shows the dilatometric curve of a sample quenched and tempered for 2 h at 100 °C

result seems to be the shift of stage I to higher temperatures after DCT. In view of the higher content of martensite and structural defects introduced by DCT (i.e. dislocations), precipitation would be expected at least at the same temperature as for Q, most likely at a lower temperature. A more detailed view of the Q dilatometry signal suggests that peak I is the result of a two consecutive contractions and that the low temperature contribution disappears after DCT. To further investigate this effect, one sample was quenched and tempered at 100 °C for 2 h. Its dilatometry curve (inset in Fig. 4a) confirms that the contraction up to 100 °C is now lacking and that only the contribution above this temperature remains. In view of the almost perfect superimposition with the peak of Q+DCT72, it is concluded that low temperature transformation occurs during DCT. It is anticipated that the contraction below 100 °C is due to a pre-precipitation stage and, in particular, to the segregation of carbon atoms to lattice defects, because clustering does not cause a significant volume decrease [14]. This is in agreement with the large amount of dislocations introduced in lath martensite by DCT [15]. On the other hand, the higher intensity of the cementite precipitation peak and the sheer disappearance of the austenite decomposition in Q+DCTx samples are directly related to the martensitic transformation at low temperature.

In relation to the soaking time at −196 °C, dilatometry curves suggest that the time of storage in boiling nitrogen (i.e. 5 min, 29 h or 72 h) has a limited effect, if at all, on the tempering behaviour of AISI D2 (Fig. 4a). In fact, the same conclusions drawn for Q+DCT72 (points a-b) can be extended to DCT0 and DCT29. Nevertheless, a systematic increase in CTE in the temperature interval 450–550 °C with longer soaking time is observed along with shifts of the small peaks in this temperature range. This sug-

gests a modification of the precipitation reactions with soaking time. Further investigation is needed to clarify the origins of these peaks.

DSC curves (Fig. 4b), displaying the enthalpy changes related to the various phase transformations, show a marked influence of DCT and the soaking time at −196 °C. After prolonged storage time in LN the signals become more and more exothermic (curves are rotated anticlockwise), particularly at higher temperature. Considering that these are subtracted curves, this effect can be interpreted with a lower exothermic contribution during the second run: in other words, due to the slower kinetics of transformations occurring at higher T and the limited time available during isochronal tempering, transformations cannot complete during the first run and do it during the second one [16]. Prolonged DCT appears to improve the transformations during the first tempering. This effect appears to be active from low temperature: the first exothermic shoulder observed below 100 °C, corresponding to C clustering [5] is enhanced by DCT. Apparently, in the temperature range of transition carbide precipitation (80–220 °C) no peak is observed in DSC: this is plausibly due to the relatively low enthalpy change associated to this precipitation and the partial overlap with clustering at lower temperature and with cementite precipitation at higher temperature. Cementite precipitation (peak II) is enhanced by DCT, in agreement with dilatometry. Because of the strong overlap, the peaks related to retained austenite decomposition (peak III) and secondary carbide precipitation (peak IV) cannot be distinguished easily. Along with the higher amount of retained austenite in Q, a stronger exothermic peak could be expected. On the other hand, the crystallographic parameters of martensite and retained austenite (Fig. 3) do not provide evidence for structural

differences to justify such a different behaviour for Q and Q+DCTx samples. New DSC measurements are ongoing to further investigate these effects.

## CONCLUSIONS

The influence of DCT on the phase transformations occurring during tempering of AISI D2 was investigated. Independently from the storage time in LN (5 min, 29 h and 72 h), DCT causes the partial transformation of retained austenite and a hardness increase. Furthermore, the coefficient of thermal expansion is reduced as compared to the quenched material and the volume expansion associated with decomposition of RA is less pronounced, because more martensite is present. For the same reason, the volume contraction due to cementite precipitation from martensite is more pronounced. A final important effect of DCT is the shift of the onset of transition carbide precipitation to higher temperature. Preliminary results confirm that storage in LN leads to the disappearance of a volume effect below 100 °C on tempering, which would imply that segregation of carbon to lattice defects has occurred prior to tempering. DSC indicated an effect of the storage time at -196 °C during DCT on the kinetics of the precipitation reactions in-between stages II and III.

## REFERENCES

1. **Carlson E.A.** Cold treating and cryogenic treatment of steel, ASM Handbook 4, ASM International / Metals Park, Ohio, 1991. P. 203–206.
2. **Pellizzari M., Molinari A.** Deep cryogenic treatment of cold work tool steel. 6th Int. Tooling Conference. 2002 Sept. 10–13; Karlstad, Sweden; 2002. P. 547–557.
3. **Collins D.N., Dormer J.** Deep cryogenic treatment of a D2 cold-work tool steel // *Heat Treat. Met.* 1997; 3:71.
4. **Collins D.N.** Deep cryogenic treatment of tool steels: a review // *Heat Treat. Met.* 1996; 23:40–42.
5. **Cheng L., Brakman C.M., Böttger H., Korevaar B.M., Mittemeijer E.J.** The tempering of Iron-Carbon martensite; Dilatometric and Calorimetric Analysis // *Met. Trans. A.* 1988; 19A:2415–2426.
6. **Gavriljuk, Sirosh V.A., Petrov Y.N., Tyshchenko A.I., Theisen W., Kortmann A.** Carbide precipitation during tempering of a tool steel subjected to deep cryogenic treatment // *Metall. Mater. Trans.* 2014; A45:2453–2465.
7. **Kokosza A., Pacyna J.** Evaluation of retained austenite stability in heat treated cold work tool steel // *J. Mater. Process. Technol.* 2005; 162–163:327–331.
8. **Bala P., Pacyna J., Krawczyk J.** The influence of the kinetics of phase transformations during tempering on the structure development in a high carbon steel // *Arch. Metall. Mater.* 2007; 52:113–120.
9. **Morra P.V., Bottger A.J., Mittemeijer E.J.** Decomposition of iron based martensite. A kinetic analysis by means of differential scanning calorimetry and dilatometry // *J Therm Anal Cal.* 2001; 64:905–914.
10. **Villa M., Pantleon K., Somers M.A.J.** Enhanced carbide precipitation during tempering of sub-zero Celsius treated AISI 52100 bearing steel / *Proceedings of the heat & surface engineering conference and expo, Chennai, 2013.*
11. **Preciado M., Pellizzari M.** Influence of deep cryogenic treatment on the thermal decomposition of Fe-C martensite // *J Mater Sci.* 2014; 49:8183–8191.
12. **Genzel C., Denks I.A., Klaus M.** The materials science beamline EDDI for energy-dispersive analysis of subsurface residual stress gradients // *Mater. Sci. Forum.* 2006; 524–525:193–198.
13. **Villa M., Pantleon K., Somers M.A.J.** Evolution of compressive strains in retained austenite during sub-zero Celsius martensite formation and tempering // *Acta Mater.* 2014; 65:383–392.
14. **Van Genderen M.J., Isav M., Böttger A., Mittemeijer E.J.** Aging and Tempering Behavior of Iron-Nickel-Carbon and Iron-Carbon Martensite // *Met. Trans. A.* 1997; 28A:545–561.
15. **Kelkar R., Nash P., Zhu Y.** The mechanism of property enhancement in M2 tool steel by cryogenic treatment. 45th MWSP Conference Proceedings. 2003. P. 13–19.
16. **Menegante V.** Master degree thesis, University of Trento, AY 2018–2019.

## DEVELOPMENT OF THE COMPLEX TECHNOLOGIES BASIS FOR PRODUCTION OF A NEW COLD-ROLLED LOW-CARBON AND ULTRA-LOW-CARBON STEELS GENERATION WITH IMPROVED COMPLEX PROPERTIES

A.I. Zaitsev<sup>1a</sup>, S.V. Denisov<sup>2</sup>, V.E. Telegin<sup>2</sup>, A.V. Koldaev<sup>1b</sup>, I.G. Rodionova<sup>1</sup>, A.B. Stepanov<sup>1</sup>

<sup>1</sup> I.P. Bardin Central Research Institute of Ferrous Metallurgy (TsNIIchermet). Moscow, Russia

<sup>2</sup> PJSC Magnitogorsk Iron and Steel Works (MMK). Magnitogorsk, Russia

<sup>a</sup> aizaitsev1@yandex.ru, <sup>b</sup> koldaevanton@gmail.com

The original principles of achieving a complex of high service properties, quality characteristics of cold-rolled low-carbon 08U and ultra-low-carbon IF, IF-HS automotive steels based not on the traditional method to achieve the lowest degree of impurities, interstitial elements, but on giving them a favorable form of existence. A series of experimental laboratory heats was carried out and rolled steel sheets were produced from low-carbon 08U and ultra-low-carbon IF, IF-HS steels. The achievement of high and stable indicators of strength, yieldability, formability, corrosion resistance and other properties is confirmed.

**Keywords:** low-carbon 08U steel; ultra-low-carbon IF, IF-HS steel; cold-rolled steel; hot galvanized steel; strength; yieldability; formability; corrosion resistance; impurities; interstitial elements; manufacturing practice.

Modernization of existing and, especially, creation of new effective technological items in the developing automotive industry, high-speed railway transport, building and construction, other industries makes it necessary to manufacture elements and assemblies of increasingly complex shape by progressive methods of stamping. However, usually used for these purposes cold-rolled, including coated, low-carbon and ultra-low-carbon steels have insufficient yieldability and formability, which makes it impossible to obtain stamped products of complex shape. There are cracks, other defects on the metal surface, often even when the stamping products have a relatively simple form, which involves significant damage, complexity or inability to improve the design, technical characteristics of new high-speed vehicles, equipment, structures, etc.

Another equally important characteristic of cold rolled low-carbon and ultra-low-carbon steels is their corrosion resistance. There are no requirements for it until now. As a result, on the surface of rolled products, including foreign manufactured one, in a short period of time, sometimes less than necessary for its transportation to the place of processing, there are traces of cosmetic and/or even perforating corrosion. The use of metal, polymer and other types of protective coatings does not allow to solve the formulated problem and, in many cases, is not advisable consid-

ering technical and economic reasons. In addition, factors that reduce the corrosion resistance of steel often lead to a significant decrease in the adhesion of protective coatings applied to its surface. The noted circumstances, especially in difficult environmental and climatic conditions of Russia, lead to a significant reduction in the efficiency and service life of various technological items.

Finally, an important factor that has a negative impact on the competitive ability of the products is associated with the relatively high cost of low-carbon and ultra-low-carbon steels, due to the insufficient level of their production technologies. In particular, the need for the use of pure charge materials, low efficiency of expensive micro-alloying components using, the lack of scientific approaches and effective technological methods, in a single unified sequence of metal processing stages, the practice of obtaining different strength classes steel with high levels of other service properties from cold-rolled products of ultra-low-carbon steels of one chemical composition.

In accordance with the noted circumstances, one of the most important and up-to-date problems is the creation of effective technologies for the production of a new generation of cold-rolled (including coated) low-carbon and ultra-low-carbon steels with fundamentally improved yieldability, formability, corrosion resistance (the relative elongation of 50–60%, the co-

efficient of normal plastic anisotropy,  $r = 2.2-2.5$ , the coefficient of deformation hardening,  $n = 0.24-0.26$ , the resistant against local corrosion) with the expansion of the raw material

base, reducing costs. The achievement of the stated technical parameters of the manufactured rolled products will allow the manufacturing of forged metal products of complex shape that are widely demanded by the manufacturers of transport and other engineering, building and construction industry.

The solution of this problem is extremely difficult, requires the development and use of fundamentally new, unparalleled, scientific, technical and technological solutions. First of all, the achievement of high service properties complex, quality characteristics of cold-rolled low-carbon 08U and ultra-low-carbon IF, IF-HS automotive steels based not on the traditional method to achieve the lowest degree of impurities, interstitial elements, but on giving them a favorable form of existence. According to the results of theoretical and experimental studies of a large number of laboratory and industrial metal samples, it was found that the implementation of the formulated progressive approach should be based on the creation and use of adequate forecasting methods and effective technological methods for controlling the structural state, non-metallic inclusions, forms of the impurities presence, phase precipitates, including nanoscale at all stages of steel production. For this purpose, an integrated prediction approach, phase composition analysis, structural state and properties of steel [1], including:

- physico-chemical, kinetic prediction of the formation conditions of nonmetallic inclusions, phase precipitates, and the forms of impurities presence,
- electron microscopic study of their characteristics,
- determination of the interstitial elements content in solid solution by internal friction.
- integrated tests of mechanical and other properties of steel,
- physical and chemical analysis of the results with the establishment of the composition, process parameters influence on the rolled products properties.

The main advantage of this approach is the ability to:

- establishment of optimal steel production technological parameters for given

Table 1. Chemical composition of experimental steels, wt.%

№	C	Si	Mn	P	S	Cr	Ni	Al	Ti	N	Nb	B
1	0.004	0.024	0.12	0.009	0.006	0.03	0.01	0.04	0.065	0.004	–	–
2	0.004	0.02	0.18	0.008	0.005	0.03	0.02	0.045	0.052	0.006	0.003	0.0003
3	0.004	0.017	0.41	0.037	0.004	0.03	0.02	0.057	0.031	0.006	0.04	0.0003

chemical composition, providing the highest and most stable complex of properties;

- production of different strength and drawing categories rolled products from steel of equal chemical composition;

- determination of the most efficient alloying systems, schemes of production for producing steels with the specified properties.

Its even more important advantage is detailed scientific principles allowing not only to make the most effective the development of new and improvement of existing steels and their production technologies with minimal cost, but also to reveal the essence, direction and intensity of the processes and phenomena occurring in the processing of metal. This can be illustrated by the example of ultra-low carbon microalloyed (stabilized) titanium steels. Their high rates of yieldability, formability are achieved by complete binding of the interstitial elements– carbon and nitrogen, which occur in solid solution, in stable carbonytride and other types of phase presipitates. Prediction of the conditions of their formation, as a rule, is made using empirical relationships or thermodynamic methods for calculating the phase composition of steel [2]. In particular, the calculation results for steel composition №1 (Table 1) are shown in Fig. 1.

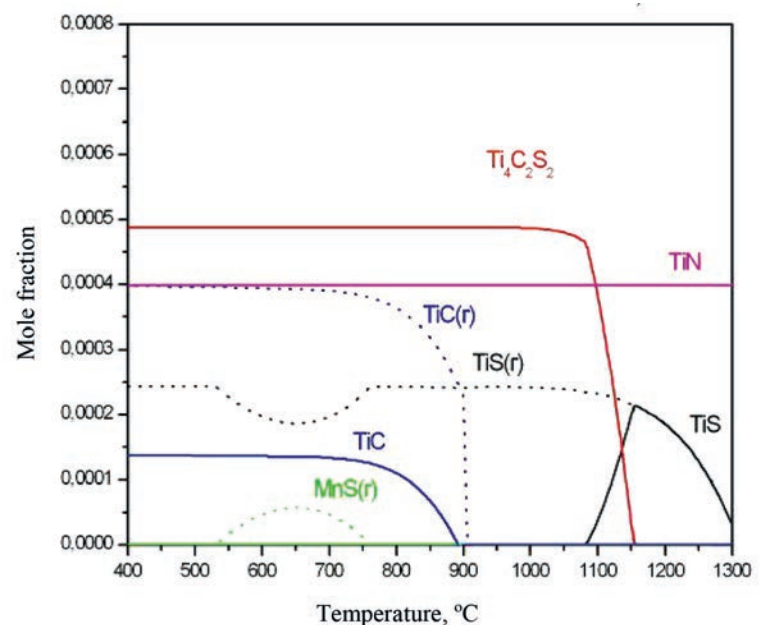


Fig. 1. The temperature dependence of the mole fractions of all possible phase precipitates in the investigated steel

As can be seen from the data in figure 1, the main types of phase precipitates in the investigated steel are TiN, TiS,  $Ti_4C_2S_2$ , and TiC. The temperature dependences of their molar fractions shown by solid lines are found from thermodynamic equilibrium condition. However, from the results of a wide range of experimental studies it was found that as a rule thermodynamic equilibrium is not achieved during hot rolling of steel. This can lead to a change not only in the quantity but also in the types and sizes of the present phase precipitates. In particular, as can be seen from the data in figure 1, if the transformation of TiS to  $Ti_4C_2S_2$  does not have enough time to finish, it becomes possible to form MnS precipitates and the amount of TiS precipitates increases. At the same time, a significant amount of TiS secretions remains in the steel. The change in the characteristics of phase precipitates leads to a change in the structural state and properties of steel. The use of the complex approach formulated above allows not only to reveal the reason of such changes, but also to develop effective technological methods of its correction.

This circumstance is used to unify the chemical composition of steel or the development of so-called cassette technologies for the rolled products manufacturing of different grade and/or categories of strength, drawing from steels of the equal composition. In particular, the results of the study of steel compositions №№ 1, 2 (Table 1) showed the following. On the basis of a reasonable choice of parameters of hot, cold rolling and recrystallization annealing in units of periodic (bell furnaces) and continuous operation, it is possible to create a technology for the production of cold-rolled and hot-galvanized steel, both with a low yield point (less than 140–170 MPa) and a strength class 180. High values of elongation (more than 50%) are contemporary achieved. From steel composition №3 obtained cold-rolled steel sheet with thickness of 0,6 mm meets the requirements for rolling strength classes 180 and 220, with high values of elongation. These circumstances show a high reasonability of establishing a cluster of technologies for the manufacturing of cold-rolled products annealed in bell-type furnaces with different classes of strength, improved yieldability and formability from IF, IF-HS steels of the equal composition. At the same time, it was found that the processes of phosphorus segregation along the grain boundaries can be neglected in the development of annealing modes in bell-type furnaces of cold-rolled steel from IF steels. The highest rates of elongation were obtained for cold rolled products, hot rolled products for which were produced using high degrees of compression at the final stage of hot rolling. This leads to a more

intensive grain refinement with obtaining of a homogeneous structure and the formation of phase precipitates. High values of yield strength and elongation confirms this conclusion. Steel sheets with thickness of 0.8, 1.0 mm obtained from steel composition №1 (Table 1), almost meets the requirements for rolling strength class 180, with a elongation more than 50%.

Achieving of a high complex performance (strength characteristics, yieldability, formability) of rolled products is confirmed by the results of metallographic investigation of its structure after simulated annealing in bell-type furnaces. In all cases, a homogeneous ferritic microstructure was obtained.

According to the results of detailed studies, it is clearly established that obtaining of high performance complex of cold-rolled steel, including coated steel, is depend on every stages of steel processing. Moreover, the processes occurring in their implementation are interrelated. In steelmaking, first, it is important to obtain a given chemical composition of the characteristics of non-metallic inclusions, which can subsequent evolve.

It is established that the corrosion resistance of cold-rolled steel of low-carbon 08U and IF, IF-HS steels is primarily determined by the presence of corrosion-active non-metallic inclusions based on aluminum spinel. Their content naturally increases with an increase in the concentration of aluminum, regardless of the type and composition of steel (Fig. 2), as well as the content of MgO in the cover slag is more than 10.5–12.5 wt.%. They acquire corrosion activity due to the deposition of MnS and other sulfide phases on the surface.

On the other hand, the formation of complex non-metallic inclusions on the basis of aluminum-magnesium spinel with sulfide deposition, as well as MnS precipitates can be the basis for the subsequent deposition of cementite [3] (Fig. 3). This fact in conjunction with the controlled deposition capability of

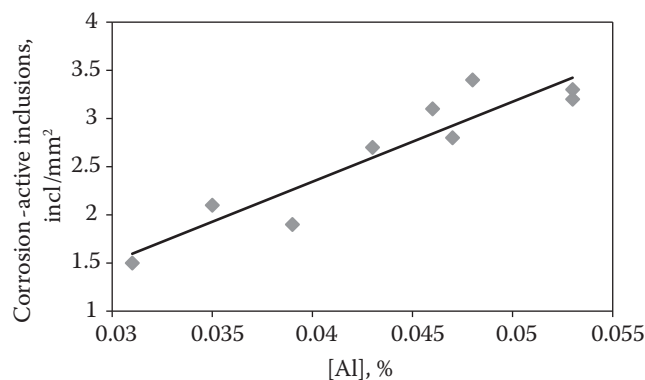


Fig. 2. Dependence of the aluminium concentration on the corrosion-active non-metallic inclusions content in rolled low carbon steel 08U and IF, IF-HS

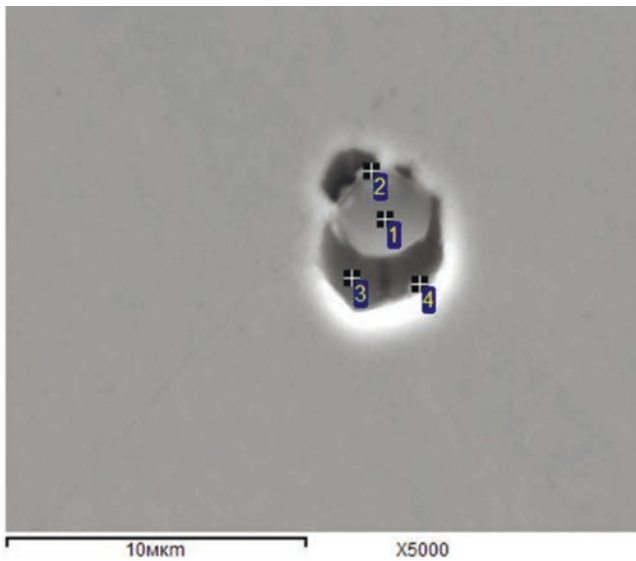


Fig. 3. Cementite precipitate on the surface of complex non-metallic inclusion of MnS and aluminum spinel (1 – MnS, 2 – aluminum spinel, 3, 4 – cementite)

aluminum nitride on the surface of manganese sulfide is a key technique of significantly increase the yieldability and formability of low-carbon steel 08U. In this case, they can be used instead of much more expensive IF steels.

It was found that the key parameters controlling the complex of high performance properties and quality of cold-rolled products, including coated, is the homogeneity of the microstructure, as well as the completeness of the solid solution purification from the interstitial elements. This is promoted by reduced heating temperature of the billet before rolling, finishing temperature of rolling in the range 880–900 °C, high coiling temperature 710–730 °C.

It is shown that the degree of deformation during temper rollong should be limited by the level of 0.7% to ensure high yieldability and formability of ultra-low-carbon steels. Its further increase leads to a significant increase in the yield strength. For low-carbon steels of 08U minimum values of the yield strength in the absence of the yield line on the stress-

strain curve were observed at the degree of deformation equal to 0,8%.

Using the formulated principles and approaches, a series of experimental laboratory melting and rolling of low-carbon 08U and ultra-low-carbon type IF, IF-HS steels were conducted. The achievement of high and stable levels of yieldability, strength, formability and other properties is confirmed. The results of tests of rolled products of low-carbon type 08U and ultra-low-carbon type IF, IF-HS steels indicate that the achieved level of yieldability and formability up to 10–15% higher than the best analogues. For IF-steels rolled products, including high carbon (about 0.06%) and impurities content, high ductility (880–54–55%), formability, exceeding the characteristics of analogues, were achieved. Corrosion resistance of the developed steels up to 2–3 times higher than the characteristics of the best analogues are obtained by providing a low content of inclusions based on aluminum spinel with a significant content of the sulfide component.

*Правильно?*

*The study was carried out by an agreement on subsidy (project No. 075-11-2018-170, 26.11.2018). Unique identifier of the project RFMEFI62418X0050.*

## REFERENCES

1. Zaitsev A.I. Prospective directions for development of metallurgy and materials science of steel // Pure and Applied Chemistry. 2017. Vol. 89, No. 10. P. 1553–1565.
2. Zaitsev A.I., Rodionova I.G., Pavlov A.A., Shaposhnikov N.G., Grishin A.V. Effect of composition, structural state, and manufacturing technology on service properties of high-strength Low-carbon steel main bimetal layer // Metallurgist. 2015. Vol. 59, No. 7. P. 684–692.
3. Zaitsev A.I., Stepanov A.B., Karamysheva N.A., Rodionova I.G. Advancement of the properties of structural steels by creating an optimum form of existence of impurities and nonmetallic inclusions // Metal Science and Heat Treatment. 2016. Vol. 57, No. 9. P. 531–538.

# DEEP CRYOGENIC TREATMENT OF HIGH SPEED STEELS

Patricia Jovičević Klug<sup>1,2</sup>, Bojan Podgornik<sup>1</sup>

E-mail  
нужен???

<sup>1</sup>Institute of Metals and Technology. Ljubljana, Slovenia

<sup>2</sup>Jožef Stefan International Postgraduate School. Ljubljana, Slovenia

High speed steels (HSS) are commonly used for punches, broaches, drills, milling cutters, tool bits, gear cutters, saw blades, jointer and planer blades, etc. [1, 2]. Barron [3] recognized that cryogenic treatment improves properties of cutting tool steels (HSS). Special type of cryogenic treatment is deep cryogenic treatment (DCT). DCT is a type of cryogenic treatment, where material is subjected to temperatures below  $-150\text{ }^{\circ}\text{C}$ , normally to temperatures of liquid nitrogen ( $-196\text{ }^{\circ}\text{C}$ ) [3–7]. Sub-zero treatment causes changes in microstructure, which are induced due to formation of new grains, changes in grain size, movement of dislocations, alteration of crystal structure, change of solubility of atoms, and lastly the new phase formation. The performance of HSS and later of produced tools are subject to selection of HSS type (main alloying elements), proper design, tool manufacturing accuracy and application of proper heat treatment, including DCT [7]. Representatives of high speed steels treated by DCT found in the literature are 1.0044 [8], 1.0338 [9–14] performance of cryogenically treated M35 high speed steel (HSS), 1.3207 [15], 1.3242 [16, 17], 1.3243 [18, 19], 1.3247 [20], 1.3255 [20], 1.3355 [20], 1.3343 [19, 21–27] there are issues debated upon, in respect of the treatment parameters, extent of benefits experienced in different materials, underlying mechanism and pretreatment conditions. A study on the improvement in wear resistance and the significance of treatment parameters in different materials has been made. It is found that cryogenic treatment imparts nearly 110% improvement in tool life. It is even superior to TiN coatings. The underlying mechanism is essentially an isothermal process. The microstructure and tempering response of Cr-V ledeburitic steel Vanadis 6 subjected to sub-zero treatment at  $-196\text{ }^{\circ}\text{C}$  for 4 h have been examined with reference to the same steel after conventional heat treatment. The obtained experimental results infer that sub-zero treatment significantly reduces the retained austenite amount, makes an overall refinement of microstructure, and induces a significant increase in the number and population density of small globular carbides with a size 100–500 nm. At low tempering temperatures, the transient M3C-carbides precipitated, whereas their number was enhanced by sub-zero treatment. The presence of chromium-based M7C3 precipitates was evidenced after tempering at the temperature of normal secondary hardening; this phase was detected along with the M3C. Tempering above  $470\text{ }^{\circ}\text{C}$  converts almost all the retained austenite in conventionally quenched specimens while the transformation of retained austenite is rather accelerated in sub-zero treated material. As a result of tempering, a decrease in the population density of small globular carbides was recorded; however, the number of these particles retained much higher in sub-zero treated steel. Elevated hardness of sub-zero treated steel can be referred to more completed martensitic transformation and enhanced number of small globular carbides; this state is retained up to a tempering temperature of around  $500\text{ }^{\circ}\text{C}$  in certain extent. Correspondingly, lower as-tempered hardness of sub-zero treated steel tempered above  $500\text{ }^{\circ}\text{C}$  is referred to much lower contribution of the transformation of retained austenite, and to an expectedly lower amount of precipitated alloy carbides."

In this study, a systematical approach in DCT of selected HSS (1.3243, 1.3343 and 1.3395) has been performed. To provide the representative results also one hot work tool steel (1.2367) and one martensitic stainless steel (1.4057) were selected for the same treatment. Additional steels were chosen with regards to martensite start temperature ( $M_s$ ), to be comparable to selected HSS. This research is focused on induced changes in microstructure and resulting properties including hardness, strength, fracture toughness, bending fatigue strength and wear resistance. Thus it provides one of the first systematical approach studies in dealing with DCT of HSS.

**Keywords:** deep cryogenic treatment (DCT); high speed steels (HSS); martensite start temperature ( $M_s$ ); hardness, toughness, wear resistance.

## REFERENCES

1. Roberts G., Krauss G., Kennedy R. Tool Steels, 5th edition, ASM International. 1998.
2. da Silva F.J., Franco S.D., Machado Á.R., Ezugwu E.O., Souza A.M. Performance of cryogenically treated HSS tools. *Wear*. 2006; 261(5–6):674–85.
3. Barron R.F. Do treatment at temperature below  $-120\text{ }^{\circ}\text{F}$  help increase the wear resistance of tool steels? Here are some research findings that indicate they do // *Heat Treating*. 1974; 5(14):14–7.
4. Iacopi F., Choi J.H., Terashima K., Rice P.M., Dubois G. Cryogenic plasmas for controlled processing

of nanoporous materials // *Physical Chemistry Chemical Physics*. 2011; 13(9):3634–7.

5. Dumasia C.A., Kulkarni V.A., Sonar K. A Review on the Effect of Cryogenic Treatment on Metals // *International Research Journal of Engineering and Technology* [Internet]. 2017; 4(7): 2402–6. Available from: <https://irjet.net/archives/V4/i7/IRJET-V4I7490.pdf>
6. Prudhvi K., Lakshmi V.V. Cryogenic Tool Treatment. 2016; 9(9):1204–11.
7. Podgornik B., Paulin I., Zajec B., Jacobson S., Leskovšek V. Deep cryogenic treatment of tool steels // *Journal of Materials Processing Technology*. 2016; 229: 398–406.

8. **Pradeep A.V., Satya Prasad S.V., Suryam L.V., Kesava Rao Y., Kesava D.** Effect of Cryogenic Treatment on Tool Life of HSS Tool (S400) and Surface Finish of the Material in Turning of SS304. IOP Conference Series: Materials Science and Engineering. 2016; 149(1).
9. **Çiçek A., Klvak T., Uygur I., Ekici E., Turgut Y.** Performance of cryogenically treated M35 HSS drills in drilling of austenitic stainless steels // International Journal of Advanced Manufacturing Technology. 2012; 60(1–4): 65–73.
10. **Suresh A.R., Rajendran I.** Investigations on Deep Cryogenically Treated Low Alloy Steel Impregnated with WS2. Materials Today: Proceedings [Internet]. 2018; 5(2): 6736–45. Available from: <https://doi.org/10.1016/j.matpr.2017.11.332>.
11. **Surberg C.H., Stratton P., Lingenhölle E.** The influence of cold treatment on case-hardened steel // Heat Treating Progress. 2008; 8(2): 45–8.
12. **Bensely A., Senthilkumar D., Mohan Lal D., Nagarajan G., Rajadurai A.** Effect of cryogenic treatment on tensile behavior of case carburized steel-815M17 // Materials Characterization. 2007; 58(5): 485–91.
13. **Ciski A., Babul T., Duchek M.** Sub-zero treatments of case-carburized 18CrNiMo7-6 steel. In: 9th Youth Symposium on Experimental Solid Mechanics. 2010. P. 108–11.
14. **Senthilkumar D.** Influence of deep cryogenic treatment on hardness and toughness of En31 steel Influence of deep cryogenic treatment on hardness and toughness of En31 steel. Advances in Materials and Processing Technologies [Internet]. 2018; 00(00): 1–9. Available from: <https://doi.org/10.1080/2374068X.2018.1530426>.
15. **Dhokey N.B., Hake A.R.** Instability in wear mechanism and its relevance to microstructural features in cryotreated T42. Tribology – Materials, Surfaces & Interfaces [Internet]. 2013; 7(4): 193–200. Available from: <http://www.tandfonline.com/doi/full/10.1179/1751584X13Y.0000000047>.
16. **Dhokey N.B., Dandawate J.V., Rawat R., Dhokey N.B., Dandawate J.V., Rawat R.** Effect of Cryo-soaking Time on Transition in Wear Mechanism of M2 Tool Steel. ISRN Tribology [Internet]. 2013; 2013: 1–6. Available from: <http://www.hindawi.com/journals/isrn.tribology/2013/408016/>
17. **Dhokey N.B., Hake A., Kadu S., Bhoskar I., Dey G.K.** Influence of cryoprocessing on mechanism of carbide development in cobalt-bearing high-speed steel (M35) // Metallurgical and Materials Transactions A: Physical Metallurgy and Materials Science. 2014; 45(3):1508–16.
18. **Alava L.A., Artola G., Guinea I., Muro M.** On the Influence of Cryogenic Steps on Heat Treatment Processes // Materials Performance and Characterization [Internet]. 2017; 6(5): 837–49. Available from: <http://www.astm.org/doiLink.cgi?MPC20170017>.
19. **Pellizzari M.** Influence of deep cryogenic treatment on the properties of conventional and PM high speed steels // Metallurgia Italiana. 2008; 100(8): 17–22.
20. **Shanmugam K., Pathak S.D.** Study on the effect of cryogenic treatment of T1, T4 and M42 high-speed steels // Indian Journal of Science and Technology. 2016; 9(41): 7–10.
21. **Mohan Lal D., Renganarayanan S., Kalanidhi A.** Cryogenic treatment to augment wear resistance of tool and die steels // Cryogenics. 2001; 41(3): 149–55.
22. **Zurecki Z.** Cryogenic Quenching of Steel Revisited: Air Products and Chemicals, Inc. 2005; 1–9.
23. **Jurčí P., Dománková M., Ptačinová J., Pašák M., Kusý M., Priknerová P.** Investigation of the Microstructural Changes and Hardness Variations of Sub-Zero Treated Cr-V Ledeburitic Tool Steel Due to the Tempering Treatment // Journal of Materials Engineering and Performance. 2018; 27(4): 1514–29.
24. **Surberg C.H., Stratton P., Lingenhölle K.** Effect of deep cold treatment on two case hardening steels // Acta Metallurgica Sinica (English Letters). 2008; 21(1): 1–7.
25. **Hradil D., Duchek M., Hrbáčková T., Ciski A.** Gas Nitriding With Deep Cryogenic Treatment of High-Speed Steel // Acta Metallurgica Slovaca [Internet]. 2018; 24(2): 187. Available from: <http://www.qip-journal.eu/index.php/ams/article/view/1058>.
26. **Huang J.Y., Zhu Y.T., Liao X.Z., Beyerlein I.J., Bourke M.A., Mitchell T.E.** Microstructure of cryogenic treated M2 tool steel // Materials Science and Engineering A. 2003; 339(1–2): 241–4.
27. **Somers M.A.J., Christiansen T.L.** Low temperature gaseous surface hardening of stainless steel // Thermochemical Surface Engineering of Steels. 2015; 171(11):52–23.
28. **Jaswin A., Dhasan M.L.** Effect of Cryogenic Treatment on Corrosion Resistance and Thermal Expansion of Valve Steels // International Journal of Engineering Technology, Management and Applied Sciences. 2015; 3(3): 2349–4476.
29. **Senthilkumar D., Rajendran I.** Influence of Shallow and Deep Cryogenic Treatment on Tribological Behavior of En 19 Steel // Journal of Iron and Steel Research International. 2011; 18(9): 53–9.
30. **Levine M., White C.** Material damping experiments at cryogenic temperatures // Optical Materials and Structures Technologies. 2003; 5179: 165–76.

# CORRELATION BETWEEN MECHANICAL AND ACOUSTIC PROPERTIES OF LOW-CARBON STEEL AFTER STATIC TEST

A.V. Levina, V.P. Levin, L.R. Botvina

Baikov Institute of Metallurgy and Materials Science, RAS, Moscow, Russia

nas-levina@yandex.ru

Damage of low-carbon steel after tensile test was estimated using nondestructive methods, including methods of measuring microhardness, attenuation coefficient of ultrasonic waves and aspect ratio of steel grains. A new informative damage parameter was proposed, namely, slope coefficient of cumulative distributions of microhardness, and correlation between physical (acoustic) and mechanical (microhardness, grain aspect ratio) properties of material was established.

**Keywords:** damage; nondestructive methods of testing; microhardness; attenuation coefficient of ultrasonic waves; grain aspect ratio.

## INTRODUCTION

The process of damage accumulation in construction elements during operation is inevitable, hence diagnostics of material with using nondestructive methods is needed on every loading stage. Since degradation of structure occurs due to appearance of defects of different origin, complex of nondestructive methods of testing allowing to measure physical and mechanical properties of material is needed for damage estimation.

One of abundantly used method of diagnostics of structural components is ultrasonic method that consists in measuring the attenuation coefficient of ultrasonic waves directly during usage of the structure. It has been established that with increase of number of defects (pores, microcracks) the attenuation coefficient of ultrasonic waves increases [1, 2]. Measure of microhardness is also effective method for damage estimation. In papers [3, 4], methods of statistical evaluation of microhardness were proposed by introducing new parameters including coefficient of inhomogeneity of material structure and

variation coefficient. The authors of works [5, 6] proposed new approaches to assessing the state of a material by using dimensionless parameters reflecting the interrelation of material properties and microindentation characteristics.

The methods of nondestructive testing given above have selective sensitivity to structural changes and stress-strain states, therefore, it is necessary to apply a combination of these methods. As a consequence, the purpose of this work was to measure microhardness and attenuation coefficient of ultrasonic waves of investigated steel and to establish the relationship of these parameters with local damage characteristics (local reduction of area and aspect ratio of grains on the specimen surface).

## EXPERIMENTAL PROCEDURE

The study was performed in ten zones on the surface of a flat low-carbon steel (0.2% C) specimen with dimensions of 220×20×5.6 mm (Fig. 1). These zones were located at different distances (Table 1) from the

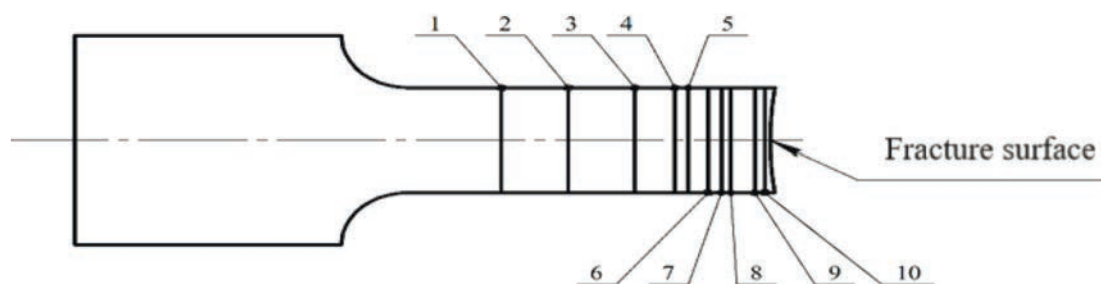
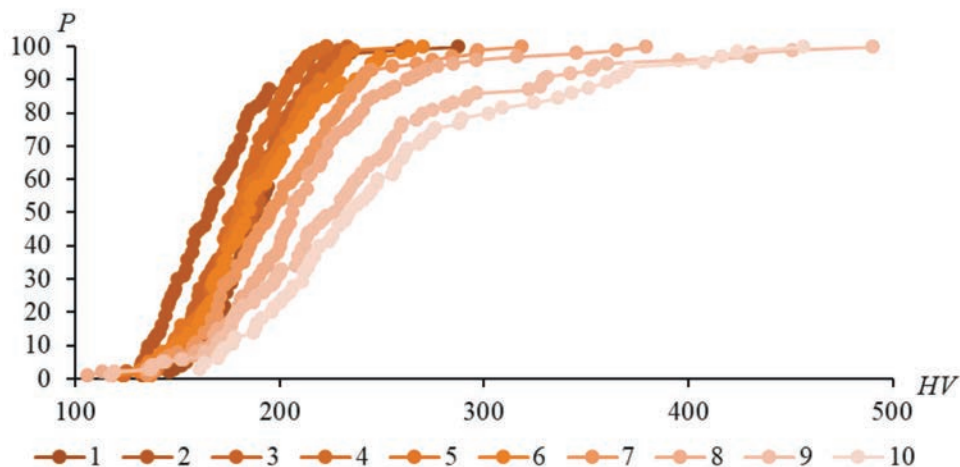


Fig. 1. Measuring zones of microhardness values  $HV$ , attenuation coefficient of ultrasonic waves  $\alpha$ , local reduction of area of the sample  $\Psi^*$ , % and aspect ratio of grains  $\xi$

Table 1. The local reduction of area of the sample in sections 1-10, located at different distances from the fracture surface

PROPERTIES OF SECTIONS 1-10										
Nº of section (Fig. 1)	1	2	3	4	5	6	7	8	9	10
$\Psi^*$ , %	0	3.26	7.82	13.44	19	24.74	31.49	32.68	35.59	38.46
Distance from fracture surface, mm	40.22	31.02	20.45	14.08	12.31	9.27	7.28	5.88	2.28	0.78

Fig. 2. Cumulative probability distributions  $P$  of the microhardness  $HV$  of investigated specimen in sections 1-10

fracture surface after static test. Using the EPOCH 4 flaw detector, the attenuation coefficient of ultrasonic longitudinal waves  $\alpha$  in the frequency range 2.25–20 MHz was estimated. An optical microscope Neophot 32 equipped with a digital camera and image-processing program were used to estimate aspect ratio of grains. Microhardness measurements were carried out on the semi-automatic Wolpert 402MVD microhardness meter, and 100 measurements were made in each designated zone for subsequent plotting of cumulative distributions.

## RESULTS AND DISCUSSION

According to the measurement data, cumulative microhardness distributions were plotted. To describe these distributions the following relation was proposed:

$$P = \frac{a}{1 + e^{-\beta(x-x_c)}} [1],$$

where  $a$  and  $x_c$  are constants,  $\beta$  is the slope of microhardness cumulative distributions. It was found that the slope  $\beta$  is informative parameter, the coefficients  $a$  and  $x_c$  practically do not change.

As local reduction of area  $\Psi^*$ , % increases, the slope of the cumulative distributions described by relations (1) decreases, indicating an increase in the

microhardness values caused by hardening of steel (Fig. 2). For this reason, the indicator  $\beta$  can be considered as an informative parameter characterizing the degree of material hardening.

The attenuation coefficient of the ultrasonic waves was measured in the same sections as the microhardness measurements. From the measurements it follows that an increase of  $\alpha$  at 20 MHz is the most significant (Fig. 3a). As can be seen from Fig. 3b, the change in the attenuation coefficient of ultrasonic waves correlates with the change in the average value of microhardness (Fig. 4). From Fig. 4 it follows that with an increase in the average value of microhardness, the attenuation coefficient of the ultrasonic wave increases. The exponential relation describes the obtained dependence:

$$\alpha = Ae^{HV^*} [2],$$

with the coefficient of determination  $R^2 = 0.9$ .

The study of the microstructure of the specimen after fracture (Fig. 5a, b) showed that steel grains elongate during the deformation process. For the evaluation of this elongation in each investigated section (Fig. 1), the aspect ratio of grains  $\xi$ , equal to the ratio of the longitudinal ( $a$ ) and transverse ( $b$ ) grain sizes (Fig. 5c), was estimated. The character of the change in the parameter  $\xi$  with an increase in the local reduction of area  $\Psi$ , % turned out to be similar to the character of the change in the average value of the microhardness and the attenuation coefficient of

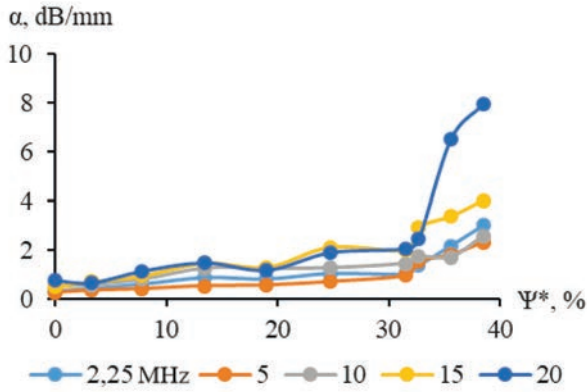


Fig. 3. *a* – Change in attenuation coefficient of ultrasonic waves in function of reduction of area at different frequencies of ultrasonic waves

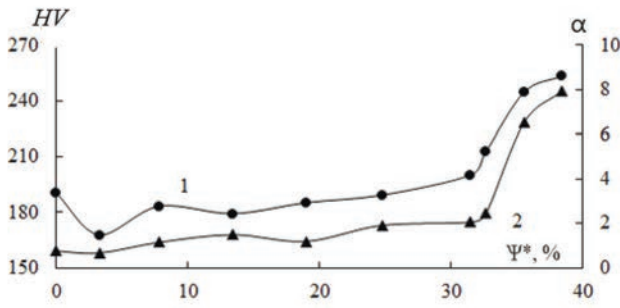


Fig. 3. *b* – Correlation between the average microhardness value  $HV^*$  (1), the attenuation coefficient of ultrasonic waves  $\alpha$  at  $f = 20$  MHz (2) and reduction of area  $\Psi^*$ , %

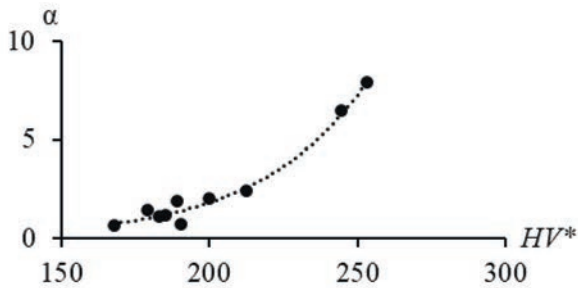


Fig. 4. Correlation between the attenuation coefficient of ultrasonic waves  $\alpha$  and the average microhardness value  $HV^*$

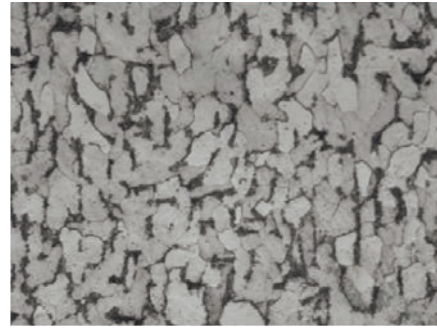


Fig. 5. *a* – Microstructure of non-deformed specimen

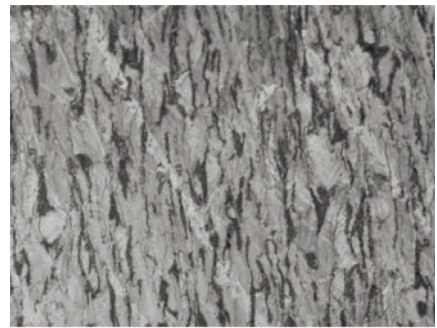


Fig. 5. *b* – Microstructure of specimen near fracture surface

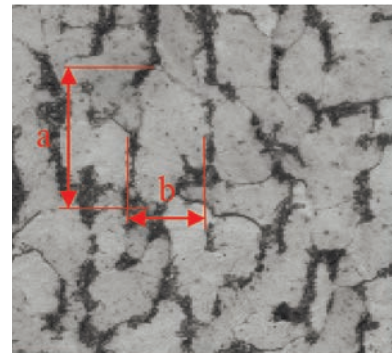


Fig. 5. *c* – Method for measuring aspect ratio

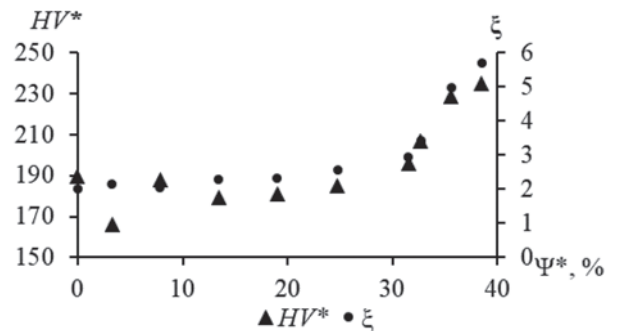


Fig. 6. Correlation between of aspect ratio of grains  $\xi$ , the average microhardness value  $HV^*$  and reduction of area  $\Psi^*$ , %

ultrasonic waves (Fig. 6). The beginning of intensive formation of the neck of the sample corresponding to local reduction value of area  $\Psi^* = 32\%$  causes a significant increase in the measured parameters  $\alpha$ ,  $HV^*$  and  $\xi$ . It should be noted that at the same value of  $\Psi^*$ , %, an intensive decrease in the slope coefficient  $\beta$  of the cumulative microhardness distribution occurs. Based on the data obtained, the dependences of the local damage characteristic, that is, the grain as-

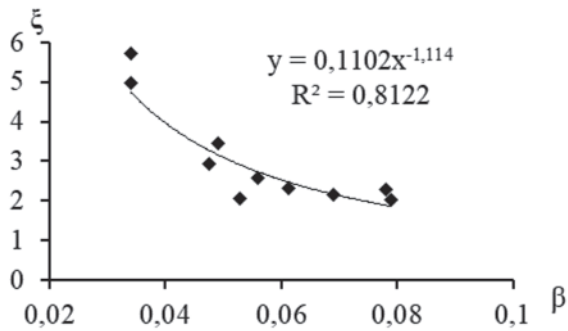


Fig. 7. *a* – Correlation between aspect ratio of grains  $\xi$  and slope coefficient of cumulative distributions of microhardness  $\beta$

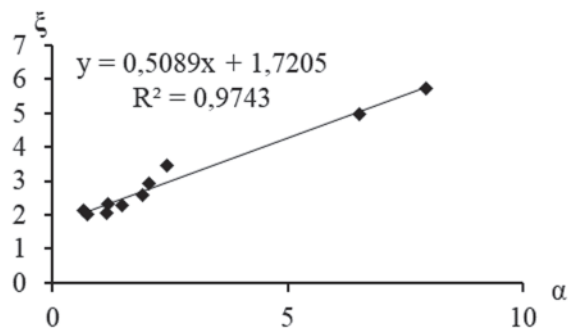


Fig. 7. *b* – Correlation between aspect ratio of grains  $\xi$  and the attenuation coefficient of ultrasonic waves  $\alpha$

pect ratio on the slope parameter  $\beta$  and the attenuation coefficient of ultrasonic waves  $\alpha$  (Fig. 7*a, b*) were plotted.

## CONCLUSIONS

A new informative parameter  $\beta$ , which characterizes the change in the slope of the cumulative distributions of microhardness values due to material hardening during deformation, was proposed

Correlation dependences of the physical parameter of ultrasonic attenuation  $\alpha$  on average value of microhardness were obtained.

The dependences of the degree of local deformation characterized by aspect ratio of grains on both the slope coefficient of cumulative microhardness distributions  $\beta$  and the attenuation coefficient of ultrasonic waves  $\alpha$  were established.

The research was carried out with support from Russian science foundation, project № 19-19-00674.

## REFERENCES

1. **Rohlin L.L.** Akusticheskie svoystva legkih splavov [Acoustic properties of light alloys]. Nauka. 1974.
2. **Truell R., Elbaum C., Chick B.B.** Ultrasonic methods in solid state physics. Academic press. 2013.
3. **Lebedev A.A., Nedoseka S.A., Muzyka N.R., Volchek N.L.** Ocenka sostoyania metalla trub posle dlitelnoy ekspluatatsii v sisteme magistralnyh gazoprovodov [Assessment of the condition of metal pipes after long-term operation in the system of gas pipelines]. Avtomaticheskaya svarka. 2003.
4. **Romanov A.N., Filimonova N.I.** Strukturnaya i deformacionnaya neodnorodnost konstrukciionih materialov i rassredotochennoe treshchinoobrazovanie pri ciclicheskom nagruzhении [Structural and deformation heterogeneity of structural materials and dispersed crack formation under cyclic loading]. Pervaya mezhdunarodnaya konferencia «Deformaciya i razrushenie materialov». 2006, Vol. I. P. 32–35.
5. **Minh-Quy L.** Material characterization by instrumented spherical indentation // Mechanics of Materials. 2012, Vol. 46. P. 42–56.
6. **Thai-Hoan P., Quang-Minh P., Seung-Eock K.** Identification of the plastic properties of structural steel using spherical indentation // Materials Science and Engineering: A. 2018, Vol. 711. P. 44–61.

# PIPELINE STEELS FOR SOUR SERVICE: CHEMICAL COMPOSITION, THERMOMECHANICAL TREATMENT, MICROSTRUCTURE AND PROPERTIES

A.A. Kholodnyi, Yu.I. Matrosov, G.A. Filippov, M.Yu. Matrosov

I.P. Bardin Central Research Institute for Ferrous Metallurgy, Moscow, Russia  
kholodnyi.aa@gmail.com

About a 30% reserves of the natural gas and oil contain  $H_2S$  impurities, which, in the presence of moisture, form an acidic medium and can lead to pipeline destruction by the mechanisms of hydrogen-induced cracking (HIC) and sulphide stress cracking (SSC). With the growing number of hydrocarbon fields being developed with a high content of  $H_2S$ , the demand for gas and oil large diameter pipes with high resistance to HIC and SSC increases. Comprehensive studies have been carried out to determine the effect of the chemical composition and thermomechanical processing on the microstructure, mechanical properties and resistance to HIC and SSC of rolled plates from low-alloy pipe steels. Optimal concentration of segregating (C, Mn) elements, controlled rolling and accelerated cooling modes provide the high resistance to destruction in  $H_2S$ -containing media due the formation of a homogeneous ferritic-bainitic microstructure without developed central segregation heterogeneity was determined. According to the research results, the technology for manufacturing of plates grade X52MS-X65MS was developed.

**Keywords:** low-alloy pipe steel; thermomechanical treatment; hydrogen-induced cracking; sulfide stress cracking; microstructure; non-metallic inclusion; central segregation; mechanical properties.

## INTRODUCTION

In recent years, the number of developed gas and oil fields with an increased content of  $H_2S$  grows, while previously such fields were considered to be of little use for operation. This is explained by the depletion of «clean» fields, which have been the main source of hydrocarbons for many decades. This leads to growth demand for gas-oil pipes, which are much more cracking resistant in an aggressive  $H_2S$ -containing medium. To prevent damage of pipelines transmitting «sour gas» special requirements have been developed for the resistance of pipe metal to failure in  $H_2S$ -containing media. The fulfilment of such requirements is necessary to ensure a long-life operation of the pipes [1–4].

is iron ionization:  $Fe \rightarrow Fe^{2+} + 2e$ . Cathodic reaction leads to formation of atomic hydrogen that steel may absorb. Hydrogen in atomic form is present in steel in the form of interstitial impurity in a crystal lattice or is accumulated in non-metallic inclusion, grain and phase boundaries, within pores, etc. In areas of a non-uniform steel matrix it may be transferred into molecular form ( $H_2$ ), having a significant volume, which leads to occurrence of excess internal pressure, high tensile stresses, and to crack formation, propagating predominantly through hard and coarse structural components [3–6].

Steel failure under action of hydrogen may proceed by two mechanisms: cracking, arising without stresses, and cracking with action of residual and/or applied stresses. In the first case cracking develops in the form of cracks parallel to the surface of rolled product/pipe, and is signified by the term Hydrogen-Induced Cracking (HIC). Hydrogen cracks arise in areas with high non-metallic inclusion density and areas of anomalous structure (banding, central segregation inhomogeneity). Cracking arising under action of stresses is signified by the term Sulfide Stress Cracking (SSC). This form of failure is connected with metal embrittlement by atomic hydrogen present with a crystal lattice. In this case, it is also necessary to consider

## MECHANISMS OF STEEL FRACTURE IN $H_2S$ -CONTAINING MEDIA

During contact with moisture  $H_2S$  dissolves with it and as a result of reaction dissociates with formation of hydrogen ions ( $H_2S \leftrightarrow HS^- + H^+$ ), which leads to a reduction in pH and increase in medium acidity. This medium provokes electrochemical corrosion, and as a result of anodic reaction there

crack formation caused by the pressure of molecular hydrogen [2, 6].

## FACTORS AFFECTING THE HIC AND SSC RESISTANCE OF PIPE STEELS IN SOUR SERVICE

The negative effect of aggressive  $H_2S$ -containing wet media in transported gas and oil causes disruption of continuity and failure of pipes by the mechanisms of HIC and SSC and is determined by a number of factors related to the metallurgical properties of the pipe metal and include the chemical composition, microstructure, the shape and distribution of non-metallic inclusions, strength properties, internal stresses. The accumulation of atomic hydrogen, which saturates the steel, as well as its recombination into the molecular form occur at structure discontinuities such as interphase interfaces between non-metallic inclusions and steel matrix. This leads to the appearance of internal gas pressure and tensile stresses, which, after exceeding a certain critical level, initiate the crack nucleation. The stress level depends on the shape of the inclusions, their size, quantity, distribution, and distance from the plate/pipe surface. Due to the specific features of crystallization and solidification of a continuously cast slab, most non-metallic inclusions, harmful impurities (S, P), and alloying elements (Mn, Nb, C) are concentrated in the axial zone. Therefore, special attention upon the production of continuously cast slabs for plates intended for sour gas resistant pipes is paid to the measures aimed at increasing steel cleanliness from non-metallic inclusions and reducing centreline segregation [5–9].

The main non-metallic inclusions detrimentally affecting the cracking resistance of the plates from pipe steels in  $H_2S$ -containing media are as follows: inclusions based on manganese sulfide (MnS), inclusions of a complex composition based on niobium and titanium carbonitrides (Ti, Nb)(C, N), oxide-sul-

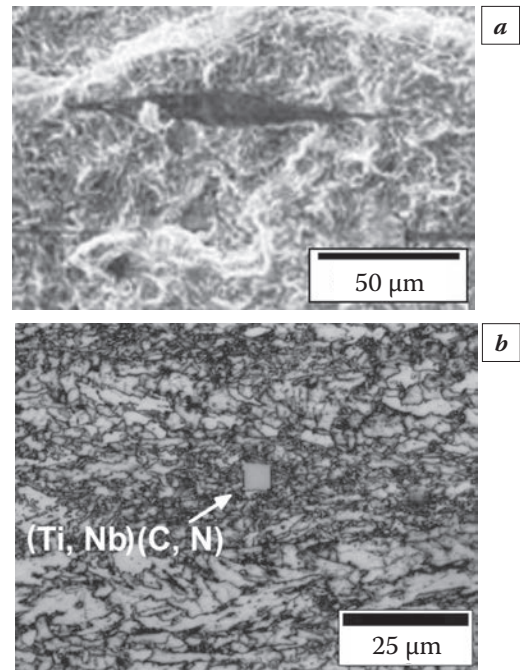


Fig. 1. Non-metallic inclusions in the centerline segregation zone of the plate:

*a* – manganese sulfides (MnS); *b* – complex carbonitride composition based on (Ti, Nb)(C, N) [5, 10]

fide inclusions of complex composition (Fig. 1). The modern level of metallurgical technology of steel-making, out-of-furnace processing, and continuous casting can provide minimum contamination of the slab by non-metallic inclusions.

The predominant sites of the nucleation and propagation of hydrogen cracks in the plates of high cleanliness from non-metallic inclusions are extended segregation bands of increased hardness in the zone of central structural heterogeneity of the plates. In the plates produced by different TMCP regimes, the hydrogen-induced cracks propagate in the axial zone along coarse extended segregation bands with regions of high-carbon structures such as lamellar pearlite, degenerate pearlite, high-carbon upper bainite, twinned high-carbon martensite with retained austenite, and acicular bainitic ferrite with interlayers of retained austenite along the lath boundaries (Fig. 2).

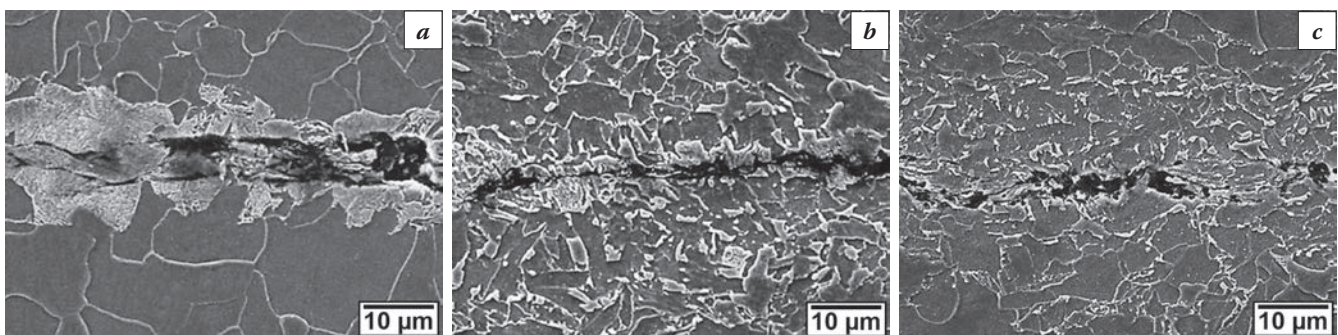


Fig. 2. Hydrogen-induced crack in the centerline segregation zone of the plate, SEM: *a* – lamellar pearlite; *b* – high-carbon upper bainite; *c* – twinned high-carbon martensite with retained austenite

## EFFECT OF ACCELERATED COOLING

The structure formation in the central segregation zone and in the base metal of the plates is mainly affected by the conditions of hot plastic deformation and cooling. For the development of the thermomechanical treatment regimes for HIC resistant plates from pipe steels, their effect on the formation of the axial zone microstructure responsible for the HIC resistance of the plates are taken into account [8, 9]. The microstructure formation in the centerline zone is characterized by some specific features associated, first of all, with a higher content of segregating elements, which is inherited from continuously cast slabs. The effect of the post-deformation cooling parameters such as start temperature of accelerated cooling ( $T_{sc}$ ), finish temperature of accelerated cooling ( $T_{fc}$ ), and cooling rate ( $V_c$ ) on the HIC resistance of rolled plates was investigated (Fig. 3) [10].

On the basis of the experimental results one conclude that, as the start temperature of accelerated cooling is above the  $Ar_3$  temperature, the microstructure is more uniform over the plate thickness and less susceptible to HIC than that formed upon accelerated cooling from the temperature below  $Ar_3$  (Fig. 3a). This is explained by the enrichment of undecomposed austenite with carbon and alloying elements upon the  $\gamma \rightarrow \alpha$  polymorphic transformation occurring upon slow cooling when the  $T_{sc} < Ar_3$ . The decomposition of such austenite can occur in the pearlitic and bainitic regions, as well as with the formation of the MA-constituent. In this case, the difference between the steel matrix and the segregation bands in hardness increases, which promotes the nucleation and propagation of hydrogen-induced cracks.

If accelerated cooling stop temperature is relatively high ( $T_{fc} \geq 580$  °C), the structure formed in the axial zone of the plates contains a second phase in the form of coarse pearlite bands. At a lower finish temperature of accelerated cooling ( $T_{fc} \leq 450$  °C) bands with regions of the MA-constituent can form. Such high-carbon structures are favourable for the nucleation and propagation of hydrogen-induced cracks. The optimum range of the finish temperatures of accelerated cooling for the steels under study is the lower range of the bainitic transformation region -  $T_{fc} \sim 500$  °C (Fig. 3b). The ferritic-bainitic microstructure formed in the axial zone at such temperatures is more uniform and less susceptible to HIC than the structures formed upon cooling to higher or lower temperatures.

With an increase in the cooling rate from 2 to 25 °C/s, a significant increase in the HIC resistance

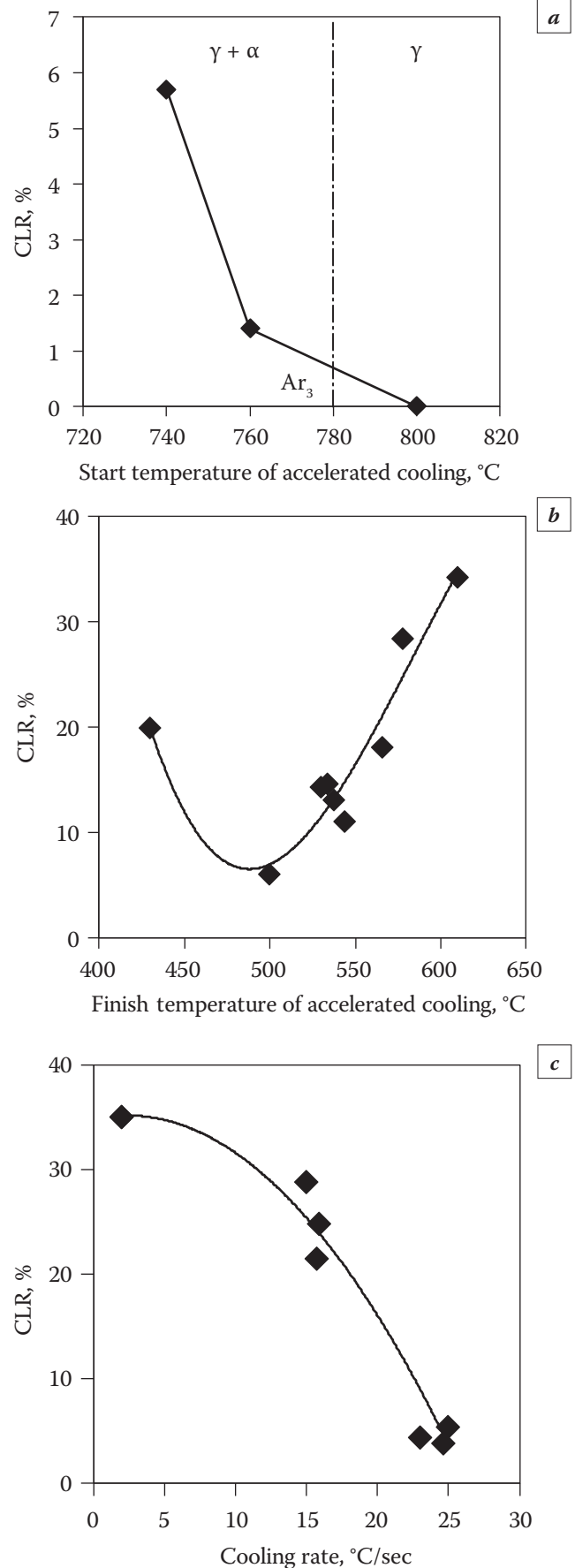


Fig. 3. Effect of start temperature (a), finish temperature (b) and rate (c) of accelerated cooling on the crack length ratio (CLR) of the plates [10]

of the plates (Fig. 3c). An increase in the microstructural homogeneity over the plate thickness and an increase in the HIC resistance of the plates with increasing cooling rate is associated with a decrease in the rate of the diffusion of carbon and other elements into austenite upon phase transformations. This allows one to reduce the amount of non-decomposed austenite regions enriched with alloying elements, primarily with carbon, and to reduce the number and extension of the bands consisting of unfavourable transformation products such as pearlite, high-carbon bainite, and MA-constituent, which adversely affect the HIC resistance.

### EFFECT OF CHEMICAL COMPOSITION

The chemical composition of steel, especially the content of strongly segregating elements – C and Mn – affects the degree of central segregation in the slab and, as a consequence, the segregation heterogeneity in the axial zone of the plates. On the other hand, the chemical composition both in the base metal and in the axial zone affects the kinetics of the polymorphic transformation upon cooling of the plate after rolling, and this also determines the degree of chemical and microstructural heterogeneity of the rolled products [7].

The effect of carbon content changing from 0.04 to 0.08% (Mn = 1.25–1.35%) and manganese concentration from 0.65 to 1.35% (C = 0.06%) on the central segregation heterogeneity and HIC resistance of the plates 20–25 mm thick manufactured by controlled rolling followed by accelerated cooling has been studied (Fig. 4) [10]. The plates were cooled from the  $\gamma$ -region to bainitic transformation range ( $T_{fc} = 490$ – $530$  °C) at a rate of more than 20 °C/sec.

The carbon content substantially affects the microstructure of the axial zone of the plates. At 0.04%C, a slight structural heterogeneity is seen in the axial zone in the form of a narrow segregation band. As the carbon content increases to 0.08%, the central structural heterogeneity becomes more pronounced, which is expressed in an increase in the number of segregation bands. A decrease in the carbon content, other things being equal, resulted in a substantial increase in the HIC resistance of the plates. The CLR parameter on average decreased from 12.5% at 0.08%C to 0% at 0.04%C.

The estimation of the effect of manganese on the susceptibility to HIC of the plates processed by the above regimes shows that the reduction in manganese content positively affects the HIC resistance of the plates from the test steels. The HIC parameter reached zero at a manganese content of about 0.90%.

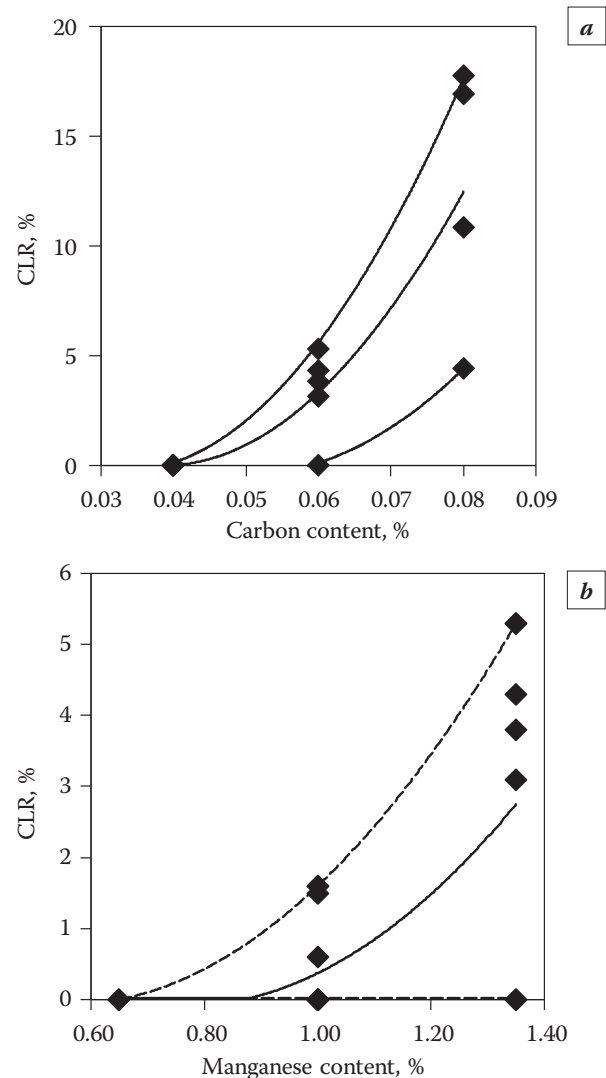


Fig. 4. Effect of carbon (a) and manganese (b) content on the crack length ratio (CLR) of the plates [10]

### IMPROVEMENT OF SSC RESISTANCE

The effect of TMCP technology on SSC resistance was studied on plates (wt.%: 0.05 C, 0.92 Mn, 0.001 S, 0.90 (Cr + Ni + Cu + Mo), 0.090 (Ti + Nb + V)) produced by three technologies [11] (Table 1, Fig. 5):

- high-temperature controlled rolling (CR) with completion of deformation in the  $\gamma$ -region ( $T_{fr} = 855$ – $859$  °C) and air cooling, i.e., HCR;
- low-temperature CR with finish of deformation in the ( $\gamma + \alpha$ )-region ( $T_{fr} = 718$ – $720$  °C) and air cooling, i.e., LCR;
- high-temperature controlled rolling ( $T_{fr} = 855$ – $859$  °C) followed by accelerated cooling (AC) from the  $\gamma$ -region ( $T_{sc} = 808$ – $817$  °C;  $T_{fc} = 517$ – $520$  °C;  $V_c = 23$ – $26$  °C/sec), i.e., HCR + AC.

Plates produced by HCR technology has significantly lower strength and greater ductility compared with plates after LCR and HCR + AC. After treat-

Table 1. Microstructure, mechanical properties and test results for SSC resistance of plates [11]

TMCP scheme	Structure type	Mechanical properties					SSC resistance with load coefficient (k) 0.72 of $\sigma_{0.5 \text{ norm}}$								
		$\sigma_{0.5}$ , N/mm <sup>2</sup>	$\sigma_B$ , N/mm <sup>2</sup>	$\delta_{2\gamma}$ , %	$\sigma_{0.5}/\sigma_B$	KV <sup>-20</sup> , J	370 N/mm <sup>2</sup>			400 N/mm <sup>2</sup>			425 N/mm <sup>2</sup>		
							1	2	3	1	2	3	1	2	3
HCR	F + P	391	480	53	0.81	305/295/321	57	35	20	17	12	18	10	15	14
		393	484	51	0.81	280/315/304	47	85	29	18	55	10	21	15	20
LCR	F(def)+P	522	576	36	0.91	290/297/329	720	720	720	720	720	720	245	170	290
		521	575	37	0.91	285/345/235	720	720	720	720	720	720	80	154	178
HCR+AC	F+B	471	576	44	0.82	373/390/358	720	720	720	720	720	720	720	720	720
		479	578	38	0.83	345/354/324	720	720	720	720	720	720	720	720	720

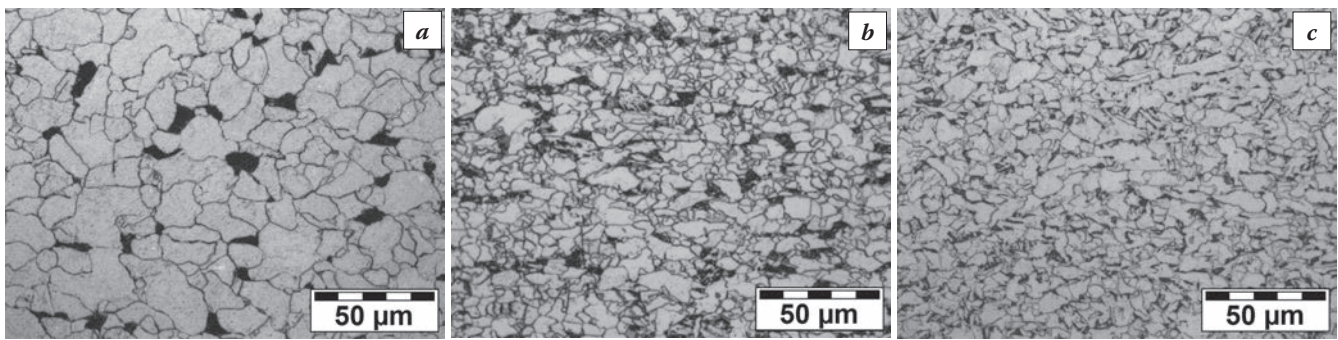


Fig. 5. Microstructure of steel produced by different thermomechanical treatment technologies, OM: a – HCR; b – LCR; c – HCR + AC [11]

ment by HCR technology plates had a ferrite-pearlite microstructure (matrix of polygonal ferrite and uniformly distributed areas of lamellar pearlite) (Fig. 5a). With completion of rolling in the two-phase ( $\gamma + \alpha$ )-region (LCR technology) a microstructure was obtained consisting of deformed polygonal ferrite and lamellar pearlite (Fig. 5b). Accelerated cooling from the austenitic region after rolling (HCR + AC technology) makes it possible to form a microstructure consisting of a matrix of quasipolygonal ferrite and areas of high-carbon bainite and cementite over ferrite grain boundaries (Fig. 5c).

Test specimen resistance to SSC was determined from results of testing specimens with different loads ( $\sigma_{\text{test}} = k \times \sigma_{0.5 \text{ norm}}$ ): coefficient  $k$  was 0.72, and  $\sigma_{0.5 \text{ norm}}$  was 370, 400, and 425 N/mm<sup>2</sup>. Testing with load coefficient  $k = 0.72$  within the limits of 370–400 N/mm<sup>2</sup> showed that all specimens prepared from plates after LCR and HCR + AC withstood testing and did not fail for 720 h. All specimens of steel with a ferrite-pearlite microstructure after HCR having lower strength than steel after HCR, also with a ferrite-pearlite structure, failed. On testing with load  $0.72 \times 425$  N/mm<sup>2</sup> specimens of plates with a ferrite-pearlite microstructure treated by HCR and LCR technology did not withstand testing for SSC, but specimens of steel with a

ferrite-bainite microstructure after HCR + AC did not fail sooner than 720 h. It may be concluded that with an increase in the strength of steel with a ferrite-pearlite microstructure there is an increase in SSC resistance. At the same time, with comparable value of strength properties a steel ferrite-bainite microstructure has greater SSC resistance compared with a ferrite-pearlite microstructure.

The effect of post-deformation accelerated cooling on SSC resistance was studied on plates (wt.-%: 0.10 C, 1.36 Mn, 0.002 S, 0.44 (Ni + Cu); 0.094 (Ti + Nb + V)), produced by two CR + AC schedules [11]:

- schedule 1: end of deformation in the single phase  $\gamma$ -region ( $T_{\text{fr}} = 793\text{--}801$  °C) followed by accelerated cooling from the two-phase ( $\gamma + \alpha$ )-region ( $T_{\text{fr}} = 757\text{--}761$  °C) with intensity of 12–13 °C/sec;
- schedule 2: end of deformation and start of accelerated cooling from the single phase  $\gamma$ -region ( $T_{\text{fr}} = 832\text{--}837$  °C,  $T_{\text{sc}} = 796\text{--}800$  °C) with a faster cooling rate of 20–21 °C/sec. The accelerated cooling stop temperature was 545–575 °C.

The microstructure of plate prepared by schedule 1 consisted of a matrix of polygonal and quasipolygonal ferrite with areas of degenerated pearlite and high-carbon bainite (Fig. 6a). Steel of plate treated by schedule 2 had a finer ferrite-bainite microstructure

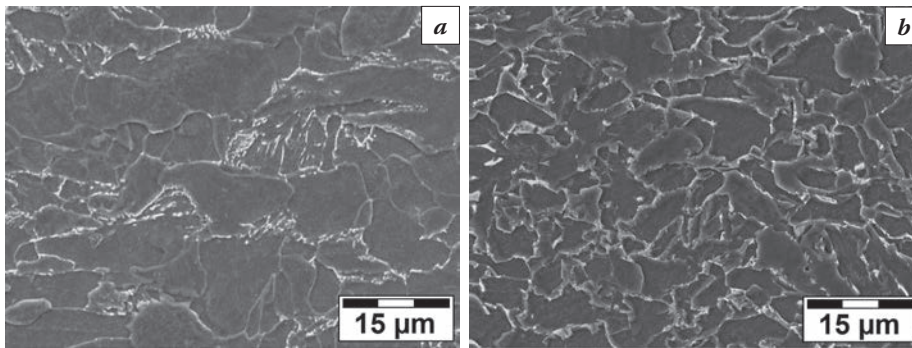


Fig. 6. Microstructure of plates from steel grade X60 produced by CR+AC technology, SEM: *a* – schedule 1 ( $T_{fr} = 801\text{ °C}$ ;  $T_{sc} = 757\text{ °C}$ ;  $T_{fc} = 550\text{ °C}$ ;  $V_c = 12\text{ °C/sec}$ ); *b* – schedule 2 ( $T_{fr} = 837\text{ °C}$ ;  $T_{sc} = 800\text{ °C}$ ;  $T_{fc} = 555\text{ °C}$ ;  $V_c = 21\text{ °C/sec}$ ) [11]

consisting of quasi-polygonal ferrite with areas of high-carbon bainite (Fig. 6*b*).

In spite of some differences in the microstructure the test CR + AC regimes provided comparable mechanical properties and corresponded to strength grade X60. After treatment by schedule 1 steel had low SSC resistance: with load coefficient  $k = 0.60$  of six of the test specimens three specimens failed in 79–168 h, and with  $k = 0.72$  all six specimens failed in the period 22–61 h. In this case specimens of steel treated by schedule 2 did not fail for 720 h after testing with  $k = 0.60$  and  $0.72$ . Therefore, use of post-deformation cooling from the austenitic region at a rate of not less than  $20\text{ °C/sec}$  provides formation of a finer microstructure, which leads to an increase in steel SSC resistance.

## INTEGRATED PRODUCTION CONCEPT AND MANUFACTURING TECHNOLOGY OF STEELS FOR PIPES ORDERED FOR SOUR SERVICE

As the requirements for sour service gas pipeline steels become more severe, all steps in the manufacture of such steels have to be optimized, especially with the aim of a clean steel with minimized inclusions and with homogeneity of microstructure which is a consequence of reduced center segregation of slabs. The general strategy of production for sour service steels relies on: vacuum treatment by tank degassing; very low sulfur content ( $\leq 0.001\%$ ) and CaSi treatment for shape control to prevent MnS; minimization of segregation and contamination by inclusions during continuous casting of slabs; controlled rolling with accelerated cooling after final rolling with specific temperatures; microstructure control by limit of  $C \leq 0.07\%$ ,  $Mn \leq 1.10\%$  and  $P \leq 0.015\%$  contents. During production certain deviations or in-

cidents are possible having significant influence on HIC and SSC and no or minor influence on other properties. For that reason a special adapted quality control system steel must be developed that is able to state a deviation of actual values and to decide if such plates must be prohibited from release and delivery or additionally tested to prove conformity with specification. With all the measure explained above it is possible to produce steel plates for sour

service with consistent property profiles even in big quantities [12].

The data on the production of plates 20.0 mm thick for the manufacture of the X52MS, X56MS, X60MS, and X65MS grade large-diameter LSAW pipes ordered for sour service are considered in [10]. For the reduction of the central segregation heterogeneity of the continuously cast slabs and plates, the heats contained  $C \leq 0.07\%$  and  $Mn \leq 1.00\%$ , and the mass fraction of harmful impurities was limited to the level  $S \leq 0.001\%$  and  $P \leq 0.010\%$ . All experimental heats were alloyed with  $Cu+Ni+Cr \leq 0.80\%$ , and the heats from the X60MS and X65MS grade steels additionally contained Mo. The steels were microalloyed with complex additions of  $Ti+Nb+V \leq 0.120\%$ . The use of the optimal chemical composition and continuous casting technology ensured the centreline segregation of slabs at a level of 1.5–2.0 according to the Mannesmann method.

Thermomechanical processing of plates in the two-stand plate mill was carried out using technology of controlled rolling followed by accelerated cooling. The start temperature of the accelerated cooling was above the phase transformation start temperature ( $Ar_3$ ). The accelerated cooling stop temperature was at least  $520 \pm 30\text{ °C}$ . The cooling rate was over  $20\text{ °C/sec}$ .

The plates have a fine-grained ferritic-bainitic microstructure with a slight central structural heterogeneity and high cleanliness from non-metallic inclusions. The mechanical properties of the plates met the specified requirements for steels. All plates exhibited a high HIC and SSC resistance.

## REFERENCES

1. API Specification 5L. Specification for line pipe, 45 ed., 2012. P. 164.

2. International standard ISO 3183:2012. Petroleum and natural gas industries – Steel pipe for pipeline transportation systems, 2012. P. 179.
3. NACE Standard TM0284-2016. Standard Test Method «Evaluation of Pipeline and Pressure Vessel Steels for Resistance to Hydrogen-Induced Cracking», 2016, Houston. P. 20.
4. ANSI/NACE Standard TM0177-2016. Standard Test Method «Laboratory Testing of Metals for Resistance to Sulfide Stress Cracking and Stress Corrosion Cracking in H<sub>2</sub>S Environments», 2016, Houston. P. 77.
5. **Ishikawa N., Endo S. et al.** Material design of high strength/heavy gauge linepipes for sour service // Proceedings of the Microalloyed Steels for Sour Service International Seminar. São Paulo, Brazil, 20–22 August 2012. USA: CBMM, 2014. P. 135–154.
6. **Yamada K. et al.** Influence of metallurgical factors on HIC of high strength ERW line pipe for sour gas service // International Conference on Technology and Applications of HSLA Steels. 3–6 October 1983, Philadelphia, Pennsylvania. P. 835–842.
7. Sour gas resistant pipe steel, Niobium Information. № 18/01. CBMM/NPC, Düsseldorf (Germany), 2001.
8. **Bufalini P., Pontremoli M., Aprile A.** Accelerated cooling after control rolling of line-pipe plates influence of process conditions on microstructure and mechanical properties // Proceedings of the International Conference on Technology and Applications of HSLA steels, Philadelphia, Pennsylvania October 3–6, 1983. P. 743–753.
9. **Tamehiro H. et al.** Effect of accelerated cooling after controlled rolling on the hydrogen induced cracking resistance of line pipe steel // Transactions of the Iron and Steel Institute of Japan. 1985. 25. 982–988.
10. **Shabalov I., Matrosov Yu., Kholodnyi A. et al.** Pipeline Steels for Sour Service. Topics in Mining // Metallurgy and Materials Engineering. Springer, Cham. 2019.
11. **Kholodnyi A.A., Kuznechenko Y.S., Matrosov Yu.I. et al.** Improvement of Low-Alloy Pipe Steel Sulfide Stress Cracking Resistance // Metallurgist. 2019. 63: 58–65.
12. **Schwinn V., Thieme A.** TMCP Steel Plates for Sour Service Linepipe Application : International Seminar «Pipe Seminar Modern Steels for Gas and Oil Transmission Pipelines, Problems and Prospects» / Proceedings. Moscow, 15–16 Mar. 2006. P. 165–172.

# CONTROL OF AUSTENITE STRUCTURE EVOLUTION DURING TMCP IN MICROALLOYED STEELS

A. Chastukhin, D. Ringinen, L. Efron

OMK Vyksa Steel Works. Vyksa, Russia

chastuhin\_av@vsw.ru, ringinen\_da@vsw.ru, lefron@omk.ru

A continuous demand for plates for X60–X120 pipes with high toughness and cold resistance requires the development of new methods of additional grain refinement at all stages of thermo-mechanical control processing (TMCP). An effect of structure formation during slab reheating was studied. Physical models of secondary recrystallization during reheating and austenite recrystallization at roughing rolling of Nb-microalloyed pipeline steels were developed. Grain refinement during hot deformation was studied through physical modelling. Using the recrystallization model, new rolling schedules were introduced. Industrial trials were conducted; the effect of reheating and deformation parameters on cold resistance of steel was investigated. Implementation of the results of given study into production practice made it possible to produce plates with excellent properties, including strength, toughness, and cold resistance.

**Keywords:** recrystallization; grain refinement; pipeline steels; hot rolling; gleeble.

## INTRODUCTION

Fracture resistance of a pipeline strongly depends on pipe steel toughness. The toughness depends on dispersity and uniformity of final structure of rolled metal. Formation of such structure is possible only by controlled rolling (CR) which includes slab reheating, roughing and finishing rolling and accelerated cooling. Each stage plays a specific role in metal structure formation, and thus affects final product structure-sensitive properties. For microalloyed high-strength pipe steels slab reheating and roughing rolling are important CR stages, since they determine to a significant extent solid solution composition, austenite grain size and austenitic structure uniformity, on which depend such rolled product properties as low-temperature impact toughness and drop weight tear tests.

Parameters of the slab reheating on one hand are determined by equipment production limitations and on the other by a requirement for formation a desired austenite structure before roughing rolling. At some cases, for Nb-microalloyed steels abnormal grain growth (AG) could happen in slab during heating and soaking [1]. This phenomenon is known as secondary recrystallization (SR) [2, 3]. The reason of the AG is partial dissolution of the Nb(C, N) particles, which leads to increase of boundary mobility of some grains and as result a rapid growth of individual grains. This means when choosing heating temperature and slab

soaking time in a furnace it is extremely important to consider the possibility of developing the AG, leading to formation of a nonuniform grain size structure before the start of roughing rolling. Prevention of the AG during slab reheating has a high-priority, because even after sequence hot deformations the austenite inhomogeneity persists and has a negative influence on toughness [1].

Rough rolling is also the very important part of the CR. The main goal of the stage is reduction of the relatively large initial austenite grain size and improvement of structure uniformity by the sequence of recrystallizations between passes. However, it is necessary determine appropriate thermomechanical parameters of roughing rolling to avoid partial recrystallization which results in heterogeneous austenite structure prior to finishing rolling and hence deterioration of structure-sensitive properties.

Obtaining optimal slab reheating and roughing rolling parameters by stepwise changing the industrial processing is complicated and quite expensive. For this reason, the study of the AG during slab reheating and the recrystallization behavior during roughing rolling is indispensable for creating controlled rolling processing and achieving high properties of rolled metal. The models make it possible to create new and to correct existing technologies of the controlled rolling, significantly increase toughness and ensure the production of rolled metal for the main pipelines like the South Stream.

## MATERIAL AND EXPERIMENTAL PROCEDURE

Twenty Nb-microalloyed steels X60–X120 grades were studied in this work (wt.%: C = 0.04–0.09; Si = 0.12–0.35; Mn = 0.4–2.0; Nb = 0.03–0.08; Ti = 0–0.02; Mo = 0–0.30; Ni+Cr+Cu = 0.11–0.92, Ti/N = 0–6.5).

## GRAIN GROWTH

In order to study the effects of soaking temperature and soaking time during heating of slab on austenite grain structure, specimens with a size of 10×10×15 mm were cut from 1/4 of the thickness of industrial slabs (>300 mm). Specimens were placed in a tube furnace with an inert atmosphere (argon), heated to 1080–1250 °C (average heating time to these temperatures was 50 min), held at constant temperature for 30–190 min. and then water quenched for the structure analysis.

## RECRYSTALLIZATION AND RECRYSTALLIZED GRAIN SIZE

Three types of recrystallization are known to occur during the roughing rolling: dynamic recrystallization (DRX), metadynamic recrystallization (MDRX) and static recrystallization (SRX) between the deformations. DRX takes place directly during deformation if pass strain exceeds a critical strain  $\varepsilon_c$ . If DRX achieves certain volume fractional, then MDRX begins immediately after deformation. Else, after incubation time the SRX begins and, in this case, is responsible for softening behavior and austenite grain size.

In order to characterize recrystallization kinetics, two types of compression tests were performed in this investigation: single compression test and double compression test. Cylindrical specimens with a diam-

eter of 10 mm and a height of 15 mm were cut from industrial plates. Before tests all specimens were heat treated with the aim of dissolving of carbonitrides of microalloying elements. For this purpose, specimens were heated to 1250 °C in the tube furnace with the argon atmosphere, soaked for 30 min and then water quenched. Thermomechanical simulator Gleeble 3800 was used for experiments with preset temperature and strain rate conditions. Single compression tests were carried out to determine the critical strain and model parameters associated with the DRX. Double compression tests were performed for study MDRX and SRX kinetics. All tests were implementing in the temperature range of 900–1170 °C and in the strain rate range of 0.1–10 s<sup>-1</sup>. For microstructure analysis, the specimens were water quenched immediately after interpass time. The microstructure observations and grain size measurements were implemented at the same region for all the specimens, the region is located at the ¼ of high and ¼ of diameter of specimen.

Validation of the model was also carried out with laboratory compression tests on Gleeble. During these tests the specimens were compressed different number of the deformations with variant deformation parameters. All the specimens were water quenched and used for austenite grain size measurement. The experimental results were compared with calculated in the model.

## SLAB REHEATING MODEL

After heating and soaking tests, it was concluded that all specimens could be separated in three types: with fine-grained ( $\approx 60 \mu\text{m}$ ), coarse-grained ( $\approx 1\text{--}6 \text{ mm}$ ) and mixed austenite structure (Fig. 1).

Furthermore, the results of the observations could be combining into a structural condition map. And the structural maps of steels with different chemical composition are also different (Fig. 2). It is clear that position on the Temperature axis of the

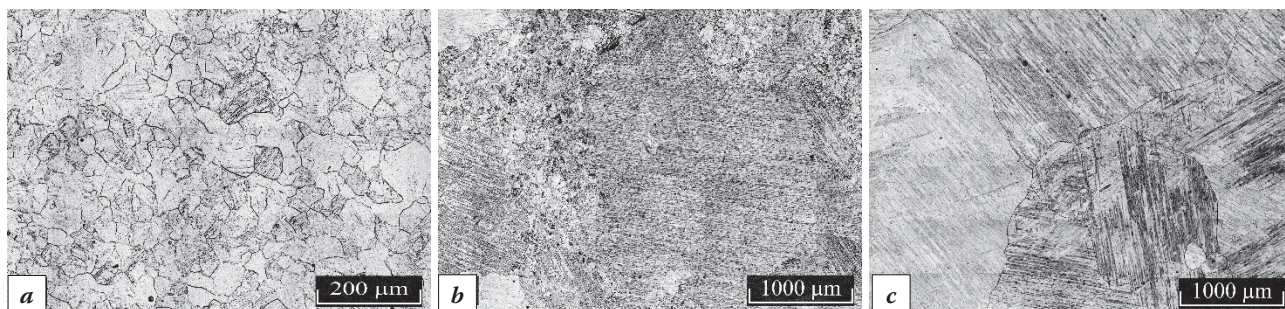


Fig. 1. Different types of austenite structure in the specimens of X100 after heating and soaking tests: *a* – fine grains ( $T=1160 \text{ }^\circ\text{C}$ ,  $t=90 \text{ min}$ ); *b* – nonuniform grains ( $T=1190 \text{ }^\circ\text{C}$ ,  $t=90 \text{ min}$ ); *c* – coarse grains ( $T=1220 \text{ }^\circ\text{C}$ ,  $t=90 \text{ min}$ )

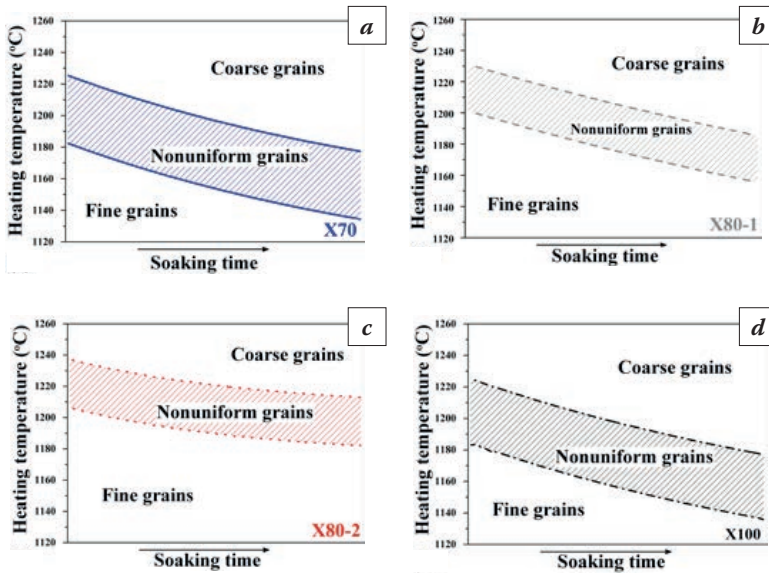


Fig. 2. **Structural condition maps:** *a* – X70 (0.05%C; 0.02%Ti; 0.05%Nb; Ti/N=4.9); *b* – X80-1 (0.06%C; 0.02%Ti; 0.04%Nb; Ti/N=2.8); *c* – X80-2 (0.06%C; 0.02%Ti; 0.07%Nb; Ti/N=6.5); *d* – X100 (0.06%C; 0.02%Ti; 0.05%Nb; Ti/N=2.8)

lower boundary and width of the nonuniform region varies in different steels.

Studies on TEM showed that in all steels in the initial state there are: 1) large particles of complex carbonitrides TiNb(C, N) with a dendritic form and a size of 1–6  $\mu\text{m}$ ; 2) TiN particles of rectangular shape and size from 0,5 to 5  $\mu\text{m}$ ; 3) «star-like» particles up to 0,5  $\mu\text{m}$  in size with a central part of TiN and «rays» from Nb(C,N); 4) dispersed uniformly distributed Nb (C, N) particles with sizes from 5 to 20 nm. Dispersed TiN particles, which could restrain migration of grain boundaries at high heating temperatures, are not detected.

Analysis of samples with a fine-grained and mixed austenite structure made it possible to conclude that the reason for the abnormal grain growth is the dissolution of niobium carbonitride particles with dimensions 5–20 nm.

The differences in position of a border of the abnormal growth beginning are associated with solvus temperature of the niobium carbonitride  $T_{\text{Nb(C,N)}}$  for the investigated steels [4]. The solvus temperatures for these steels were determined by ThermoCalc® program. It was found that for the start of SR, superheating above  $T_{\text{Nb(C,N)}}$  is required (Fig. 3). The required superheat decreases with increasing holding time (Fig. 4). With decreasing  $T_{\text{Nb(C,N)}}$ , the value of the required superheat increases due to the reduction of the braking force restraining the migration of boundaries.

In the industrial process it is important to know what soaking time we could use for holding the slabs

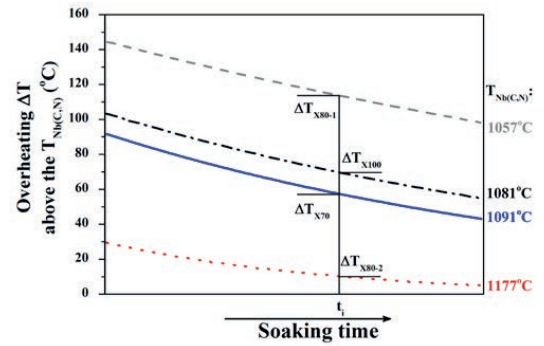


Fig. 3. **Dependence of the required overheating for the AG on the soaking time for steels with the different  $T_{\text{Nb(C,N)}}$**

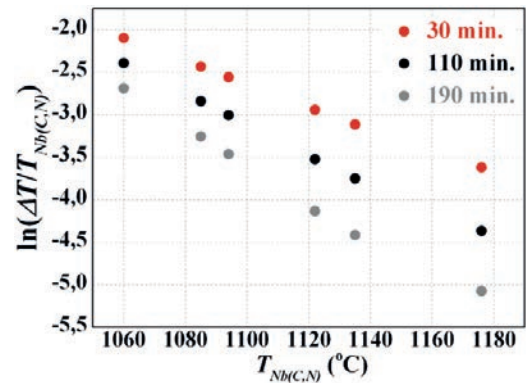


Fig. 4. **Dependence of the overheating value  $\Delta T$  on  $T_{\text{Nb(C,N)}}$  and soaking time**

any chemical composition at the target heating temperature in the furnace.

The equation for soaking time calculation is shown below (Eq. 1):

$$t = \frac{\ln\left(\frac{T_H - T_{\text{Nb(C,N)}}}{T_{\text{Nb(C,N)}}}\right) + b \cdot T_{\text{Nb(C,N)}} - d}{a \cdot T_{\text{Nb(C,N)}} + c}, \quad (1)$$

$t$  – maximum soaking time at the target heating temperature in the furnace [min];  $T_H$  – target heating temperature in the furnace [°C];  $T_{\text{Nb(C,N)}}$  – equilibrium solvus temperature of the niobium carbonitride in the steel [°C];  $a, b, c, d$  – the equation parameters.

The solvus temperature in Eq. 1 could be calculated by Eq. 2, which was obtained through variation of the chemical elements content when calculating in ThermoCalc®.

$$T_{\text{Nb(C,N)}} = \lg\left([C]^{203.7} \cdot [\text{Nb}]^{285.4}\right) + 32.2[\text{Si}] - 1.42[\text{Mn}] - 2.6[\text{Cr}] + 6.9[\text{Cu}] + 17.34 \cdot \left| 3.42 - \frac{[\text{Ti}]}{[\text{N}]} \right| + 1698, \quad (2)$$

[C], [Nb], [Si], [Mn], [Cr], [Ti], [N] – the chemical elements contents in the steel [wt.%].

According to the obtained dependence, the value of the equilibrium dissolution temperature of Nb(C, N) is mainly determined by the content of carbon and niobium in the steel, as well as by the deviation of the ratio of Ti/N concentrations from stoichiometric.

The temperature of dissolution is affected by the content of such elements as Si, Mn, Cr and Cu, but to a much lesser extent. The influence of the other elements can be neglected. The accuracy of the calculation with the new formula, in comparison with the values obtained in the ThermoCalc®, for all the steels under study is  $\pm 5^\circ\text{C}$ .

The equations Eq. 1 and Eq. 2 become the basis of the new program tool for reheating parameters calculating that was created for technologists. The tool allow evaluation of the target temperature and the appropriate soaking time for steels any chemical composition clearly and in short time. The calculated reheating parameters could be used for obtaining uniform austenite structure jointly with maximum possible dissolution of the carbonitride particles prior to roughing rolling. Industrial application of the tool showed significant improvement of the cold resistance of the Nb-microalloyed rolled metal for pipes.

## HOT ROLLING RECRYSTALLIZATION MODEL

The evolution of the austenite microstructure during rolling was modeled by equations based on

equations in Table 1 and deformation parameters (strain per pass, strain-rate, temperature, interpass time). The coefficient of determination between experimental and calculated results exceeds 0.94 (Fig. 5).

For a specific deformation sequence, the model was applied for each deformation pass, calculating the microstructure at the entrance of the subsequent

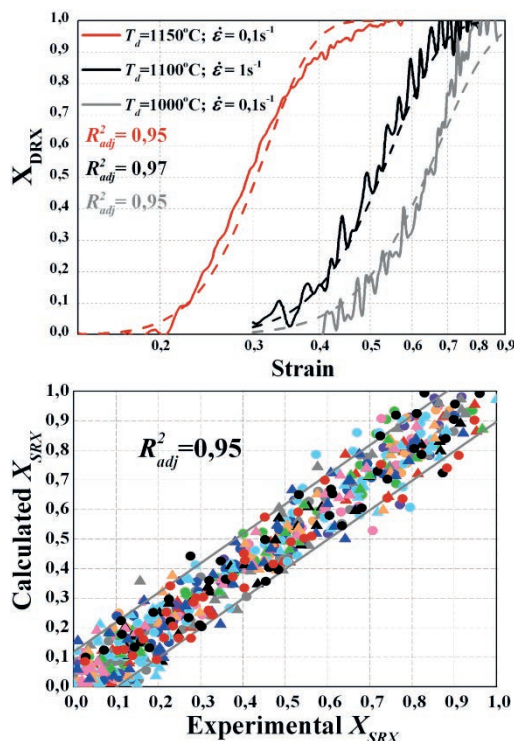


Fig. 5. Accuracy of volume fraction of recrystallization calculating

Table 1. Main equations of HRRM

Dynamic Recrystallization	Metadynamic Recrystallization
$\varepsilon_{Ci} = A_{def} d_{i-1}^q \left( \dot{\varepsilon}_i \cdot \exp \left[ \frac{Q_{def}}{RT_i} \right] \right)^m \quad (3) [7]$	$\varepsilon_{MDRXi} = t_{50MDRXi} \cdot \dot{\varepsilon}_i \left[ \frac{\ln \left( \frac{1}{1-0.1} \right)}{0.693} \right]^{n_{DRX}} + \varepsilon_{Ci} \quad (6)$
$\varepsilon_{50i} = A_{DRX} \dot{\varepsilon}_i^u d_{i-1}^w \cdot \exp \left[ \frac{Q_{DRX}}{RT_i} \right] \quad (4) [8]$	$t_{50MDRXi} = A_{SRX} \varepsilon_{MDRXi}^p \dot{\varepsilon}_i^k d_{i-1}^v \cdot \exp \left[ \frac{Q_{SRX}}{RT_i} \right] \quad (7)$
$X_{DRXi} = 1 - \exp \left[ -0.693 \left( \frac{\varepsilon_i - \varepsilon_{Ci}}{\varepsilon_{50i}} \right)^{n_{DRX}} \right] \quad (5) [8]$	$X_{MDRXi} = 1 - \exp \left[ -0.693 \left( \frac{t_{ipi}}{t_{50MDRXi}} \right)^{n_{SRX}} \right] \quad (8)$
Static Recrystallization	Grain Size and Residual Strain
$t_{50SRXi} = A_{SRX} \varepsilon_i^p \dot{\varepsilon}_i^k d_{i-1}^v \cdot \exp \left[ \frac{Q_{SRX}}{RT_i} \right] \quad (9) [9]$	For each recrystallized level:
$X_{SRXi} = 1 - \exp \left[ -0.693 \left( \frac{t_{ipi}}{t_{50SRXi}} \right)^{n_{SRX}} \right] \quad (10) [9]$	$d_i = B \varepsilon_i^s d_{i-1}^f \cdot \exp \left[ \frac{Q_{RX}}{RT_i} \right] \quad (11) [10]$
	$\varepsilon_{ri} = 0$
	For each unrecrystallized level:
	$d_i = d_{i-1} \quad (12)$
	$\varepsilon_{ri} = 0.9 \varepsilon_{i-1} \quad (13)$

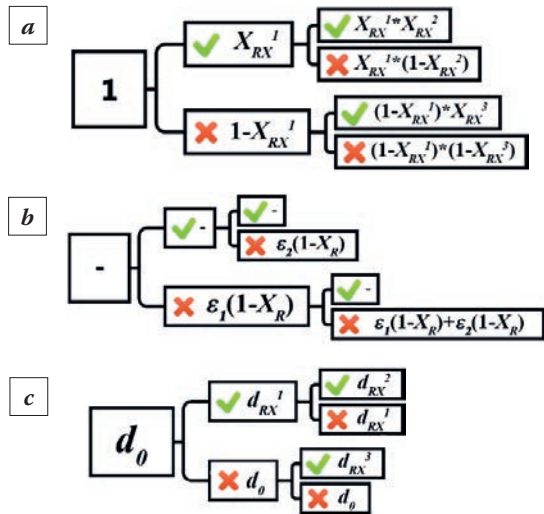


Fig. 6. Tree-structure of: a – recrystallized and unrecrystallized zones; b – retained strain; c – grain size

pass. The model is organized following a tree-structure, the depth being equal to the number of passes and each level is divided into two branches, the recrystallized and the unrecrystallized zones, respectively (Fig. 6).

These areas are treated independently for subsequent deformation, this method being reported in the literature as the law of mixtures [4–6]. This introduces the complexity of managing an increasing number of different structures throughout the deformation process. For the recrystallized volume fraction  $X_{RX}$ , it is assumed that the residual deformation is zero, while for the unrecrystallized fraction all the strain imparted in the previous pass is retained. Recrystallized zones are characterized by the values of the mean recrystallized grain sizes, while unrecrystallized grain size assumed is equal to the initial size for the zone. The mean grain size after each pass is calculated as the sum of the multiplications of the grain sizes and the volume fraction of the respective zones.

This complex model was designed in a form of a simple and convenient software tool which, in a visual form, provides information on the part of recrystallization between the passes, the change in the average grain size during rolling, and gives a qualitative assessment of the uniformity of the austenite structure after hot rolling.

The model accuracy was verified using Gleeble 3800 compression tests to simulate various roughing modes and using laboratory rolling of wedge specimens into one and two passes (Fig. 7). The agreement of the calculations with all validation test results is shown on Fig. 8, the corresponding determination coefficient is  $R^2_{adj} = 0.88$ .

Analysis of twenty Nb-microalloyed steels prompted investigation the obvious relation between kinetic

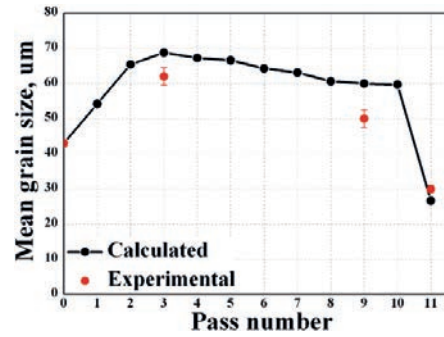


Fig. 7. Comparison of the calculated change of the mean grain size during a strain sequence with values after tests

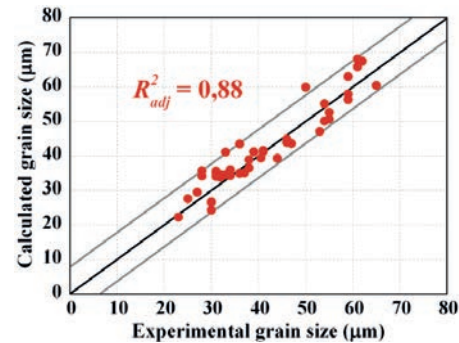


Fig. 8. Accuracy of calculated results compared with grain sizes after validation tests

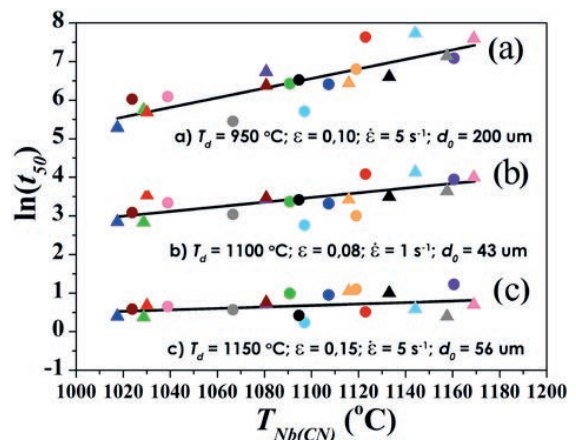


Fig. 9. Dependence of recrystallization kinetic on  $T_{Nb(C,N)}$

of static recrystallization and equilibrium solvus temperature of niobium carbonitride which strongly depends on chemical composition of steel (Fig. 9).

The sensitivity of the recrystallization kinetics to the value of  $T_{Nb(C,N)}$  increases with decreasing temperature, strain and strain rate due to more effective inhibition of austenite grain boundaries migration in steels with a high precipitation temperature of Nb(C, N) particles against the background of a general decrease in the driving force of recrystallization.

This opens the possibility of calculating the kinetics of recrystallization even if there is a deviation of chemical composition of steel. In order to evaluate of

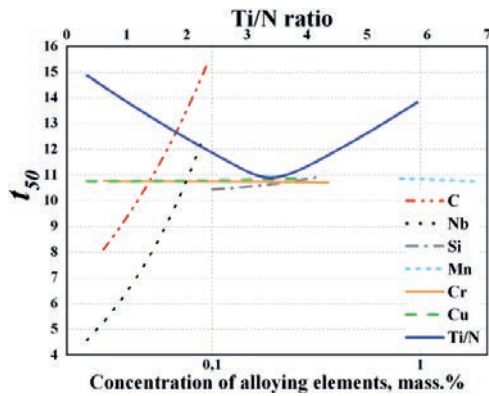


Fig. 10. Influence of alloying elements and Ti/N ratio on static recrystallization kinetic

SRX kinetics the equation was created (Eq. 3).

$$t_{50} = \exp\left[\ln(\varepsilon^{k_1} \dot{\varepsilon}^{k_2}) + k_3 \exp\left(-\frac{1}{mT_d}\right) + f_1\right] T_{\text{Nb(C,N)}} + \ln(\varepsilon^{k_4} \dot{\varepsilon}^{k_5} d_0^{k_6}) + k_7 \exp\left(-\frac{1}{mT_d}\right) + f_2, \quad (3)$$

$k_1, k_2, k_3, k_4, k_5, k_6, k_7, m, f_1, f_2$  – coefficients;  $\varepsilon, \dot{\varepsilon}, T_d$  – strain, strain rate and deformation temperature (°C);  $T_{\text{Nb(C,N)}}$  – equilibrium solvus temperature of niobium carbonitrides.

It has been shown and experimentally confirmed that an increase in the carbon and nitrogen content (with a Ti/N ratio lower than the stoichiometric ratio) leads to an increase in the precipitation temperature of Nb(C, N) dispersed particles, which hinder migration of the grain boundaries and slow down the recrystallization. An increase in the Ti content (for  $\text{Ti/N} > 3.42$ ) and Nb also increases the recrystallization time due to an increase in the concentration of atoms of these elements in the austenite and the enhancement of the solute drag effect (Fig. 10).

Based on a complex model, the HRRM software tool has been created that allows developing the TMCP regimes that provide for the formation of a dispersed and homogeneous structure, to evaluate the evolution of the austenite structure with a change in the chemical composition of the steel. Analysis of test results showed a strong decrease in unsatisfactory KCV and DWT tests from 2.25% in 2012 to 0.05% in 2018.

## SUMMARY

1. Evolution of austenite grain size in Nb-microalloyed steels X60–X120 grades during heating and soaking in a furnace with various target temperatures and soaking times was investigated. It was found out, three types of the austenite structures are possible after slab reheating: fine-grained ( $\approx 60 \mu\text{m}$ ), coarse-grained

( $\approx 1\text{--}6 \text{ mm}$ ) and mixed. The evolution of the investigated steels structure could be represented as a structural map in Heating temperature – Soaking time axes.

2. Correlation between the start of abnormal grain growth during heating and solvus temperature of the niobium carbonitride  $T_{\text{Nb(C,N)}}$  in a steel was established. Overheating above the solvus temperature is required for abnormal grain growth. The equation for allowable soaking time without the abnormal growth at target temperature, which is above the solvus temperature, was determined.

3. To improve dispersion and uniformity of austenite structure before the start of finishing rolling the Hot Rolling Recrystallization Model was developed. The model allows determination of a mean austenite grain size after multipass deformations for wide steel grades interval. The determination coefficient of calculated and experimental results is  $R^2_{\text{adj}} = 0.88$ .

## REFERENCES

1. Ringinen D.A., Chastukhin A.V., Khadeev G.E. et al. Evolution of Austenite Grain Structure and Microalloying Element Precipitation During Heating of Steel of Strength Class K65 (X80) for Rolling // Metallurgist. 2014. 57. 996–1004.
2. Gorelik S.S., Dobatkin S.V., Kaputkina L.M. Recrystallization of metals and alloys, third ed. Moscow: MISIS, 2005.
3. Novikov V.Y. Second recrystallization. Moscow : Metallurgy, 1990.
4. Anelli E. Application of Mathematical Modelling to Hot Rolling and Controlled Cooling of Wire Rods and Bars // ISIJ Int. 1992. 32. 440–449.
5. Fernández A.I., López B., Rodríguez-Ibabe J.M. Modeling of Partially Recrystallized Microstructures for a Coarse Initial Nb Microalloyed Austenite // Scr. Mater. 2002. 46. 823–828.
6. Uranga P., Fernández A.I., López B., Rodríguez-Ibabe J.M. Modeling of Austenite Grain Size Distribution in Nb Microalloyed Steels Processed by Thin Slab Casting and Direct Rolling (TSDR) Route // ISIJ Int. 2002. 44. 1416–1425.
7. Guoliang J., Fuguo L., Qinghua L. et al. Research on the dynamic recrystallization kinetics of Aermet100 steel // Materials Science and Engineering A 527. 2009. 2350–2355.
8. Siciliano Jr. F., Minami K., Maccagno T.M. Mathematical Modeling of the Mean Flow Stress, Fractional Softening and Grain Size during the Hot Strip Rolling of C-Mn Steels // ISIJ Int. 1996. 36. 1500–1506.
9. Sellars C., Whiteman J. Recrystallization and grain growth in hot rolling // Met. Sci. 1979. 40. 189–194.
10. Hodgson P., Gibbs R. A Mathematical Model to Predict the Mechanical Properties of Hot Rolled C–Mn and Microalloyed Steels // ISIJ Int. 1992. 32. 1329–1338.

# EFFECT OF TEMPERATURE AND CATALYST ON THE OXIDATION OF OIL USED FOR THE MAR-TEMPERING OF GEARS

D. Scott MacKenzie<sup>1</sup>, Pedro Luiz Pioli<sup>2</sup>, John Kim<sup>3</sup>

<sup>1</sup>FASM, Houghton International, Inc., USA, smackenzie@houghtonintl.com

<sup>2</sup>Houghton International, Inc., Brazil, pedro.pioli@houghtonintl.com

<sup>3</sup>Houghton International, Inc., USA, jkim@houghtonintl.com

Mar-tempering oils are used to control the distortion of precision parts, by the reduction of thermal gradients, and to allow martensite to transform uniformly. Elevated oil temperatures are used, greater than 120 °C. This means that very high quality base oils and additives are used to prevent oxidation of the oil. A review of the mechanism of oxidation of mar-tempering oils will be provided.

The operating temperature of the mar-tempering oil is used to control distortion. As a general rule, the higher the temperature, the lower the distortion. However, even minor changes in the operating temperature can have a large impact on the life of the quench oil. An oxidation study showing the effects of temperature on the life of three oils will be presented. The effects of different catalysts on the oxidation and life of mar-tempering oil will also be presented.

**Keywords:** quenching; oil; temperature; oxidation; catalyst; martempering.

## INTRODUCTION

Engineered quench oil is governed by the desired quenching performance; the necessary thermal and oxidative stability, and finally price or market considerations. Quenching performance is generally considered to be the heat transfer characteristics and the thermal stability of the oil. This includes having an acceptable flash temperature that is a minimum of 50°C above the expected use temperature; low sludge forming tendency; long life; and the necessary quenching speed.

Premium quality heat-treating quenching and martempering oils are formulated from refined base stocks (usually paraffinic) of high thermal stability with additives to improve performance and increase tank life. These additives are a combination of specially chosen ingredients compatible with the base oil; in particular, carefully selected and tested anti-oxidants, which retard the aging process.

Quench oils degrade from four primary reasons: oxidation; thermal degradation; contamination; and additive depletion. This is aggravated by residues on parts, washer residues from oil reclaimed from washers; high energy density heater or radiant tubes, and excessive peak temperatures. The addition of robust additive packages prolongs a quenchant life and provides for repeatable quenching.

Oxidation of quench oil is caused by exposure to oxygen. As operating temperatures increase, the kinetics of oxidation approximately double with each

10 °C. This is especially true with mar-tempering oils because of their elevated temperature of use.

Thermal degradation is from exposure to temperatures that cause the base oil and additive package to change. This results in the formation of insoluble products of reaction that can cause deposits on parts and sludge the quench tank.

Contamination can be from many sources. Water, dust, scale and soot are not the direct result of oil degradation, but can contribute to other degradation issues. Soot can act as nucleation sites for thermal degradation products, and can mimic oxidized oil.

Additive depletion is normal and expected. The anti-oxidants are consumed as part of their function. Anti-oxidants are replenished as make-up oil is added.

The oxidation mechanism of quenching oils is very complex [1–6]. The presence of Iron and Copper catalyze the reactions and play an important part in chain initiation reaction. Typically reactions are slow at room temperatures but become increasingly faster above 100 °C. This is why, for high quality quenching oil, “cold” oils (those used below 80 °C) do not experience the severe oxidation with attendant increases in viscosity and Total Acid Number (TAN) that Mar-tempering oils experience. A schematic of the oxidation process is shown in Fig. 1.

The side reactions of the formation of aldehydes and ketones are probably the most important in maintenance of quench oils because their subsequent reactions eventually form sludge and deposits. While there are a number of different paths that lead to the

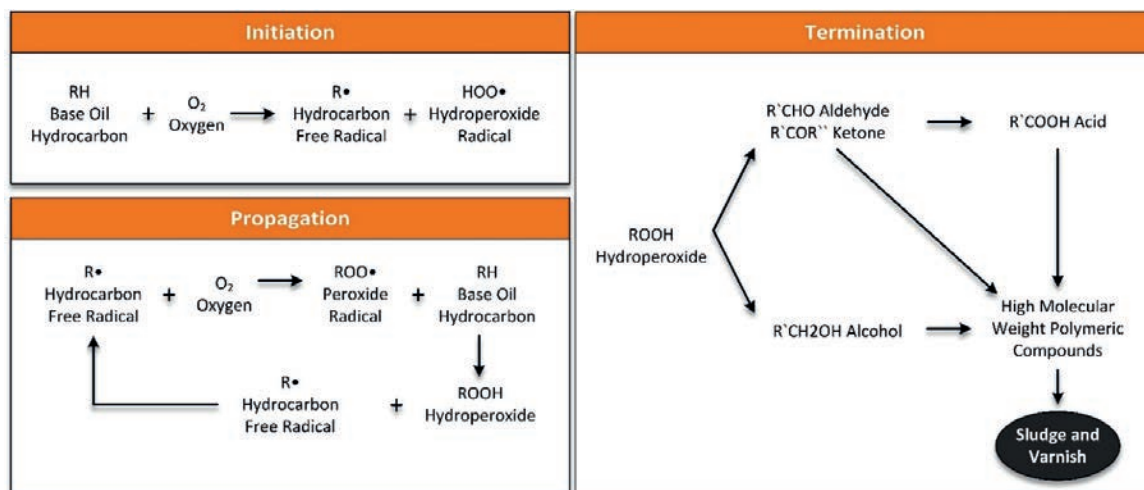


Fig. 1. Schematic of the mechanism of quench oil oxidation

formation of aldehydes and ketones, the most accepted mechanisms are shown below:



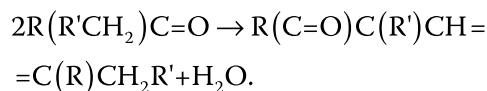
The last reaction above is a chain termination that consumes two peroxy radicals and produces an alcohol and a carbonyl compound. The polarity of the hydrocarbon will increase, but the molecular weight will be unchanged. This also means that the viscosity, flashpoint will also be unchanged.

As the oxidation increases, the acid levels from the formation of carboxylic acids increase. This increase leads to further oxidation because the carboxylic acids promote oxidation. This is why, once oil starts to oxidize, it does so in an exponential fashion, with the oxidation rapidly increasing. Carboxylic acids are formed by the oxidation of aldehydes and ketones. This is measured by ASTM D664. It is a measure of the amount of organic acids present in the oil, and is useful for determining when staining is likely, or the oil is reaching the end of its useful life. For most oil quenchants, when the TAN (Total Acid Number) is greater than 1.5–2.0, it is indicative of staining or deposits on parts being quenched.

As oils become increasingly oxidized, whether in the quench tank, or in oxidation tests, the viscosity increases. This occurs by condensation reactions that become important as the levels of aldehydes and ketones increase. These reactions are known as Aldol Condensations [3].

These reactions are the primary source of viscosity increases in quench oils. The formation of low molecular weight polymers and other hydrocarbons are the result of the “Aldol Condensations”, and can result in staining and other deposits. The viscosity of the quenchant increases as the number of condensation reactions increase. This would occur with severely oxidized mar-tempering oil.

The condensation products described in the above section have a limited solubility in the quenchant. These are high molecular weight oligomers. These are molecules that have a few monomer units, in contrast to a polymer that can have an unlimited number of monomers. As oil oxidizes the amount of carboxylic acids will increase. These acids are very effective catalysts for Aldol condensation reactions. These then convert the low molecular weight carbonyl compounds into higher molecular weight oligomers:



As the reactions progress, chemical changes in the oligomers will result in making them insoluble in the quench oil. At this point the insoluble oligomers will precipitate from the quench oil and create sludge on the bottom of the quench tank, and deposits on the hot metal part.

The higher kinetic rate of aromatic group oxidation increases sludge and deposits. Because paraffinic oils have fewer aromatic groups than naphthenic oils, paraffinic oils are preferred for quenchants. Metal scale and soot, base oil sulfur, additive sulfur can also promote the formation of sludge and deposits. Soot can also act as a nucleation site for the formation of oligomers formation, resulting in oligomers coated



Fig. 2. Deposits on ring gears due to severely degraded quench oil

soot particles. These accumulate at the bottom of the quench tank in low velocity areas, and are deposited on parts (Fig. 2).

## EFFECT OF CATALYST – EXPERIMENTAL PROCEDURE

Testing was conducted according to ASTM D 943 “Standard Test Method for Oxidation Characteristics of Inhibited Mineral Oils.” [7], modified by eliminating the use of water. Standard copper coils were used. To test the effect of different catalysts, the copper coil was plated with nickel. Testing was conducted at 121 °C. Oxidation was measured by Viscosity (ASTM D445) [8], Total Acid Number (ASTM D664) [9], and by FTIR. Measurements for viscosity and TAN were taken at various intervals. The oil used was Houghton Mar-Temp 3530. The results of the oxidation testing

as measured by TAN are shown in Fig. 3 and the viscosity testing is shown in Fig. 4. Results of FTIR testing is shown in Fig. 5.

The oxidation testing clearly showed that copper was a very strong catalyst for oxidation of Mar-Temp 3530. Nickel plating showed a very mild effect, and exhibited very little oxidation during the life of the test. When examined using FTIR, the oil exposed to the copper coil showed extensive oxidation while the oil exposed to the nickel plated coil showed very little oxidation. The FTIR scans of the new oil and the oil exposed to the nickel coil were practically identical.

The use of nickel plating for the prevention of carburization has merit in the reduction of oxidation. However, additional testing must be performed to demonstrate that the diffusion of nickel will not change the local composition of the part, and change the local hardenability. The use of a copper strike under the nickel plating to improve plating adhesion would help

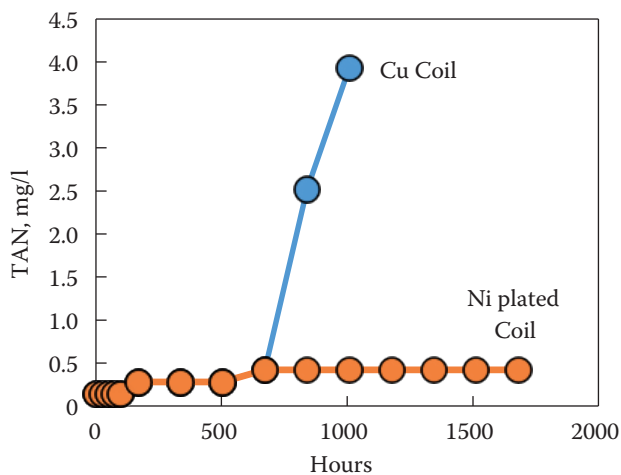


Fig. 3. Total Acid Number by ASTM D664 for copper coil and nickel plated coil

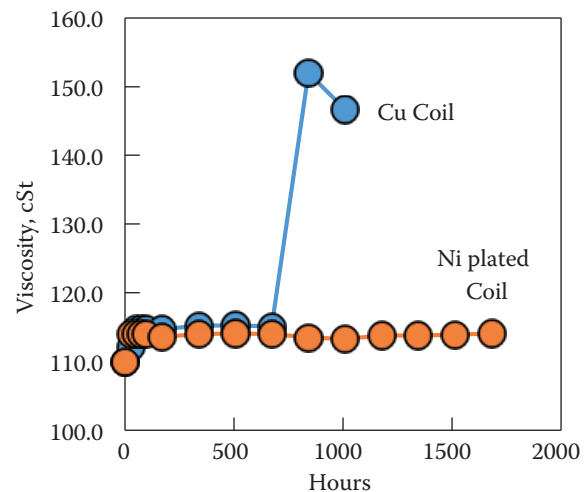


Fig. 4. Kinematic viscosity testing per ASTM D445 for the copper coil and nickel plated coil

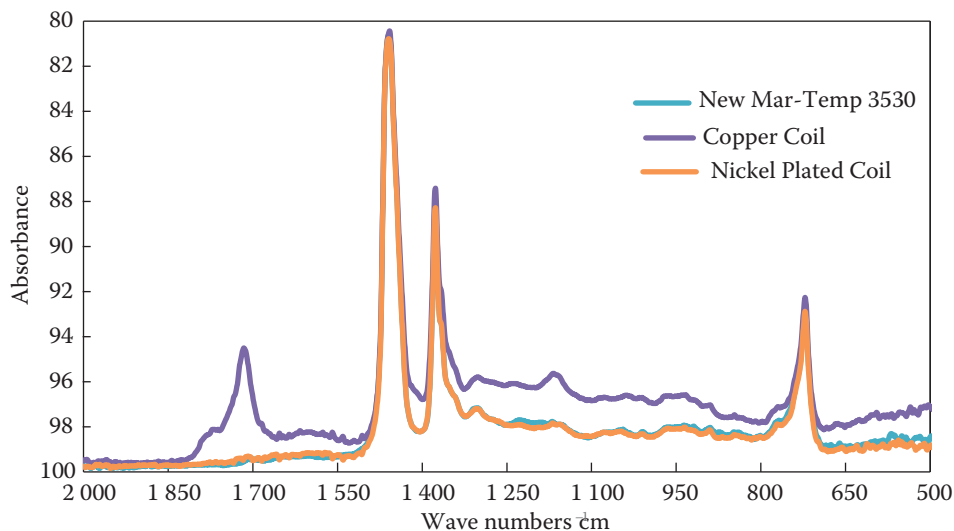


Fig. 5. FTIR of new Mar-Temp 3530 compared to oils exposed to the copper coil and the nickel plated coil

reduce nickel diffusion, and provide additional protection from the diffusion of carbon during carburization. Additional investigation is underway to evaluate the effect of nickel plating during high temperature carburization to evaluate the diffusion of nickel.

The oxidation testing clearly showed that copper was a very strong catalyst for oxidation of Mar-Temp 3530. Nickel plating showed a very mild effect, and exhibited very little oxidation during the life of the test. When examined using FTIR, the oil exposed to the copper coil showed extensive oxidation while the oil exposed to the nickel plated coil showed very little oxidation. The FTIR scans of the new oil and the oil exposed to the nickel coil were practically identical.

The use of nickel plating for the prevention of carburization has merit in the reduction of oxidation. However, additional testing must be performed to demonstrate that the diffusion of nickel will not change the local composition of the part, and change the local hardenability. The use of a copper strike un-

der the nickel plating to improve plating adhesion would help reduce nickel diffusion, and provide additional protection from the diffusion of carbon during carburization. Additional investigation is underway to evaluate the effect of nickel plating during high temperature carburization.

## EFFECT OF TEMPERATURE – EXPERIMENTAL PROCEDURE

Three mar-tempering oils used for the quenching of gears were evaluated to ASTM D4336 [10]. The physical properties of the new oils are shown in Table 1. Temperatures used were 130 °C and 160 °C. These temperatures are commonly used for mar-tempering. Copper, carbon steel and aluminum strips were used as catalysts in the oxidation process. The sample size was 200 mL of fluid. The catalyst strips were immersed in the oxidation tube.

Table 1. Physical properties of the oils investigated

Characteristics	Method	Oil A	Oil B	Oil C
Color	ASTM D1500	2.5	2.0	<1.5
Appearance	MIH 052	Clear Liquid	Clear Liquid	Clear Liquid
Density 20 °C - g/cc	ABNT NBR71478	0.891	0.882	0.881
Visc. 40°C, cSt	ABNT NBR10441	223.60	93.85	80.04
Visc. 100°C, cSt	ABNT NBR10441	19.12	10.87	9.85
VI	ASTM2270	96	100	102
TAN, mg KOH/g	MIH 004	0.28	0.05	0.09
Flash Point, °C	ABNT NBR11341	268	240	262

Table 2. Results of the oxidation testing to ASTM D4336

	Oil A @130°C		Oil A @160°C		Oil B @130°C		Oil B @160°C		Oil C @130°C		Oil C @160°C	
Hours	Visc.40°C	TAN										
0 hours	223.60	0.28	223.60	0.28	93.85	0.05	93.85	0.05	103.70	0.09	80.04	0.09
8 hours	224.87	0.24	233.60	0.82	94.96	0.22	95.30	0.39	103.90	0.25	84.50	0.36
16 hours	226.30	0.28	237.40	0.61	94.07	0.38	95.70	0.66	105.40	0.29	85.90	0.85
24 hours	227.20	0.41	240.50	0.55	94.28	0.39	100.90	0.82	105.70	0.37	86.56	1.21
32 hours	229.80	0.44	244.90	0.87	94.37	0.46	103.40	1.15	105.87	0.45	87.54	1.96
40 hours	231.80	0.46	245.00	0.99	94.49	0.50	105.60	2.13	105.99	0.52	90.81	2.36
48 hours	232.05	0.49	251.90	1.29	94.66	0.55	109.90	2.70	106.11	0.57	92.11	2.93
56 hours	233.20	0.50	254.70	1.45	95.78	0.57	118.70	3.20	106.88	0.59	94.40	3.45
64 hours	233.51	0.78	–	–	95.80	0.69	–	–	107.60	1.04	–	–
72 hours	235.80	0.82	–	–	95.89	0.70	–	–	107.80	1.1	–	–
80 hours	235.85	0.85	–	–	95.97	0.72	–	–	107.82	1.13	–	–
88 hours	235.92	0.91	–	–	96.70	0.79	–	–	108.48	1.19	–	–

Правильно?

An air flow of 14 liters/minute was passed through the oxidation tubes. The tubes were heated to the testing temperatures of 130 °C and 160 °C. The appearance of the samples, as well as viscosity [8] and TAN [9] were measured at 8 hour intervals. Testing was terminated when the TAN of the samples exceeded 3.0 mgKOH/g. Results of the testing is shown in Table 2.

The testing shows that the oxidation rate is much faster at 160 °C than at 130 °C. The oxidation rates at 160 °C are at least twice the oxidation rates at 130 °C. The viscosity, as well as the quality of the oxidation package, plays a critical effect on the thermal stability of the oil over extended use.

In practical terms, while increasing the temperature of the oil can show benefits of decreasing distortion, the life of the oil is reduced by half or more. A cost-benefit analysis weighing the benefits and savings associated with parts having lower distortion (reduced straightening, lower residual stress, etc.) must be weighed against the shortened life of the oil; and the increased consumption and disposal costs of the oil. The selection of an oil that is resistant to the increased oxidation rates (robust antioxidant package and higher viscosity) is important to cost effective mar-tempering.

## CONCLUSIONS

In this short paper, we have showed the effects of different materials in the oxidation of oil. The use of copper as a local prevention of carburization severely increases the oxidation rate of the oil. The use of nickel shows great promise in reducing oxidation of the oil. The use of a nickel plating instead of copper would substantially reduce staining and extend the life of a quench oil. However, additional work is necessary to reduce the diffusion of nickel into the part, resulting in changes in local hardenability. The use of a copper strike prior to nickel plating would improve plating adhesion, and may mitigate the diffusion effects. This work will be the subject of an additional paper to be presented once the work is complete.

Increasing the temperature of the quenchant is an effective method of reducing distortion and residual stresses in heat treated components. However, increasing the temperature by only 30°C, which is a small increase in temperature in metallurgical terms, can drastically impact the life of the oil. We have shown that this small temperature can more than halve the life of the oil. The cost of shortening the

life of the oil by at least half, must be weighed against the benefits of reduced distortion. Finally, it is important that the proper oil be chosen to operate at the desired temperature. The oil must provide consistent quenching, as well as resist oxidation at the desired temperature of operation.

## ACKNOWLEDGEMENTS

The authors wish to thank the management of Houghton International, Inc., for allowing this material to be presented. Further the authors would like to thank the Organizing Committee of the 26<sup>th</sup> Congress of the International Federation of Heat Treatment and Surface engineering, for accepting my paper to the conference.

## REFERENCES

1. **Colclough T.** «Lubricating Oil Oxidation and Stabilization,» in Atmospheric Oxidation and Antioxidants, Vol. II, G. Scott, Ed., Amsterdam, Elsevier Science B. V., 1993. P. 1–70.
2. **Gatto V., Moehle W., Cobb T., Schneller E.** Oxidation Fundamentals and Its Application to Turbine Oil Testing // J. ASTM. April 2006. Vol. 3. P. 1.
3. **March J.** «The Aldol Condensation,» in Advanced Organic Chemistry, 3rd ed., New York, John Wiley & Sons, 1985. P. 829–834.
4. **Rasberger M.** «Oxidative Degradation and Stbilization of Mineral Oil Based Lubricants,» in Chemistry and Technology of Lubricants, R. M. Motier and S. T. Orszulik, Eds., London, Blackie Academic and Professional Publishing, 1997. P. 98–143.
5. **Scott G.** Atmospheric Oxidation and Antioxidants, Amsterdam: Elsevier Publishing Company, 1965.
6. **Shlyapnikov Y.A.** Antioxidant Stabilization of Polymers // Russ. Chem. Rev. 1981. Vol. 50. P. 581–600.
7. ASTM, Standard Test Method for Oxidation Characteristics of Inhibited Mineral Oils // ASTM, 2018.
8. ASTM, Standard Test Method for Kinematic Viscosity of Transparent and Opaque Liquids (and Calculation of Dynamic Viscosity) // ASTM, 2018.
9. ASTM, ASTM D664: Standard Test Method for Acid Number of Petroleum Products by Potentiometric Titration // American Society of Testing and Materials International, West Conshohocken, PA.
10. ASTM, D 4636: Standard Method for Corrosiveness and Oxidation Stability of Hydraulic Oils, Aircraft Turbine Engine Lubricants and Other Highly Refined Oils // ASTM, Conshohocken, PA, 2017.

# VACUUM HEAT TREATMENT OF AS CAST HIGH-SPEED STEEL OF M2 TYPE

A.S. Chaus, M. Bračík, M. Sahul, M. Dománková

Slovak University of Technology in Bratislava, Faculty of Materials Science and Technology in Trnava,  
Institute of Production Technologies. Trnava, Slovakia  
alexander.chaus@stuba.sk

The influence of vacuum heat treatment on the microstructure of as cast AISI M2 type high-speed steel was studied. The primary focus was on the behaviour of eutectic carbides during both softening and homogenisation annealing as well as austenitisation. The effect of tempering on the microstructure, including secondary carbide precipitation, and the properties of the steel was also studied. Specimens were prepared by casting into ceramic moulds both in vacuum furnace and in open air. The softening and the homogenisation annealing were carried out in a vacuum furnace at 800 °C for 90 min and 1200 °C for 2, 4 and 8 h, respectively. For austenitisation, the specimens were heated up to 1180 °C and held at this temperature for 3 min followed by high pressure nitrogen quenching. Triple tempering at 540 °C for 2 h (two times) and then at 580 °C for 2 h was carried out. To study microstructure SEM and TEM electron microscopy, X-ray diffraction analysis, and energy dispersive spectroscopy were used. The relationship between the microstructure and the properties was established.

**Keywords:** vacuum; cast state; microstructure; eutectic carbides; austenite eutectoid; decomposition.

## INTRODUCTION

Heat treatment allows obtaining a given set of technological and service properties of high-speed steels (HSSs) such as machinability and grinding, hardness, strength, toughness, red hardness and wear resistance [1, 2]. Usually, the first operation is softening annealing, which is performed at a temperature 800–850 °C. This operation primarily results in the softening of the microstructure to improve machinability, but it does not have a noticeable effect on the morphology and distribution of eutectic carbides. An increase of the annealing temperature to 950 °C leads to a certain thinning of the eutectic carbide network at the grain boundaries, which is accompanied by an increase in toughness of cast HSSs after heat treatment [3]. However, in order to eliminate the eutectic carbide network more completely, so-called diffusion or homogenisation annealing carrying out at high temperatures has to be used [3]. From the point of view of the as cast microstructure transformation upon annealing, behaviour of different eutectic carbides plays a key role. This can be primarily attributed to the decomposition of metastable  $M_2C$  carbide [4–8] that is not the case of  $M_6C$  and  $MC$  carbides.

After the machining, the tools are subjected to hardening heat treatment which involves quenching and tempering. Tempering in most cases completes the heat treatment of HSSs. The processes occurring during tempering of HSSs and determining the change

in their properties are described in detail in [9–11]. It is worth mentioning that the precipitation of a variety of special carbides of alloying elements from the super-saturated martensite is particularly important for the formation of the red hardness of HSSs. However, the origin of the secondary carbides precipitated in the different HSSs is open question. Moreover, in general the effect of vacuum heat treatment on the microstructure and properties of as cast HSSs has not been investigated thoroughly. Taking into account the above-mentioned, the influence of vacuum heat treatment on the microstructure and properties of AISI M2 type HSS obtained by the foundry technology was studied.

## EXPERIMENTAL PROCEDURE

Commercially available AISI M2 HSS was used to prepare liquid metal. A nominal chemical composition of the steel was as follows, in wt. %: 0.80–0.90C, max 0.45 Mn, max 0.45 Si, 3.8–4.6 Cr, 5.50–7.00W, 1.50–2.20V, 4.50–5.50 Mo, 4.3–5.20 Co, max 0.035P, max 0.055S, and Fe as balance. To cast the steel, a roll-over induction furnace and a vacuum induction furnace were used. A pouring temperature was 1557 and 1550 °C for the gravity and vacuum casting, respectively. Two types of ceramic shell moulds containing a zircon/silica primary coat without and with addition of a cobalt aluminate ( $CoAl_2O_4$ ) were used. The ceramic shell moulds were heated and fired before cast-

ing at 1050 °C for 90 min in a rotary hearth furnace. After casting, the annealing of cast samples was carried out in argon at  $800 \pm 10$  °C in a pit vacuum furnace for 90 min followed by their cooling with a cooling rate 17 °C/h to 600 °C, then the samples were replaced to a cooling chamber where they were cooled to an ambient temperature. After annealing, specimens for mechanical tests and metallographic analysis were fabricated, which prior to austenitisation were preheated at 600, 800 and 1050 °C to minimise thermal shock. For austenitisation, the specimens were heated up to 1180 °C and held at this temperature for 3 min followed by high pressure nitrogen quenching. This treatment was carried out using a vacuum furnace. Triple tempering in a vacuum furnace at 540 °C for 2 h (two times) and then at 580 °C for 2 h completed the heat treatments of the specimens.

The metallographic specimens were prepared by standard grinding and polishing procedures. The microstructure was observed with a scanning electron microscope (SEM) a JEOL JSM-7600F, equipped with an Oxford Instruments Energy Dispersion Spectroscopy (EDS) facility. The identification of secondary carbides was done by selected area electron diffraction using transmission electron microscopy (TEM) of carbon extraction replicas and thin foils. The carbon extraction replicas were obtained from mechanically polished and etched surfaces. The replicas were stripped from the specimens in the 3% solution of  $\text{HNO}_3$  in  $\text{C}_2\text{H}_5\text{OH}$  at 20 °C and 20 V. The thin foils were prepared by mechanical pol-

ishing and jet-electropolishing. TEM observations were performed using a JEOL 200 CX and Philips 300 CM microscopes operated at 200 kV and 300 kV, respectively.

## RESULTS AND DISCUSSION

### Microstructure in as cast state

The microstructure of the studied samples in as cast state was studied in details elsewhere [12]. Solidification in ceramic moulds in both cases led to a microstructure containing bainite, minor amount of retained austenite,  $\delta$ -eutectoid and some volume of eutectic carbides, as shown in Fig. 1. According to the results presented in Table 1, after casting  $\text{M}_2\text{C}$  eutectic dominated in the microstructure of both samples being of plate-like or rod-like morphology, depending on the casting conditions. In the gravity cast sample  $\text{M}_2\text{C}$  eutectic precipitated mainly into coarse plate-like morphology (Fig. 1a) and in the vacuum cast sample in the form of considerably finer  $\text{M}_2\text{C}$  rod-like eu-

Table 1. The volume fraction of eutectics in the as-cast microstructure of the studied M2 HSS, vol. %

Eutectic	Gravity cast sample	Vacuum cast sample
Total volume fraction	13.02±1.37	8.68±1.10
$\text{M}_2\text{C}$ , rod-like	3.13±0.31	5.34±0.53
$\text{M}_2\text{C}$ , plate-like	8.73±1.02	2.25±0.28
$\text{M}_6\text{C}$ , fishbone	1.16±0.19	Not found
MC, branched petal-like	Not found	1.09±0.16

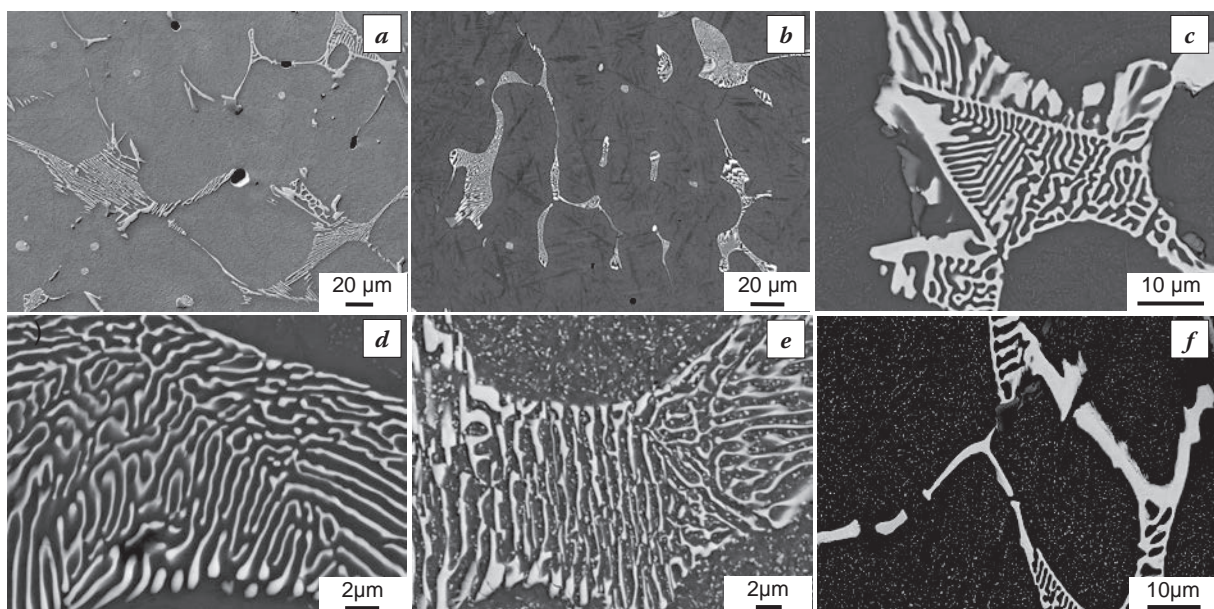


Fig. 1. Microstructure of the (a, c, f) gravity and (b, d, e) vacuum cast samples after (a–d) casting and (f, e) softening annealing

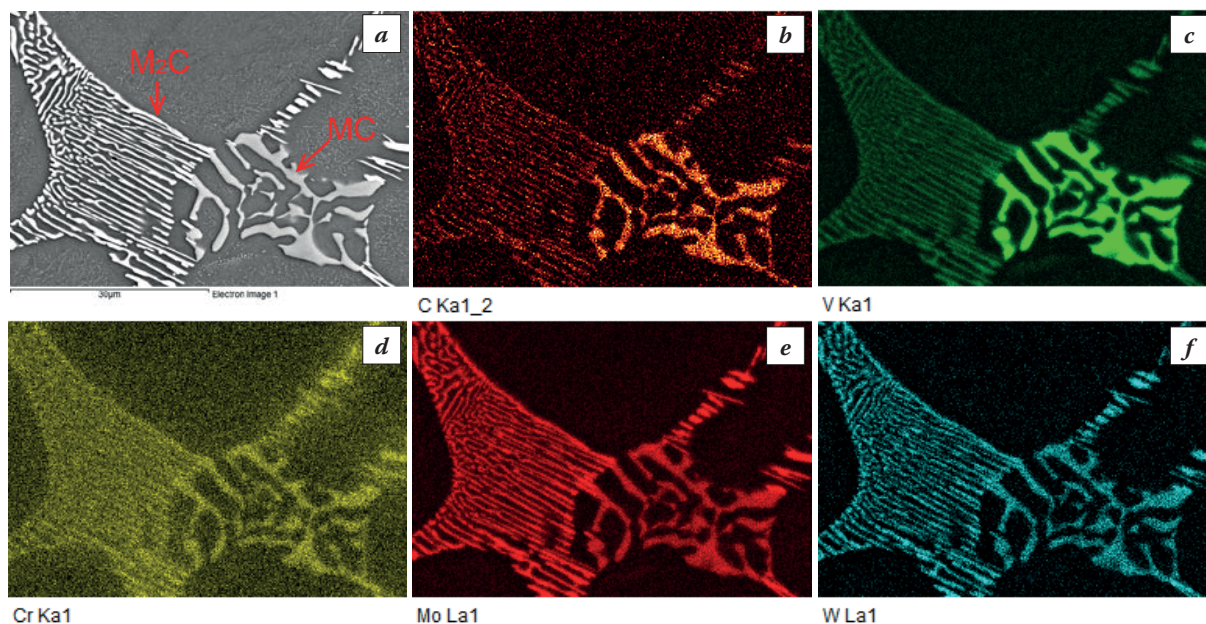


Fig. 2. SEM image showing typical  $M_2C$  and MC eutectic colonies in the as-cast microstructure of the vacuum cast sample (a) and EDS elemental maps of the area (b–f). Adopted from [12]

tectic (Fig. 1b and d). As can be seen from Table 1, the volume fractions of other eutectics, i.e.  $M_6C$  (Fig. 1c) and MC (Fig. 2a), were significantly smaller than that of  $M_2C$  one. The microstructure of the matrix and the eutectic constituent was found to be finer in the case of vacuum cast sample that was explained by the effect of the cobalt aluminate addition to the primary coat of the ceramic mould for vacuum casting that resulted in increased number of nuclei sites in the melt [12]. It was also shown in [12] that due to inoculating effect of the cobalt aluminate, concentration of alloying elements in the matrix was higher for the vacuum cast sample that, in turn, resulted in the lower volume fraction of eutectic constituent in the as cast microstructure (see Table 1). In the cast state all the above-mentioned eutectic carbides exhibited uniform distribution of carbon and the principal alloying elements in the bulk of these carbides particles as illustrated, for example, for  $M_2C$  and MC eutectic carbides in Fig. 2. The vacuum casting provided strong purification of the melt with respect to the content of gases and solid non-metallic impurities in the steel [12].

### Microstructure after softening annealing and homogenisation annealing

The microstructure of the matrix after softening annealing consisted of the fine products of austenite eutectoid decomposition and was practically similar in both cases, as illustrated for the vacuum and gravity cast samples in Fig. 1e and f, respectively. It is worth mentioning that all the eutectic carbides kept

their initial morphology. However, the higher temperature stability of  $M_6C$  eutectic carbide compared to  $M_2C$  was somewhat indicated by the fact that after softening annealing at 800 °C, the eutectoid products of austenite decomposition were not observed in the matrix of the  $M_6C$  eutectic colonies, as shown in Fig. 1f, but were observed between carbide particles in the colonies of  $M_2C$  eutectic (Fig. 1e). Nevertheless, the fine eutectoid mixture of ferrite and carbides, formed in the primary grains of the matrix during annealing, is clearly visible in both cases.

The results of metallographic studies performed after high-temperature annealing at 1200 °C were described in details elsewhere [13]. It was shown that after 2 h of homogenisation heat treatment the products of  $M_2C$  carbide decomposition were already seen in both carbides with plate-like and rod-like morphology that was primarily attributed to the precipitation of MC carbide precipitates in the bulk of the initial  $M_2C$  particles. The nucleation of the MC carbide started both inside the initial  $M_2C$  carbide, when  $M_2C$  particles were large enough (Fig. 3a), and at the carbide/matrix interface in the case of slender carbide particles (Fig. 3b). This process appeared to be more intensive in the carbide with plate-like morphology compared with rod-like one that can be explained by higher content of V in the former [6, 12]. In contrast, a change in the initial morphology of  $M_6C$  and MC carbides did not occur after two hours of exposure [13].

With increasing treatment time from 4 to 8 h, V and Cr segregation in the initial  $M_2C$  carbide was getting stronger (Fig. 3c–e) that was a consequence of the progressive growth and coarsening of the MC particles

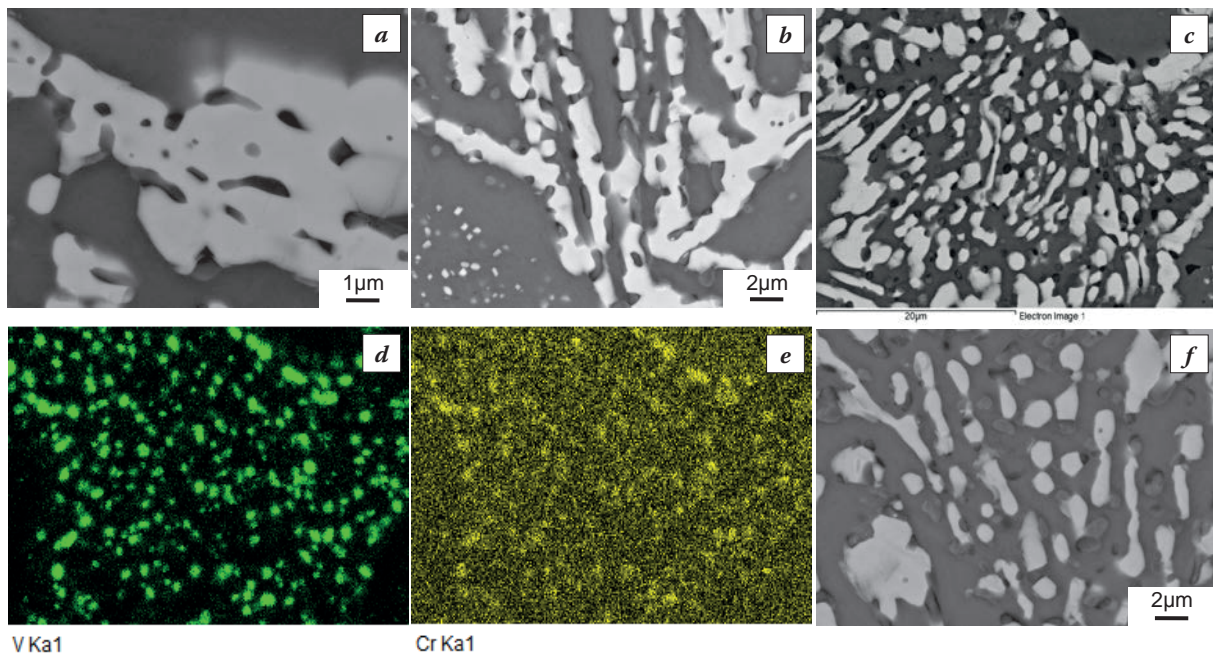


Fig. 3. SEM images showing (a, b) MC precipitates in the bulk of initial  $M_2C$  carbide particles after 2h homogenisation annealing and (c, f) mixtures of  $M_6C$  and MC carbides formed at decomposition of  $M_2C$  during 8 h homogenisation annealing, and EDS elemental maps of (d) V and (e) Cr in the area shown in (c). (c–f) Adopted from [13]

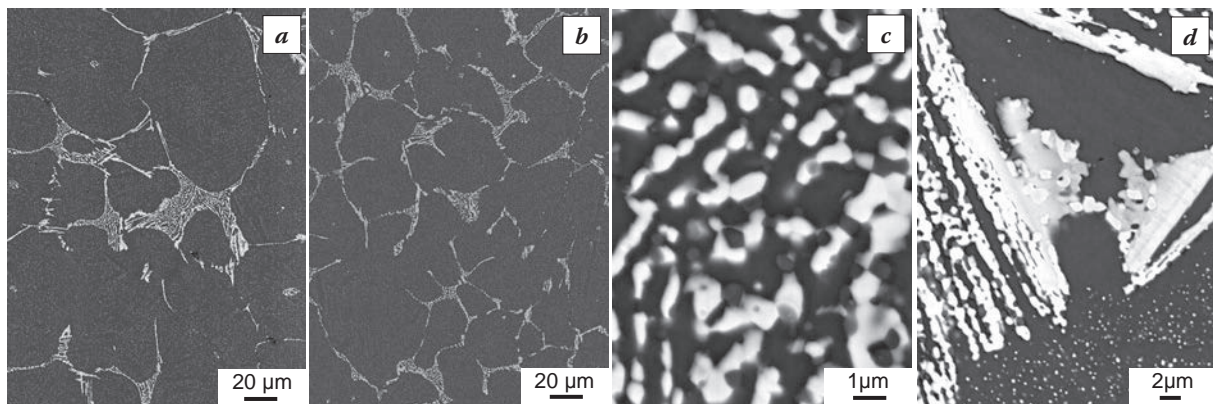


Fig. 4. Microstructure of the (a, c, d) gravity and (b) vacuum cast samples after full heat treatment

precipitated from  $M_2C$  carbide during its decomposition. Moreover, the longer homogenisation time also resulted in a stronger fragmentation of  $M_6C$  carbide particles that together with the coarsening of MC carbide particles led to the formation of a distinct mixture of these carbides to be products of the  $M_2C$  carbide decomposition (Fig. 3f). It should be stressed that the above-mentioned microstructural changes of  $M_2C$  eutectic carbide could result in improved toughness of the cast HSSs due to the formation of thinner eutectic carbide networks at the matrix primary grain boundaries.

### Microstructure in heat-treated state

After heat treatment, the microstructure of both samples consisted of the undissolved eutectic

carbides, the fine secondary carbides, the small “islanders” of  $\delta$ -eutectoid and the tempered martensite with very little retained austenite, as shown in Fig. 4a and b. It is seen from these figures that decomposition process of the initial  $M_2C$  eutectic carbide occurred during the heat treatment in both samples. However, the coarser products of the decomposition were revealed in the case of the gravity cast sample. For example, Fig. 4c shows a mixture of the completely fragmented  $M_6C$  and MC carbide particles formed during the decomposition of the original  $M_2C$ . In contrast, Fig. 4d illustrates the partial decomposition of the  $M_2C$  carbide particle that was only observed in the case of a larger size of  $M_2C$  particles in this sample. As a result, such larger particles in their periphery regions consisted of the above-mentioned mixture whilst the core of the given par-

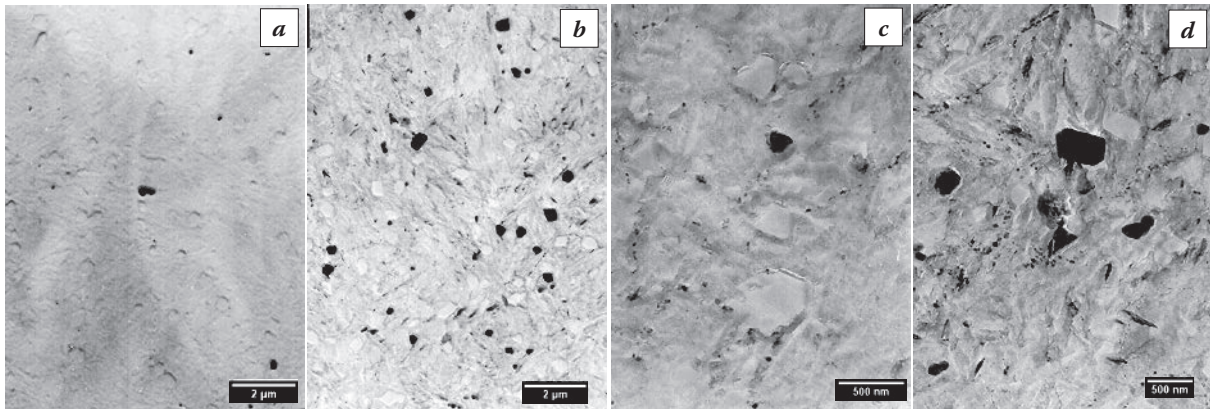


Fig. 5. TEM micrographs of (a, b) larger and (c, d) smaller secondary carbide particles in the microstructure of the (a, c) gravity and (b, d) vacuum cast samples after full heat treatment

ticle, i.e. original  $M_2C$ , appeared to be undecomposed [12]. In this context it is worth noting that incompletely decomposed particles of the larger  $M_2C$  carbide enhanced carbide heterogeneity of the steel.

Since the origin, size, morphology and distribution of secondary carbides have great impact on the red hardness of HSSs, these parameters were also thoroughly examined. In particular, with respect to size, two types of secondary carbide particles were detected by the TEM analysis in the tempered samples. Fig. 5a and b shows the distribution of larger carbide particles in the gravity and the vacuum cast samples, respectively. As can be seen from these figures the vacuum cast sample contained a greater number of larger secondary carbide particles with primarily angular shape, which size for both samples varied in the range of 150–400 nm. This is consistent with a higher concentration of carbon and alloying elements in the matrix as was reported in [12]. Amount of smaller secondary carbide particles, 20–40 nm in size in both cases, was also greater in the vacuum cast sample, as can be seen in Fig. 5c and d. According to the indexation of the diffraction patterns of the larger secondary carbide particles, these precipitates were found to be  $M_6C$  and  $MC$  carbides, whereas the smaller secondary carbide particles were identified as  $MC$  and  $M_2C$  [12].

### Evaluation of mechanical properties

Mechanical properties of both samples are presented in Table 2. The microhardness after casting were in line with the bainitic matrix of these

Table 2. Mechanical properties of the studied M2 HSS samples after the heat treatment [12]

Property	Gravity cast sample	Vacuum cast sample
Hardness, $HV_{10}$	$803.8 \pm 7.7$	$801 \pm 11.7$
Red hardness, $HV_{10}$	$686.7 \pm 4.9$	$720.6 \pm 6.3$
Impact toughness, $MJ/m^2$	$0.065 \pm 0.028$	$0.101 \pm 0.016$
Bending strength, MPa	$1597 \pm 64$	$1781 \pm 64$

samples. In general, the microhardness was a bit higher after the vacuum casting that can be attributed to a larger content of carbon and alloying elements in the matrix of the sample cast in vacuum that was explained by a larger undercooling of the melt under the effect of the cobalt aluminate particles which increased number of nuclei sites for the solid solution at the first stage of the nucleation [12]. After the heat treatment the hardness of both samples was practically similar, whilst the red hardness was a bit higher for the sample fabricated by the vacuum casting. This can be attributed to stronger secondary carbide precipitation in the vacuum cast sample that was proved by the TEM analysis.

As can be seen from Table 2 vacuum cast sample had higher impact toughness and bending strength compared with the gravity cast one that was related to its general microstructure refinement and the purification of the metal discussed above.

### ACKNOWLEDGMENTS

The financial support of the grants from the Ministry of Education, Science, Research and Sport of the Slovak Republic VEGA 1/0747/19 and APVV-16-0057 is gratefully acknowledged.

## REFERENCES

1. **Roberts G. ., Krauss G., Kennedy R.** Tool Steels, fifth ed. Ohio: ASM International, 1998.
2. **Campbell F.C.** Elements of metallurgy and engineering alloys. Ohio: ASM International, 2008.
3. **Revis L.A., Lebedev T.A.** Structure and properties of cast cutting tools (in Russian). Leningrad: Mashinostroenie, 1972.
4. **Fredriksson H., Hillert M., Nica M.** Scand. // J. Metall. 1976. 8. 111–122.
5. **Zhou X., Fang F., Jiang J., Zhu W., Xu H.** // Mat. Sci. Technol. 2012. 28. 1499–1504.
6. **Chaus A.S.** // Mater. Sci. Technol. 2014. 30. 1105–1115.
7. **Chaus A.S., Porubski J.** // Met. Sci. Heat Treat. 2014. 55. 583–591.
8. **Chaus A.S., Bogachik M., Uradnik P.** // Phys. Met. Metallogr. 2011. 112. 470–479.
9. **Pippel E., Woltersdorf J., Pöckl G., Lichtenegger G.** // Mater. Charact. 1999. 43. 41–55.
10. **Yan F., Shi H., Fan J., Xu Z.** // Mater. Charact. 2008. 59. 883–889.
11. **Chaus A.S., Dománková M.J.** // Mater. Eng. Perform. 2013. 22. 1412–1420.
12. **Chaus A.S., Bračik M., Sahul M., Dománková M.** Vacuum. 2019. 162. 183–198.
13. **Chaus A.S., Sahul M., Bračik M.** Diff. Found. 2019. 22. 24–33.

## HEAT TREATMENT WITH INTERCRITICAL HEATING OF DUCTILE IRON

Piotr Nawrocki<sup>1,2</sup>, Karolina Lukasik<sup>3</sup>, Kamil Wasiluk<sup>4</sup>, Dawid Myszka<sup>5</sup>

<sup>1</sup> Heat Treatment Department, Institute of Precision Mechanics. Warsaw, Poland

<sup>2,3,5</sup>Department of Metal Forming and Casting, Warsaw University of Technology. Warsaw, Poland

<sup>4</sup>Department of Surface Engineering, Warsaw University of Technology. Warsaw, Poland

p.nawrocki@wip.pw.edu.pl

Ductile iron with ausferritic matrix obtained as a result of austenitization and then austempering is characterized by a combination of high strength properties along with good wear resistance and good ductility. Austenitization in intercritical temperatures is described in the literature, but the phenomena associated with the use of this range preceded by austempering in cyclic processing is not fully understood. The paper attempts to evaluate the influence of heat treatment within the intercritical field on the microstructure and properties of austempered ductile iron (ADI) with an increased content of Mo, Ni and Cu elements. The aim of the work was to maximize the fragmentation of the ductile iron matrix microstructure by selecting a low temperature of isothermal transformation, i.e. 40°C above Ms temperature in the lower bainite range. Heat-treated cast iron was subjected to dilatometer tests, microstructure research, hardness and impact tests. It was found that cyclic heat treatment and the use of the intercritical range during austenitizing may affect the strong grain refining of austenitic grain and achieving high fracture toughness

**Keywords:** austempered ductile iron (ADI); intercritical temperature; impact properties; dilatometric tests; bainitic transformation.

### INTRODUCTION

The best compromise between high strength and good ductility in nodular cast iron is obtained by performing a heat treatment of austempering, consisting of two steps: austenitization above A1 temperature, usually between 820–900 °C, fast cooling to the temperature within range of 200–400 °C and isothermal hold in that temperature [1]. As a result, an unique microstructure is formed, consisting of a mixture of high carbon content austenite ( $\gamma_{HC}$ ) and ferrite plates ( $\alpha$ ), called ausferrite. This structure can be achieved with proper cooling rate after austenitization to prevent diffusive transformations in inhomogeneous as-cast microstructure [2, 3]. Microsegregation of alloying elements often causes necessity of preliminary treatment, ex. normalization or ferritization, especially when treated element has a variable cross-section.

Main parameters of austempering are time and temperature of austenitization and time and temperature of austempering. Increment of austenitization temperature results in higher carbon concentration in austenite which causes better hardenability but also increases total time of ausferritic transformation. Decrement of austenitization temperature increases driving force of austenitic transformation, which can lead to significant refinement of micro-

structure. Considering the above, austenitization temperature should be minimized to a level sufficient to achieve 1.1–1.3 wt.% of carbon concentration in austenite. Temperature of austempering affects the kinetics of ausferritic transformation and morphology of forming microstructure. Austempering within lower range of transformation temperatures results in higher fraction of thin bainitic ferrite plates in final microstructure and, subsequently, lower content of carbon-enriched austenite. The amount of high carbon content austenite in such microstructure is too low to ensure good plasticity while maintaining high strength. Formation of martensite during cooling to low austempering temperature can also occur. With an increment of austempering temperature a decrement of mechanical strength and improvement of plasticity is observed [4]. Numerous studies [5–8] on optimization of ausferritic transformation that have been published often are concentrated on analyzing only a narrow range of austempering temperatures. Recently, a number of papers regarding austenitization in the intercritical zone have been published [9, 10]. In paper [9] analyzed series of intercritical austenitizing temperatures ranging from 775 to 900 °C with subsequent austempering performed at 300 and 400 °C on a conventional unalloyed ductile iron. Reported results showed that all mechanical properties increased with intercritical austenitizing tempera-

tures till an optimum austenitizing temperature of 830 °C. At this optimum processing condition, tensile strength of 974 MPa and very high toughness of 166 J was achieved. This paper aims to estimate the influence of prior heat treatment and austenitization within intercritical zone parameters on microstructure and properties of an austempered ductile iron. It is also an attempt to comprehensively solve the problem of selection of transformation parameters using dilatometric tests, which enable designing standard heat treatment of nodular cast iron, but above all are a starting point for the design of complex processing variants, eg with pre-treatment or intercritical.

## MATERIALS AND METHODS

For the purpose of experiment a database of heat treated ductile cast iron, containing chemical composition, heat treatment, properties and microstructure data from over 100 published papers and own research, was created. Collected data was used to choose chemical composition of a ductile iron, optimal for obtaining good mechanical properties after heat treatment in a variety of different cast modules. Selected chemical composition is shown in Table 1.

The material was cast as Y2-shaped standard test blocks by the Foundry Institute in Krakow. Casting were performed in medium frequency induction furnace with loading capacity of 50 kg. The cast batch was composed of special crude iron containing C – 4,30 wt.%, Si – 0,40 wt.%, Mn – 0,03 wt.% and steel scrap. Spheroidisation was performed at 1400 – 1420 °C at the vat bottom using FeSiMg9, followed by a modification using FeSi75. Samples for spectrometric analysis were produced (Table 2) and the melt was casted at 1350 °C to bentonite-bounded sand moulds. The microstructure of the obtained ductile iron in the as-cast state is presented in Fig. 1. Based on unetched metallographic samples observation the amount of graphite nodules was estimated to be 11%. The obtained castings were cut into smaller samples (Fig. 2), which were subject to a heat treatment.

Table 1. Chemical composition of ductile iron (wt. %)

	C	Si	Mn	Ni	Cu	Mg
<b>min.</b>	3.40	2.,40	0.20	1.80	0.50	0.055
<b>max.</b>	3.55	2.50	0.35	2.00	0.80	0.060

Table 2. Chemical composition of ductile iron (wt. %)

C	Si	Mn	Mo	Ni	Cu	Mg
3.55	2.5	0.35	0.55	1.90	0.5	0.058

Heat treatment parameters for investigated ductile iron were determined after dilatometric study of phase transformation kinetics. Cylindrical samples for dilatometric experiment with diameter of 3 mm and length of 10 mm were cut from Y2 blocks using EDM. Experiments were carried out on Bahr DIL 805 Pro quenching dilatometer. Heat treatment of bulk samples for metallographic and mechanical experiments was conducted in resistant furnace and fluidized bed. Microstructure observation was performed on metallographic samples using an scanning electron microscope JEOL JSM-IT100 scanning electron microscope in Institute of Precision Mechanics in Warsaw at magnifications in the range of x1000 and x5000. The HRC surface hardness tests were performed using an Wilson hardness tester, performing 3 readings on each of the samples. Charpy impact test was carried out according to EN ISO 148-1\_2011 standard using Zwick/Roell Charpy pendulum with impact energy of 300 J. For this test, standard sized 10 x 10 x 55 mm unnotched samples were utilized.

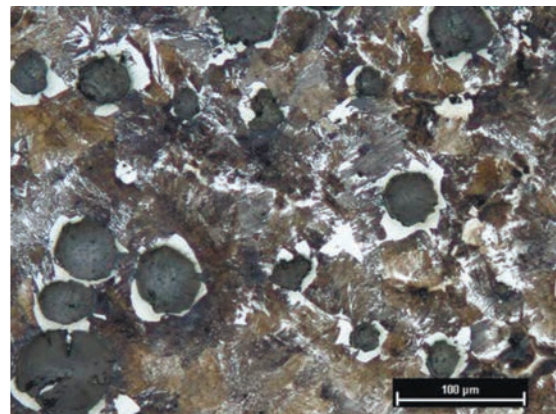


Fig. 1. Microstructure of the obtained Mo-Ni-Cu cast iron (etched with nital)

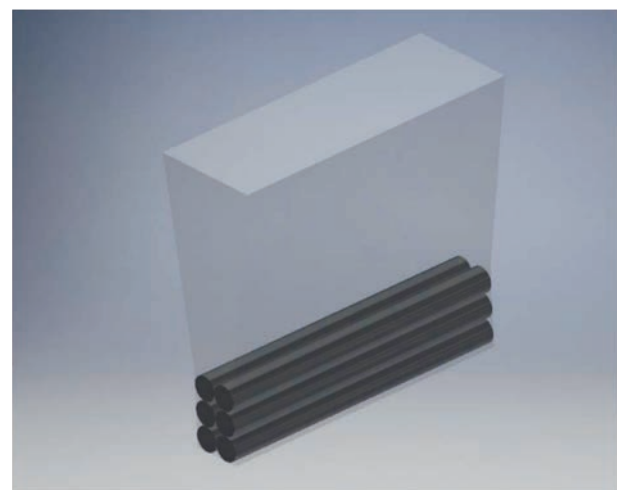


Fig. 2. Casting with specimens for heat treatment and dilatometric examinations

## Heat treatment

The first step to design a heat treatment was determination of characteristic temperatures by dilatometric study. Fig. 3 shows fragment of change of sample's length against temperature plot from the dilatometric experiment of heating sample from ambient temperature to 1050 °C at heating rate of 2 °C/min which allows to determine  $A_{c1}$ s (start of eutectoid transformation) and  $A_{c1f}$  (finish of eutectoid transformation).  $M_s$  temperature were determined from the dilatometric test of austenitizing at 900 °C with subsequent cooling to ambient temperature at cooling rate of 50 °C/s (Fig. 4).

The aim of treatment was maximum refinement of microstructure while avoiding proeutectoid ferrite. Designed process was consisted of double

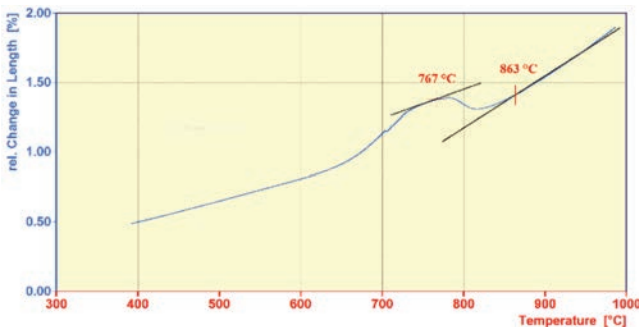


Fig. 3. Dilatometric diagram for the tested Mo-Ni-Cu cast iron

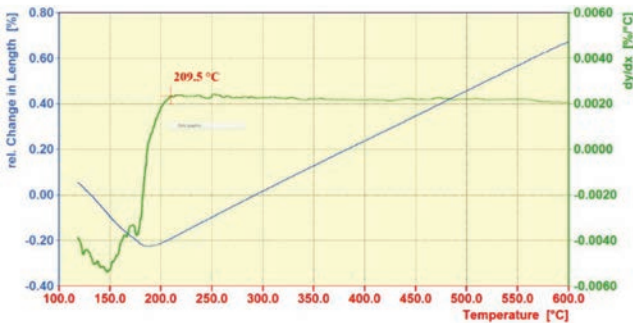


Fig. 4. Dilatometric diagram for the tested Mo-Ni-Cu cast iron shows  $M_s$  temperature

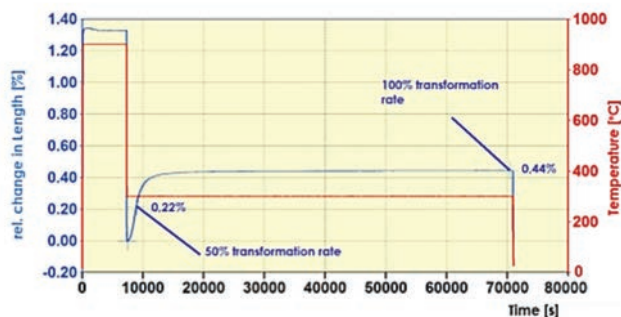


Fig. 5. Dilatometric diagram for the tested Mo-Ni-Cu cast iron shows ausferritic transformation at 300 °C

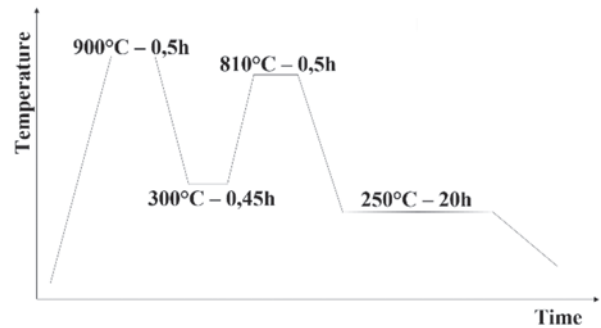


Fig. 6. Schemes of conducted heat treatment process of Mo-Ni-Cu ductile iron

austempering with first ausferritic transformation stopped at 50% rate (Fig. 6). Time to 50% of ausferritic transformation at given temperature was determined through dilatometric experiment. Assuming that carbides precipitation during isothermal hold at ausferritic transformation temperature is suppressed or negligible due to silicon content, change of length during that hold can be associated solely with austenite to bainitic ferrite transformation. Hence, a given percentage of sample's total length increment corresponds with same percentage of transformation progress (Fig. 5) Immediately after obtaining 50% of transformation material were partially austenitized within intercritical zone and austempered at low temperature for a time sufficient to close processing window. The maximum refinement of the ductile iron matrix microstructure was assumed by selecting a low temperature of isothermal transformation, i.e. 40 °C above  $M_s$  in the bottom bainite range. On the basis of dilatometric plots (Fig. 3 and Fig. 4) the temperature of 250 °C were determined (for 20 hours to complete the 100% ausferrite transformation).

## RESULT AND DISCUSSION

### Microstructure

Fig. 7 and Fig. 8 shows the obtained cast iron microstructure after heat treatment of dilatometric and bulk samples.

The metallographic analysis indicates refinement of the matrix microstructure of the ductile iron after applied heat treatment process within the zone of intercritical heating. The microstructure of both dilatometric and regular samples after heat treatment is characterized by a bainitic matrix. Dilatometric samples featured a uniform microstructure refinement (Fig. 7), while in the case of regular samples large laths of ferrite were also observed (Fig. 8).

Occurrence of large ferrite was distinctive for areas of variable chemical composition in a non-homo-

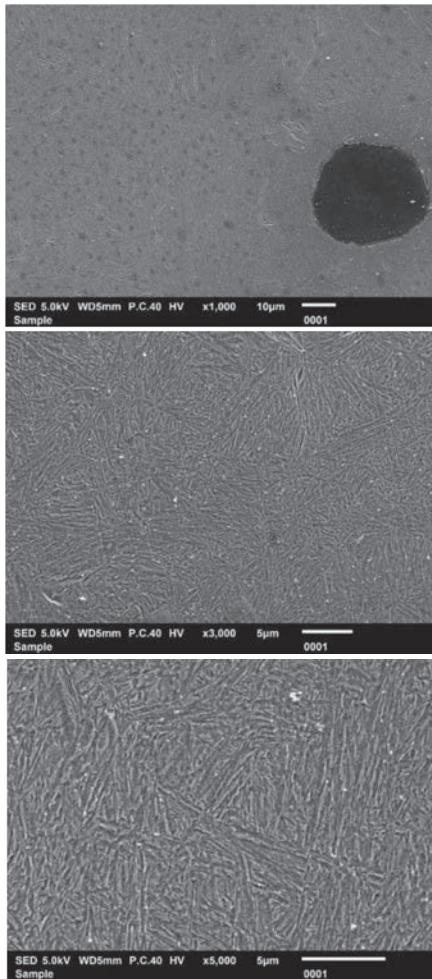


Fig. 7. Microstructure of tested dilatometric samples of cast iron after heat treatment (etched with 3% nital)

geneous matrix of nodular iron. Their formation may be associated with greater thermal inertia comparing to dilatometer samples. However, these plates constitute a small percentage of the matrix microstructure while most of observed ausferrite was characterized by grain refinement even below 100 nm. This gives grounds for concluding that the ausferritic transformation at a respectively low intercritical temperature and prior heat treatment allows the formation of a nanostructured ausferrite matrix of a ductile iron.

### Hardness and impact tests

Table 2 and Table 3 present the obtained results from hardness and impact measurements, in the form of mean values from the measurement along with the standard deviation. Two different loads during the hardness test, smaller 0.2 kG and larger-1 kG were used to illustrate the difference between matrix and whole material. Hardness results indicate a higher hardness value for dilatometer samples. Dif-

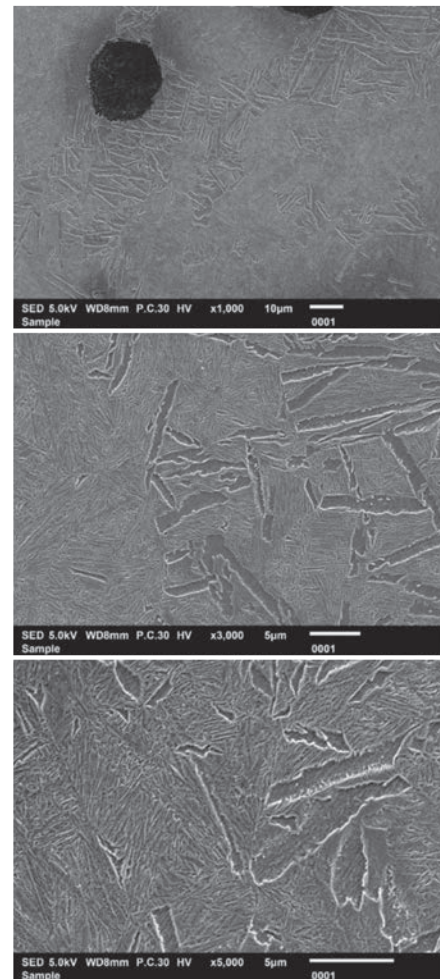


Fig. 8. Microstructure of tested metallography samples of cast iron after heat treatment (etched with 3% nital)

ference in HV0.2 hardness between dilatometric and metallographic sample was about 20%. This results from the matrix microstructure after heat treatment processes. Presence of large ferrite plates observed in metallographic samples was the cause of hardness decrement. Furthermore, measured hardness of the material can be associated with other properties, like tensile strength, due to developed database (Fig. 9).

The average impact value for the tested ductile iron is approximately 45 [J] (Table 3), which should be considered as a good result compared to ADI obtained after conventional heat treatment. Similar studies by the authors described in [6] confirm that reheating of ductile iron above the A1 temperature after the first austempering allows to achieve high impact values (Table 4).

### SUMMARY

Obtained results show that proposed heat treatment of ductile iron, consisting double austemper-

Table 3. Average hardness values for heat treatment of Mo-Ni-Cu cast iron

	HV1 kg (HB)	HV200 g
Regular sample	485±48 (460)	500±48
Dilatometric sample	552±54 (532)	622±23

Table 4. Average toughness values for heat treatment of Mo-Ni-Cu cast iron

Number of measurement	K [J]
1	52.8
2	34.3
3	47.6
Average	45.0 ±9.5

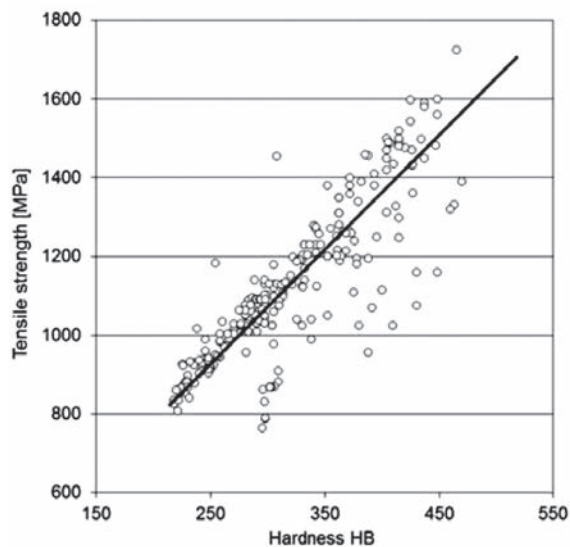


Fig. 9. Dependence of tensile strength on HB hardness for ausferritic ductile iron; base on own data

ing with intercritical austenitization can produce very fine microstructure. A careful design of specific time-temperature parameters of prior austempering ensures uniform distribution of alloying elements within the matrix. Secondary austenitization in the intercritical zone resulted in partial bainitic ferrite to austenite transformation and more even carbon distribution which provided greater nucleation rate of bainitic ferrite during second austempering. Small but significant amount of proeutectoid ferrite was also observed in bulk samples; its location in matrix microstructure suggests it formed in areas of microsegregation of alloying elements. Absence of proeutectoid ferrite in dilatometric samples was probably caused by greater austenitization time to cross section ratio than in bulk samples. Greater volume of latter would require significantly longer austenitization time to achieve similar effect like in dilatometric samples. Good mechanical properties of investigated

ductile iron after double austempering indicate considerable potential for new discoveries in the field of strong microstructure fragmentation through cyclic thermal interactions.

## ACKNOWLEDGMENTS

This work was supported by the National Centre for Research and Development NCBiR project no PBS3/B5/45/2015.

## REFERENCES

1. **Artola G., Gallastegi J., Izaga J.** Austempered Ductile Iron (ADI) Alternative Material for HighPerformance Applications // International Journal of Metalcasting. 2017; 11, 131–135.
2. **Kobayashi T., Yamada S.** Effect of holding time in the ( $\alpha$ + $\gamma$ ) temperature range on toughness of specially austempered ductile iron // Metallurgical and Materials Transactions A, 1996; 27:1961–1971.
3. **Putatunda S.K., Panneerselvam S., Alshwigi M.** Development of nanostructured austempered ductile cast iron (ADI): 28th ASM heat treating society conference. 20–22 October 2015. Detroit, USA; ASM International.
4. **Kim Y., Shin H., Park H., Lim J.D.** Investigation into mechanical properties of austempered ductile cast iron (ADI) in accordance with austempering temperature // Materials Letters. 2008; 62: 357–360.
5. **Jianghuai Y., Putatunda S.K.** Influence of a novel two-step austempering process on the strainhardening behaviour of austempered ductile cast iron (ADI) // Materials Science and Engineering A. 2004; 382: 256–279.
6. **Mahmoud F.H.** Effect of second step austempering temperature and time on the impact properties of twostep austempered SG-cast iron // Journal of Al Azhar University Engineering Sector. 2010; 5: 59–65.
7. **Aristizabal R., Foley R., Druschitz A.** Inter Metalcast (Intercritically Austenitized Quenched and Tempered Ductile Iron // International Journal of Metalcasting. 2012; 6: 7–14.
8. **Nawrocki P., Wasiluk K., Łukasik K., Myszka D.** Influence of preheat treatment on mechanical properties of austempered ductile cast iron // Archives of Foundry Engineering, Komisja Odlewnictwa Polskiej Akademii Nauk Oddział w Katowicach. 2018; 18: 176-180.
9. **Chen J.K., Tsai J.S., Chen B.T.** Toughening of ADI austenitized in inter-critical region, TMS-The Minerals // Metals and Materials Society. 2011; 3: 701–708.
10. **Aristizabal R., Foley R., Druschitz A.** Intercritically austenitized quenched and tempered ductile iron // International Journal of Metalcasting, 2010; 7–14.

# INFLUENCE OF ACCELERATED SPHEROIDISATION ON QUENCHING PROCESS AND RESULTANT MECHANICAL PROPERTIES IN SPRING STEEL 54SiCr6

Jakub Kotous<sup>a</sup>, Jaromír Dlouhý<sup>b</sup>, Daniela Nacházelová<sup>c</sup>

COMTES FHT a.s. Dobřany, Czech Republic

<sup>a</sup>jkotous@comtesfht.cz, <sup>b</sup>jdlohy@comtesfht.cz, <sup>c</sup>dnachazelova@comtesfht.cz

This article is aimed at the accelerated spheroidisation and refinement (ASR) achieved by induction heating in 54SiCr6 spring steel. ASR is much faster than conventional soft annealing and produces a fine microstructure. This has a considerable influence on material behaviour during quenching. If the quenching process is controlled well, improved mechanical properties can be obtained after tempering. For the spring industry it is very important to achieve high ultimate and yield strengths and maintain the desired ductility. The ASR process can increase strength characteristics and retain the ductility characteristics, such as elongation and reduction of area. This is also reflected in better resistance against brittle fracture.

In this experiment, the impact of various microstructures in 54SiCr6 spring steel on hardening behaviour was investigated. Specimens with three different microstructures were produced. Two microstructures contained spheroidised carbides and were achieved by accelerated annealing ASR and by conventional soft annealing. The third structure was ordinary lamellar pearlite which was produced by hot rolling. Quenched and tempered microstructures were observed using electron microscopy (SEM) and their mechanical properties were tested in the tempered state.

**Keywords:** 54SiCr6; accelerated spheroidisation; ASR; austenitization; refinement.

## INTRODUCTION

The usual way to achieve spheroidised structure in steel is soft annealing. It tends to be a time and energy consuming operation. Therefore, there efforts to accelerate this process without impairing the resulting properties. The technique which is commonly used today involves heating above or cycling about the  $A_{c1}$  temperature in a furnace. However, these processes, too, take several hours. Another alternative is the “Accelerated Spheroidisation and Refinement” (ASR). This process can be performed using thermal [1] or thermomechanical treatment [2]. It uses phase transformations to rapidly accelerate the spheroidising process. The great advantage of ASR is fast. It takes several minutes. The resulting microstructure is fine-grained, because the low time of treatment restricts structure coarsening [3–5]. A structure of this type undergoes transformation more readily, and therefore at a faster rate. As previous experiments show [6], this manifests itself in quenching temperature differences which can reach 60 °C.

The ASR can be used with many low-alloy steels, including 100CrMnSi6-4 bearing steel, 90MnCrV8

tool steel and 51CrV4 spring steel. The applicability of ASR mainly depends on chemical composition by reason of diffusion-controlled partial austenitization and divorced eutectoid transformation which occur during the process. Therefore, it is limited by the speed of movement of the phase interface which should not be too slow [7, 8]. This movement is retarded by higher levels of alloying elements, for instance. There was a problem with higher silicon content in the 54SiCr6 experimental steel. This ferrite-forming element hinders carbon diffusion and increases the resistance of cementite to spheroidisation [9]. This in turn affects the ASR and soft annealing processes. The ASR was modified by including isothermal holds. Soft annealing was altered by using slower cooling rate.

The main goal of this work was the optimizing of the quenching process of 54SiCr6 spring steel with three different initial structures and comparing the mechanical properties after tempering. The three microstructures prior to quenching were hot rolled structure of lamellar pearlite, a spheroidised structure after soft-annealing and spheroidised structure after accelerated spheroidising annealing (ASR).

Table 1. Chemical composition of 54SiCr6 steel (wt. %)

C	Si	Mn	P	S	Cr	Mo	Ni	Cu	Ti	V	Fe
0.57	1.51	0.68	0.008	0.003	0.75	0.03	0.1	0.1	0.003	0.003	bal.

## Materials and methods

The material under investigation was 54SiCr6 steel, which is used widely for the manufacture of springs. The batch used for the experiments was made at COMTES FHT a.s. The chemical composition of the steel is given in Table 1.

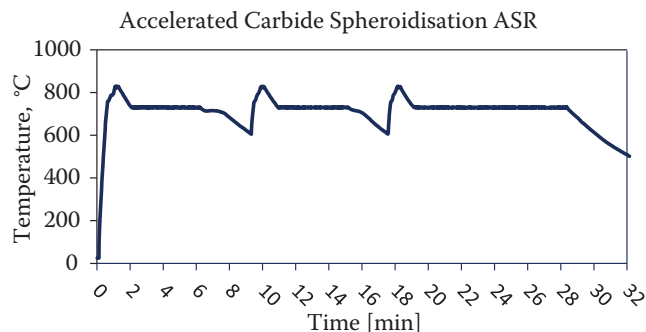
The steel was cast in a vacuum induction furnace, then forged to blocks, hot-rolled and air-cooled after rolling. This process produced the first initial structure for experiments, lamellar pearlite (identified as HR, hot-rolled). Spheroidising annealing was performed by two different methods. One was conventional soft annealing (SA) in an electrical air furnace. The material was held just above the  $A_{c1}$ . If a temperature below  $A_{c1}$  were used, much longer time at temperature would have been necessary.

The soft annealing sequence was as follows: heating at 10 °C/min to 720 °C, then at 15 °C/hour to 770 °C, holding for 5 hours, furnace cooling at 5 °C/hour to 720 °C, then at 25 °C/hour to 650 °C, free cooling in the furnace to 400 °C and afterwards cooling in still air. The total duration of the soft annealing sequence till the samples were removed from furnace was 27 hours.

The second spheroidising annealing was the ASR process carried out in medium-frequency induction heating equipment. Temperature was measured with a thermocouple welded onto the samples. The ASR sequence consisted of three short thermal cycles.

The ASR sequence (Fig.1) was as follows: heating at 19 °C/s to 820 °C, holding for 15 seconds, cooling in still air (at approx. 1.5 °C/s) to 725 °C and holding for 5 minutes. This was followed by cooling in still air to 600 °C. The second cycle was identical. In the third cycle, the holding time at 725 °C was extended to 10 minutes. The final step was cooling in still air to ambient temperature. The sequence is shown in Fig. 2. The total duration of the spheroidisation stage was approximately 30 minutes. Holding at 725 °C was necessary to prevent formation of new cementite lamellae in the steel. Otherwise, the processing time can be half [10].

Soaking prior to hardening was carried out using electrical air furnaces. Quenching temperatures were in the range from 810 °C to 910 °C and the soaking time were 20 and 40 minutes. The quenching medium was oil. Samples were then tempered at 400 °C/ 2 hours followed by air-cooling.



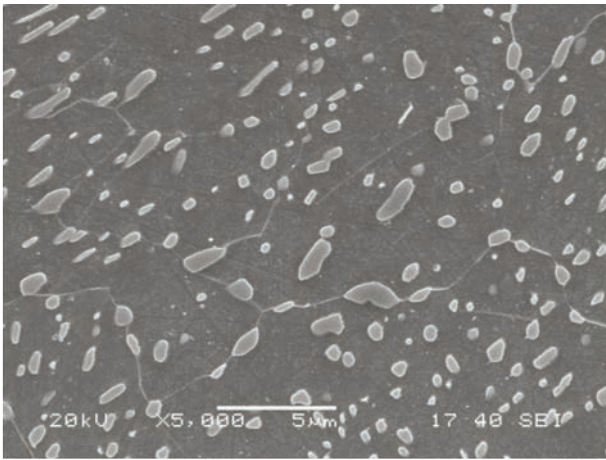


Fig. 3. Microstructure after soft annealing (SA), 207 HV10

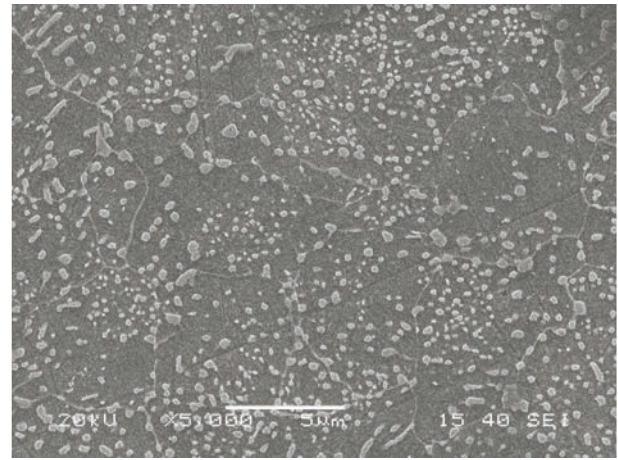


Fig. 4. Microstructure after accelerated annealing ASR, 224 HV10

duced large globular particles up to 2  $\mu\text{m}$  in size. The ASR sequence (Fig. 4) led to densely-dispersed four times smaller globular cementite particles (no more than 0.5  $\mu\text{m}$ ). It led to higher hardness after accelerated spheroidisation (ASR):  $224 \pm 5$  HV10. Hardness after soft annealing was  $207 \pm 1$  HV10. Both values meet the delivery specifications for 54SiCr6 steel annealed to obtain globular cementite [11].

### Quenching and tempering

Quenching was performed from 810, 830, 850, 870, 890  $^{\circ}\text{C}$ , and 910  $^{\circ}\text{C}$ , a temperature which was added for the soft-annealed state. Soaking time prior to quenching were 20 and 40 minutes. Based on previous experience [3], it was assumed that a lower quenching temperature would be sufficient for the material after ASR. Quenching temperatures of 810 and 830  $^{\circ}\text{C}$  were thus chosen. The temperatures

recommended in material data sheets are 840  $^{\circ}\text{C}$  or higher [11].

Quenching temperature at 810  $^{\circ}\text{C}$  was too low. Ferrite was found in the microstructure of every samples. HR sample contained considerably less ferrite compared to after SA and ASR. The structure was fully austenitized at 830  $^{\circ}\text{C}$  and the structure was consisted only of martensite and undissolved carbides (Fig. 5). Undissolved carbides were very fine globules and homogeneously distributed through the material. Observed globular carbides were created by incomplete dissolution of lamellar cementite. The amount of undissolved carbides decreased with increasing quenching temperature up to and including 870  $^{\circ}\text{C}$ , see Fig. 6. Undissolved carbides were only rarely observed at 890  $^{\circ}\text{C}$ . This anticipated trend was similar in routes which contained soaking for 40 minutes: all cementite was dissolved at 870  $^{\circ}\text{C}$ . The presence of ferrite and undissolved carbides depended on aus-

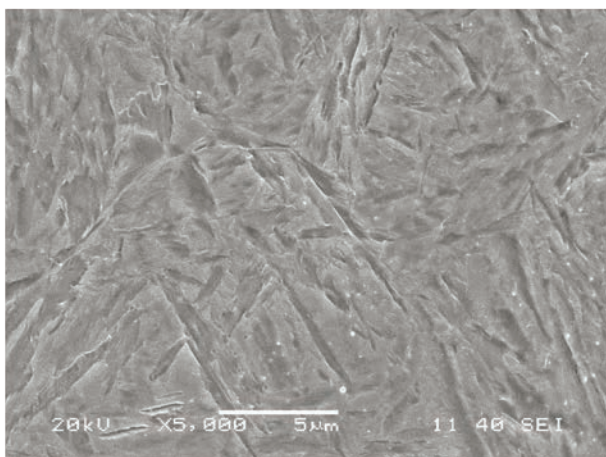


Fig. 5. Microstructure of quenched HR 830  $^{\circ}\text{C}$  / 20 min

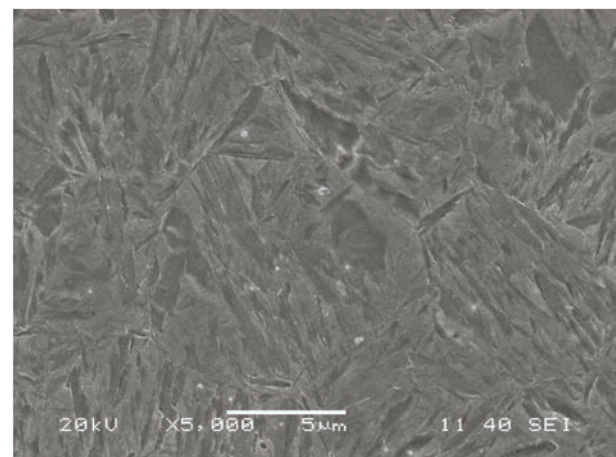


Fig. 6. Microstructure of quenched HR 870  $^{\circ}\text{C}$  / 20 min

Table 2. Austenitizing: the highest quenching temperature which 54SiCr6 steel still contained a particular phase

	Condition prior to quenching					
	Hot rolling (HR)		Soft annealing (SA)		Accelerated annealing ASR	
Soaking time [min]	20	40	20	40	20	40
Ferrite	810 °C	810 °C	850 °C	830 °C	810 °C	810 °C
Undissolved cementite	870 °C	850 °C	910 °C	890 °C	870 °C	850 °C

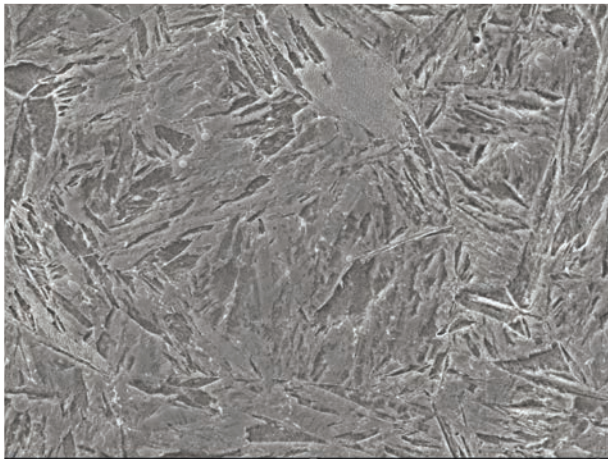


Fig. 7. Microstructure of quenched SA 910°C/20 min

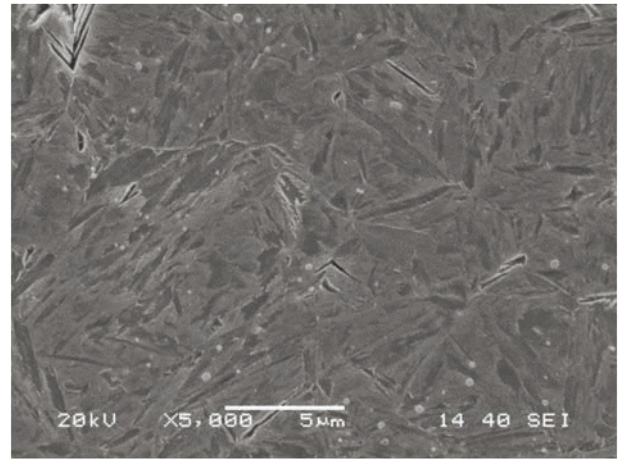


Fig. 8. Microstructure of quenched ASR 830°C/20

tenitizing parameters for all initial states, as illustrated in Table 2.

The soft-annealed material exhibited a completely different behaviour during austenitization. Ferrite grains were found even after quenching at 850 °C (20 min). Large globular carbides dissolved significantly more slowly. Undissolved globular cementite was found in the material after quenching from 910 °C (Fig. 7).

Globular carbides after ASR showed a similar behaviour to lamellar pearlite. The temperature of 830 °C was the lowest to bring about complete transformation of ferrite to austenite (Fig. 8). Undissolved carbides had almost the same size as those in quenched HR material. However, they were dispersed more densely in the martensitic matrix. No differences were found among the martensite matrices produced by quenching materials in the different initial states.

During tempering, cementite precipitated within and along martensitic plates. Apart from the size of undissolved cementite particles, no differences were found among tempered microstructures obtained in all specimens.

Hardness was in according to the microstructure, as seen in Table 3 (austenitizing for 20 min). Yet, the dissolution of the remaining cementite particles did not lead to any significant increase in the final hardness. Once all ferrite had transformed to austenite, as

Table 3. Results of hardness for 20-minute austenitizing during quenching

Quench. temp. [°C]	Hardness HV10					
	Post-quench			Post-temper		
	HR	SA	ASR	HR	SA	ASR
810	733 ± 2	600 ± 11	683 ± 2	543 ± 6	462 ± 2	533 ± 1
830	753 ± 2	667 ± 7	756 ± 4	553 ± 2	515 ± 3	547 ± 2
850	742 ± 6	702 ± 11	752 ± 5	552 ± 2	530 ± 4	554 ± 1
870	749 ± 9	742 ± 4	754 ± 6	534 ± 7	544 ± 2	548 ± 6
890	750 ± 7	745 ± 4	757 ± 4	549 ± 1	547 ± 4	546 ± 4
910	–	746 ± 8	–	–	534 ± 5	–

the quenching temperatures were increasing from sequence to sequence, hardness remained almost constant, see Fig. 9. The maximum level of hardness after quenching and tempering were similar for all initial conditions prior to quenching. When the quenching parameters were appropriate, the hardness was around 750 HV10 and the hardness after tempering was approx. 550 HV10. The same trend and similar values were found in sequences with 40-minute soaking times.

### Mechanical properties after quenching and tempering

The standard tension-deformation characteristics were evaluated: 0,2% offset yield strength (OYS),

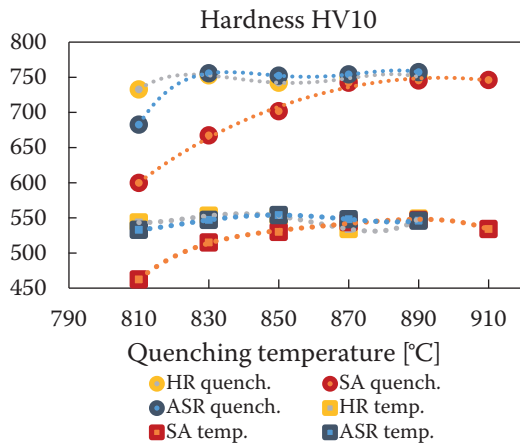


Fig. 9. Trend in hardness ( $t_a = 20$  min)

Table 4. The results of mechanical properties

Sequence	OYS [MPa]	UTS [MPa]	EL [%]	RA [%]	OYS/UTS [-]
HR 830	1720 ± 4	1909 ± 8	8.9 ± 0.3	33.5 ± 1.8	0.90
HR 850	1667 ± 1	1851 ± 6	8.3 ± 1.1	33.6 ± 0.1	0.90
HR 870	1666 ± 9	1867 ± 6	8.6 ± 0.8	30.5 ± 0.5	0.89
HR 830 (40min)	1723 ± 3	1914 ± 7	8.8 ± 0.1	32.5 ± 1.0	0.90
HR 870 (40min)	1678 ± 11	1885 ± 3	8.0 ± 0.3	30.1 ± 1.5	0.89
SA 830	1589 ± 5	1765 ± 3	8.8 ± 0.2	32.3 ± 0.1	0.90
SA 870	1634 ± 7	1832 ± 12	8.9 ± 0.2	31.4 ± 0.9	0.89
SA 890	1656 ± 10	1847 ± 1	9.6 ± 0.2	34.0 ± 1.4	0.90
SA 910	1644 ± 18	1835 ± 16	9.9 ± 0.1	35.2 ± 1.0	0.90
SA 830 (40min)	1660 ± 16	1832 ± 17	8.2 ± 0.5	33.1 ± 0.4	0.91
SA 870 (40min)	1683 ± 7	1881 ± 3	9.2 ± 0.1	33.8 ± 1.0	0.89
SA 890 (40 min)	1667 ± 20	1882 ± 15	9.8 ± 0.7	34.6 ± 0.6	0.89
ASR 830	1696 ± 19	1873 ± 13	8.8 ± 0.1	34.9 ± 0.4	0.91
ASR 850	1686 ± 11	1881 ± 1	9.3 ± 0.1	38.8 ± 0.9	0.90
ASR 870	1684 ± 19	1863 ± 10	9.7 ± 0.2	41.7 ± 1.1	0.90
ASR 830 (40min)	1716 ± 7	1881 ± 11	9 ± 0.4	38.8 ± 0.9	0.91
ASR 850 (40 min)	1683 ± 13	1883 ± 8	10.2 ± 1.2	36.5 ± 2.6	0.89
ASR 870 (40min)	1694 ± 6	1883 ± 8	9.6 ± 0.4	39.5 ± 0.4	0.90

ultimate strength (UTS), elongation (EL) and reduction of area (Ra). The results are in Table 2. Maximum tensile strength was achieved in the material containing lamellar pearlite prior quenching. Interestingly, an ultimate strength of 1850 MPa could not be exceeded after soft annealing and soaking for 20 minutes, even at higher temperatures. Similar tensile strengths were obtained at higher temperatures and twice longer soaking times in comparison to ASR – about 1880 MPa. Yield strength over 1700 MPa was only achieved after hot rolling and ASR. Mechanical properties were lower after quenching HR from higher temperature than 830 °C. This means that the microstructure with lamellar pearlite began to coarsen during austenitization. After ASR was not show this trend. The elongation and area reduction were

the highest in the hardened ASR states. Reduction of area in the ASR material was about 40%. After HR and SA about 33%. Trends of properties are shown in Fig. 10. The graph gives results for 20-minute austenitizing ( $t_a$ ) during quenching.

Based on the results, these are the most appropriate parameters for quenching: 830 °C/ 20 min. after hot rolling, where material contained lamellar pearlite; 870 °C/ 40 min. after soft annealing; and 830 °C/ 40 min. after ASR (Table 4). Fine globular carbides which formed thanks to ASR strike a compromise between the HR and SA routes. Accelerated

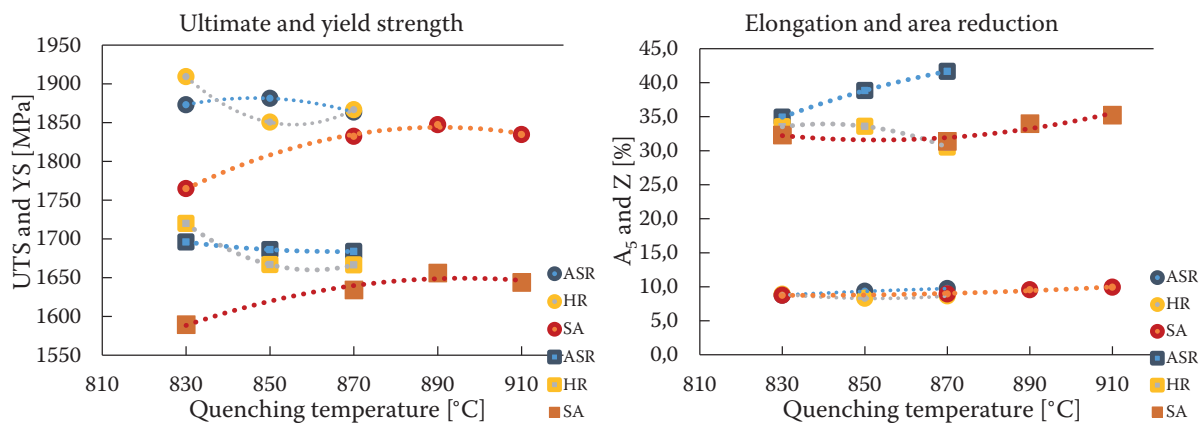


Fig. 10. Trend of mechanical properties ( $t_a = 20$  min)

spheroidisation ASR provides material with as good machinability as that upon soft annealing but the final mechanical properties achieved are similar to those after hot rolling. Nevertheless, elongation and reduction of area are improved. The differences of properties are small but the technological advantages are not negligible. Faster spheroidising treatment (ASR) brings lower quenching temperature in comparison with conventional soft annealing.

## CONCLUSIONS

The effects of three different initial microstructures on the quenching process and resulting mechanical properties were studied for spring steel 54SiCr6. The initial microstructures included lamellar cementite obtained by hot rolling (HR, 290 HV10), coarser globular cementite produced by soft annealing (SA, 207 HV10) and fine globular cementite after Accelerated Spheroidisation and Refinement (ASR, 224 HV10). The following conclusions were found:

Good final mechanical properties are achieved after hot rolling without spheroidising annealing. But lamellar cementite has worse machinability.

Spheroidising by ASR is much faster than soft annealing.

Low quenching temperature is sufficient after hot rolling and ASR. The optimal quenching temperature is 830 °C. Higher quenching temperatures are not suitable for hot-rolled material.

Quenching after soft annealing needs higher temperature and at the same time longer holding during austenitization. The suitable sequence is 870 °C/ 40 minutes.

The maximal hardness does not significantly affect initial state before quenching.

The highest ultimate strength were achieved after hot rolling – 1914 MPa. The maximal yield strength was similar after hot rolling and ASR (1723/1716 MPa). Plastic properties were the highest after ASR – 10.2% elongation, 41.7% reduction of area.

## ACKNOWLEDGEMENT

This paper was created under the project “Development of West-Bohemian Centre of Materials and

Metallurgy” No.: LO1412 financed by the Ministry of Education of the Czech Republic.

## REFERENCES

1. **Dlouhý J., Hauserová D., Nový Z.** Accelerated Carbide Spheroidisation of Chromium Bearing Steel by Induction Heating // *Adv. Mat. Res.* 2013. Vol. 739. P. 161-6.
2. **Jirková H., Hauserová D., Kučerová L., Mašek B.** Energy and Time Saving Low Temperature Thermomechanical Treatment of Low Carbon Plain Steel, *Materiali in Technologije // Materials and Technology.* 2013. Vol. 47/3. P. 335-9.
3. **Hauserová D., Dlouhý J., Nový Z.** Microstructure and Properties of Hardened 100CrMnSi6-4 Bearing Steel after Accelerated Carbide Spheroidisation and Long-duration Annealing. In: *Bearing Steel Technologies: Vol. 10, Advances in Steel Technologies for Rolling Bearings, STP 1580, 2015.* P. 389–409, ISSN 2160-2050.
4. **Mašek B., Jirková H., Kučerová L.** Rapid Spheroidization and Grain Refinement Caused by Thermomechanical Treatment for Plain Structural Steel // *Mat. Sci. For.* 2012. Vol. 706-9. P. 2770-5.
5. **Nam W.J., Bae C.M.** Coarsening Behavior of Cementite Particles at a Subcritical temperature in a medium Carbon Steel // *Scripta Materialia.* 1999. Vol. 41. P. 313-8.
6. **Hauserová D., Dlouhý J., Kotous J.** Structure Refinement of Spring Steel 51CrV4 after Accelerated Spheroidisation // *Archives of Metallurgy and Materials.* 2017. Vol. 62. P. 1473-7.
7. **Tian Y.L., Kraft R.W.** Mechanisms of Pearlite Spheroidization // *Metallurgical Transactions.* 1987. Vol. 18A. P. 1403-14.
8. **Shtansky D.V., Nakai K., Ohmori Y.** Pearlite to austenite transformation in an Fe-2.6Cr-1C alloy // *Acta Mater.* 1999. Vol. 47/9. P. 2619-32.
9. **Kwan-Ho K., Jae-Seung L. and Duk-Lak L.** Effect of silicon on the Spheroidization of Cementite in Hyper-eutectoid High Carbon Chromium Bearing Steels // *Met. Mater. Int.* 2010. Vol. 16/6. P. 871-6.
10. **Hauserová D., Dlouhý J., Nový Z.** Effect of Heating Rate on Accelerated Carbide Spheroidisation (ASR) in 100CrMnSi6-4 Bearing Steel // *Archives of Metallurgy and Materials.* 2014. Vol. 59. P. 1199–1203, ISSN 1733-3490.
11. *Saarstahl: Material specification sheet [online], [seen 31. May 2019], Available from: <https://www.saarstahl.com/sag/downloads/download/11543>.*

## “BESPOKE” COMPOUND LAYERS FOR FRETTING RESPONSE OPTIMIZATION

A. Dreano<sup>1</sup>, P. Arnaud<sup>2</sup>, E. Hériprée<sup>2</sup>, V. Aubin<sup>2</sup>, J. Laporte<sup>1</sup>, S. Fouvry<sup>1</sup>, O. Skiba<sup>3</sup>,  
G. Michel<sup>3</sup>, C. Dannoux<sup>4</sup>, V. Branger<sup>5</sup>, R. Guiheux<sup>6</sup>

<sup>1</sup>LTDS – Ecole Centrale de Lyon. Ecully, France

<sup>2</sup>MSSMat – Université Paris-Saclay. Gif-sur-Yvette, France

<sup>3</sup>IRT-M2P. Metz, France

<sup>4</sup>ALD. Grenoble, France

<sup>5</sup>Naval group. Bouguenais, France

<sup>6</sup>Safran Transmissions Systems. France

romain.guiheux@safrangroup.com

Regardless of the nitriding process used (gaseous or plasma treatment), the nitrided surface is divided into three different « layers »: the compound layer, the diffusion layer and the core which is not affected by the thermochemical treatment. Generally, industrial end-users specify to their suppliers a nitriding depth and / or hardness for the treated part. No requirement is made on the nature of the compound layer. It means that from one supplier to another, a unique depth/hardness requirement can lead to different compound layers, in terms of chemical composition, structure and thickness.

According to literature and return of experience from the different academic and industrial partners involved in the “NITRU” project of the IRT M2P, a difference in the nature of the compound layer, for instance the volume ratio of iron nitrides  $\gamma'$  and  $\epsilon$ , can impact the tribological properties of this layer.

The aim of this study is firstly to study the tribological response of different industrial compound layers for different mechanical solicitations (fretting, sliding) and conditions of lubrication; secondly to design “bespoke” compound layers regarding the solicitations applied to one specific part.

A methodology is thus proposed to reach this objective. It consists in original metallurgical characterizations of the compound layer (SEM FIB, EBSD, XRD, SDL) and in-situ mechanical tests on micro-scale specimen extracted from this layer.

**Keywords:** nitriding; compound layer; fretting; SEM; in-situ tests.

### INTRODUCTION

In industry, nitriding is a widely used thermochemical process, which aim is to increase the mechanical properties (e.g. hardness, fatigue and wear resistance) of structural parts. For low alloyed ferritic steel, the process is usually carried out between 480 °C and 580 °C and is based on nitrogen diffusion and alloying element nitrides precipitation mechanisms. Regardless of the nitriding process used (gaseous or plasma treatment), the treatment leads to the formation of a nitrided surface, which can be divided into three different « layers » : the compound layer, the diffusion layer and the unaffected core. The compound layer is usually composed of the  $\gamma'$ -Fe<sub>4</sub>N (containing around 6 %wt N) and  $\epsilon$ -Fe<sub>2</sub>-3N phases (containing around 8 %wt N up to 11 %wt) whereas the case-hardening takes place in the diffusion layer.

Generally, industrial end-users specify to their suppliers a nitriding depth and / or hardness for the

diffusion layer but no requirement is made on the nature of the compound layer. It means that from one supplier to another, a unique depth/hardness requirement can provide different compound layers in terms of chemical composition, structure and thickness. However, according to literature and return of experience from the different academic and industrial partners involved in the «NITRU» project of the IRT-M2P, its presence and nature can impact the tribological behavior of the treated parts. The aim of this study is firstly to study the tribological response of different industrial compound layers for different mechanical solicitations (fretting, sliding) and conditions of lubrication; secondly to design “bespoke” compound layers regarding the solicitations applied to one specific part. For a better understanding of the impact of the compound layer nature on tribological properties, IRT M2P industrial and academic tested several nitriding processes on the 33CrMoV12-9 steel grade, which produce similar nitriding depth (see Table 1 below).

Table 1. Description of the different compound layers studied

Different compound layer tested		
Name	Nitriding depth (mm)	Technology
Nitreg	0.11–0.19	Gaseous (AP) nitriding
Allnit		Gaseous (LP) nitriding
Plasma $\epsilon$		Plasma nitriding
Plasma $\gamma'$		Plasma nitriding
TF1AB1		Salt bath nitriding
QPQ		Salt bath nitriding

A methodology is thus proposed to reach this objective. It consists in original metallurgical characterizations of the compound layer (SEM FIB, EBSD, XRD, SDL) and in-situ mechanical tests on micro-scale specimen extracted from this layer.

### Metallurgical characterisations

Before undergoing tribological tests, the compound layers, associated to the nitrided samples listed in Table 1, were characterized with Scanning Electron Microscope (SEM), X-Ray Diffraction (XRD)

and Glow Discharge Optical Emission Spectroscopy (GDOES).

SEM micrographs of the compound layers are given in Fig. 1. They were observed from top and on cross-sections (after etching) and they exhibit different topologies and morphologies. On cross-sections, compound layers present different morphologies: Plasma  $\epsilon$ , QPQ and Nitreg shows a rather homogeneous and dense aspect whereas porosities at the top surface could be observed on Plasma  $\gamma'$ , TF1AB1 and Allnit. Cracks are also visible on the latter and TF1AB1 compound layers.

XRD analysis was used in order to determine the nature of the phases present in the near surface. Results are summarized in Table 2 and show that the compound layer was essentially constituted of  $\epsilon$ -nitrides for the two salt bath technologies and the Allnit one whereas the other technologies produced more  $\gamma'$ . XRD analysis gives no indication of the repartition of the phases throughout the layer and GDOES analyses were performed to determine it. Indeed, GDOES gives information about the mean mass fraction of the different element at a given depth. Considering the theoretical N mass fraction contained in epsilon and gamma' iron nitrides, it is possible to deduce their respective presence within the layer with respect to the depth. The GDOES analysis for Plasma  $\gamma'$  is given in Fig. 2. The latter exhi-

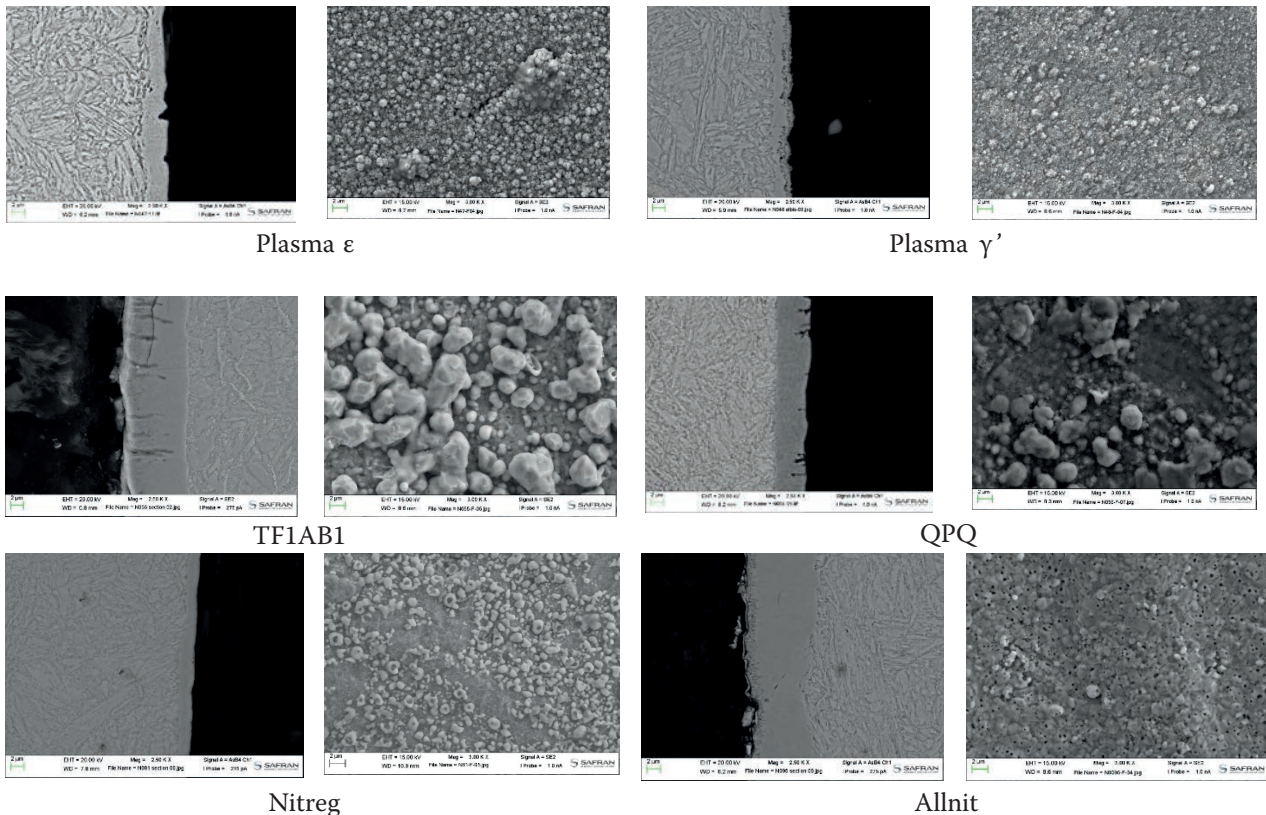


Fig. 1. Cross-section and top views of the compound layer by SEM analysis

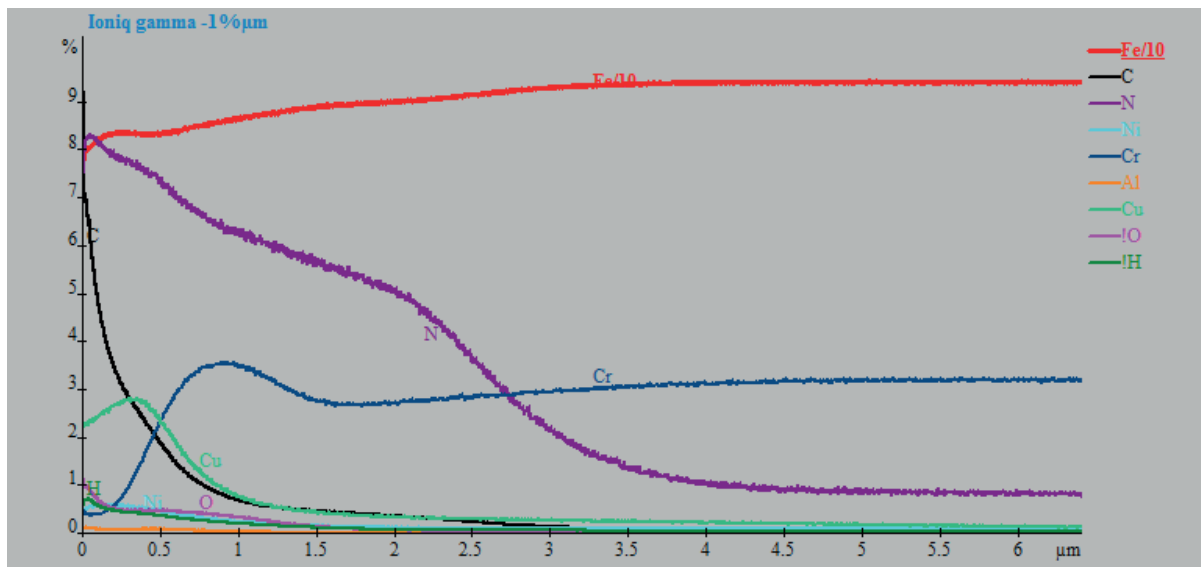
Fig. 2. GDOES analysis on Plasma  $\gamma'$  layer

Table 2. Summary of the results concerning the nature of the compound layer tested and the repartition of the iron nitrides phases

Results summary obtained on the tested compound layers					
Name	Compound layer depth ( $\mu\text{m}$ )	Nitriding depth (mm)	Epsilon	Gamma'	Technology
Nitreg	2.2	0.11–0.19	0	100	Gaseous (AP) nitriding
Allnit	9.3		70	30	Gaseous (LP) nitriding
Plasma $\epsilon$	3.6		10	90	Plasma nitriding
Plasma $\gamma'$	3.3		10	90	Plasma nitriding
TF1AB1	10		100	0	Salt bath nitriding
QPQ	4.8		75	0 (25% Oxides)	Salt bath nitriding

bits a N-weight fraction going from around 8% wt to around 2% wt from the surface to a depth of around 3  $\mu\text{m}$ , which corresponds to the compound layer. At the extreme surface, the N-weight fraction of 8% wt can be related to the presence of  $\epsilon$  phase. At 1  $\mu\text{m}$  depth, the N weight fraction drops at around 6% wt, which can be related to the presence of  $\gamma'$  phase solely. In between this range, the compound layer is likely to be a mix of both phases. From 1  $\mu\text{m}$  to around 2.5  $\mu\text{m}$ , the N-weight fraction falls steadily and this content can also be related to the  $\gamma'$  phase. Below this content, the compound layer gradually gives place to the diffusion zone.

The metallurgical results corresponding to the different compound layers studied are given in the Table 2 below. Those results confirm that, depending on the nitriding process and technology used, compound layers with different metallurgical aspects and composition were created and are likely to exhibit different tribological behaviors.

## EVALUATION OF THE TRIBOLOGICAL BEHAVIOR OF THE COMPOUND LAYERS

The wear resistance of the compound layers was tested through fretting experiments in gross slip fretting conditions in a ball-on-flat configuration [1]. Fretting is usually defined as a small amplitude reciprocating displacement. The ball had a radius of 12.7 mm and was in 100 Cr 6 whereas the flat was the nitrided sample. In the following, the wear resistance of the 100 Cr 6 samples is not discussed since most of the wear is detected on the nitrided part. Fretting tests were performed a tribometer equipped with an electromagnetic linear motor actuator, as presented in Fig. 3 a. The linear motor imparted a displacement  $\delta$  of  $\pm 100 \mu\text{m}$  at a frequency  $f$  of 5 Hz to the tribosystem. A normal load  $P$  of 7.5 N was applied though a dead weight and the value of the applied load was carefully verified before launching the experiments. The wear tests were performed by maintaining a

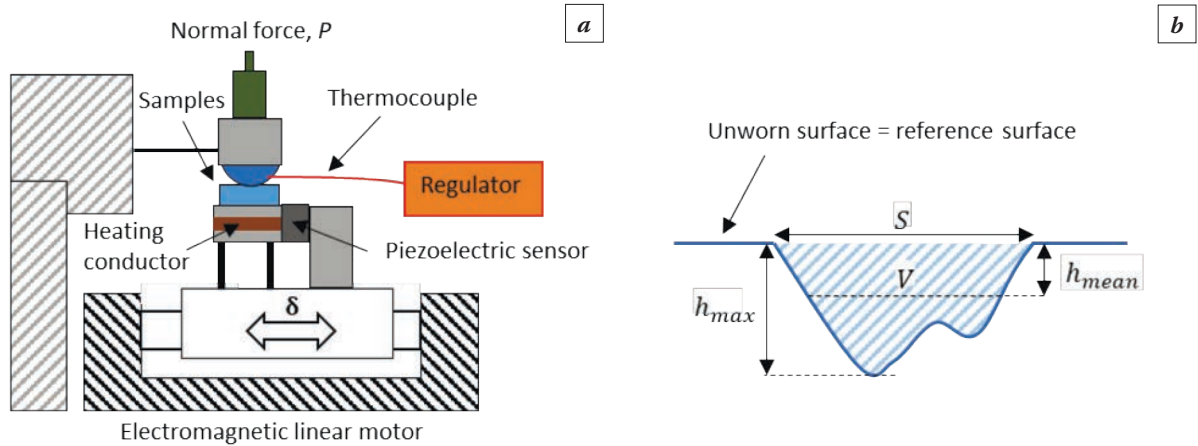


Fig. 3. *a* – Schematic illustration of the fretting wear set-up; *b* – illustration of the wear quantities through a wear track observed in cross-section

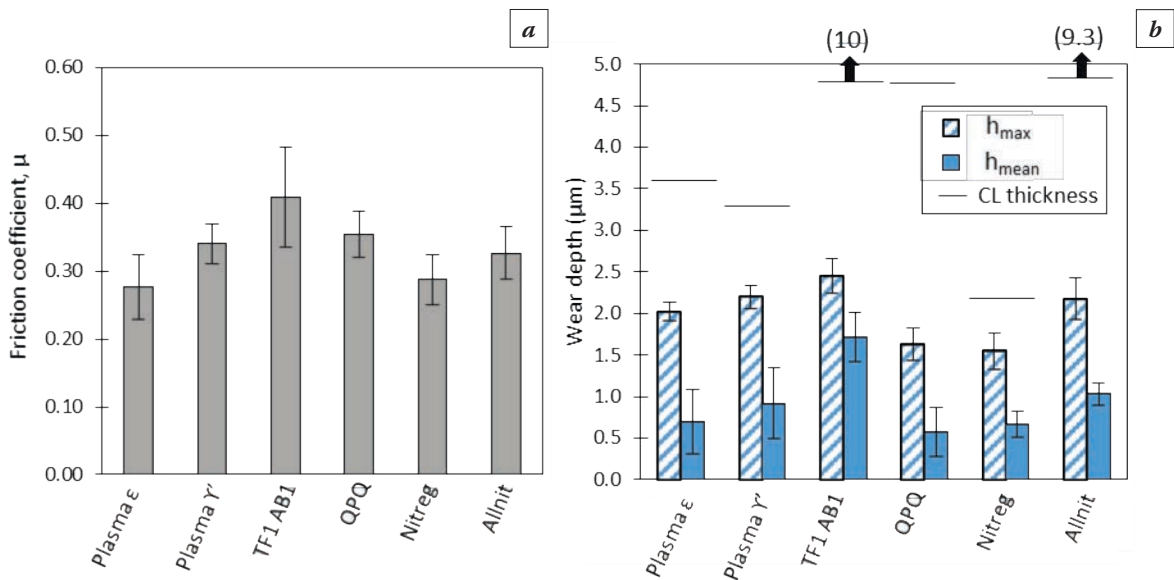


Fig. 4. Effect of the nature of the compound layer on : *a* – the mean friction coefficient; *b* – the wear depths  $h_{max}$  and  $h_{mean}$  respective of the Compound Layer (CL) thickness (indicated as horizontal black lines on the graph) ( $P = 7.5 \text{ N}$ ,  $\delta = \pm 100 \mu\text{m}$ ,  $f = 5 \text{ Hz}$ ,  $T = 80^\circ\text{C}$ ,  $N = 100\,000$  cycles). The error bars are standard deviations of several fretting tests

constant temperature  $T$  equal to  $80^\circ\text{C}$  thanks to two heating conductors. The temperature was recorded and regulated near the fretted surface. A piezoelectric sensor recorded the tangential force induced by friction,  $Q$ . The friction coefficient  $\mu$  was defined for each fretting cycle as the ratio of the maximal tangential force  $Q$  to the normal force  $P$ . Finally, the total number of fretting cycles  $N$  was chosen in order to exceed the transient period of the wear process (100 000 cycles). All the fretting tests were performed in a lubricated environment with an oil used in aeronautical systems.

After the test, the sample were cleaned in an ultrasonic bath with appropriate solvents. Optical images and 3D surface profiles were performed. A systematic procedure is proposed in order to evaluate the wear process of the compound layers, as present-

ed in Fig. 3b. From the 3D profiles, the wear volume  $V$  is measured and defined as the missing volume below the reference surface. The maximum depth of the wear track  $h_{max}$  is also measured by profilometry. Since wear volume is an extensive parameter, it is proposed to study the mean depth of the wear track  $h_{mean}$  defined by Eq. 1, where  $S$  is the area of the worn surface measured on the optical images of the wear track.

$$h_{mean} = \frac{V}{S}. \quad (1)$$

The six compound layers were tested and the results are presented in Fig. 4, where the friction coefficient and the wear depths  $h_{mean}$  and  $h_{max}$  are analyzed respective of the Compound Layer thickness (CL thickness, specified in Table 2).

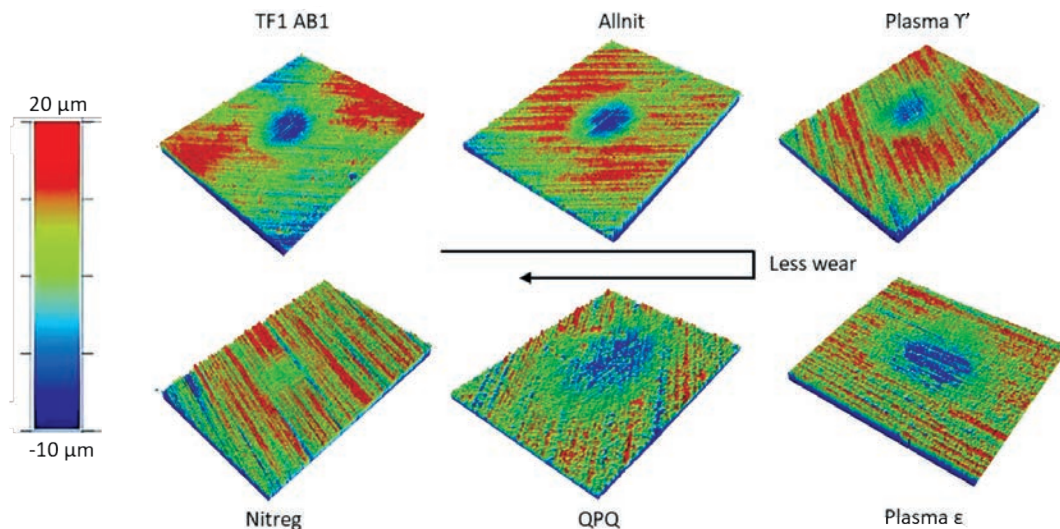


Fig. 5. 3D profiles of the wear tracks obtained by profilometry ( $P = 7.5 \text{ N}$ ,  $\delta = \pm 100 \text{ }\mu\text{m}$ ,  $f = 5 \text{ Hz}$ ,  $T = 80 \text{ }^\circ\text{C}$ ,  $N = 100\,000$  cycles)

For all specimens, the maximum wear depth is below the CL thickness, which means that the fretting experiments only consider the friction and wear resistance of the compound layers. Fig. 4 *a* shows that the nature of the compound layer has an influence on the friction coefficient. The error bars show that there are some instabilities of the friction coefficient from one test to another, especially for the TF1 AB1 layer, which also presents the higher friction coefficient (0.41). This may be due to a higher generation of wear debris during the experiments. On the contrary, the lower friction coefficient is recorded for the Plasma  $\epsilon$  and Nitreg compound layers (0.28), showing that the production of wear debris is reduced compared to TF1 AB1. In terms of wear, Fig. 4 *b* demonstrates that there is a relatively low effect of the nature of the compound layer. The maximum wear depth is observed for the TF1 AB1 sample with  $h_{\text{max}} = 2.45 \text{ }\mu\text{m}$  and  $h_{\text{mean}} = 1.72 \text{ }\mu\text{m}$ . On the contrary, the minimal wear is observed for QPQ with  $h_{\text{max}} = 1.64 \text{ }\mu\text{m}$  and  $h_{\text{mean}} = 0.58 \text{ }\mu\text{m}$  and for Nitreg with  $h_{\text{max}} = 1.55 \text{ }\mu\text{m}$  and  $h_{\text{mean}} = 0.67 \text{ }\mu\text{m}$ .

Fig. 5 presents the 3D profiles of the wear tracks for the six compound layers. Images show that, for all the compound layers except Nitreg, the wear depth is larger than the roughness of the sample. Therefore, the Nitreg compound layer seems to be particularly interesting to resist to fretting wear. In this study, the effect of the direction of the initial roughness compared to the sliding direction is not considered. Nonetheless, the initial roughness was controlled and was between  $0.37 \text{ }\mu\text{m}$  and  $0.44 \text{ }\mu\text{m}$  (Ra) for all the samples.

The nature of the compound layer has an effect on the wear process and some interesting points are

now detailed. The TF1 AB1 compound layer, which presents the higher friction coefficient and the deepest wear profile is composed of full  $\epsilon$  nitrides compound layer. This compound layer is also the thickest, around  $10 \text{ }\mu\text{m}$  (Table 2), but it exhibits porosities and even cracks (Fig. 1). Inversely, the best specimen in terms of fretting wear response appear to be the Nitreg and QPQ compound layers, which are both homogeneous, dense and with a thickness lower than  $5 \text{ }\mu\text{m}$  (Table 2 and Fig. 1). In another hand, the QPQ compound layer is composed of a mixture of  $\epsilon$  nitrides and iron oxides on top whereas the Nitreg compound layer is composed exclusively of  $\gamma'$  nitrides.

Hence, if the thickness of the layer does not affect the tribological response of the compound layer in terms of wear and friction coefficient, it seems that the composition and aspect of the compound layer can have an impact on it. Indeed, a compact compound layer made of essentially  $\gamma'$  iron nitrides or a mixture of  $\epsilon$  and iron oxides leads to a reduction of wear and friction coefficient compared to  $\epsilon$  based layers. Further investigations need to be performed by correlating the microstructure of the compound layers to the fretting response.

Finally, Fig. 6 presents the wear kinetics (the evolution of wear with the fretting cycles) of the QPQ and Nitreg specimens, which are the two best candidates in terms of wear resistance. First, Fig. 6 *a* shows that the evolution of wear volume presents different trends. The wear volume of the QPQ specimen increases rapidly during the early stage and then it completely stops after 50 000 fretting cycles. For the Nitreg specimen, after a fast increase in wear at the beginning, the wear volume keeps increasing but at a lower pace. The same statements cannot be made

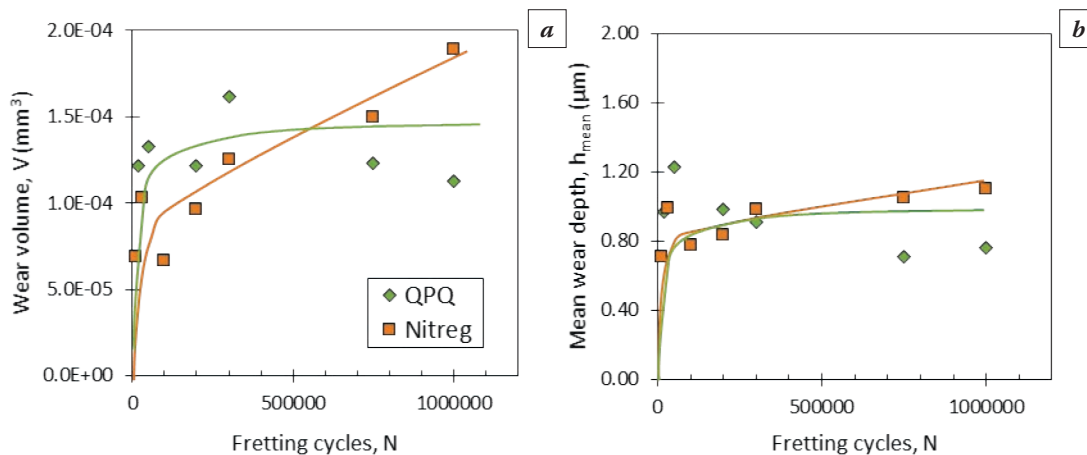


Fig. 6. Wear kinetics for the two best wear resistant compound layers: QPQ and Nitreg: *a* – wear volume; *b* – mean wear depth ( $P = 7.5$  N,  $\delta = \pm 100$  μm,  $f = 5$  Hz,  $T = 80$  °C)

regarding the mean wear depth, presented in Fig. 6 *b*, showing a similar plateau evolution for both specimens. Hence, a lateral extension of the wear track is promoted with the Nitreg compound layer, and it may be due to the formation of a tribofilm at the interface which completely changes the distribution of the contact pressure and thus the wear process. The QPQ compound layer, presenting a stable wear volume and mean wear depth over the fretting cycles appears to be the most efficient layer for protecting the interface from wear.

This study is a first attempt to understand how the compound layer can affect the friction and wear behavior. This original study shows that there is an actual effect of the nature of the compound layer on the fretting wear response of nitride specimens and further investigations on this are required.

## CONCLUSIONS AND PERSPECTIVES

This paper reports a methodology to compare tribological responses of different industrial compound layers for fretting conditions. First, a complete analysis was performed to characterize the composition of compound layer. The thickness of layer as well as the proportion and the depth localization of phase

$\varepsilon$  and  $\gamma'$  were determined by coupling SEM, XDR and SDL techniques. Then, the tribological behavior was studied under constant solicitations for all layers. These two analyses have shown correlations with layer composition and structure (porosity, crack ...). For better understanding, current investigations are focused on mechanical behavior of the layer by residual stress analysis. Indeed, a compressive residual stress can improve the tribological behavior by shifting the damage stress of the layer. However, to access the stress gradient, specific methods with SEM FIB and reverse analysis must be developed. We can mention the incremental hole method [2]. Finally, in-situ SEM micro tensile tests should allow us to obtain elastic behavior with significant volume (almost all layer thickness). Results could be compared to common methods, such as nano-indentation, to better understand the homogenization of the behavior.

## REFERENCES

1. Fouvry S., Kapsa P., Vincent L. Quantification of fretting damage // *Wear*. 1996; 186–205:200.
2. Schajer G.S. Measurement of non-uniform residual stresses using the hole-drilling method. part I stress calculation procedures // *J. Eng. Mater. Technol.* 1988.

## HEAT TREATMENT IN ACTIVE FLUIDIZED BED

E-mail  
нужен???

Tomasz Babul, Zdzisław Obuchowicz, Piotr Nawrocki

Institute of Precision Mechanics. Warsaw, Poland

New generation furnaces for fluidized thermo-chemical treatment were presented. So far, devices have been used in which source of diffusion element was gas, whereas the inert bed consisted of ceramic powders or carbides. Most often it was silicon carbide or aluminum oxide. The bed allowed for uniform gas flow throughout the entire furnace and therefore for uniform temperature in the furnace. It also allowed the working atmosphere to reach all difficult to work surfaces, such as long blind holes, small rays, etc. In the presented solution, it was proposed to change the inert bed into a bed chemically active, which is the source of the diffusing element – similarly to the pack treatment. In order to obtain fluidization, two methods were used: 1) inert gas flow, 2) vibration of the bed. The proposed solutions of the new technology of fluidal thermo-chemical treatment were verified on X153CrMoV12 steel. Metallographic tests, microhardness and surface hardness tests, microhardness distribution in the obtained layer were carried out. Measurements of wear resistance were carried out using a 3 cylinder – cone method. Obtained results were presented in the form of Lorentz curves.

**Keywords:** fluidized bed heat treatment; boriding; wear resistance.

### CLASSIC TECHNOLOGY OF HEAT AND THERMOCHEMICAL TREATMENT

The fluidized bed treatment technology has been used for thermo-chemical treatments for many years. The use of this technology results from its unique properties, which can include: 1) easy access to the furnace working space; 2) access to the furnace working chamber at any time during the process; 3) quick batch heating; 4) uniform temperature in the workspace; 5) uniform temperature on the surface and along the cross-section of the batch, regardless of its size and shape; 6) the possibility of diffusion processes on an open furnace, easy adaptation of the device to changes in the type of processing; 7) possibility of working in a wide temperature range.

In the classical treatment in a fluidized bed furnace the source of diffusion elements to the surface layer of the processed steels were gases supplied at the base of the retort, whereas the bed served mainly as a heat accumulator and distributor of uniform gas flow throughout the entire furnace volume. Fig. 1 shows a diagram in which chemically active gases (red color), affect the inert fluid bed material (yellow color) and the load to be processed. The main disadvantage of this treatment are: 1) large amounts of used working atmosphere resulting from continuous gas flow across the cross-section of the furnace working chamber; 2) relatively low heat treatment temperatures up to approx. 950–1000 °C resulting from «sticking of the bed» at higher temperatures and reducing the effect uniform fluidization; 3) difficult access of gases to the surface of long holes, internal corners, etc.

### FLUID BED TREATMENT IN THE ACTIVE BED

#### An active fluid bed in fluid treatment

The extension of fluidized bed applications and the elimination of some of the existing disadvantages of this technology became possible when using active powders as a fluidized bed. These powders are not only a source of elements diffusing into the workpiece, but also are responsible in some technological variants for the even distribution of gases. The essence and basis of these processes, however, are powders. Depending on the purpose and type of thermo-chemical treatment, powders with different chemical and phase composition, granulation and morphology are used.

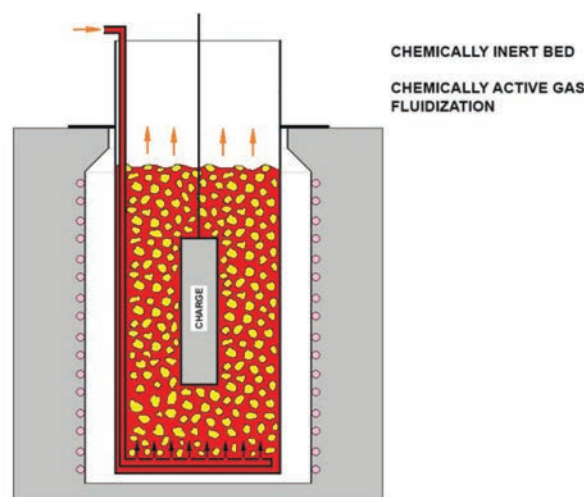


Fig. 1. Functional diagram of a typical fluidized bed furnace (red – chemically active gas, yellow – chemically inert bed)

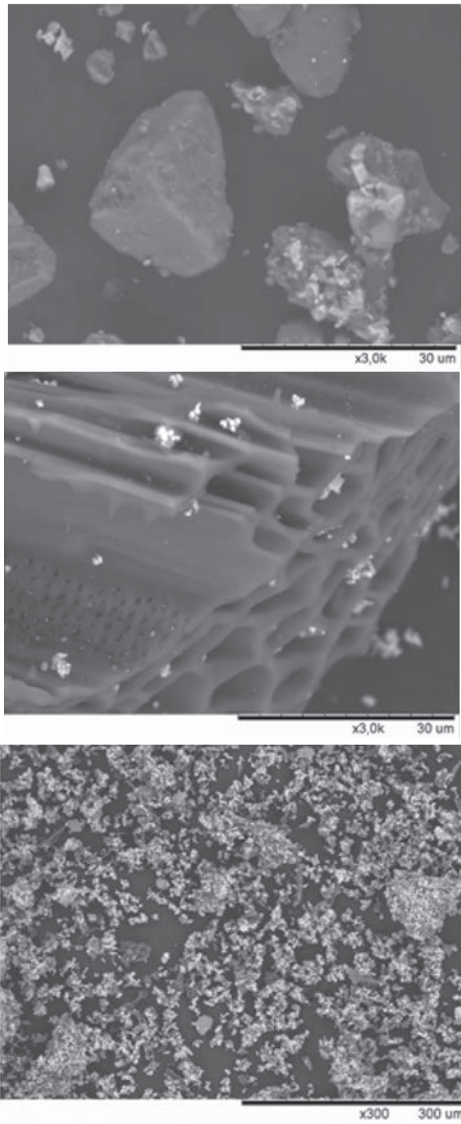


Fig. 2. View of the powder mixture for the:  
1 – boronizing, 2 – carbonitriding and nitrocarburizing  
3 – carburizing

Где позиции  
1, 2, 3?

For example, Fig. 2 shows different types of powders for boron, carbonitriding and fluidized carburizing.

### Thermo-chemical treatment in an active fluidized bed

The thermo-chemical treatment in the active fluidized bed is carried out in powder, which, as a result of selecting the appropriate chemical composition, is the source of the diffusing element to the workpiece. The gas, supplied by the distributor located at the bottom of the retort, acts as a surface activator. Stable gas flow also moves individual grains of powder in the retort during the process. Therefore, during the thermo-chemical treatment in the active fluidized bed: a) the surface of the individual grains of the powder in con-

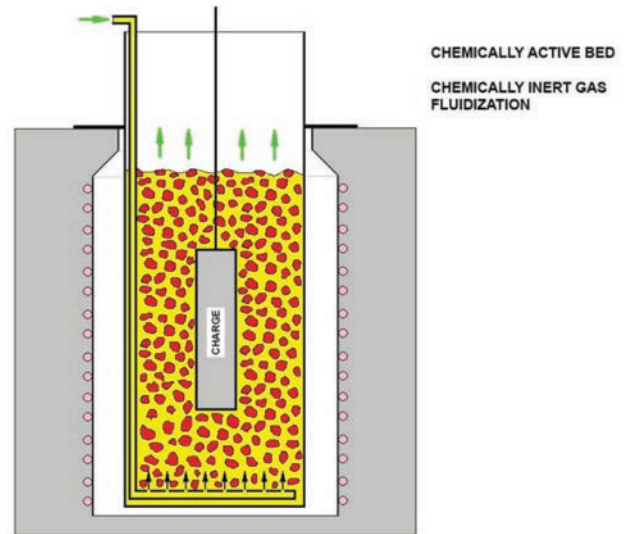


Fig. 3. Diagram of the fluidized bed new generation furnace (red – chemically active bed, yellow – chemically inert gas)

tact with the workpiece changes; b) the powder grains are in contact with the treated surface; c) the activator is also in powder delivered to the machining zone: workpiece surface – powder and thus more effectively affects the diffusion rate of individual elements. At the same time, the proposed solution allows during the process to remove the depleted deposit and supplement it with a new powder, as well as adding the activator to the deposit at any time. In Fig. 3. is a schematic diagram of the device in which the active fluidized bed was used, with the simultaneous use of a chemically inert gas. Of course, this variant can be modified by using an active bed including an active gas atmosphere.

### Thermo-chemical treatment in an active fluidized bed with vibrations

The use of vibrations for fluidization in the active bed instead of the classical use of gases drastically reduces the demand for process gases, reduces their emission to the filters as well as to the atmosphere, and at the same time reduces the costs of the process. There is no observed phenomenon of elevating micro and nanosomes of powder outside the bed. The process can be carried out using continuous vibration with the same amplitude as well as in any combination of variable amplitudes with respect to amplitude and their period, also continuous or intermittent vibration can be used. The retort and/or the load may be subjected to forced mechanical vibrations (Fig. 4). As a result of the use of vibrations, the bed has similar properties to those obtained during the introduction of both active and neutral gas.

### Thermo-chemical treatment in an active fluidized bed with vibrations

Same as gas, the vibration induces the following phenomena: 1 – the movement of the powder grains in the entire retort; 2 – even heating of the active bed in the whole volume. The vibration causes the bed to penetrate into all the technological holes in the workpiece, and thus the diffusion of elements is the same on any surface, regardless of how complicated the shape of the workpiece is. Grains of the vibrating powder mixture change their surface contact with the surface of the work piece, ensuring its contact with the grain surfaces with a high content of diffusion element and activator.

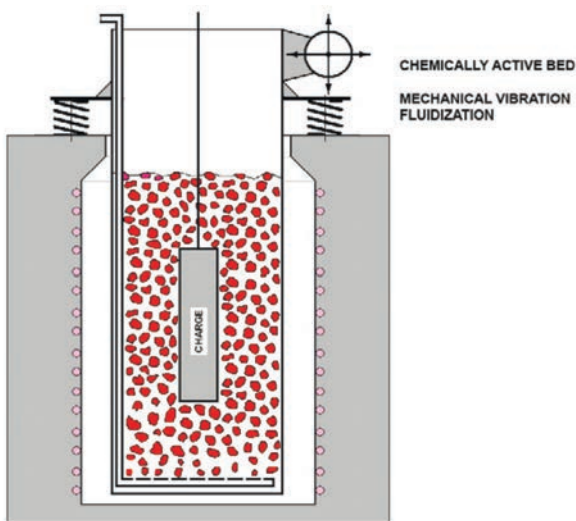


Fig. 4. Schematic of the new generation fluid bed furnace with mechanical vibrations (red – chemically active bed)

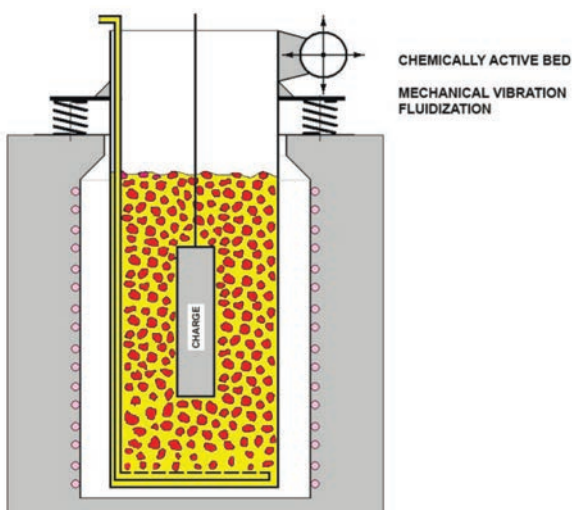


Fig. 5. Schematic of the new generation fluidized by mechanical vibrations bed furnace (red – chemically active bed, yellow – chemically inert gas)

### Thermo-chemical treatment in an active fluidized bed with vibrations and inert gas

Another solution combines the concept presented in Fig. 3 and Fig. 4. In the solution presented below, the active deposit is used, as well as gas and mechanical vibrations to obtain fluidization (Fig. 5). The use of gas and vibrations to move the bed in the retort can be done independently depending on the needs technological process and its various stages.

### BORIDING X153CrMoV12 STEEL IN AN ACTIVE DEPOSIT

The X153CrMoV12 tool steel was designed for cold work. The chemical composition of the steel was as follows

NC11LV X160CrMoV121 steel samples were in an improved condition (samples from X153CrMoV12 steel: hardening at 1030°C and one tempering at 525 °C in 2 hours in vacuum and double tempering at 600 °C for 2h at hardness ~ 57 HRC .

The boring was carried out at 960 °C, for 4h and 8h and the samples were cooled in air after the process. The results of metallographic examinations are shown in Fig. 6.

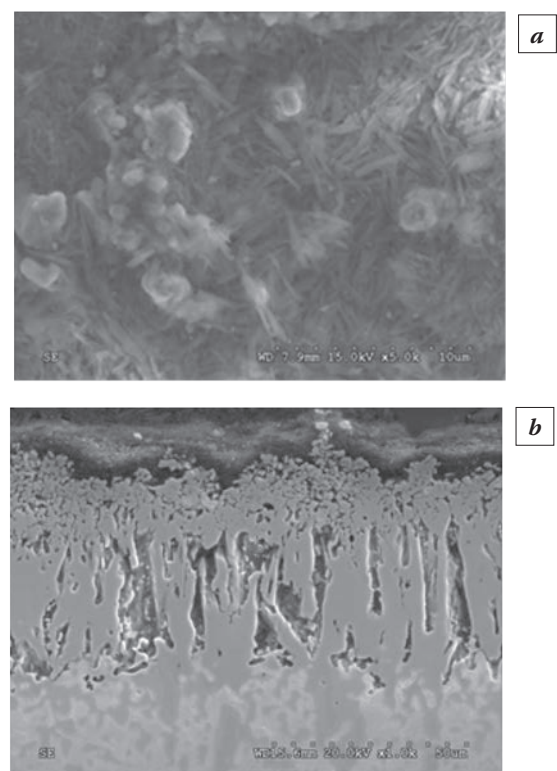


Fig. 6. View of X153CrMoV12 steel structure fluid boriding in active powder 8h at 960 °C (surface hardness 1260 HV0.1): a – sample surface; b – cross-section

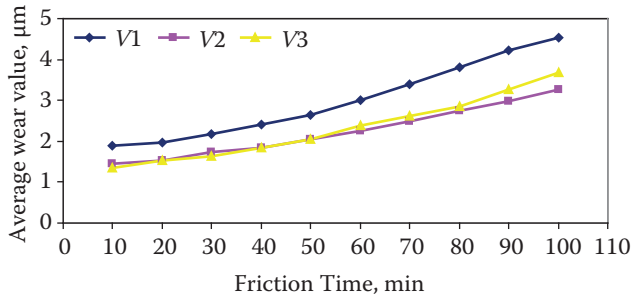


Fig. 7. Wear resistance in 3 rolls-cone system (50 MPa load)

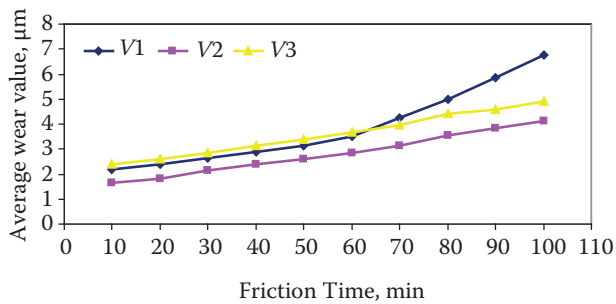


Fig. 8. Wear resistance in 3 rolls-cone system (100 MPa load)

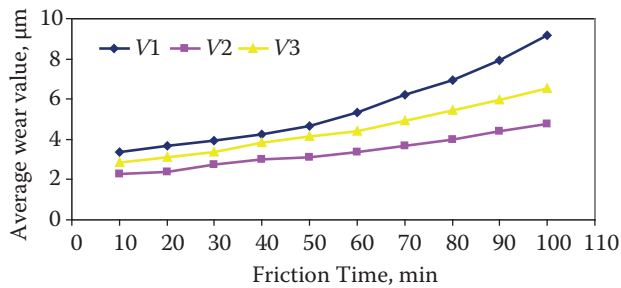


Fig. 9. Wear resistance in 3 rolls-cone system (200 MPa load)

Metallographic examinations were carried out using an Olympus 1X70 light microscope and a Hitachi S-3500N electron microscope equipped with a Thermo Noran electrodispersive X-ray spectrometer used to approximate the chemical composition of the surface layers produced on the samples. For metallographic examinations, the Axiovert 200 MAT microscope from Carl Zeiss was used, the microstructures were digitized using the AxioCam MRc5 camera.

Metallographic observations were made on processed samples, surface hardness distributions, surface microhardness measurements, three-roll and cone wear resistance tests, Amsler wear tests, impact tests were performed.

The results of abrasion measurement of the X153CrMoV12 Steel in the initial state and after drilling at different times are shown in Fig. 7–10,

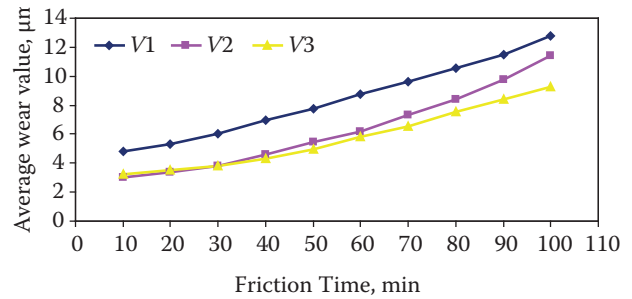


Fig. 10. Wear resistance in 3 rolls-cone system (400 MPa load)

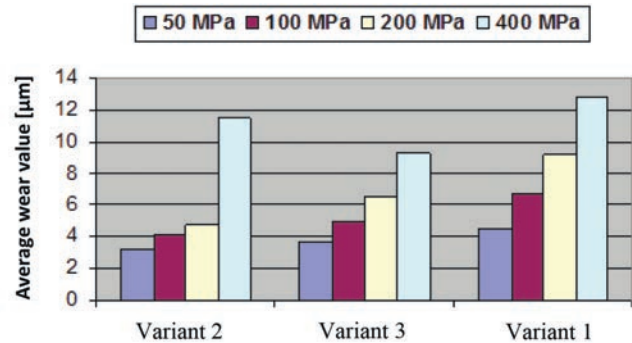


Fig. 11. Wear resistance in a 3 rolls-cone system of samples made of X153CrMoV12 steel subjected to various thermo-chemical treatments, time of friction 100 min

while the final wear values in Fig. 11. Markings on Figs 7–10: Variant 1 – after hardening and tempering, Variant 2 – boronizing in 960 °C, 4 h, Variant 3 – boronizing in 960 °C, 8h.

## SUMMARY

1. The use of active powders for fluidized bed processes gives the opportunity to conduct heat and thermo-chemical treatment processes in order to increase the functional properties of structural and tool steels.

2. The use of active powders creates the possibility of introducing new technologies to obtain the fluidizing of the bed, e.g. vibrations.

3. The use of an active deposit makes it possible to replace the current carrier of diffusion elements such as working gas, with a neutral gas and thus a significant reduction of gas emissions to the atmosphere.

4. The use of an active deposit allows its multiple use and its easy regeneration even during heat and thermo-chemical treatment processes.

5. The use of active powders for drilling in the process of thermochemical treatment results in a significant reduction of wear for steel X153CrMoV12 regardless of the applied load in the range of 50–400 MPa.

## BORON-BASED COMPOSITE DIFFUSION LAYERS FOR OPERATIONAL IMPROVEMENT OF DIES

U. Mishigdorzhyn, N. Ulakhanov

Department of Mechanical Engineering,  
East Siberia State University of Technology and Management. Ulan-Ude, Russia  
mishigdorzh@gmail.com

This research investigates a possibility of improving a set of operational properties of carbon and alloy steels by means of pure boriding and boroaluminizing (joint diffusion with boron and aluminium). A set of experimental and theoretical studies was carried out, including conducting experiments on high-temperature boriding and boroaluminizing (HTB and HTBA), metallography, phase and elemental analysis, topography investigation and mechanical characteristics of composite layers. Diffusion layers were elaborated by the treatment pastes based on boron carbide and aluminum, which were plotted on the steel surface and heated at 950–1100 °C for 2 hours with the specimens inside in a muffle furnace. As a result, diffusion layers with the typical tooth-like structure and a new composite structure were obtained on the steel surfaces. The former structure consists of iron borides FeB (outer phase) and Fe<sub>2</sub>B (inner phase), while the latter structure comprises hard phases evenly distributed in the softer matrix of solid aluminum solution in  $\alpha$ -Fe and iron aluminides. Despite iron borides, ferrotungsten Fe<sub>7</sub>W<sub>6</sub> was revealed in the composite layers on the alloy steel. It was established that layers with a composite structure are superior to layers with a traditional needle-like structure in plasticity. However, the specimens after pure boriding were slightly superior to ones after boroaluminizing in wear resistance.

**Keywords:** thermochemical treatment; boriding; boroaluminizing; treatment paste; composite structure; steel; wear resistance; surface roughness.

### INTRODUCTION

Thermal-chemical treatment can be viably utilized in mechanical engineering to adjust the metal surfaces. Depending on the diffusing element, single-component (nitriding, cementation, boriding etc.) and multi-component TCT techniques are recognized, where one or several chemical elements diffuse into the steels and alloys surface, creating compounds and solid solutions [1–4]. Boriding continues to explore the new fields of application and the range of products subjected to boriding is constantly expanding [1, 5]. Along with this, it is necessary to state that boriding is of limited use in comparison with nitriding and cementation. The constraining factors are the high brittleness of borides and the high gradient of hardness of the diffusion layer and the base metal. The researchers have achieved positive results in increasing the plasticity of the layer due to the formation of a single Fe<sub>2</sub>B-layer, which can be obtained by means of various methods of using direct and alternating current field, concentrated energy flows etc [6–10]. In many cases these methods require complex and expensive equipment.

Multi-component treatment is preferable over pure boriding. Combined diffusion of boron and a non-metal (boronitriding, borocarburing) or boron

and a metal (borochromizing, borotitanizing, boronickelizing boroaluminizing) are discussed in the sources [11–14]. Despite the obvious advantages of multi-component TCT, it should be noted that the combined processes can suppress or restrain each other. For instance, a range of experiments in powder mixture and pastes has shown that boriding and aluminizing, when performed together in one processing cycle at 900–1000 °C, compete with each other [15, 16]. As a result, the layers with predominant boron or aluminum compounds are formed. The Al content of 7–10% wt. in treatment powder or paste is the breaking point, where lower or higher Al content leads to the predominant boriding or aluminizing respectively. Thus, the above-described problem of increasing the plasticity of B-Al-layer is a particular case of solving the problem of combining boriding and aluminizing in one combined process.

According to the authors of [17], the plasticity of the borided layer lies in its structure, namely, in the composition of the structure. Creating composite layers and coatings can solve the problem of low plasticity; in addition, it can also provide an increase of mechanical and thermal properties. In some sources, this type of layers is referred to as multi-phase diffusion layers with a Charpy-type structure [18]. Among the methods for sintering this type of layers and coat-

ings are electron-beam and laser processing, thermo reactive diffusion, PVD, CVD and combinations of these methods. Thus, the formation of coatings with a composite structure can be an effective method of brittleness reducing of boron-based diffusion layers. Not last in importance is the extended transition zone, which is capable of layer adhesive enhancement and the favorable of residual stresses distribution.

The present work is devoted to the mechanical properties improvement of carbon and alloy steels by means of high-temperature pack boriding and boroaluminizing in pastes.

## MATERIALS AND METHODS

The steel 30 was used as a benchmark material, on which time-temperature treatment parameters were tested. The steel 3Kh2V8F (the analogue of AISI H21 steel) were used as the tested materials. Currently, steel 3Kh2V8F is being used as hot-work die steel in forging. The chemical composition for both steels is given in Table 1.

Diffusion layers were obtained by pack method in treatment pastes. Pastes are comprised of sodium fluoride as an activator and boron carbide for boriding. Aluminum powder was used in addition to the aforementioned chemical components for boroaluminizing, where boron carbide and aluminum ratio was 5:1, respectively. Briquettes from dried pastes with steel specimens inside were exposed in the following time-temperature range – 2 hours and 950–1100 °C.

The microstructure, microhardness and composition of treated specimens were investigated by means of optical microscopy, SEM, EDS and XRD analysis. Besides, mechanical properties, such as microhardness and wear resistance, were studied, where the latter was determined by dry sliding friction test in accordance to the block-on-ring scheme. The specimen's wear change was evaluated by its mass loss on an analytical scale. In order to reduce high roughness after boroaluminizing the final machining operation (FMO) was applied to the treated surface. FMO was implemented on a vertical milling machine with grinding tool from cubic boron nitride. Surface roughness was measurements on an optical profiler before and after FMO.

Table 1. The chemical composition of steels, wt.%

Steel grade	C	Si	Mn	P	S	Cr	Ni	Cu	W	V
30	0.17–0.24	0.17–0.37	0.35–0.65	up to 0.035	up to 0.04	up to 0.25	up to 0.3	up to 0.3	–	–
3Kh2V8F	0.3–0.4	0.15–0.4	0.15–0.4	up to 0.03	up to 0.03	2.2–2.7	up to 0.35	up to 0.03	8.5–10.0	0.3–0.6

## RESULTS

### Microstructure evolution

Experiments have shown that the layers with different thickness were formed depending on the treatment temperature. Boroaluminizing at 950 °C lead to the sandwich-structured diffusion layer with the total thickness of about 130 μm (Fig. 1a). Combined B+Al-diffusion resulted in the generation of predominantly aluminized layer, where the outer zone of the layer consists of iron aluminide FeAl at the top and a solid solution of aluminum in iron below. The inner boride zone is comprised of a chain of small iron boride crystals located at the interface layer boundary. A transition zone of coarse perlite grains with acicular ferrite on boundaries can be found beneath the layer.

Boroaluminizing at elevated temperatures of 1050 °C and 1100 °C leads to the formation of layers with composite structure, where hard phases (FeB, Fe<sub>2</sub>B and Fe<sub>7</sub>W<sub>6</sub>) are evenly distributed in the matrix of aluminum containing phases, such as FeAl, Fe<sub>3</sub>Al and α-Fe(Al) (Fig. 1b, c). The layer thickness riches 800 μm for steel 30 and 560 μm for steel 3Kh2V8F. Extended transition zone was formed below the main layer, due to carbon and alloying elements displacement from the surface to the core. The presence of transition zone can positively effect on the adhesive properties and provide favorable residual stress distribution.

Thus, treatment temperature affects highly on the layer structure, thickness and composition at combined B+Al-diffusion. On the contrary, the minor effect of the treatment temperature is visible after pure boriding in pastes. The treatment has resulted in the layer formation with the typical tooth-like structure, where the outer phase is FeB and the inner – Fe<sub>2</sub>B (Fig. 1d). The same result has been obtained in the whole temperature range of 950–1100 °C.

### Wear resistance

Wear resistance tests have shown that high-temperature boriding (HTB) and high-temperature boroaluminizing (HTBA) at 1050 °C and 1100 °C increase significantly wear resistance of treated steels (Fig. 2). Wherein, alloy steel resistance was slightly superior to the carbon steel.

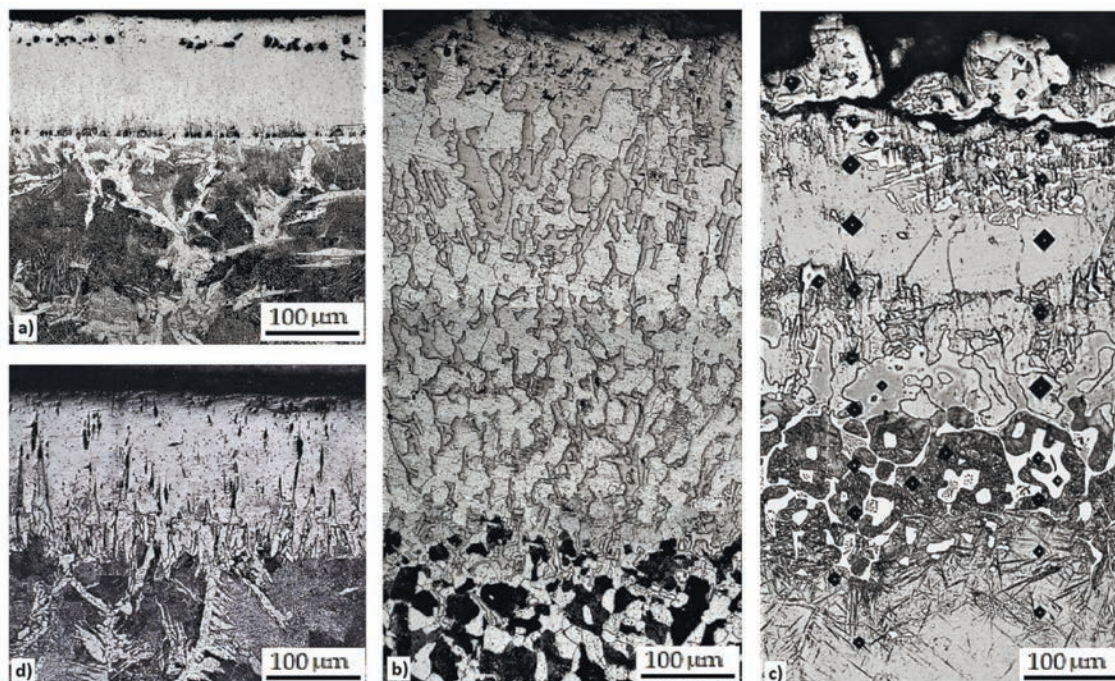


Fig. 1. Microstructures of borided and boroaluminized steels after 2-hours exposure (×200): *a* – boroaluminizing of steel 30 at 950 °C; *b* – boroaluminizing of steel 30 at 1100 °C; *c* – boroaluminizing of steel 3Kh2V8F at 1050 °C; *d* – boriding of steel 30 at 1100 °C

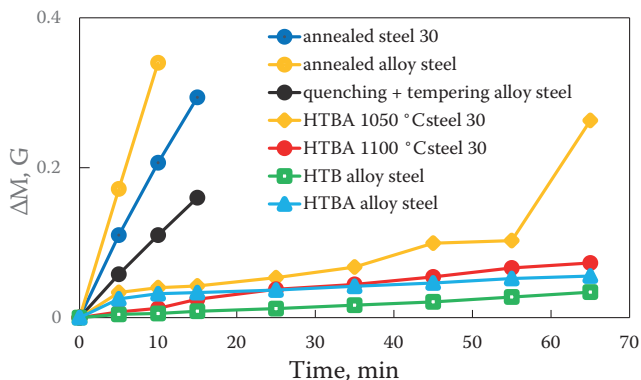


Fig. 2. Wear resistance of steels after different treatments [15]

Wear behavior of all non-treated specimens demonstrates a sharp (catastrophic) mass loss at the very beginning of the test. The similar sharp mass loss was revealed for boroaluminized steel 30 (1050 °C) after 55 minutes of abrasion, which indicate a full layer deterioration.

Borided specimen have demonstrated the highest resistance to dry friction. In the meantime, specimens after boroaluminizing possesses corresponding slope of the wear curve. In prospect, the layers with composite structure, containing boron and aluminum compounds, is preferable to resist oxidation and wear over pure boriding.

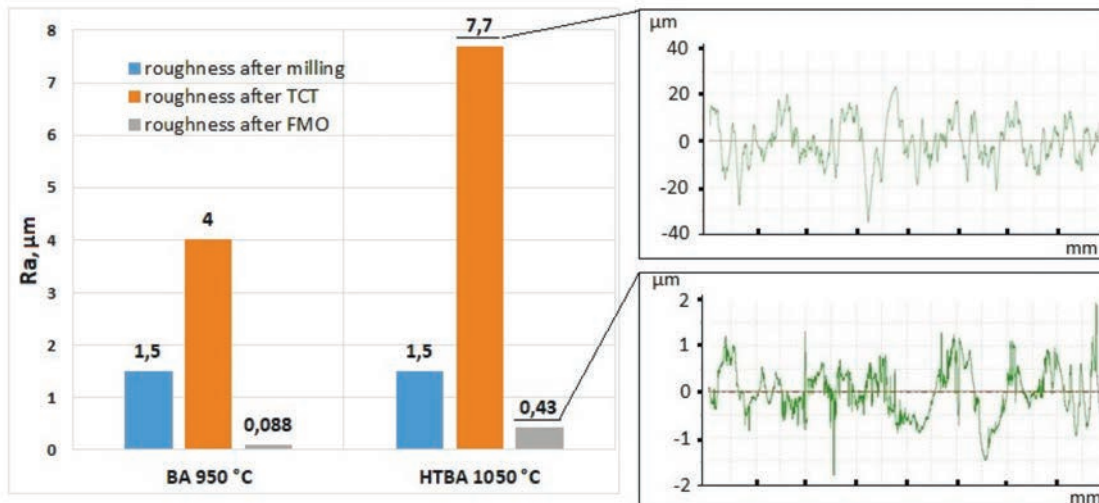


Fig. 3. Surface roughness profiles of steel 3Kh2V8F after different treatments

## Surface roughness

Boriding is notable for its ability to provide minor roughness of treated surface. The combined B+Al-diffusion results in significant roughness rising from initial to Ra 1.5  $\mu\text{m}$  to Ra 7.7  $\mu\text{m}$  (Fig. 3). The high surface roughness can be reduced by applying the final machining operation (FMO). In the meantime, functional properties the surface are provided to the full extent by the remaining zones of the layer.

## CONCLUSIONS

Boriding and boroaluminizing lead to significant wear resistance improvement of carbon and alloy steels.

The layer with the composite structure is formed as result of boroaluminizing at 1050 °C and 1100 °C, where hard phases (FeB, Fe<sub>2</sub>B and Fe<sub>7</sub>W<sub>6</sub>) are evenly distributed in the matrix of aluminum containing phases.

Combined diffusion with boron and aluminum is preferable in comparison with pure boriding due to potential resistance to oxidation and punching load.

## ACKNOWLEDGMENTS

This research was funded by RFBR, grant number № 18-38-00939.

## REFERENCES

1. **Kulka M.** Trends in thermochemical techniques of boriding. In *Current Trends in Boriding // Engineering Materials*; Springer: Cham, Switzerland, 2019. P. 17–98.
2. **Rohr V., Schütze M., Fortuna E., Tsipas D.N., Milewska A., Perez F.J.** Development of novel diffusion coatings for 9–12% Cr ferritic-martensitic steels (SUNASPO): In *Novel Approaches To Improving High Temperature Corrosion Resistance // European Federation of Corrosion Publication*; Schütze, M., Quadackers, W.J., Eds.; Woodhead Publishing, 2008. Vol. 47. P. 176–192.
3. **Voroshnin L.G., Mendeleeva O.L., Smetkin V.A.** Teoriya i tekhnologiya khimiko-termicheskoy obrabotki [Theory and technology of Chemical and Thermal Processing]. Minsk, Belarus: Novoje znanije, 2010. P. 304.
4. **Czerwinski F.** Thermochemical treatment of metals. In *Heat Treatment: Conventional And Novel Applications*; Czerwinski F., Eds.; In Tech Open Access: Rijeka, Croatia, 2012. P. 73–112.
5. **Campos-Silva I., Palomar-Pardavé M., Pérez Pastén-Borja R., Kahvecioglu Feridun O., Bravo-Bárce-**

**nas D., López-García C., Reyes-Helguera R.** Tribocorrosion and cytotoxicity of FeB-Fe<sub>2</sub>B layers on AISI 316 L steel // *Surf. Coat Technol.* 2018. 349. 986–997.

6. **Keddam M., Kulka M.A.** kinetic model for the boriding kinetics of AISI D2 steel during the diffusion annealing process // *Prot. Met. Phys. Chem. Surf.* 2018. 54. 282–290.

7. **Timur S., Kartal G., Eryilmaz O.L., Erdemir A., inventors.** Ultra-fast boriding of metal surfaces for improved properties. United States patent US 8951402 B2. 2015 Feb 10.

8. **Xie F., Sun L., Cheng J.** Alternating current field assisted pack boriding to Fe<sub>2</sub>B coating // *Surf. Eng.* 2013. 29. 240–243.

9. **Kulka M., Pertek A.** Characterization of complex (B+C+N) diffusion layers formed on chromium and nickel-based low carbon steels // *Appl. Surf. Sci.* 2003. 218. 114–123.

10. **Novakova AA, Sizov IG, Golubok DS, Kiseleva TYu, Revokatov PO.** Electron-beam bonding of low-carbon steel // *J. Alloys Compd.* 2004. 383. 108–112.

11. **Pertek A., Kulka M.** Characterization of complex (B+C) diffusion layers formed on chromium and nickel-based low carbon steel // *Appl. Surf. Sci.* 2002. 202. 252–260.

12. **Bartkowska A., Bartkowski D., Piasecki A.** Effect of diffusion borochromizing on microstructure, microhardness and corrosion resistance of tool steel with different carbon content // *Journal of Achievements in Materials and Manufacturing Engineering.* 2017. 80. 49–55.

13. **Bartkowska A., Pertek A., Popławski M., Bartkowski D., Przystacki D., Miklaszewski A.** Effect of laser modification of B-Ni complex layer on wear resistance and microhardness // *Optics and Laser Technology.* 2015. 72. 116–124.

14. **Sizov I.G., Mishigdorzhyn U.L., Leyens C., Vetter B., Furmann T.** Influence of thermocycle boroaluminizing on strength of steel C30 // *Surf. Eng.* 2014. 30. 129–133.

15. **Mishigdorzhyn U., Sizov I.** The influence of boroaluminizing temperature on microstructure and wear resistance in low-carbon steels // *Mater. Perform Charact.* 2018. 7. 252–265.

16. **Sizov I.G., Mishigdorzhyn U.L., Polyansky I.P.** Boroaluminized carbon steel: *Encyclopedia of Iron, Steel and Their Alloys*; Colás R, Totten GE, Eds. Taylor and Francis: New York, USA, 2016. P. 346–357.

17. **Krukovich M.G., Prusakov B.A., Sizov I.G.** Plasticity of boronized layers. Springer International Publishing: Switzerland, 2016. P. 111–227.

18. **Zemskov G.V., Kogan R.L.** Mnogokomponentnoye diffuzionnoye nasyshcheniye metallov i splavov [Multi-component diffusion saturation of metals and alloys]. *Metallurgiya*: Moscow, Russia, 1981. P. 208.

# EFFECT OF AlN PARTICLE SIZE ON ABNORMAL GRAIN GROWTH DURING CARBURIZATION

Naohide Kamiya, Yuuki Tanaka, Keisuke Inoue

Automotive steel research sect. No.1, corporate research & development center, Daido Steel Co., Ltd, Japan  
n-kamiya@bw.daido.co.jp

The effect of AlN particle size on abnormal grain growth in case hardening of steel was investigated in detail by using small-angle X-ray scattering (SAXS) analysis. To prepare various AlN sizes, pre-heating by full-solution treatment at 1573 K, and by precipitation treatment at 1423 K and 1273K were carried out before normalization. After the same normalization on the three samples, the total volumes of the AlN evaluated by the electrolytic extraction method were almost the same. Then, from the results of SAXS, the AlN size in the samples that underwent precipitation treatment at 1423 K and 1273 K was larger than that of the non-precipitation-treated sample.

By carburizing the three samples at from 1323 K to 1373 K, it was confirmed that abnormal grain growth was observed only on the samples that underwent precipitation treatment at 1423K and 1273 K. By SAXS measurement of the samples after carburizing, it was clarified that smaller AlN before carburizing can remain small even at higher carburizing temperatures. This result suggests that abnormal grain growth is strongly affected by the AlN size before carburizing.

**Keywords:** abnormal grain growth; aln size; small angle x-ray scattering; case hardening steel; normalization; pinning energy.

## INTRODUCTION

Carburized steel is used for power transmission parts in automobiles and industrial machinery, and in recent years, shortening the carburizing time has been aimed for through carburizing treatment at higher temperatures. However, raising the temperature in carburizing treatment is also prone to causing abnormal grain growth in the course of carburizing. Abnormal grain growth is known to cause various practical problems, such as an increase in heat-treatment strain and a decline in fatigue strength. For this reason, investigations and theoretical analyses have been conducted regarding the causal factors leading to abnormal grain growth, as a result of which it is now known that ensuring the following characteristics is effective for restraining abnormal grain growth: small variations in such particle size; large amount of pinned grains; and small particle radiuses for the pinned grains (1).

As for AlN, although it has been reported that increasing the Al and N content for a larger AlN amount at the time of carburizing does restrain abnormal grain growth (2), there has been no report on what the effects of pre-carburization AlN particle sizes are.

The pinned grains in case hardening steel are nanosized, so evaluations of their particle radiuses are being conducted by using transmission electron microscopes (TEM), but the current issues faced are

that the volume viewed in the field of vision is small, making only localized information available for the particle radiuses, and that it thus takes time to evaluate the particle radiuses. In recent years, however, there have been reports on the utilization of small-angle X-ray scattering (hereinafter called "SAXS") in evaluating the distribution of the nano-precipitate grain sizes contained in steel (3), leading to expectations that conducting evaluations for large volumes would be possible for AlN also, and that using high-luminance synchrotron radiation would expedite the measurement process.

In this study, based on SCr420, a typical case hardening steel, samples were created by changing the pre-heating treatment methods to provide the specimens, and regarding the AlN particle radiuses as evaluated through SAXS, an investigation was conducted on their effects on abnormal grain growth.

## EXPERIMENTAL PROCEDURE

In this study, with JIS-SCr420 as the basic component, steel materials with additions of Al for 0.033 mass % and of N for 0.016 mass% were used, as shown in Table 1.

For the specimens, after smelting in an electric furnace, round bars with  $\phi 30$  mm were created through hot working, with heat treatment performed

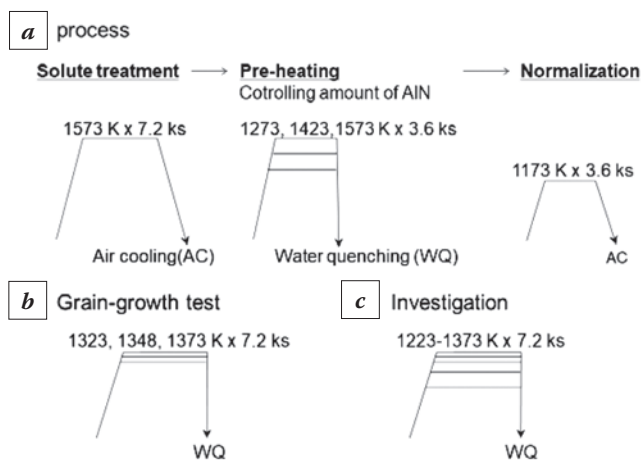


Fig. 1. Heat treatment conditions

Table 1. Chemical composition (mass %)

Fe	C	Si	Mn	Cr	Al	N	O
Bal.	0.19	0.22	0.75	1.02	0.033	0.016	0.0013

thereafter at 1573 K for 7.2 ks, with the purpose of forming an AlN solid solution (Fig. 1a).

As shown in Fig. 1a, a key aim of this study was to change the AlN particle radii after normalization in accordance with the differences in the pre-normalization AlN solid solution amount, and to investigate their effects on abnormal grain growth at the time of carburizing. Pre-normalization heating and holding was carried out at 1573, 1423 and 1273 K for 3.6 ks, then normalization heating and holding at 1173 K for 3.6 ks with radiational cooling in the atmosphere were carried out. For evaluating and estimating the AlN amount contained in the materials after normalization, electrolysis was performed by using a solution of 10% acetylacetone – 1% tetramethyl ammonium chloride – methanol, exposing the precipitates on the surface. After suction filtration using a filter with a radius of 0.2  $\mu\text{m}$ , an analysis was conducted for Al in the residual substances through inductively coupled plasma atomic emission spectroscopy (ICP-AES) (hereinafter referred to as “extraction analysis”), and presuming that all the O content in the components is a part of  $\text{Al}_2\text{O}_3$ , a subtraction was performed to arrive at the calculated value. Fig. 3 shows the AlN amount through the extraction analysis after normalization. An equivalent AlN amount was confirmed, irrespective of the preheating treatment.

For investigating the effects of a pre-normalization preheating treatment temperature on the AlN particle radius after normalization, the average particle radius of AlN (hereinafter called “ $r_0$ ”) was evaluated and estimated according to the following method. For the mea-

surements through SAXS, the Beamline BL8S3 of the Aichi Synchrotron Radiation Center, the synchrotron radiation facility of the Aichi Science & Technology Foundation in Aichi, Japan, was used. The X-rays were applied for 900 s to the specimens with their thickness adjusted to 30  $\mu\text{m}$  or less, under the conditions of a wavelength of 0.092 nm and a camera length of 4 m, for conducting the measurements. The  $r_0$  and particle size distribution for AlN were evaluated and estimated as follows. The shape of AlN was assumed to be a sphere, and its particle size distribution was considered as log-normal distribution, for the profile fitting and evaluation. To check the appropriateness of the evaluation and estimation results derived through SAXS, thin film materials normalized after the pre-normalization heat treated at 1573 K were observed with a scanning transmission electron microscope (STEM).

To investigate how the AlN particle radius, as explained in the preceding section, affect the occurrence of abnormal grain growth after carburizing, the specimens that underwent heating and holding in the atmosphere for 7.2 ks at 1323 K, 1348 K, and 1373 K, and cooling in water thereafter were checked under an optical microscope, as to whether there was any abnormal grain growth, as shown in Fig. 1b. The evaluation for abnormal grain growth was conducted this time around through quasi-carburizing, without the actual carburizing process. Regarding the judgment on the existence of abnormal grain growth, when any large grain with a grain size number of 5 or less as stipulated under JIS G 0551 was observed, this was judged as abnormal grain growth.

An investigation was conducted on how the pre-carburizing AlN particle radius affect the AlN amount and their average particle radius  $r_0$  during carburization. As for the AlN amount and  $r_0$ , after the heating and holding at the temperatures from 1223 K to 1373 K for 7.2 ks and the cooling in water, as shown in Fig. 1c, extraction analysis was conducted for the specimen to derive the AlN amount, in a way similar to the process as described in the preceding section, and the AlN particle radii were evaluated and estimated based on the SAXS measurement.

## RESULTS

### The AlN particle radii after normalization

Fig. 2 shows the SAXS profile for the samples after normalization. The horizontal axis in Fig. 2 shows the logarithm of  $q=4\pi\sin\theta/\lambda$ , a function of the scattering angle  $\theta$  and the wavelength  $\lambda$ , while the vertical axis shows the logarithm of the scattering intensity  $I$  for each  $q$  value. The gray line in Fig. 2 shows the

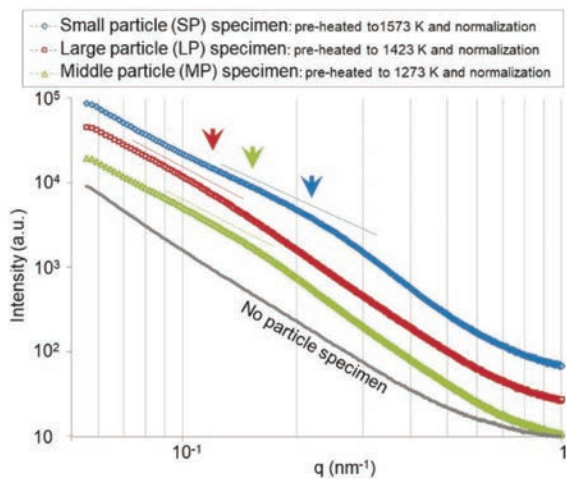


Fig. 2. SAXS profiles of pre-heated to (a) 1573 K, (b) 1423 K and (c) 1273 K for 3.6 ks and normalization

SAXS profile when AlN is absent, with the SAXS attenuation for  $q$  showing monotonously gentle curves on the high  $q$  side. On the other hand, as shown by the arrows in Fig. 2, the SAXS profiles for the specimens used in this study have a hump-shaped transition region (hereinafter called “the hump”) between the gentle and rapid attenuation regions for the scattering intensity regarding  $q$ , which does not exist in the gray-line profile. The more the hump tends to exist in the regions with high  $q$  values, it shows that more small-sized scatterers exist in the regions also (3). Based on the results of the extraction analysis and the observations through TEM as described later, these scatterers were considered to be AlN particles, and comparisons were made for the effects of the pre-normalization heat treatment temperatures on the AlN particle radiuses normalized thereafter.

A look at the arrows in Fig. 2 shows that the specimen for which the hump as indicated by the arrow exists in the regions with the highest  $q$  levels (meaning that AlN with the finest particles exist) was the specimen that was normalized after the pre-normalization heat treatment at 1573 K (hereinafter called “the SP specimen,” with SP standing for Small Particle). In contrast, the specimen for which the hump exists in the regions with the lowest  $q$  levels (meaning that AlN with the coarsest particles exist) was the specimen that was normalized after the pre-normalization heat treatment at 1423 K (hereinafter called “the LP specimen,” with LP standing for Large Particle). The specimen with the size of the AlN particles between the above two was the specimen normalized after the pre-normalization heat treatment at 1273 K (hereinafter called “the MP specimen,” with MP standing for Mid-size Particle). Based on this results, it became possible to change the AlN particle radiuses while retaining an equivalent AlN amount.

For 40 AlN particles, the radius values were measured with STEM. The SAXS trend matches that of the particle size distribution derived through STEM, based on which it is considered that the scatterers detected through SAXS are indeed AlN particles, and that the evaluation results for their particle size distribution are appropriate.

### The effects of the average particle radius $r_0$ of AlN on abnormal grain growth

To investigate how differences in the pre-carburizing AlN particle radiuses affect the temperatures at which abnormal grain growth occurs, quasi-car-

Specimen	Pre-heating temperature	AlN amount	$r_0$	1323 K	1348 K	1373 K	
a	SP	1573 K	0.086 vol. %	7.1 nm	Fine Grain (FG)	FG	FG
b	LP	1423 K	0.090 vol. %	12.5 nm	FG	Abnormal Grain Growth (AGG)	AGG
c	MP	1273 K	0.086 vol. %	10.3 nm	FG	AGG	AGG

Fig. 3. Optical micrographs of  $\gamma$  grains after quasi-carburizing for 7.2 ks of SP (a), LP (b) and MP (c) specimens

burizing was performed for the SP, LP, and MP specimens as explained in the previous section, with the temperature of 1323 K, 1348 K and 1373 K retained respectively for 7.2 ks, after which the specimens were rapidly cooled. Fig. 3 shows examples of the grain structures observed, and the results of whether there was any abnormal grain growth. Also shown in the figure are the results of evaluation and estimation for the average particle radius  $r_0$  of AlN and amount of AlN. Whereas performing quasi-carburizing for the LP specimen with a large pre-carburizing  $r_0$  value and for the MP specimen with a fairly large  $r_0$  value at 1348 K resulted in coarse grains being observed and the occurrence of abnormal grains, fine grains were retained for the SP specimen with the small pre-carburizing  $r_0$  even after the quasi-carburizing at 1373 K, with no abnormal grain occurrence observed. The smaller the pre-carburizing  $r_0$  value, the more possibility of restraining abnormal grain growth.

## DISCUSSION

The AlN amount and the behavior for  $r_0$  at the time of carburizing was considered. As shown in Fig. 4a, heating and holding was performed for 7.2 ks in the atmosphere, followed by rapid cooling and the AlN amount measurements, for each of the SP, LP, and MP specimens. The AlN amount before the quasi-carburizing is also shown by the white outlined marks on the vertical axis to the left and equilibrium AlN amount derived from reported solubility (4–6) is shown by line. There is a declining trend for the AlN amount due to quasi-carburizing at any temperature, and the higher the temperature, the larger the decline there is, and matches equilibrium AlN amount derived from solubility reported by Houghton (6). It

is considered that this is because of increases in the amount of solid solution Al and N, with effects on a decline in the pinning force at the carburizing temperatures. At the same time, no clear difference was observed in the AlN amount among the SP, LP, and MP specimens at the same carburizing temperature, so it is believed that the effects of any differences in the pre-carburizing AlN particle sizes on the decline in the AlN amount are small.

For evaluation and estimation of the AlN particle sizes during carburization, after holding each of the SP, LP and MP specimens in the atmosphere for 7.2 ks, they were rapidly cooled. Fig. 4(b) shows the  $r_0$  values after quasi-carburizing at each of the temperatures between 1223 K and 1373 K. The effects of the quasi-carburizing temperatures on the  $r_0$  values are small up to 1323 K, and there were only slight increases in  $r_0$  even at the quasi-carburizing temperature of 1348 K or higher, as shown in Fig. 4b. The white outlined marks on the vertical axis on the left show the pre-carburizing  $r_0$  values also, revealing that the pre-carburizing  $r_0$  levels for AlN have mostly been retained as they were, even after the quasi-carburizing. For this reason, similar differences in the  $r_0$  values remained among the SP, LP and MP specimens even after the quasi-carburizing process.

Based on these results, it is considered within the scope of this study that the pinning for AlN has a considerable effect on whether abnormal grains emerge. Therefore, a comparison was made for the pinning force after heating and holding each specimen at the temperature from 1223 to 1373 K for 7.2 ks, on the basis of the pinning energy. According to Zener's equation (7), the pinning energy is derived by the following equation.

$$\Delta G_{pin} = \frac{3 \sigma V f}{2 r} [1].$$

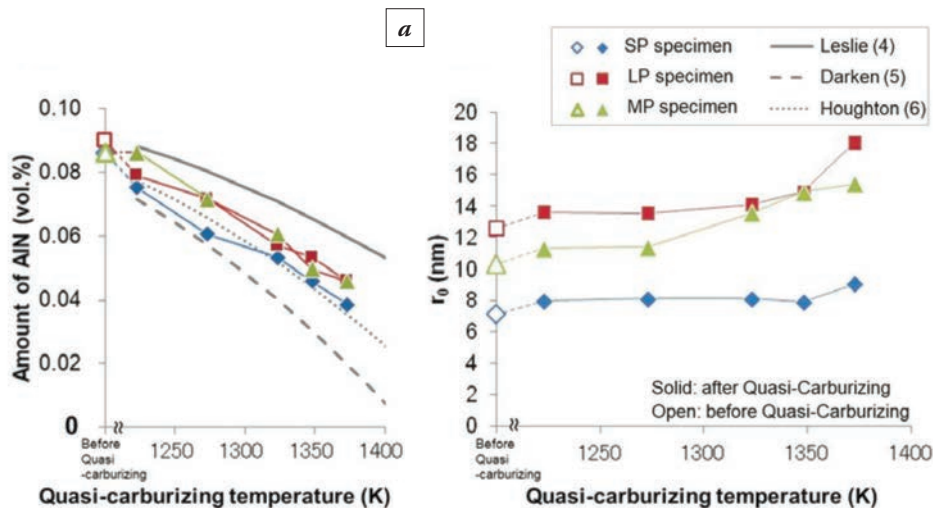


Fig. 4. Amount of AlN (a) and Average AlN radius ( $r_0$ ) of SP, LP and MP (b) specimens heated to 1223–1373 K for 7.2 ks

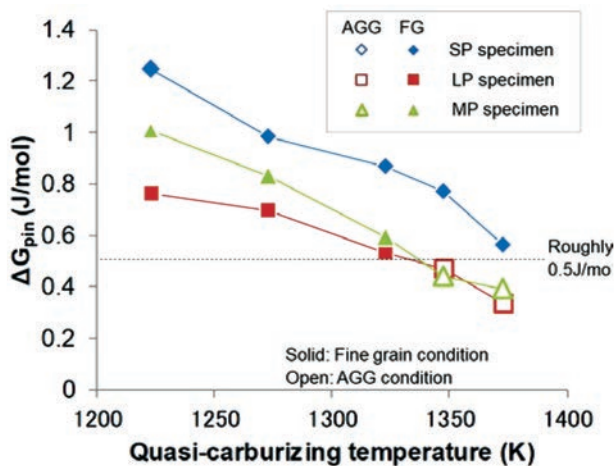


Fig. 5. Pinning energy of SP, LP and MP specimens heated to 1223–1373 K for 7.2 ks

With the surface energy  $\sigma$  at  $0.7 \text{ J/m}^2$  and the molar volume  $V$  at  $1.26 \times 10^{-5} \text{ m}^3/\text{mol}$ , the AlN amount and its average particle radius  $r_0$  at the time of heating and holding at each temperature for 7.2 ks were used for the volume fraction for pinned particles  $f$  and the particle radii of the pinned particles  $r$ . Fig. 5 shows the pinning energy of each specimen heating and holding at the temperature from 1223 to 1373 K for 7.2 ks. Although the pinning energy of each specimen decreases with high quasi-carburization temperature, the value of LP and MP specimens is less than that of SP specimens at any quasi-carburization temperatures and the value of LP and MP specimens decrease below  $0.5 \text{ J/mol}$  after quasi-carburization at 1348 K and 1373 K as shown in Fig. 5, there was any abnormal grain growth at that temperatures, on the other hand, the pinning energy of SP specimen keeps higher even after quasi-carburization at 1373 K for 7.2 ks. In this equation, the differences between the SP specimen and the LP and MP specimens exist in the volume fraction  $f$  for the AlN particles and the average particle radius  $r$  for AlN. However, as shown in Fig. 4a, there were scarcely any differences in the AlN amount, while the results in Fig. 4b show that there was a 44% difference in the reciprocals for the pre-carburizing  $r_0$  values, so it is considered that the pre-carburizing AlN particle radii have substantial effects on whether abnormal grains appear.

## SUMMARY

For case hardening steel, an evaluation was conducted on the pre-carburizing average particle radius  $r_0$  for AlN through small angle X-ray scattering (SAXS), and an investigation was conducted on the effects of the particle radii on the occurrence of

abnormal grain growth after carburizing, as a result of which the following facts became clear.

It became clear that the smaller the pre-carburizing average particle radius  $r_0$  for AlN, the higher the temperatures at which restraining the occurrence of abnormal grain growth is possible. This is because there is only a slight increase in the pre-carburizing average particle radius  $r_0$  for AlN and the smallness of the particle size is retained, even at practical carburizing temperatures.

## ACKNOWLEDGMENT

In conclusion and last but not least, we would like to express our heartfelt gratitude to Professor Masato Ohnuma in the Faculty of Engineering, Graduate School of Hokkaido University, who gave us a lot of precious advice as we conducted the analysis of small-angle scattering for this study; to Professor Kenji Kaneko in the School of Engineering, Graduate School of Engineering of Kyushu University, who gave us a lot of valuable advice as we conducted research using STEM; and to Mr. Tomonori Koyama of Kyushu University, who greatly helped us with the STEM observations.

## REFERENCES

1. Nishizawa T. Grain growth in single- and dual-phase steels. *Trans // Iron Steel Inst. Jpn.* 1984. 70: 1984–1992.
2. Kubota M., Ochi T. Development of anti-coarsening extra-fine steel for carburizing // *Nippon Steel Technical Review.* 2003. 378: 72–76.
3. Satoh K., Sato S., Ohnuma M., Naruse T., Kim Y., Ebata T., Suzuki S., Wagatsuma K. Small-angle X-ray scattering studies on aging precipitation of high-strength soft-magnetic stainless steels // *ISIJ int.* 2017. 57: 2028–2033.
4. Leslie W.C., Rickett R.L., Dotson C.L., Walton C.S. Solution and precipitation of aluminium nitride in relation to the structure of low-carbon steels // *Trans. ASM.* 1954. 46: 1470–1499.
5. Darken L.S., Smith R.P., Filer E.W. Solubility of Gaseous Nitrogen in Gamma Iron and Effect of Alloying Constituents – Aluminum Nitride Precipitation // *J. Metall.* 1951. 191: 1174–1179.
6. Houghton D.C. Equilibrium solubility and composition of mixed carbonitrides in microalloyed austenite // *Acta metall. mater.* 1993. 41: 2993–3006.
7. Smith C.S. Grains, phases, and interphases: an interpretation of microstructure // *Trans. Metall. Soc. AIME.* 1948. 175: 15–51.

## LOW-TEMPERATURE LIQUID BORONIZING OF STRUCTURAL STEELS

S.G. Tsikh<sup>1</sup>, A.A. Krasulya<sup>2</sup>, K.D. Polinovsky<sup>3</sup>, V.N. Skorobogatykh<sup>1</sup>, A.S. Pomelnikova<sup>2</sup>

<sup>1</sup> NPO «CNIITMASH». Moscow, Russia

<sup>2</sup> Bauman Moscow State Technical University. Moscow, Russia

<sup>3</sup> «ITSU». Moscow, Russia

krasulya230593@gmail.com

The influence of the low-temperature liquid boronizing modes on the depth of the boride layers on the samples of previously toughened steel 25Cr1MoV was researched. The X-ray phase diffraction analysis, scanning transmission electron microscopy and corrosion resistance tests were carried out.

**Keywords:** low-temperature liquid boronizing; heat-resistant steel 25Cr1MoV.

### INTRODUCTION

The operational durability of parts and assemblies of modern equipment is mainly determined by the ability of relatively thin surface layers of their working bodies to resist various types of wear, corrosion, fatigue failure, etc. This is due to the fact that the surface layers of parts are loaded more intensively than the core during the operation. Accordingly, the resulting stresses on the surface have maximum values, which leads to loss of performance ability of both the surface layer and the whole part. Unfortunately, there are no versatile strengthening technologies. Well-known and widely used technologies of surface strengthening, such as nitriding, cementation and nitrocarburizing, have proved successful in the conditions of metal-to-metal friction under high contact loads, but their efficiency is dramatically reduced in the presence of abrasive particles in the contact zone. This is because the hardness of the abrasive particles is higher than the hardness of the surface of the part. Among diffusion methods, only boronizing can form a strengthened layer on the surface consisting of iron borides with a hardness of more than 2000 HV [1–7], which is significantly higher than the hardness of most abrasive materials (for example, the hardness of the most common abrasive – quartz – does not exceed 1240 HV [8]).

Due to the fact that the modulus of elasticity of FeB is 4.0–4.5 times higher than that of quartz (343...400 GPa and 77...97 GPa, respectively [1–7, 9]), during the contact under the loading of a boride layer and an abrasive grain it is mainly quartz is subjected to elastic distortion, but not iron boride. The

calculation according to the method given in [10, 11] shows that with a two-phase structure (FeB + Fe<sub>2</sub>B) of the boride layer and a quartz grain size up to 1 mm, the nominal depth of its penetration into the boride layer is less than 1 micron, and the maximum possible depth (for acute-angle juts) is 3...4 microns. This suggests that in order to provide a long service life of boride layers, a thickness of 10...15 μm is sufficient, since their wear is a result not of gradual abrasion, but of fatigue mechanism. In this case, at first, the growth of microcracks in the boride layer occurs, and then the detachment of some sections of the boride layer from the matrix takes place. Thus, the wear resistance of the boride layer is primarily determined not by its thickness, but by fatigue resistance.

However, with such a small thickness of the boride layer, it is necessary that the elastic limit in compression of the metal base exceeds the tensile strength of the abrasive grains. Otherwise, plastic deformation of the metal base will take place, which may cause cracking of the boride layer. The calculation shows that the specified elastic limit is provided by the hardness of the metal base of at least 26 HRC. In practice, it is accepted that a certain margin of hardness should be provided and the lower hardness limit of the part's core should not be less than 28 HRC, and in some cases even at a higher level (30...45 HRC) [12]. Therefore, the existing technologies of high-temperature (at 850 °C and above) boronizing almost invariably need the subsequent operation of toughening (quenching and high-temperature tempering) to give the part's core high strength characteristics. However, boronizing followed by quenching leads to

the formation of a large number of microcracks in the boride layer and, consequently, to a falloff in its fatigue resistance [13], and in some cases, in corrosion resistance [4]. In addition, due to high hardness of the boride layer, it is impossible to carry out finishing machining treatment after boronizing. Therefore, quenching after boronizing is unacceptable due to the inevitable quenching distortion for the parts which have strict requirements on their size and shape.

A significant increase in the fatigue resistance and, probably, in the corrosion resistance of the boride layer can be achieved by boronizing after toughening. Moreover, in order to maintain a sufficiently high hardness of the core of the part, the boronizing temperature should not exceed the temperature of the preceding tempering, i.e. low-temperature (580...660 °C) liquid boronizing (LLB) should be used. But the standard bath compositions used for high-temperature liquid boronizing are unsuitable for LLB because they do not provide an acceptable kinematic viscosity of the melt.

Earlier, the authors [14–16] have developed and tested several versions of the compositions for LLB baths, but they turned out to be unsuitable for practical use because of high kinematic viscosity of the melt.

The main objectives of this work are choosing steel grades with sufficient resistance to tempering, namely – with the ability to provide not lower than 28 HRC level of hardness of the core after LLB;

– development of boronizing modes for the creation of rational structures of the surface layer, providing practically its ultimate performance.

To solve the problem, the technology of LLB “Rubonit” was developed. This is a technology of low-temperature liquid boronizing (580–660 °C) in chloride salts medium with additions of boron oxide. Boron oxide is a catalyst for the reactions of active boron formation, which diffuses into the surface of steel. The developed composition has a rather low viscosity and a high water solubility.

## MATERIALS AND RESEARCH METHODS

Chromium, molybdenum, vanadium, tungsten and niobium alloyed steels form carbides and intermetallic compounds which are resistant to coagulation. These steels have a rather high resistance to tempering. However, as shown in [1–4], the speed of boronizing process decreases dramatically in the presence of these elements. Thus, to ensure a suf-

ficient thickness of the boride layer, the content of these elements in the steel should be at a minimum level at which the specified value of heat resistance can be provided. Proceeding from this and on the basis of the analysis of reference data, heat-resistant steel of pearlitic class 25Cr1MoV was chosen for research and working out the operational modes. Its chemical composition is given in Table 1.

Taking into account the reference information on the heat resistance of the selected steel grade, LLB in the “Rubonit” melt was carried out at the temperature range 600...660 °C for 8...32 hours. Preliminary toughening of the samples was carried out according to the mode: quenching from 900 °C and tempering at 600 °C for 2 hours. We chose the tempering temperature slightly lower compared to that recommended by State Standard 20072-74, because of the convenience for researching the effect of temperature and duration of LLB on the mechanical properties of the core.

The research of the samples’ microstructure and the chemical composition of the phases was carried out on a JSM-6060A scanning electron microscope (Jeol, Japan) equipped with a JED-2300 energy dispersion spectrometer (Jeol, Japan) and on a Neophot 30 optical microscope.

X-ray diffraction phase analysis was carried out on a DRON-3M general-purpose diffractometer (CuK $\alpha$  radiation, with a monochromator). Registration and processing of the data were performed using the software package “GLRDIF”.

Transmission microscopy was performed on a JEM 200CX electron microscope. The diffusion layer of iron borides was studied in a transverse to the surface plane. The final thinning was conducted in the PIPS II ion polishing unit in argon medium. The surface layer was protected from thinning with a layer of tin-lead solder. The measurement of the surface layers and the core hardness was carried out on a “DuraScan 20” microhardness tester with a load of 100 g. The microhardness tester was controlled using a personal computer equipped with “ecos Workflow” software.

## RESULTS AND DISCUSSION

The kinetics of steel 25Cr1MoV boronizing is governed by a parabolic law (Table 2), the dependence of the boride layer depth on the temperature is exponential (Table 3), that completely corresponds to the theory of chemical kinetics.

Table 1. Chemical composition of steel 25Cr1MoV according to State Standard 20072-74 [17]

C	Si	Mn	Cr	Mo	V	Ni	Cu	P	S
0.22–0.29	0.17–0.37	0.4–0.7	1.5–1.8	0.25–0.35	0.15–0.3	up to 0.25	up to 0.2	up to 0.03	up to 0.025

Table 2. The dependence of the core hardness and the depth of the boride layer on the duration of the process LLB (temperature of boronizing – 640 °C)

The duration of boronizing, h	8	16	24	32
Core hardness, HV 0.1 (GPa)	310 (3,04)	300 (2,94)	280 (2,75)	270 (2,65)
Boride layer depth, micron	10...11	13...15	15...17	17...19

Table 3. The dependence of the core hardness and the depth of the boride layer on the temperature of the LLB process (duration of boronizing – 14 hours)

Boronizing temperature, °C	600	620	640	660
Core hardness, HV 0.1	330	320	300	250
Boride layer depth, micron	6...8	9...10	12...14	16...18

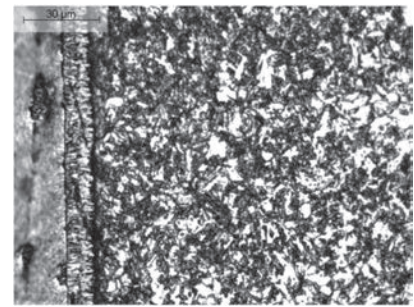


Fig. 1. The structure of steel 25Cr1MoV after toughening and LLB «Rubonit» treatment

Based on the results obtained, the optimal LLB mode for this steel grade was selected, which provides a combination of sufficient boride layer depth and core hardness: temperature 640 °C, time of treatment – 14 hours.

As a result of boronizing of steel 25Cr1MoV according to the “Rubonit” technology, a compositional layer 12... 14 μm of depth is formed on the surface. This layer has no cracks and consists of several zones (Fig. 1). X-ray structural method reveals two phases - on the surface of FeB (Fig. 2a), under which the zone Fe<sub>2</sub>B is located (Fig. 2b).

The foils were cut from the boronized layer and studied by means of electron transmission microscopy. This research showed the presence of only two phases in the boride layer (Fig. 3) and the presence of special carbides in the core.

It is not possible to determine the type of crystal lattice of the surface zone acicular structure (Fig. 3a) because of the high imperfection of the structure. According to X-ray diffraction analysis, this phase corresponds to FeB boride.

An analysis of the electron diffraction patterns obtained from the needles of the second zone from the edge of the sample (Fig. 3b) showed that the crystal lattice of the studied phase corresponds to a body-centered tetragonal lattice with parameters  $a = 5.06$ ;  $b = 5.06$ ;  $c = 4.24$ . This lattice corresponds to iron boride Fe<sub>2</sub>B with the space group I4/mcm, which agrees with the X-ray diffraction data (Fig. 2b).

In the diffusion zone (Fig. 3c) the needles of the Fe<sub>2</sub>B phase “grow” into the initial solid solution. An α-solid solution with inclusions of special carbides (Me<sub>7</sub>C<sub>3</sub>, Me<sub>23</sub>C<sub>6</sub>, and MeC) is found in the core (Fig. 3d).

The surface phase of FeB (Fig. 3a) is represented by disordered needles which have a lamellar structure of unclear nature (mainly microtwinned). The boundaries between the needles are diffused. The depth of some needles reaches 0.15 microns.

The Fe<sub>2</sub>B zone (Fig. 3b) is represented by the needles strictly oriented perpendicular to the surface.

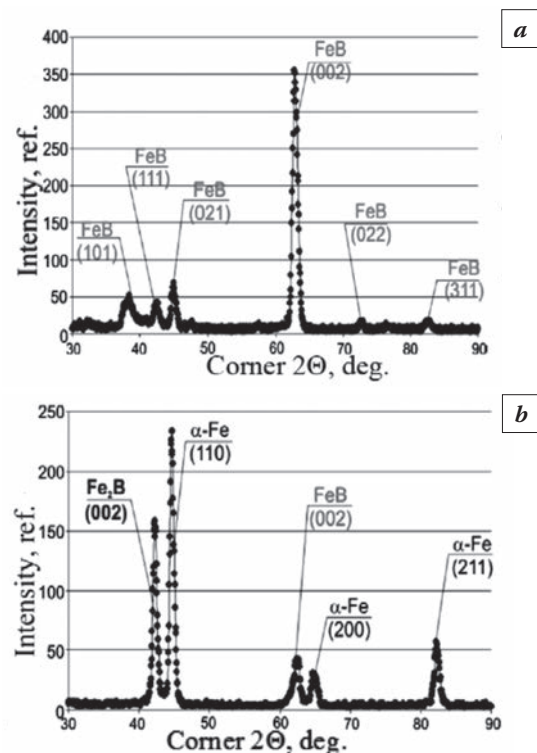


Fig. 2. X-ray diffraction patterns: from the surface (a) and after removal of a layer ~ 9 microns (b) of steel 25Cr1MoV after toughening and LLB “Rubonit” treatment

They have clear boundaries. The observed needles width is 0,2–0,8 μm. Unlike the surface layer, the Fe<sub>2</sub>B layer is formed by only one row of needles, i.e. its depth is determined by the length of the needles themselves, which is 5–6 μm. At the boundaries between adjacent needles there is no solid solution of α-iron, the junction between the needles is tight, in some places there are particles of foreign inclusions (Fig. 3b). In the diffusion zone (Fig. 3c), where the needles grow into the initial solid solution, the needles have rounded, thinner ends. There is the α-solid solution between the ends. There is no additional precipitate at the border between the needles and the α-solid solution. The dark edging which is visible in some figures around the needles is the tilt boundary of two phases in the sample.

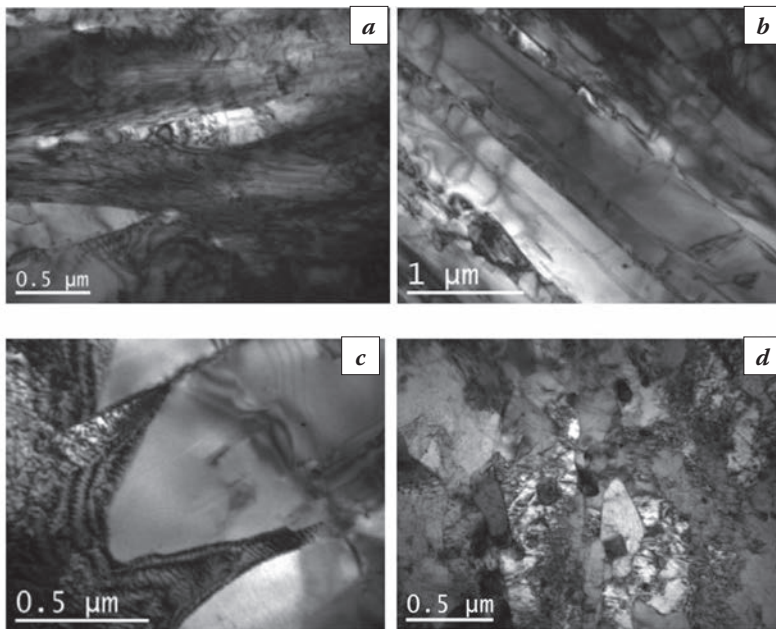


Fig. 3. The fine structure of steel 25Cr1MoV after toughening and LLB «Rubonit» treatment: *a* – the surface (the sample surface is on the right); *b* – the distance from the surface of 8...9 microns; *c* – the distance from the surface 11...12 microns; *d* – the core

Thus, the technology LLB «Rubonit» allows to get high-quality strengthened layers at low (up to 660 °C) temperatures, which are high-tempering temperatures for many structural steels (especially heat-resistant). After experimental verification, this technology can substitute nitriding, nitrocarburizing, galvanic chrome plating for friction pairs in the presence of abrasive particles.

## CONCLUSIONS

The failure mechanism in the presence of abrasive particles of the friction pairs surface strengthened by boronizing is analyzed.

It was found that the wear of boride layers occurs due to fatigue failure, therefore, their wear resistance is determined primarily not by the layer's thickness, but by its fatigue strength. Theoretical estimation shows that the thickness of 10...15 microns is sufficient to provide high wear resistance of boride layer. In this case, the hardness of the core should be at least 26 HRC. Such a value of hardness, as a rule, can be achieved only in toughened steel.

The technology of LLB «Rubonit» has been developed for strengthening of the parts made of heat-resistant steels at the temperatures not exceeding high-tempering temperatures. The mode of boronizing optimization was carried out, which allows to obtain the rational structures of the surface layer, providing maximum fatigue strength.

## REFERENCES

1. Ворошнин Л.Г., Ляхович Л.С., Панич Г.Г., Протасевич Г.Ф. Структура сплавов системы Fe-B // *Металловедение и термическая обработка металлов*. 1970. № 9. С. 14–17.
2. Ворошнин Л.Г., Ляхович Л.С. Борирование стали. М.: *Металлургия*, 1978. 239 с.
3. Прогрессивные методы химико-термической обработки / Под ред. Г.Н. Дубинина, Я.Д. Когана. М.: *Машиностроение*, 1979. 184 с.
4. Крукович М.Г. Разработка теоретических и прикладных аспектов управления структурой и свойствами борированных слоев и их использование при производстве транспортной техники: Дисс. докт. техн. наук. М., 1995. 416 с.
5. Anvil Kumar Sinha. Boriding (Boronizing) // *ASM Handbook*. V. 4. Heat Treating. 1998. P. 437–447.
6. Thomas W.R., Leak G.M. Condition of Boron in Alpha Iron // *Nature*, 1955. July 2. Vol. 176, № 4470. P. 29–31.
7. Самсонов Г.В., Серебрякова Т.И., Неронов В.А. Бориды. М.: *Атомиздат*, 1975. 376 с.
8. Самсонов Г.В, Борисова А.А. и др. Физико-химические свойства окислов. Справочник. М.: *Металлургия*, 1978. 472 с.
9. Кристаллический кварц (электронный ресурс – сайт ООО «Тидекс» [http://www.tydexoptics.com/ru/materials/for\\_transmission\\_optics/crystal\\_quartz/](http://www.tydexoptics.com/ru/materials/for_transmission_optics/crystal_quartz/))
10. Крагельский И.В. Трение и износ. М.: *Машиностроение*, 1968. 480 с.
11. Икрамов У.А. Расчетные методы оценки абразивного износа. М.: *Машиностроение*, 1987. 288 с.
12. Зинченко В.М. Инженерия поверхности зубчатых колес методами химико-термической обработки. М.: Изд. МГТУ им. Н.Э. Баумана., 2001. 303 с.
13. Карпенко Г.В., Похмурский В.И., Далисов В.Б., Замиховский В.С. Влияние диффузионных покрытий на прочность стальных изделий. К.: *Наукова думка*, 1977. 168 с.
14. Чернов Я.Б., Анфиногенов А.И., Шуруп Н.И. Борирование сталей в ионных расплавах. Екатеринбург: УрО РАН, 2001. 223 с.
15. Ляхович Л.С., Косачевский Л.Н., Крукович М.Г., Туров Ю.В. Состав расплава для низкотемпературного борирования // Авт. свид. № 406971 С23С – Оpubл. в Б.И. 1973, № 46.
16. Ляхович Л.С., Косачевский Л.Н., Крукович М.Г., Туров Ю.В. Состав расплава для низкотемпературного борирования // Авт. свид. № 418571 С23С – Оpubл. в Б.И. 1974, № 9.
17. ГОСТ 20072-74 Сталь теплоустойчивая. Технические условия (с Изменениями N 1, 2).

# ECOLOGICAL AND PRACTICAL PROCESS COMPARISON OF PLASMA AND GAS NITRIDING–NITROCARBURIZING FOR USERS

Thomas Müller, Andreas Gebeshuber, Martin Aigner

RÜBIG GmbH & Co KG, Austria

thomas.mueller@rubig.com, andreas.gebeshuber@rubig.com, martin.aigner@rubig.com

For heat treatment processes the associated cost reduction per component, the precise temperature control, quality reproducibility and the increase in energy efficiency are becoming increasingly important in the future. In addition mainly economic considerations and aspects are coming to the fore and are driving the R&D in the thermochemical treatment industry. Based on the advanced developments in the field of furnace and process technology the trend is more and more versus environmental friendly and in the meantime economical methods like plasma nitriding. Nevertheless from the technical point of view not all applications can be handled by plasma assisted nitriding technology. So a coexistence of several different innovative and conservative nitriding technologies will remain, with the focus of reducing the environmental impact of nitriding. The differences – advantages and disadvantages – of the technologies plasma – ion – nitriding and gas nitriding will be demonstrated from the user's point of view. Further to analyze and evaluate the environmental/ecological impact of the compared technologies Life Cycle Assessments are shown. By using these data the competitiveness from an ecological point of view can be demonstrated.

**Keywords:** plasma nitriding; gas nitriding; ecological heat treatment; efficient heat treatment; Environmental heat treatment.

## INTRODUCTION: NITRIDING TECHNOLOGIES

### Needs of industry and why nitriding?

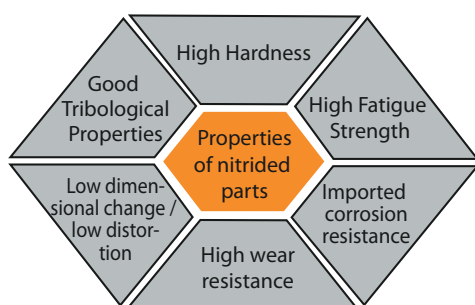
Nitriding (further on nitriding is including nitro-carburizing) is a thermochemical hardening method of diffusing N (N+C) into the surface of steel components or cast iron components. The main goal of nitriding is the increase of surface hardness to improve wear resistance and the creation of superficial compressive stresses (stress profiles) to optimize fatigue properties – see Fig. 1. In comparison to other thermochemical processes nitriding is performed at temperatures below 590 °C. Therefore only the surface is modified and no phase transformation of the core takes place. The minimized dimensional change and distortion during the nitriding process is a big advantage of this technology. Additionally to improved wear

and fatigue properties subsequent post treatments like post-oxidation can influence the corrosion behavior.

For iron the solubility of N is shown in Fig. 2. By changing nitriding intensities and parameters different surface structures and corresponding properties can be adjusted. This varies from just nitrogen enriched zones up to the formation of nitrides/nitride precipitations and phase transformation (gamma prime, epsilon phase) of the surface area due to higher N, C concentrations.

The main influencing process parameters on the “nitriding intensity” and the nitriding results are

- Composition of nitrided alloy
- Process temperature [ $T$ ]
- Process duration [ $t$ ]
- Availability of atomic N/C by different gas mixtures, surface reactions, activation
- Surface condition



Component properties	Major influence by	
	Compound layer	Diffusion layer
wear resistance	X	
fretting	X	
Corrosion protection	X	
high temp.-strength	X	X
fatigue		X
compressive strength		X

Fig. 1. Summary of steel properties influenced by nitriding

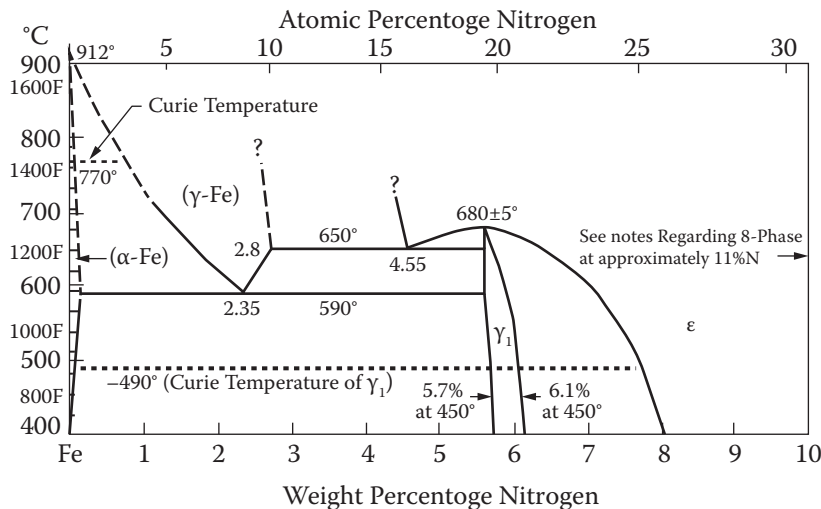


Fig. 2. Iron – nitrogen equilibrium phase diagram [1]

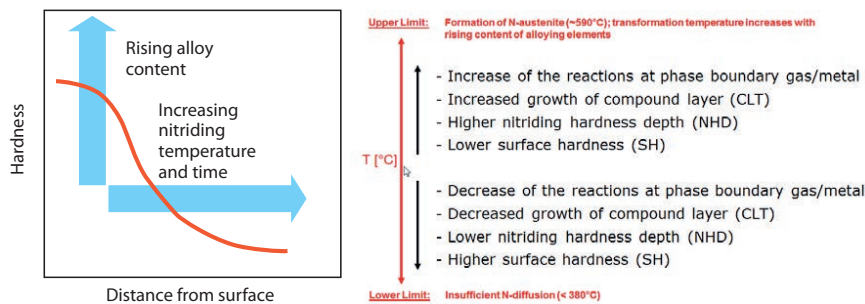


Fig. 3. Principle scheme of parameter influences on the nitriding result



Fig. 4. Pit – horizonal – bell type furnace configuration [4]

and can be summarized for the nitriding depth [ND] in the below shown approximation and are illustrated in Fig. 3:

$$ND \approx \sqrt{k \frac{N}{X} D_N^\alpha t}, [1]$$

$N$  – nitrogen content;  $X$  – content of nitride formers;  $k$  – correction value;  $D_N^\alpha$  – diffusion coefficient of nitrogen in ferrite.

An example of a nitrided hardening tempering steel is shown in Fig. 3.

## Gas nitriding

Gas nitriding is carried out in most cases in retort furnaces (different furnace types see Fig. 4) at a tem-

perature of 480 °C to 580 °C under slight over pressure conditions. The nitrogen source is gaseous ammonia, whereas it has to be mentioned that ammonia is poisonous even in low concentrations and has to fulfil higher safety regulations.

The process can be sketched in a simplified form as follows: The heating up of the batch usually takes place in protective nitrogen atmosphere. For better activation of the surface pre-oxidation in the temperature range of 300 °C to 450 °C could be carried out. Depending on the desired nitriding results ammonia containing gas mixtures are added to the furnace atmosphere at nitriding temperature. The catalytic decomposition of the ammonia on the workpiece surface produces activated nitrogen, which can diffuse into the surface of the workpiece (see Fig. 5). Through a continuous flow of the fresh gas mixture the dissociated ammonia is continuously replaced. The gas mixture flow through the batch is usually ensured by a gas guiding cylinder and a powerful convection ventilator. For nitrocarburizing a carbon source is added to the treatment gas in addition to the nitrogen-donating ammonia. This can be for example  $\text{CO}_2$ ,  $\text{CO}$ , ... The gas nitrocarburizing temperature of typically 550–590 °C is higher compared to those of the gas nitriding process.

Post-oxidation (e.g., water vapour or air) provides significantly improved corrosion resistance by passivating the compound layer with an oxide layer (see Fig. 5).

Nowadays nitriding processes are sensor controlled. This means based on the analysis of the atmosphere ( $\text{H}_2$  or  $\text{H}_2/\text{O}_2$ ) the nitriding potential – nitriding intensity – can be controlled. The potential is calculated from the partial pressures of  $\text{NH}_3$  and  $\text{H}_2$  and based on this ratio the gas flow can be adjusted. Using this method the flexibility and efficiency of nitriding cycles and of installed gas nitriders can be improved.

## Plasma nitriding

As an alternative technology plasma nitriding or ion nitriding has been used for decades. During the

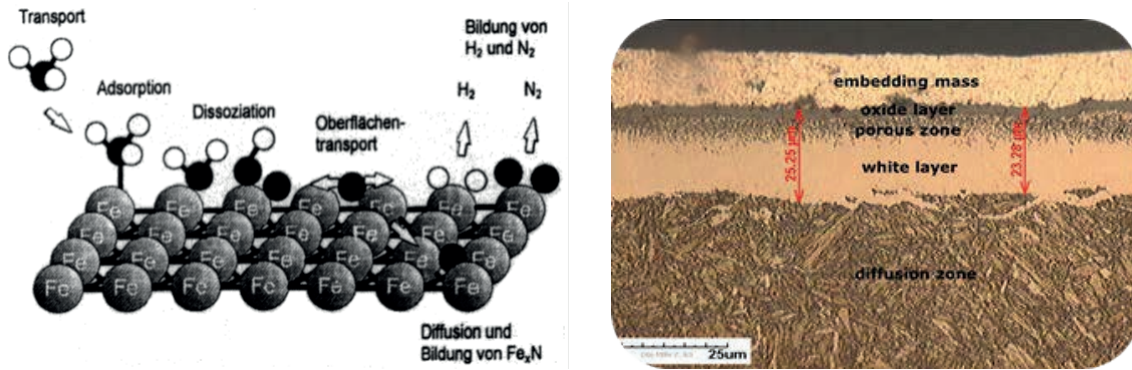


Fig. 5. Reaction schematics and results of gas nitriding process [4]

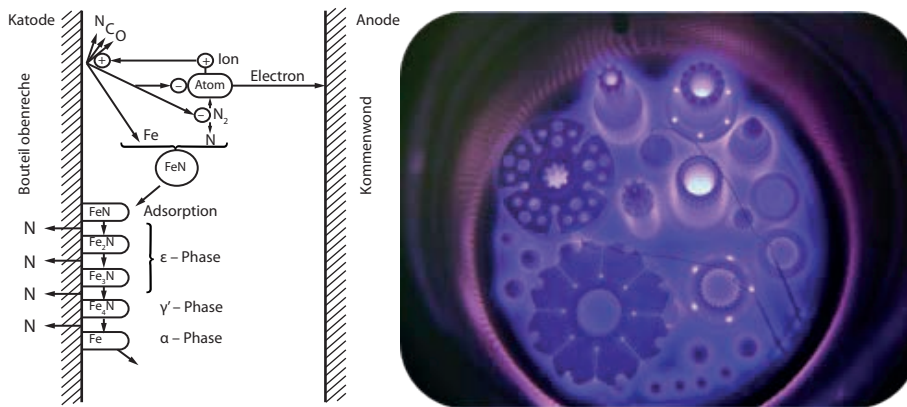


Fig. 6. Schematic molecular reaction model of plasma-nitriding process [2]

early 90's there was a technological shift in the plasma nitriding hardware from cold to hot wall technology. Since then the industrial usability and efficiency of this technology is given. Due to the better controllability, flexibility and reproducibility of processes any further results and statements are only referred to hot wall – externally heated and cooled – furnace technology. Plasma nitriding in comparison to gas nitriding is a low pressure process. Due to the low pressure system very little gas quantities are needed and further only nontoxic gases are used. Therefore there is a big advantage in respect to environmental/legal requirements and for the integration of the heat treatment in e.g. assembly lines. Essentially nitrogen and hydrogen are used for this process and for nitrocarburizing carbon sources like  $\text{CH}_4$ ,  $\text{CO}_2$  are added. The nitriding principles are comparable with the gas nitriding with the difference of the N source. As  $\text{N}_2$  as nitrogen source is chemically stable at nitriding temperature, an activation by a glow discharge plasma is used. One of several model explanations for plasma nitriding based on Kölbl is shown in Fig. 6.

Plasma nitriding processes are carried out at a pressure in the range of 0.2 to 8 mbar and can be used even at very low temperatures like  $>200^\circ\text{C}$  if needed. For achieving a glow discharge a low pressure system is needed and the batch has to be electroni-

cally separated from the wall. By applying a voltage between the furnace wall and the components, which is usually between 400 and 600 V during the process, diffusible N and/or C is produced. As a result, a glow discharge with a high degree of ionization (plasma) is generated and consequently covering the parts. Nitrogen ions are accelerated to the surface of the workpiece leading to the formation of nitrogen-rich nitrides. The decomposition of

these nitrides produces active nitrogen, which can diffuse into the workpiece surface. Plasma nitriding processes are completely automated and can be fully integrated in management systems like ERP, PPS, ... (see Fig. 7).

### Practical criteria for the choice of process – gas or plasma nitriding

The coexistence of the described technologies shows that there is the need for the advantages of both technologies. Even the technological gap is getting smaller and smaller, several arguments pro/con still exist. Table 1 shows an overview of criteria on the choice of nitriding technology.

This means that there is an optimum nitriding technology for each application and a very wide field of activity, which can be handled by both technologies. Derived from this criteria the optimum nitriding process can be chosen by considering the main benefits of both, gas and plasma nitriding (see Table 2).

### Life cycle assessment

Based on the nitriding life cycle analysis, a comparison of a gas and plasma nitriding process was

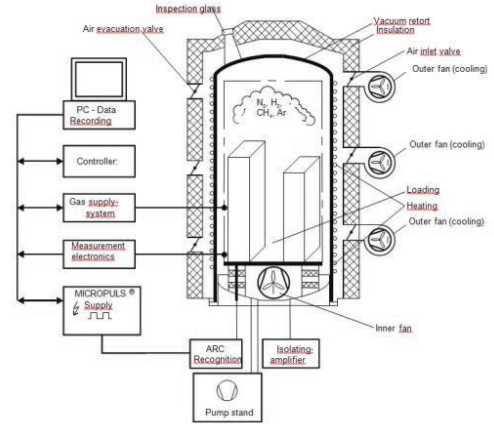


Fig. 7. GUI (graphic User Interface) and schematic set up of a state of the art plasma nitriding system [4]

Table 1. Overview of process choice criteria [4]

Major criteria for nitriding process choice			
Economical	Environmental	Related to alloy	Application/component
Equipment invest	Carbon footprint	Unalloyed steel	Surface quality
Infrastructure invest	CO/CO <sub>2</sub> /NO <sub>x</sub> exhaust gases	Low / medium alloyed steel Cr < 12%	Bulk vs. separated part load
Process costs: Energy costs Media costs Process duration	Integration of surface treatment in assembly lines	High alloyed steel Cr > 12%	Component geometry
Maintenance costs	Cleanliness of technology		Partial nitriding
Life cycle costs	Life cycle costs		Metallurgical specifications
Equipment availability			
Pre treatment – washing/ cleaning			
Partial nitriding			

Table 2. Differentiation matrix gas / plasma nitriding [4]

	GAS NITRIDING	PLASMA NITRIDING
Pores in the compound layer	High	Low
Distortion risk	Low	Very low
Partial nitriding	Expensive (with paint cover)	Very easy (with metal masks)
Temperature	> 480°C	Only economical limitation
Bulk material (see Fig. 8)	Yes	Impossible
Treatment of high-chromium steel (Cr > 12%)	Impossible (loss of corrosion resistance)	Possible (obtained corrosion resistance)
Treatment of sintered steel	Problematic	Possible
Environmental protection (see Fig. 9)	With limitation / Toxic gases used	Harmless / No limitation
Costs	Depending on industrial application advantages for both technologies	
Surface Activation	Only through prior process	Sputtering possible
Uniform layer thickness on the component even with complicated geometry	Possible	With limitation

done. The life cycle assessment was limited to the system operation period due to the fact that environmental impact of assembly and liquidation for both types are comparable (see Fig. 9). Starting with

the engineering and assembly, the main difference in the cost and environmental impact is visible in the period of the system operation till the final liquidation of it.



Fig. 8. Example of typical gas nitriding (left) and plasma nitriding load (middle, right) [4]

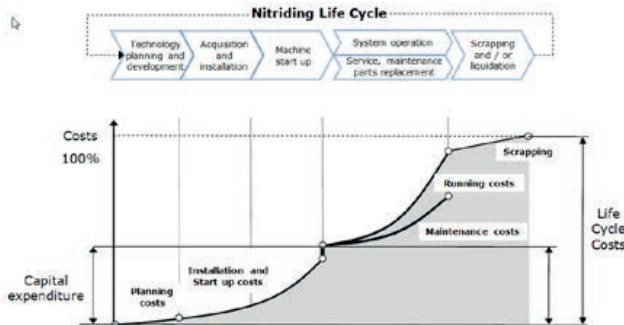


Fig. 9. Principle structure of life cycle analysis for nitriding equipment [3]

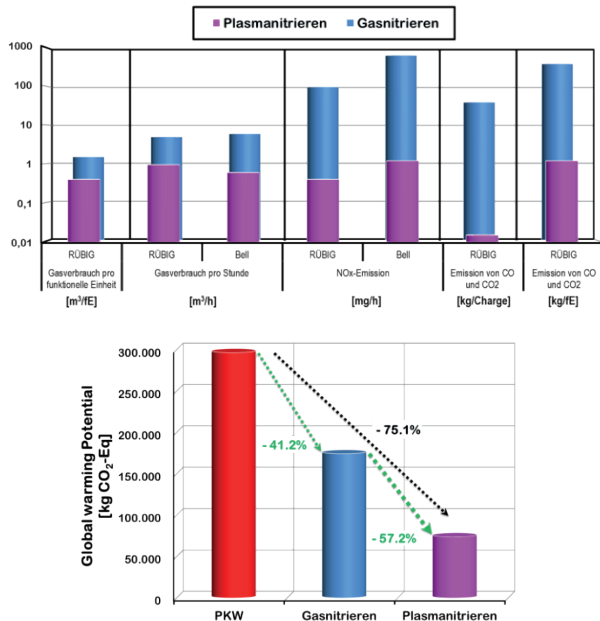


Fig. 10. Comparison results for environmental impact and global warming potential [3]

For the assessment two furnace installations with similar size and same load components and capacity were investigated. The systems were simulated in Umberto and assessed with the Cumulative Energy Demand CED.

The mayor difference of the compared technologies is the media consumption in regards of heating energy and process gases. For the plasma nitriding the total amount of process gases can be reduced by a factor  $>10$ . Furthermore, no post treatment of the waste gases has to be done. In Fig. 10 therefore the impact on the amount of greenhouse gases is obvious. Based on these data and

further comparison in literature (i.e. T. Bell) it could be shown, that the positive effect on environmental influence of low pressure nitriding processes compared to atmospheric nitriding processes (gas nitriding) is proven.

## SUMMARY

Gas and plasma nitriding processes have established themselves as independent processes in heat treatment. Both methods have their strengths and weaknesses. The application, technical specification is decisive, which nitriding technology is more suitable for the application. Nevertheless, based on an increased environmental pressure and the stricter environmental requirements low pressure applications as plasma nitriding are getting of higher importance. In relation to life cycle aspects further the low pressure plasma nitriding technology is more competitive.

Furthermore the recent R&D achievements on low pressure technology like plasma nitriding are leading to a high economical competitiveness of plasma nitriding, which gives an additional focus on these technologies in the future.

## REFERENCES

1. Practical Nitriding and Nitrocarburizing, ASM International.
2. Kölbl J. Die Nitridschichtbildung bei der Glimmentladung, Forschungsbericht des Landes NRW; Nr.155. Köln; Opladen; Westdeutscher Verlag; 1965.
3. Analysis and technology comparison of plasma and gas nitriding using Life Cycle Assessment: S. Leichtenmüller, C. Gallien. Montanuniversität Leoben.
4. RÜBIG GmbH & Co KG internal document.

# NITRIDED GEARS ENGINEERING: BENDING FATIGUE STRENGTH PREDICTION FROM PROCESS PARAMETERS

Simon Thibault<sup>1</sup>, Vincent Argoud<sup>1,2</sup>, Stéphane Gourdin<sup>1</sup>

<sup>1</sup> Safran Tech, M&P Dept. Magny-les-Hameaux, France

<sup>2</sup> LAMPA, Arts et Métiers ParisTech Angers. Angers, France

simon.thibault@safrangroup.com

Нет  
аннотации



**Keywords:** gear; nitriding; bending fatigue; hardness; residual stress.

## INTRODUCTION

When working temperature is too high for classical carburized steels, nitriding is an efficient alternative for gears case hardening. Obviously, the time necessary to achieve a given case depth is largely increased due to the low temperature at which it is performed. This is mainly true for high power transmission systems, which require high gear module and consequently high nitriding depth [1]. As a consequence, in an ideal co-engineering approach, both Stress and Process Engineer have to deal with two challenges. First, the Stress Engineer has to define local material requirements, which warrant reliability of the working gear. Secondly, as the final strengthening decreases when nitriding time increases [2, 3], the Process Engineer has to find an optimum solution complying with net nitriding depth (deep nitrided gears are generally grounded after nitriding [4]) and case mechanical properties. The aim of the present study is to propose a global model linking process parameters to fatigue resistance for a given loaded structure, especially for gear tooth bending fatigue. This can be achieved thanks to previous work of the authors [3] coupled with local fatigue criterion [5–9] based on mechanical parameters that have to be identified for the steel of interest.

## EXPERIMENTAL PROCEDURE

Rods were extracted from a 80 mm diameter E33CrMoV12 grade steel at normalized and annealed

state. Then, different heat treatments were applied, as detailed in the Table 1, to achieve different pre-nitriding states. The quenched and stress-relieved state is not a conventional pre-nitriding state, but allows achieving superior surface and core hardness. Near net shape notched specimens were extracted from the rods. Nitriding treatments were performed in an ALD industrial nitriding furnace. The atmosphere during nitriding was controlled by a H2SMART™ system (UPC). Regulation of the nitriding potential  $K_N$  was performed by adjusting ammoniac ( $\text{NH}_3$ ) and dissociated ammoniac ( $\text{N}_2 + \text{H}_2$ ) flow rates. Nitriding time was set to 120 hours, nitriding temperature was 520 °C or 550 °C and nitriding potential  $K_N$  was 3 atm<sup>-0.5</sup>. The seven final configurations are presented in Table 1.

After nitriding (or after heat treatment for un-nitrided specimens) notches were ground in order to reduce the diameter by 200 μm, to achieve the final geometry and remove the compound layer. The final specimen has a notch of 0.9 mm radius and a 5.9 mm effective diameter, leading to stress concentration factor,  $k_f$ , of 1.65. Microstructure in cross section was observed by optical microscopy after Nital and Murakami etching. Cross section hardness profiles were obtained with micro hardness testing machine using Vickers indenter. For each configuration, a simple coupon followed the manufacturing route in order to obtain the residual stress profile, very difficult to get in the notch, for which only a surface measurement was performed. Residual stress assessment was carried out by X-ray diffraction using Cr-K $\alpha$  radiation on the {211} diffracting plane of  $\alpha$ -Fe. Electro-chemi-

Table 1. Selected heat treatment and nitriding conditions

Configuration	Heat treatment conditions	Hardness before nitriding (HV0.2)	Nitriding condition (Temperature, °C / Time, hours / $K_N$ , atm <sup>-0.5</sup> )
665-0	Oil quenched and tempered at 665 °C during 2 hours	350	No nitriding
665-520			520 / 120 / 3
665-550			550 / 120 / 3
615-0	Oil quenched and tempered at 615 °C during 2 hours	400	No nitriding
615-520			520 / 120 / 3
615-550			550 / 120 / 3
180-520	Oil quenched and stress relieved at 180 °C during 2 hours	550	520 / 120 / 3

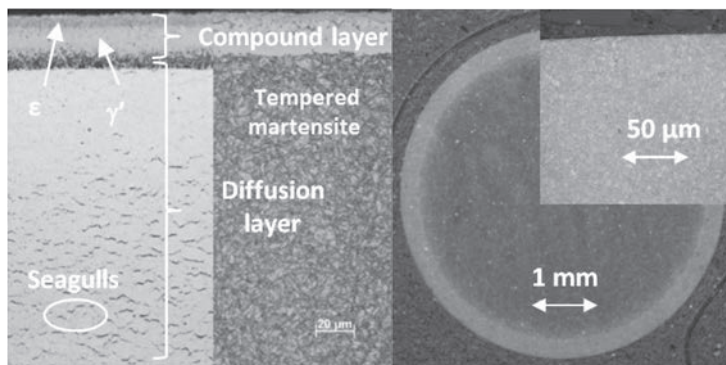


Fig. 2. Microstructure of as-nitrided coupon after Murakami (left side) and Nital (right side) etching, and residual nitrided case on fatigue specimen after grinding (right) revealed by Nital etching

cal surface layer removal was performed for in-depth profiling. Rotating bending fatigue tests (load ratio  $R_\sigma = -1$ ) were conducted at room temperature, at 50 Hz, and with a four-point loading configuration. Fatigue limit was estimated thanks to the stair-case method and Dixon-Mood data analysis. The tests ended at specimen failure or if the specimen did not fail after  $10^7$  load cycles. Fractographic examination of the failed specimen was performed using a scanning electron microscope.

Table 2. Summary of the experimental results

Configuration	NHD (after grinding)	Mean surface hardness	Mean core hardness	Surface residual stress	Normalized fatigue limit $\sigma_D$	Crack initiation location
665/0	–	295	–	–22*	0.39	Surface
615/0	–	389	–	–101*	0.52	
665/550	0.61	756	301	–257	0.95	
665/520	0.47	863	306	–249	0.99	
615/550	0.68	832	382	–164	0.96	
615/520	0.48	942	411	–199	1.00	
180/520	0.51	1006	486	–188	0.96	

\*Resulting from grinding.

## RESULTS

Microstructure (presented in Fig. 2 for the as nitrided coupon) is typical for nitrided martensitic steel and consists in a fine tempered martensite with some intergranular precipitates also called “seagulls”, under a  $\epsilon+\gamma'$  compound layer. Macrographic observations reveals the homogeneity of nitriding on the working section of the specimen, and confirms the removal of compound layer (see Fig. 2).

The main results of fatigue tests, associated to corresponding hardness and surface residual stress are summarized in the Table 2. The reported nitriding hardening depth  $NHD$  corresponds to the depth where hardness is 100 points over the core one. What will be called macroscopic fatigue limit,  $\sigma_D$ , corresponding to the first principal stress applied at the surface, is given for a 50% of failure probability, and is normalized for confidentiality reasons. All specimens presented evidence of surface crack initiation, so residual stress values are only reported for the surface. As expected, combination of prior heat treatment and nitriding conditions led to different

surface hardness values and fatigue limits. *NHD* is almost totally linked to nitriding conditions, and is not considered as an influent factor since crack initiated at surface in all cases.

**MODEL FORMULATION**

The results presented in Table 2 were used for the identification of a local fatigue criterion which assumes that failure occurs if local stress overpasses the local fatigue limit. In this approach, local stress includes residual stress and applied cyclic stress. Intrinsic local fatigue limit of the material is linked to the local metallurgy which can be roughly linked to the local hardness. For each configuration, knowing, at the crack initiation location, hardness, residual stress and cyclic applied stress, the fatigue limit corresponding to different hardness can be estimated using the classical multiaxial fatigue criterion of Crossland. Failure occurs if the criterion, defined as follows, is verified:

$$(1 - \alpha) \frac{\Delta J}{2} + \alpha I_{\max} = \beta, \tag{1}$$

where the left term is the Crossland equivalent stress.  $\frac{\Delta J}{2}$  is the alternated octahedral shear stress defined for a given material point by equations (2) and (3), where  $\sigma_{i\max}$  and  $\sigma_{imin}$  are the temporal maximum values of applied principal stresses during cyclic loading:

$$\frac{\Delta J}{2} = \sqrt{\frac{1}{2} [(\sigma_{a1} - \sigma_{a2})^2 + (\sigma_{a2} - \sigma_{a3})^2 + (\sigma_{a3} - \sigma_{a1})^2]} \tag{2}$$

$$\text{with } \sigma_{ai} = \frac{\sigma_{i\max} - \sigma_{imin}}{2}. \tag{3}$$

As residual stress is a mean stress, it does not modify the  $\Delta J/2$  value.  $I_{\max}$  is the maximum temporal value of the trace of the effective stress tensor  $\overline{\overline{\sigma_{eff}(t)}}$  for a given material point during the cycle defined by (4). Assuming the tensor of residual stress  $\overline{\overline{\sigma_R}}$  is equi-biaxial, and due to proportionality of the loading, then:

$$I_{\max} = \max_t (tr[\overline{\overline{\sigma_{eff}(t)}]}) = \max_t (tr[\overline{\overline{\sigma(t)} + \overline{\overline{\sigma_R}}]}) = tr \begin{bmatrix} \sigma_{1\max} + \sigma_R & 0 & 0 \\ 0 & \sigma_{2\max} + \sigma_R & 0 \\ 0 & 0 & \sigma_{3\max} \end{bmatrix} \tag{4}$$

where  $\overline{\overline{\sigma(t)}}$  is the stress tensor resulting from the applied cyclic loading, and  $\sigma_R$  is the residual stress estimated by XRD.  $\beta$  is the fatigue limit for a given cyclic loading (in the case of the formulation we use, it represents the traction-compression fatigue limit) and  $\alpha$  depicts the sensitivity of the material fatigue resistance to hydrostatic stress. It is assumed that  $\alpha$  is not affected by nitriding, so a previously identified  $\alpha$  value is used. As mentioned before, we assume that the fatigue limit  $\beta$  depends on hardness and rewrite it,  $\beta(HV)$ . Since crack initiation always appeared at surface ( $z = 0$ ) in our case, we can write:

$$(1 - \alpha) \frac{\Delta J(z=0)^*}{2} + \alpha I_{\max}(z=0)^* = \beta(HV(z=0)), \tag{5}$$

where terms with \* are calculated with the applied cyclic loading corresponding to the macroscopic fatigue limit  $\sigma_D$  (see Table 2). The cyclic applied stress tensor at crack initiation location (surface), for our specimen, was computed by finite elements analysis, and is given in equation (6):

$$\overline{\overline{\sigma_{\max}(z=0)}} = \begin{bmatrix} \sigma_D & 0 & 0 \\ 0 & 0.18\sigma_D & 0 \\ 0 & 0 & \approx 0 \end{bmatrix} = -\overline{\overline{\sigma_{\min}(z=0)}}. \tag{6}$$

In order to achieve the calibration of the criterion for the material,  $\beta$  is calculated from equation (5) for the seven configurations proposed in the Table 2. An empirical relationship is then established between  $\beta(z=0)$  and the surface hardness, as proposed in Fig. 3, in the 300 HV – 1000 HV range.

If depth hardness profile is known, this relation can be used to describe the evolution of local fatigue limit for a given nitrided case through its depth  $z$ , following the equation (7):

$$\beta(z) = a HV^2(z) + bHV(z) + c. \tag{7}$$

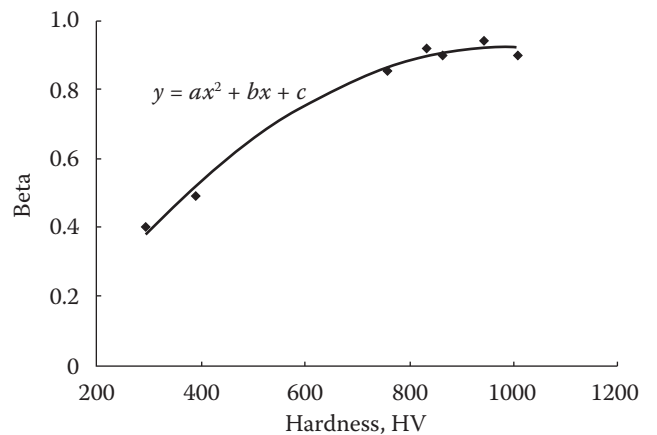


Fig. 3. Identified  $\beta$  values for the different configurations, and corresponding best fit between  $\beta(z=0)$  and surface hardness

For any cyclic loading and any nitriding condition, the initial fatigue criterion can be expressed with the equation (8), where the left term will be called “Crossland equivalent effective stress”:

$$(1-\alpha)\frac{\Delta J(z)}{2} + \alpha\left(\max_t(\overline{\overline{\sigma(t,z)}}) + 2\sigma_R(z)\right) = aHV^2(z) + bHV(z) + c \quad (8)$$

## APPLICATION OF THE LOCAL CRITERIA FOR PERFORMANCE OPTIMIZATION

Based on previous work [3] hardness and residual stress profiles can be predicted from nitriding process parameters, as presented in Fig. 4. Using equation (7) and the predicted hardness,  $\beta$  can be estimated. In addition, the residual stress prediction is giving the necessary information to calculate the Crossland equivalent effective stress for a given applied stress distribution.

This distribution was computed by elastic finite elements analysis, for three geometries of spur gear tooth, loaded at the highest point of single tooth contact (HPSTC, [1]). The through-depth evolutions of principal stresses were normalized by the maximum value of the first principal stress  $\sigma_1$ , which can be assimilated to the macroscopic stress (see Fig. 5).

Finally, we can find, for each configuration (nitriding parameters and geometry), the lowest macroscopic stress that verifies the local fatigue criterion, which is the macroscopic fatigue limit of the structure. All the following results are calculated for a load ratio  $R_\sigma = -1,2$  which is actually applied to a driving-driven tooth [1]. Depending on the applied stress distribution and nitriding profiles, the fatigue criterion can be verified (see Eq. 8) at the surface or in subsurface region, as presented in Fig. 6.

The “Crossland equivalent applied stress”, calculated without residual stress, is given for information. One can note that it is almost the same for both nitriding conditions, but failure occurs at the end of the nitrided case, and at lower local stress for the second configuration. A wide range of nitriding configurations (see Fig. 4) for the three geometries was computed. An example of the response surface for a given geometry is presented in Fig. 7, where the reported macroscopic fatigue limit  $\sigma_D$  corresponds to the maximal first principal applied stress at surface leading to failure,  $\sigma_D = \sigma_1^*(z=0)$ . The left part of the surface corresponds to what is referred to “under-nitrided” tooth, for which cracks initiate in sub-surface due to insufficient nitriding depth. The ridge of the surface corresponds to the optimum nitriding conditions where a transition is observed between sur-

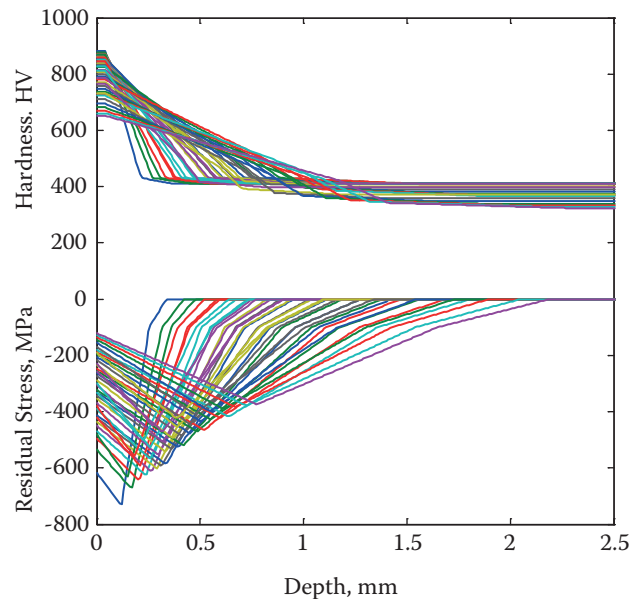


Fig. 4. Computed hardness and residual stress profiles for the range of 500–580 °C and 20–160 hours with 20 °C and 20 hours steps

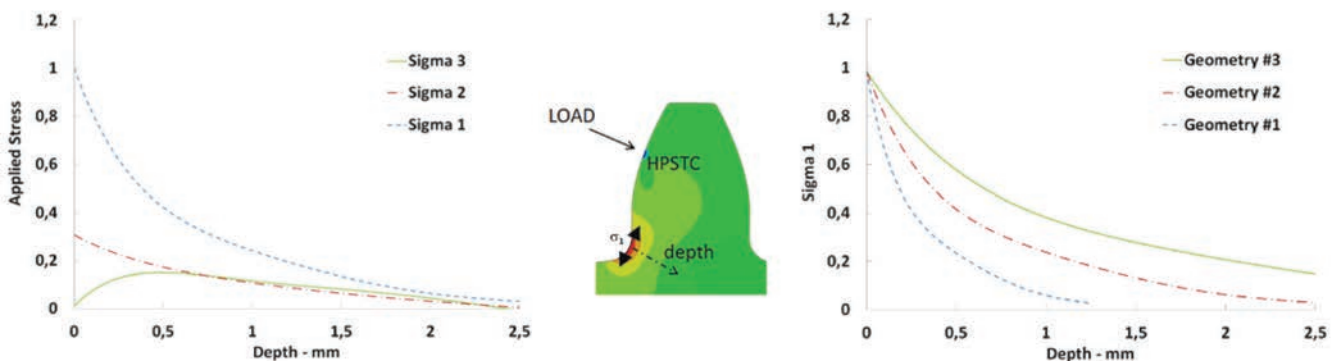


Fig. 5. Principals stresses evolution through the depth (left) in the critical section, when load is applied at HPSTC (center). Effect of the tooth size on the first principal stress distribution through the depth (right). The first and third geometries respectively correspond to the smaller and the bigger tooth

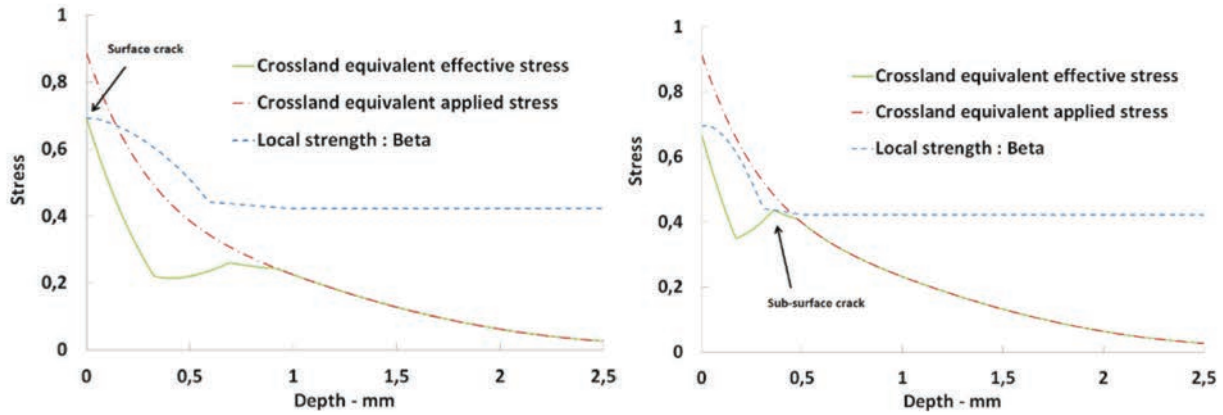


Fig. 6. Illustration of configurations (one configuration = nitriding + geometry + loading) where the local fatigue criterion is verified at surface (left) and in sub-surface (right)

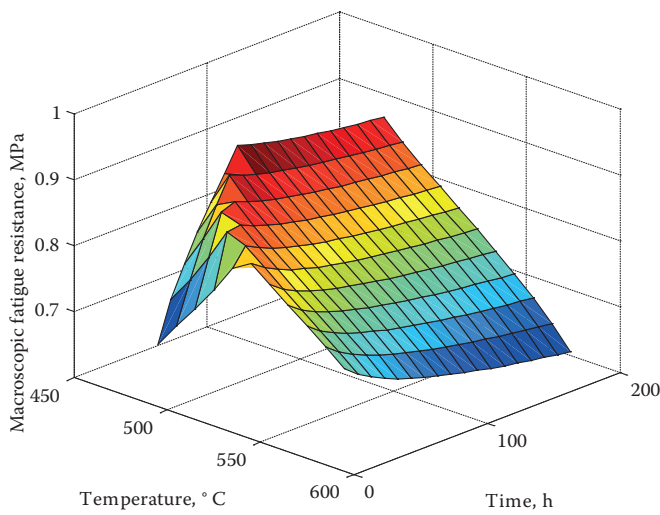


Fig. 7. Response surface of macroscopic fatigue resistance  $\sigma_D$  as a function of nitriding time and temperature

face and subsurface crack initiation. Overpassing this ridge is the “over-nitrided” region. Fatigue resistance decreases because of a drop in hardness and surface compressive residual stresses induced by nitriding time and temperature increase. This result is in accordance with literature [5, 10, 11]. These authors observed a transition between subsurface / surface crack initiation during fatigue tests performed on different geometries nitrided in the same conditions. This is quite the same phenomenon since they played on the stressed volume versus nitrided volume ratio.

The results of calculation for all nitriding conditions combined with the three geometries were regrouped in a single graph where the macroscopic fatigue resistance is reported as a function of the  $NHD/m$  ratio, where  $m$  is the normal module of the teeth, which represents roughly its size and has a big influence on the applied stress profile through the

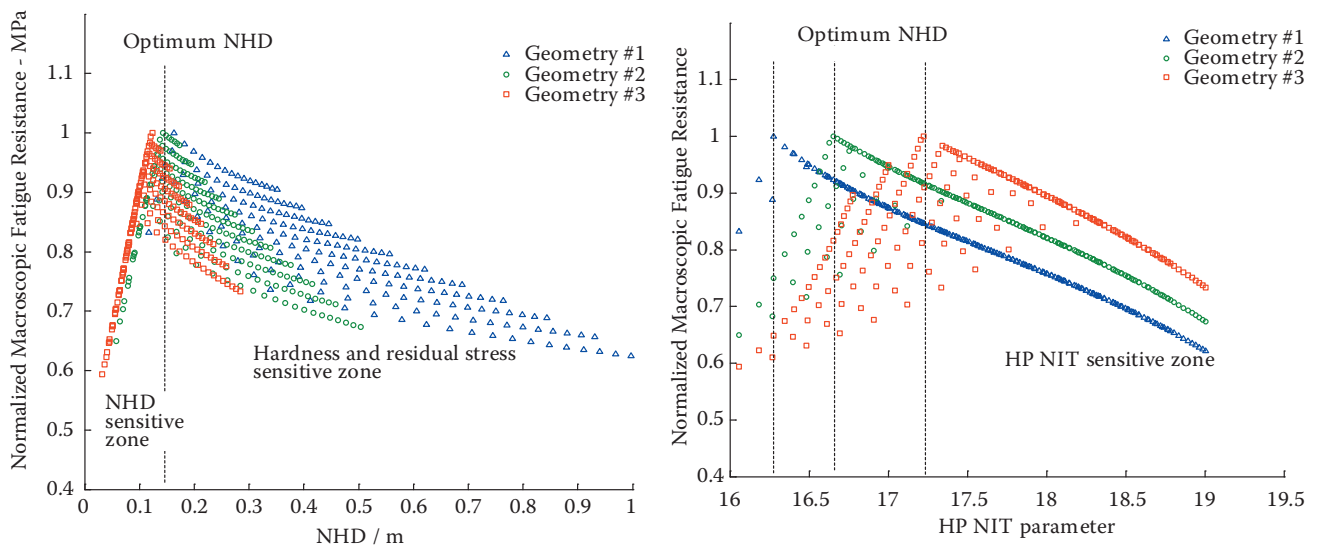


Fig. 8. Macroscopic fatigue limit as a function of  $NHD/m$  ratio for every tested configuration (left) and as a function of the nitriding parameter  $HP_{NIT}$  (right)

depth (see Fig. 5). We can clearly see the two regions mentioned before. In the under-nitrided region, we observe a strictly linear relation between fatigue resistance and  $NHD/m$ , doesn't matter the nitriding conditions to reach this  $NHD/m$  value. For all geometries, the optimum  $NHD$  seems to be  $0,15 m$ . This is in good correlation with reported results of fatigue tests performed on gear teeth [12]. In the over-nitrided region, fatigue resistance is not anymore dependent on  $NHD$  but rather on nitriding conditions and corresponding surface hardness and residual stress. As demonstrated in previous work [3], both surface hardness and residual stresses can be linked to the so called  $HP_{NIT}$  parameter based on the Hollomon Jaffe model.

$$HP_{NIT} = \frac{(T + 273.15)(20 + \log_{10}(t))}{1000} \quad (9)$$

Where  $T$  and  $t$  are respectively, nitriding temperature ( $^{\circ}C$ ) and time (hours). In this region, fatigue resistance is, thus, also driven by this parameter as shown in Fig. 8. Note that these results are only valid for the present mechanical configuration (bending of notched part).

## CONCLUSION

- Different initial metallurgical states allowed to reach different nitrided cases configurations
- An empirical relationship between hardness and fatigue resistance was established from fatigue tests on notched specimens, independent from residual stresses.
- Parameters of a local fatigue criterion were identified and used to predict fatigue resistance gear teeth of different geometries and for different nitriding conditions. These results are in good agreement with literature.
- Based on these predictions, the nitriding conditions maximizing the fatigue resistance is obtained for  $NHD$  is  $0,15$  time the normal module.
- If  $NHD$  is lower than this optimum value, bending fatigue is driven by  $NHD$  but if it is higher, fatigue resistance is driven by the  $HP_{NIT}$  parameter.

## ACKNOWLEDGEMENTS

The authors thank the French IRT-M2P Institute (Metz) for realizing nitriding treatments.

## REFERENCES

1. ISO 6336 3 & 5: Edition 2006/2003. Calculation of Load Capacity of Spur and Helical Gears.
2. **Spies H.J.** Case Structure and Properties of Nitrided Steels // Comprehensive Materials Processing. Elsevier. 2014. Vol. 12.
3. **Thibault S. et al.** A simple model for hardness and residual stress profiles prediction for low-alloy nitrided steel, based on nitriding-induced tempering effects // J. Heat Treatm. Mat. 73, 2018.
4. **Davis J.R.** Gear materials properties and manufacture // ASM International. 2005.
5. **Weil H. et al.** Optimization of gaseous nitriding of carbon iron-based alloy based on fatigue resistance modelling // Int. J. Fatigue. 2018. 110.
6. **Ghribi D. et al.** Comparative study of the tooth flank fracture in cylindrical gears, Efficient method to assess the risk of the tooth flank fracture on the cylindrical gears. CETIM, VDI Congress 2015.
7. **Hyde T.R. et al.** A methodology for modelling the effects of nitriding on fatigue life // Journal of Materials: Design and Applications. 2008.
8. **Genel K.** Estimation method for the fatigue limit of case hardened steels // Surface and Coating Technology. 2005.
9. **Hassani S.M. G. et al.** The effect of nitriding, severe shot peening and their combination on the fatigue behavior and micro-structure of a low-alloy steel // International Journal of Fatigue. 2014.
10. **Spies H.J.** Fatigue behaviour of nitrided steels // Steel Research. 1993.
11. **Limodin N. et al.** Fatigue strength improvement of a 4140 steel by gas nitriding: Influence of notch severity // Material Science and Engineering A. 2006.
12. **Tobie T. et al.** Optimizing Gear Performance by Alloy Modification of Carburizing Steels // Metals. 2017. 7, 415.

# RESEARCH FOR HEAT TREATMENT SIMULATION ON HYPER CARBURIZING PROCESS CONSIDERING WITH SEGMENTATION OF ALLOY ELEMENTS

Tsuyoshi Sugimoto<sup>1a</sup>, Dong-Ying Ju<sup>2b</sup>

<sup>1</sup>Nissan Motor Co., Ltd, Saitama Institute of Technology, Japan

<sup>2</sup>Saitama Institute of Technology, Japan

<sup>a</sup> tsuyoshi-sugimoto@mail.nissan.co.jp, <sup>b</sup> dyju@sit.ac.jp

Now on the day, the progress of electric vehicle, there is an increasing demand for smaller and lighter drivetrain gears for automobiles. To reduce the size and weight of the gears, pitting fatigue failure due to the rise in the operating temperature of the tooth surface becomes a problem. Therefore, hyper carburizing or carbonitriding shall be used the measure of these problems. The spread of low pressure carburizing furnaces capable of treating hyper carburizing with low cost is expanding the utilization of hyper carburizing. However, in hyper carburizing, the change in hardenability of the materials occurs due to the segregation of alloying elements during precipitation of cementite carbide, and the hardness of the parts differ from those of ordinary carburizing. In this research, we clarified the segregation behaviour of Cr, which are alloy elements, during the precipitation of carbides. The heat treatment simulation in consideration of this is investigated the prediction method of heat treatment quality in actual parts. It was found that Cr had different segregation states depending on the formation mechanism of precipitation. Using these, we realize the heat treatment simulation for steel products that could ensure sufficient quality overall with gear-shaped parts and improve heat treatment quality.

**Keywords:** hyper carburizing; precipitation; heat treatment simulation; segmentation.

## INTRODUCTION

To increase the strength of gear parts for automobiles, improvement of hardness, durability against decrease in hardness during use, and improvement in tempering softening resistance become issues [1]. To avoid such phenomena, techniques such as carbonitriding or hyper carburizing are often used. However, conventionally, in case of hyper carburizing, there is a problem that the treatment time is several times as long as the ordinary carburizing method. In the case of carbonitriding, a separate nitrogen supply device is required, which is expensive.

Since the low pressure carburizing method has become popular in recent years and it has become easy to introduce high contents carbon exceeding the cementite solubility limit on the part surface, it becomes possible to shorten the process time drastically with hyper carburizing [2]. However, since low pressure carburizing has large shape dependence [3], there is a characteristic that the carbon concentration is heavy in the edge part than the flat part or the concave part. This shape dependency becomes a problem of this method.

In this research, we tried quality prediction by simulation of low pressure hyper carburizing, with

considering shape dependencies. We tried to predict the carbon content distribution, precipitate amount, coast cementite precipitation, chemical segmentation and hardness.

## EXPERIMENTAL PROCEDURE

To compare experimental and simulation results, gear-shaped samples shown in Fig. 1 of JIS SCM20H shown in Table 1 were subjected to hyper carburizing under the conditions shown in Fig. 2. The first half before intermediate cooling is called primary carburizing, and the subsequent part is called secondary precipitation process.

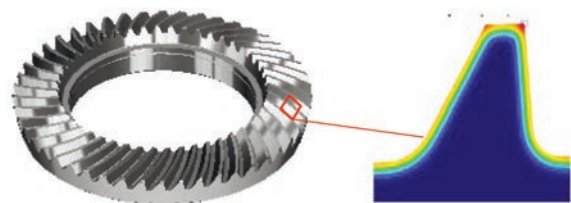


Fig. 1. Gear shape used in this research and calculated tooth section

Table 1. Gear specification used in this research

SPECIFICATION	
GEAR TYPE	HYPOID GEAR
MODULE	3.12
TARGET ECD	0.9mm @ pitch point
MATERIAL	JIS SCM420H

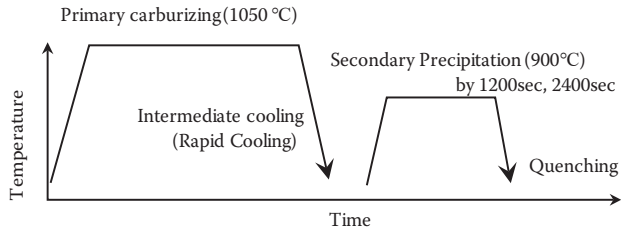


Fig. 2. Heat treatment condition discussing in this reserach

As for the carburizing condition is shown in Fig. 2, the primary carburizing condition was set to 1.5Cwt% on flat part which does not become hyper eutectoid at the carburizing temperature on 1050 °C. The hardness was measured after secondary precipitation. Likewise, the amount of precipitates was specified after secondary precipitation process, and how precipitation progresses during carburization and secondary precipitation was specified.

## SIMULATION PROCEDURE

The carburizing, precipitation and hardness is calculated by heat treatment simulation.

The precipitation model in response to the above experiment and the formulated equation up to the primary carburizing and the second precipitation was examined. On the primary carburizing process, the surface reaction of carburizing was determined according carburizing occurred with cementite and graphite as intermediate products [4]. The cementaite on primary and secondary treat will remaind and it became coast and fine cementite. It was assumed that cementite precipitation increased from existing precipitation nuclei as a starting point and particle size increased with diffusion rate growth formulation.

In addition to the calculation of precipitation hardness was predicted. Hardness predicted separately for matrix phase and cementite phase, and predicted total hardness by taking weighted sum of these. The hardness of the matrix phase was examined from the sum of each phase (martensite, bainite, ferrite and pearite) and cooling calculation on quenching with carbon concentration value taken

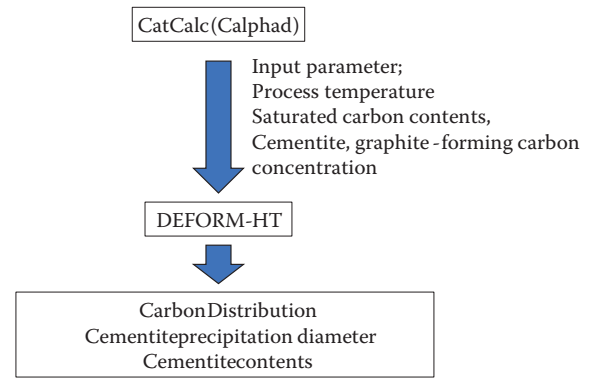


Fig. 3. Schematic of hyper carburizing simulation

into consideration with Jominy values change with Cr segmentation [5]. The hardness of cementite was assumed to be constant. It is assumed that the overall hardness rises as the increase of cementite effected by increasing in cementite grain size.

The actual calculation was carried out by the method shown in Fig. 3. The cementite-graphite precipitation contents at treating temperature for treatment temperature was calculated by using Cat Calc. Using these results, carbon diffusion at primary carburization was calculated by SFTC DEFORM-HT<sup>®</sup> and carbon contents distribution after primary carburizing was obtained. The difference between the carburizing after the primary carburization and the cementite equilibrium carbon contents at the secondary precipitation temperature was determined and used as the driving force for the diffusion rate growth during the secondary precipitation. The coast cementite precipitation is calculated with exceeded than cementite solute contents after first precipitation calculation.

For grain growth during secondary precipitation, calculations were performed with DEFORM-HT<sup>®</sup> using a user function incorporating diffusion rate growth. After secondary diffusion, precipitation size is estimated. Quenching analysis was carried out to determine the hardness distribution of the matrix phase considering with Cr segmentation around cementite precipitations. The effect of Cr segmentation is considered with the change of Jominy value with FIELD method. By obtaining this weighted sum of cementite hardness distribution and cementite amount, the hardness distribution after high concentration carburization was obtained.

## RESULTS

### Verification on primary carburizing

Fig. 4 shows changes in carburizing temperature, cementite precipitated carbon concentration

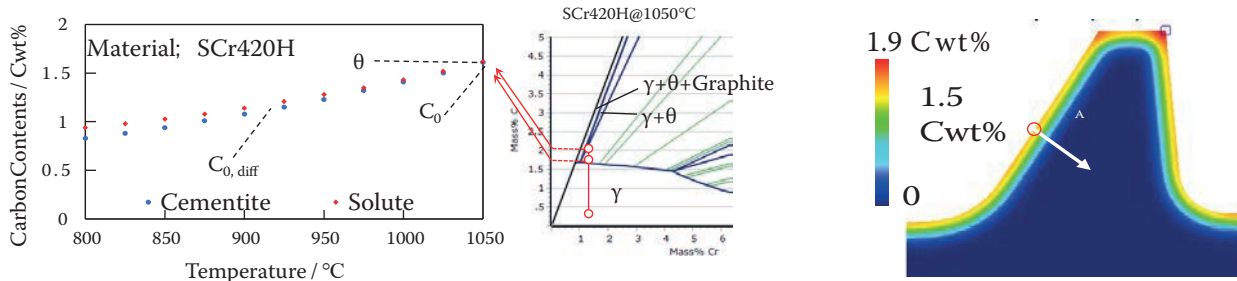


Fig. 4. Soluble contents calculated by calphad method

(a) Carbon distribution

and solid solution carbon contents. As the treatment temperature rises, it can be seen that the solid soluble carbon contents is rising. In vacuum carburizing, the pulse carburizing method is often used in many cases. In this case, it was assumed that carbon flowing in cementite equilibrium occurred at the surface of the pulsed carburizing gas, and surface reaction did not occur at the time of pulse when purge gas was flowing. Carbon diffusion inside the part was calculated according to Fick's second law as shown in (1). The diffusion multiplier was in accordance with Well et al. 1950 [6].

$$D(C, T) = \exp(18.5 - 1.5C + \frac{546C^2 + 2361C - 19410}{T}) \quad (1)$$

$C_0$ ; Surface carbon contents,  $C$ ; carbon contents,  $T$ ; Temperature.

The calculated and comparable experimental carbon contents is shown in Fig. 5 a, b. The carbon contents distribution in the flat part was in good agreement with experiment and analysis. In addition, excessive carburization phenomenon at the edge portion, which is a problem for gear parts, was well reproduced as shown in Fig. 6.

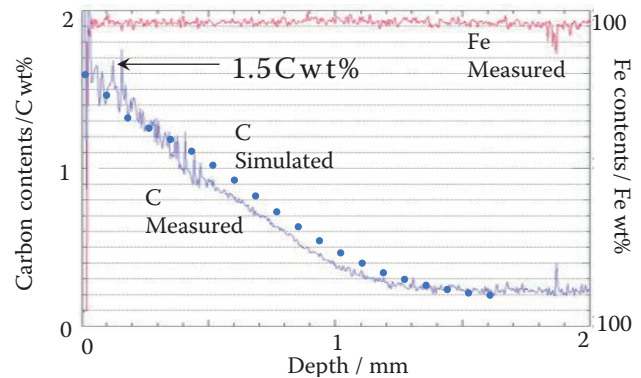


Fig. 5. Carbon contents distribution after primary carburizing

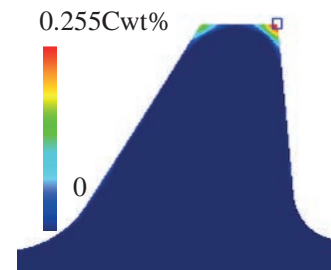


Fig. 6. Coast cementite distribution with exceeded carbon contents

### Verification on secondary precipitation

It was assumed that precipitation during secondary diffusion follows diffusion rate growth [6, 7]. Diffusivity growth is a precipitation mode assuming that particles precipitate according to the formula shown in (2), and it is a precipitation mode assuming that the elements migrate and precipitate from the surrounding area where precipitation nuclei already exist. This  $K$  is estimated by fitting calculation as  $K = 3.6 \times 10^{-3}$ . This precipitation calculation has good correlation with experimental values[8] as shown in Fig. 7.

$$r = K(Dt)^{0.5} \quad (2)$$

$r$ ; Precipitation diameter ( $\mu\text{m}$ ),  $D$ ; Precipitation driving force ( $C \text{ wt}\%$ ),  $t$ ; Secondary diffusion time (s),  $K$ ; constant depend on each condition.

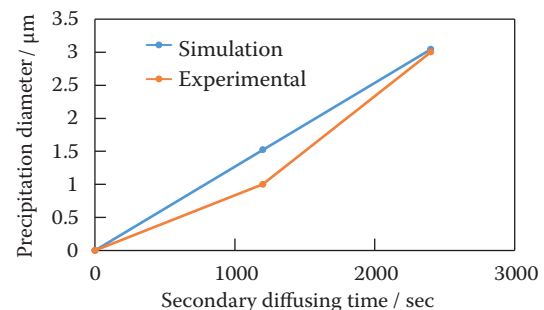


Fig. 7. Comparing of cementite precipitation growth

### Verification on Cr segmentation

The absorption measurement results of Cr to cementite after primary carburizing are shown on the right of Fig. 8a. In the cementite, there is very high

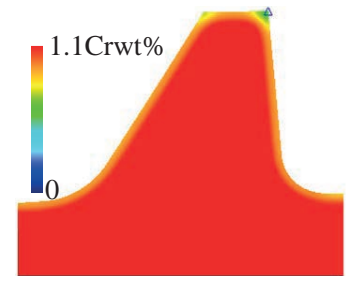
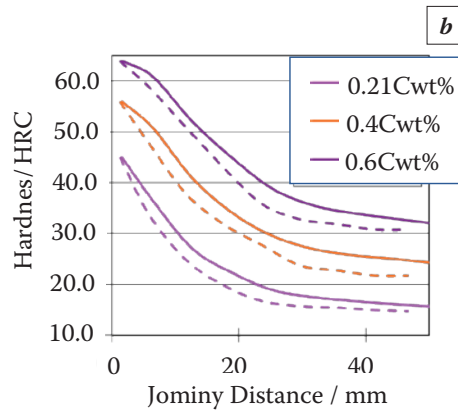
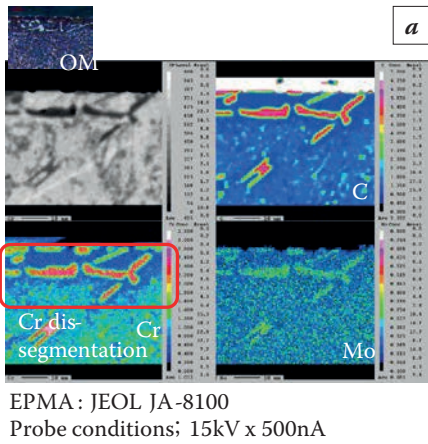


Fig. 9. Cr contents in matrix after primary carburizing

Fig. 8. Cr absorption and Jominy value change: a – Segmentation detail by EPMA; b – Jominy value change with Cr segmentation

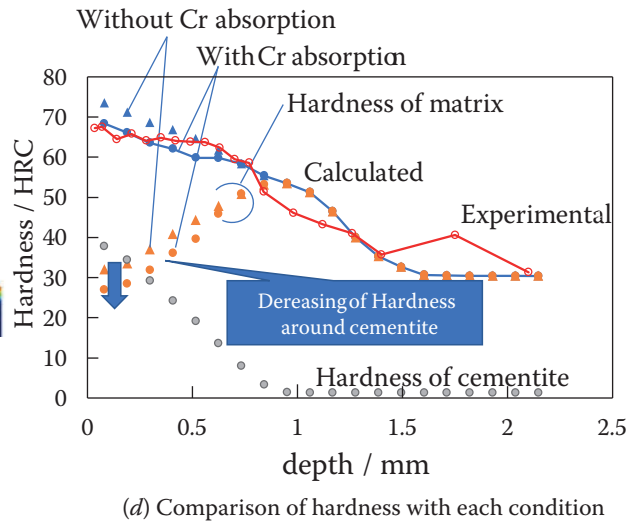
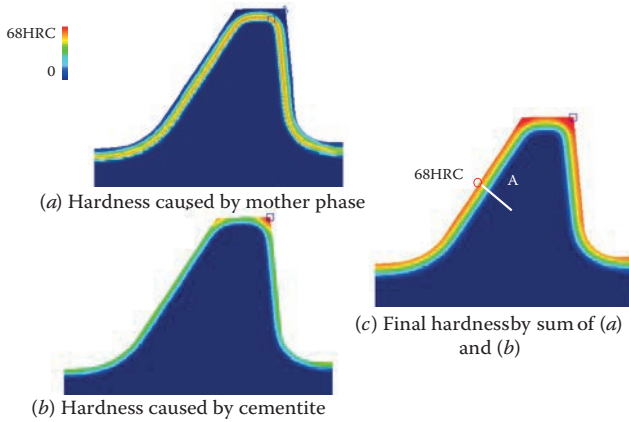


Fig. 10. Hardness calculation result

Cr contents. Then, there is largely Cr decreasing is occurred around cementite precipitations. This is occurring in a wide range around precipitations.

The change of the Jominy value by the decreasing of Cr calculated by the FIELD method is shown in Fig. 8b. The Cr absorption distribution is calculated with coast cementite distribution in proportionally.

### Hardness distribution after secondary precipitation

Fig. 9 shows the state of the hardness distribution after hyper carburizing. Fig. 10a is the hardness distribution caused by matrix phase hardening. Fig. 10b is the hardness distribution caused by cementite precipitation. The total hardness is calculated by the sum of hardness of cementite and matrix phase. The hardness distribution roughly agrees with the experimental value and the calculated value as shown in Fig. 10c, and the hardness of the hyper carburizing

can be predicted in advance by this case. The effect of Cr absorption is calculated with modified Jominy curve shown as Fig. 8 is shown in Fig. 10d. The experimental and calculated hardness has good correlation. To consider Cr absorption, the hardness accuracy on the surface of parts is increased.

### CONCLUSION

To investigate the conditions for applying low pressure hyper carburizing to the actual part shape, the quality simulation method was performed. Carbon content distribution analysis considering with the dependence of the actual part shape can be carried out by conducting the carbon diffusion analysis incorporating the precipitation condition using the CALPHAD method together. We succeeded in macroscopically predicting precipitation particle size and hardness by conducting a secondary precipitation analysis using the carbon amount exceeding

the eutectoid carbon concentration similarly determined by the CALPHAD method as the precipitating dynamics. Coast cementite precipitation and its segmentation of Cr is considered in these calculations.

## REFERENCES

1. **Abe S., Ikeda S.** High Pitting Fatigue Strength Steels based on Super-carburizing // KOBE STEEL ENGINEERING REPORTS. 2004. Vol. 54, No. 3. P. 21–24.
2. **Todo S., Imataka H., Sueno H.** // Japan Steel Engineering report. 406 (2016). 13–18.
3. **Jones K.D., Krauss G.** // Heat Treat. 79 (1980). 188.
4. **Morita T., Hanyuda T.** Tetsu-to-Hagane. 2006. Vol. 92, No. 4. P. 36–41.
5. **Field J.** // Met. Prog. 43(1943), 3. 402.
6. **Wells C., Batz W., Mehl R.F.** // Trans. AIME. 1950. Vol. 188. P. 553.
7. **Klein S., Mujica L., Walter M., Weber S., Theisen W.** // J Mater Sci. 2017. Vol. 52. P. 375–390.
8. **Tanaka K., Ikehata H., Takamiya H., Mizuno H.** Calculation of Microstructure in Vacuum-carburizing Incorporating Kinetics Modeling of Grain-Boundary Cementite // Tetsu-to-Hagané. 2011. Vol. 97. P. 3, 32–37.
9. **Sugimoto T., Ju D.Y.** // Journal of Mechanics Engineering and Automation. 1 (2019). 33–39.

## FEATURES OF BORONIZED LAYERS FORMATION ON PRE-CARBURIZED STEELS

M.S. Tsikh<sup>1</sup>, A.A. Krasulya<sup>1</sup>, A.A. Mironova<sup>2</sup>, A.D. Metlyakov<sup>2</sup>

<sup>1</sup> Bauman Moscow State Technical University. Moscow, Russia

<sup>2</sup> Perm State University. Perm, Russia

M.99@mail.ru

The types of surface failure in condition of abrasive media are analyzed. The technological modes of surface treatment providing multi-zone structures with the ability to control the phase composition, depth and hardness of each zone are developed.

**Keywords:** carburizing; boronizing; bainite; iron boride.

### INTRODUCTION

Effective performance of any wear-resistant coating mostly depends on the type of wear. The traditional diffusion methods of surface strengthening (carburizing, nitriding, etc.) are very effective in metal-to-metal friction where fatigue wear, seizure wear and fretting occur. At the same time, they are ineffective with abrasive wear. Among the diffusion strengthening methods, only boronizing processes can improve wear resistance in abrasive media since the hardness of a boride layer is significantly higher than the hardness of many abrasive materials.

However, boride layers are far less resistant to impact abrasive wear due to their tendency to brittle spalling. This process is significantly developed in the presence of plastic deformation of the zones adjacent to the boride layer. In this case, initially the growth of microcracks in the boride layer and their transformation into macrocracks occurs, and then detachment of individual sections of the boronized layer from the matrix takes place.

Boronizing of high-strength steels followed by quenching is one of the solutions to this problem. The main danger in the implementation of such a treatment is the increased risks of quenching cracks formation in the boride layer and unacceptably high values of the parts distortion. In this regard, the main objective of this work is the development of a surface strengthening technology that allows obtaining rational compositional structures in order to provide

the ultimate performance of the surface under abrasive wear conditions.

The following aspects of the problem are resolved in this study:

- the types of surface failure in condition of abrasive media are analyzed;
- quantitative criteria are developed for assessing the quality of the strengthened layer for abrasive wear conditions;
- technological modes of surface treatment, providing multi-zone structures with the ability to control the phase composition, depth and hardness of each zone are developed.

### Materials and research methods

Medium-carbon steel 30XГСА (30CrMnSi), widely used in mechanical engineering for the manufacture of the parts with different types of treatment (carburizing, nitriding), was chosen as the material for research.

The study of the samples' microstructure and the chemical composition of the phases was carried out on a JSM-6060A scanning electron microscope (Jeol, Japan) equipped with a JED-2300 energy dispersion spectrometer (Jeol, Japan) and on a Neophot 30 optical microscope.

X-ray diffraction phase analysis was carried out on a DRON-3M general-purpose diffractometer (CuK $\alpha$  radiation, with a monochromator). Registration and processing of the data were performed using

the software package “GLRDIF”. The measurement of the surface layers and the core hardness was carried out on a “DuraScan 20” microhardness tester with a load of 100 g.

The intensity of abrasive wear is substantially determined by the ratio of the hardness of a wearable material  $H_M$  and of an abrasive  $H_A$ . If the ratio of  $H_A/H_M$  is less than 1 then so-called elastic edging of the material by the abrasive particle takes place [1]. In this case, the wear proceeds rather slowly and the destruction of the surface is of fatigue nature [2].

If the ratio of  $H_A/H_M$  is slightly higher than 1 then the abrasive particles embed into the material to a small depth while plastic edging of the material occurs, i.e. a dented scratch remains on the material but without formation of the chips. In this case, the wear proceeds almost an order of magnitude faster than during fatigue wear [3].

When the ratio  $H_A/H_M$  reaches a value of 1.3...2.2 (known as “critical hardness of an abrasive”) the ratio of penetration depth of an abrasive particle into the metal to the rounded radius of the particle reaches a certain critical value at which scratching is accompanied by the separation of wear products in the form of chips. Plastic edging turns into microcutting [1]. This process leads to unacceptably rapid destruction of the material surface (almost two orders of magnitude faster than during fatigue wear) [3].

Among the most common natural abrasives, quartz has the greatest wear effect on the working surfaces of machine parts and tools. Its hardness varies from 950 to 1220 HV [4].

On this basis, high wear resistance of a wearing part can be provided by the hardness of the surface layer above 1220 HV (72 HRC), reasonable wear resistance – by a hardness not lower than 1220 /1.3 = 940 HV (68 HRC). For this reason, the most common methods of surface strengthening (carburizing, nitrocarburizing, nitriding) are ineffective for abrasive wear, since they can hardly provide hardness of even 940 HV.

Under abrasive wear conditions, such a method of surface strengthening as boronizing is effective enough. It provides hardness from 1320...1800 HV for single-phase ( $Fe_2B$ ) layers and to 1800...2200 HV for two-phase ( $Fe_2B + FeB$ ) layers [5].

However, the described types of surface failure refer to a particular case of abrasive wear: the abrasive particles interact with the metal without impacts (friction either in the abrasive or in the flow of abrasive particles in liquid or gas at low impinging angles). But under the conditions of actual products operation in the presence of impact loads (in particular, gas and water abrasive wear), the boride layers have

increased wear despite their high hardness. It should be noted that with gas or water abrasive wear, the rate and intensity of wear are greatly influenced by the kinetic energy of abrasive particles and their impinging angle to the surface of metals. In many cases, the parts operation under the conditions of abrasive, gas and water abrasive wear requires a certain margin of viscosity and plasticity of the core, which is provided with a hardness of 30...45 HRC. But the optimal combination of mechanical properties usually takes place in the range of 38...43 HRC (370...420 HV) [7]. As practice shows, this value of hardness is insufficient to prevent plastic deformation of the metal base and, as a consequence, spalling of boride coatings.

The indentation and spalling of the boride layer during the operation can be prevented by:

- creation of a solid layer under the boride layer;
- increase the ductility of the boride layer;
- creation of the compression stresses in the boride layer which prevent the growth of microcracks [6].

The presence of the solid underlayer is a prerequisite for the boride layer effective operation under the conditions of elastic deformation and a fatigue-type wear. The most important requirement for this underlayer is not its high hardness, but maximum values of the fatigue limits and elasticity of compression.

These parameters reach their maximum with a hardness of 58–60 HRC (650–700 HV) for most steel grades. However, not every treatment mode leads automatically to the achievement of this hardness. Both the depth of the solid underlayer and carbon content and distribution, as well as the underlayer’s microstructure play an important role in the process: for example, the carbon content of 0.6...0.7% is optimal for martensitic microstructure, 0.8...1.0% – for bainitic microstructure and 0.7...0.8% – for a mixture of martensite with secondary bainite.

The level of compressive stresses in the boride layer depends on the composition and microstructure of both the solid underlayer and the metal base. Therefore, the optimization of this parameter is provided by an expedient choice of carburizing and subsequent heat treatment modes.

The fracture patterns analysis in various types of abrasive wear enables to describe the requirements for the base material and the strengthened layer in order to provide maximum wear resistance of the parts surface. The base material must have a hardness of 30...45 HRC after the heat treatment and provide a certain margin of viscosity and plasticity.

The surface hardness must be higher than 1220 HV (the hardness of the main abrasive particles). The

strengthened layer should have a sufficient depth and an absence of cracks. To prevent spalling of the strengthened layer, especially when exposed to impact loads of the abrasive on the metal surface, the zones directly located under the boride layer should provide maximum values of fatigue limit and elasticity of compression. These parameters reach their maximum with a hardness of 58–60 HRC (650–700 HV) for most steel grades.

Based on the theory of “Surface engineering of parts by chemical heat treatment methods” [7] consisting in the ability to design composite multi-zone structures of the surface layer with the opportunity to control its phase composition, structure, depth and hardness, we proposed a two-stage technology ‘Carbo-bor’. The essence of this technology is the sequential saturation of the steel surface, first with carbon and then with boron, followed by volume heat treatment.

Carburizing was carried out in an automated unit of the company “Uttis” according to the following mode:  $t = 930^{\circ}\text{C}$ , exposure 15 hours, the carbon potential of the furnace atmosphere  $\sim 0.8\text{--}0.9\%$ . This mode of carburizing provides a carburized layer  $\sim 1.4\text{--}1.6\text{ mm}$  of depth with a carbon content in the surface layer  $\sim 0.8\%$ . This carbon content was chosen to prevent the presence of ferrite in the carburized

layer because ferrite can contribute to the process of plastic deformation in the carburized layer. This carbon content was also chosen to reduce an amount of carbides because they lead to brittle spalling.

The boronizing was carried out on the equipment of our own production at a temperature of  $800^{\circ}\text{C}$  for 3 hours. To carry out the process we developed salt melts based on sodium tetraborate with the addition of amorphous boron in an amount of up to 5%.

The exposure in the boronizing melt was immediately followed by the quenching in the oil heated up to  $100^{\circ}\text{C}$ . The tempering was carried out at  $200^{\circ}\text{C}$  for 2 hours.

As a result of treatment of 30XTCА steel with the ‘Carbo-bor’ technology, the composite structure of the surface layer is formed (Fig. 1) consisting of several zones.

The surface zone (Fig. 1a) about 70 microns of depth with a hardness of  $1900\text{ HV}_{0.1}$  (Fig. 1c) consists of borides  $\text{FeB}$  and  $\text{Fe}_2\text{B}$ , according to X-ray structural analysis (Fig. 2) data. A two-phase acicular structure of borides is observed by means of electron microscopic analysis (Fig. 1b).

No cracks are found in the surface layer. There is a martensitic zone of the carbonized layer with a depth of up to 1.5 mm (Fig. 1a) and with a hardness of up to  $600\text{ HV}_{0.1}$  under the boride layer. The core structure corresponds to the sorbitol-bainite mixture with a hardness of 35–40 HRC.

Thus, the developed ‘Carbo-Bor’ technology allows to obtain the strengthened layers corresponding to quantitative criteria for assessing the quality of the composite layer.

A distinguishing feature of ‘Carbo-bor’ technology is the ability to control the structure, phase composition, depth and hardness of the strengthened layer. It is known [6] that single-phase boride layers have a much greater reserve of plasticity than two-phase ones. Two-phase layers ( $\text{FeB} + \text{Fe}_2\text{B}$ ) begin to peel off during plastic deformation of 1.5–3%, and single-phase ( $\text{Fe}_2\text{B}$ ) – during 3.0–4.5%. How-

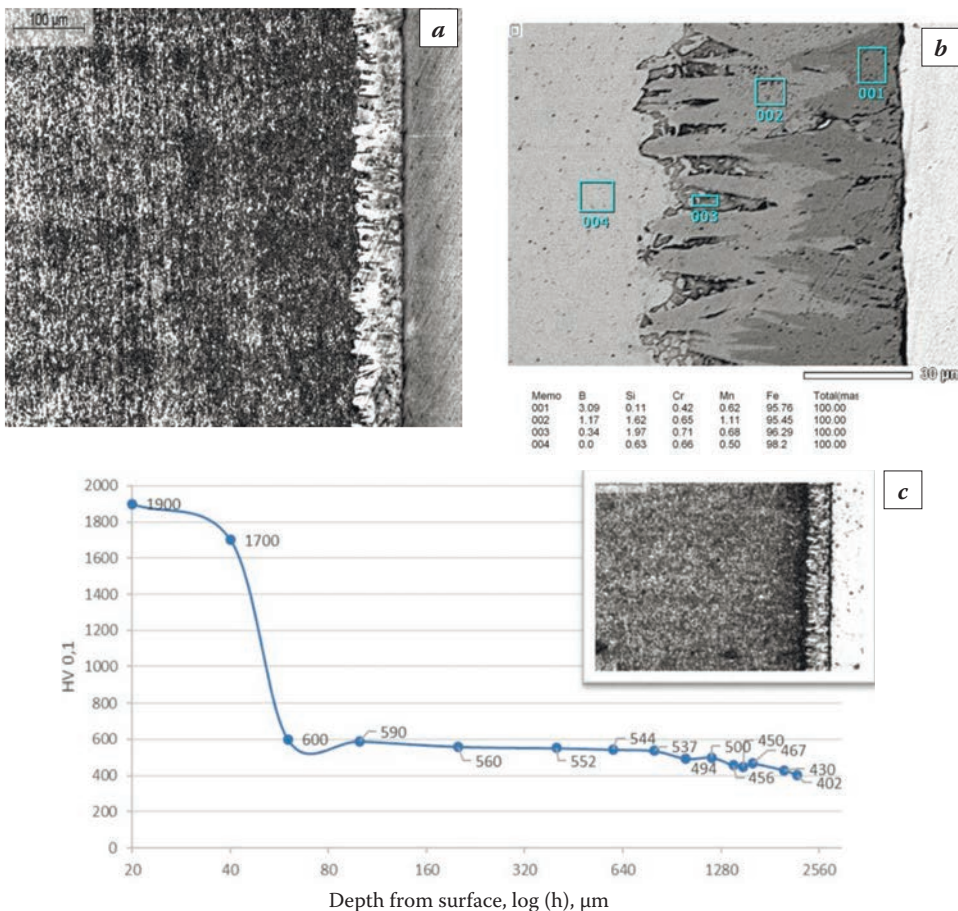


Fig. 1. Structure of steel 30CrMnSi (a, b) and the distribution of microhardness (c) in the depth of the strengthened layer after ‘Carbo-bor’ technology treatment

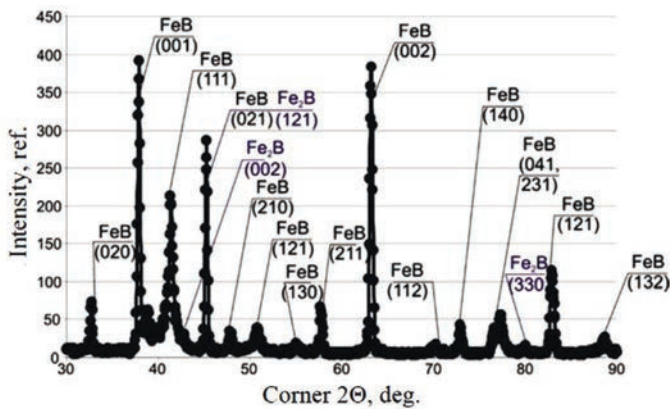


Fig. 2. X-ray diffraction pattern of the surface of steel 30CrMnSi after the 'Carbo-bor' technology treatment

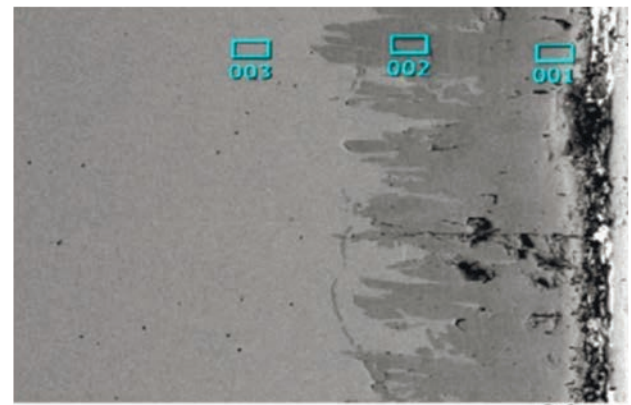
ever, the maximum values of hardness and wear resistance of the boride layer are achieved namely with a two-phase structure of the strengthened layer. The high-temperature boronizing modes with isothermal heating exposure (700 °C) were developed which allow to form a large number of centers of  $Fe_2B$  phase and to control the degree of acicularity and density of the layer at the initial stage of the process. As a result of the treatment, the boronized layer is composed as a two-phase structure corresponding to the Charpy principle: the FeB phase is formed not as a continuous zone, but as isolated needle inclusions in the  $Fe_2B$  phase layer. Such a structure of a boronized layer significantly increases its plasticity, and the presence of inclusions of the FeB phase should provide almost the ultimate characteristics of surface wear resistance in abrasive media.

The compositions and modes of boronizing in melts depleted in active boron to a concentration of 8,5–10%, insufficient for the formation of a continuous layer of the FeB phase (Fig. 3) are also tested during the study. A similar structure of the boride layer is obtained when the parts are transferred, at the final stage, from the active bath to the neutral (chloride-potassium) bath, where diffusion resorption of the FeB borides occurs.

Thus, the correct choice of methods and technological modes of carburizing and boronizing allows to cover a wide range of operating conditions for parts and tools, including the conditions of abrasive and water-abrasive wear.

## CONCLUSIONS

In order to provide high abrasive wear resistance, it is necessary that the wear is of fatigue nature. This condition is satisfied if the hardness of the abrasive  $H_A$  is lower than the hardness of the wearing surface  $H_M$ .



Memo	B	Cr	Fe	Total(mass%)
001	16.01	1.35	82.64	100.00
002	10.56	1.62	87.82	100.00
003	0.00	1.55	98.45	100.00

Fig. 3. The structure of the boride layer after the treatment in molten salt depleted in active boron

The quantitative criteria are developed for assessing the quality of the strengthened layer for abrasive wear conditions: the base hardness is 35–45 HRC, the surface hardness is above 1220 HV, the hardness of the underlayer is 58–60 HRC. The presence of cracks is unacceptable.

The 'Carbo-bor' technology has been developed which allows to obtain two-phase and single-phase boride layers with an increased margin of plasticity. The presence of the carburized underlayer provides the fatigue type of the surface abrasive wear and results in the ultimate hardness and wear resistance characteristics of the strengthened layer.

## REFERENCES

1. Крагельский И.В. Трение и износ. М.: Машиностроение, 1968. 480 с.
2. Елагина О.Ю. Технологические методы повышения износостойкости деталей машин. Брянск: изд. БГТУ, 2010. 112 с.
3. Макаров А.В., Коршунов Л.Г., Счастливцев В.М., Солодова И.А., Яковлева И.Л. Структура и абразивная износостойкость закаленных и отпущенных заэвтектоидных углеродистых сталей. // ФММ. 2004. Т. 98, № 4. С. 96–112.
4. Самсонов Г.В., Борисова А.А. и др. Физико-химические свойства окислов. Справочник. М.: Металлургия, 1978. 472 с.
5. Ворошнин Л.Г., Ляхович Л.С. Борирование стали. М.: Металлургия, 1978. 239 с.
6. Крукович М.Г., Прусаков Б.А., Сизов И.Г. Пластичность борированных слоев. М.: Физматлит, 2010. 384 с.
7. Зинченко В.М. Инженерия поверхности зубчатых колес методами химико-термической обработки. М.: Изд. МГТУ им. Н.Э. Баумана, 2001. 303 с.

# INVESTIGATION OF STRUCTURE AND PROPERTIES FROM ALUMINUM MATRIX COMPOSITE MATERIALS PRODUCED BY SELECTIVE LASER MELTING

T. Tarasova, R. Ableyeva<sup>a</sup>, G. Gvozdeva

Moscow State University of Technology Stankin. Moscow, Russia

<sup>a</sup> riana\_abl@mail.ru

An integrated study of AlSi10Mg powders and high strength Al 7075 was made. This work establishes correlation of particle-size distribution and granular morphology composition to standard requirements for powders used in additive manufacturing. The main selective laser melting interaction parameters (laser power, scanning speed, layer thickness, particle-size distribution) on the process stability and the sizes of the deposited layers were established. As the result of experimental research the connection between selective laser melting parameters and the structure of the researching material was established, the conditions for obtaining an aluminum based composite material with strengthening particles of the second phases were determined. The influence of the selective laser melting parameters on physical and mechanical properties of investigated material (corrosion resistance, density, hardness, surface roughness) was established, comparative results of specimens electrochemical corrosion investigations after selective laser melting and cast specimens from alloy-analogue were presented. This work demonstrates obtained rational regimes for aluminum based composite material with strengthening particles of the second phase.

**Keywords:** selective laser melting; aluminum alloy; AlSi10Mg; Al7075; corrosion; mechanical properties; microstructure.

## INTRODUCTION

The machine-building complex development in the direction of energy efficiency and resource saving requires searching for new solutions which combines technological methods of manufacturing products and creation of new materials with an unusual properties combination. All this relates to additive manufacturing intensively developed in the country and in the world. In recent years, a special attention in the additive manufacturing has been paid to aluminum-based alloys. Aluminum and its alloys are widely used in aerospace and automotive industries due to high corrosion resistance, low density, high thermal and electrical conductivity, etc. For metallic materials, in particular for aluminum alloys, perspective and actively developing technologies in additive manufacturing are selective laser melting technologies. AlSi12 and AlSi10Mg alloys have become the most spread aluminum alloys used in selective laser melting technology [1, 2]. However, the strength characteristics of these alloys do not meet the requirements of the aerospace industry [3, 4].

In this regard, the purpose of this work is to study the influence of the SLM parameters on AlSi10Mg alloy and the least studied high-strength alloy Al7075.

## EXPERIMENTAL PROCEDURE

For this investigation, the samples were made by selective laser melting technology to investigate and determinate SLM parameters window of aluminum alloys using special SLM system ALAM (advanced laser additive machine), developed and assembled at MSTU STANKIN. This system was equipped with ytterbium fiber laser  $P = 200$  W with a wavelength  $\lambda = 1.075$   $\mu\text{m}$ .

Samples were manufactured using Phenix Systems PM100 selective laser melting (PLP) machine (in the Laboratory of Diagnostics and Industrial Process Engineering (DIPI) at the National Engineering School of Saint-Etienne, France). The laser source used within this machine is an ytterbium fiber laser with continuous radiation at a wavelength of 1075 nm and a maximum radiation power of  $P = 200$  W with 70  $\mu\text{m}$  spot size. The process was carried out in a closed chamber filled with argon to prevent oxidation. An industrial machine EOSINT M 280 (German) with maximum laser power of 400 W and the beam diameter of 100  $\mu\text{m}$  was used to manufacture samples for tensile tests and finished product.

For samples manufacturing different scanning strategies were used (one zone, two zones, criss

cross). The materials investigated in this study are two aluminum alloys AlSi10Mg and Al 7075.

The particle size distribution was measured using the optical measuring apparatus called Alpa500 NANO (OcchioSA, Belgium) with Callisto software for statistical data processing. Chemical composition, particle shape and distribution of the elements of aluminum alloy powders were determined using TESCAN VEGA 3 LMN scanning electron microscope (Czech Republic) using scanning electron microscopy.

The quality of the obtained tracks, as well as the microstructure of the samples, were analyzed using a ZEISS Axioscope A1 optical microscope. Sample density was calculated using Adobe Photoshop CS5. The cross sections of the samples were examined for the presence of pores using a ZEISS Axioscope A1 optical microscope with a x5 zoom. For this purpose, the pictures were converted to black and white images using a constant threshold value. Then the ratio of the number of black pixels to the white pixels was calculated for each image giving the porosity.

Microhardness of the specimens was measured on a BUEHLER Omnimet MHT 5104.S. The measurements were taken by placing the samples under a load of 100 grams for approximately 10 seconds. To improve the material properties, in this case microhardness, heat treatment was used in a vacuum furnace.

Corrosion resistance analysis of the samples was conducted using P-30-PJ potentiostat-galvanostat with a three-electrode cell setup. Silver chloride was used as the reference electrode and platinum was used as the counter electrode. To test the corrosion resistance samples were immersed in 3% NaCl solution. The measurements were carried out at an ambient temperature of  $20 \pm 2$  °C.

Roughness measurements were carried out on a profilometer Hommelwerke

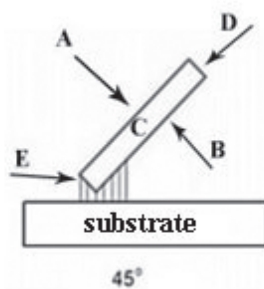


Fig. 1. Direction of manufacturing specimens for roughness measurement

Hommel Tester T8000. Samples roughness tests were manufactured in accordance with Fig. 1, the roughness value was measured in planes A, B, lateral planes C, D, E, both in the longitudinal and in the cross-section.

The tensile stress tests were carried out on equipment WDW 300EIII (Time Group Inc., China). Cylindrical reference specimens were made in one basic technological mode in three scanning directions – 0°, 45°, 90° – in an amount of not less than 5 pieces in every direction.

## RESULTS AND DISCUSSION

The particle size distribution analysis and particle shape analysis showed compliance with ASTM standard for aluminum alloys powders recommended for additive manufacturing (Fig. 2).

AlSi10Mg cube specimens (7×7×7 mm) were additively manufactured. After a series of experiments, the basic parameters set of selective laser melting for this alloy were determined as following: laser power 150 W, scanning velocity 400 mm/s, layer thickness 50 μm, hatch distance 160 μm, temperature in the chamber 70 °C, argon atmosphere, two zones scanning strategy.

Also some series of specimens were made from Al7075 powder. The range of parameters was chosen in the same range as for the AlSi10Mg alloy. After a series of experiments the basic parameters set of selective laser melting for Al7075 alloy were determined as following: laser power 150 W, scanning velocity 400 mm/s, layer thickness 60 μm, hatch

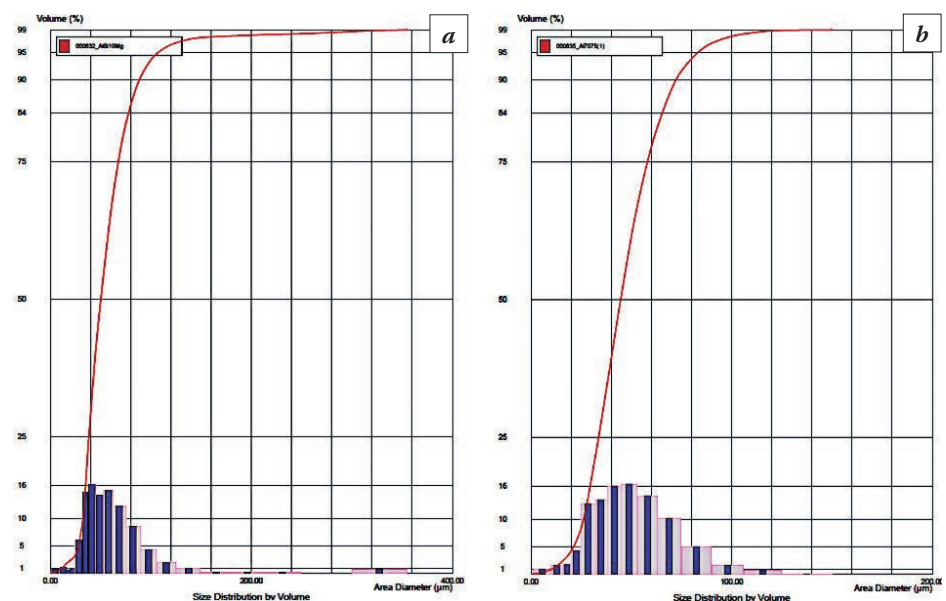


Fig. 2. Powder size distribution of (a) AlSi10Mg, (b) Al7075

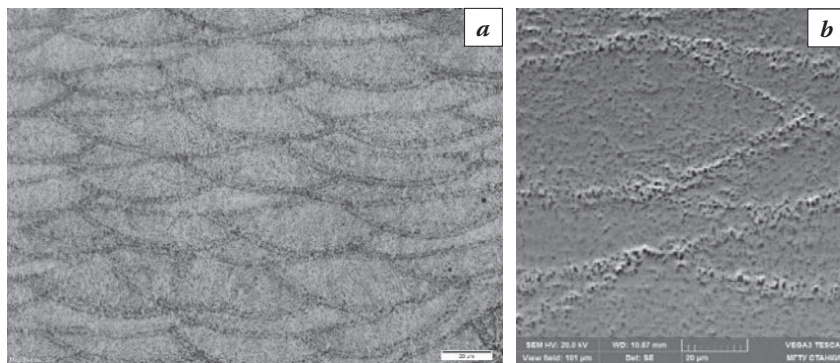


Fig. 3. Microstructure of AlSi10Mg SLM (a) zoom x20, (b) zoom x2050

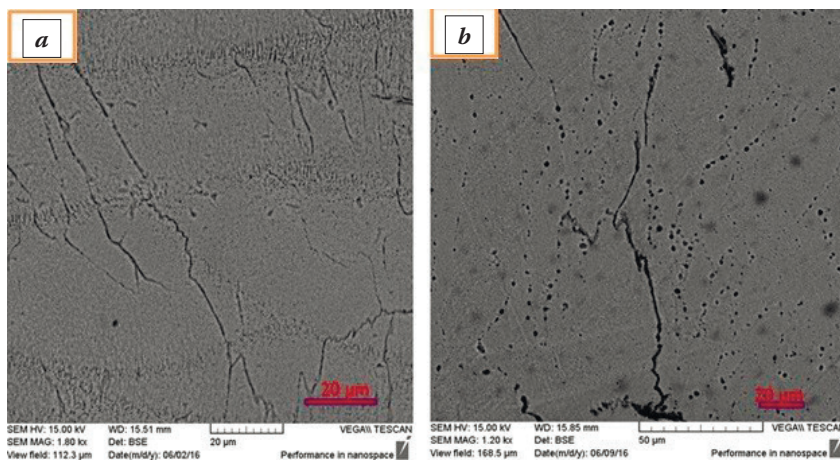


Fig. 4. Microstructure of the specimen (a) with heat treatment, (b) without heat treatment

Table 1. Surface roughness  $Ra$ ,  $\mu\text{m}$

Surface roughness, $Ra$ , $\mu\text{m}$	Plane A	Plane B	Plane C	Plane E	Plane D
Longitudinal section	4.367	5.291	4.774	5.532	7.768
Cross section	3.927	4.855	4.689	6.009	4.973

distance 160  $\mu\text{m}$ , temperature in the chamber 27  $^{\circ}\text{C}$ , argon atmosphere, crisscross scanning strategy, the laser scanning was rotated 30 $^{\circ}$  between consecutive layers to lead a better overlapping.

The microstructure of AlSi10Mg after SLM was investigated. Specimens were obtained using above-mentioned basic parameter set. Fig. 3 shows the microstructures of AlSi10Mg specimens obtained by SLM method. This microstructure clearly shows boundaries of melting zones in the shape of semi-ellipses forming during laser scanning process. The material structure is typical for specimens after SLM. Cellular fine structure consist of aluminum solid solution with uniformly distributed Si and Mg phase along the grain boundaries, which has been confirmed earlier in works [5, 6]. The shape and size of

the cells differs along the track section.

In addition, microstructure investigation of specimens from Al7075 powder after SLM were made (Fig. 4). This exposed the presence of uniaxial dendritic structure, which in the cross section has cellular structure. Investigating microstructure before and after heat treatment it was revealed that after heat treatment dendrites are dissolved and the secondary phase precipitates are clearly visible in the microstructure (Fig. 4).

The samples were manufactured using basic parameters set and a number of experiments were done, in particular, microhardness tests. Heat treatment was used to improve the value of material microhardness [7, 8].

The specimens were artificially aged in an air furnace at two different temperatures, 121  $^{\circ}\text{C}$  and 177  $^{\circ}\text{C}$ . The first aging step was done at 121  $^{\circ}\text{C}$  for 55 min, and the samples were then water quenched. The second aging step was done at 177  $^{\circ}\text{C}$  for 55 min. After that, the microhardness of heat-treated samples was examined. Results revealed an increased value of microhardness for the heat treated Al7075 specimen in comparison with non-heat treated specimen by 11% (The average microhardness value of heat treated specimen is 138 HV, of non-heat treated specimen is 124 HV).

The obtained values of roughness are represented in Table 1. It was determined that the surface roughness in longitudinal section is greater than in cross section. The highest value of surface roughness in longitudinal section is in the E plane, and in the cross section is in the D plane. The surface roughness of aluminum alloys after SLM is similar to the surface roughness after casting.

The corrosion tests were carried out on samples fabricated from AlSi10Mg powder with different surface roughness. The aim of this investigation is to determine the influence of surface roughness on corrosion resistance. Each experiment was repeated 10 times for each specimen. The specimen with  $Ra = 18.207$  surface roughness was manufactured using following parameters: laser power 150 W, scan-

Table 2. Corrosion measurements obtained from polarization curves for samples with different surface roughness

Material	Surface roughness $Ra$ , $\mu\text{m}$	Corrosion potential $E$ , mV	Corrosion current, A
AlSi10Mg	18.207	-762	$5.01 \cdot 10^{-6}$
AlSi10Mg	4.367	-727	$3.16 \cdot 10^{-6}$

Table 3. Corrosion measurements obtained from polarization curves

Material	Corrosion potential $E$ , mV	Corrosion current $I$ , A
Cast alloy	-537	$3.1 \cdot 10^{-7}$
AlSi10Mg (polished)	-462	$3.3 \cdot 10^{-7}$

ning velocity 1300 mm/s, hatch distance 50  $\mu\text{m}$ , and sample with  $Ra=4.367$  surface roughness was manufactured using these parameters: laser power 150 W, scanning velocity 400 mm/s, hatch distance 160  $\mu\text{m}$ . The average values of corrosion tests for the samples with different surface roughness presented in Table 3.

This revealed that the corrosion potential of the sample with greater surface roughness was lower -762 mV vs. -0.745 V for the sample with lower surface roughness (-727 mV), while the corrosion current was relatively elevated  $5.01 \cdot 10^{-6}$  A vs.  $3.16 \cdot 10^{-6}$  A.

For the second series of experiments potentiodynamic polarization curves for the cast aluminum alloy (AlSi10Mg alloy analogue) and printed aluminum alloy (polished AlSi10Mg) were measured. Each experiment was repeated 10 times for each specimen. Table 3 presents the averaged data. Fig. 5 represents potentiodynamic polarization curves obtained in 3% NaCl solution.

Corrosion potential of printed alloy (-462 mV) was relatively shifted to higher values in compare with cast alloy (-537 mV), which indicates improved corrosion resistance. The corrosion current of these two samples differs insignificantly ( $3.3 \cdot 10^{-7}$  A for printed sample and  $3.1 \cdot 10^{-7}$  A for cast sample). These results showed that printed samples have better corrosion resistance.

The tensile strength results of horizontally and vertically oriented specimens made of AlSi10Mg alloy are presented in Table 4.

The tensile tests of samples manufactured in different directions showed that vertical specimens mostly have lower strength properties than horizontal ones, which has been confirmed in works [9, 10]. The relative elongation of the samples shows a similar dependency: the  $\delta$  value for horizontal samples is higher.

Also, a comparison was made between printed and cast samples from AlSi10Mg alloy. The mechanical properties of the samples produced by the addi-

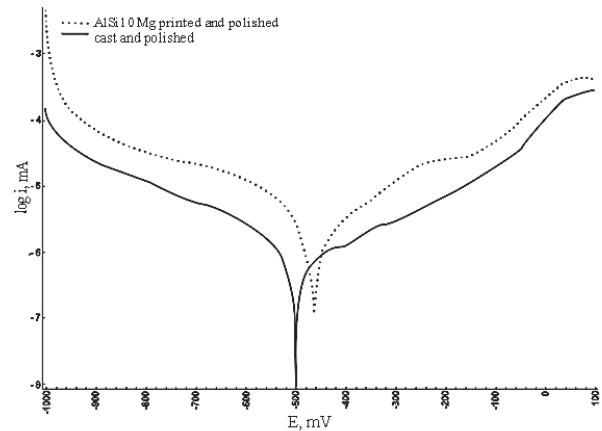


Fig. 5. Potentiodynamic polarization curves of cast and printed samples

Table 4. Tensile strength of AlSi10Mg alloy

Sample orientation	Ultimate tensile strength $\sigma_B$ , MPa	Elongation $\delta$ , %
0	370	13
45	345	15
90	330	12
Cast alloy AK9Ch	230	3

tive manufacturing exceed the mechanical characteristics of cast alloys.

Prototype of the “bracket” part was produced by SLM of AlSi10Mg powder according to the developed parameter set. The purpose of the bracket is fastening the doors in the aircraft. Topological optimization was made which allowed reducing the weight of the structure. The weight of the “Bracket” part produced by the SLM technology was reduced 1.3 times compared to the cast part. The part was manufactured on the EOS M280 machine. Fig. 6a, b shows the prototype of the “bracket” part, obtained by SLM from AlSi10Mg alloy.

## CONCLUSIONS

Basic parameter set was established.

Research showed the possibility to obtain three-dimensional objects from Al7075 alloy using selective laser melting.



Fig. 6. Bracket from AlSi10Mg powder was manufactured by selective laser melting technology (a) on the substrate, (b) after support structures are removed

Heat treatment allowed increasing the average value of samples microhardness compared to samples without heat treatment.

The results obtained by the present study in terms of immersion tests and potentiodynamic polarization analysis indicate that printed samples showed better corrosion resistant in comparison with cast sample.

Surface roughness obtained results showed that the surface roughness in longitudinal section is greater than in cross section.

Mechanical tests of samples produced in different directions demonstrate that in most cases vertical samples have lower strength properties than horizontal ones, which has been confirmed in previous works.

## REFERENCES

1. Grigoriev S.N., Tarasova T.V., Gvozdeva G.O., Nowotny St. Solidification behavior during laser microcladding of Al-Si-alloys // *Journal of Mechanical Engineering*. 2014. 6: 389–394.
2. Тарасова Т.В., Гвоздева Г.О. Структурообразование в заэвтектических сплавах системы Al-Si при лазерной обработке поверхностей // *Упрочняющие технологии и покрытия*. 2012. 12: 35–40.
3. Louvis E., Fox P., Sutcliffe C.J. Selective laser melting of aluminium components // *Journal of Materials Processing Technology*. 2011. 211: 275–284.
4. Kang N., Coddet P., Liao H., Baur T., Coddet C. Wear behavior and microstructure of hypereutectic Al-Si alloys prepared by selective laser melting // *Applied Surface Science*. 2016. 378: 142–149.
5. Thijs L., Kempen K., Kruth J.-P., Van Humbeeck J. Fine-structured aluminium products with controllable texture by selective laser melting of prealloyed AlSi10Mg powder // *Acta Materialia*. 2013. 61: 1809–19.
6. Manfredi D., Calignano F., Krishnan M., Canali R. Additive Manufacturing of Al alloys and aluminium matrix composites (AMCs) // *Intech*. 2014. 3–34.
7. Emani S.V., Benedyk J., Nash P., Chen D. Double aging and thermomechanical heat treatment of AA7075 aluminum alloy extrusions // *Journal of Materials Science*. 2009. 44: 6384–6391.
8. Sobol' O.V., Andreev A.A., Grigor'ev S.N., Volosova M.A. Vacuum-arc multilayer nanostructured TiN/Ti coatings: structure, stress state, properties // *Metal Science and Heat Treatment*. 2012. 1: 28–33.
9. Noriko Read, Wei Wang, Khamis Essa, Moataz M. Attallah. Selective laser melting of AlSi10Mg alloy: Process optimisation and mechanical properties development // *Materials and Design*. 2015. 65: 417–424.
10. Kempen K., Thijs L.J., Van Humbeeck, Kruth J.-P. Mechanical properties of AlSi10Mg produced by Selective Laser Melting // *Physics Procedia*. 2012. 39: 439–446.

## WAYS OF ULTRASONIC ADDITIVE MANUFACTURING DEVELOPMENT

D.S. Fatyukhin, R.I. Nigmatzianov, A.V. Sukhov

Moscow Automobile and Road Construction State Technical University (MADI), Moscow, Russia  
mitriy2@yandex.ru

The most dynamically developing type of manufacturing technologies are additive ones. Technologies of layer-by-layer synthesis of metal materials are of particular interest. Ultrasonic additive manufacturing is based on the mutual diffusion of the material layers to be joined. The technology of ultrasonic additive manufacturing includes the welding of metal layers using friction and pressure and the following contour milling. The main directions of development of ultrasonic layer-by-layer synthesis of metallic materials are: the use of low-cost materials and an increase in printing speed. The cost of materials for this type of processing is much less than powder, therefore, the cost of products obtained using ultrasonic additive technology is many times lower. In addition, a significant advantage of the technology is the possibility of obtaining composite products of complex shape from dissimilar materials, such as steel, titanium, copper, etc. Increasing the speed of printing consists of the possibility of using thick layers of foil and the choice of rational processing modes.

**Keywords:** ultrasound; additive technologies; layer-by-layer synthesis; processing modes; oscillatory system; diffusion.

### INTRODUCTION

The widespread use of high-performance, environmentally friendly ultrasound technology currently improves the reliability and durability of engineering products, components and machine parts. Perspective directions of the use of ultrasound are the practical implementation of inventions that open up fundamentally new directions in engineering and technology of mechanical engineering [1, 2].

The most dynamically developing direction of production technologies are additive. Of particular interest are the technology of layered synthesis of metallic materials. The most common additive technology for producing metal products is the method of layer-by-layer selective laser melting of metal powders (SLS technology). The technology consists in selective melting of a thin layer of metal powder with a laser beam in accordance with the geometry of the section of the part corresponding to each powder layer [3]. The difficulty of obtaining and the high cost of powders for SLS technology are significant factors hindering the wider use of this production method. In addition, the process is associated with the melting of the material, which does not allow to achieve high performance technology. The use of other methods of combining particles of a material, such as diffusion, allows one to eliminate the listed disadvantages. One of the methods for obtaining permanent connections is ultrasonic.

### THE MECHANISM OF ULTRASONIC WELDING OF METALS

Since the middle of the last century, ultrasonic welding technology has been developed and successfully used in industry. According to GOST 2601–84, ultrasonic welding – pressure welding, carried out when exposed to ultrasonic vibrations.

The connection is formed when superimposed ultrasonic vibrations on the parts being welded to be compressed. The required compression force is relatively small from tenths to hundreds of N. The mechanical energy of ultrasonic vibrations creates compressive and tensile stresses as well as shear stresses in the connection elements. When the stresses exceed the yield strength of the materials being welded, plastic deformation occurs. Deformation and high-frequency vibrations cause the destruction of oxide films and the setting of materials. At the same time, the temperature in the setting zone does not exceed 200...250 °C, therefore the structure and properties of the materials being welded change slightly.

The main areas of application of ultrasonic welding is the production of compounds from thin-sheet materials and wire. In addition, ultrasonic welding is widely used in the manufacture of microcircuits, chips, electronic parts.

As well as ultrasonic welding, ultrasonic additive technology is based on the mutual diffusion of the joined layers of material [4]. The process consists in

welding layers of metal under the action of friction and pressure, after which the final contour milling is performed.

## ULTRASONIC ADDITIVE TECHNOLOGY AND EQUIPMENT

The concept of ultrasonic additive technology (UAM-technology) was developed by Fabrisonic. The technology refers to the hybrid, because it is implemented using additive and subtractive modules. The first stage is layer-by-layer ultrasonic fusing of the foil, the second is mechanical machining on a CNC machine [5].

Layer-by-layer ultrasonic surfacing is carried out according to the scheme shown in Fig. 1.

The four-half-wave ultrasonic oscillatory system consists of a radiator and a waveguide concentrator. The magnetostriction emitter creates longitudinal oscillations with an amplitude  $\xi$ , which are transmitted to the concentrating waveguide. The cylindrical waveguide-hub is made in the form of a stepped shaft, the central part of which has a broadening and is a roller. The ultrasonic vibrating system roller is pressed with a force  $P$  to the package and rolled without slipping over the sheets of metal foil with rotation frequency  $n$ , which determines the flow  $S$ .

As a result, in the place of contact of the foil sheets, the oxide film is destroyed, plastic deformation and heat release occur, which is sufficient for diffusion penetration of molecules of one metal into another. Foil layers are welded.

The main parameters of the process are  $P$  – force normal pressure;  $S$  – longitudinal feed tool;  $\xi$  is the amplitude of oscillations of the instrument. The processing mode is selected depending on the foil thickness and material properties, such as yield strength and hardness.

## CONCLUSIONS

Given the above, we can distinguish the main directions of development of ultrasonic layer-by-layer synthesis of metallic materials: the use of inexpensive materials and increase printing speed. Since the industry offers a wide range of foils, the choice of material is not difficult. The cost of materials is much less than powder, in connection with this, the cost of products obtained by using ultrasonic additive tech-

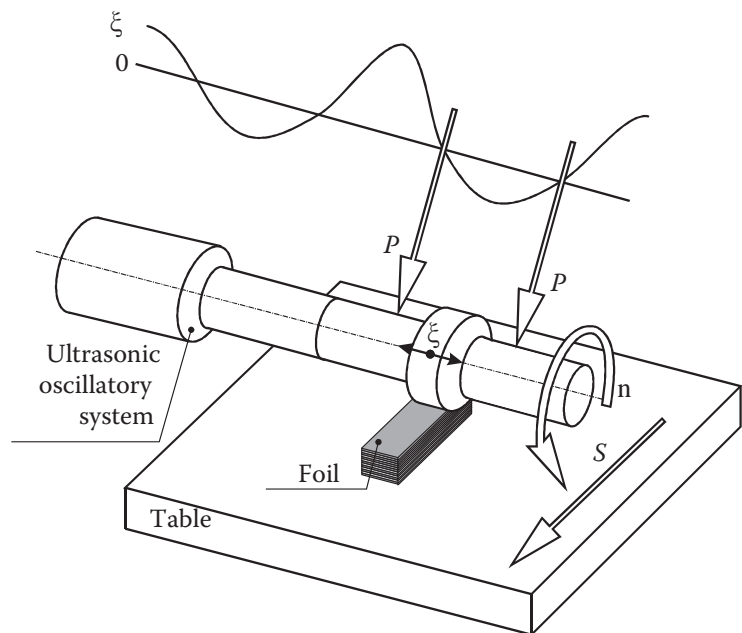


Fig. 1. **The scheme of ultrasonic additive processing:**  $P$  – force normal pressure;  $S$  – longitudinal feed tool;  $n$  is the frequency of rotation of the tool;  $\xi$  – the amplitude of the instrument

nology is many times lower. In addition, a significant advantage of the technology is the possibility of obtaining composite products of complex shape from dissimilar materials, such as steel, titanium, copper, etc. Increasing the speed of printing consists of the possibility of using thick layers of foil and the choice of rational processing modes.

## REFERENCES

1. Prikhodko V.M., Nigmatzyanov R.I., Sundukov S.K., Fatyukhin D.S. Innovative technological processes using ultrasound // Science intensive technologies in mechanical engineering. No. 73. P. 11–14.
2. Prikhodko V.M., Fatyukhin D.S. Ultrasound technologies at the modern stage of development of mechanical engineering // Science intensive technologies in mechanical engineering. No. 62. P. 37–42.
3. Antonova V.S., Osovskaya I.I. Additive technologies: textbook / HSE SPbSUITD. St. Petersburg, 2017. 30 p.
4. Nigmatzyanov R.I., Sundukov S.K., Fatyukhin D.S., Grib V.V., Kartsov S.K. Additive Manufacturing with Ultrasound // Russian Engineering Research. 2017. Vol. 37, No. 12. P. 1070–1073.
5. Fabrisonic L.L.C. Fabrisonic wins additive manufacturing patent [Internet]. Available from: <https://www.todaymotorvehicles.com/article/fabrisonic-additive-located-welding-subtractive-022717/>

# SUBMICRON STRUCTURE FORMATION AT SELECTIVE LASER MELTING OF WC-Co

A.V. Gusarov, R.S. Khmyrov, P.A. Podrabinnik, T.V. Tarasova

Moscow State Technological University STANKIN, Moscow, Russia  
av.goussarov@gmail.com

The thermal cycle of additive manufacturing by selective laser melting (SLM) is less than a millisecond. It causes high thermal gradients in the laser interaction zone. Standard WC-Co hard alloys often crack at SLM. To find compositions resistant to cracking at SLM, micron-size Co and nano-size WC powders were mixed in various proportions. Optical microscopic study of the samples obtained by SLM revealed microcracks at 50 wt% WC content while cracking is not observed at 25 wt% WC. X-ray diffraction study of the samples indicated supersaturated Co-based solid solution. Furthermore, ternary carbide of  $\eta$ -phase is revealed at 50 wt.% WC. Thus, cracking is associated with the brittle  $\eta$ -phase. The solid solution consists of columnar grains formed at quenching from liquid phase. The diameter of columns decreases from 1–2  $\mu\text{m}$  at the scanning speed of 10 mm/s down to 0.2–0.5  $\mu\text{m}$  at the scanning speed of 50 mm/s. After annealing at 700 °C for 3.5 hours, micron-sized and submicron carbides precipitate from the supersaturated solid solution. Such a post-treatment increases the micro-hardness after SLM.

**Keywords:** additive manufacturing; cracking; hard alloy; laser processing; post processing.

## INTRODUCTION

Selective laser melting (SLM) is an additive technology offering the possibility to build parts from powders of various, even refractory, materials. The thermal cycle of this process is less than a millisecond. Therefore, it is not always sufficient for homogenizing the chemical composition and complete powder consolidation. On the other hand, high cooling rate of the order of  $10^6$  K/s is favorable for formation of highly non-equilibrium phase composition and fine crystalline structure. The serious drawback of SLM is high thermal gradients in the laser-interaction zone. Many conventional materials with insufficient plasticity, for example standard WC-Co hard alloys, crack due to thermal shocks accompanying SLM. Various modifications of the composition, customized powders and SLM regimes were studied to reduce the number of defects and improve the microstructure and properties of SLM-fabricated WC-based hard alloys [1–4]. The present work studies the WC-Co system. The objectives are finding compositions, which do not crack at SLM, and studying the influence of the process parameters on the microstructure.

## MATERIALS AND METHODS

The powders of Co with 2  $\mu\text{m}$  mean particle size and WC with 70 nm mean particle size were used as initial materials (Fig. 1). They were mixed in various proportions and then treated for 2 hours in ball mill Retsch PM 100 at 200 r.p.m. to attain uniform distribution of Co and WC particles in the mixture (Fig. 2a). Energy dispersive elemental analysis (see Fig. 2b) confirmed that the chemical composition is uniform. Samples for SLM were prepared by depositing a thin layer of the powder mixture of 50–100  $\mu\text{m}$  thickness on the surface of 4 mm thick WC-20% Co (BK20) sintered substrate shown in Fig. 3. The powder layer is fused with the substrate by a scanning laser beam with spot diameter of 100  $\mu\text{m}$ , wavelength of 1.064  $\mu\text{m}$ , and incident power up to 170 W.

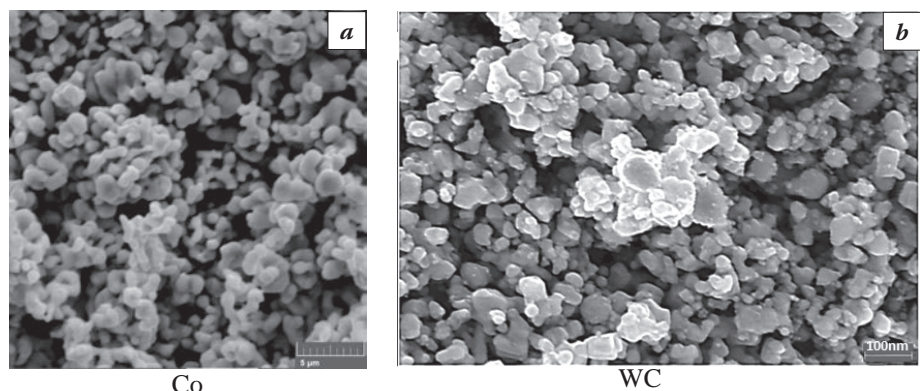


Fig. 1. Initial powders of 2  $\mu\text{m}$  cobalt (a) and 70 nm tungsten carbide (b)

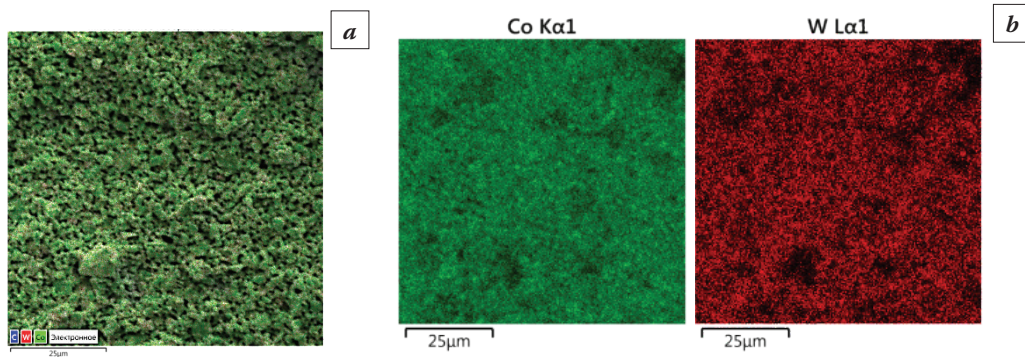


Fig. 2. Powder mixture of 50 wt% Co and 50 wt% WC: *a* – general view; *b* – distribution of elements

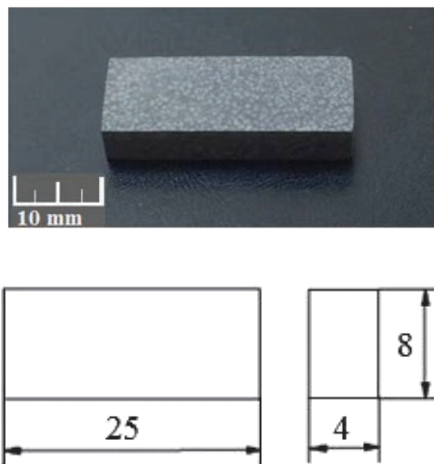


Fig. 3. General view and dimensions of BK20 substrates

Laboratory setup ALAM shown in Fig. 4 is used for powder deposition, sample positioning, and laser scanning. The study of microstructure of the laser-treated samples was performed on a Scanning Electron Microscope (SEM) «Tescan Vega 3» (Tescan a.s., Brno, Czech Republic) equipped with an Oxford Instruments (Abingdon, UK) as well as on optical microscope Olympus (Japan). Phase composition was studied by X-ray diffractometer PANalytical Empyrean Series 2 with Co  $K_{\alpha}$  radiation. Microhardness is measured on microhardness tester Qness Series Q10A.

## RESULTS AND DISCUSSION

Table 1 lists the studied powder compositions. Only composition 25 provided the absence of cracks in the remelted material. Fig. 5 compares optical micrographs of two remelted layers with different compositions obtained at the same SLM parameters: laser power 50 W and scanning speed 100 mm/s. Vertical cracks are observed in the left micrograph. X-ray diffraction analysis indicates that the sample



Fig. 4. Setup ALAM for selective laser melting

of composition 25 consists of a supersaturated Co-based solid solution while ternary carbide  $W_3Co_3C$  ( $\eta$ -phase) is additionally detected for composition 50. Since  $\eta$ -phase is brittle, the material containing it is prone to cracking. It is also worth pointing out that the cracks are located generally in the bands of darker contrast shown in Fig. 5b. Fig. 6 shows such a band at higher magnification. The band contains nano-size inclusions while the surrounding regions of clearer contrast are uniform. These inclusions are probably  $\eta$ -phase. The distance between the darker bands approximately corresponds to the period of la-

Table 1. Powder compositions

	WC-Co		
Composition	25	50	75
WC, wt.%	25	50	75
Co, wt.%	75	50	25

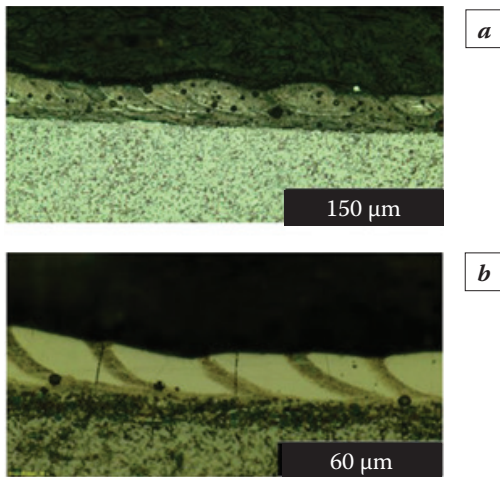


Fig. 5. Single laser-remelted layer at the content of WC, wt.%,: 25 (a) and 50 (b)

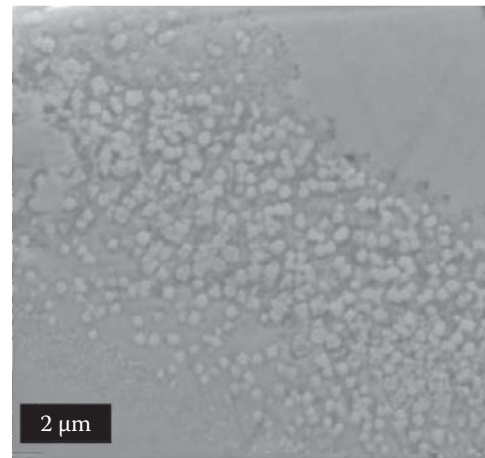


Fig. 6. The band of darker contrast in the structure 50 wt.% WC

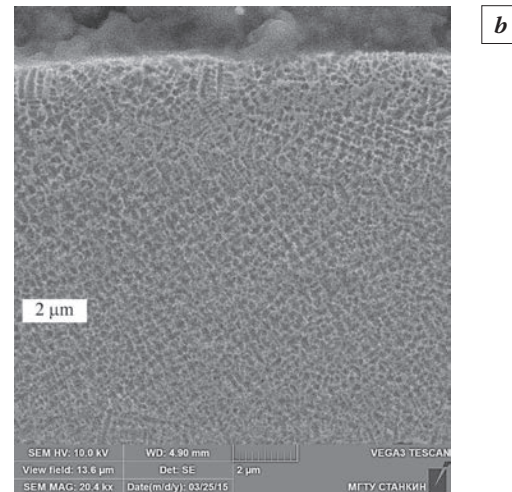
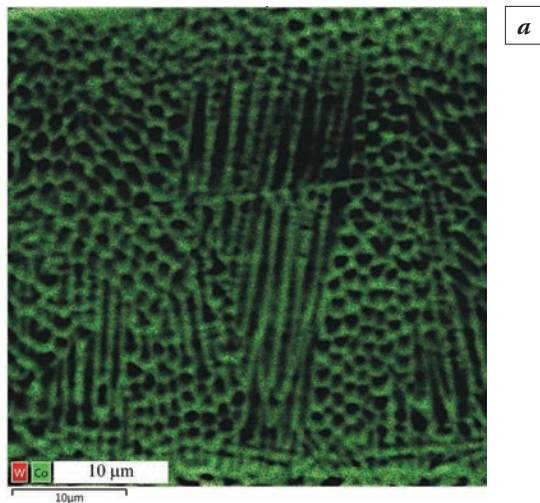


Fig. 7. Structure of supersaturated Co-based solid solution formed at 25 wt.% WC and scanning speed: 10 mm/s (a) and 50 mm/s (b)

ser scanning (hatch distance). Thus, their formation is related to the periodicity of the thermal influence of the laser beam.

The probable mechanism for the formation of such a structure is as follows. First, supersaturated Co-based solid solution is formed at quenching from liquid phase. Note that the cooling rate at SLM can attain  $10^6$  K/s or even be greater [5]. The nuclei of  $\eta$ -phase can be formed at quenching. However, the growth of the carbide particles is controlled by diffusion. The diffusion is slow and the cooling is fast. Therefore, no precipitation is observed in the primary supersaturated phase. Consider a portion of material remelted by a laser scan. The next laser scan passes at a hatch distance from this portion. This is why its thermal influence is insufficient to melt this portion of material again but can be sufficient to intensify the thermally-activated diffusion growth of carbides. Thus, the bands of the precipitated carbide can be explained by the thermal influ-

ence of the laser scan followed after the given portion of powder is fused. The arc-like shape of the band resembles the shape of an isotherm around a localised heat source. The absence of precipitation for composition 25 (see Fig. 5) can be explained by a lower degree of supersaturation. At low supersaturation and high cooling rate, even nucleation can be suppressed.

Fig. 7 shows the structure of the primary solid solution which is columnar grains typical for quenching from liquid phase. The diameter of grains considerably decreases with the scanning speed from  $\sim 2$   $\mu\text{m}$  at 10 mm/s to  $\sim 200$  nm at 50 mm/s. It confirms the theoretical conclusion that the cooling rate at SLM is approximately proportional to the scanning speed [5]. Generally, the finer the grain structure, the better mechanical properties. This is why higher scanning speed at SLM is favorable. The presence of carbide inclusions is not desirable during the SLM process because of the risk of cracking. However, they may

Table 2. Influence of the thermal post-treatment on microhardness

Microhardness	
Before	After
540 HV	700 HV

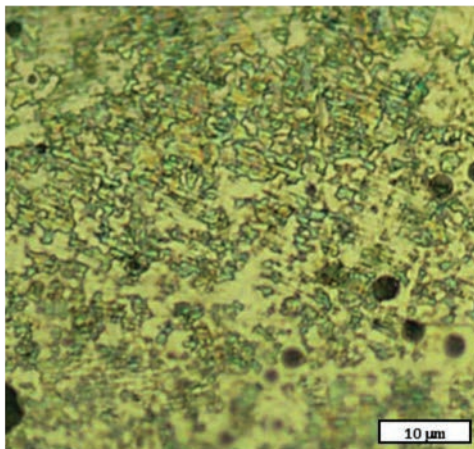


Fig. 8. Precipitation of carbides at 25 wt.% WC after post-treatment

improve mechanical properties of the material. This is why a sample with composition 25 was post-treated in a furnace at 700 °C for 3.5 hours. Figure 8 shows that carbides do precipitate increasing microhardness from 540 HV to 700 HV (See Table 2). Thus, the crack-free microstructure with carbide inclusions, which ensures better mechanical properties, can be obtained by SLM followed by a thermal post-treatment.

## CONCLUSION

Supersaturated Co-based solid solution is formed at quenching from liquid phase after laser fusion of powder. For composition 50, precipitation of ternary carbide  $\eta$ -phase is observed during SLM process, which can be due to thermal influence of the following laser scan after powder fusion. The carbide precipitation at SLM is not desirable because it can

make the material brittle and less resistant to thermal shocks at laser treatment. This is why the material can crack at composition 50. Cracks are not observed for composition 25. The Co-based solid solution consists of columnar grains with the diameter considerably depending on the scanning speed at SLM. The cooling rate at SLM increases approximately proportional to the scanning speed. This is why the grain diameter decreases from  $\sim 2 \mu\text{m}$  at 10 mm/s to  $\sim 200 \text{ nm}$  at 50 mm/s. A thermal post-treatment is proposed to obtain carbide inclusions after SLM. This post-treatment increases the microhardness.

## ACKNOWLEDGEMENT

This work is supported by Russian Science Foundation (Grant Agreement No. 15-19-00254).

## REFERENCES

1. Wang X.C., Laoui T., Bonse J., Kruth J.P., Lauwers B., Froyen L. Direct selective laser sintering of hard metal powders: Experimental study and simulation // *Int. J. Adv Manuf Technol.* 2002; 19: 351.
2. Gu D., Meiners W. Microstructure characteristics and formation mechanisms of in situ WC cemented carbide based hardmetals prepared by Selective Laser Melting // *Materials Sci. Eng.* 2010; 527: 7585.
3. Domashenkov A., Borbely A., Smurov I. Structural modifications of WC/Co nanophased and conventional powders processed by selective laser melting // *Materials Manufacturing Processes.* 2017; 32: 93.
4. Cavaleiro A.J., Fernandes C.M., Farinha A.R., Gestel C.V., Jhabvala J., Boliat E., Senos A.M.R., Vieira M.T. The role of nanocrystalline binder metallic coating into WC after additive manufacturing // *Appl. Surf. Sci.* 2018; 427: 131.
5. Gusarov A.V., Yadroitsev I., Bertrand Ph., Smurov I. Model of radiation and heat transfer in laser-powder interaction zone at selective laser melting // *J. Heat Transfer.* 2009; 131: 072101.

# APPLICATION OF DIFFERENT MEASURING TECHNIQUES FOR CHARACTERIZATION OF QUENCHING PROCESSES IN WATER BASED POLYMER SOLUTIONS

Frerichs Friedhelm, Lübben Thomas

Leibniz Institute for Materials Engineering, IWT. Bremen, Germany

frerichs@iwt-bremen.de

During the last decades many heat treating workshops substitute quenching oils with water soluble polymers. Without any doubt this type of quenching fluid has many advantages. For example the good environment properties and the opportunity to adjust the quenching power between oil and water quenching. Partially oil similar quenching condition can be achieved. Nevertheless some critical aspects must be considered. During the quenching of steel parts with polymer solutions explosion like phenomena can occur which are often accompanied by large cooling rate changes. These “explosions” can lead to pressure waves and vibrations in the quenching tank which are able to displace even heavy components in a quenching load and are therefore a risk for the safety of workers and machines. The mechanisms leading to this phenomenon are from the knowledge of the authors not fully understood. Therefore different measuring techniques were applied to investigate and understand the quenching in water based polyalkylene glycol and polyvinylpyrrolidone solutions. First of all near surface temperature measurements inside the workpieces were carried out. But additionally video documentations of the quenching processes and acoustical and electrical measurements inside the quenching tank were done. The electrical measurements detect the changes of the electrical conductivity between the workpiece and an electrode in the quenching tank. The acoustic measurements inform about fast changes of the state of the vapor and polymer films at the surface. The summary of all simultaneous measurements enable a better assessment of the quenching with water polymer solution.

**Keywords:** quenching behavior; water soluble polymers; Polyalkylenglykol (PAG); Polyvinylpyrrolidon (PVP); investigation techniques.

## INTRODUCTION

Heat treatment and quenching is used to control material properties of metal components. In this framework immersion quenching in evaporating liquids like water and oil is a widely used technique in heat treatment workshops, because these methods provide higher heat transfer coefficients than gas and liquid salt quenching techniques. The heat transfer coefficients achieved in water are very high and might induce thermal stresses and even cracks whereas immersion cooling with oil is softer with the accompanied disadvantage that the resulting cooling rate is maybe too small for generating a proper micro structure with a sufficient hardness.

Heat transfer rates between water and oil can be achieved by aqueous polymer solutions. Water soluble organic polymers like polyvinylpyrrolidone (PVP) or polyalkylene glycol (PAG) have become commercially available for quenching since the middle of the last century [1–3]. Polymer quenchants offer a number of possibilities to adjust the quenching process. The kind of the polymer and the concentration allow to vary the cooling properties of the water based quenching media [4, 5].

In any case the controlled extraction of heat is very important during quenching. In this context immersion quenching in evaporating fluids have some disadvantages. The heat transfer mechanism are complex and consists of the three phases film boiling, nucleate boiling, and convection [6]. Especially the transition from film to nucleate boiling – the rewetting of the sample surface – is a complex process which can lead to a strong position dependence of the heat transfer coefficient of the cooled work pieces. These effects are even much more complex, if water polymer solutions are applied. In that case the wetting and rewetting might occur several times during one quenching process. Furthermore the reproducibility of the quenching results is not high and depends strongly on agitation conditions. Fig. 1 gives an example for the poor reproducibility of such quenching processes. Up to now the mechanisms, which lead to the repeating wetting and rewetting and the poor reproducibility, is unknown.

To get more information about the quenching process, simultaneous temperature, video, and sound measurements are carried out and compared. Sound measurements with a hydrophone [7] are useful because the rewetting process during water polymer

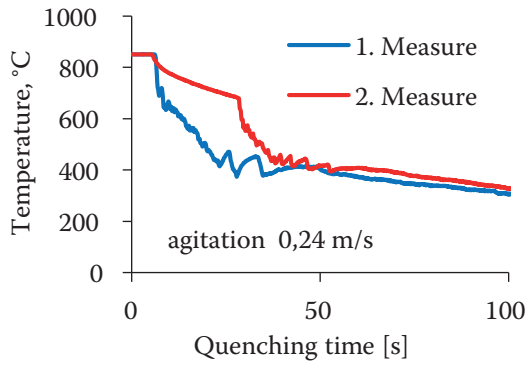


Fig. 1. Quenching process (austenitic cylinder, length 100 mm, Ø 50 mm 20% water polymer solution type PVP, 35°C, agitation speed 0.24 m/s (source: own measurements))

quenching is accompanied by very noisy sounds. Furthermore by the aim of electric conductivity measurements between sample and an electrode inside the tank [8] more information about the state of the vapor and polymer film around the workpiece surface during the quenching process can be collected.

Each of these measuring techniques delivers parts of the necessary information for understanding the different events of the quenching process in water based polymer solutions. Due to a comparison of all available information a better understanding of the processes in the quenching tanks can be achieved. In this contribution the results of the above mentioned measuring techniques will be exemplarily shown and discussed. Finally the applicability of the investigated measuring methods in industrial quench tanks will be assessed.

### Experimental Setup

Application-oriented experiments were carried out by use of a 240 l quenching tank with transparent sidewalls in combination with a vertical tube furnace (Fig. 2, left). For generation of different kinds of flow, special equipment can be integrated into the quenching tank. With respect to the lateral sample surface of a cylinder axial, radial and circular flows were investigated. The middle picture of Fig. 2 shows exemplarily such an equipment for axial flow. By use of a pump (not visible in the figure) and an upwards oriented outlet nozzle the quenchant is pressed inside a transparent (polymethylmethacrylate – PMMA) tube. To avoid a direct flow onto the bottom of the cylinder a sphere is mounted in the middle of the tube below the sample (Fig. 3, left).



Fig. 2. Arrangement of furnace and quench tank (left); equipment for axial flow (middle); hydrophone and coil for current measurements (right)

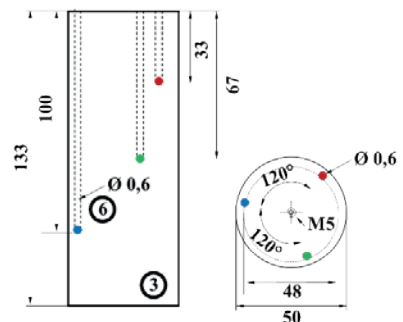
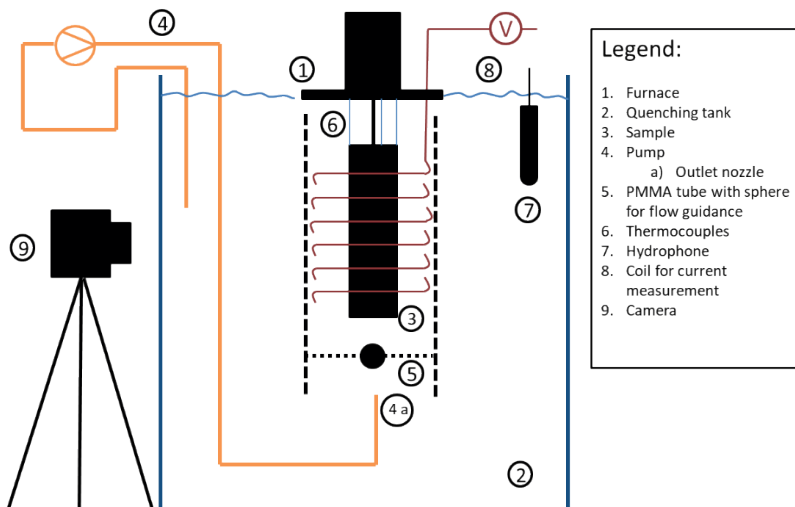


Fig. 3. Experimental setup (left). The cylinder with boreholes for thermocouples. Colored spots indicate the positions of the three thermocouples inside the sample (right)

The quenching process was observed by a video camera (GC PX 100 JVC Kenwood Cooperation) with a resolution of 1920×1080 Pixel and a rate of 50 frames/s. To record the noises during the quenching experiments the hydrophone H2a from Aquarian Audio & Scientific was placed inside the quenching tank, see Fig. 2 (right) and 3 (left). The hydrophone sensor is capable of picking up sounds from below 20 Hz to over 100 KHz. The audio measurements were recorded, visualized, and analyzed by the software *audacity*.

To receive more information about the quenching process the electric current between the sample surface and an electrode around the sample was measured. This idea was used in the past by Tensi ([8]). The boiling phase and perhaps a polymer film at the surface can electrically isolate the sample completely or partial. Additionally modifications of the polymer solution between sample surface and electrode for example by vapor bubbles will lead to changes of the global electric conductance of this system, too. As a result the measured current can give integral information about the wetted surface and the polymer film at the surface. Within the electrical system the current between the sample and a coil which is wrapped around the sample was measured, see Fig. 2 (right) and 3 (left). The applied direct voltage between sample and coil was 4 V. The advantage of the coil is the good observability of the surface during the quenching process.

To achieve information about cooling rate and cooling homogeneity the cylindrical samples were equipped with three thermocouples, see Fig. 3 (right). The dimensions of the austenitic cylinders (1.4305 [9]) investigated by this equipment were  $\varnothing 50 \text{ mm} \times 133 \text{ mm}$  with a mass of about 2 kg. The advantage of austenitic steel is the absence of latent heat and scaling during quenching. The holes for the thermocouples were bored by EDM. They start at the upper cylinder surface and end at different depths in 33 mm, 67 mm, and 100 mm. The distance to the

lateral surface was for all bores 1 mm. In circumferential direction the bores are arranged with an angle of  $120^\circ$  between them. The samples were heated up to  $850^\circ\text{C}$  and were moved from an upper position inside the vertical tube furnace (Fig. 2, left) into a lower position inside the quench tank.

For the concentration of the polymer solutions typical values were chosen which are used in industrial applications, too. Two different PVP were investigated. One with a relative short polymer chain, one with a relative long chain. The concentration of the short-chain and the long-chain PVP was 15%, for PAG 18%. The bath temperature for both kinds of PVP was  $25^\circ\text{C}$  and  $55^\circ\text{C}$ . For the PAG a constant bath temperature of  $35^\circ\text{C}$  was applied.

## RESULTS

Observations during a quenching process with explosive like rewetting

Fig. 4 shows exemplarily the measurements during a quenching process of a cylinder in a water-poly-

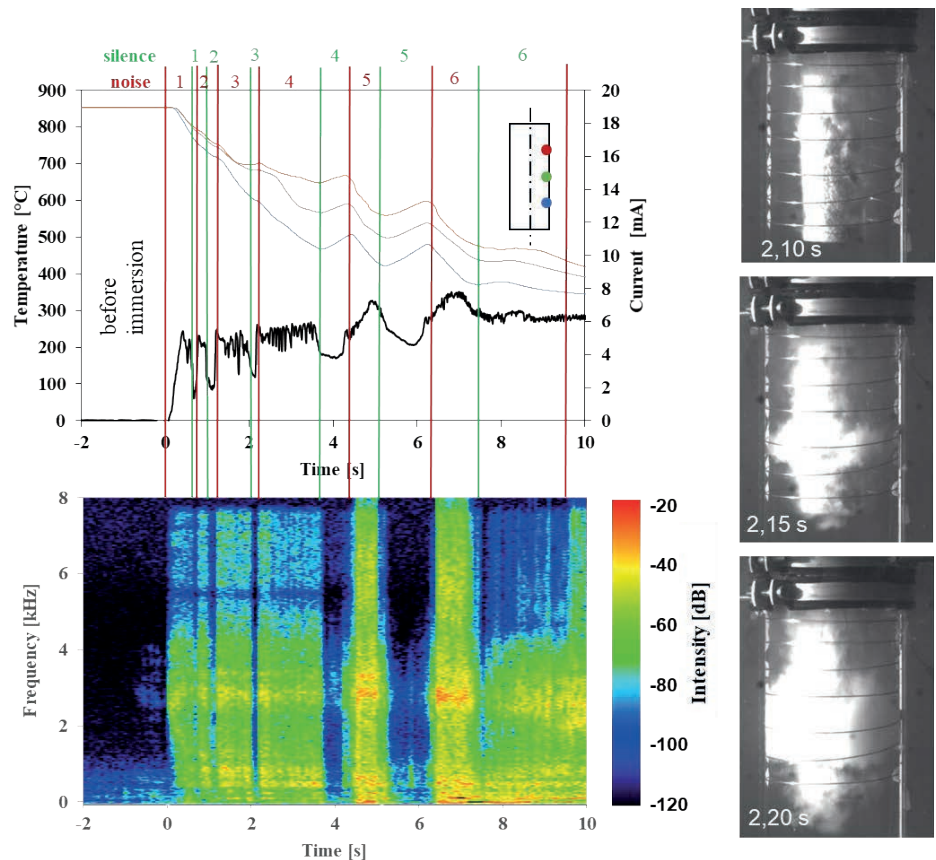


Fig. 4. Quenching of a sample with  $\varnothing 50 \text{ mm}$  in water polymer solution with a long-chained PVP, axial flow  $0.14 \text{ m/s}$ , bath temperature  $25^\circ\text{C}$ . Cooling curves and current as function of time (top) and time dependent frequency spectrum (bottom, left). Selected frames of the simultaneous recorded video film at the beginning of the 4<sup>th</sup> noisy sequence (right)

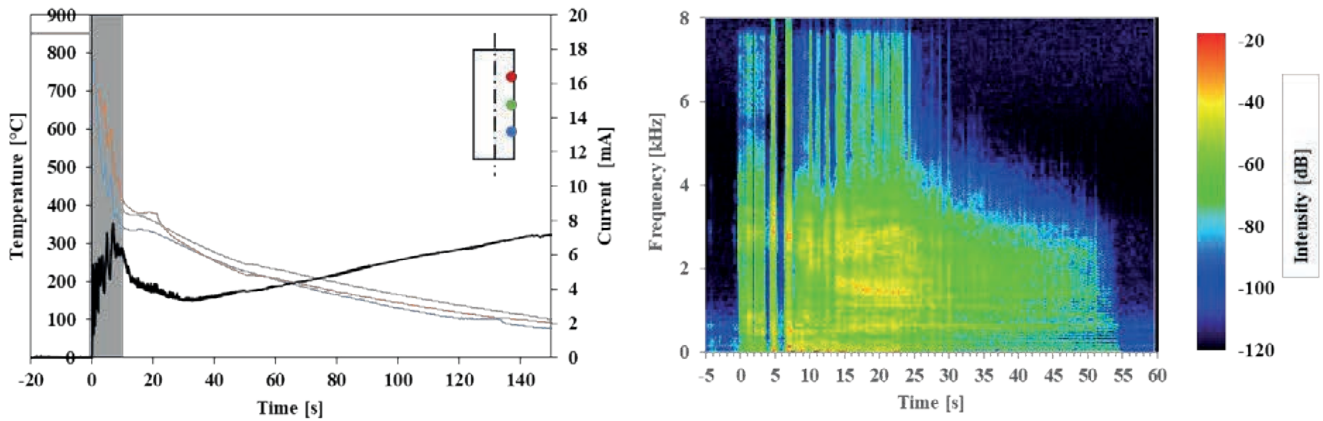


Fig. 5. Same measurement as Fig. 4 (grey area) (left). Sound measurement until 60 s (right)

mer solution with a long-chain-PVP, an axial flow of 0.14 m/s, and a bath temperature of 25 °C. In the upper part the temperature and current measurements are summarized. The lower part represents the audio measurement with the hydrophone. Before immersing the hot cylinder into the quenching liquid (time = 0 s, first red line) the frequency spectrum of the audio recording shows only low intensities for frequencies lower than one kHz. The signal results from more or less constant background sound (for example the pump) which can principally be filtered out. The recorded sounds about 1s before the cylinder immersed into the quenching liquid was generated by the motion of the sample from the furnace to the quenching tank. Such single events cannot be filtered out. They are disturbances in the spectrum. The intensity of the generated noise due to the quenching process itself should be significant higher than the background and single disturbances.

After immersion the measurements can be divided into different sequences marked in Fig. 4 with red and green lines. Red lines mark the beginning of sequence with relative loud noises, green lines the beginning of relative silent sequences. During the first 10 s 6 noisy and 6 silent periods are clearly distinguishable. Within this period the temperature and the current measurements correlate with the recorded sounds. Immediately after the sample had contact with the quenching liquid the current increases for a few tenth of a second and the temperature at all measuring positions decrease monotonously. At the same time the corresponding noise spectrum changes significantly. The sound contains frequencies up to about 8 kHz with relative high intensities between -80 to -40 dB. The spectrum is more or less independent from time during this period.

After about 0.6 s the first sequence with low noise generation begins. The current decreases in that moment rapidly. This behavior can be identified three times during the first two seconds of the quench-

ing process (until sequence 3). Within the 4<sup>th</sup> noisy sequence the mean current increases slightly with superimposed very fast fluctuations. During this period the position dependency of the cooling curves increases in such a way that a temperature gradient from bottom to top with a maximum temperature difference of about 180 °C results. At the same time the sound spectrum shows only some very short and therefore slightly visible vertical lines with lower noise generation. The fast fluctuations of the current and the sound had no visible consequences for the cooling curves. The 4<sup>th</sup> silent sequence reveals a decrease of the current with only small fluctuations and a temperature increase of about 25 °C at all measuring positions. Within the sequences 5 and 6 the rise and fall of current and sound repeats. The temperature at all measuring positions change contrarily in respect to current and sound measurements.

Fig. 4 (right) shows some frames of the simultaneous recorded video film. The first frame represents a moment at the transition time between the 3<sup>rd</sup> silent and the 4<sup>th</sup> noisy sequence. Within the next two frames a cloudy area in the middle of the cylinder occurs which spreads and becomes larger with a high velocity. The average propagation speed was estimated to 0.6 m/s.

Fig. 5 (left) represents temperatures and current measurements until 150 s quenching time for the same measurement given in Fig. 4. The grey field marks the time period of Fig. 4. Between 10 and approximately 25 s the current decreases and the cooling rate becomes very small. The recorded sound shows a more or less constant acoustic signal. After that period (>30 s) the current increases whereas the sound signal decreases continuously. At the same time the temperature falls continuously. The recorded sound at the right hand side decreases significantly after about 50 s. But the current increases at the same more and more. This happens possibly because of a polymer layer at the surface. Before 25 s the PVP layer perhaps grows or reduces the content

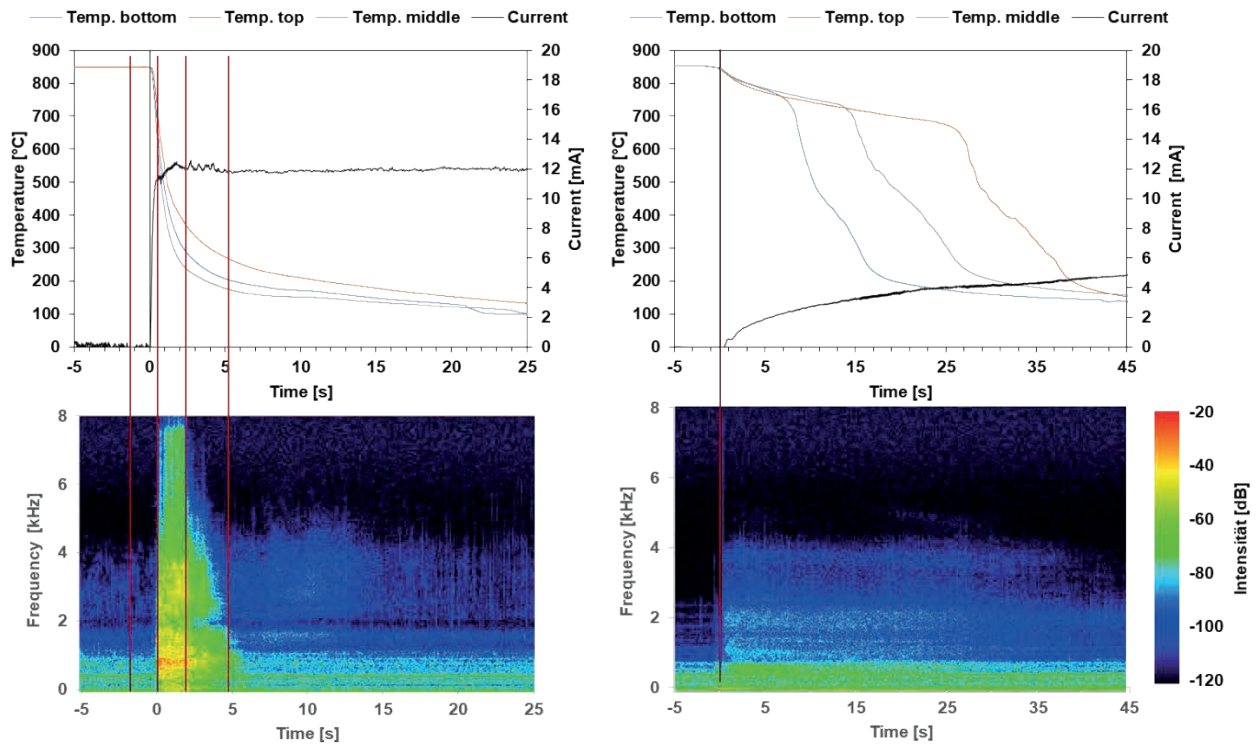


Fig. 6. Short-chain-PVP, axial agitation 0.5 m/s, 24 °C (left) and short-chain-PVP circular agitation 0.5 m/s, 56 °C (right)

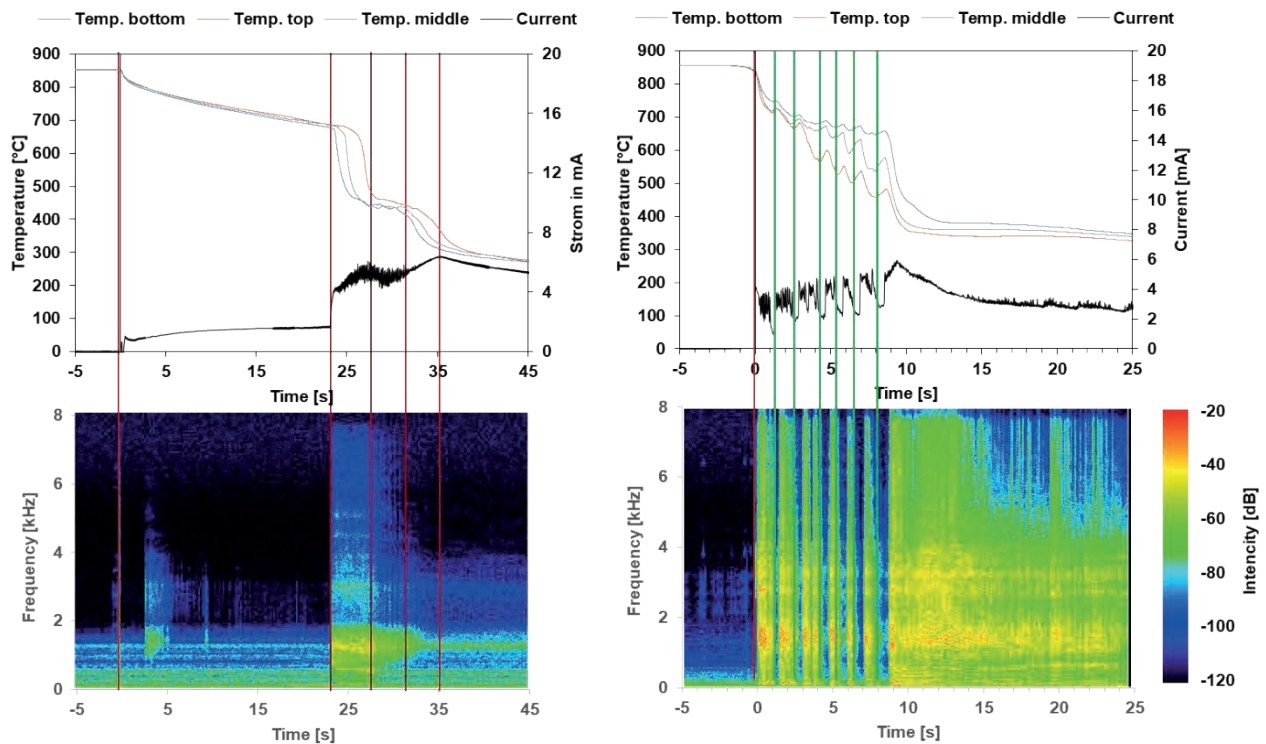


Fig. 7. PAG, circular 0.5 m/s, 35 °C (left) and long-chain-PVP circular 0.5 m/s, 21 °C

on water because of the high sample temperatures above 300 °C. As a result the electrical and thermal conductivity decreases. After 30 s the polymer film probably dissolved slowly in water. As a consequence of the disappearance of the layer the current and the cooling rate increases again.

The Fig. 6 and 7 represent results and comparisons of other quenching variants. The results reveal a large range of quenching behaviors. The quenching with 25 °C short-chain PVP with a 0.5 m/s axial agitation, see Fig. 6 (left) offers a rapid cooling without any reheating. The current increases rapidly to a more or

less high constant value. A Leidenfrost-effect is not observable. A circular agitation with the same quenchant but higher bath temperature reveals a relative slow quenching rate with a pronounced Leidenfrost-effect, see Fig. 6 (right). In that case the current increases slowly with the rewetting of the samples surface. The noise generation is low.

The results of Fig. 7 (left) were generated by a PAG quenchant with a circular agitation with 0.5 m/s. They offer a pronounced very stable vapor phase, which disappears rapidly over the complete surface after about 22 seconds accompanied with a significant noise generation. Simultaneously with the rewetting the current increases rapidly. A reheating was not detected. The results on the right hand side of Fig. 7 were generated by a long-chain PVP with the same circular agitation than in Fig. 7 (left). In that case 6 reheatings occur which were accompanied in every case with silent sequences (green lines) and significant decreases of the measured current.

## CONCLUSION

The application-oriented experiments presented in figures 4 to 7 show that a wide range of quenching scenarios can be generated with water polymer solutions. Changes of the kind of polymer, the agitation, and the bath temperature can have a significant impact on the quenching process. The experiments show that explosive like collapses of the vapor layer are more likely if long chained PVP solutions are used. Short chain polymers lead to more rapid cooling processes without reheating. Circular agitation tends to a reduced cooling rate.

The analysis of the different measuring techniques shows, that a combination of the used techniques deliver important information of the processes during quenching in water polymer solutions. A restriction to only one measuring technique would conceal relevant details which are necessary for a comprehensive evaluation of the complex processes. The surface near temperature measurement are important to predict the finally generated microstructure and hardness. The sound measurement gives the opportunity to check the processes inside the tank. This is important because the explosion like phenomena inside the quenching tank provoke perhaps strong pressure waves which are able to move parts which can lead to considerable damages of the tanks and the quenched workpieces. The current measurement gives details about the layer of vapor and polymer films around the surface of the quenched workpieces. This is important to understand the quenching mechanisms.

In many commercial quenching tanks are no possibilities to install thermocouples or video cameras. The sound and/or the current measurements can be in this case a feasible method to monitor the quenching process. The experimental experiences show that sound measurements are the easiest way to control quenching in water polymer solutions. The hydrophones are not expensive, the recording is possible with simple software tools like audacity or others. Overall this method offers the possibility to evaluate quenching process with water polymer solutions in commercial hardening workshops and adjust the changeable parameter to get the best quenching result.

## ACKNOWLEDGEMENTS

This project has been funded by «Arbeitsgemeinschaft industrieller Forschungsvereinigungen AiF» through financial resources from «Bundesministerium für Wirtschaft und Energie» based on a decision of the German Bundestag and within the «AWT Arbeitsgemeinschaft Wärmebehandlung und Werkstofftechnik» at contract IGF 19115 N.

## REFERENCES

1. **Hilder N.A.** Polymer Quenchants // Heat Treatment of Metals. 1986. 1. P. 15–25.
2. **Hilder N.A.** The Behaviour of Polymer Quenchants // Heat Treatment of Metals. 1987. 2. P. 31–46.
3. **Beitz T.** Substitution of quenching oils with high risk of fire by waterbased quenchants – without flames and fumes // HTM. 2007. 62, 4. P. 163–166.
4. **Haaf F., Sanner A., Straub F.** Polymers of N-Vinylpyrrolidone: Synthesis, Characterization and Uses // Polymer Journal. 1985. 17, 1. P. 143–152.
5. **Burgdorf E.H.** Abschreckfehler beim induktiven Randschichthärten // HTM. 1989. 44, 3. P. 179–182.
6. **Canale L.C.F., Luo X., Yao X., Totten G.E.** Quenchant characterization by cooling curve analysis // ASTM Spec. Tech. Publ. 2010; 1523 STP; 2. P. 861–899.
7. **Ravnik F., Grum J.** Relation between Sound Emission Occurring during Quenching and Mechanical Properties of the Steel after Quenching. Ravnik, F. & Grum // J. Berg Huettenmaenn. Monatsh. 2010. P. 155–119. <https://doi.org/10.1007/s00501-010-0547-x>.
8. **Totten G.E., Tensi H.M.** Using Conductance Data to Characterize Quenchants // Heat Treat. Prog. 2002. 2.5. P. 39–42.
9. **Frerichs F., Lübben Th., Fritsching U., Lohner H., Rocha A., Löwisch G., Hoffmann F., Mayr P.** Simulation of gas quenching // Journal de Physique. 2004. IV, 120. P. 727–735.

# INSTRUMENTED INDENTATION APPLICATION FOR EXPRESS CONTROL OF MATERIALS SURFACE LAYERS MECHANICAL PROPERTIES AFTER VARIOUS TREATMENT

V.M. Matyunin, A.Yu. Marchenkov, A.L. Goncharov, A.P. Sliva, Nuha Abusaif

Moscow Power Engineering Institute. Moscow, Russia

MatiuninVM@mpei.ru

The authors' developments in instrumented indentation application to determine the mechanical properties of the materials surface layers after various types of treatment are summarized. The advantages and disadvantages of existing techniques are noted and new solutions are proposed for a more reasonable evaluation of the Young's modulus, hardness, strength and crack resistance of the processed surface layers. Several examples of surfaces mechanical properties evaluation after the electron-beam surface hardening, chemical heat treatment and the application of hardening coatings are given.

**Keywords:** instrumented indentation; ball indenter; hardness; young's modulus; elastic compliance; indentation curve; electron-beam heat treatment; chemical heat treatment; coating.

## INTRODUCTION

When developing new technologies and using existing technologies for the materials surface layers treatment, it is necessary to provide a defined level of physical, mechanical and service properties. Such technologies include heat treatment, chemical heat treatment, thermo mechanical treatment, treatment with concentrated energy flows, coatings, etc. Sometimes combined processing methods are used for this purpose, for example, chemical heat treatment combined with the concentrated energy flows processing [1]. Regardless of the technology type the mechanical properties characterize the quality of the processed material and confirm or refute the correctness of the technological processing modes choice. As for coatings, the achieved level of mechanical properties reflects the validity of the choice of their compositions, thicknesses and application modes.

Most often, the micro hardness method is used to determine the mechanical properties of the processed surface layer. However, despite the significance of the micro hardness, it is not enough for evaluation of material strength, ductility and crack resistance. A more effective method for this purpose is the instrumented indentation, which has been successfully developed in recent decades [2–9]. To date, several instrumented indentation standards have been enacted, which regulate the methods of testing materials with the registration of indentation curves

and determination of hardness and Young's modulus. For example, the following GOST R 8.748-2011 (ISO 14577-1:2002), GOST R 56232–2014, GOST R 8.904–2015 (ISO 14577-2:2002), GOST R 56474–2015 state standards are valid in Russia. It should be noted that in the Russian state standard GOST R 56232–2014 not only the method for determining the hardness and the Young's modulus was considered and described, but also the method for converting the ball indentation curve to the tensile diagram in a plastic region. At the same time, there are several difficulties and limitations in evaluation of mechanical characteristics using the indentation diagram. The possibility of mechanical properties evaluation with a defined accuracy depends on many factors, for example, the surface quality of the test material, grain size, loading and strain rates, scale range of indentation, device elastic compliance, etc.

## EXPERIMENT METHODOLOGY

Instrumented indentation experiments were performed on the MPEI-TA installation [9] and the universal testing machine Instron 5982, prepared for testing by indentation. Fig. 1 shows the loading and measurement units of the MPEI-TA and the Instron 5982.

Ball indenters with different radii  $R$  were used:  $R = 0.5$  mm indenter made of high-hard hardened

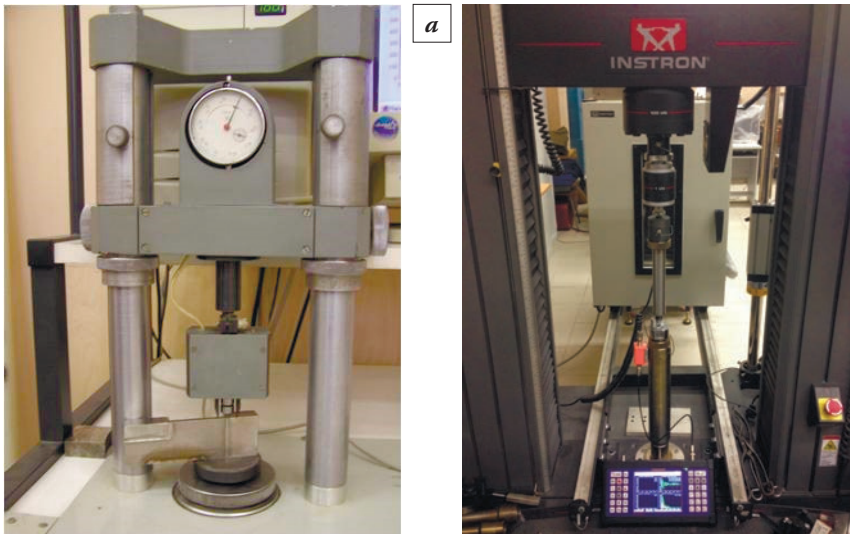


Fig. 1. Loading and measurement units of the MPEI-TA (a) and Instron 5982 (b) prepared for testing by instrumented indentation

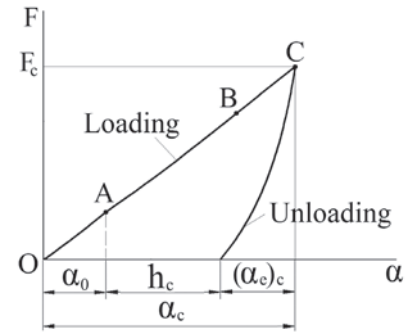


Fig. 2. Instrumented indentation diagram “ $F - \alpha$ ” scheme:

$\alpha_0$  – ultimate elastic displacement at the elastic indentation;  $F_c$  – ultimate indentation load;  $h_c$  – indent residual depth;  $\alpha_c$  – elastoplastic displacement under the  $F_c$  indentation load;  $(\alpha_e)_c$  – elastic part of the elastoplastic displacement  $\alpha_c$  under load  $F_c$

steel and  $R = 0.2$  mm diamond indenter. During each indentation a diagram “load  $F$  - elastoplastic displacement  $\alpha$ ” was registered.

A scheme of the instrumented indentation diagram “ $F - \alpha$ ” obtained with ball indenter and containing the loading and unloading curves is performed in Fig. 2. The initial stage  $OA$  corresponds to an elastic indentation, herewith in subsequent sections  $AB$  and  $BC$  an elastoplastic indentation occurs.

The elastic stage  $OA$  can be clearly identified by indentation with ball indenters of large radii. In this stage the dependence of the indentation load  $F$  on the elastic convergence  $\alpha_0$  is described by the Hertz equation:

$$F = \frac{4 \cdot R^{0.5}}{3 \left[ \frac{1 - \nu_m^2}{E_m} + \frac{1 - \nu_i^2}{E_i} \right]} \cdot \alpha_0^{1.5}, \quad (1)$$

where  $\nu_m$  and  $\nu_i$  – Poisson’s ratios of the tested material and the indenter material respectively;  $E_m$  and  $E_i$  – Young’s moduli of the test material and the indenter material respectively.

The  $AB$  stage can be approximated by a equation:

$$F = k \cdot \alpha^m, \quad (2)$$

where  $k$  and  $m$  are the coefficients depending on the tested material properties, herein  $k$  depends on indenter radius  $R$ , and  $1 < m < 1.5$ .

On the  $BC$  diagram stage, the dependence of  $F$  on  $\alpha$  becomes direct and  $m$  is equal to 1. The value of  $\alpha_B$ , where the loading curve becomes straight, depends on the mechanical properties of the tested material,

primarily on the ultimate uniform strain under tension (i.e. elongation). Usually, for structural materials it is occurred when the loading degree is about  $F/R^2 = 1200 \dots 2000$  N/mm<sup>2</sup>.

The instrumented indentation diagram “ $F - \alpha$ ” can be used to evaluate the Young’s modulus  $E_m$  and Brinell hardness  $HB_t$ , which is calculated from the elastoplastic indent depth  $t_c$  under the ultimate indentation load  $F_c$ . However, as it was shown by numerous authors’ experiments, the accuracy and repeatability of  $HB_t$  and  $E_m$  evaluation depends largely on the method of the “ $F - \alpha$ ” diagram analysis and accounting the elastic compliance of the indentation device.

Five different methods for estimating the elastic compliance of the indentation device are described in Russian state standard GOST R 8.904–2015, and each of them has its advantages and disadvantages. However, the main indicator of the correctness of the elastic compliance evaluation is the  $E_m$  value. We can consider that the elastic compliance evaluation is correct if the  $E_m$  value, determined by indentation matches well with the  $E_m$  value, which was determined by tension test with an extensometer. The authors of this paper found that the best results of the  $E_m$  determining by indentation are obtained when evaluating of the device elastic compliance is performed by the registration of diagram elastic region ( $OA$ ) with subsequent Hertz equation (1) application for the elastic displacement calculation [10]. It was established that the difference  $\Delta\alpha$  between the elastic displacement  $\alpha_0$  estimated by “ $F - \alpha$ ” diagram and the elastic displacement  $(\alpha_0)'$  calculated using the Hertz equation (1), is uniquely related to  $F$ . How-

ever, it should be noted that the elastic part  $(\alpha_e)_c$  of the total elastoplastic displacement  $\alpha_c$  under load  $F_c$  differs from the  $(\alpha_0)_c$ , where the  $(\alpha_0)_c$  is the theoretical value of elastic displacement in the assumption that elastic indentation occurs before  $F_c$ . This difference is explained by the impact of plastic deformation depending on the indent residual depth  $h_c$ . Correction  $\lambda$  on the plastic deformation effect has the following form [11]:

$$\lambda = \left( 1 + \frac{2h_c}{(\alpha_e)_c} \right)^{1/3}. \quad (3)$$

Then

$$(\alpha_0)_c = \lambda \cdot (\alpha_e)_c. \quad (4)$$

Using the eq. (1) in view of (3) and (4), the tested material Young's modulus  $E_m$  can be evaluated:

$$E_m = \frac{1 - \nu_m^2}{1.333 \cdot (\alpha_c - h_c) \sqrt{R(\alpha_c + h_c)} - \frac{1 - \nu_i^2}{E_i}}. \quad (5)$$

Experiments performed on steels, aluminum alloys and magnesium alloys show that the relative difference of the  $E_m$  values, determined by indentation and tension test, does not exceed 10%. If  $E_m$  is initially known, it is possible to determine the material hardness  $(HB_t)_c$ :

$$(HB_t)_c = \frac{F_c}{2\pi R t_c}, \quad (6)$$

where  $t_c$  is the indent depth  $t_c$  under the ultimate indentation load  $F_c$ , which is calculated by the following equation:

$$t_c = h_c + \gamma(\alpha_c - h_c), \quad (7)$$

where  $\gamma = E_i / (E_i + E_m)$ .

In case of the equality of  $E_m$  and  $E_i$ ,  $\gamma$  is equal to 0.5 and

$$t_c = \frac{h_c + \alpha_c}{2}. \quad (8)$$

It should be noted that the hardness  $(HB_t)_c$  on BC indentation diagram section is equal to the maximum hardness  $(HB_t)_{\max}$ .

Another relationship for ball indentation, which was firstly established by A. Martens, connects the indentation load  $F$  with the indent depth  $h$  in a certain initial range:

$$F = kh, \quad (9)$$

where  $k$  is the constant for a defined material.

The authors of this paper established that eq. (9) is fair up to B point of the indentation diagram. From (9) it follows that the parameter

$$q = \frac{F}{Rh}, \quad (10)$$

is in fact the hardening modulus of the tested material for ball indentation in plastic region.

In [12] it was established that the material hardness at the yield point  $HB_y$  during the transition from elastic to elastoplastic strain can be determined by the following equation:

$$HB_y = \frac{q}{2\pi(1+\gamma)}. \quad (11)$$

In case of the equality of  $E_m$  and  $E_i$ , equation (11) takes the form:

$$HB_y = \frac{q}{3\pi}. \quad (12)$$

Numerous tests of structural steels differing in structure and mechanical properties have shown that the relationship between tensile yield strength  $R_{0.2}$  and hardness at the yield point  $HB_y$ , as well as between ultimate tensile stress  $R_u$  and ultimate Brinell hardness  $(HB_t)_{\max}$  is sufficiently stable and can be approximated by the following expressions (all values are presented in MPa):

$$R_{0.2} = 0.321 \cdot HB_y - 20.4. \quad (13)$$

$$R_u = 0.31 \cdot (HB_t)_{\max}. \quad (14)$$

Experimental verification of eq. (13) and (14) shows that the relative difference of the  $R_{0.2}$  and  $R_u$  values, determined according to the indentation diagrams, compared with the same mechanical characteristics determined by the tension test, does not exceed 10%.

The proposed methods for the evaluation of  $E_m$ ,  $HB_y$ ,  $(HB_t)_{\max}$ ,  $R_{0.2}$  and  $R_u$  were used to estimate the mechanical properties of the materials surface layers hardened by electron beam quenching, coating and chemical heat treatment.

Fig. 3 shows the instrumented indentation diagrams for 40Kh13 steel (0.4% C, 13% Cr, Fe balanced) before and after electron-beam quenching (Fig. 3a), for 18KhGT steel (0.18% C, 1.2% Cr, 1% Mn, 0.06% Ti) before and after TiN coating (Fig. 3b) and for the 4KhMFS (0.4% C, 1.6% Cr, 1% Mo, 0.4% V, 0.7% Si) steel before and after the chemical heat treatment (Fig. 3c).

## RESULTS AND DISCUSSION

The results of the mechanical properties determination shown in Table 1 as well as indentation dia-

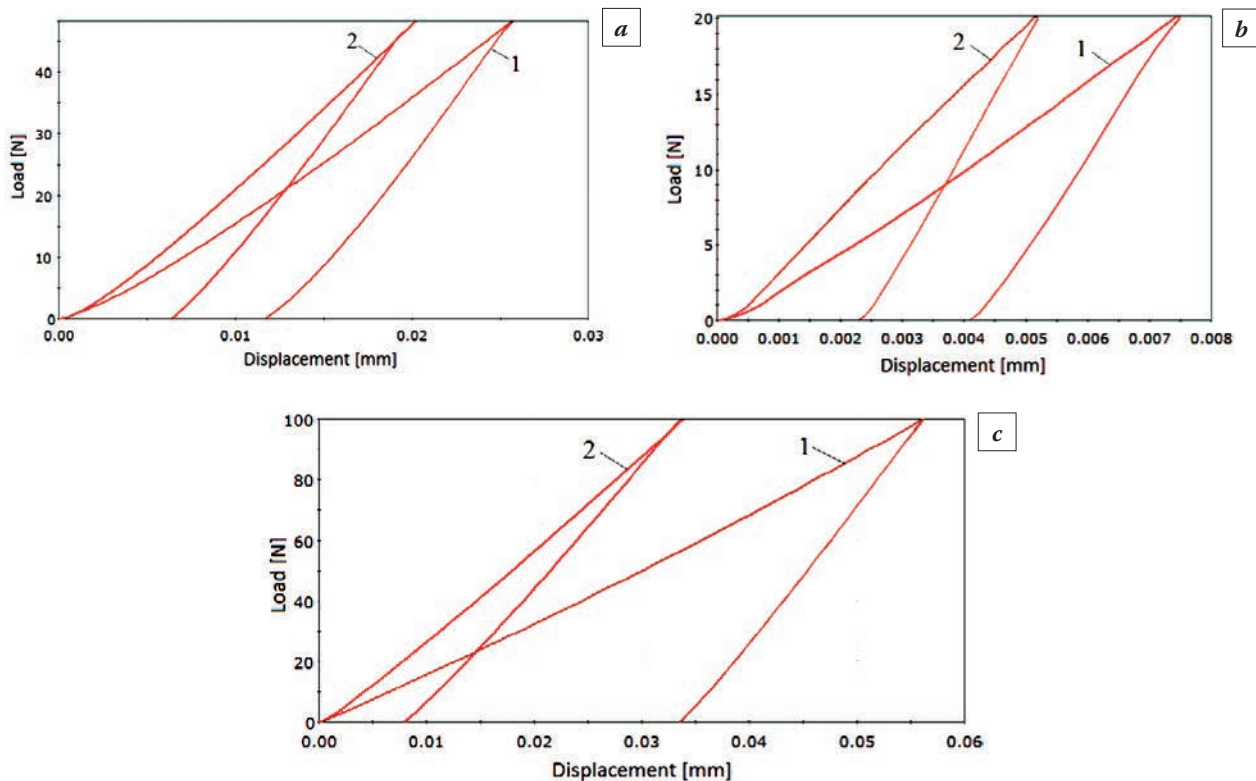


Fig. 3. Instrumented indentation diagrams before (1) and after (2) surface treatment: *a* – 40Kh13 steel (electron-beam quenching); *b* – 18KhGT steel (TiN coating); *c* – 4KhMFS (chemical heat treatment) (metallization (Cr + Ni) when using ablation). Indenter:  $R = 0.2$  mm diamond ball

Table 1. Mechanical properties of the materials surface layers before and after processing

Material (processing method)	Before / after processing	Tested material mechanical characteristics						
		Young's modulus $E_m$ , MPa	Hardening parameter $q$ , MPa	Hardness at the yield point $HB_y$ , MPa	Ultimate hardness $(HB_t)_{max}$ , MPa	Yield stress $R_{0.2}$ , MPa	Ultimate stress $R_u$ , MPa	$R_{0.2}/R_u$
40Kh13 steel (electron-beam quenching)	Before	198 289	19 208	1 648	2 502	508	776	0.654
	After	222 844	35 463	3 074	4 061	966	1 260	0.767
18KhGT steel (TiN coating)	Before	213 477	23 927	2 066	3 682	643	1 141	0.564
	After	282 332	42 654	3 683	4 179	1162	1 295	0.897
4KhMFS (chemical heat treatment)	Before	228 583	14 426	1 253	2 139	382	663	0.576
	After	270 952	61 312	5 396	6 082	1 712	1 885	0.908

grams shown in Fig. 3 make it possible to estimate their change after various types of surface layers processing. Indentation diagrams visually reflect these changes by their relative positions. It should be noted the significant increase of  $q$ ,  $(HB_t)_{max}$ ,  $HB_y$ ,  $R_{0.2}$ ,  $R_u$  as well as  $R_{0.2}/R_u$  ratio of all the tested samples after the processing. The increase in all the above characteristics indicates a strong hardening of each material after its treatment. At the same time, the Young's moduli values  $E_m$  have changed slightly (up to 10%). An increase of the  $R_{0.2}/R_u$  ratio after the materials processing usually indicates the plasticity reduction.

The closer this ratio is to 1, the higher the probability of brittle destruction. However, there were no visible radial or annular cracks near the indents after the indentation. It indicates the sufficient crack resistance of the treated materials. The crack formation usually can be detected on the indentation diagrams in the form of sharp bends or failures of the loading curve. This is also confirmed by the acoustic signals recording in the process of indentation diagram registration [13]. At the moment of crack formation, a sharp impulse of acoustic emission signal as well as indentation loading failure is occurred. From the values of the

indentation load  $F_{cr}$  and the elastic-plastic displacement  $\alpha_{cr}$ , corresponding to the fracture in the indentation diagram, it is possible to calculate the specific energy  $\omega_{cr}$  spent on the crack formation regardless of its type. The higher the value of  $\omega_{cr}$ , the higher the crack resistance of the treated surface layer.

## CONCLUSION

This paper presents new possibilities for determining the materials processed surface layers mechanical properties by instrumented indentation with a ball indenter. The main sections of indentation diagram that reflect the stages of the material elastic and elastic-plastic strain are considered. A method for determining not only Young's modulus and hardness, but also the parameters of hardening and strength of a tested material is presented. The experimental results of the mechanical properties evaluation of the steel surface layers, strengthened by electron-beam quenching, chemical-thermal treatment and coating are given.

## ACKNOWLEDGEMENTS

The research was carried out in the Moscow Power Engineering Institute (Moscow, Russia) with the financial support of the Ministry of Education and Science of the Russian Federation in accordance with base part of state assignment, project no. 11.8088.2017/8.9.

## REFERENCES

1. **Prikhodko V.M., Petrova L.G., Chudina O.V.** Metal physics basis for hardening technology development. 2003. P. 308.

2. **Bulychev S.I., Alekhin V.P.** Materials instrumented indentation test. 1990. P. 224.

3. **Giannakopoulos A.E., Suresh S.** Determination of elastoplastic properties by instrumented sharp indentation // Scr. Mater. 1999. 40: 1191-8.

4. **Oliver W.C., Pharr G.M.** Measurement of hardness and elastic modulus by instrumented indentation: Advances in understanding and refinements to methodology // Mater. Res. Soc. 2004. 19: 3-20.

5. **Hamada A.S., Haggag F.M., Portera D.A.** Non-destructive determination of the yield strength and flow properties of high-manganese twinning-induced plasticity steel // Mater Sci Eng. 2012; 558: 766-70.

6. **Das G., Ghosh S., Sahay S.K.** Use of ball indentation technique to determine the change of tensile properties of SS316L steel due to cold rolling // Mater. Let. 2005; 59: 2246-51.

7. **Toparli M., Koksali N.S.** Hardness and yield strength of dentin from simulated nano-indentation tests // Computer Methods & Programs in Biomedicine. 2005. 77: 253-7.

8. **Golovin Y.I.** Nano indentation and its advantages. 2009. P. 312.

9. **Matyunin V.M.** Indentation in the materials mechanical properties diagnosis. 2015. P. 288.

10. **Matyunin V.M., Marchenkov A.Y., Abusaif N., Stasenko N.A.** Evaluation of elastic compliance of the hardness tester during the instrumented indentation of materials. Industrial Laboratory // Materials Diagnostics. 2019. 85(4): 57-63.

11. **Drozd M.S., Matlin M.M., Sidiyakin Y.I.** Elastoplastic contact deformation calculations. 1986. P. 224.

12. **Matyunin V.M., Marchenkov A.Y., Volkov P.V.** Determination of the metal yield stress from the ball instrumented indentation diagram. Industrial Laboratory // Materials Diagnostics. 2017. 83(6): 57-61.

13. **Matyunin V.M., Marchenkov A.Y., Stasenko N.A.** Specific energy of elastoplastic deformation required for crack formation at indentation of hardening coatings // Inorganic materials. 2018. 54(15): 98-101.

Не указан источник

# MEASUREMENT OF COOLING CURVES AND VISUALIZATION OF BOILING PHENOMENON ON DISK PROBE

Hideo Kanamori<sup>1</sup>, Tsuyoshi Sugimoto<sup>3</sup>, Riki Homma<sup>4</sup>, Dong-Ying Ju<sup>2</sup>

<sup>1</sup> Graduate School of Saitama Institute of Technology. Saitama, Japan

<sup>2</sup> Advanced Science Institute, Saitama Institute of Technology. Saitama, Japan

<sup>3</sup> Nissan Motor Co., Ltd. Kanagawa, Japan; and Department of Engineering, Saitama Institute of Technology. Saitama, Japan

<sup>4</sup> Lubricants Research Laboratory of Idemitsu Kosan Co., Ltd. Chiba, Japan

dyju@sit.ac.jp

In this paper, the visualization technique of PIV is used to observe the complex heat flow phenomenon of nucleate boiling and film boiling when the high temperature circular plate is put into the low temperature oily coolant. Through the research herein, the heat prevalence in the first stage of nucleate boiling around the disk and the formation of bubbles in the cooling medium and the formation of the vapor film on the lower surface of the circular plate are clearly revealed. At the same time, combined with the cooling curve measurement of the lower surface of the circular plate, the heat flow and heat transfer phenomenon on the lower surface of the circular plate and the heat conduction behavior and mechanism inside the circular plate are revealed. The effectiveness of the experimental and analytical methods was determined by comparing the visualization results with the simulation results.

**Keywords:** disk specimen; cooling curves; piv analysis; vapor bubbles; film boiling; nucleate boiling; convection; laser oscillator; quenching.

## INTRODUCTION

When a high temperature metal part is placed in a liquid coolant with lower temperature, the coolant will suddenly boiling. This boiling phenomenon has an important influence on the heat conduction behavior and deformation behavior of high temperature metal parts. For example, material structure, strain control and quality control after quenching of mechanical parts are very important [1]. In quenching process, steam film and boiling bubbles often occurring on the boundary layer between quenching steel and quenching liquid take large effects on their heat transfer with coolant. The steam film formed on the machinery parts during quenching parts didn't only reduces the heat transfer efficiency but also lead to uneven heat transfer which often results in heterogeneous microstructure in turn and mechanical properties of quenching parts. The mechanism of boiling film and its effect on the heat transfer is still open to research as a strong coupling problem of multi-physics phenomena. As the request on high quality parts such as gears and shaft for automobiles, studying the boiling heat transfer and developing high efficient heat treatment has attracted much attention. In this research, the formation and movement of bubbles in boiling film during quenching process are investigat-

ed with high-speed video camera by PIV technology as means of visualization method [2–7].

In this paper, the few thermocouples are directly soldered to the surface of a SUS304 parallel circular plate. When the circular plate is heated to a high temperature of 850 °C and rapidly put into the oil coolant, it will bring about a complicated thermal fluid phenomenon of nucleate boiling and film boiling. In this paper, a method was examined that can reproduce discontinuous transition processes leading to nucleate boiling, vapor film formation, stagnation and collapse of the formed film, and nuclear boiling while convection cooling. Here, three thermocouples were directly welded to the upper and lower surfaces and inside of the SUS303 parallel circular plate to measure the cooling curve when the circular plate was heated to a high temperature of 850 °C and the oily coolant was quickly added. At the same time, the visual heating technology of PIV is used to measure the complex heat flow phenomenon of nuclear boiling and film boiling when the high temperature circular plate is put into the low temperature oily coolant. Through the research herein, the heat prevalence in the first stage of nucleate boiling around the disk and the formation of bubbles in the cooling medium and the formation of the vapor film on the lower surface of the circular plate are clearly revealed. There-

fore, the heat flow and heat transfer phenomena on the lower surface of the disk and the heat conduction behavior and mechanism inside the disk are revealed. In addition, the heat flow analysis method is used to simulate the heat flow around the circular plate. The effectiveness of the experimental and analytical methods was determined by comparing the visualization results with the simulation results.

## EXPERIMENTAL METHOD

### Measurement of cooling curve

As shown in Fig. 1, the disk of SUS304 was embedded in the support ring, diagonally drilled at the angle of  $6.74^\circ$  to the horizontal from the side of the ring toward the center of each of the upper and lower surfaces of the test piece, and the center of each of the upper and lower surfaces. Part of the K thermocouple junction is pulled out by spot-welding the element wire to 2–10  $\mu\text{m}$  directly under the part and fixed with silver paste. This specimen, ring and K thermocouple were uniformly heated to  $850 \pm 1^\circ\text{C}$  in a furnace as shown in Fig. 1, charged into a coolant having an oil temperature of  $60^\circ\text{C}$ , and the cooling curve was measured.

### Sample Coolant

As a sample coolant, commercially available cold quench oil and Daphne Bright quench having the properties shown in Table 1 were used at oil temperature  $T_0 = 60^\circ\text{C}$ .

### Visualization and thermal flow simulation

In order to observe the thermal enthalpy behavior of the first stage of boiling and measure its streamline, a 4K camera “GoPro HERO 6 Black CHD-HX-601-FW” manufactured by ZEN International Corporation and an Nd: YVO 4 laser SOC are used. The laser beam is emitted by a transformed crystal having a wavelength of 532 nm which the schematic diagram

Table 1. Property of Coolant

Quenching oil : Daphne Bright Quench				
Temperature, $^\circ\text{C}$	Density, $\text{g}/\text{m}^3$	Viscosity, $\text{mm}^2/\text{sec}$	Conductivity, $\text{W}/\text{m}\cdot\text{K}$	Specific Heat, $\text{J}/\text{g}\cdot\text{K}$
60	834.9	14.94	0.1315	2.03
70	828.7	11.20	0.1307	2.07
80	822.5	8.667	0.1300	2.11

of system shown in Fig. 3. The Streamline measurement method of the thermal flow field is based on PIV technology by using of “LD-pumped green laser JUNO EX” made by Showa Optronics Corporation. Also, PIV (Particle Image Velocimetry) analysis was performed using “FLOgraph-PIV” software made by Photron Co., Ltd. from the image obtained from the high-speed camera.

On the other hand, in order verify the PIV analysis results, the CFD fluid analysis also was performed using analysis function Turbulance model;  $k - \epsilon$  method, Multiphase flow model and VOF method in software of Solver STAR - CCM + Ver. 11.06.011.

## EXPERIMENTAL RESULTS AND DISCUSSION

### Results of cooling curve

Fig. 3a show the measurement results of cooling curves on upper surface and lower surface and cen-

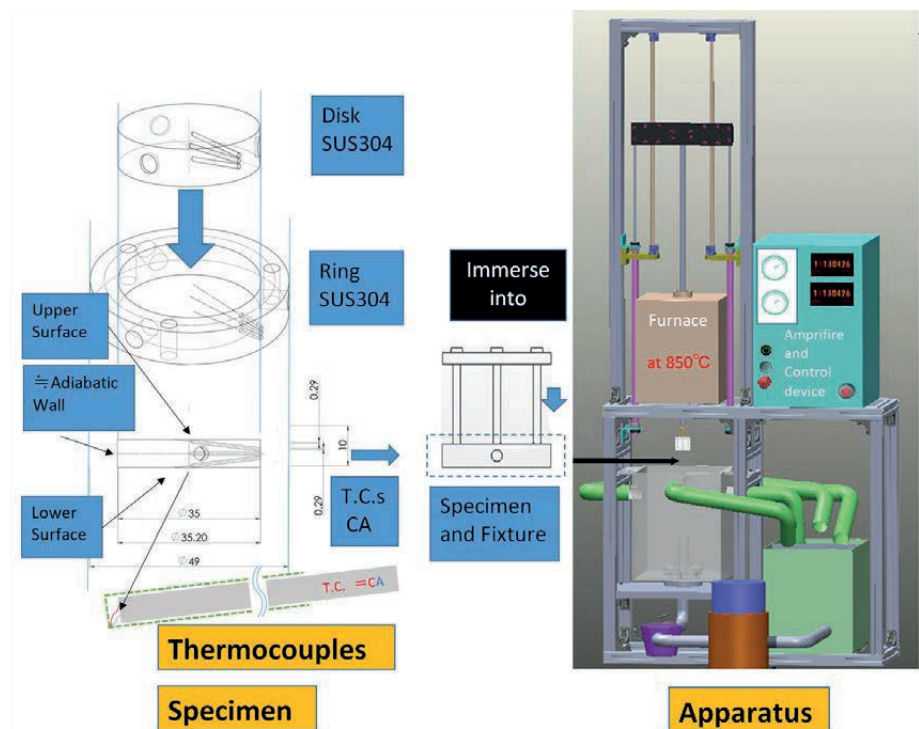


Fig. 1. Structure and shape of disc probe – left side, Schematic diagram of experimental equipment – in right side

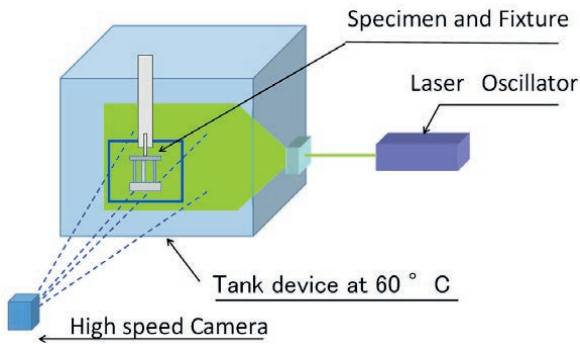


Fig. 2. Schematic diagram of visualization device

tral of the disk specimens. When the thermocouple was installed at 0 mm (10 μm or less) directly below the surface (hereinafter referred to as 0 mm just below the surface), cooling started at about 0.5 s, up to 826 °C, a first boiling stage was formed in which the vapor film was not formed on the lower surface of the test specimen, Then a cooling curve showing the temperature change of slow cooling covered over the vapor film for more than a few seconds was observed. Here, the vapor film start temperature was observed as 826 °C, and immediately after that, the vapor film on the lower surface stabilized and collapsed at 698 °C. after 6.2 sec as shown in Fig. 3b. On the other hand, on the upper surface of the specimen, a cooling curve of temperature change leading to nucleate boiling, which is more rapidly cooled from the first boiling stage up to 0.6 s (0.1 s longer than the lower surface) immediately after cooling started, was observed in Fig. 3a and Fig. 3b.

The cooling curve measured on the side between the ring and the disk specimen assuming a heat insulating wall is shown in Fig. 3a. As a result, even if considering the aspect, the result does not change, so it can be seen that insulation in the experiment is secured.

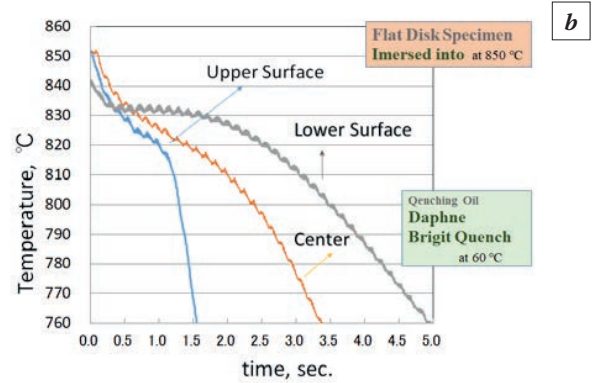
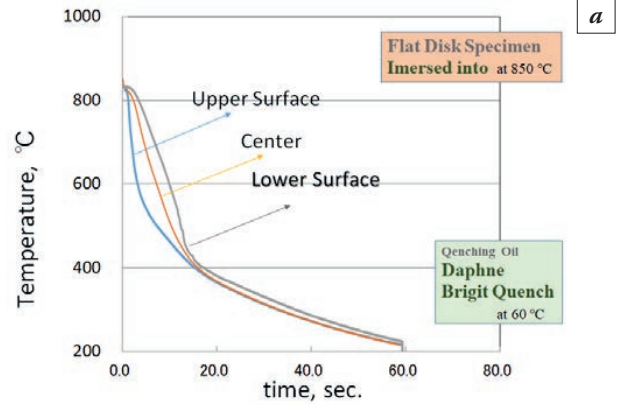


Fig. 3. Measured Cooling Curves: a – Cooling curves of the entire cooling process; b – Boiling first stage cooling curve

Results of visualization

Fig. 4 show the images captured with the high-speed camera and the results of PIV analysis. No steam film is generated on both the upper and lower surfaces at the first boiling stage up to 0.22 sec. Even after 0.22 sec, steam film is formed on the upper surface from 0.22 to 1.12 s, and then nucleus boiling was started, and it was cooled rapidly. Now, it was found that the PIV analysis result, the flow lines, showed that was standing up vertically upper direction. On

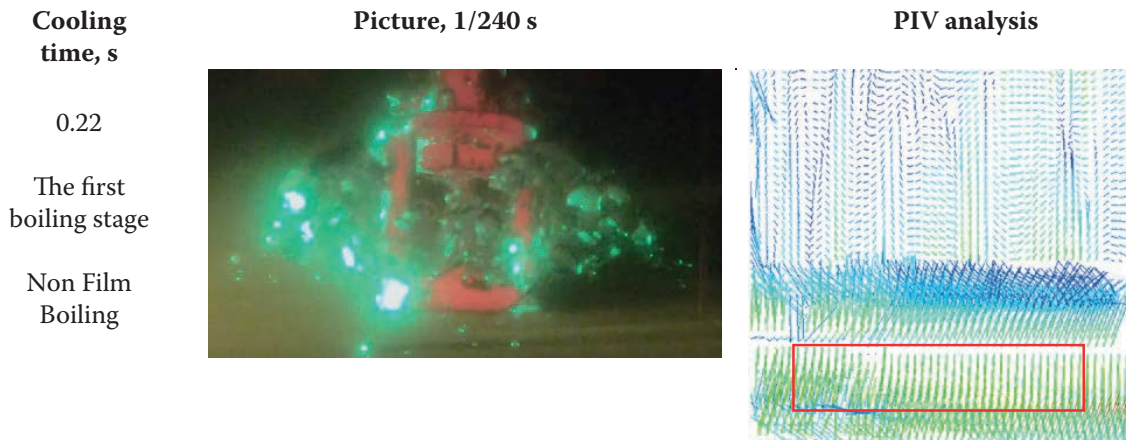


Fig. 4.1. Seen of cooling at the first boiling stage

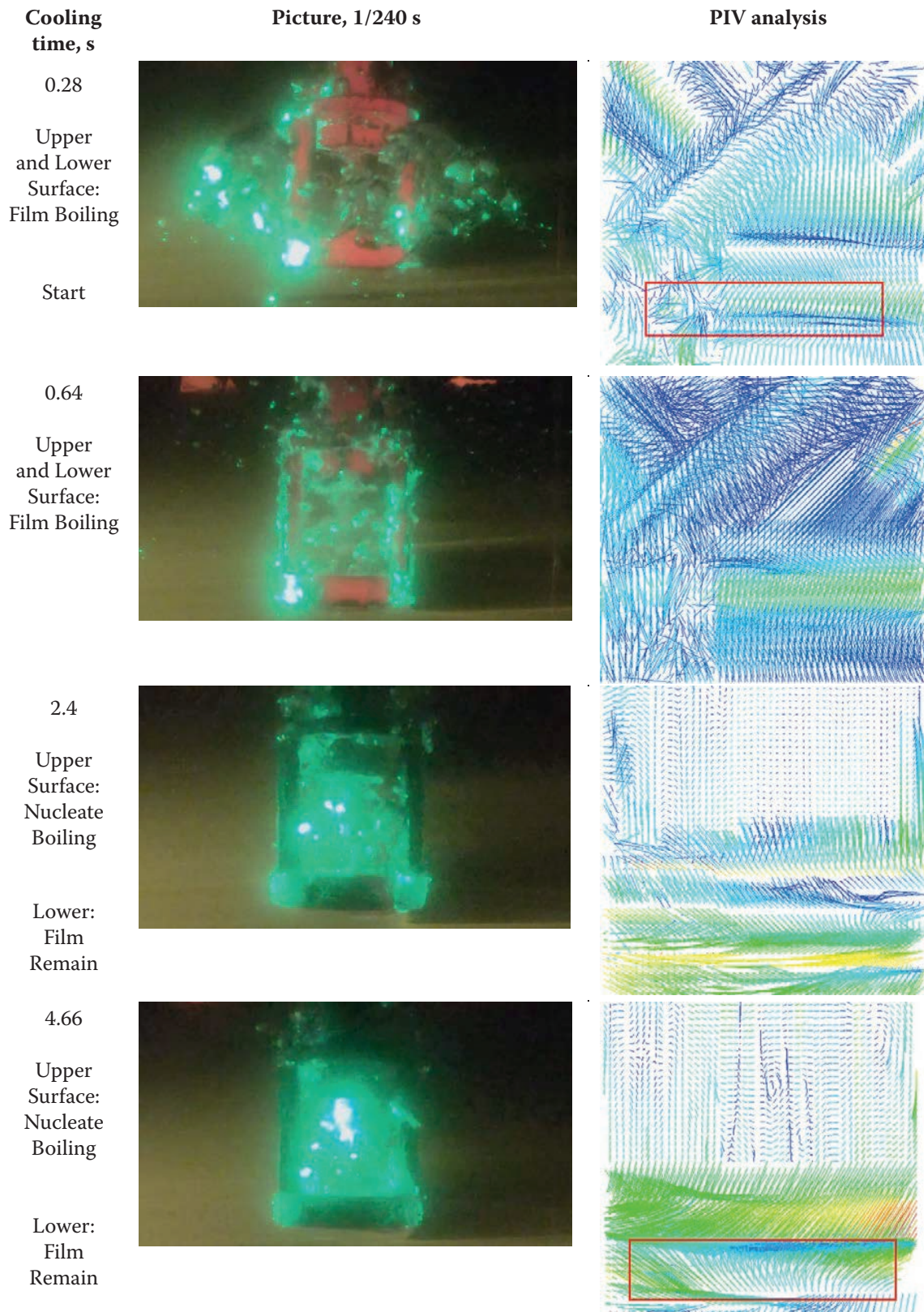


Fig. 4.2. Seen of cooling at film boiling to nucleate boiling stage

the other hand, vapor film under the bottom surface disintegrated from 0.28 to 12 seconds. The steam film formation at the same time and then remained to over 60 seconds. The observation that were cooling curves and image and the analysis result coincided

with the result, and the phenomenon captured as a temperature change could be visualized. However, as a temperature change, one that reliably reflects the information on the surface, that is, one in which the thermo-couple element wire was spot welded and

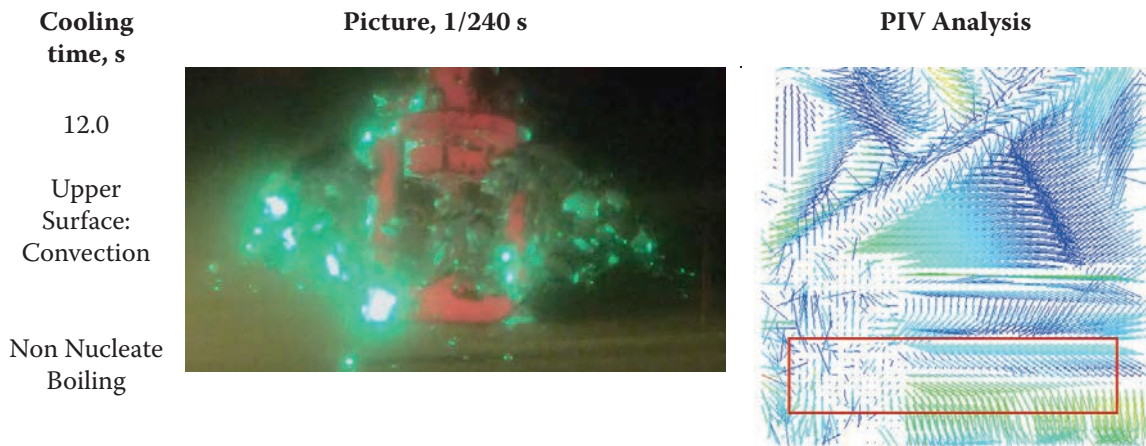


Fig. 4.3. Seen of cooling at convection stage on upper surface and boiling film remained under lower surface, there were not nucleate regim

fixed to 0 mm just under the surface in this case corresponded thereto. In addition, it was observed that the image in which the vapor film formed on the lower surface rotated was caught, and the vapor film in cooling in the presence of the vapor film did not remain at the fixed position.

## CONCLUSIONS

By fixing the contact point of the welded thermocouple element wire just under the surface, it was possible to measure detailed surface temperature and its change. Cooling of lower surface accompanying formation of steam film and no vapor film occurs Nucleate boiling cooling state on the upper surface and the violent cooling state in the first boiling stage preceding it are captured as temperature change and supported by image, PIV analysis It was possible to obtain data to become, and to approach the substance.

## REFERENCES

1. **Dhir V.K.** Investigation of Mechanisms Associated with Nucleate Boiling Under Microgravity Conditions //

Proceedings of the Third Microgravity Fluid Physics Conference. NASA CP-3338, 1996. P. 153-158.

2. **Yano T., Mukai R., Ju D.Y.** Bubbling and Breaking Visualization of Steam Film in Quenching Process of Carbon Steel // Proceeding of 10th Int. Symp. on Flow Visualization, Kyoto, August 26-29. Int. Flow Visualization Society. P. F0348-F0352.

3. **Suzuki K., Ju D.Y.** Cooling performance evaluation and visualization of thermal flow in gas cooling process // J-stage. 2006. Vol. 26, No. 2. P. 155-158. DOI:https://doi.org/10.3154/jvs.26.Supplement2\_155.

4. **Ju D.Y., Saito D., Suzuki T.** Evaluation and Visualization of Heat Transfer Behavior of Quenchant // Journal of the Visualization. 2005. Vol. 25, No. 2. P. 177-180.

5. **Dong-Ying J.U., Hiromichi Saito, Zhang Zhong Bo, Katsumi Ichitani.** Visualization of thermal flow on domain near to quenching products // Journal of the Visualization (Japanese). 2006. Vol. 26, No. 2. P. 151-154.

6. **Takahiro Suzuki, Dong-Ying J.U.** Cooling performance evaluation and visualization of thermal flow in gas cooling process // Journal of the Visualization (Japanese). 2006. Vol. 26, No. 2. P. 155-158.

7. **Dong-Ying J.U., Takahiro Suzuki, Youichi Watanabe, Takashi Sugioto.** Visualization of Thermal Flow and Surface Temperature Filed of Quenched Material in Gas-Quenching Process // Journal of the Visualization (Japanese). 2007. Vol. 27, No. 2. P. 35-36.

## FRACTODIAGNOSTICS: TASKS AND METHODS

L.R Botvina

A.A.Baikov Institute of Metallurgy and Materials Science. Moscow, Russia

lbotvina@imet.ac.ru

The need for the development of new interdisciplinary strength science - fractodiagnosics is justified. The subject of study of this science is a specimen fracture surface, and the goal is a qualitative and quantitative description of the loading history that caused the fracture.

The tasks and methods of fractodiagnosics used for the analysis of static, cyclic and dynamic loading are considered. They allow to estimate by the fracture surface parameters the duration of the development of a fatigue crack, the nominal stress, which resulted in fracture, the critical temperature of brittleness and the critical values of other characteristics controlling fracture in the interval of ductile- brittle fracture. The mechanisms and stages of crack growth at mixed loading modes, as well as in conditions of corrosion medium are studied. The fractographic features of crack growth caused by material structure and a local stress state are revealed; general regularities of fracture surface formation at different scale levels are established. The fracture criteria characterizing macro- and microrelief of fracture surfaces at various stages of cyclic, static and dynamic loading are proposed.

**Keywords:** fractodiagnosics; fracture surface; failure analysis; fracture mechanism; loading history.

### INTRODUCTION

In some cases, factors acting on the structural element and not taken into account in the calculation lead to accidental fracture. The study of the history of such failures and the identification of the cause of the accident makes it possible to optimize the construction or material structure and justify the frequency of monitoring of the structural elements. A fracture surface contains a lot of information about the loading history. Already in the 16th century, the fracture surface was used to assess the quality of the metal. In 1722 R.A. Reomeur began to use a microscope to study the macro- and microrelief of fracture surface and proposed the classification of fracture surface. In our country, the first studies on the analysis of fracture surface are associated with the name of D.K. Chernov, who assessed the quality of heat treatment of the metal by appearance of fracture surface.

### OBJECTIVES AND METHODS OF FRACTODIAGNOSTICS

Electron microscopy has given new impetus to the development of fractographic research. In our country, this happened in the early 70s, abroad – a few years earlier. What are the results of this 50-year period of intensive development of fractography?

1. The main mechanisms and types of fracture are identified. There are few of them, namely, dimples,

facets of cleavage and intergranular fracture, fatigue striations, ridges, scars, tongues, plateaus, beach marks and a number of particular features characteristic of individual materials and types of fracture, most of which are associated with the fracture of individual structural elements. Changes in the main mechanism of crack development under the action of various factors in different materials are studied. The models for the formation of fracture surface relief features are proposed. Thus, enormous qualitative fractographic information of a descriptive character has been obtained concerning a specific material and sample tested under specific conditions. Such information is important, but it is difficult to use it when analyzing the fracture of the same material under slightly different conditions.

2. Much less quantitative fractographic information allowing to associate fracture surface parameters with characteristics evaluated by other methods, namely, by methods of X-ray structural analysis, acoustic emission, methods of fracture mechanics and analysis of the structure of the material was obtained. There are a small number of works in which the fractograms are processed by statistical methods.

3. So far, few methods have been proposed that allow evaluating some characteristics of a material based on using the fracture surfaces of structure elements appeared in service conditions. However, they require careful verification by statistical processing and stand testing.

4. Despite the fact that there is tremendous fractographic information related to certain materials and certain types of loading, there is almost no works devoted to the general laws of formation of the fracture surface relief for different types of loading. This impoverishes our understanding of the process of fracture, does not allow us to use in this analysis the general approaches that are addressed in other areas of science and technology.

In other words, to solve problems of diagnostics using fracture surface, a scientific basis is needed. In [1], the necessity of creating a new interdisciplinary strength science – fractodiagnostics, the subject of study of which should be a fracture surface and the goal is a qualitative and quantitative description of the loading history that caused the fracture is based.

Highlight fractodiagnostics into a separate section of materials science (similarly pathology anatomy in medicine) will contribute to its development and solving the problem of ensuring the reliability of the material of a structure.

Fractodiagnostics should combine many areas in strength, micro- and macro-mechanics of fracture, material science, and physics of solid. It should link the strength and kinetic parameters of fracture development with the characteristics of fracture surface relief and general fracture regularities under static, dynamic, cyclic loading at low and high temperatures, under conditions of friction and wear, the action of corrosive media, vacuum and other factors. Within the framework of fractodiagnostics, particular and general fractographic regularities of crack development in various materials should be found.

These regularities must be associated with the structure of the material and its damage, strength parameters, the rate of crack development and the size of the plastic zone, with the characteristics evaluated by calculation and also experimental laboratory testing.

Qualitative and quantitative methods of macro- and microanalysis of fracture surface using optical and scanning electron microscopy, X-ray diffraction and fractal analysis methods, as well as physical methods of non-destructive testing can be used as methods of fractodiagnostics, allowing to assess the material damage and the crack length.

One of the fundamental tasks of fractodiagnostics should be the assessment the stages of the crack development process by fracture surface and the description of the microrelief that characterizes each stage. Assessment of the stages of development of fracture and transitional values of strength characteristics seems to be necessary both for understanding the nature of the process of fracture under various types of loading, and for establishing the relationship

between physical and mechanical approaches to its analysis. This interrelationship is required to ensure the reliability of the structure, improve its calculation methods and damage diagnosis.

The results of such studies, including the study of the kinetics of the fracture process in steels, aluminum and titanium alloys under cyclic, static and dynamic loading using the methods of fractography and fracture mechanics, are set out in [1–3].

The stages and mechanisms of crack development are studied, the transitional values of fracture parameters that control the transition from one stage to another are evaluated, and the relationship of these parameters with fracture characteristics, plastic zone kinetics at the crack tip and loading conditions is established.

The mechanisms and kinetics of crack growth under conditions of corrosion medium, as well as under mixed loading modes, are considered. New methods of diagnostics have been developed, which enable to restore the loading history using the parameters of fractures of parts and structural elements, estimate the duration of fatigue crack growth, the critical temperature of brittleness and the nominal stress at which failure occurred.

Investigation of the crack development process revealed not only the features of crack growth in structural materials caused by the structure of the material and loading conditions, but also some common patterns of the fracture process, which are reflected in many particular strength effects and in a certain stages of crack growth.

The existence of common patterns of fracture formation is confirmed by the fact that many, if not all, features of fracture surfaces of rocks are similar to those observed on fracture surfaces of metal specimens. In rocks, just as in metallic materials, for example, under certain conditions, a ductile-brittle transition occurs, which is associated with the intensity of tectonic deformation [4].

The identification of such a transition by analysis fracture surfaces provides information on geological phenomena associated with a change in tectonic deformation, in particular, with a change in seismicity. In this case, information on tectonic processes occurring in the earth crust many years ago can be obtained from fracture surfaces.

However, the works devoted to the detailed description of fracture surfaces of rocks are still few, so the fractographic approach is only beginning to be widely used in tectonophysics and the results of its use are much more modest compared to the results obtained on metals. So far, the terminology is being clarified, the mechanisms are classified, and possible hypotheses are expressed.

Thus, a new field of science should unite specialists studying the process of fracture surface formation at various scale levels, differing in several orders, from microscopic to global, including the formation of fracture surfaces in mountain regions.

The development of fractodiagnostics of different-scale objects should make it possible to understand the general laws of the process of fracture and to establish the relationship between the calculated, predictable and actual characteristics of materials in different loading conditions. This will contribute to the development of mechanical engineering and tectonophysics, as well as an understanding of the fundamental properties of nature.

*The study was carried out with the support of the Russian Science Foundation, project No. 19-19-00674.*

## REFERENCES

1. **Botvina L.R.** Fracture kinetics of structural materials. Moscow: Nauka, 1989. P. 230.
2. **Klevtsov G.V., Botvina L.R., Klevtsova N.A., Lymar' L.V.** Fractodiagnostics of fracture of metallic materials and structures. Moscow: MISiS, 2007. P. 260.
3. **Botvina L.R.** Fracture: kinetics, mechanisms, general regularities. Moscow: Nauka, 2008. P. 334.
4. **Bahat D.** Tectonofractography. Berlin, Heidelberg, New York, London: Springer – Verlag, 1992. P. 354.

# THE TRIBOLOGICAL PROPERTIES OF THE HEAT RESISTANT STEEL AFTER A COMPLEX THERMO-CHEMICAL TREATMENT

M.Yu. Semenov<sup>1</sup>, A.E. Smirnov<sup>1</sup>, A.S. Mokhova<sup>1</sup>, A.P. Alekhin<sup>1</sup>

<sup>1</sup>Bauman Moscow State Technical University, Moscow, Russia  
Semenov.m.yu@bmstu.ru

Tribological properties of the dispersion-hardened heat resistant Cr-Ni-Mo-martensitic steel have been investigated after vacuum carburizing, heat treatment and final nitriding by the glow discharge technology. This steel is heat resistant up to temperatures higher than 450 °C, hence final nitriding is possible. This complex thermo-chemical treatment has some advantages over common carbonitriding and pre-nitriding carburization. The properties after complex treatment were compared with properties of the steel after carburizing and heat treatment. The dry friction coefficient after complex treatment was 0.3–0.4, i.e. lower than dry friction coefficient of carburized samples which is equal to 0.7–0.8. Surface hardness values of completely treated samples and samples after carburizing were equal to 1000 and 830 HV respectively. The wear intensity of carburized samples after subsequent nitriding was decreased by 3 times (from  $0.89 \times 10^{-10}$  up to  $0.27 \times 10^{-10}$ ). One can presume that the resistance to seizing of steel would also increase significantly after complex treatment. At the same time values of the contact fatigue resistance of completely treated samples and carburized samples in the same conditions with a lubrication are practically equal (near 1750 MPa). This equality shows that the contact fatigue resistance depends mostly on strength of carburized layer but not on the surface hardness. According to our theoretical study the maximum of contact stress highly dependent on the friction coefficient. So, the performance of complexly treated samples under conditions of high friction, temperature and stress can be determined only after dry abrasive wear tests. Furthermore, the complex thermo-chemical treatment was used for a new dispersion-hardened steel alloyed by Co and rare earth elements. The surface hardness after the treatment was 900–950 HV, but the carburized layer and core hardness both decrease by 25–30 HV.

**Keywords:** heat resistant steel; friction; wear; carburizing; nitriding.

## INTRODUCTION: A COMPLEX HEAT TREATMENT

The efficiency of modern high-loaded and high-speed gears for aerospace and automotive applications is determined mainly by such properties of the surface layer of wheels as contact endurance, resistance to abrasive and adhesive wear, and seizure resistance. Primarily, a chemical-thermal treatment, commonly the carburizing or carbonitriding, is used for surface hardening of such parts, which allows to obtain extended diffusion layers with high carbon concentrations. The thermochemical treatment is followed by hardening heat treatment. In some cases, carburizing or carbonitriding may be replaced by nitriding in a glow discharge, providing greater resistance to wear due to especially high surface hardness [1].

However, as well known, a contact endurance of nitrified layers usually does not comply to the performance requirements. The complex thermo-chemical treatment combines the advantages of carburizing (the high contact endurance) and nitriding (the high wear resistance) [1].

It should be noted, that not every steel may be subjected to nitriding after vacuum carburizing and heat treatment. The necessary steel must have a heat resistance of at least 450 °C and did not lose the hardness of martensite after ion nitriding. The example of such steel is dispersion-hardened complex-alloyed steel, containing a large amount of stabilizing austenite nickel and molybdenum. The presence of chromium, molybdenum, tungsten, vanadium, and niobium provides large amount of hard carbide particles after carbon saturation [2].

It should be noted that conducting of expensive thermal and thermochemical treatment in low-pressure atmospheres for high-quality steel is in accordance with modern concepts. The high-quality steel must be subjected to an advanced processing to realize completely its innovative potential [3].

The idea to provide the complex thermo-chemical treatment was proposed firstly by Gorockiewicz et al [4]. However, only a special steel alloyed by 9.5% Ni and 18% Co entitled as Ferrium C61 was subjected by such treatment. The surface hardness of steel was equal to 70 HRC (1100 HV).

This study is aiming to determine properties of steel after complex thermo-chemical treatment.

## MATERIALS AND METHODS

Composition of steel used to this research is shown in Table 1.

### Methods

The complex thermo-chemical treatment combined consists of carburizing in low pressure (vacuum carburizing) acetylene atmosphere during 5 hours (C), tempering during 6 hours (T), quenching in an argon stream (Q), triple tempering during 1.5 hours (T), and cold treatment during 2 hours (CT). The nitriding treatment (NT) in a glow discharge atmosphere of 95% N<sub>2</sub> + 5% H<sub>2</sub> was applied as finishing treatment. Nitriding duration was 15 h at pressure of 500 Pa and cathode voltage of 400 V (Fig. 1). Associazione Italiana di Metallurgia. All rights reserved. Super Duplex Stainless Steels (SDSSs).

In this work, the acetylene feed rate during cyclic carburizing was developed in a two-cycle fashion to provide a high value of contact fatigue endurance. The first group of cycles with long booster stages provides the intensive carbon saturation of the surface, while the second group of cycles with brief booster stages provides the diffusion redistribution of the carbon concentration and saturation of the near-surface region of the layer. This sequence of cycles provides an extended carbide saturated region; smooth

carbon distribution; and, as a result, smooth hardness distribution. This structure of the diffusion layer contributes to the high limit of the contact fatigue endurance. Nitriding in glow discharge was used as the additional modification of the surface layer. The nitriding process temperature must not exceed the temperature of the final tempering; this prevents the softening of the hardened layer and core during nitriding.

Metallographic analysis was carried out using an Olympus GX-51 microscope with 200× and 500× magnifications. Specimen surfaces for light microscopy were prepared by standard technique. Duro-metric analysis included hardness measurements of the samples surfaces by Rockwell using the TP5006-02 device at a 150 kg load and microhardness measurements using the DuraScan device at a 0.1 kg load. Standard etchant to reveal the microstructure of steel was 3–5% HNO<sub>3</sub> solution in C<sub>2</sub>H<sub>5</sub>OH.

The contact fatigue endurance was determined using rotating samples with diameters of 30.2 mm and widths of 18 mm in accordance with the rolling-sliding pattern (Russian standard GOST 25.501–78) using the Sh-17 double contact roll machine. The sliding velocity, type of oil, and its temperature were selected to be close to the operational conditions of high-loaded and high-speed gear wheels. The total rolling rate was 25.47 m/s. The sliding velocity on the lagging surface of the roller was 0.75 m/s, while the specific slide on this surface was 6.1%. An industrial oil grade of I-20A was used in the contact zone of the rolls with the counter bodies to provide necessary lubrication.

Table 1. Chemical composition of steel 13Kh3N3M2VFB-Sh

CONTENT OF ALLOYING ELEMENTS, WT%											
C	Cr	Ni	Mn	Mo	W	Si	V	Nb	Al	S	P
0.10–0.15	3.0–3.4	2.7–3.0	0.3–0.6	1.9–2.3	0.2–0.5	0.17–0.37	0.05–0.15	0.05–0.15	≤0.04	≤0.015	≤0.025

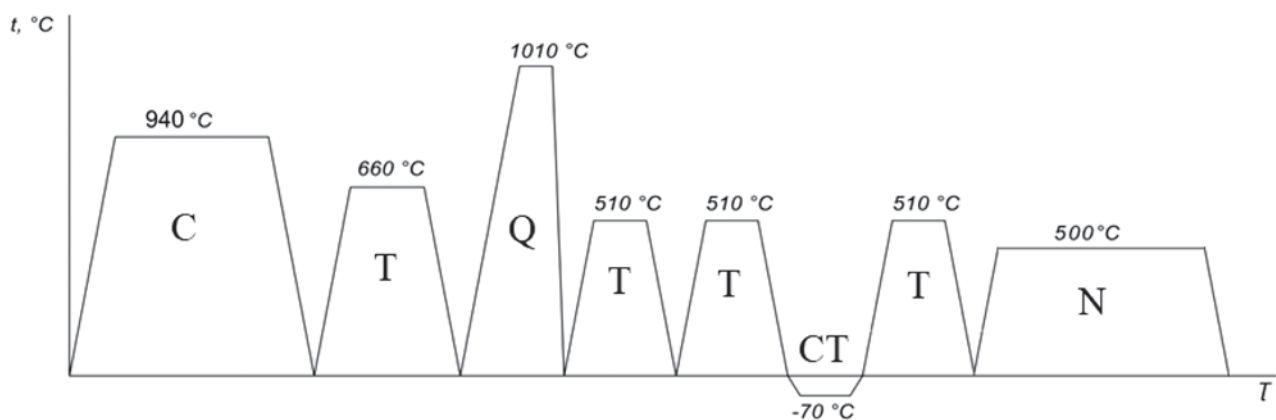


Fig. 1. A complex treatment of steel

The wear resistance was determined on prismatic samples with dimensions of  $12 \times 6 \times 4$  mm. The eight-position test bench developed at the Blagonravov Institute of Machines Science Russian Academy of Sciences was used, which involves the reciprocating motion of matching samples with flat friction surfaces and plastic lubricant grade Litol-24. Average speed in the friction couple was 0.19 m/s and the distance of sample motion was 40 mm. Quenched high carbon steel with a hardness of 59–60 HRC was used as a counter body. The wear of the hardened layer was determined based on the test result within 15 h at a pressure of 10 MPa (705.6 N). The value of the wear intensity was determined according to Russian Standard GOST 27674–88 by calculating the weight loss during the test.

A dry friction coefficient and dry wear intensity were determined using a tribometer NANOVEA in conditions of normal load of 30 N and rotational speed of 300 rpm. Steel balls ( $\varnothing 3.5$  mm) with hardness of 59–60 HRC were used as counter body.

## Results and discussion

After vacuum carburizing, strengthening heat treatment, the samples microstructure includes martensite, carbides of the cementite type, and fine particles of Cr, Mo, W, V, and Nb carbides.

The microstructure of the diffusional layer of steel 13Kh3N3M2VFB-Sh after the complex thermochemical treatment includes external dark-etching nanostructured nitrided zone and the internal carburized layer (Fig. 2). The boundary between the layers is quite clear. So, the thickness of the nitrided zone can be easily determined. The thickness of the nitrid-

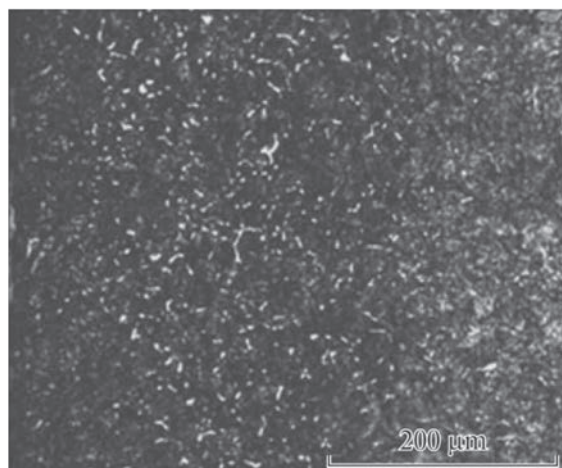


Fig. 2. Microstructure of 13Kh3N3M2VFB-Sh steel after vacuum carburizing at 940 °C for 5 h, strengthening heat treatment, grinding, and nitriding in glow-discharge at 500 °C for 15 h x 500

ed zone in the samples is about 0.25 mm according to the measurement results. It is necessary to mention, that there is not any hard nitride layer formed on the sample surface due to the selected nitriding mode.

After carburizing, and hardening heat treatment hardness is equal to 63 HRC. The measurement of the layer hardness after the complex thermochemical treatment by the Rockwell method gave only 62 HRC due to the small thickness of the nitrided layer. However, the measurement of the nitrided layer microhardness gave more 1000 HV (this is near to 66 HRC). For comparison, the Vickers hardness of carburized layers is equal to 830 HV. The hardness curves are represented in Fig. 3.

The average value of the contact fatigue endurance limit of 13Kh3N3M2VFB-Sh steel samples after the complex thermochemical treatment was 1754 MPa. Interesting, that after nitriding contact fatigue endurance limit value of this steel is equal to 1580 MPa. A contact fatigue endurance limit value of complex-alloyed heat-resistant steel 16Kh3N3MF-BAYu-Sh after vacuum carburizing estimated by the described method was only 1763 MPa [1].

Simultaneously the wear intensity of steel 13Kh3N3M2VFB-Sh samples after the complex thermochemical treatment was determined as  $0.31 \times 10^{-10}$ . For comparison, a wear intensities of this steel hardened samples after the carburizing process and the nitriding process is equal to  $0.27 \times 10^{-10}$  and  $0.89 \times 10^{-10}$ , respectively [1].

It should be noted, that effective contact stresses on the surface increase significantly with friction increasing according to theoretical calculations results [5]. The effective contact stresses determine the performance of gears both in terms of resistance to wear and seizure, and contact endurance.

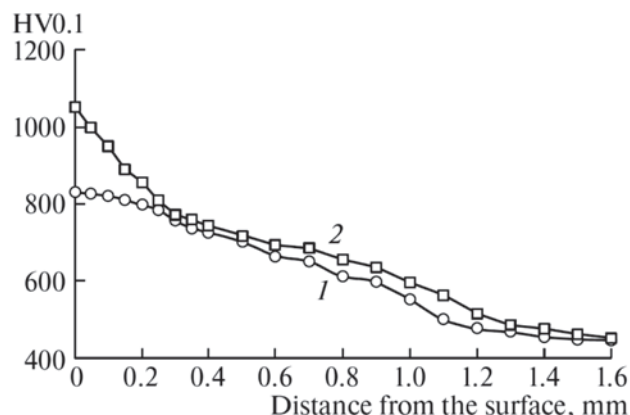


Fig. 3. Distribution of microhardness over distance from surface of 13Kh3N3M2VFB-Sh steel sample (1) after vacuum carburizing, strengthening heat treatment, and grinding and (2) after complex thermochemical treatment

Consequently, it is very important, that the dry friction coefficient after complex treatment is equal to 0.3–0.4, i.e. lower than dry friction coefficient of carburized samples which is equal to 0.7–0.8. The decrease of friction coefficient can be explained because of adhesion decrease after the finishing nitriding [5]. In the same time a dry wear intensity was reduced from  $1.02 \times 10^{-7}$  after vacuum carburizing, and quenching, to  $0.58 \times 10^{-7}$  after the complex thermo-chemical treatment.

So, the combined performance of complexly treated samples in conditions of high friction, temperature and stress can be determined only after dry abrasive wear tests in high load, and high temperature.

The complex thermo-chemical treatment was applied for high-loaded turbopump engine gears. Furthermore, the complex thermo-chemical treatment was used for a new dispersion-hardened steel alloyed by cobalt and rare earth elements [6]. The surface hardness after the treatment was 900–950 HV, but the carburized layer and core hardness both decrease by 25–30 HV. An ultimate strength is equal to 1935 MPa at least, and a heat resistance no worse than 500 °C, for aircraft applications. Due to microalloying by rare earth elements an accelerated process of vacuum carburizing at a high temperature (980 °C) prevents formation of a carbide grain-boundary network, which is inadmissible for the required level of contact fatigue resistance of gears.

Also, the complex thermo-chemical treatment has some advantages over common carbonitriding and pre-nitriding carburization. First of all, we have to decrease a temperature of the carbonitriding to 880 °C. So, the velocity of a diffusional saturation by carbon and nitrogen atoms will be also strongly decreased according to exponential law in respect of temperature. Also, we can not achieve the nitrogen concentration on the surface more than 0.2–0.3 mass %. The final hardness of surface not very differ from carburized layers.

The pre-nitriding can be used only to decrease austenite grain size. Free nitrogen atoms will diffuse from the surface under a carbon gradient influence and the nitrogen can not achieve significant concentrations in the layer.

## CONCLUSIONS

The complex thermo-chemical treatment of the dispersion-hardened heat resistant Cr-Ni-Mo containing martensitic steel allows to achieve the hardening effect, which was previously achieved on a cobalt alloyed steel only by Gorockiewicz et al [4].

The complex thermo-chemical treatment of the dispersion-hardening steel provides wear resistance in conditions of lubrication like nitrided layers and much larger than carburized layers. At the same time the contact fatigue resistance of steel 13Kh-3N3M2VFB-Sh after the complex thermo-chemical treatment near equal to contact fatigue endurance of carburized layers.

Furthermore, the decrease of the dry friction coefficient and dry wear intensity could give great opportunities especially for use in aerospace and automotive applications.

Some modes of complex thermochemical treatment are recommended for special cobalt containing steel with additionally micro-alloying by rare earth metals for aviation and space applications.

## REFERENCES

1. **Smirnov A.E., Mokhova A.S., Semenov M.Yu., Kuxsenova L.I., Fakhurtdinov R.S.** Mixed-Surface Impregnation of Gear Wheels Made of 13Kh3N3M2VFB-Sh Age-Hardenable Integrally Alloyed Steel Aimed at Improving Surface Hardness, Wear-Resistance, and Back-to-Back Endurance // *Journal of Machinery Manufacture and Reliability*. 2017; 46: 404–408. Available from: <http://dx.doi.org/10.3103/S1052618817040173.01.09.2017>.
2. **Lashnev M., Smirnov A.E., Semenov M.Yu.** Use of vacuum carbonitriding for raising the seizure resistance of gears from steel VKS-10 // *Metal Science and Heat Treatment*. 2013; 55: 29–33. Available from: <https://doi.org/10.1007/s11041-013-9574-z.09.05.2013>.
3. **Otto F.J., Herring D.H.** Vacuum carburizing of aerospace and automotive materials // *Heat Treating Progress*. 2005; 5.1: 33–37.
4. **Gorockiewicz R., Adamek A., Korecki M.** Steels for vacuum carburizing and structure of the carburizing layer after low pressure carburizing. *Industrial Heating // The International Journal of Thermal Technology*. 2007; 16.
5. **Semenov M.Yu.** Assessing the impact of the conditions of friction in the contact endurance of gears from a complex-alloyed heat resistant steels subjected by thermo-chemical treatment (in Russian) // *Problemy chernoj metallurgii i materialovedeniya*. 2015; 1: 70–79.
6. **Smirnov A.E., Fakhurtdinov R.S., Semenov M.Yu., Gromov V.I., Kupryakova N.A., Seval'nev G.S.** Application of complex thermochemical treatment for reinforcing high-strength precipitation-hardening heat resistant steel microalloyed with REM // *Metal Science and Heat Treatment*. 2018; 60: 450–453. Available from: <https://doi.org/10.1007/s11041-018-0299-x.04.12.2018>.

# EFFECT OF COMBINED GAS NITRIDING AND DEEP CRYOGENIC TREATMENT ON WEAR BEHAVIOUR OF AISI D2 STEEL

David Hradil<sup>1</sup>, Michal Duchek<sup>1</sup>, Miroslav Šugár<sup>1</sup>, Piotr Nawrocki<sup>2</sup>

<sup>1</sup> COMTES FHT. Czech Republic

<sup>2</sup> IMP WARSAW. Poland

dhradil@comtesfht.cz, mduchek@comtesfht.cz, msugar@comtesfht.cz, piotr.nawrocki@imp.edu.pl

Gas nitriding conducted in ammonia atmosphere with subsequent heat treatment in combination with deep cryogenic treatment (DCT) produces unique nitrided layers with higher wear resistance. Layers with specific properties result from the dissolution of subsurface layers of iron nitrides and subsequent nitrogen diffusion into the substrate during austenitization. Deep cryogenic treatment is used between the quenching and tempering steps. Fine precipitates of carbonitrides are formed during DCT and the tempering process. The aim of the research is comparing the novel nitrided layers with conventionally nitrided layers. The experimental steel was AISI D2 with equivalents DIN 1.2379 / X153CrMoV12. Different approaches of nitriding were evaluated and compared based on hardness measurement and the extensive wear testing by the Pin-On-Disc and 3 rolls cone methods in different conditions of testing (load, temperature, duration, etc.). The higher wear resistance were proved in inverse approach of nitriding. New approach of gas nitriding leads to considerable savings in processing time.

**Keywords:** AISI D2; gas nitriding; Deep cryogenic treatment; Pin-On-Disk; 3 rolls cone.

## INTRODUCTION

Process of gas nitriding is the most common process of nitriding, there are also other possibilities, i.e. plasma nitriding, molten salt baths nitriding or nitriding in appropriate powders. This process is usually used in the machinery or toolmaking industries to obtain better tribological properties and fatigue performance of steels, the characteristics are achieved by compressive stresses generated in the surface.

The gas nitriding process for most of the tool steels takes place at relatively low temperatures ranging from 490 to 590 °C. The most common temperatures are between 500 and 520 °C. The main reasons for choosing of these low temperatures are influence on transformation temperatures in Fe-N diagram (limited to temperature 590 °C) and impact of tempering temperature that is usually before nitriding. Tempering temperature must be higher than nitriding temperature, i.e. about 30 ÷ 50 °C. Otherwise, there will be risk of unwanted tempering of the steel during the nitriding process, resulting in the decrease in the core hardness. The disadvantage of gas nitriding at low temperatures is the necessity of very long periods of tens of hours to achieve the desired thickness of the nitriding layer with required microstructure known as the  $\alpha$ -phase. Nitrogen diffusion is very slow at low temperatures. Another reason for this slow and relatively long lasting process is preven-

tion of creating of the compound layer (composed by  $\epsilon$ -phase ( $\text{Fe}_3\text{N}$ ) and  $\gamma'$ -phase ( $\text{Fe}_4\text{N}$ )). Compound layer is not required in case of nitriding sharp or very difficult shapes tools. Compound layer is very hard, but also very brittle, the edge breaking can follow after inappropriate nitriding. To decrease period of nitriding, higher temperature of nitriding is used. At the increased temperatures, the nitrogen saturation is faster. In view of the risk of significantly lowering the core of the material during nitriding at elevated temperatures, increasing the nitriding temperature is not optimal. From this point of view, a procedure where nitriding precedes quenching and tempering processes seems to be very suitable [1–3].

Hardening of nitrided layer consists in heating the part (the austenitization) followed by rapid cooling by overpressure of shielding gas or other quenching medium. As a result of this heat treatment process, a martensitic structure is forming in the region of the nitrided layers which is additionally hardened by aging. During austenitization, nitrogen is migrated to the subsurface, resulting in (M)-C-N carbonitrides with different structural properties from the original nitrided layer. An important process is also the tempering, which is in the inverse nitriding process carried out in an active atmosphere of dissociated ammonia. The reason for tempering in the dissociated ammonia is to prevent further migration of nitrogen to greater depth from the surface of the component. Temper-

ing in an atmospheric furnace would result in a local depletion of the subsurface layer by nitrogen, thereby significantly reducing of the subsurface hardness in the nitrated layer. Several procedures are available for steel hardening. Their detailed descriptions are given in [4, 5].

Deep cryogenic treatment (DCT) is defined as an add-on process to conventional heat treatment, with process temperature up to  $-196\text{ }^{\circ}\text{C}$ , with holding times in range of hours to days. It is generally used for increasing the hardness in the sub-surface layer, reduction amount of retained austenite, stabilizing martensite for dimensional and geometric stability of the precision parts, to improve wear resistance for most of steel grades. DCT is in most cases applied between quenching and tempering process. The reason for this order is to promote grain refinement and precipitation of fine carbonitrides contain the alloying elements [6].

According Stratton [7], DCT leads to several microstructural changes, below  $-130\text{ }^{\circ}\text{C}$ , retained austenite transforms to martensite same way as in cold treatment ( $-80\text{ }^{\circ}\text{C}$ ). Cooling down to deepest temperature (up to  $-196\text{ }^{\circ}\text{C}$ ) causes decomposition of primary martensite by time-dependent transformation. It resulted in the nucleation of plenty coherent nanometric carbides. These processes are starting during DCT, however the process is done during tempering period. The considerable improvement in wear resistance is supposedly caused by newly-formed carbides. DCT improves wear resistance in the most steel grades and lead to longer lifetime of tools [8, 9]. AISI D2 steel was investigated in several studies, the deepest one was conducted by Das et al. [10–12]. One of their biggest survey was mapping of time at  $-196\text{ }^{\circ}\text{C}$ , that will lead to highest wear resistance. The wear resistance grown up to holding time 36 hours. This type of tool steel is used for various industrial

Table 1. Chemical composition of experimental steel

Chemical composition, wt. %									
C	Si	Mn	Cr	Ni	Mo	V	W	P	S
1.58	0.39	0.32	11.51	0.14	0.80	0.94	0.038	0.017	0.001
Cu	Al	Co	Nb	Ti	B	Fe			
0.043	0.004	0.026	0.013	0.014	<0.001	bal.			

application, e.g. stamping or forming dies, punches, blades for knives and shears and tens of others.

## MATERIAL AND METHODS

The chemical composition of steel AISI D2 (with equivalents DIN 1.2379 / X153CrMoV12) used in this experiment is given in Table 1. Its chemical composition was measured using the Q4 TASMAN optical emission spectrometer (Bruker Elemental GmbH, Germany). The thermochemical treatment (TCT) was based on conventional gas nitriding at relatively low temperature ( $515\text{ }^{\circ}\text{C}$  / 24 hours) combine with DCT ( $-170\text{ }^{\circ}\text{C}$  / 12 hours), as a spare variant were used inverse nitriding at increased temperature ( $580\text{ }^{\circ}\text{C}$  / 6 hours) also combine with DCT ( $-170\text{ }^{\circ}\text{C}$  / 12 hours). Conventional approach of nitriding were conducted after hardening and tempering. Inverse approach of nitriding were conducted with nitriding as a first operation, followed with subsequent hardening and tempering in active ammonia atmosphere ( $530\text{ }^{\circ}\text{C}$  / 5 hours). Details about temperatures, dwell times,  $\text{NH}_3$  dissociation, etc. are shown in Table 2. Main reason for tempering in active ammonia atmosphere (with increased dissociation 70%) was to prevent nitrogen diffusion into the substrate of the steel, which would caused nitrogen depletion of the subsurface area. The experiment was based on a comparison of the properties of both

Table 2. Sequence information, detail of used TCT process parameters

Sequence designation	Sequence information					NH <sub>3</sub> diss. (%)	
<b>Conventional nitriding (+ DCT)</b>							
N24	Austenitizing 1040 °C / oil	–	Tempering 540 °C / 2 hours	Nitriding 515 °C / 24 hours		30	
N24C	Austenitizing 1040 °C / oil	DCT 170 °C / 12 hours	Tempering 540 °C / 2 hours	Nitriding 515 °C / 24 hours		30	
<b>Inverse nitriding (+ DCT)</b>							
N6	Nitriding 580 °C / 6 hours	Austenitizing 1040 °C / oil	–	Tempering in ammonia 530 °C / 5 hours	45	70	
N6C	Nitriding 580 °C / 6 hours	Austenitizing 1040 °C / oil	DCT 170 °C / 12 hours	Tempering in ammonia 530 °C / 5 hours	45	70	

nitriding approaches, and at the same time, the effect of cryogenic processing was observed. DCT was always applied in selected modes immediately after hardening. All nitriding processes were carried out in ammonia gas in container placed in a pit furnace. The treatment was controlled by regulating the ammonia flow, and monitored using water-based dissociation meter for measuring content of dissociated ammonia. Hardening was carried out in atmospheric furnace, quenched to the oil. Deep cryogenic treatment was performed in CES-CTC (C.E.S NV, Belgium) cryogenic chamber. The specimens were prepared by means of standard metallographic techniques of grinding and subsequent polishing. The microstructures were revealed by etching with 10% Nital. The microstructures were documented using a Zeiss Axio Observer (Carl Zeiss Microscopy GmbH, Germany) optical microscope. The Vickers hardness profiles were measured by Struers DuraScan-50 (Struers ApS, Denmark). The wear resistance was measured at the ambient temperature and elevated temperature 100 °C using Pin-On-Disc method. Another testing were conducted using 3 rollers-cone system with continuous lubrication of samples, at constant unit pressure of 100 and 200 MPa. By this method only sequences with inverse nitriding were tested. Conical counter-specimen was made of 100

Cr6 steel hardened to hardness 64 HRC and ground to a roughness  $Ra = 0.32 \mu\text{m}$  (same roughness as surface of tested specimens).

## RESULTS AND DISCUSSION

Metallographic analysis were done using optical microscope. Before etching by Nital, the samples were prepared by cutting perpendicular to the surface, embedded into resin by hot pressing and then there were ground and polished. The thickness of diffusion layer was measured using microscope software. According metallographic measurement the thickness of diffusion layer for conventional gas nitriding (Fig. 1) was 245  $\mu\text{m}$  for sequence N24 and 190  $\mu\text{m}$  for sequence N24C. Compound layer was up to 30  $\mu\text{m}$ . Inverse nitriding showing lowest thickness of diffusion and compound layer. Thickness of diffusion layer was measured using microscope software on value 120  $\mu\text{m}$  for both inverse sequence, compound layer was only 5  $\mu\text{m}$ . Microstructure is composed in all cases of TCT by tempered martensite and carbides undissolved during austenitization.

Hardness profile curves were measured using Vickers hardness HV 0.3 (Fig 2). Conventional gas

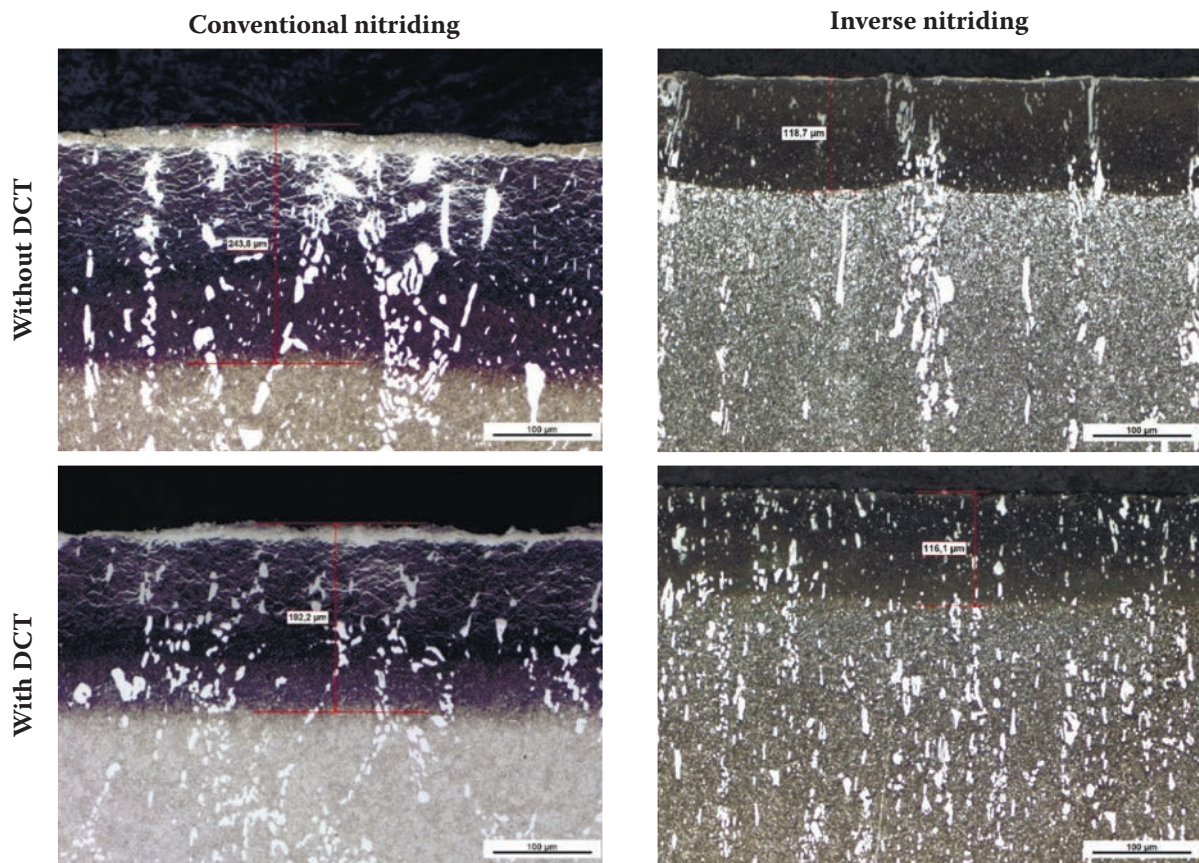


Fig. 1. Microstructure of nitrided layers (N24, N24C, N6 and N6C), with diffusion layer measurement by software

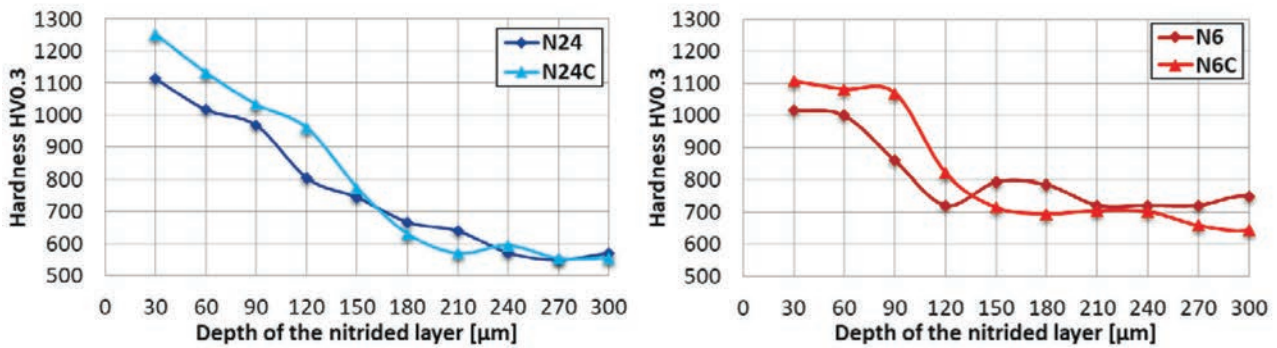


Fig. 2. Hardness curves for conventional nitriding (left) and inverse nitriding (right)

nitriding designated as N24C achieved subsurface hardness up to 1250 HV 0.3, it is approx. about 150 HV 0.3 higher subsurface hardness than after conventional nitriding without DCT. The core hardness of after conventional nitriding is almost similar from 550 to 580 HV 0.3. According Nht criterion (defined as a vertical distance from the surface to the point at which the hardness is still 50 HV higher than the core hardness) the depth of nitrided layer is 230 µm (N24) and 180 µm (N24C). These values correspond with microstructure software evaluation of the depth. DCT caused increased hardness in subsurface layer, it's probably caused by very small precipitates that increasing effect of nitriding including presence of α-phase and precipitation of nitrides (CrN).

Inverse nitriding has lower values of subsurface hardness. The maximum subsurface hardness is 1100 HV 0.3 for sequence N6C. There is same tendency for increased values of hardness in case of sequence with DCT. The difference we can find in stability and depth with increased amount of hardness. In case of sequence N6C the hardness is increased up to depth 90 µm. Core hardness is relatively higher comparing with conventional nitriding, for both sequences were achieved same value 650 HV0.3. This value according Nht correspond with depth 120 µm (N6) and 150 µm (N6C), the results almost correspond with microstructure software evaluation of the depth.

Deep cryogenic treatment is typically used for expected improvement in wear resistance. For testing of wear resistance were used 2 methods, pin-on-disc and 3 rolls-cone. The principle of pin-on-disc test is forcing a ball into the surface of a rotating flat specimen. The ball indenter was pressed by a defined force (exerted by a weight) against the specimen. AISI D2 is intended for cold working, there are also situation when materials are ex-

posed to the increased temperatures (e.g. high friction, impossibility of cooling or extreme working conditions). It was the reason why testing was conducted besides ambient temperature also at temperature 100 °C. The surface of the flat samples were prepared by grinding with waterproof SiC sanding paper (Grain size 15 µm) and then cloth for polishing (grain size 3 µm), surface loss was only 5 µm. The reason for surface grinding and polishing was inequality and insufficient roughness of the testing surface, integrity of the surface was not disturbed. Each testing for each sequence was done on 2 specimens.

The test parameters for all specimens were as follows:

- 6 mm diameter ball indenter (Al<sub>2</sub>O<sub>3</sub>)
- 13 N load
- 120 rpm
- 3 mm radius of wear track
- ambient temperature; 100 °C
- 15000 cycles / 276.75 m (number of cycles / path travelled by the ball indenter)

The wear rate was calculated from the test data using (1). The wear track volume was evaluated using a contact profilometer. Its value was found as the mean from 8 readings around the track.

$$W = \frac{\text{Wear track volume}[\mu\text{m}^3]}{\text{Load}[\text{N}] \times \text{Path travelled by ball indenter}[\text{m}]}$$

The result of the were rate are graphically showed in Fig. 3. The order of the columns is according TCT

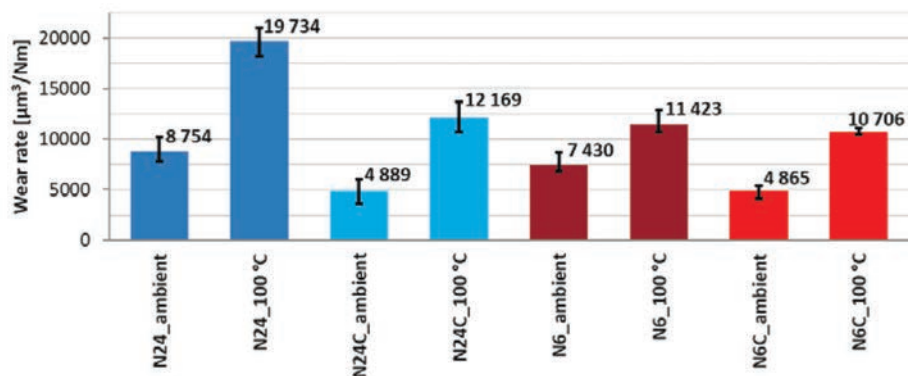


Fig. 3. Results of wear rate, 4 sequences (N24, N24C, N6, N6C), 2 testing conditions

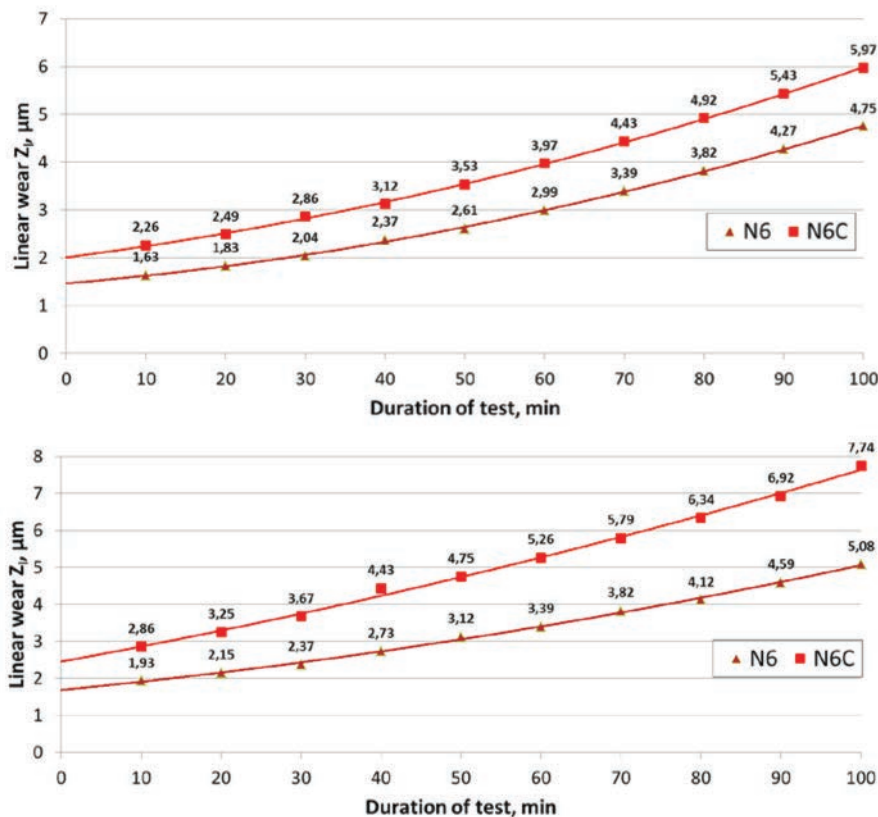


Fig. 4. Results of 3 rolls-cone testing, testing unit pressure 100 MPa (upper diagram) and 200 MPa (lower diagram)

sequence and testing temperature (ambient and 100 °C). When we compare only same nitriding regimes with or without DCT, we can see that sequences with DCT are more resistant (lower wear rate = higher wear resistance) than regimes without DCT. Most significant results are at ambient temperature. Wear rate is almost 45% lower compared to same nitriding (N24C) without DCT (N24). At the increased temperature of testing the tendency is similar, wear rates are lower about 38%. Sequences with inverse nitriding N6 and N6C showed the results comparable to conventional nitriding sequences. Samples treated with DCT has lower value of wear rate (35% for ambient temperature, 7% at 100 °C). Deviations of measurement (black lines) shows lowest and highest wear rate wear rate of each testing. We can see that more stable values are in case of inverse nitriding with DCT (N6C). The effect is probably caused by very stable hardness to depth in subsurface layer. The result show us, that measured hardness is only micro-characteristics of the material. Testing on Pin-on-Disc show us macro-characteristics of the material with relatively low loading force.

The 3 rolls-cone testing method were used for comparing with results from Pin-on-Disc test. Only sequences with inverse nitriding were tested. Testing of all sequences is planned in next investigation.

The results of wear resistance test in the form of diagrams of linear wear as a function of time are shown in Fig 4. For testing were used unit pressure 100 and 200 MPa. All samples were characterized by the wear with a regular course, manifesting the occurrence of steady friction state in the entire course of wear, except running-in period. From the diagram we can see the worst results for sequence with DCT (decrease approx. about 25% at 100 MPa loading and about 35% at 200 MPa loading). Process pressures and loads are significantly higher compared to Pin-on-Disc test. There results more correspond to real behavior of the nitrided layer and are more relevant for higher loading application. For better understanding of real wear resistance it is necessary conduct some industrial testing with real parameters of operating conditions on real

tools. All these methods show us only tendencies that can be different, influenced by process parameters of each type of tool.

## CONCLUSION

New approach to nitriding process is unique in order of the operation. This approach allow us increased temperature of nitriding, another innovation is tempering in reactive atmosphere. In this investigation deep cryogenic treatment were used for increasing of subsurface hardness. As we can see in hardness curves, both sequences with used DCT process shows better hardness properties in subsurface layer. This effect is caused by precipitation of finer carbides, that increased effect of newly formed nitrides due to nitriding. With nitriding at increased temperatures, the entire treatment can be shortened (by least 13 hours) which greatly reduces the cost and harmful gas emissions. After conventional nitriding with DCT, the hardness is approx. 150 HV 0.3 higher at subsurface area compared to a process without DCT. Inverse nitriding caused significant increase in hardness to depth, when we used DCT process, the hardness was approx. 1100 HV 0.3 up to depth 90 μm. The microstructure focused on diffusion layer

almost correspond with the depth of nitrided layers stated using Nht criterion.

Wear resistance testing were based on Pin-on-disc testing and 3 rolls-cone testing. Results of wear rate (Pin-on-Disc) showed higher wear resistance for sequences with used DCT process. The wear rate were lower up to 45%. This method used only very small forces, for better understanding of wear resistance method 3 roll-cone were used. There were tested only sequences with inverse approach of nitriding. From the results of linear wear we can see difference in both tests. 3 rolls-cone method shows significantly better results for sequence N6, which is without DCT. The worst result for DCT sequence can be caused by higher tempering temperature / decrease of macro hardness, that wasn't investigate. Pin-on-Disc method used small forces of loading, so this effect was not visible. For better understanding of real wear resistance it is necessary conduct some industrial testing with real parameters of operating conditions on real tools.

## ACKNOWLEDGEMENT

This paper was completed with support from the Inter-Eureka programme (LTE117 project "CRYO-NITRIDE") and programme "Development of West-Bohemian Centre of Materials and Metallurgy" No.: LO1412 financed by the Ministry of Education of the Czech Republic.

## REFERENCES

1. **Yeh S.H., Chiu L.H., Chang H.** Effects of gas nitriding on the mechanical and corrosion, properties of SACM 645 Steel // *Engineering*. 2011. 3. 942–948.
2. **Karamis M.B., Yildizli K., Aydin G.C.** Sliding/rolling wear performance of plasma nitrided H11 hot working steel // *Tribol. Int.* 2012. 51. 18–24.
3. **Conci M.D., Bozzib A.C., Franco A.R.** Effect of plasma nitriding potential on tribological behaviour of AISI D2 cold-worked tool steel. *Wear*. 2014. 317. 188–193.
4. **Ciski A., Wach P., Tacikowski J., Babul T., Šuchmann P.** Heat treatment of nitrided layer formed on X37CrMov5-1 hot working tool steel, In.: *COMAT 2016, Pilsen, IOP Conference Series // Materials Science and Engineering*. 2017. Vol. 179. P. 1–8, DOI: 10.1088/1757-899X/179/1/012013.
5. **Fattah F., Mahboubi F.** Comparison of ferritic and austenitic plasma nitriding and nitrocarburizing behavior of AISI 4140 low alloy steel // *Materials & Design*. 2010. Vol. 31, No. 8. P. 3915–3921, DOI: 10.1016/j.matdes.2010.03.008.
6. **Podgornik B., Paulin I., Zajec B., Jacobson S., Leskovšek V.** Deep cryogenic treatment of tool steels // *Journal of Materials Processing Technology*. 2016. 229. 398–406. DOI: 10.1016/j.jmatprotec.2015.09.045.
7. **Stratton F.P.** Optimizing nano-carbide precipitation in tool steels // *Materials Science and Engineering A449*. 2007. 809–812.
8. **Šuchmann P., Nižňanská J.** Deep cryogenic treatment of H11 hot working tool steel // *Journal of Achievements in Materials and Manufacturing Engineering*. 2015. 73/1. 21–26.
9. **Hradil D., Duchek M., Hrbáčková T., Ciski A.** Gas nitriding with deep cryogenic treatment of high-speed steel // *Acta Metallurgica Slovaca*. 2018. Vol. 24, No. 2. P. 187–193.
10. **Das D., Dutta K.A., Toppo V., Ray K.K.** Effect of deep cryogenic treatment on the carbide precipitation and tribological behavior of D2 steel // *Materials and Manufacturing Processes*. 2007. 22/4. 474–480.
11. **Das D., Dutta K.A., Ray K.K.** Correlation of microstructure with wear behavior of deep cryogenically treated AISI D2 steel // *Wear*. 267/9-10. 2009. 1371–1380.
12. **Das D., Dutta K.A., Toppo V., Ray K.K.** Inconsistent wear behavior of cryotreated tool steels: the role of mode and mechanism // *Materials Science and Technology*. 2009. 25/10. 1249–1257.

# COMBINATION OF THERMOCHEMICAL TREATMENT METHODS WITH ULTRASOUND

V.M. Prikhodko<sup>1,2a</sup>, D.S. Simonov<sup>2b</sup>, T.D. Dmitriev<sup>2c</sup>, Lotof Yassin Qeblawi<sup>2d</sup>

<sup>1</sup>Russian Academy of Sciences. Moscow, Russia

<sup>2</sup>MADI. Moscow, Russia

<sup>a</sup>prikhodko@madi.ru, <sup>b</sup>dimsimonov94@mail.ru, <sup>c</sup>916739@mail.ru, <sup>d</sup>lotof.qeblawi@gmail.com

The paper discusses the combination of thermochemical treatment of critical parts in transport equipment with ultrasonic action. Combined processes of surface modification, which combine thermochemical treatment and electro-physical action, allow obtaining the required operational properties unattainable by other technologies: fatigue strength, wear resistance, contact endurance and corrosion resistance. The combination of thermochemical process with ultrasound is carried out in two ways: when using process fluid, and with ultrasonic plastic deformation. Nitriding is used as the thermochemical treatment method; ultrasonic action is produced by special ultrasonic vibrating systems, which allow regulating the acoustic power in a wide range, from tenths to 50 W/cm<sup>2</sup>. The experimental results confirm the preliminary conclusions about the possibility of optimizing the nitriding process by its acceleration and increasing the case depth when exposed to ultrasound. Ultrasonic plastic deformation improves the roughness of the workpiece surface. Studies show that during the operation, the mechanical characteristics, including the fatigue strength of materials, largely depend on the state and properties of the surface layer, therefore, a reasonable choice and design of technological processes to get products with properties that best meet the conditions of operation is an actual problem.

**Keywords:** thermochemical treatment; nitriding; ultrasound; surface plastic deformation; magnetostrictive transducer; combined technologies; surface roughness; surface layer.

## INTRODUCTION

The actual modern trend of functional coatings formation is to develop combined technological processes using existing and new methods of steel surface modification, taking into consideration the operational requirements of products [1]. Ensuring required properties of product surface is an important component of improving the entire part quality, since many operational properties, such as wear resistance, fatigue strength, contact endurance, corrosion resistance, depend almost entirely on the state and properties of the surface layer. The formation of highly resistant modified layers and coatings on low-cost carbon and low-alloy steels contributes to an increase in the service life of products and reduces the consumption of materials used, the costs of their production and processing. This paper discusses the possibility of combining known methods of surface treatment – thermochemical and ultrasonic.

Both ultrasonic and thermochemical methods are widely used to improve the operational properties of product surface. Combining the advantages of multistage ultrasonic processing and thermochemical treatment allows using not only the positive technological manifestations of each of the methods, but also creating synergistic effects from the combined use of ultrasound and diffusion saturation [2].

Thermochemical treatment, as a rule, is accompanied by diffusion saturation of steel surface with some element (for example, carbon, nitrogen, aluminum, chromium, etc.). Saturation is carried out by the corresponding element diffusion from the external medium at high temperature.

## RESEARCH RESULTS

As known, [3] thermochemical treatment includes three elementary processes:

- dissociation – obtaining the diffusing element in an atomic state in a saturating medium as a result of chemical reactions;
- adsorption – the contact of the diffusing element atoms with the surface and the formation of chemical bonds with the metal atoms;
- diffusion of the saturating element atoms deep into the metal.

As a rule, the diffusion in the solid phase is the limiting stage of the saturation process. This stage determines the rate of formation of the diffusion layer (the surface layer of the part that differs from its core in chemical composition, structure, and properties). Diffusion layer thickness depends on the duration of the saturation process, the temperature and

concentration of the diffusing element in the saturating medium.

The most well-known thermochemical treatments are: carburizing, carbonitriding, cyaniding and nitriding. This paper focuses on nitriding in combination with ultrasound.

Nitriding is the process of diffusion saturation of metal surface layer with nitrogen. This is done to increase the hardness, wear resistance of the surface, endurance and resistance to corrosion in different environments.

Ultrasonic effect on process fluid has a significant impact on the results of the thermochemical treatment, contributing in most cases to obtaining effects that are not achievable under normal conditions without the use of ultrasound.

In this work, combined technological processes of ultrasonic and thermochemical treatment are investigated in order to form the functional properties of the surface layer on steels, taking into account the operational requirements of products. This task is carried out in a comprehensive manner by applying ultrasonic technologies at all stages of the formation of a modified layer by the thermochemical method: preliminary ultrasonic treatment before the thermochemical one for surface preparation, subsequent ultrasonic finishing after the thermochemical treatment, and simultaneous thermochemical treatment in a liquid medium with superimposed ultrasonic vibrations. It is planned to include in the combined processes the application of ultrasonic vibrations on the liquid medium, as well as ultrasonic surface plastic deformation. As already noted, the main type of thermochemical treatment used is nitriding, which is a low-temperature method that allows preserving both the preformed structure of the part core and the reinforcing effects that are achieved with preliminary ultrasonic treatment. During saturation with nitrogen and simultaneous ultrasonic treatment, phenomena associated with the activation of the release of dispersed nitride phases by the precipitation hardening mechanism are expected.

A distinctive feature of experiments with ultrasound is that we use an ultrasonic vibrating system of the original design that allows us to reach acoustic powers up to  $50 \text{ W/cm}^2$  and higher, which roughly corresponds to vibrations amplitude reaching 50 micrometers. The ultrasonic vibrating system is a 3x – half-wave vibrating system (Fig. 1), consisting of a sonotrode, a waveguide, a transducer – a magnetostrictor and a cooling jacket.

Surface plastic deformation is an effective method for hardening parts surface by creating compressive stresses on it [4]. The method of surface plastic de-

formation using an ultrasonic tool differs from conventional burnishing in that its tool vibrates with an ultrasonic frequency (approximately 22.000 Hz). During treatment, the tool is pressed against the surface to be treated with a constant force  $F_n$ . As with conventional burnishing, the tool moves over the surface by rotating the workpiece at a speed  $V_r$  and moving the tool along the generating line with a speed  $V_s$ , Fig. 2

The effect of ultrasonic pretreatment on the surface roughness is shown in Fig. 3, 4. With ultrasonic treatment, the average height of the surface irregularities decreases. A comparison of the surface roughness profiles of pre-hardened steel and ground steel 45 samples before and after ultrasonic treatment shows that ultrasonic treatment significantly changes the roughness. The surface acquires a more regular texture, and the average height of the peaks and valleys is significantly reduced. In particular,  $R_a$  has been decreased from 0.63 to 0.16 microns.

The pressing force  $F_n$  of the ultrasonic tool against the surface being processed has significant influence on the magnitude of surface roughness of the samples ( $R_a$  or  $R_z$ ) [5]. Smaller roughness values are achieved with lower pressing forces  $F_n$ .

To study the effect of ultrasonic waves on the process of nitriding in gaseous and liquid media, we chose structural carbon steel 35X10A, which is used in the manufacture of such parts as gears, pins, and

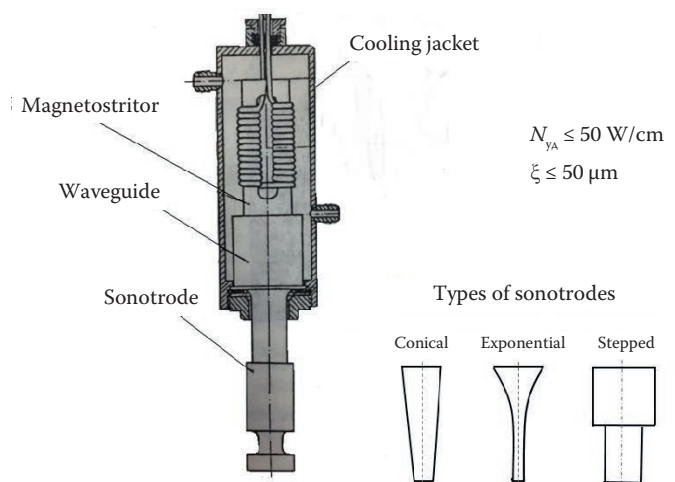


Fig. 1. Ultrasonic vibrating system (developed in MADI)

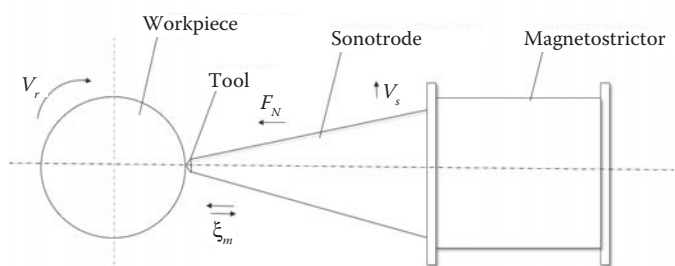


Fig. 2. Surface plastic deformation using an ultrasonic tool

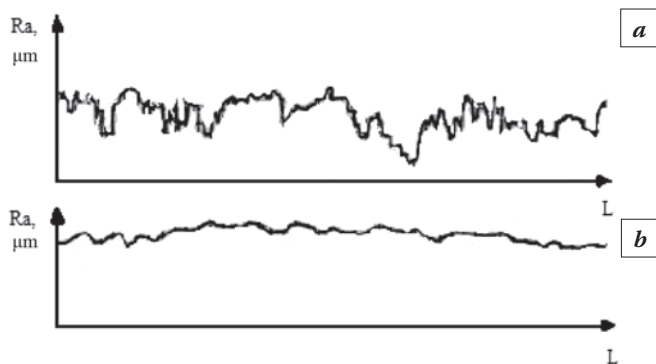


Fig. 3. Surface roughness profiles of steel 45 samples before (a) and after (b) ultrasonic treatment

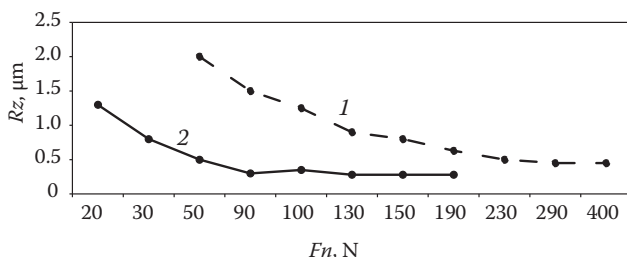


Fig. 4. The relationship between the height of irregularities  $R_z$  on samples of steel 12X18H9T and the pressing force  $F_n$  of a deforming tool with a head radius  $R_h = 3$  mm, without ultrasound (1) and with ultrasonic (2) vibrations with  $\xi = 5$   $\mu\text{m}$

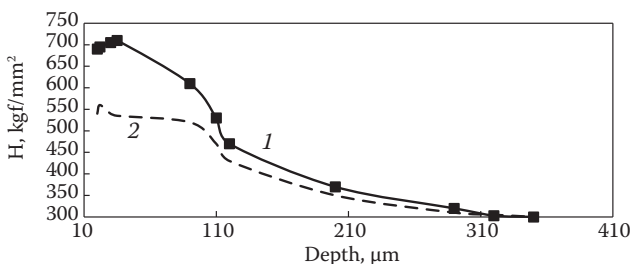


Fig. 5. The hardness distribution over the depth of the nitrated layer of steel 35X10A by liquid nitriding: 1 –with ultrasound; 2 – without ultrasound

bushings. The transmission of ultrasonic vibrations to the samples was carried out due to their tight attachment to the sonotrode [6]. Nitriding was carried out in a molten salt bath consisting of sodium (21% NaCl) and calcium (48%  $\text{CaCl}_2$ ), with passing ammonia through the bath at a temperature of 540–560 °C and holding up to 12 hours.

The following key patterns of the process are identified. Ultrasound stimulates the process of liquid nitriding by passing ammonia in the bath. An increase in the depth and microhardness in the main region of the nitrated layer is traced. With gas nitriding, a significant increase in hardness is guaranteed according to a comparison with liquid ultrasonic nitriding.

The results of the experiments are presented graphically in Fig. 5. It can be seen that ultrasound

has a large effect on the microhardness of the samples surface to a depth of up to  $\approx 300$   $\mu\text{m}$ , increasing it by 1.3–1.6 times its value compared to simple nitriding.

## CONCLUSION

Combined methods of surface modification are effective technologies for the formation of required operational properties of critical parts in transport equipment.

The possibilities of combining thermochemical treatment (in our case, nitriding) with ultrasonic action, both in a liquid medium and on a solid body using the method of surface plastic deformation, are considered.

Ultrasonic treatment in a molten salt bath, consisting of NaCl 21% and  $\text{CaCl}_2$  48% with passing ammonia through the bath, to saturate the workpiece surface layer with nitrogen allows speeding up the process and to achieve 1.3–1.6 times higher microhardness compared to the same nitriding process without ultrasound.

Ultrasonic surface plastic processing of ground steel 45 samples levels the surface roughness and reduces the  $R_z$  value. The value of  $R_a$  is significantly reduced when the force pressing the tool against the workpiece is lowered by  $\approx 2$  times.

Further research is aimed at optimizing the combination of thermochemical treatment with ultrasound, both in sequential thermochemical and ultrasonic treatments, as well as with combined, simultaneously performed nitriding and ultrasound operations.

## REFERENCES

1. Smolentsev V.P., Smolentsev E.V. Bulletin of the Rybinsk State Aviation Technological Academy. P.A. Solovyov, 2017, No. 2 (41). P. 5–9.
2. Petrova L.G., Gladova G.V., Chudina O.V. Materialovedenie (Materials Science), Moscow, MADI (GTU), 2008. 288 p.
3. Lakhtin Yu.M. Osnovi metalovedeniy (Fundamentals of metallurgy), Moscow, INFRA - M., 2013. P. 154–186.
4. Prikhodko V.M. Yl'trazvykovye tehnologii pri proizvodstve, ekspluatatsii i remonte transportnoy tehniki (Ultrasonic technologies in the production, operation and repair of transport equipment). Moscow: Tehpoligrafcentr, 2003. 253 p.
5. Prikhodko V.M., Petrova L.G., Chudina O.V. Metallofizicheskie osnovy razrabotki yprochniyushih tehnologiy (Metal physics basis for the development of hardening technologies). Moscow: Mashinostroenie, 2003. P. 182–187.
6. Byront V.S. Primenenie yl'trazvuka pri termicheskoy obrabotke metallov (The use of ultrasound in the heat treatment of metals). Moscow: Metallurgy, 1978. 168 p.

# ELECTROPLATING ON THE SURFACE OF STEELS AFTER ULTRASONIC TREATMENT

O.V. Chudina, P. Bringulis

Moscow automobile and road construction state technical University (MADI). Moscow, Russia

Pavel.bringulis@gmail.com

The proposed new method of applying electroplating on the surface of structural steels subjected to primary ultrasonic treatment under cavitation conditions, allows you to create a protective coating with a diffusion sublayer 1.8–2 times more than after standard technologies.

**Keywords:** electroplating; ultrasonic treatment; surface plastic deformation; microstructure.

## INTRODUCTION

Electroplating coatings are actively used to protect steels from corrosion and to increase the wear resistance of machine parts used in various industries. The advantages of electroplating technologies are low process temperatures, usually not higher than 100 °C, which does not cause deformation of the product, and a short duration of 30...60 minutes, including preparatory and finishing operations. The thickness of the coating is 20...40 microns.

The main disadvantage of electroplating coatings is their weak adhesive properties, since there is no diffusion sublayer. During the operation of products, especially under cyclic loads, cracks are formed in the coating, leading to penetration of moisture or other aggressive environmental components under the coating, which causes corrosion of the base metal.

Another way to improve the corrosion resistance of products is chemical heat treatment, in particular chrome plating, which allows to obtain protective corrosion-resistant coatings with a diffusion underlayer of the same thickness. However, chemical heat treatment processes are carried out at temperatures above 1000 °C for 6 hours or more. In this case, there is a deformation of products, they require fine-tuning. In addition, at high temperatures grows a large grain of austenite, which remains after cooling, which dramatically reduces the characteristics of strength, ductility and toughness.

In connection with the above task of this work is the development of the technology of applying protective coatings on parts of cars and agricultural machines by electroplating, possessing not only high protective properties, but also good adhesion with

the base metal. To solve this problem, it is proposed to apply the technology of ultrasonic processing of products on the steel surface to develop an advanced dislocation structure, which allows penetration of the metal of the coating metal and increase the thickness of the electroplated coating. There are various methods of ultrasonic action on the surface of metals, in particular, surface plastic deformation of structural steels and alloys by the methods of force action of ultrasound [1].

Another method of ultrasound exposure to a steel surface is cavitation, which occurs in a liquid medium during the cleaning process. Ultrasonic cleaning is used everywhere at the industrial enterprises and at repair of machine-building, road equipment. Thus, the development of electroplating deposition technology with preliminary ultrasonic cleaning is advisable. The purpose of this work is to study the effect of ultrasonic and galvanic treatment on the structural state of the surface of structural steels.

## RESEARCH METHODOLOGY

For research, samples of Armco iron of a cylindrical shape with a diameter of 12 mm, samples of steel 45, 10X18H9 and 38MH2YA cylindrical shapes with a diameter of 10 mm were used as a model material.

The technique of ultrasonic processing of samples involves immersing them in a liquid working medium and the effect of a source of acoustic oscillations — a rod-type piezoelectric transducer with an acoustic frequency that is located at a distance of  $f_{pu} = 20-30 = 3-6$  kHz, mm which is located at a distance of  $l = 3-6$  mm from the surface to be treated.

The amplitude of the vibrational displacements  $\xi$  varied from 7  $\mu\text{m}$  to 40  $\mu\text{m}$ , and the duration of exposure – from 20 to 60 minutes.

Galvanizing was carried out in the electroplating workshop of OJSC Corporation Moscow Institute of Thermal Technology using a standard technology consisting in immersing the product in an electroplating bath, comprising  $\text{ZnSO}_4 \cdot 7 \text{H}_2\text{O}$  – 140 g / l,  $\text{N}_2\text{SO}_4$  – 10 g / l,  $\text{NaCl}$  – 25 g/l, at pH = 2, temperature 20 ° C, in transmission for 30 min. Metallographic studies were performed on an Axiovert 25 CA Carl Zeiss light microscope. The microhardness of the hardened layer was measured on a PMT-3 microhardness meter.

## DISCUSSION OF RESEARCH RESULTS

In modern engineering in the manufacture and repair of automotive engineering, ultrasound methods are widely used to clean the surface from contamination. Ultrasonic cleaning can be both a finishing treatment [1, 2] and intermediate before applying a reinforcing coating on the surface [3]. Available publications on the effect of ultrasonic cleaning in liquid detergents on the state of the surface are mainly devoted to the study of erosion surface destruction processes under ultrasonic action. However, there are practically no studies of the effect of ultrasonic cavitation on the change in the structure and properties of the surface layer of the materials being processed.

The article [4] shows that during the operation of a magnetostrictive transducer in the ultrasonic frequency range in a liquid, cavitation processes develop, which are accompanied by: 1 – the formation of cumulative liquid jets as a result of the collapse of cavitation bubbles; 2 – formation of shock waves generated from the zone of collapse of cavitation bubbles, and 3 – the emergence of a collective shock wave. The cumulative effect of all three of these processes has a significant impact on the surface of steel products, causing surface plastic deformation and, as a result, hardening.

In the works [2, 5, 6] it was shown that by the nature of the effect produced and by the duration of existence in the sound field, cavitation bubbles can be divided into slamming and pulsating. The process of erosion destruction is mainly the result of the slamming of bubbles. When the cavitation bubble collapses, a shock

wave arises, which develops significant pressure. If the shock wave encounters an obstacle in its path, then it destroys its surface. Repeated exposure in the same area of a large number of individual collapsing bubbles leads to significant damage. There are a lot of cavitation bubbles, and their collapse occurs many thousands of times per second, therefore, the mechanism of erosive surface destruction of solids is accumulative. At the beginning of the impact of bubbles on the surface, elastic deformations predominate, then, accumulating in size, the deformations become plastic, and metal is destroyed.

In accordance with the classical concepts of hardening mechanisms acting during plastic deformation in metals, the increase in surface hardness is mainly due to an increase in the density of dislocations in the surface layer. Studies in [7] showed that, using ultrasonic treatment, it is possible to achieve an increase in the hardness of the surface layer of the metal being processed up to 40%. The authors showed that, in addition to an increase in the density of dislocations, there is observed a refinement of the grain and an increase in the microstrain of the crystal lattice, which are unevenly distributed over the treated surface. Such non-uniform microstresses on the surface of the samples are the result of complex unsteady hydrodynamic processes occurring in liquids under acoustic impact conditions and play the role of stress concentrators. It is known that in the presence of stress concentrators, the mechanical properties of products, especially those operated under cyclic and shock loads, are reduced. To obtain a uniformly hardened layer, it is sufficient to apply technological methods consisting in changing the position of the workpiece during ultrasonic treatment with respect to the transducer.

In Fig. 1 shows the microstructure of Armco iron and steel 10X18H9 after ultrasonic treatment for 45 minutes with an amplitude of vibrational displacement

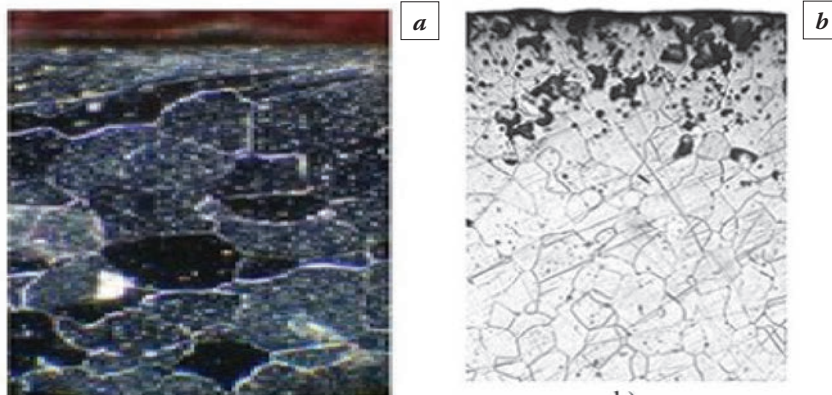


Fig. 1. Microstructures of (a) Armco iron and (b) steel 10X18H9 after ultrasonic treatment for 45 minutes with an amplitude of vibrational displacements  $\xi = 7 \mu\text{m}$ ,  $\times 250$

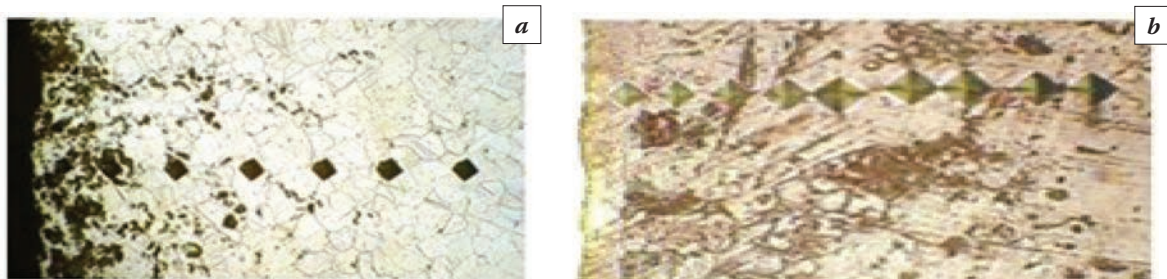


Fig. 2. Comparison of the microstructure and hardness of Armco iron (a) and steel 45 (b) after ultrasonic treatment for 30 min at  $\xi = 7 \mu\text{m}$  (a) and  $\xi = 15 \mu\text{m}$  (b)

ments  $\xi = 7 \mu\text{m}$ . It is seen that in the near-surface layer at a depth of 80...100  $\mu\text{m}$  a new structure with increased hardness is formed (Fig. 2), which is a consequence of the formation of a dislocation structure, and the reinforced layer on the austenitic matrix has a greater thickness than on the ferritic.

With an increase in the amplitude of the vibrational displacements, the intensity of the ultrasonic effect increases, which leads not only to the formation of a layer with a developed dislocation structure on the sample surface, but also to the refinement of grain, which additionally increases the surface hardness.

It has been established that the thickness of the hardened layer mainly depends on the technological parameters of the RCD. Fig. 3 shows the dependences of the influence of the amplitude of vibrational displacements and the duration of treatment on the

thickness of the hardened layer for Armco iron and steel 40X. It was established experimentally that the maximum thickness of hardening without disturbing the integrity of the surface is provided on the model material – Armco iron and steel 10X18H9 after 30 minutes of processing and reaches 70 microns. To obtain a hardened layer of the same thickness on steels 45 and 38X2MIOA, ultrasonic treatment is carried out for 40...45 minutes.

According to the results of experimental studies, the preferred technological modes of ultrasonic exposure were determined, ensuring maximum dislocation hardening without disturbing the integrity of the product surface. For steels with a ferritic and austenitic structure, the amplitude of vibrational displacements  $\xi = 7...30 \mu\text{m}$  and the processing time – 15...30 minutes are optimal. And for steels with

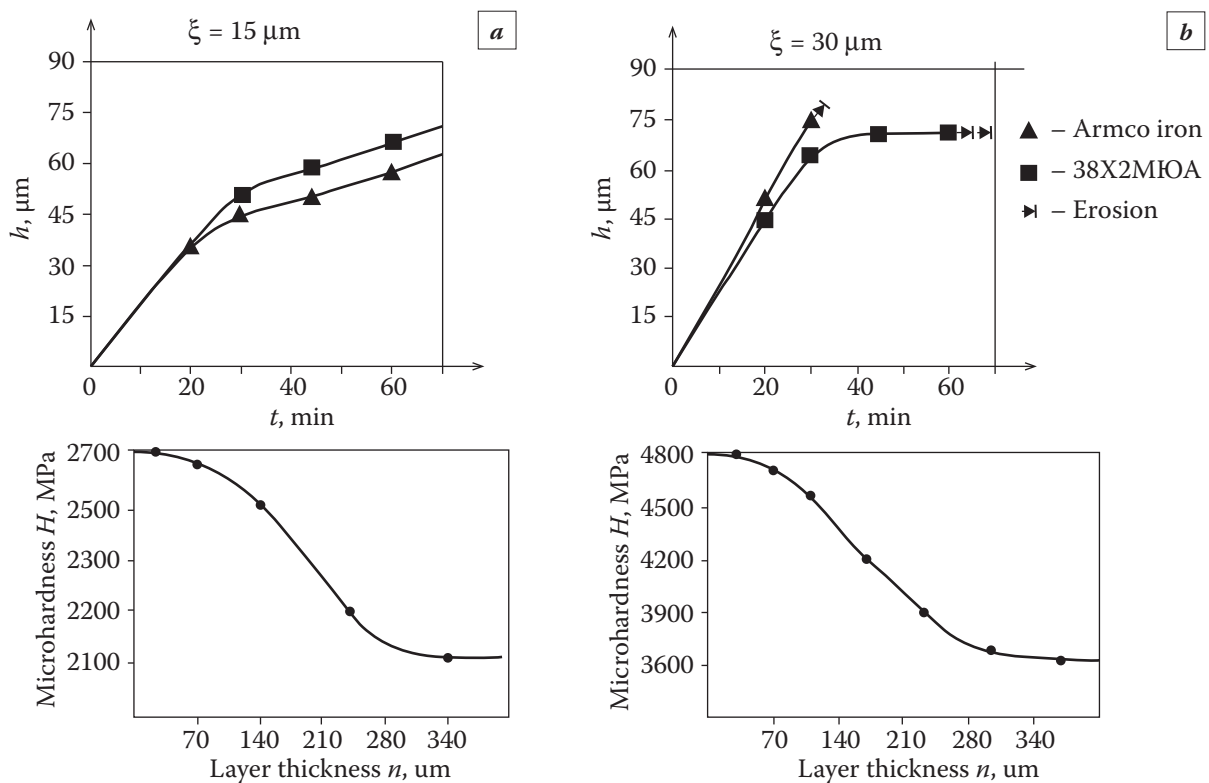


Fig. 3. The influence of the amplitude of oscillatory displacements  $\xi$  and the duration of ultrasonic processing on the thickness of the reinforced armco iron layer (▲) and steel 38X2MIOA (■): a – with the amplitude of oscillatory displacements  $\xi = 15 \mu\text{m}$ ; b – with the amplitude of oscillatory displacements  $\xi = 30 \mu\text{m}$

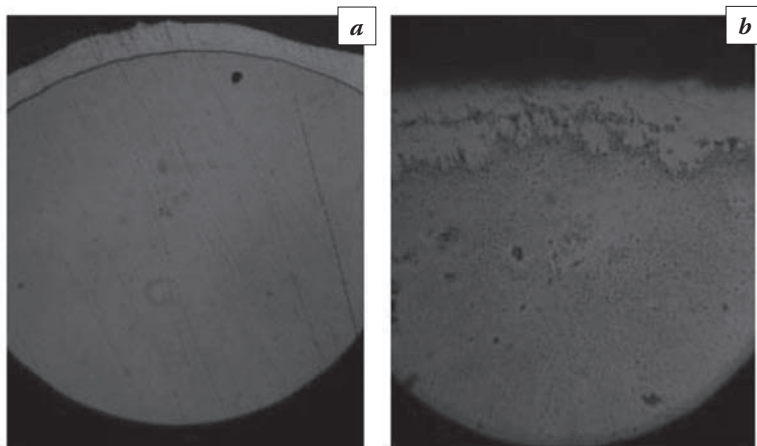


Fig. 4. The microstructure of the steel surface 38MH2UA: *a* – after the standard galvanizing technology,  $\times 100$ ; *b* – after processing by the combined technology: RCD + galvanizing,  $\times 100$

pearlitic structure –  $\xi = 15...50$  microns and duration – 30...60 minutes.

Ultrasonic treatment of steels according to the proposed modes increases the micro-hardness of the surface layer by 1.3...1.5 times. It is established that the level of dislocation hardening largely depends on the structure of steel. The greatest hardening is achieved in steels with austenitic structure, to a lesser extent with ferritic, and in steels with pearlitic structure, the level of hardening depends on the carbon content: the more carbon in steel, the smaller the increase in hardness in the surface layer of the steel being processed.

In Fig. 4*a* shows the microstructure of the surface layer of steel 38X2MUA treated according to the standard galvanizing technology described above. The resulting thickness of the protective coating is 45 microns. It can be seen that there is a clear phase boundary between the coating and the base metal, which indicates the absence of a diffusion sublayer and, as a result, poor adhesion of the coating to the substrate.

In Fig. 4*b* shows the microstructure of 38MH2YA steel with a coating obtained by ultrasonic treatment in water with an amplitude of vibrational displacements  $\xi = 45 \mu\text{m}$  for 45 minutes and subsequent galvanizing using standard technology. It is seen that the thickness of the protective coating increased by 1.8...2 times compared with the standard treatment. In addition, it can be seen that the zinc coating penetrated deep into the metal, and an underlayer was formed, ensuring a reliable and tight fit of the coating with the substrate. This effect was achieved due to the fact that, in the process of ultrasonic treatment, a developed dislocation structure was created in the surface layer, contributing to the penetration of zinc atoms into the metal.

## FINDINGS

1. A new method of electroplating on the surface of structural steels, subjected to preliminary ultrasonic treatment under conditions of cavitation, is proposed. The method allows to form a protective coating with a diffusion underlayer with a thickness of 1.8...2 times greater than after the standard technology.

2. It has been established that ultrasonic action allows forming a layer with a developed dislocation structure on the surface, which increases the microhardness of the surface layer 1.3...1.5 times, and the level of hardening depends on the steel structure, and the thickness of the hardened layer depends on the technological parameters processing. It has been established that the greatest hardening is achieved in steels with austenitic structure, to a lesser extent with ferritic, and in steels with pearlitic structure, the level of hardening depends on the carbon content: the more carbon in the steel, the smaller the increase in hardness in the surface layer of the steel being processed.

Как правильно?

## REFERENCES

1. Abramov O.V., Prikhodko V.M. Moshhnyj ul'trazvuk v metallurgii i mashinostroenii (Powerful ultrasound in metallurgy and mechanical engineering), Moscow, Janus-K, 2006, 688 p.
2. Panov AP Ul'trazvukovaja ochildka precizionnyh detalej (Ultrasonic cleaning of precision parts). Moscow: Mashinostroenie, 1984. 88 p.
3. Alisov V.E., Chudina O.V. Jefferktivnost' ispol'zovanija instrumenta s iznosostojkimi pokrytijami, Sbornik nauchnyh trudov. Moscow: VNIINSTRUMENT, 1985. P. 111–113.
4. Buravova S.N. // Zhurnal tehicheskoj fiziki. 1998. Vol. 68, No. 9. P. 58–64.
5. Agranat B.A., Bashkirs V.I., Kitaygorodsky Y.I. Ul'trazvukovaja ochildka. Fizicheskie osnovy ul'trazvukovoj tehnologii (Ultrasonic cleaning. Physical basis of ultrasound technology). Moscow: Nauka, 1970. P. 165–252.
6. Tyavlovsky M.D., Fastovets E.P., Alefirenko V.M. Ul'trazvukovaja ochildka RJeA i priborov (Ultrasonic cleaning devices and CEA). Minsk: Nauka i tehnika, 1984. 239 p.
8. Chudina O.V., Alexandrov V.A., Fatyuhin D.S. Uprochnajushhie tehnologii i pokrytija. 2011. No. 2. P. 3–6.

# SIMULATION OF LOW-PRESSURE CARBURIZING WITH ACETYLENE FOR INDUSTRIAL APPLICATIONS

Thomas Waldenmaier, Hermann Autenrieth

Robert Bosch GmbH, Germany

thomas.waldenmaier@de.bosch.com, hermann.autenrieth@de.bosch.com

A Modern industrial case hardening is carried out in vacuum furnaces by carburizing components with pulsed acetylene offers at low-pressure. If the hardenability of the used case hardening steel is sufficient usually a more gentle high speed gas quenching is applied as hardening process step. With this kind of heat treatment you can prevent internal oxidation and unwanted decarburization. Furthermore you can carburize complex geometries highly uniform with acetylene as low-pressure process and omit subsequent cleaning steps, as the hardening process is dry. Thus metallic bright components are produced in a robust way with less distortion. However, one of the major backdrafts is that applying acetylene to the components leads to strong carbide formation especially at threads, bore intersections and edges in a short time. These carbides might be solved partly again by diffusion phases in which no acetylene is offered or a hard-machining process have to be applied to remove the carbide enriched surface layers from critical functional areas. If hard-machining cannot be carried out in a matter of costs or geometrical accessibility usually you have to find a compromise solution in regard to the complexity of the geometry and other requirements as the case hardening depth and surface hardness. To minimize a time-consuming and cost-intensive experimental approach for identifying an appropriate heat treatment solution it is necessary to predict the carbide formation and distribution within the geometry. The intention of this study is to model the carbide formation of low-pressure carburization processes for industrial applications as e.g. gears.

**Keywords:** low-pressure carburizing; carbide formation; case hardening; simulation; mass transport.

## INTRODUCTION

Thermochemical heat treatment processes are widely applied for components of diesel injection systems and gear boxes. With this kind of processes it is possible to meet requirements in regard to wear resistance, strength and fatigue strength. An unwanted surface damage caused by internal oxidation can be avoided due to the utilization of low-pressure processes. An already well established process is the low-pressure carburizing with acetylene [1]. One disadvantage of the process is that carbides are formed very fast which might be critical for the components fatigue strength.

Increasingly more simulation tools are used to avoid time and cost consuming experimental process developments. Furthermore new products have less time to market and components are increasingly more complex with more demanding requirements. Therefore, the modeling of mass transport of thermochemical heat treatment processes is an appropriate approach for simulation based component design. However, the existing mathematical mass transport model introduced by Sauerborn for low-pressure carburizing [2] has been further simplified for computational time reduction and a model ap-

proach was amended for predicting geometry areas where carbide precipitations can be found after the case hardening. The thereby developed mathematical model is described in the following chapter.

## MODEL OF CARBON TRANSPORT

A schema of a typical low-pressure carburizing process is given in Fig. 1. After heating the batch the carburization of the components begins with pulsed acetylene offers separated from each other by diffusion phases in which the furnace is either evacuated or purged with nitrogen. To achieve the desired surface near carbon concentration and the case hardening depth a final diffusion phase is applied. In the given example a single hardening process is intended. Therefore, the batch is cooled down for a perlitisation step and afterwards heated again for a final austenitisation step before the components are quenched by a high speed gas quenching process. As the carbon diffusion is neglectable slow under 800 °C the carbon transport is only calculated for the red marked areas beginning with the first acetylene offer.

Within an acetylene offer, the gas is introduced in a furnace and very well distributed in short time

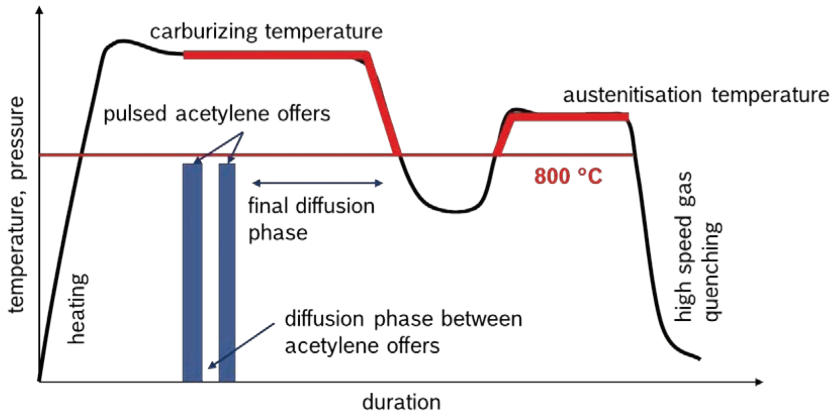


Fig. 1. Schematic time-temperature curve for low pressure carburizing in single hardening. The red marked areas are considered by the model

(< 1 s) in the whole treatment chamber. Due to the very high carbon availability of acetylene the carburizing of the component surface starts immediately. Depending on the process parameters (temperature, pressure and gas flow rate) carbon saturation is achieved within 60 to 100 s. Carbides are formed when the carbon saturation of the iron matrix is reached. To reduce the risk of overcarburizing diffusion phases are introduced between acetylene offers. The surface near carbon concentrations decrease by carbon diffusion. Gets the local carbon concentration under the carbon saturation the carbides are solved again. This additional carbon keeps the concentration close to the saturation concentration. However, depending on the geometry of the component, the carbides are often not solved completely again, e.g. at edges or threads. For a second or further acetylene offer the carbon saturation is achieved faster as the carbon concentration does not fall to the basic carbon concentration after the first diffusion phase [2–4].

The following assumptions and boundary conditions are used in the developed carbon transport model:

- homogeneous temperature distribution in the metal component,
- sufficient acetylene offer for uniform batch treatment,
- the gas transport of acetylene to the component surface is neglected,
- the surface reactions for the decomposition of acetylene to atomic carbon and molecular hydrogen as well as the solving of carbon atoms on interstitial sites are neglected,
- for the first acetylene offer a linear ramp is used to describe the increase of the surface near carbon concentration from the basic carbon concentration to carbon saturation concentration,
- for all further acetylene offers the surface near car-

bon concentration is set immediately to the carbon saturation concentration.

Basis for the calculation of the carbon saturation concentration  $x_{C,S}$  is the temperature dependent approach for austenitic iron by Montevecchi, whereby the temperature  $T$  has to be given in Kelvin [5]:

$$x_{C,S} = 1.67 \cdot 10^{-10} \cdot T^3 + 6.13 \cdot 10^{-7} \cdot T^2 + 7.21 \cdot 10^{-4} \cdot T - 0.706 \text{ [wt\%]}. \quad (1)$$

To describe the carbon saturation concentration for the investigated case hardening steel 20MnCr55 (1.7149) an alloy factor  $k_A$  was introduced with the value 1.06. The alloy dependent carbon saturation concentration  $x_{C,SA}$  can be calculated by equation (2):

$$x_{C,SA} = \frac{x_{C,S}}{k_A} \text{ [wt\%]}. \quad (2)$$

As mentioned above the formed carbides are solved in the diffusion phases. The longer an acetylene offer  $\tau_A$  takes, the longer carbides can be formed  $\tau_C$  and the more time  $\Delta\tau_S$  is needed to solve the carbides in which the carbon concentration stays at the saturation level. The carbide formation time  $\tau_C$  is equal to the acetylene offer time  $\tau_A$ . Only for the first acetylene offer it has to be reduced by 60 s to consider the ramp time to reach carbon saturation for the first time. The prolongation time  $\Delta\tau_S$  at saturation level can be calculated with equation (3).

$$\Delta\tau_S = A_0 \cdot \tau_C^{A_1} \text{ [s]} \text{ with } A_0=1.08 \text{ and } A_1=0.97 \quad (3)$$

The carburization  $\tau_A$  time is prolonged by  $\Delta\tau_S$ , the subsequent diffusion time  $\tau_D$  is reduced by  $\Delta\tau_S$ :

$$\tau_A = \tau_A + \Delta\tau_S \text{ [s]} \text{ and } \tau_D = \tau_D - \Delta\tau_S \text{ [s]}. \quad (4)$$

The approach of Collin was chosen to calculate the concentration and temperature dependent carbon diffusion coefficient, whereas the temperature  $T$  has to be given in Kelvin and the carbon concentration  $x_C$  in wt%, [6]:

$$D_C = \frac{1.43 \cdot 10^{-4} \exp\left[\frac{-19900}{T}\right] \left[2.42 \cdot 10^{-1} x_C \exp\left[\frac{6790}{T}\right]\right]}{(1 - 23.2 x_C)} \left[\frac{\text{m}^2}{\text{s}}\right] \quad (5)$$

To identify critical areas where carburization carbides were formed and not fully solved again it is convenient to indicate zones with carbon concentrations higher than 0.8 wt%.

## VALIDATION OF CARBON TRANSPORT MODEL

In a first step the mathematical model was verified in regard to the CHD and surface carbon concentration with simple cylindrical specimens (diameter 28 mm, height 3 mm) made from 20MnCrS5 (1.7149) for three different case hardening depths (CHD) – 0.50 mm, 0.75 and 1.00 mm. The process parameters for the carburizing and diffusion steps are given in Table 1.

The batch build-up was always done with one specimen (for further investigations) and with additional parts of the same material with a total surface of ca. 1 m<sup>2</sup>. The batches were heated in a single vacuum chamber furnace (Ipsen furnace, type VUTK-(AvaC)-524) to 800 °C under convection mode with 1.5 bar nitrogen. The heating step to the carburizing temperature of 960 °C was carried out under vacuum. After the carburizing (with 6 mbar acetylene) and diffusion (under vacuum) steps, the batches were cooled down to 600 °C for a perlitisation step (60 min) and subsequent heated-up to 870 °C again. On this temperature the batches were austenitized for 20 min. The hardening was carried out with high-pressure gas quenching by 10 bar nitrogen. The deep freezing to –80 °C and the final tempering process took 2 h at 180 °C in a single chamber furnace (Heinrich furnace).

For validating the carbon transport model, the case hardening depths were measured with a Vickers hardness tester (Leco device, type LM247AT) and the surface near carbon concentration with a glow-discharge spectrometer (Spectrumba device, type GDA650). The results are summarized in Table 2.

The measured case hardening depths and surface near carbon concentrations are in good accordance to the predicted values. It has to be mentioned that the measurement accuracy is about +/- 0.02 wt% for the glow-discharge spectrometer.

With a sufficient high acetylene flow rate the range of validity for the developed model is:

- acetylene pressure 4 mbar < 10 mbar,
- carburizing temperature between 800 and 1050 °C,

- no limitation in number of acetylene offers / diffusion phases.

## EXAMPLE OF USE

As an example for the usage of the model an application for a uniform carburizing of hollow cylinder specimens for dilatometer measurements is given in the following.

Objective of the approach was to investigate phase changes during quenching of carburized steel specimens made from 18CrNi8 (1.5920) in dependency of the carbon content. For this purpose specimens were manufactured and carburized with a desired carbon concentration of 0.73 wt% for the test cross section. A sketch of the specimen and its axes of symmetry is showed in Fig. 2.

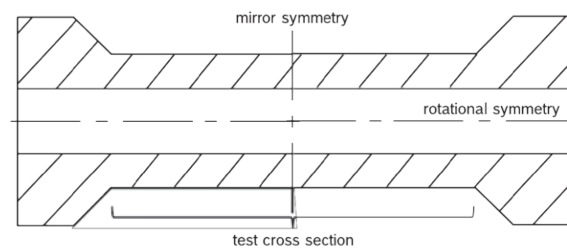


Fig. 2. Sketch for dilatometer specimen made from 18CrNi8 (1.5920)

Table 1. Experimental design for case hardening of specimens made from 20MnCrS5 (1.7149)

CARBURIZING AND DIFFUSION PARAMETERS						
process step	CHD 0.50 mm		CHD 0.75 mm		CHD 1.00 mm	
	C <sub>2</sub> H <sub>2</sub> offer, s	diffusion, s	C <sub>2</sub> H <sub>2</sub> offer, s	diffusion, s	C <sub>2</sub> H <sub>2</sub> offer, s	diffusion, s
1	180	600	240	600	300	600
2	130	1320	210	600	300	600
3	–	–	150	3550	250	600
4	–	–	–	–	180	6670

Table 2. Comparison between experimental and simulation results for cylindrical specimens made from 20MnCrS5 (1.7149)

CARBURIZING AND DIFFUSION PARAMETERS			
	CHD 0.50 mm	CHD 0.75 mm	CHD 1.00 mm
measured surface carbon concentration, wt%	0.71	0.68	0.66
simulated surface carbon concentration, wt%	0.71	0.67	0.66
measured case hardening depth, mm	0.51	0.76	1.01
simulated case hardening depth, mm	0.49	0.76	1.01

Table 3. Heat treatment parameters for hollow cylinder specimens made from 18CrNi8 (1.5920)

HEAT TREATMENT PARAMETERS				
process parameters		carburizing parameters		
carburizing temperature	920 °C	step	C <sub>2</sub> H <sub>2</sub> offer, s	diffusion, s
acetylene flow rate	1500 l/h	1	500	300
acetylene pressure	10 mbar	2	400	300
diffusion phases	vacuum	3	300	300
soft furnace cooling	nitrogen	4	250	300

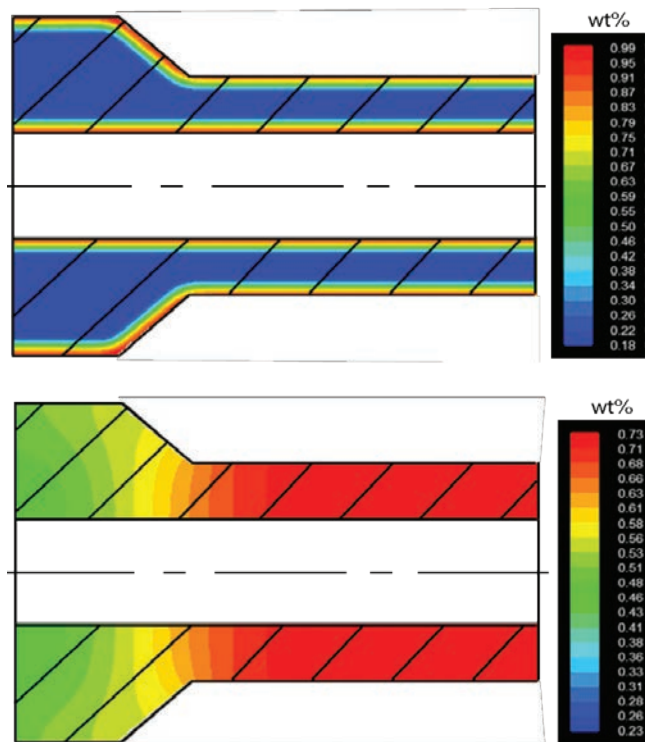


Fig. 3. Simulation results of carburized hollow cylinder specimens made 18CrNi8 (1.5920)

For reducing the necessary computational time the mirror symmetry was exploited and the resulting rotational symmetry was modeled in the commercial software ANSYS FLUENT®. The process parameters for carburizing the specimens are given in Table 3.

The simulation results are presented in Fig. 3. On the left hand side the carbon distribution is showed after the fourth carburizing step and on the right hand side after additional 20 h of diffusion on carburizing temperature for homogenizing the carbon concentration in the test cross section. The results show an uniform carbon distribution with the desired carbon concentration of 0.73 wt% in the test cross section of the specimen. The measured car-

bon concentration was about 3% higher at 0.75 wt% which was sufficient accordant to the objectives.

## CONCLUSION

The authors are aware of the severe simplification, but with this model it is possible to run several simulations to design a low-pressure carburizing process for complex geometries within only a couple of hours. A comparable process design with the original complete model of Sauerborn [2] would take approximately 1 month of computational time [2]. Additionally it is possible:

- to consider e.g. longer diffusion times to reduce the risk of carbide formation in critical area depending on the calculated carbon concentrations,
- to estimate the necessary finish machining tolerances by considering the predicted carbide formation,
- and to define carbide critical areas for check positions which can be used in test specifications.

## REFERENCES

1. Clausen B., Hoffmann F., Zoch H.-W. Beeinflussung der Randschicht durch die Einsatzhärtung // HTM Journal of Heat Treatment and Materials. 2008. Vol. 63, No. 6. P. 326–336.
2. Sauerborn C. Modellierung der Stoffübertragung beim Niederdruckaufkohlen mit Acetylen. Dissertation, University of Karlsruhe, 2008.
3. Hagymási L., Waldenmaier T., Schwarzer J., Schulze V., Reimert R. Experimentelle Untersuchung und Modellierung des Niederdruck-Carbonitrierens // HTM J. Heat Treatm. Mat. 66 (2011) 4. P. 230–238.
4. German Federal Ministry of Education and Research (BMBF): Final report of research project: Durchbruch der breiten Anwendung von Vakuumverfahren beim Einsatzhärten (DAVE). Grant number: 03X2506, 2005–2007.
5. Montevecchi I. Carburizing of steels: optimum furnace and application of process control computers // Studies in Surface Science and Catalysis. 1980. S. 1–5.
6. Collin R., Gunnarson S., Thulin D. A mathematical model for predicting carbon concentration profiles of gas-carburized steel // Journal of The Iron and Steel Institute. 1972. 10. P. 785–789.

# ACETYLENE DECOMPOSITION DURING LOW PRESSURE CARBURIZATION TREATMENT: MODELLING AND OPTIMISATION OF THE PROCESS

E. Vyazmina<sup>1</sup>, G. Mougín<sup>1</sup>, J. Sheng<sup>1</sup>, S. Jallais<sup>1</sup>, L. Coudurier<sup>2</sup>, F. Januard<sup>3</sup>

<sup>1</sup>Air Liquide R&D, Paris Innovation Campus. France

<sup>2</sup> Air Liquide, Technology Center. Germany

<sup>3</sup> Air Liquide Head Office. France

Elena.Vyazmina@airliquide.com

The low-pressure carburization (LPC) treatment of metal pieces is needed to increase the hardness of the metal surface in the presence of a carbon-bearing material, for instance acetylene. LPC is performed at high temperature (approximately 850–950 °C) and low pressure (<30 mbar). In general, the reaction of acetylene decomposition under these conditions is considered at infinite time and high temperature, where the final products of the chemical reactions are hydrogen and carbon. However, although the decomposition of C<sub>2</sub>H<sub>2</sub> is fast, this hypothesis is not correct. Most hydrogen atoms recombine to form hydrogen molecules, yet some of them remain linked to carbon, leading to different types of hydrocarbons. In terms of molecule mass and C/H ratio, they can be ranked in an ascending sequence: small molecules (H<sub>2</sub>, CH<sub>4</sub>, C<sub>2</sub>H<sub>4</sub>, C<sub>2</sub>H<sub>6</sub>, C<sub>6</sub>H<sub>6</sub> etc.), polycyclic aromatic hydrocarbons (PAHs), fine-crystalline graphite and pyrolytic carbon (soot). PAHs are carcinogenic and soot can damage the furnace functioning. The current investigation is based on kinetic modeling of the acetylene decomposition in the atmosphere of a reactor. For this modeling 3 comprehensive mechanisms are considered to understand the formation of PAHs and soot during the treatment inside the furnace. Simulations results are in good agreement with experimental data. Parametric studies show that higher temperature and pressure accelerate the decomposition of C<sub>2</sub>H<sub>2</sub>. Nevertheless, higher pressure and higher temperature increase the quantity of Large PAHs and soot. Simulations suggest a set of operational conditions of the furnace (temperature, pressure, flow rate or residence time) to reduce the harmful species. A new approach of monitoring and mitigation of soot formation is also suggested.

**Keywords:** carburization; low pressure; acetylene; pyrolysis; soot formation; optimisation.

## INTRODUCTION

Heat treatment of the metal surface is a processing of industrial materials to make them resistant to wear and fatigue. One of such thermo-chemical process is carburization. It is based on the surface enrichment by carbon when the metal is in the austenite state. The depth of the hardening is directly linked to the temperature and the processing time, so-called residence time. The process consists of four principal steps: heating, carburization, quenching and annealing. Quenching mainly affects the metal properties of the diffusion zone increasing its hardness and improving its resistance to the fatigue.

Heating process brings the treated metal piece into the austenite state. Carburization usually uses acetylene (C<sub>2</sub>H<sub>2</sub>) to bear the carbon into the metal surface. During the carburization stage acetylene decomposes at high temperature and activated carbon diffuses into the metal surface.

Although carburization has been developed for decades, the reaction pathways taking place inside the treatment furnace at low pressure are still not

fully understood. Consequently, the process is not entirely optimized. The primary target of this paper is to shed a light on the chemical decomposition C<sub>2</sub>H<sub>2</sub> in the furnace atmosphere during the low-pressure carburization process via simulations. Several suggestions to optimization of the furnace performance and monitoring of soot are also suggested. Simulations are performed using software CHEMKIN PRO 17.1 using the model of perfectly stirred reactor.

## PYROLYSIS OF ACETYLENE

### Pyrolysis

Acetylene is a chemical compound with the formula C<sub>2</sub>H<sub>2</sub>. As a simplest alkyne, acetylene is unsaturated due to its two carbon atoms, which are bonded together with a triple bond. The carbon-carbon triple bond places all four atoms in the same straight line, with CCH band angle of 180°. This triple bond makes the pyrolysis of C<sub>2</sub>H<sub>2</sub> very complicated involving si-

multaneous processes of complex gas phase reactions leading to multiple products including small molecules like  $H_2$ ,  $C_2H_4$ ,  $C_3H_4$ , polycyclic aromatic hydrocarbons (PAHs) and soot. Heterogeneous reactions lead to a deposition of pyrolytic carbon on the substrate surface [1].

Acetylene pyrolysis involves thousands of species. In current paper, three models describing  $C_2H_2$  pyrolysis are used (Table 1).

Table 1. Models for description of  $C_2H_2$  pyrolysis

Model	Mechanism	Applicability
K. Norinaga [2]	227 species, 827 reactions	Concentration of specific PAHs
T. Bensabath [3]	364 species, 1245 reactions	Concentration of specific PAHs
C. Saggese [4]	350 species, 16700 reactions	Growing of soot particles, 900K-2500K

## Polycyclic aromatic hydrocarbons

Polycyclic aromatic hydrocarbons (PAHs) are formed with several aromatic cycles by carbon rings connected through consecutive reactions involving acetylene as a major space. PAHs are very harmful for human health. Several of them are classified as priority pollutants by the Environment Protection Agency of the United-States (EPA-PAHs). Understanding of PAH formation is important to make safer and cleaner low-pressure carburization processes.

Soot is a carbonaceous solid product obtained by a combustion of fuels when combustion conditions are sufficiently fuel-rich, where polymerization/condensation reactions of the fuel take place. Soot is an undesirable product: it destroys the pump system,

dampers the diffusion and adsorbs large number of toxic hydrocarbon. Since there is no oxygen in the decomposition system during carburization, theoretically large quantity of soot will form. An important progress has been made recently in understanding of soot formation. The formation of soot from hydrocarbon consists of complex chemical and physical steps, including pyrolysis, formation of polycyclic aromatic hydrocarbon, particle inception, coagulation, surface growth, carbonization, agglomeration [5].

To model the formation of PAH and soot it is essential to perform kinetic simulations. Previous validations [6, 7] of models from Table 1 gave reasonable agreement with experimental data. References [6, 7] also demonstrated that higher pressure accelerates the decomposition of acetylene. However, at the same time it increases the mass fraction of PAHs and soot in the treatment furnace. Simulations demonstrated that for the resident time of 20 s and temperature of 880 °C soot starts to form at for pressure of 8 mbar and higher. Based on this investigation Vyazmina et al. [7] recommended keeping the pressure low inside the furnace (less than 10 mbar).

## INFLUENCE OF TEMPERATURE ON $C_2H_2$ PYROLYSIS

### Conversion of PAHs to Large PAH and soot

Vyazmina et al. [6, 7] demonstrated the influence of another governing parameter on the reactions: temperature. From one hand, higher temperature accelerates the decomposition, from another hand the decomposition produces more PAHs. Fig. 1 demonstrates that almost all the EPA-PAHs have a maxi-

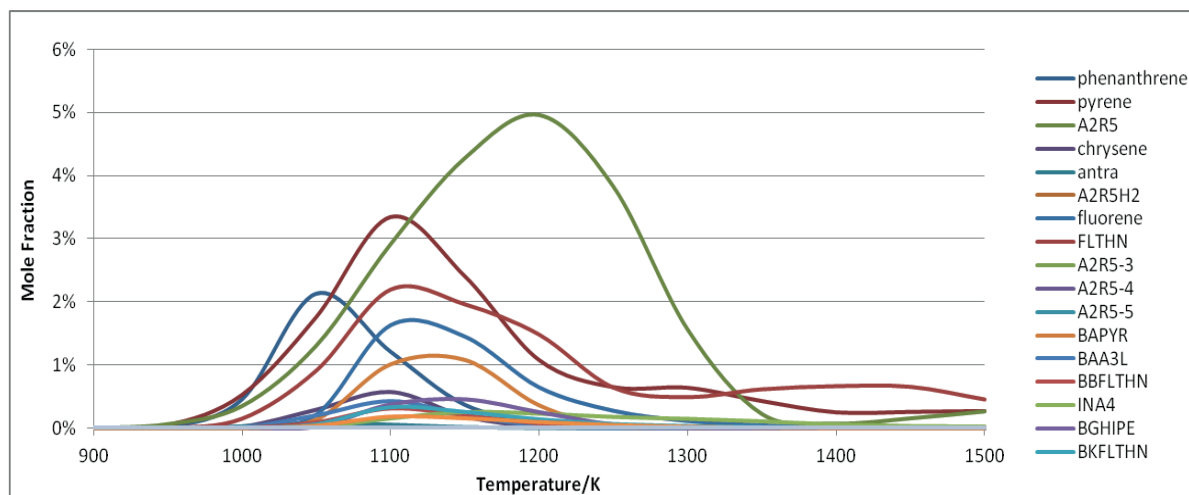


Fig. 1. Mole fraction of EPA-PAHs as function of temperature, 45 mbar, 100 s

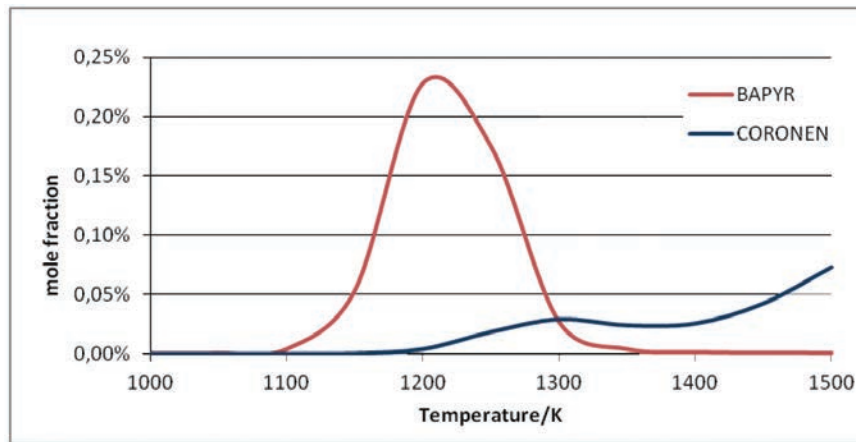


Fig. 2. Mole fraction of Benzo[a]pyrene (or BAPYR) and coronene as function of temperature, 20 mbar, 20 s

imum mole fraction. Benzo[a]pyrene (BAPYR) is one of the most toxic EPA-PAH. Another PAH coronene, co-called super-benzene is the largest PAHs in the T. Bensabath mechanism [3]. These two PAHs can be considered as representative for understanding of the conversion PAHs to Large PAHs at different temperatures.

When BAPYR reaches its highest concentration, coronene starts to form. This may indicate that EPA-PAHs turn into large PAHs. As the reaction proceeds, smaller cycles combine themselves into bigger cycles as temperature rises. This agglomeration will lead to the soot formation.

Vyazmina et al. [7] showed that for acetylene pyrolysis at  $T < 830$  °C there is no soot (20 mbar and residence time of 20 s). Above this threshold, soot quantity jumps. This behavior was confirmed experimentally [8]. This means that there is a critical condition for the soot formation as temperature increases.

### Critical conversion rate

The critical condition demonstrates that there is a series of critical points as  $(t, T, P)$  for  $C_2H_2$  pyrolysis where soot starts to form.

The critical condition is of a great importance: it reveals a possibility to control the formation of soot. Therefore, a lot of simulations are done to study this phenomenon. Critical conditions can be expressed by three parameters: residence time  $t$ , temperature  $T$  and pressure  $P$ .  $t$  is fixed to 10 s, 20 s and 40 s. For each residence time,  $P$  varies from 5 mbar up to 20 mbar. For a given combination of residence time  $t_c$  and pressure  $P_c$ , temperature decreases until reaching a critical point. Fig. 3 shows critical points, each series corresponding to a different residence time.

For a residence time of 10 s, as the pressure increases, the critical temperature decreases. When the pressure increases,  $C_2H_2$  decomposes faster and PAHs grow faster, hence it is easier to form the soot.

For 0.02 atm (20 mbar) pressure and the residence time increase, the critical temperature decreases. Longer residence time means more time to form soot in the system.

At 1150K for furnace pressure of 5 mbar, the residence time must be less than 40 s. If the furnace pressure is 8 mbar, then the residence time should be less than 20 s. If the furnace pressure is 10mbar, the residence time should better within 10 s, see Fig. 3.

Three series of critical points are plotted on Fig. 4.

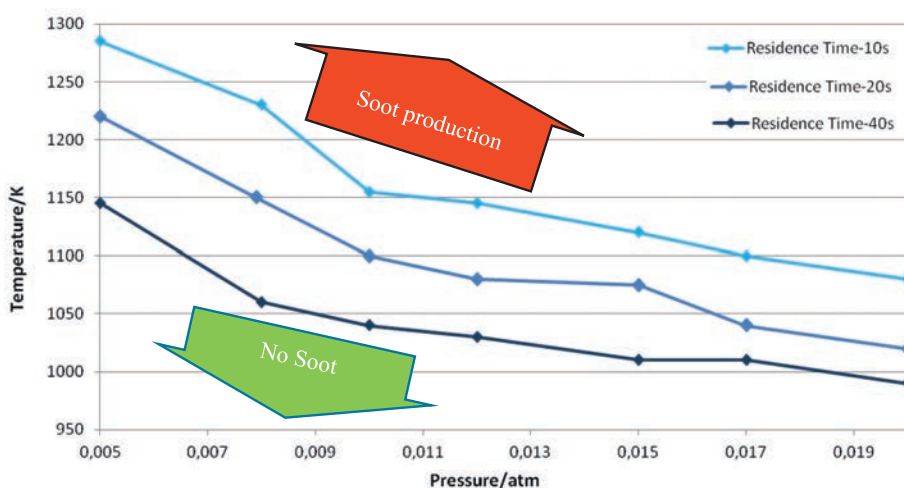


Fig. 3. Critical points for three residence times: 10 s, 20 s and 40 s

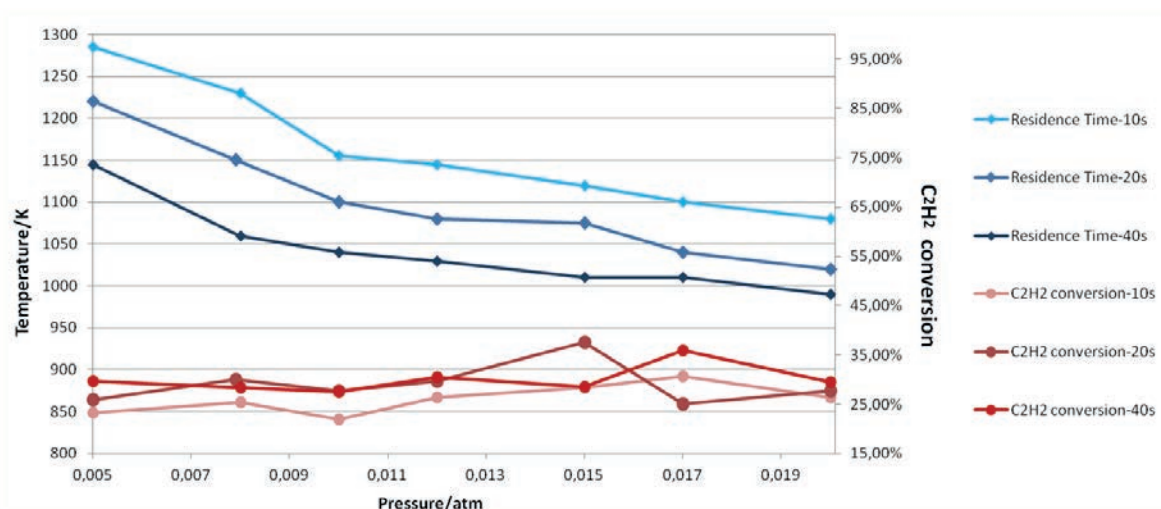


Fig. 4. The critical conversion rate of  $C_2H_2$

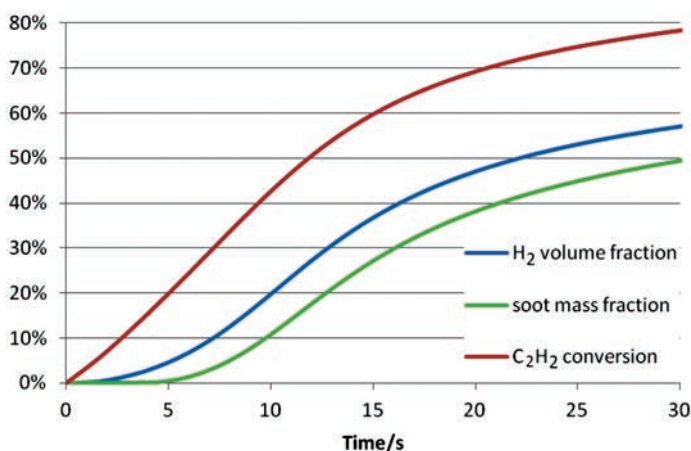


Fig. 5.  $H_2$  volume fraction as function of time, 1120 K, 20 mbar, C. Saggese model

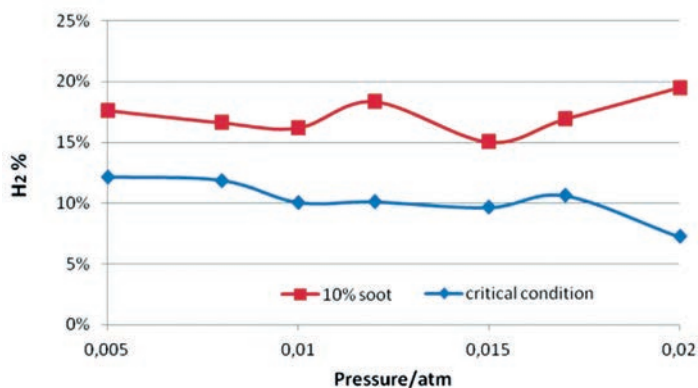


Fig. 6.  $H_2$  volume fraction at critical conditions (residence time 10 s) and at 10% soot

As long as the reaction condition is controlled under the critical point, there should be not much soot. However, in the industrial process, residence time could not be limited to just these three times considered here. Pressure range may be also much larger. Thus, a more general approach

is developed. Fig. 5 shows the conversion rate of  $C_2H_2$  for each critical condition to understand how much  $C_2H_2$  decomposes at each critical point.

Red curves represent the conversion rate of  $C_2H_2$ . Blue dot at 0.02 atm, 40 s represents a critical condition (40 s, 0.02 atm, 990 K) and the corresponding critical conversion rate of  $C_2H_2$  is 29%. The critical conversion rates of  $C_2H_2$  are always in between 20–30% (average 28%), whatever the critical condition is. Hence, when 30% of  $C_2H_2$  is decomposed, the soot starts to form.

$H_2$  is also a product of  $C_2H_2$  decomposition. Fig. 5 shows a correlation between hydrogen production and acetylene pyrolysis. According to Fig. 4, the point (1120 K, 0.02 atm) is above the 10s-residence-time line. Therefore, there should be soot formation at (10 s, 1120 K, 0.02 atm), see Fig. 5. At 10 s, there is 10% soot in the system. Moreover, when the soot starts to form at 5s, the critical conversion rate of  $C_2H_2$  is 22%, which is within the critical range of 20%–30%.

Hydrogen is produced by its extraction when aromatic cycles grow. Therefore, the formation of hydrogen is directly linked to the formation of PAHs and soot. As is showed on Fig. 5, as soot grows, hydrogen volume fraction increases. The gap between the hydrogen volume fraction and soot mass fraction is a constant and it equals to 10%. Therefore, the following correlation can be used to predict the mass fraction of soot in the furnace:

$$\text{soot \%} = H_2\% - 10\%.$$

More simulations are done to verify this correlation. It appears that this simple cor-

relation is valid for large spectrum of pressures (Fig. 7).

The blue curves on fig. 6 corresponds to  $H_2$  volume fraction at the critical conditions (residence time 10 s, no soot) and red curve represents  $H_2$  volume fraction when there are 10% soot in the furnace. At the critical condition, the soot only starts to form (soot % is 0)  $H_2$  volume fraction is around 10%. Furthermore, when there is 10% soot formation,  $H_2$  volume fraction is close to 20%.

Hence, hydrogen volume fraction can be used as a simple indicator of soot fraction in the furnace system. Monitoring the hydrogen concentration can help to reduce the quantity of soot in the furnace and hence to control better the treatment process.

## CONCLUSION

The behavior of  $C_2H_2$ , PAHs and soot during the pyrolysis is investigated. For  $C_2H_2$  pyrolysis, simulations results are in good agreement with experimental data. Parametric studies show that higher temperature and pressure accelerate the decomposition of  $C_2H_2$ . Either higher pressure or higher temperature increase the formation of large PAHs. There is always a critical condition for  $C_2H_2$  where soot starts to form. This condition corresponds to the conversion rate of  $C_2H_2$  approximately within 20–30%. Moreover, the volume fraction of hydrogen can be considered as an indicator of soot formation. A correlation between the volumetric fraction of hydrogen and the mass fraction of soot is found. Hence, hydrogen volumetric fraction can be used as a simple indicator of soot formation in the industrial furnaces. Monitoring the hydrogen concentration can help to reduce the quantity of soot formed in the furnace and hence to better control the treatment process.

## ACKNOWLEDGEMENTS

Special thanks to Dawid Nadolski for his valuable comments on the draft.

## REFERENCES

1. <http://www.reactiondesign.com/products/chemkin/chemkin-2/>
2. **Norinaga K., Deutschmann O.** Analysis of gas compounds in chemical vapor deposition of carbon from light hydrocarbons // *Carbon*. 2006. 44. 1790–1800.
3. **Bensabath T., Monnier H., Glaude P.-A.** Detailed kinetic modeling of the formation of toxic polycyclic aromatic hydrocarbons (PAHs) coming from pyrolysis in low-pressure gas carburizing conditions // *Journal of Analytical and Applied Pyrolysis*. 2016.
4. **Saggese Ch., Frassoldati A.** A kinetic modeling study of polycyclic aromatic hydrocarbons (PAHs) and soot formation in acetylene pyrolysis // *Energy Fuels*. 2014. 28, No. 2. 1489–1501.
5. **Ruiz M.P.** Influence of the temperature on the properties of the soot formed from acetylene pyrolysis // *Chemical Engineering Journal*. 2006.
6. **Sheng J., Vyazmina E., Jallais S., Bustamante-Valencia L., Bruchet P., Richard F.-P.** Carbonitriding: kinetic modeling of acetylene decomposition at high temperature and low pressure // *A3TS Congress, Nice, France*, June. 2017.
7. **Vyazmina E., Sheng J., Jallais S., Bustamante-Valencia L., Bruchet P., Richard F.-P.** Carbonitriding: kinetic modeling of acetylene decomposition at high temperature and low pressure // *Matériaux & Techniques (Mattech)*. 2018. Vol. 106, No. 1. <https://doi.org/10.1051/mattech/2018033>.
8. **Sánchez N.E., Millera Á., Bilbao R., Alzueta M.U.** Polycyclic aromatic hydrocarbons (PAH), soot and light gases formed in the pyrolysis of acetylene at different temperatures: Effect of fuel concentration // *Energy Fuels*. 2012. 26, No. 8. 4823–4829.

# DISTORTION OF A FIXTURE HARDENED PLANET GEAR BLANK – A FINITE ELEMENT SIMULATION STUDY

Hannes Birkhofer<sup>1</sup>, Ben Taylor<sup>2</sup>, Thomas Lübben<sup>1</sup>

<sup>1</sup>Leibniz-Institute for Materials Engineering IWT, Bremen, Germany

<sup>2</sup>Aerospace Transmission Technologies – ATT, A Joint Company of Liebherr-Aerospace  
and Rolls-Royce, Friedrichshafen, Germany

birkhofer@iwt-bremen.de

Power transmitting components in aerospace applications require precise production processes with minimal resulting distortion. Press quenching or fixture hardening is a heat treatment technique utilized to control dimension and form changes of parts by constraining their shrinkage. Phase transformations during the quenching process lead to significant dimensional changes and plasticity effects. Due to highly nonlinear physical phenomena exact forecast of shrinkage for an individual steel grade is extremely challenging. Conditions in the fixture, high temperatures, oil flow and available space in the tool limit opportunities to measure temperature and distortion of the part in situ. State of the art simulation techniques such as Finite element modeling can significantly enhance the possibilities to investigate the fixture hardening process. The simulation study aims to analyse distortion of a gear blank (base body of the gear) with emphasis on thermal and plasticity effects. A thermo-mechanical 2D axisymmetric model of a fixture hardening process including contact and transformation plasticity effects, implemented in Abaqus® with user subroutines is used. Dilatometer experiments are carried out to determine phase transformation data. Model validation is achieved by comparing simulated temperature curves with measurements from an instrumented gear. The effect of different mandrel sizes is investigated with regards to plasticity, transformation plasticity and thermal strain. Fixture hardening is compared to free quenching in oil. The resulting distortion is analysed in depth comparing the influence of the different settings and their contribution to distortion of the part.

**Keywords:** fixture hardening; transformation plasticity; heat treatment; distortion; quenching simulation; steel bs s156 (16NiCrMo16-5).

## INTRODUCTION

Fast and continuous growth of air traffic has led to increased demands in safety and efficiency of aerospace transport. An aircraft engine technology step change aiming at higher power output and less fuel consumption is the introduction of geared turbofans. Gear box components require highly accurate production processes with minimal resulting distortion. Fixture hardening is a heat treatment technique utilized to tightly control dimension and form changes of parts by constraining their shrinkage. Oil flow guidance and mandrel dimension are key parameters of fixture hardening tool design. The resulting heat transfer coefficient in the fixture dictates the time of contact, the developing contact pressure and resulting deformations. Setting the correct mandrel size is critical in order to achieve high quality results. Due to highly nonlinear physical phenomena exact forecast of shrinkage for an individual steel grade is extremely challenging [1]. Finite Element Method (FEM) simulations are used to model the heat treatment process [2].

This study discusses the difference between free quenching and fixture hardening with respect to dis-

tortion. Further emphasis is a comparison of two different mandrel diameters and the resulting distortion: Results show good agreement between measured and simulated temperature curves. Distortion of the inner and outer radius is investigated. Fundamental differences between free quenching and fixture hardening are highlighted. Improvement of distortion for larger mandrel radii is demonstrated.

## MATERIALS AND METHODS

The steel grade and the methodology of simulating the fixture hardening process is presented in the following section. Briefly the mathematical framework, selected material data, geometry and mesh as well as boundary conditions and specifics of the simulated heat treatment are presented. The investigated heat treatment process consists of a sequence of several steps leading to the part's final geometry: Austenitising and carburising, slow cooling to room temperature and most importantly austenitising and fixture hardening followed by removal of the mandrel and free cooling in air to room temperature. The final

state after mandrel removal will be discussed in this work.

## Mathematical framework

A coupled thermo-mechanical-metallurgical model of a fixture hardening process of a power transmission gear blank was implemented within a FEM framework [3–5]. The temperature field is calculated by Fourier's heat equation. Carburising is modelled via Fick's second law. Diffusion based phase transformations are described by a combined approach according to Johnson-Mehl-Avrami (JMA) and Leblond [6–8]. The diffusionless martensitic transformation is modeled by the Koistinen-Marburger equation [9]. The total strain rate equilibrium of the mechanical field is divided into individual contributions:

$$\dot{\epsilon}_{ij} = \dot{\epsilon}_{ij}^e + \dot{\epsilon}_{ij}^p + \dot{\epsilon}_{ij}^{th} + \dot{\epsilon}_{ij}^{pt} + \dot{\epsilon}_{ij}^{tp}. \quad (1)$$

Where  $\dot{\epsilon}_{ij}$  is total strain rate composed of,  $\dot{\epsilon}_{ij}^e$  – elastic,  $\dot{\epsilon}_{ij}^p$  – plastic,  $\dot{\epsilon}_{ij}^{th}$  – thermal,  $\dot{\epsilon}_{ij}^{pt}$  – isotropic phase transformation and  $\dot{\epsilon}_{ij}^{tp}$  transformation plasticity strain rates. Linear mixture rules are applied for all described effects. Elasticity strain rates are given in terms of the Young's modulus and Poisson's coefficient [10]. Thermal and phase transformation strain is calculated in a combined approach according to [11]:

$$\epsilon_{ij}^{th} + \epsilon_{ij}^{pt} = \sqrt[3]{\frac{\rho(T_0, P_0)}{\rho(T, P)}} - 1. \quad (2)$$

Where  $\rho$  is the phase dependent density and  $T$  is temperature. Density of the phases is calculated from the sum of thermal and transformation strain. The transformation plasticity effect is implemented using a linearized approach [12] as follows:

$$\dot{\epsilon}_{ij}^{tp} = \frac{3}{2} K s_{ij} \frac{df(p)}{dp} \frac{dp}{dt}. \quad (3)$$

Where  $K$  is the transformation plasticity constant and  $s_{ij}$  is the deviatoric stress tensor. Kinetics are affected by the saturation function  $f(p)$ , in the interval [0,1], where  $p$  is the transformed phase volume.

## Material data

Steel grade for this study is 16NiCrMo16-5 (MSRR 6010, 1.6722) having a chemical composition (wt.%): 0.1 C, 0.3 Mn, 0.2 Si, 1.0 Cr, 2.0 Ni, 4.0 Mo and 0.1 Cu. Dilatometer experiments with through carburized specimens of 16NiCrMo16-5 of different carbon contents have been carried out. The experiments yielded martensitic transformations only, for a wide range of cooling rates. Retained austenite was measured by X-ray diffraction for the dilatometer specimens at room temperature. Based on these experiments phase transformation material data has been obtained by fitting recorded dilatometry data to the JMA and Koistinen-Marburger equations using the retained austenite data as validation for the transformed phase volumes. Martensitic transformation is modeled by the Koistinen-Marburger equation [9]. Material and phase transformation parameters were implemented as carbon and phase dependent. Thermo-physical data was partially taken from a dataset for alloy 20MnCr-5 published in [13]. Further unpublished data from the SFB 570, Distortion Engineering programme, and from a material data base provided by a project partner was implemented.

## Geometry and mesh

The model geometry was implemented based on a 3D CAD model of a gear blank according to Fig. 1.

Rotational symmetry enables 2D representation of the gear blank. A 4-node axisymmetric quadrilateral bilinear displacement temperature element type was used. The mesh consists of 65,088 elements, with refinements underneath the surface in order to account for steep gradients in those areas. Maximum distance between two nodes on the sur-

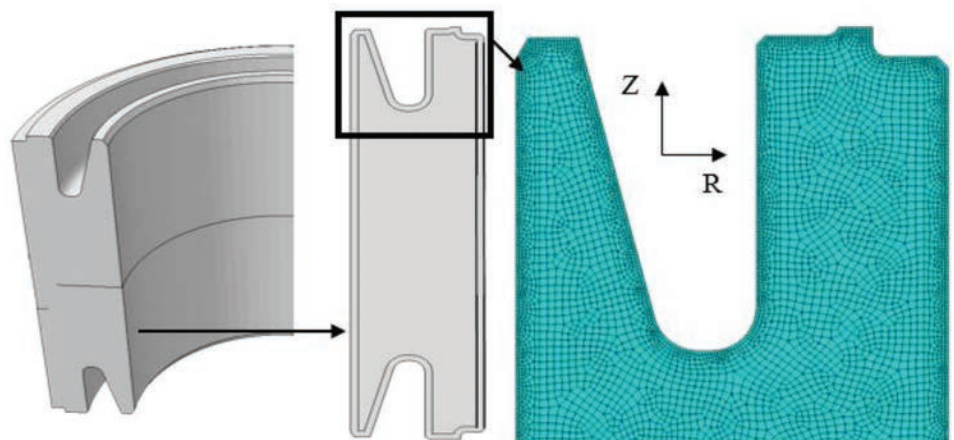


Fig. 1. Implemented gear blank geometry and near surface mesh of the 2D axisymmetric model

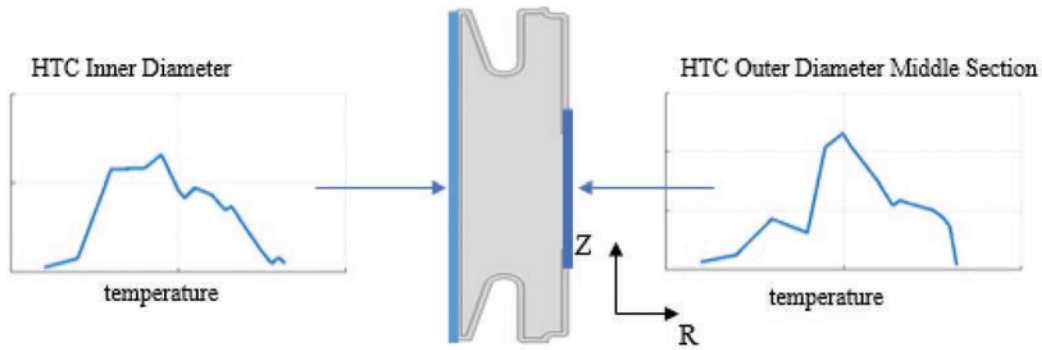


Fig. 2. Examples of inversely calculated HTCs for two selected surfaces (inner and outer diameters). HTC calculated by project partner based on temperature measurements in a quenching press

face is 0.3 mm. Mesh optimization for convergence was carried out. The mandrel is represented by an analytical rigid body without assigned material properties.

### Boundary conditions

Displacement constraints consider rotational symmetry about the cylinder axis of the gear blank and also prevent translation about the  $z$ -axis. Thermal boundary conditions depend on the process step: During heating and furnace cooling a constant Heat Transfer Coefficient (HTC) is applied. For the fixture hardening step HTCs have been inversely calculated based on temperature measurements by a project partner. The calculated HTCs have been provided to the author. The gear blank surface is divided into several zones for the fixture hardening step. For each zone a separate location and temperature dependent HTC is applied. Two selected HTCs are presented in Fig. 2.

For the free quenching simulation a temperature dependent HTC of oil W72 is used. Data for the HTC of oil W72 is based on previous works at IWT, published in [14]. Cooling is assumed to be uniform over the surface of the gear blank due to strong agitation of the oil.

### Simulated process steps

The following process steps with resulting displacements are simulated: Carburising, air cooling, austenitising and quenching, mandrel removal. Heat transfer is assumed to be homogeneous over the part for constant heating and slow cooling steps. The fixture hardening step consists of austenitising, a slow cooling step in order to reach the desired hardening temperature and quenching. During the fixture

hardening step quenching with the described HTCs as shown in Fig. 2, is simulated. Thermal shrinkage, phase transformations and contact lead to considerable changes of the geometry. The final step, removing the mandrel, takes place at room temperature and leads to the release of elastic energy which can introduce further distortion.

### Study parameter

The main study parameter is the influence contact with the mandrel on distortion of the part. In order to systematically understand resulting displacements results from three different simulation setups are compared. First free quenching in oil without contact is matched up with quenching in the fixture with contact. Secondly the influence of a much larger mandrel diameter of + 0.5 mm than the nominal one on distortion is analysed.

### RESULTS

For validation of thermal history measured temperature curves are compared to simulated temperature curves for two positions. Fig. 3 shows this comparison.

The temperature comparison shows good overall agreement with the exception of two time periods where the curves deviate from each other. The described transport and resting inside the press in the beginning for a temperature region above 750 °C is not replicated perfectly. For lower temperatures below 250 °C the simulated temperature curve on the left hand side deviates from the measured one. The overall quality of the simulated temperature curve is considered excellent, since good agreement is achieved in the region with steep temperature reduction where most of the shrinkage and phase

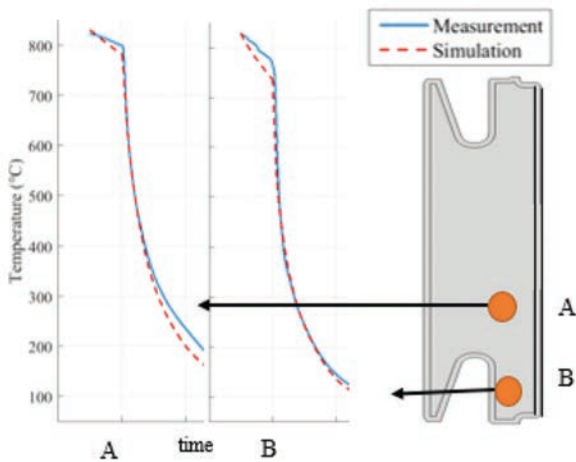


Fig. 3. Measured and calculated temperature curves for two position, A and B inside the gear blank during fixture hardening

transformations take place. Martensite start for the bulk of the material, the non-carburised body is well above 300 °C and thus the martensite transformation for this region can be modelled realistically. For free quenching thermal history has not been recorded. The implemented HTC has been experimentally determined by [14].

Displacement of the gear blank, scaled by a factor of 25, for free quenching and fixture hardening with the nominal diameter is shown in Fig. 4. The volume of transformed martensite is illustrated. At room temperature the martensite transformation in the gear body is nearly finished at 96% transformed volume with 4% retained austenite. The case yields lower volume fractions of martensite of approximately 73% due to higher carbon contents.

For a detailed analysis of the distortion the relative displacement in  $\mu\text{m}$  per mm over the normalised height of the gear blanks is plotted in Fig. 5. All three cases are displayed:

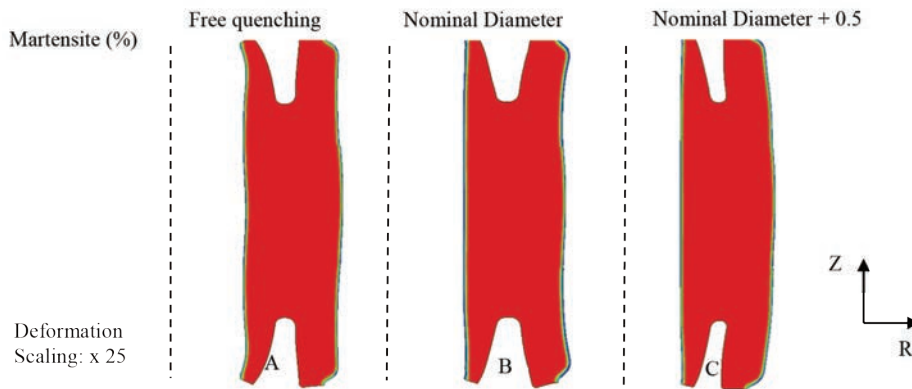


Fig. 4. Contour plot, martensite volume fraction, deformation scale factor: 25. A – Free quenching, oil W72; no contact. B + C – Fixture hardening, oil W21 with contact during quenching, plot with mandrel removed, B – nominal diameter C – nominal diameter + 0.5 mm

relative displacement in  $\mu\text{m}$  per mm over the normalised height of the gear blanks is plotted in Fig. 5. All three cases are displayed:

The straightening effect of the contact of the gear blank with the mandrel can most clearly be detected on the inner radius. While free quenching (Fig. 4 and Fig. 5 A) yields a wavy shape with a buckling in the middle section, fixture hardening yields a much straighter inner radius (Fig. 4 and Fig. 5 B). For cases B) and C) buckling of the middle section is mostly suppressed and folding of the bottom and tip, between  $\pm 0.8$  and  $\pm 1$  normalised height, is reduced by contact of the part with the mandrel. The recess area displays a similar pattern for both simulation setups, free quenching and fixture hardening. The inner part bends towards the axis of rotation while the outer gear arms bend in the opposite direction. The free quenching shape of the outer radius differs significantly from the fixture hardening one, compare (Fig. 4, Fig. 5 A and B). Free quenching yields a pattern with an elevated middle section similar to the one of the inner radius. On the

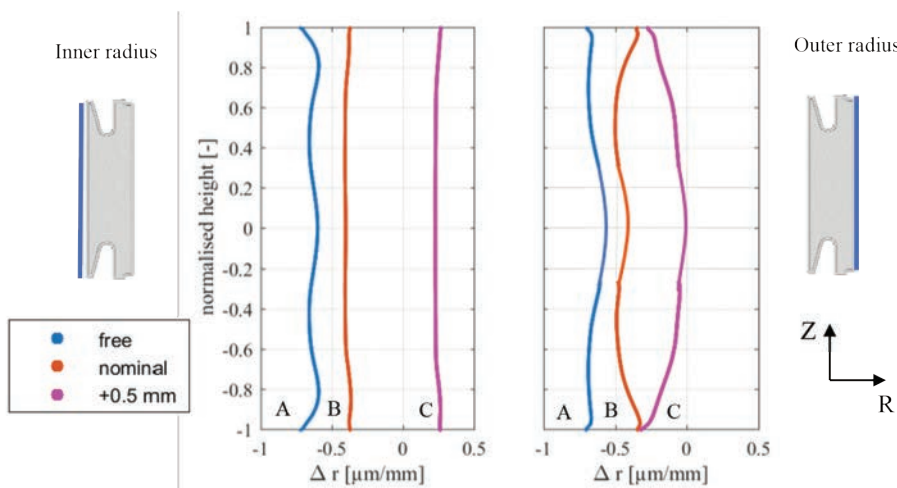


Fig. 5. Relative displacement in  $\mu\text{m}$  per mm for free quenching, fixture hardening with nominal mandrel diameter and fixture hardening with large mandrel diameter. Top: Inner radius. Bottom: Outer radius

outer radius this pattern gets reversed during fixture hardening. The bottom and top parts are elevated while the middle section appears to be pushed back slightly. An interesting shape change occurs when the mandrel diameter is increased. The outer diameter bends outwards while bottom and tip bend inwards to form an overall barrel shape that is not formed for the nominal diameter.

## DISCUSSION AND CONCLUSION

The main conclusions of the presented study concern differences between free quenching and fixture hardening and the effect of the increased nominal mandrel diameter on distortion. As expected a strong straightening effect of the mandrel on the inner radius has been documented. The outer radius however distorts slightly more when fixture hardened. The outer gear arms bend outwards stronger than when free quenched. As an effort to understand and enhance process control the mandrel diameter has been increased. Resulting dependency of distortion of the outer radius on mandrel diameter is non-linear. Two different types of shapes develop: A barrel shape for the large diameter and a shape with bottom and tip bending outwards for the nominal diameter. The two observed shapes allow the conclusion that an optimum with minimal distortion possibly exists between the two observed outcomes. The mandrel diameter acts as an effective process parameter to influence distortion of the outer radius. Straightening as well as distortion as a result of contact and plasticity effects have been demonstrated. Based on the presented results the focus of ongoing research is validation of distortion of the model by coordinate measuring machine readings. For a deeper understanding an analysis of the developing contact pressure for different simulated mandrel diameters is planned.

## ACKNOWLEDGEMENTS

The authors would like to thank the Federal Ministry for Economic Affairs and Energy (BMWi) and Aerospace Transmission Technologies (ATT) for funding this project within the Luftfahrtforschungsprogramm (LuFo), Förderkennzeichen 20T1726.

## REFERENCES

1. **Streng T., Heefß K., & Lübben T.** Dimensionally and geometrically accurate quenching of ringshaped components in fully-automated hardening presses. Proc. 19th ASM Heat Treating Society Conference. 1999. USA.
2. **Gur H., Pan J.** Handbook of Thermal Process Modeling Steels. 2001. CRC Press.
3. **Simsir C., Hunkel M., Luetjens J., Rentsch R.** Process-chain simulation for prediction of the distortion of case-hardened gear blanks // Mat.-wiss. u.Werkstofftech. 2012. No. 1–2, 163–170. P. 43.
4. **Schicchi D., Caggiano A., Lübben T., Hunkel M., Hoffmann F.** On the mesoscale fracture initiation criterion of heterogeneous steels during quenching // Materials Performance and Characterization. 2017. Bd. 1. P. 80–104.
5. **Simsir C., Gür H.C.** A FEM based framework for simulation of thermal treatments: Application to steel quenching // Computational Material Science. 2008. Bd. 44. P. 588–600.
5. **Avrami M.A.** Kinetics of phase change II, transformation-time relations for random distribution of nuclei // J. Chem. Phys. 1940. Vol. 8. P. 212–224.
6. **Johnson W.A., Mehl R.F.** Reaction kinetics in process of nucleation and growth // Trans. AIME. 1939. Bd. 135. P. 416–458.
7. **Leblond J.B., Devaux J., Devaux J.C.** Mathematical modelling of transformation plasticity in steels I: case of ideal-plastic phases // Int. J. Plast. 1989. Vol. 5. P. 551–572.
8. **Koistinen R., Marburger D.** A general equation prescribing the extent of the austenite-martensite transformation in pure iron-carbon alloys and plain carbon steels // Acta metallurgica. 1959. Vol. 7. P. 59.
9. **Wai C. et al.** Plasticity for Structural Engineers // J. Ross Publishing, 1988.
10. **Jablunka, Harste, Schwertfeger.** Thermomechanical properties of iron and iron-carbon alloys: density and thermal contraction // Steel Research International. 1991. Vol. 62, Iss. 1. P. 24–33.
11. **Wolff M., Böhm M., Dalgic M., Hüßler I.** Evaluation of models for TRIP and stress-dependent transformation behaviour for the martensitic transformation of the steel 100Cr6 // Comput. Mater. Sci. 2008. 43. P. 108–114.
12. **Hunkel M., Kagathara J., Prahl U.** The Influence of Segregations after Forming on the Heat Treatment Result of Bevel Gears // Steel research international. 2019, 02. 90(6). P. 1611–3683.
13. **Surm H., Lübben T., Hunkel M.** Konstruktions- und größenbedingte Einflüsse auf den Verzug von ölabgeschreckten Zahnradgrundkörpern – Teil 2: Ermittlung des Verzugsverhaltens mittels der Finite-Elemente-Methode // HTM J. Heat Treatm. Mat. 2017. 4. P. 215–231.

# APPLICATION OF UNIVERSAL FUNCTION APPROXIMATOR TO PREDICT HTC DURING QUENCHING

Sándor Szénási<sup>1a</sup>, Zoltán Fried<sup>1b</sup>, Károly Széll<sup>2c</sup>, Imre Felde<sup>1d</sup>

<sup>1</sup> John von Neumann Faculty of Informatics, Óbuda University. Budapest, Hungary

<sup>2</sup> Alba Regia Faculty, Óbuda University. Budapest, Hungary

<sup>a</sup>szenasi.sandor@nik.uni-obuda.hu, <sup>b</sup>fried.zoltan@nik.uni-obuda.hu, <sup>c</sup>szell.karoly@amk.uni-obuda.hu,

<sup>d</sup>felde@uni-obuda.hu

In order to achieve the desired performance of object to be heat treated, it is necessary to know the Heat Transfer Coefficient (HTC), which describes the amount of heat exchange between the workpiece and the cooling medium. The task of HTC's prediction belongs to the Inverse Heat Transfer Problems (IHCP), which cannot be solved by direct numerical methods. The several methods used to solve the IHCP are based on heuristic search algorithms, like Genetic Algorithms, or Particle Swarm Optimisation, and other methods using swarm theory. In these cases, each instance (chromosome/particle) represents a possible HTC function, and the fitness value is presented as the squared difference of the measured and the simulated cooling curves using the evaluated HTC values. The results of these methods are promising; however, the processes need hundreds of instances and thousands of iterations. Therefore, the number of fitness function evaluations (which needs an entire simulation of cooling down) is significantly high, making the process very time-consuming. This paper suggests a special application of Artificial Neural Networks, the universal function approximator. After the time-consuming training process, this network is capable of giving prompt estimations about the nature of the HTC function sought. This estimation would be a useful input for additional fine-tuning algorithms and finally for complex simulation of Heat Treatment Operations.

**Keywords:** IHCP; machine learning; neural network; quenching.

## INTRODUCTION

There are several procedures to solve the IHCP. Most of them are based on heuristic search algorithms, like Genetic Algorithms (GA) [1]–[3], or Particle Swarm Optimization (PSO) [4]–[6]. The results of these are very promising; it is possible to accurately predict the HTC function from the temperature function. However, the hundreds of required instances (particles/chromosomes) and thousands of iterations make these processes very time-consuming [7].

Artificial Neural Networks (ANN) are computing systems originally inspired by the biological neural networks of animal brains [8]. These systems can recognize and learn patterns by considering examples (training phase) and use these patterns to predict the output for unknown inputs. ANNs are applicable for general computing tasks without any prior knowledge about the given area. They automatically generate identifying characteristics from the training data that they process. The base component of these networks is the artificial neuron, which is a simplified model of the biological neuron of the brain. Like synapses in the biological brain, artificial neurons also have connections, making them able to transmit signals from one to another.

Beyond pattern recognition, ANNs are also applicable for function approximation (also known as regression). As a supervised learning method, it uses a set of example pairs of input/output data and tries to find a function mapping one value of these pairs to the other. Both the input and the output elements of these pairs can be multidimensional floating-point arrays. The universal approximation theorem states [9] that a feed-forward artificial network containing a single layer with a finite number of artificial neurons can approximate any continuous functions on compact subsets of  $R_n$ , under mild assumptions on the activation function. According to this, it is possible to give the discrete values of a temperature function as the input, and the values of an HTC function as the output. Our aim is to build a network that is capable to predict the main characteristics of the HTC function based on the temperature data.

The rest of this paper is structured as follows: the next section contains details about the used input and output data and the architecture of the neural network (layers, nodes, loss function, etc.). The third section presents the performance of the system, and the final section focuses on the conclusions.

## METHODOLOGY

### Input and output data

The main bottleneck of several machine learning projects is the availability and quality of training datasets. This is true for our case as well, training the ANN needs HTC functions and the corresponding temperature functions. Due to the high number of requested data series (millions of function pairs), it is not possible to use only real-world measurements. Instead, we randomly generated millions of potential HTC functions. Using our already existing GPU based Direct Heat Conduction Solver (DHCP) algorithm, it was possible to generate the cooling curves for these within a reasonable time. These series were used as the input and output data pairs.

It is common to split the whole dataset into smaller parts:

Training dataset – the model is initially fit on this (80% of the full dataset).

Validation dataset – it provides an unbiased evaluation while tuning the hyperparameters of the model (10% of the full dataset).

Test dataset – it is used for the unbiased final evaluation of the final model trained on the training dataset and fine-tuned with the validation dataset (10% of the full dataset).

This paper does not deal with hyperparameters; therefore, we use only the training and test datasets.

HTCs are continuous functions in the selected temperature range (0 °C – 850 °C). These functions must be discretized to make them available as the output of a neural network. Eq. 1. shows the process of creating a  $d$  dimensional output vector  $Y$

$$Y[i] = HTC\left(\frac{850^\circ\text{C}}{d}t\right) \quad (1)$$

$i \in N \mid 1 \leq i \leq d,$

We used  $d = 85$ , storing the values of the HTC function by 10.

Temperature functions are continuous in the time range 0 sec – 120 sec (simulations were executed during this time interval). The neural network can better recognise patterns and correlations if the range of interpretation is the same for the input and output vectors. To achieve this, the temperature function was inverted (to get the time values for given temperatures) and differentiated (to get the elapsed time between given temperature states). This function is discretized in a similar way as Eq. 1. Because of the derivation, the dimension of the input vector is  $d-1 = 84$ .

The loss is specified by the summarized absolute difference between the original HTC ( $Y$ ) and the predicted HTC function ( $Y_{\text{pred}}$ ) values. Our goal is to minimise this value.

$$\text{loss} = \frac{1}{d} \sum_{i=1}^d |Y[i] - Y_{\text{pred}}[i]|.$$

### Building the network

This paper presents a multi-layered neural network based universal function approximator implemented by the Keras and the TensorFlow frameworks in Python. In our primary tests, we used 64 hidden neurons for the training.

Fig. 1. shows the main building blocks of the basic model. It has a first dense (also known as fully connected) layer, which requires an input tensor of  $b \times 85$ , where  $b$  is the batch size (which is not part of the model, it is determined during the runtime of the training process) and 85 is the size of the input temperature vector. The output of this layer is a tensor of  $b \times 64$ , where 64 is the number of hidden neurons.

In the second activation layer, it has rectified linear units (ReLU) to calculate Eq. 2 for all values of the  $b \times 64$  tensor.

$$f(x) = \max(0, x). \quad (2)$$

This tensor is the input of the third dense layer, which calculates the predicted output values as a tensor with dimensions  $b \times 86$ , where 86 is the size of HTC vectors.

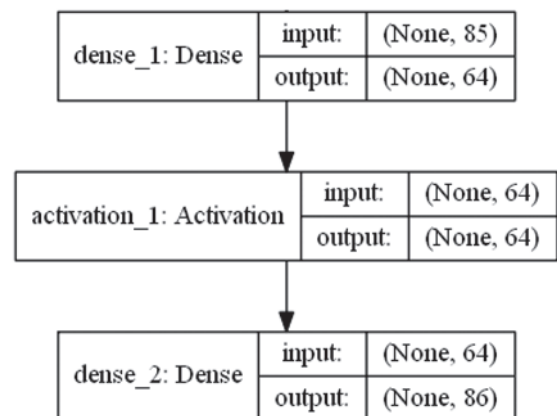


Fig. 1. Universal function approximator

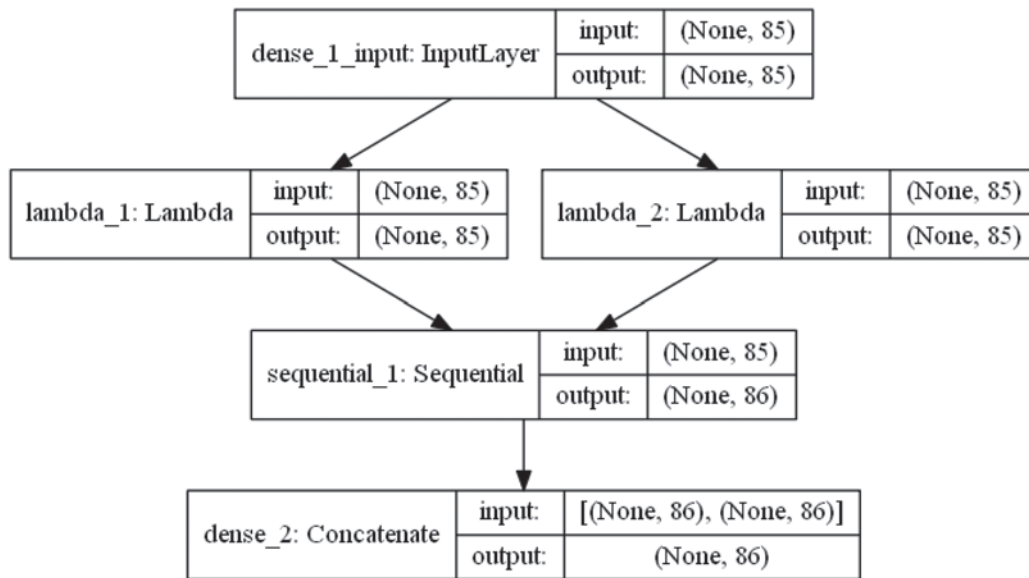


Fig. 2. Distributed universal function approximator

## Using multiple GPUs

To speed-up, the training process, multiple graphics accelerators (GPUs) were used. The Keras built-in multi-GPU model was used, which distributes the calculation intensive work between the available devices. Based on the used two NVIDIA GeForce Titan Black graphics cards, the training model was changed to a distributed one presented in Fig. 2.

This “two-tower” pattern makes it possible to assign the gradient calculation task to different devices. It creates multiple replicas to distribute calculations and some additional operations to accumulate these results to have the correct gradient for each training iteration.

It is well visible in Fig.3. (generated by the TensorBoard application), that some nodes (calculations) are assigned to GPU 0 (green nodes), and to GPU 1 (blue nodes), meanwhile several technical nodes remain in the CPU (cyan nodes). The location of grey nodes is unknown; however, these should be processed by the CPU.

## EVALUATION

10 million random HTC functions were generated with the associated temperature functions.

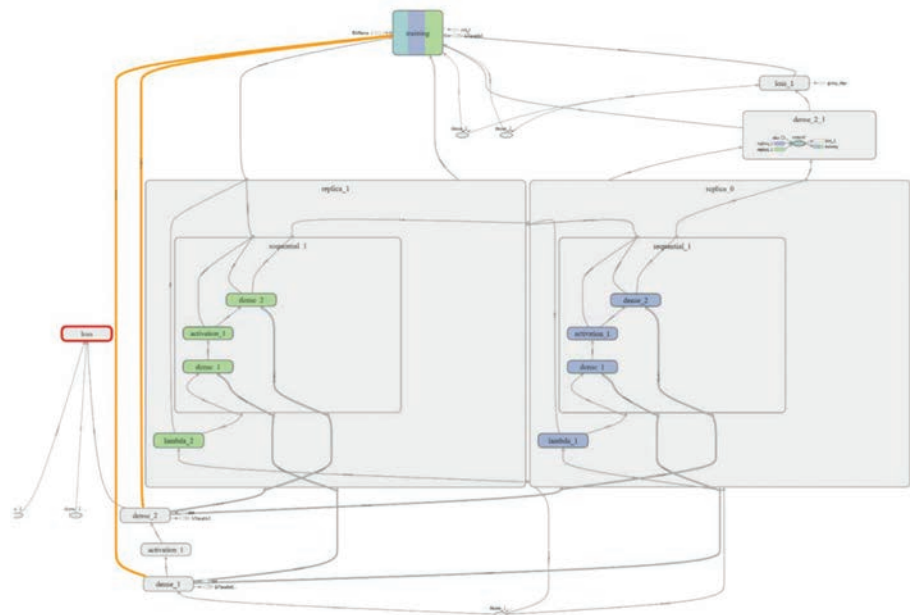


Fig. 3. TensorBoard visualisation of the multi-GPU model

After the presented discretization, inversion, derivation operations, the size of the datasets become more than 10 GB. Implementation of the presented model was done using the Python Keras library on TensorFlow backend. Training the model takes about 2 weeks using the dual NVIDIA GeForce Titan Black configuration.

Using the test dataset for the unbiased final evaluation gives very promising results. Fig. 4. shows two examples from the test dataset. The blue lines show the original randomly generated HTC; the red lines show the generated temperature records. The green lines show the output of the ANN, the predicted HTC for the given temperature function (without any knowledge of the original HTC).

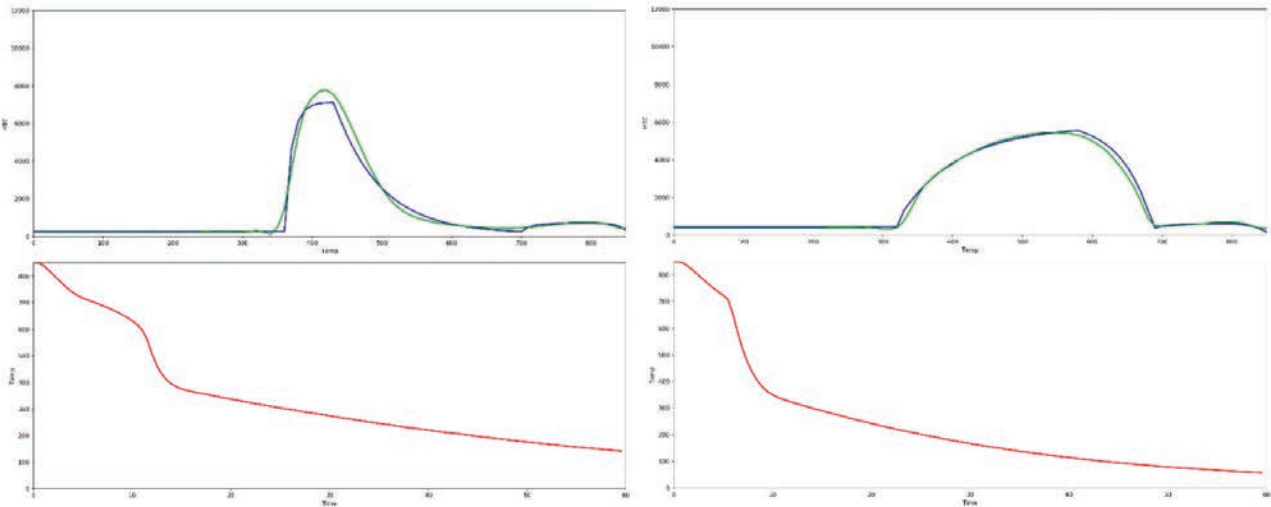


Fig. 4. Unbiased predictions given by the ANN after the training process

As visible, there are no exact matches, but the characteristics of the predicted HTC and the original HTCs are very similar. The ANN can determine the two peak points of the function, and it was able to approximate the shape of the transitions.

## CONCLUSIONS

The prediction of the ANN is not as accurate as the result of the already existing heuristic algorithms, but it has some advantages. It is significantly faster: after the one-time resource intensive learning process, it can give prompt results.

Consequently, a well-configured universal function approximator can estimate the heat transfer coefficient based on the temporal data series. Moreover, this prediction of the ANN can be a good starting point for the further heuristic methods instead of starting these from random locations.

As a further work, we would like to find the best hyperparameters for the ANN (learning rate, number of hidden neurons, etc.) and fine-tune the HTC/temperature function to output/input vector mapping method.

## ACKNOWLEDGEMENTS

We acknowledge the financial support of this work by the Hungarian State and the European Union under the EFOP-3.6.1-16-2016-00010 project. The authors would like to thank NVIDIA Corporation for providing graphics hardware through the CUDA Teaching Center program.

## REFERENCES

1. Colaço M.J., Orlande H.R.B., Dulikravich G.S. Inverse and optimization problems in heat transfer // J. Brazilian Soc. Mech. Sci. Eng. 2006. Vol. 28, No. 1. P. 1–24.
2. Özisik M.N., Orlande H.R.B. Inverse Heat Transfer: Fundamentals and Applications // Taylor & Francis, 2000.
3. Szénási S., Felde I. Configuring Genetic Algorithm to Solve the Inverse Heat Conduction Problem: in 5th International Symposium on Applied Machine Intelligence and Informatics (SAMI2017), 2017. P. 387–391.
4. Sun S.C., Qi H., Ren Y.T., Yu X.Y., Ruan L.M. Improved social spider optimization algorithms for solving inverse radiation and coupled radiation–conduction heat transfer problems // Int. Commun. Heat Mass Transf. 2017. Vol. 87. P. 132–146.
5. Vakili S., Gadala M.S. Effectiveness and Efficiency of Particle Swarm Optimization Technique in Inverse Heat Conduction Analysis // Numer. HEAT Transf. PART B-FUNDAMENTALS. 2009. Vol. 56, No. 2. P. 119–141.
6. Felde I., Szénási S., Pintér G., Shi W., Colas R., Zapata-Hernández O. Parallel PSO method for estimation heat transfer coefficients: in 23rd International Federation of Heat Treatment and Surface Engineering Congress 2016 (IFHTSE 2016), 2016.
7. Szénási S., Felde I. Configuring Genetic Algorithm to Solve the Inverse Heat Conduction Problem // Acta Polytech. Hungarica. 2017. Vol. 14, No. 6. P. 133–152.
8. Mitchell M. An introduction to genetic algorithms // Comput. Math. with Appl. 1996. Vol. 32, No. 6. P. 133.
9. Cybenko G. Approximations by superpositions of sigmoidal functions // Approx. Theory its Appl. 1989.

# IDENTIFICATION OF HEAT TRANSFER COEFFICIENTS AND SIMULATION OF QUENCHING DISTORTIONS ON DISK PROBE

Hideo Kanamori<sup>1</sup>, Dong-Ying Ju<sup>2</sup>

<sup>1</sup> Graduate School of Saitama Institute of Technology. Saitama, Japan

<sup>2</sup> Advanced Science Institute, Saitama Institute of Technology. Saitama, Japan

dyju@sit.ac.jp

In this paper, a pool cooling experiment was conducted in which a SUS304 flat plate specimen, in which a vapor film tends to remain, was placed horizontally in hardened oil, and the cooling situation was determined by fixing the contact point of the welded thermocouple wire directly below the surface. The above cooling process was captured from the cooling curve obtained as the transition of the temperature change. As a result, the first boiling stage was observed before vapor film formation on both upper and lower surfaces, and from the subsequent vapor film stage, the temperature transition was observed following the cooling process which greatly differs between the upper and lower surfaces. From the cooling curve obtained above, the heat transfer coefficients  $h_1(T)$  and  $h_2(T)$  which differ depending on the temperature are identified in inverse problems using the analytical solution of the heat conduction equation for the flat plate. From the heat conduction analysis by the finite element simulation code «COSMAP» using this data, the situation of heat treatment strain occurrence when receiving different cooling on upper and lower surfaces was calculated. A series of techniques can assess the effect of coolants on heat treatment strain, which is considered the biggest problem in heat treatment processes. In addition, it can be used to understand the behavior of the coolant in pool cooling, cause analysis and prediction.

**Keywords:** disk specimen; cooling curves; boiling-heat transfer coefficient; inverse method; heat conduction equation; quenching; simulation; distortion.

## INTRODUCTION

Two systems with temperature differences of several hundred degrees different by several tens of mass make contact, and the liquid system on the low temperature side with large mass changes several °C or less in temperature during cooling, the solid on the high temperature side with small mass from 850 °C. In the cooling process where it is cooled to 200 °C or less, the liquid has a boiling behavior of [1, 2], and in the case of steel on the solid side, stress / strain accompanied by structural transformation, thermal contraction, expansion, etc. The behavior of the cooling process proceeds while affecting each other [3, 4]. The whole change becomes a combination of them, and the prediction is a very difficult problem. In addition, the residual of the steam film in quenching causes unexpected uneven cooling and causes the generation of troublesome heat treatment distortion. On the other hand, concrete information is also provided to people with little knowledge and experience, and it is expected for designers and experts that the analysis method by CAE simulation that enables quantitative prediction and setting can be spread [4–6].

Film boiling, nucleate boiling, and convection specific to the liquid obtained by measuring the surface temperature of the specimen surface when the silver cylindrical specimen specified by the heat treatment liquid cooling performance test method specified in JIS K 2242 heat treatment oil cooling performance test method A cooling curve can be obtained that shows the process of cooling by heat transfer. However, as a result of the difference in the surface condition of silver and steel, it has been found that there is a subtle difference in the vapor film generated on the surface and its collapse behavior [14–16]. Moreover, in the case of the above-mentioned JIS K 2242 test piece, since the temperature is measured on the side, there is a problem that it is not possible to grasp the residual of the vapor film and the behavior of coming off from the top.

So, in this report, we use austenitic SUS304 steel whose surface is similar to steel and does not have structural transformation in measurement of cooling curve, and it is a circular plate-like test piece that the vapor film remains on the lower surface and vapor film does not stagnate immediately. We performed an experiment with. Using the one-dimensional heat conduction equation that describes cooling from two

parallel planes and its analytical solution, the heat transfer coefficient of the upper surface and the lower surface in the boundary condition equation were sequentially determined inversely at the temperature. In addition, the heat transfer coefficient at the side of the disk is also identified from the cooling curve, and the heat transfer coefficient of the disk surface is substituted into the heat treatment simulation code (COSMAP) to perform heat treatment simulation of the disk model of SCM420 and calculation. As compared with the quenching deformation obtained in and the deformation measured in the experiment, highly accurate prediction of the quenching strain was realized.

## METHOD OF IDENTIFYING HEAT TRANSFER COEFFICIENT

### Measurement of cooling curve

A disk-shaped test specimen made of SUS304 with a diameter of 35.0 mm and a thickness of 10.0 mm is fixed in a ring-like jig having an outer diameter of 49.0 mm and an inner diameter of 35.2 mm as shown

in Fig. 1a. Fixing is performed with 3 set screws with contact area of about  $1 \text{ mm}^2$  or less from the ring side face. Thereby, a gap of 0.1 mm was formed on the side of the disk test piece and the side face of the ring-like jig to form a heat insulating wall.

The schematic diagram of experimental equipment was shown in Fig. 1b. In addition, oblique holes were made at an angle of  $6.74^\circ$  with respect to the horizontal from the side surface of the ring toward the immediate center of each of the upper surface and the lower surface of the test specimen, respectively, and the element wires were drawn and welded at  $2\text{--}10 \mu\text{m}$  just below the center of each of the upper surface and the lower surface fix the thermocouple contact with silver paste. The specimen, ring and K thermocouple were uniformly heated to  $850 \pm 1^\circ\text{C}$  in a furnace as shown in Fig. 2 and placed in a sample coolant at a liquid temperature of  $T_0 = 60^\circ\text{C}$ . Immersed in to above specimen for about 0.28 s, and cooling is started. Measure the relationship between the upper surface temperature and the lower surface temperature and the elapsed time  $t$  to obtain the cooling curves of the upper surface and the lower surface.

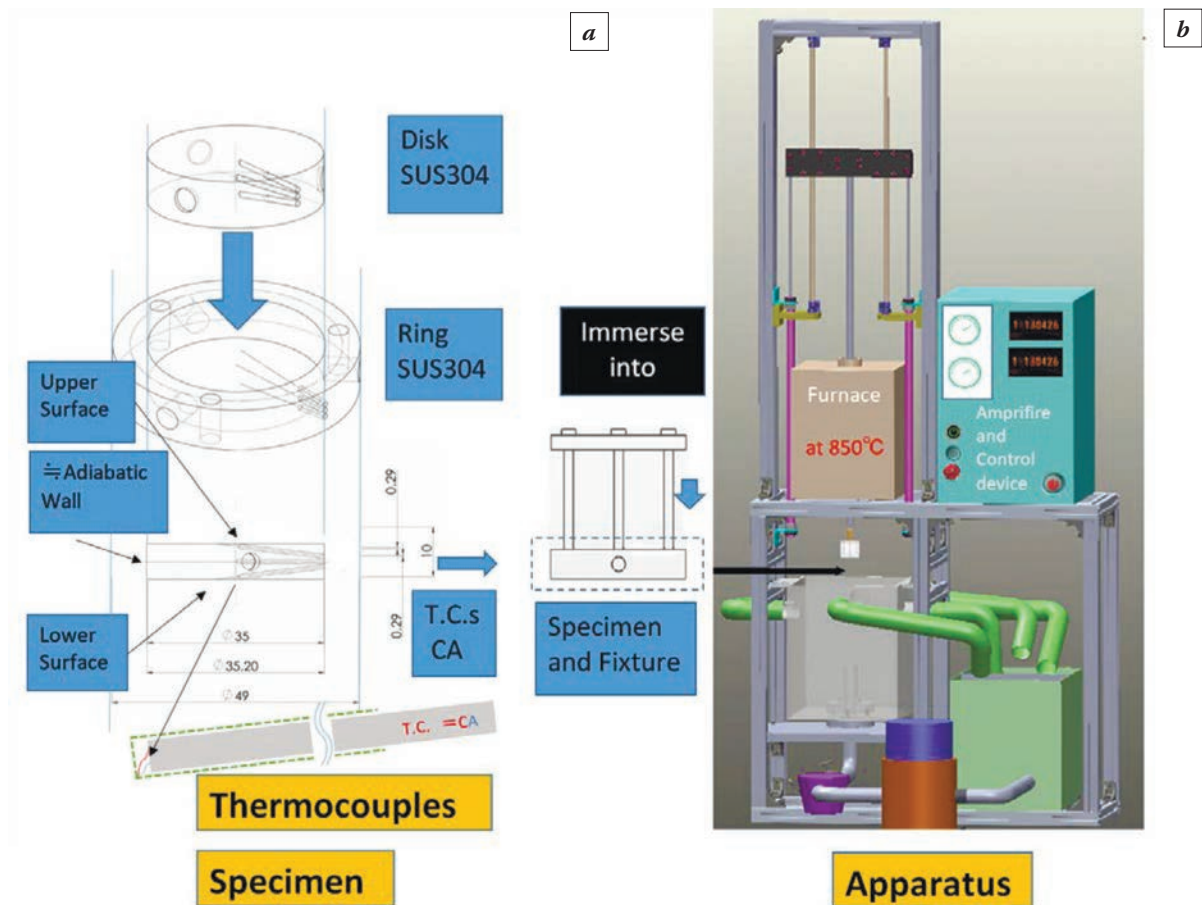


Fig. 1. Structure and shape of disc probe left side, Schematic diagram of experimental equipment in right side

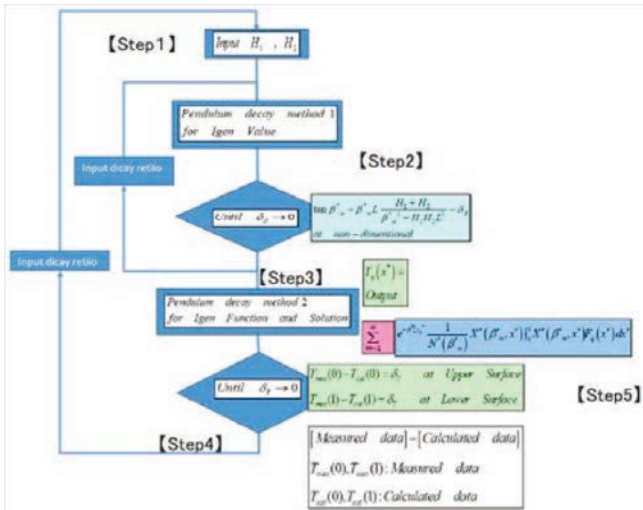


Fig. 2. The procedure of identification of heat transfer coefficient from flat plate cooling curves by inverse method

Table 1. Property of Coolant

Quenching oil : Daphne Bright Quench				
Temperature, °C	Density, g/m <sup>3</sup>	Viscosity, mm <sup>2</sup> /sec	Conductivity, W/m·K	Specific Heat, J/g·K
60	834.9	14.94	0.1315	2.03
70	828.7	11.20	0.1307	2.07
80	822.5	8.667	0.1300	2.11

### Experimental equipment and sample Coolant

For the measurement, an experiment was conducted using a cooling tester manufactured by Nisho Engineering Co. Ltd. as shown in Fig. 1b.

As a sample coolant, commercially available cold quench oil, Daphne Bright quench having the properties shown in Table 1 were used at oil temperature  $T_0 = 60\text{ }^\circ\text{C}$ .

### THEORY OF INVERSE ANALYSIS

#### Thermal conduction equation

One-dimensional equation as (1),

$$\frac{\partial^2 T^*(x^*, t^*)}{\partial x^{*2}} = \frac{\partial T^*(x^*, t^*)}{\partial t^*} \quad 0 \leq x^* \leq 1, \quad 0 \leq t^* \quad (1)$$

where

$$x^* \equiv \frac{x}{L}, \quad t^* \equiv \frac{\alpha t}{L^2}, \quad T^* \equiv \frac{T - T_\infty}{T_0 - T_\infty}$$

and in order to describe the thermal behavior, reflecting the cooling curves were paused “q” step.

In each time, for q<sup>th</sup> step,  
 $t = t_q, \tau_q^* = t_q^* - t_{q-1}^*$  in  $0 \leq x^* \leq 1$   
 $\tau_q$  is time interval, and initial condition is

$$T^* = F(x^*) \text{ for } t^* = 0, \text{ in } 0 \leq x^* \leq 1 \quad (3)$$

And then boundary conditions as,

$$-\frac{\partial T^*}{\partial x^*} + H_1 L T^* = 0 \text{ at } x^* = 0, t^* > 0 \quad (4)$$

$$k_2 \frac{\partial T^*}{\partial x} + h_2 T = 0 \text{ at } x = L, \tau_q \geq 0 \quad (5)$$

where

$$\alpha = k = \frac{k}{c_p \rho} : \text{Thermal Diffusivity, m}^2/\text{s}$$

k : Heat Conductivity, W/m·K

$c_p$  : Isobaric Specific Heat, J/kg·K

$\rho$  : Density, kg/m<sup>3</sup>

$h_1$  : Heat Transfer Coefficient of the top surface, W/m<sup>2</sup>·K

$h_2$  : Heat Transfer Coefficient of the bottom surface.

The heat transfer coefficients on both sides of the disk can be expressed as follows:

$$H_1 \equiv h_1/k_1 \text{ and } H_2 \equiv h_2/k_2. \quad (6)$$

Analytical solution of (1), (2), (3), (4), (5) shown as

$$T^*(x^*, t) = \sum_{m=1}^{\infty} \exp(-\beta_m^{*2} \tau_q^*) \frac{1}{N^*(\beta_m^*)} \times X^*(\beta_m^*, x^*) \int_0^1 X^*(\beta_m^*, x^*) F(x^*) dx^* \quad (7)$$

And the normalization integral as

$$N(\beta_m^*) = \int_0^L [X(\beta_m^*, x^*)]^2 dx^* \quad (8)$$

Eigenfunction and eigenvalue,  $\beta_m^*$  as

$$X_m^*(\beta_m^*, x^*) = \beta_m^* \cos \beta_m^* x^* + H_1 L \sin \beta_m^* x^* \quad (9)$$

$$\tan \beta_m^* = \frac{\beta_m^* L (H_1 + H_2)}{\beta_m^{*2} - H_1 H_2 L^2}. \quad (10)$$

The heat transfer coefficients on the upper and lower surfaces of the parallel flat disk shown in the above boundary conditions (4) and (5) can be expressed by equations including eigenfunctions and eigenvalues. Here, when an appropriate heat transfer coefficient of a certain temperature region is identified and can be substituted into the equation, the adopted calculated temperature distribution as the initial condition of the next time step and the calculation can be continued. Calculations corresponding to all temperatures of the cooling process are thus carried out.

## Identification of heat transfer coefficient

The heat transfer coefficients of parallel two planes corresponding to the respective temperatures of the cooling process are obtained by the following procedure and Fig. 2.

First, the time interval is 1 to 3 °C in the region where the surface temperature changes from the vapor film stage to the nucleate boiling stage, where the change of the surface temperature changes drastically, the relatively slow change of the surface temperature change that shifts to the convection cooling after the end of nucleate boiling region is set each time it is cooled by 6 to 12 °C. For each time interval, identify “and” with the following steps 1–5. When the difference between the measured value of the temperature on the disk surface and the calculated value of the surface of each of the lower surfaces calculated from one and the other is greater than the allowable value  $\delta$  ( $= 0.2$  °C. this time) Added a program that repeats slight modification until it becomes less than or equal to the value of  $\delta$  so that a value close enough to the measured value is obtained.

In the first step, an initial value should be substituted. The second step, a plurality of eigenvalues which are series solutions of functions satisfying the equation. The next third, substitute the above equation (2) into the equations, and calculate the temperature of each part of the disk from the equation. The four step, repetition calculation is performed so that the difference between the above measured value and the calculated value from the lower surface becomes less than the allowable value  $\delta$ . The final step, even if the difference between measured value and calculated value of one side, eg upper side, becomes  $\delta$  or less, it is not always the case that the measured value and the calculated value of the lower side are in agreement ( $\delta$  or less), so reset again, go back to four step, Repeat steps 4–5 until the measured values and the

calculated values of the top and bottom faces match. Changes in the value of the temperature of the upper surface that has changed this time will have an influence on it, so we need to change it again to make it. We will repeatedly identify such gangs. In order to make the calculated value coincide with the measured value and bring the difference between them to the target  $\pm \delta$  or less, a method of setting the change amount to be smaller each time and ending the wandering was adopted in Fig. 2.

## RESULTS AND DISCUSSION

### Cooling curves

The cooling curve measurement result of the sample coolant is shown in Fig. 3 At the same time as the specimen heated to 850 °C was charged into the coolant, vapor bubbles of the sample coolant rising from the surface were observed on the upper surface of the specimen. On the upper surface of the test piece, a first boiling step of 0.23 sec up to 836.6 °C, was observed immediately after the start of cooling, and then a cooling curve was obtained in which film boiling region at once until 1.26 sec up to 816.0 °C, so it could be recognise the specific temperature. On the other hand, under the lower surface of the specimen, the first boiling stage where no vapor film was formed like the upper surface was observed for 0.23 sec up to about 833.7 °C. Slow cooling which was covered over a stable vapor film for more than 10 seconds after that was observed.

On the lower surface seemed remained stable boilingfilm under the surface, until 12.06 sec at 524.5 °C. Thereafter, the lower surface shifted to nucleate boiling and was cooled with a curve parallel to the upper surface, and both surfaces migrated to convection cooling from around 500 to 400 °C.

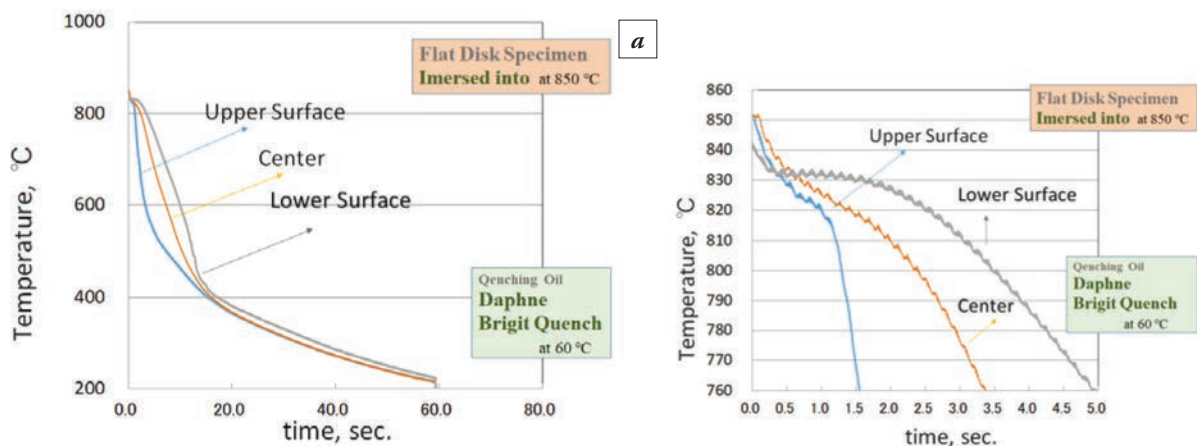


Fig. 3. Measured Cooling Curves: *a* – Cooling curves of the entire cooling process; *b* – Boiling first stage cooling curve. Temperature measured just below the surface

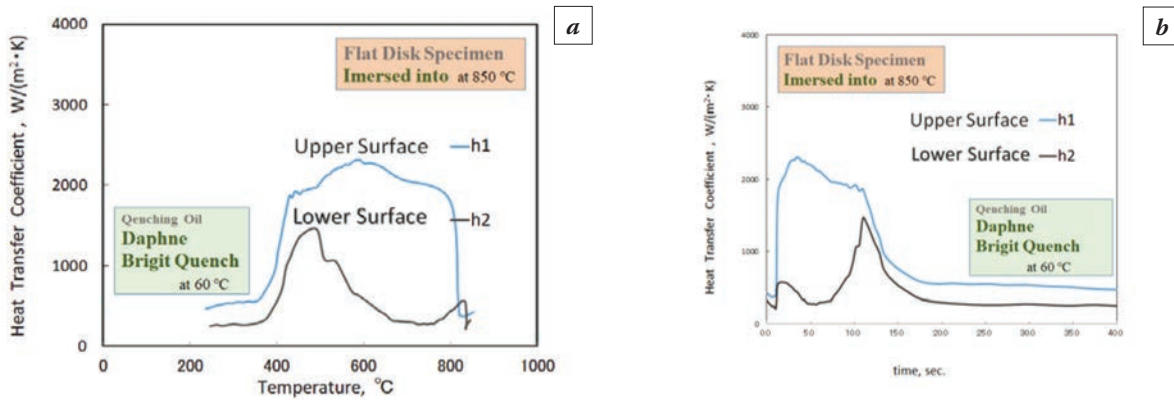


Fig. 4. Heat transfer coefficient  $h_1(T)$  and  $h_2(T)$

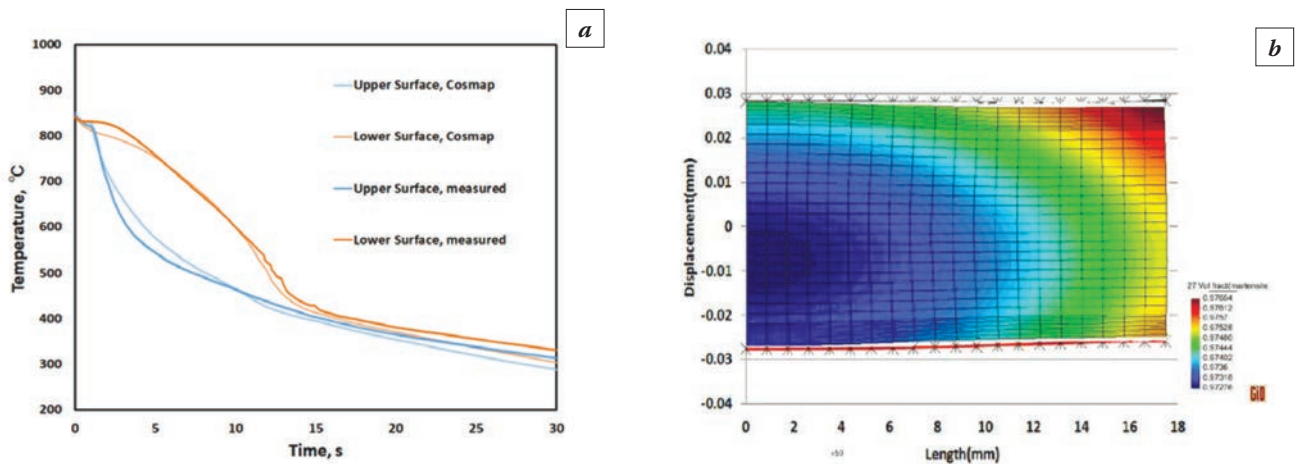


Fig. 5. Comparison of simulation results and measured data: *a* – Cooling curves of SUS304 steel; *b* – Quenching Distortion of SCM420 steel

## Heat transfer coefficient

From the cooling curves data in Fig. 3, the temperature-dependent heat transfer coefficient of parallel two planes was identified by the method in 3.2, and the relationship with temperature is shown in Fig. 4*a* and the time course is shown in Fig. 4*b*. Both the upper and lower surfaces undergo a film boiling stage where the lower surface drops to 300 W/(m<sup>2</sup>·K) after the first boiling stage, and nucleate boiling cooled at about 2250 W/(m<sup>2</sup>·K) from around 700 °C. The change from the 480 °C to 320 W/(m<sup>2</sup>·K) convection cooling changes from the first boiling stage to the nucleate boiling of 2700 W/(m<sup>2</sup>·K) directly from the first boiling stage and changes from near 350 °C to 500 W/(m<sup>2</sup>·K) or less, it can be seen from Fig. 4*b*. It is inferred that the peak occurrence of 2800 W/(m<sup>2</sup>·K) in Fig. 4*a* is a change that occurs in response to a small inflection point near 6s in the top cooling curve in Fig. 4.

## Simulation results

Cooling curves calculated from two-dimensional thermal conduction analysis of SUS304 material by inputting it to the CAE heat treatment simulation code COSMAP and the result compared with the cooling curve measurement value in Fig. 5*a*. the calculated cooling curve matched the measured value, validity of experiment, identification analysis and calculation was confirmed acknowledgment. So that, calculated quenching distortion of SCM420 material that shaped flat disk, and obtained coincident result to measured data in Fig. 5*b*.

## CONCLUSIONS

The following conclusions were obtained from this study.

1) In order to read the temperature change it is not a sheath type but a method in which a wire is

pulled out and the welded contact is fixed to the tip of an oblique hole reaching just under the surface and the surface temperature is accurately measured using a parallel two-We conducted an experiment to capture the boiling behavior of the agent.

2) Prior to formation of steam film, a quenching region at the first boiling stage was confirmed.

3) On the upper surface, a first boiling step of 0.23 sec up to 836.6 °C was observed immediately after the start of cooling, and then a cooling curve was obtained in which film boiling region at once until 1.26 sec up to 816.0 °C.

4) Using the analytical solution of the heat conduction equation describing the above 1, the temperature-dependent heat transfer coefficient was identified for each of the upper and lower faces as the boundary condition.

5) Using this, input to heat treatment simulation code COSMAP and 2 dimensional thermal conductivity analysis for SUS304 material, the calculated cooling curve matched the measured value, validity of experiment, identification analysis and calculation was confirmed.

## ACKNOWLEDGMENT

This work was supported by High-Tech Research Center in Saitama Institute of Technology in Japan. The authors also thank Ms. Katsumi Ichitani,

IDEMITSU KOSAN Co.,Ltd., for useful advice on experimental method.

## REFERENCES

1. **Tagaya M., Tamura I.** Research of Quenching Liquid: NIPPON KINZOKU GAKKI-SI. 1951–1952. Vol. 15–16, report 1-4.
2. **Dhir V.K.** Investigation of Mechanisms Associated with Nucleate Boiling Under Microgravity Conditions // Proceedings of the Third Microgravity Fluid Physics Conference. NASA CP–3338. 1996. P. 153–158.
3. **Inoue T., Nagaki S., Kishino T., Monkawa M.** // Ing. Arch. 1981. 50-5. P. 315–327.
4. **Inoue T., Ju D.Y., Arimoto K.** Proc. 1st int. Conf. Quenching and Control of Distorsion, 1992. P. 205–212.
5. **Mukai R., Ju D.Y.** Simulation of carburizing-quenching of a cylinder. Effect of carbon content on residual stresses and distortion // Journal de Physique IV (proceedings). 2004. P. 489–497. DOI: 10.1051/jp4:2004120056.
6. **Ju D.Y., Zhang W.M., Zhang Y.** Modeling and experimental verification of martensitic transformation plastic behavior in carbon steel for quenching process // Materials Science and Engineering A. 2006. Vol. 438, No. 440. P. 246–250. DOI: 10.1016/j.msea.2006.01.125.
7. **Suzuki K., Ju D.Y.** Cooling performance evaluation and visualization of thermal flow in gas cooling process // J-stage. 2006. Vol. 26, No. 2. P. 155–158. DOI:https://doi.org/10.3154/jvs.26.Supplement2\_155.

# MICROSTRUCTURE AND TRIBOLOGICAL PROPERTIES OF EXPANDED AUSTENITE FORMED IN AUSTENITIC STAINLESS STEELS BY LOW-TEMPERATURE ACTIVE SCREEN DIRECT CURRENT PLASMA CARBURISING

Youichi Watanabe<sup>1</sup>, Nobuhiko Satomi<sup>2</sup>, Haruna Ishizuka<sup>1</sup>, Kosuke Takamura<sup>1</sup>,  
Weibo Li<sup>1</sup>, Nobuyuki Kanayama<sup>3</sup>

<sup>1</sup>Nihon Parkerizing Co., Ltd. Tokyo, Japan

<sup>2</sup>Parker Trutec Inc. Ohio, USA

<sup>3</sup>Sentier Giken Co., Ltd. Shimane, Japan

yiwatanabe@parker.co.jp

By using a low-temperature plasma carburising process that combines active-screen and direct-current plasma methods at 733 K under a CH<sub>4</sub>/H<sub>2</sub> gas mixture atmosphere, an expanded austenite (S phase) which has both super-high hardness and high resistance to corrosion can be efficiently formed on the surface of austenitic stainless steels. In this paper, the microstructure of the S phase formed on SUS304 and 316 steels and effects of the S phase on mechanical and tribological properties are investigated by optical microscopy, X-ray diffraction (XRD) analysis, transmission electron microscopy (TEM) observation, tensile tests, and using a ball-on-disc tribometer and high-frequency translatory oscillation test apparatus (SRV<sup>®</sup> 5 tester). The results show that the S phase includes high-density dislocations, has a sufficient number of stacking faults and twins, and improves tensile strength while decreasing elongation. The frictional and fretting wear resistances of SUS316 steel are highly improved by forming an S phase with a thickness of 10 μm or more. The SUS 316 steel in which the S phase was formed by the low-temperature plasma carburising was also found to have good corrosion and dissolution resistance in simulated body fluids (Ringer's solutions) holding at 310 K.

**Keywords:** plasma carburising; austenitic stainless steel; expanded austenite; wear; fretting; corrosion.

## INTRODUCTION

Austenitic (γ) stainless steels such as JIS-SUS304, 310S and 316 are non-magnetic and have excellent corrosion and heat resistances. However, these steels have a relatively low structural strength even though their ductility and/or toughness are at an appropriate level. Specifically, the tensile strength of solution-heat-treated SUS304 steel is 550 to 650 MPa which is approximately the same as that of normalized plain carbon steel S35C or S40C. Frictional wear resistance is also insufficient because of low surface hardness. To increase the surface hardness of γ stainless steels with little to no loss of non-magnetism and corrosion and heat resistances in an efficient way, we have been investigating the carbon expanded austenite phase (hereinafter S phase) [1–3] formed on the surface layer by a low-temperature carburising process combined with a direct current plasma (DCP) method and an active screen plasma (ASP) method [4, 5]. This paper comprehensively describes the microstructure, strength and tribological properties of

the S phase in SUS304 and 316 steels and the expected fields in which carburised γ stainless steels can be applied.

## FORMATION OF CARBON S PHASE IN AUSTENITIC STAINLESS STEEL Low-temperature active-screen direct-current plasma (ASDCP) carburizing

The DCP method is a well-established technology in widespread use as it enables plasma to be efficiently discharged onto a processing target to form an S phase on the steel surface. However, obtaining a uniform and smooth surface is difficult due to arcing, hollow cathode effects and edge effects occurring on the surface during the operation [6]. In contrast, the ASP method can obtain a homogeneous S phase because the processing target is treated not by directly discharging plasma, but by a reactive species generated from the discharge plasma occurring on a metal screen (generally made of stainless steels) arranged

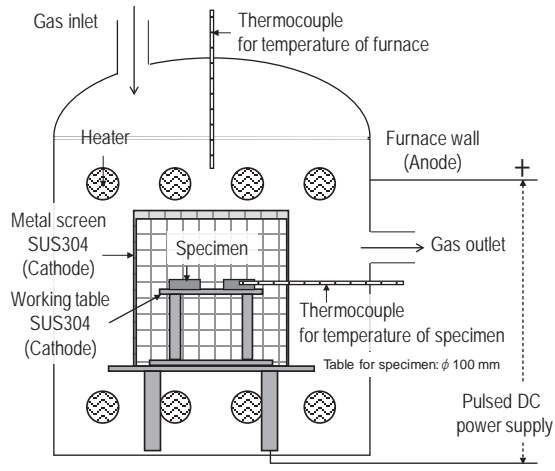


Fig. 1. Schematic of low-temperature plasma carburising system combining direct-current and active-screen plasma methods

to cover the target. The main disadvantage of the ASP method is that the S phase formation efficiency is lower than that of the DCP method, and screen components such as nickel or chromium are likely to be deposited on the processing targets, which inhibits the formation [7].

Therefore, a carburising process combining DCP and ASP has been developed to obtain an S phase effectively even at temperatures less than 733 K. The plasma carburising system used in this study is shown in Fig. 1 [4]. The vacuum furnace (designed and manufactured by NDK inc.) has a usable dimension of  $300^W \times 280^L \times 250^H$  mm and a maximum load of 20 kg per charge. The screen cage made of SUS304 stainless steel wire mesh ( $\phi 150$  mm  $\times$   $150^H$  mm, open area ratio of 59.2%) was prepared as a dual structure. The plasma was generated using a pulsed power supply (up to 1 kV-120 A, made by Rübige GmbH & Co. KG). External heaters were also used for controlling the carburising temperature. The specimen temperature was monitored by using a thermocouple set at a depth of 1 mm in the dummy specimen (made of SUS304 steel with a 24-mm diameter). The  $\gamma$  stainless steels used in this paper are SUS304 and 316 as shown in Table 1 [4]. The specimens were disc-shaped, 24 mm in diameter and 8 mm thick. The surfaces were mechanically ground and polished to a mirror finish using the emery paper of #1000 (JIS-P1200). Fig. 2 [5] shows the plasma carburising conditions to form the S phase. The specimens were carburised using a gas mixture of methane and hydrogen under 40 Pa pressure at 733 K for 14.4 ks after specimen surface contamination and the oxide film were cleaned by an ion bombardment process using an argon/hydrogen gas mixture. After the carburising, the specimens were cooled in the furnace under a reduced pressure.

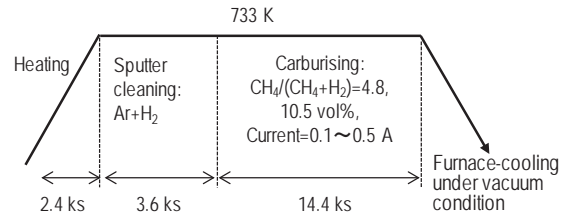


Fig. 2. Plasma carburising conditions

Table 1. Chemical compositions of austenitic steels used, mass %

	C	Si	Mn	P	S	Ni	Cr	Mo
SUS316	0.06	0.48	1.31	0.036	0.027	10.16	17.00	2.04
SUS304	0.06	0.39	1.48	0.037	0.023	8.12	18.27	-

### Microstructure, hardness and residual stress of carbon S phase

A cross-sectional view of the microstructure of an S phase, approximately 8  $\mu$ m thick, on SUS316 steel carburised under a  $\text{CH}_4$  ratio of 4.8 vol% and current value of 0.5A is shown in Fig. 3 [5]. The S phase was identified from microhardness testing results, and the shifts to a low angle side (1 to 2 degrees in  $2\theta$ ) of the (111)  $\gamma$  and (200)  $\gamma$  diffraction peaks were analysed by X-ray diffraction (XRD). The S phase in SUS316 steel has a super-high hardness of more than 800 HV on the surface and a substantial compressive residual stress of up to 1400 MPa at a depth of 3  $\mu$ m when carburised under 10.5%  $\text{CH}_4$ , 0.5 A current and at 733 K for 14.4 ks [4].

A transmission electron microscopy (TEM) observation of the surface layer (8- $\mu$ m-thick overall S phase

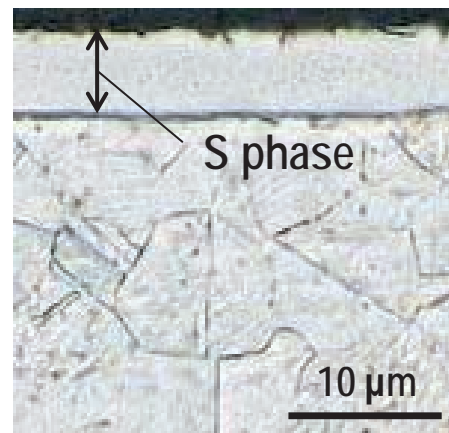


Fig. 3. Optical micrograph of cross-sectional view of SUS316 steel plasma-carburised in  $\text{CH}_4$  gas ratio of 4.8 vol.% and current value of 0.5A at 733 K for 14.4 ks (aqua regia etched)

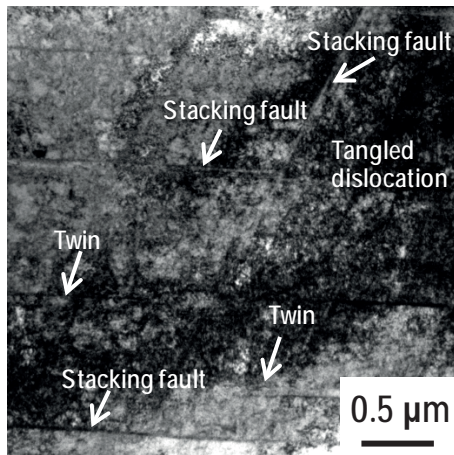


Fig. 4. Bright-field image showing the S phase (approximately 10 μm thick) of plasma-carburised SUS316 steel at a depth of 2 to 6 μm

and the underneath  $\gamma$  matrix) shown in Fig. 3 was performed using a field-emission TEM (FE-TEM, JEM-2100F, 200 kV) system with energy dispersive X-ray spectrometry (EDS). Thin-film samples for TEM observation were made by the  $\mu$ -sampling<sup>®</sup> method using the focused ion beam (FIB) system (40 kV, ion source: Ga). Fig. 4 shows bright-field images (BFIs) of the S phase. The images show that the S phase has high-density dislocations including tangled dislocations, and a sufficient number of stacking faults and twins on the surface are found throughout a depth of around 8 μm. Aoki et al. [8] reported the occurrence of high-density lattice defects such as dislocations and stacking faults in the S phase of SUS316 steel gas-carburised at 743 K from TEM observations. The FE-TEM observation also shows that there are no precipitations of chromium carbide such as  $\text{Cr}_5\text{C}_2$  and  $\text{Cr}_7\text{C}_3$  particles throughout the S phase and  $\gamma$  matrix areas. A change in the lattice parameter of the S phase was examined from the analysis results (using  $L\lambda = 3.60 \times 10^{-7} \text{ nm}^2$ ,  $L$ : camera constant and  $\lambda$ : electron beam wavelength) of selected area electron diffraction (SAED) patterns obtained from the S phase at multiple depths, as shown in Fig. 5. The lattice parameter of the S phase had expanded by up to approximately 1.7% at near surface compared to that of the  $\gamma$  matrix. Furthermore, a solute carbon concentration was calculated from the obtained lattice parameter, using the following equation [9] which describes the relationship between lattice parameter,  $a$  ( $10^{-1} \text{ nm}$ ) and carbon concentration,  $yc$  (at.%) of the S phase.

$$a = 3.5965 + (0.6029 \pm 0.0189) \times 10^{-2} yc.$$

The calculated carbon concentration in the S phase is shown as a function of depth in Fig. 6. A solute carbon of up to approximately 15.7 at.% (3.8 wt.%) penetrates the S phase at near surface. The S phase

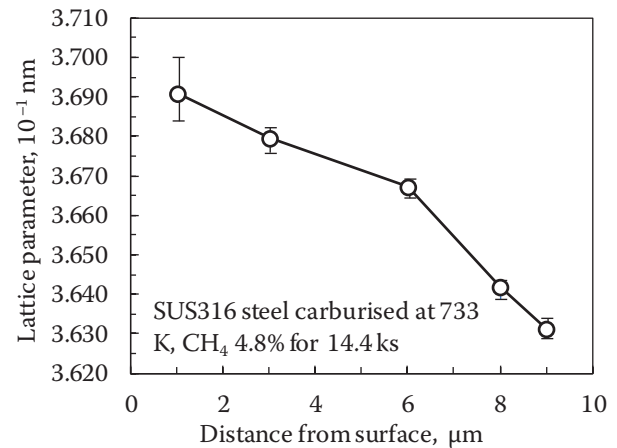


Fig. 5. Lattice parameter distribution of the S phase (approximately 10 μm thick, FCC lattice) formed in SUS316 steel as a function of distance from the surface, analysed from TEM-SAED patterns

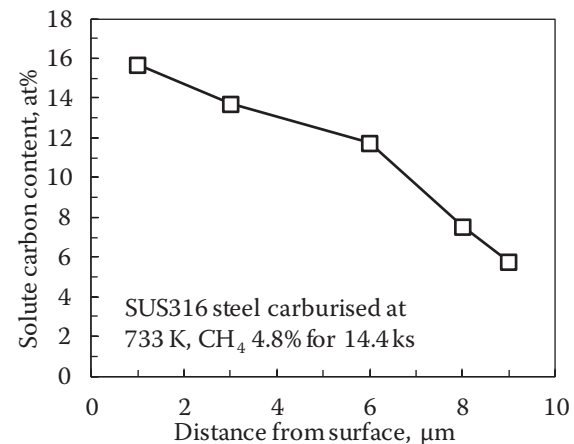


Fig. 6. Solute carbon content distribution of the S phase (approximately 10 μm thick, FCC lattice) formed in SUS316 steel as a function of distance from the surface, calculated from lattice parameters shown in Fig. 5

has a super-high hardness of over 800 HV, which is harder than normalized-and-annealed ( $\gamma$  and  $\alpha'$ ) stainless steels containing the comparable amount of carbon [4]. This is due to not only solid solution hardening by solute carbon of up to 15.7 at%, but also the existence of a high strain field that causes a high amount of lattice defects, quantified as a compressive residual stress of up to 1400 MPa.

## MECHANICAL AND TRIBOLOGICAL PROPERTIES

### Tensile test results

The result of the tensile test using a SUS316 steel specimen (gage length: 12 mm, thickness: 1.5 mm)

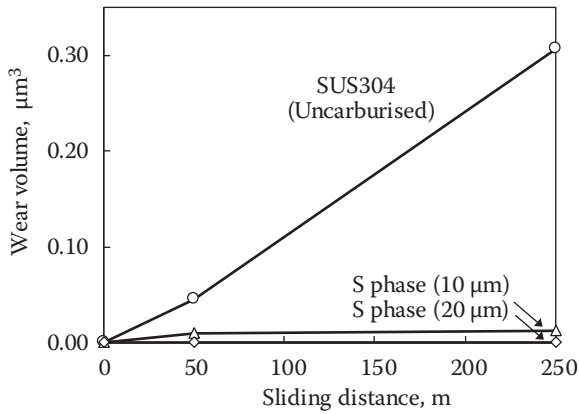


Fig. 7. Ball-on-disc tribometer test results of SUS304 steel specimens with and without the S phase of varying thickness on the surface: Wear volumes are as a function of sliding distance

shows that the tensile strength of the specimen carburised with a 12- $\mu\text{m}$ -thick S phase is 2.4% higher than that of the specimen without the S phase. The 0.5% proof stress also increased by 0.2%, while the elongation decreased to 65.1% from 63.0% by the S phase formation.

### Ball-on-disc (BOD) tribometer test results

The frictional wear properties of the SUS304 steel specimens (surface roughness:  $R_a=0.19$  to  $0.20 \mu\text{m}$ ) carburised with S phases of varying thickness were evaluated by using a BOD tribometer (made by RHESCA Co., LTD., FPR-2100) under dry conditions at 2 N loads at a sliding speed of 31.4 mm/s with an alumina ball (4.8 mm diameter) as a counter material.

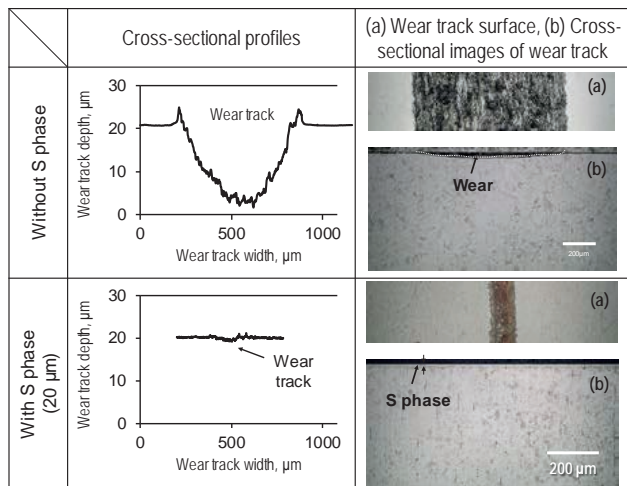


Fig. 8. Cross-sectional profiles and optical images of wear track in SUS304 steel specimens with and without a 20- $\mu\text{m}$ -thick S phase after ball-on-disc test

Fig. 7 [4] shows the wear volume as a function of the sliding distance. The cross-sectional profiles and wear track images of the specimens after sliding 250 m are shown in Fig. 8. The specimen with the S phase was found to exhibit little wear after sliding. Fine cracks visible on the cross-section of the surface were also not observed. It was confirmed that an S phase with a thickness of more than 10  $\mu\text{m}$  improves the wear resistance significantly. This excellent wear resistance of the S phase is because the occurrence and propagation of surface fine cracks which can be a cause of wear are suppressed due to the S phase's super-high hardness with an extremely high compressive residual stress as previously discussed.

### High-frequency translatory oscillation test results

To evaluate reciprocating frictional wear characteristics, including fretting wear, of the S phase, high-frequency translatory oscillation tests were carried out by using the SRV<sup>®</sup> 5 tester designed and manufactured by OPTIMOL Instruments GmbH (hereinafter SRV test). The chamber oscillation of the SRV<sup>®</sup> 5 tester and the test conditions are shown in Fig. 9 and Table 2 [5], respectively. Fig. 10 [5] shows the SRV test results carried out under a stroke of 2.0 mm and a sliding distance of 100 m without lubrication

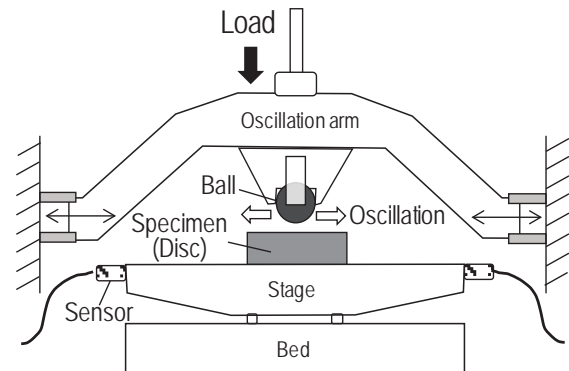
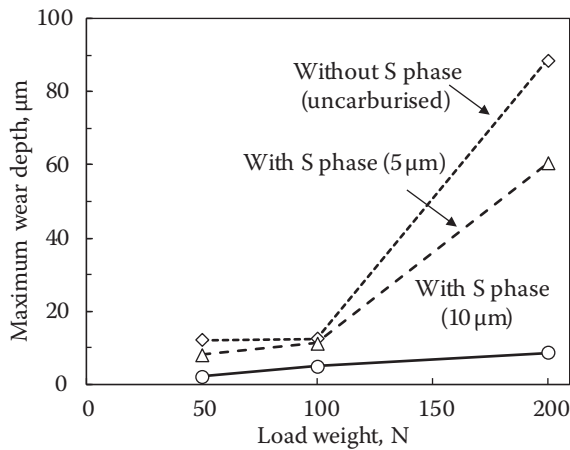


Fig. 9. Schematic of SRV<sup>®</sup> 5 tester: chamber oscillation

Table 2. SRV test conditions for evaluating tribological properties under no lubrication (dry)

Counter material	SUJ2 steel ball, F 10mm, 60HRC
Frequency [Hz]	20
Stroke [mm]	0.2, 2.0
Load weight [N] (Hertz pressure [GPa])	50 (1.73), 100 (2.18), 200 (2.74)
Sliding distance [m]	10, 50, 100
Lubrication condition	Under no lubrication (dry)

Note: Running in loading weight of 50 N and running time of 30 s before starting a test.



**Fig. 10. SRV test results of SUS316 steel specimens with and without the S phase of varying thickness on the surface (counter material:  $\phi$ 10 mm SUJ2 steel ball, frequency: 20 Hz, stroke: 2.0 mm, dry).** Maximum wear depths are as a function of load weight. Sliding distance is 100 m

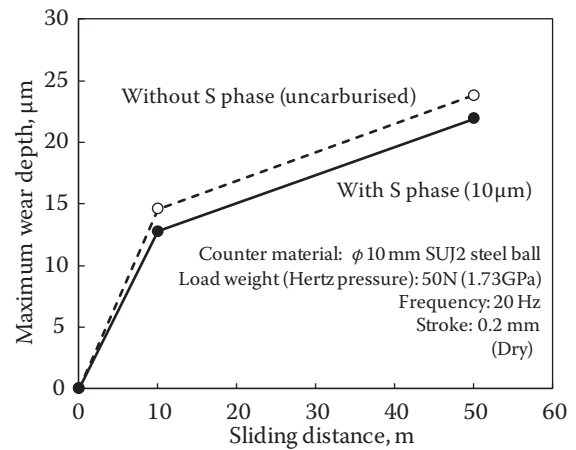


**Fig. 11. Fretting wear test result by SRV<sup>®</sup> 5 tester: comparison of maximum wear depth of SUS316 steel specimens with and without the 10- $\mu$ m-thick S phase on the surface**

at a humidity of 44 to 64%; the maximum wear depth of the SUS316 steel specimens as a function of load weight. The S phase increases the fretting wear resistance dramatically with increasing thickness. The friction coefficient of the specimen with the S phase is also found to remain relatively stable with a low value of 0.1 to 0.2 from the early stages in the test compared with that of the specimen without the S phase. Using the SUS316 steel specimen with the 10- $\mu$ m-thick S phase, the fretting wear characteristics were evaluated by the SRV test under the conditions of a very short stroke of 0.2 mm and a load weight of 50 N (1.73 GPa in terms of Hertz pressure) without lubrication. The maximum wear depth in the specimen with the S phase as a function of sliding distance is compared with that of the specimen without the S phase in Fig. 11 [5]. Fig. 12 shows the observation results of the wear track surface and wear debris after the test. Although abrasion wears like metallic adhesion indicated by arrows in Fig. 12 are observed on both surfaces of the ball (counter material) and disc (specimen) in the specimen without the S phase, those kind of wears are not clearly observed on either surface in the specimen with the S phase. The wear debris in the specimen without the S phase also has a darker

brownish-red colour than that of the specimen with the S phase. The changes in colour are due to the iron in it becoming oxidized upon exposure to air. Therefore, SUS316 steel carburised with a 10- $\mu$ m-thick S phase also has a good resistance to fretting wear.

Subsequently, to investigate the possibility of applying SUS316 steel carburised with an S phase as a biomaterial, the friction and wear characteristics of the S phase in SUS316 steel commonly used for medical purposes in Ringer's solution, which mim-

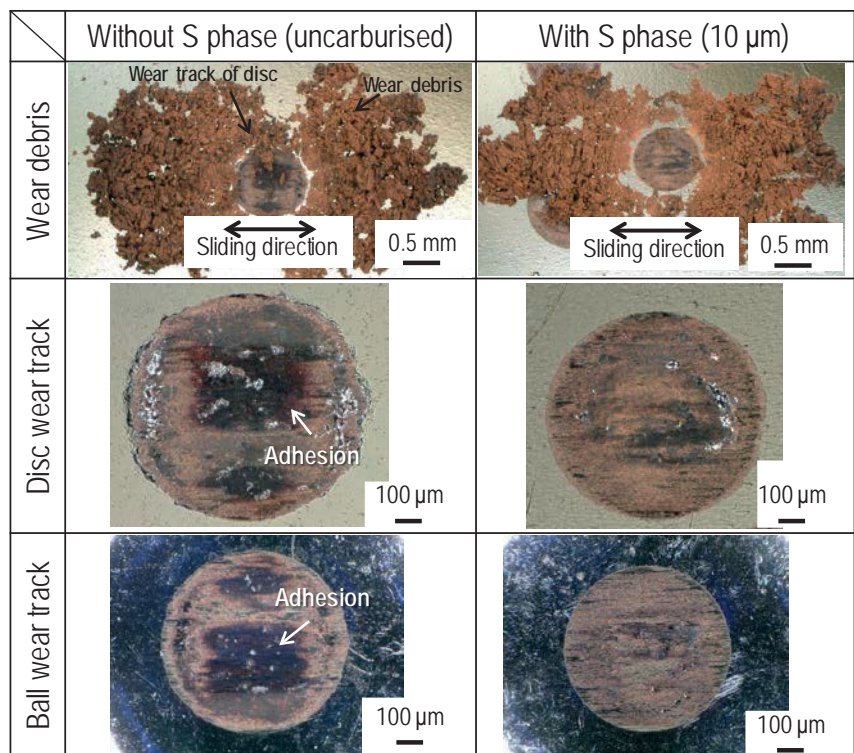


**Fig. 12. Fretting wear test results by SRV<sup>®</sup> 5 tester: disc (specimens with and without the S phase) and ball (counter material, SUJ2 steel ball) sliding surfaces after the test (sliding distance is 50 m)**

Table 3. Composition of the Ringer's solution used

(g·l <sup>-1</sup> )				
NaCl	KCl	CaCl <sub>2</sub>	NaHCO <sub>3</sub>	H <sub>2</sub> O
9.00	0.42	0.48	0.20	Bal.

Table 4. SRV test conditions for evaluating tribological properties (friction and fretting wear resistance) in the Ringer's solution

Counter materials	SUJ2 steel ball (F6 mm, 60HRC) Al <sub>2</sub> O <sub>3</sub> ball (F6 mm)
Frequency [Hz]	20
Stroke [mm]	0.2
Load weight [N] (Hertz pressure [GPa])	25 (Al <sub>2</sub> O <sub>3</sub> : 2.25, SUJ2: 1.93)
Sliding distance [m]	10
Lubrication condition	In the Ringer's solution at 310 K

Note: Running in loading weight of 25 N and running time of 30 s before starting a test.

Table 5. The mean friction-coefficients and wear volumes of SUS316 steel specimens with and without a 13- $\mu$ m-thick S phase, obtained by the SRV test in the Ringer's solution at a constant temperature of 310 K

	Mean friction-coefficient		Wear volume ( $\times 10^{-4}$ mm <sup>3</sup> )	
	Al <sub>2</sub> O <sub>3</sub>	SUJ2	Al <sub>2</sub> O <sub>3</sub>	SUJ2
Without S phase	0.48	0.55	3.10	8.57
With S phase (13 $\mu$ m)	0.38	0.39	2.16	1.25

ics a body fluid as shown in Table 3, at a constant temperature of 310 K were evaluated using the SRV<sup>®</sup> 5 tester under the conditions shown in Table 4. The mean friction coefficients and wear volumes obtained are summarized in Table 5. The wear volumes in each specimen were measured in accordance with the ASTM D7755-11 standard. For all counter materials, the specimen with the S phase was found to have a lower friction coefficient and a higher resistance to wear than the specimen without the S phase. However, the wear is likely to be accelerated by the oxidation of iron which occurs at the sliding surface due to chlorine ions contained in the Ringer's solution. Its superiority on the specimen with the S phase (mean friction coefficient: 30% decrease, wear volume: decrease to one seventh) is remarkable especially when the counter material, SUJ2 steel, also contains iron like the specimen.

## CORROSION AND DISSOLUTION RESISTANCES

The corrosion resistance of SUS316 steel with a 13- $\mu$ m-thick S phase in the above Ringer's solution

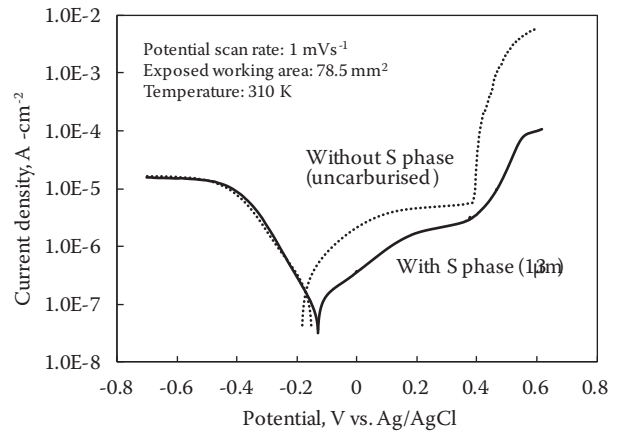


Fig. 13. Polarization curves of SUS316 steel specimens with and without a 13- $\mu$ m-thick S phase in a Ringer's solution at a constant temperature of 310 K. (Reference electrode: Ag-AgCl, Counter electrode: Pt plate)

was evaluated electrochemically at a constant temperature of 310 K. Fig. 13 shows the polarization curves of the specimen with the S phase compared with that of the specimen without the S phase. Note that these curves were measured in the Ringer's solution degassed using nitrogen. The corrosion current densities obtained from the polarization curves are  $8.6 \times 10^{-8}$  A·cm<sup>-2</sup> and  $1.5 \times 10^{-7}$  A·cm<sup>-2</sup> in the specimen with and without the S phase, respectively. The current density distribution at the anode current in the specimen with the S phase is also lower than that of the specimen without the S phase. A number of pitting corrosions up to approximately 50  $\mu$ m deep were also observed on the surface of the specimen without the S phase after the test, whereas the specimen with the S phase had no such pitting corrosion at all. The sharp rise at around 0.4 V in the anode polarization curve of the specimen without the S phase might be due to the occurrence of these pitting corrosions.

The dissolution resistances of nickel in the Ringer's solution with added hydrochloric acid (pH=1.07) were examined at a constant temperature of 310 K. As a result of analysing the nickel concentration in the solution after immersion for 20 days, the dissolution amount was 6.3 ppm and 16.9 ppm in the specimen with and without the S phase, respectively. Dissolutions of iron and chromium in the specimen with the S phase are also likewise suppressed. Thus, SUS316 steel having the S phase on the surface by the low-temperature plasma carburising is found to have a good resistance to corrosion and nickel dissolution in the Ringer's solution with increased acidity.

## CONCLUSION

A plasma carburising process combining the ASP and DCP methods performed under appropriate conditions can develop an S phase efficiently on the surface of austenitic stainless steels even at low temperatures such as 733 K or less. An S phase with a thickness of more than 10  $\mu\text{m}$  obtained by this carburising process improves resistance to various sliding wears including fretting wear by translatory oscillation even in unlubricated conditions and simulated body fluid. In addition, resistance to corrosion and nickel dissolution in the simulated body fluid also increased. This carburising process can be expected to be applied to various food and chemical manufacturing equipment, medical equipment and biomaterials fields, though the S phase to be obtained needs to be optimized for different sliding conditions required under various usage environments. It is also necessary to develop an optimized carburising facility for mass production use.

## REFERENCES

1. **Zhang Z.L., Bell T.** // Surf. Eng. 1985. 1, 2. P. 131.
2. **Ichii K., Fujimura K., Takase T.** // Technology Reports of Kansai University. 1986. 27. P. 135.
3. **Christiansen T.L., Somers M.A.J.** // Scr. Mater. 2004. 50. P. 35.
4. **Satomi N., Kanayama N., Watanabe Y., Takai O.** // Mater. Trans. 2017. 58, 8. P. 1181.
5. **Satomi N., Kanayama N., Ishizuka H., Watanabe Y., Takai O.** // Netsushori. 2018. 58, 2. P. 17 (in Japanese).
6. **Georges J., Cleugh D.** // Active Screen Plasma Nitriding (Stainless Steel 2000, Mancy, Cambridge, 2001). P. 377.
7. **Fugube T., Nishimoto A.** Proc. 80<sup>th</sup> Nihon Netsushori Gijyutsu kyokai Annual Conference // JSHT. 2015. P. 3 (in Japanese).
8. **Aoki K., Shirahata T., Tahara M., Kitano K.** // Proc. Stainless Steel 2000-Thermochemical Surface Engineering of Stainless Steel, T. Bell and K. Akamatsu ed. 2001. P. 389.
9. **Hummelshøj T.S., Christiansen T.L., Somers M.A.J.** // Scripta Materialia. 2010. 63, 7. P. 761.

# SURFACE HARDENING OF STEEL NANOCARBON MATERIALS DURING LASER AND ELECTRON-BEAM TREATMENT

O.V. Chudina<sup>1</sup>, A.V. Eletsky<sup>2</sup>, E.V. Terentyev<sup>2</sup>

<sup>1</sup>MADI. Moscow, Russia

<sup>2</sup>National Research University «MEI». Moscow, Russia

Chudina\_madi@mail.ru

---

Surface strengthening of structural steels with carbon nanomaterials using laser and electron-beam heating is studied. It is shown that during laser treatment the maximum microhardness of a modified layer is achieved in a strengthened zone up to 70  $\mu\text{m}$  thick with  $q = 9 \times 10^4 \text{ W/cm}^2$ , and with electron beam treatment in a strengthened zone up to 300  $\mu\text{m}$  thick with  $q = 4.6 \times 10^4 \text{ W/cm}^2$ . It is established that in both cases with optimum treatment regimes strengthening is due to forming martensite, a cellular structure, and grain disintegration.

**Keywords:** modification; steel; laser treatment; electron-beam treatment; carbon materials; microhardness; microstructure.

---

## INTRODUCTION

Currently in various branches of engineering there is continuous expansion of use of concentrated energy flows (CEF), among which there are streams of electrons and ions, plasma jets, laser radiation, etc. This is due to the possibility of flexible control of the CEF energy characteristics, relative simplicity of process automation, and parameter optimization. Those used most extensively in industry are processes of treating materials with laser radiation and electron streams. In spite of the difference in physical essence and technical formulation between these methods there is much in common since their geometric and energy parameters in the production range of power density  $q = 10^4 - 10^5 \text{ W/cm}^2$  appear to be similar to each other.

An important achievement of laser and electron-beam treatment is the possibility of contact-free rapid and strict dispensing of energy to a treated material surface, which It is possible to use for surface hardening of metals and alloys with both thermal and chemical treatment.

Analysis of existing scientific research has shown that laser treatment for surface hardening of structural and tool materials has been studied quite well, and there are publications on laser hardening and surface modification of steels and alloys [1–4]. An electron beam is mainly used during welding materials that are difficult to weld, including various materials, and also for cutting and preparing holes [1]. In spite of the apparent advantages of electron-beam

treatment, such as high productivity and effective protection of strengthened metal from interaction with gases, there is almost no information about use of it for surface hardening steels and alloys. In view of this it is very important to study the effect of electron-beam action on the structure and properties of structural materials, and also comparison of them with laser treatment.

Currently surface strengthening of steels employing laser heating is used mainly for components operating under wear and contact load conditions. With cyclic loading of components technology of laser surface strengthening has limited application. This is explained by features of metal treatment methods with highly concentrated energy sources when at the boundary of the main metals with a melting zone a significant temperature gradient arises, which is accompanied by development of tensile stresses, and as a consequence a tendency towards crack formation [5]. This disadvantage is overcome by heating, although the level of metal strengthening achieved by laser treatment is considerably reduced. In view of this it is important to find new ways of increasing the efficiency of laser energy for surface strengthening of steels.

Currently in view of the discovery of a new class of carbon nanomaterials (CNM), such as fullerenes, graphene, carbon nanotubes, etc., there is interest from researchers in the possibility of creating strengthened coatings based on similar structures [6].

In spite of a significant amount of work devoted to the problem of strengthening structural materials

using nanocarbon coatings with subsequent treatment by highly concentrated energy sources, so far there is almost no systematic study of the effect of nanocarbon materials on structure formation of a strengthened layer after their introduction into a steel surface by means of CEF. In view of this the aim of the present work is to study the effect of production parameters of laser and electron-beam treatment, such as power density, and also the type and thickness of previously applied amorphous nano-structured carbon, on steel surface structure and properties.

## METHODS OF STUDY

Specimens used for the study were low-carbon steel (about 0.04% and about 0.08% C) at whose surface a paste was applied consisting of amorphous nano-structured carbon and benzene.

Amorphous nano-structured carbon was prepared by extraction of fullerenes from soot, which formed the plasma of an arc discharge with a graphite electrode in a helium atmosphere. Extraction of fullerenes was carried out in a SOXHLET type unit. The specific surface of the soot remaining after fullerene extraction measured in a SORBI-M unit comprised  $233 \pm 4 \text{ m}^2/\text{g}$ . Soot was ground carefully in a mortar by means of a pestle, after which it was mixed with benzene to a uniform suspension composition in the ratio 100 : 1 (by weight). Specimens for strengthening were immersed in a suspension, dried for days in air at  $50^\circ\text{C}$ , and then with aim of improving adhesion were annealed in a furnace in a weak stream of argon (up to  $100 \text{ cm}^3/\text{min}$ ) for 20 min at  $600^\circ\text{C}$ . The weight of the coating obtained about 16 mg, and its thickness was  $20 \mu\text{m}$ , which corresponded to a coating density of about  $1 \text{ g}/\text{cm}^3$ .

Laser treatment of steel specimens containing about 0.04% C, was performed in an ALFA-200C unit at a wavelength of 1064 nm, and pulse energy up to 50 J; the laser beam was focused on a spot 3.5 mm in diameter and the radiation intensity was varied from 2 to 20 J, and the pulse duration from 1 to 9 m/sec.

Electron-beam treatment of steel specimens containing about 0.08% C was conducted in an AÉLTK-12 unit with a beam current from 3 to 15 mA in a continuous regime with a movement rate of 50 mm/sec and scanning in a transverse direction with frequency of 1000 Hz and amplitude of 2.5 mm, which with an effective beam diameter of 0.5 mm made it possible to obtain a treated "track" with width up to 2.5 mm. Under these conditions the duration of action on a metal surface was about 10 m/sec.

Metallographic study was carried out on transverse microsections using a Zeiss Observer.Z1m light microscope at a magnification of  $\times 1000$ .

Surface hardness was measured in an Emco-Test DURASCAN-20 hardness meter with a load of 1 N. Microhardness measurement of individual structural components was performed in accordance with GOST 9450–76 in an automated Instron Tukon 2500 hardness meter.

## RESULTS AND DISCUSSION

Dependences were obtained for the effect of production parameters of laser and electron-beam treatment of low-carbon steel on thickness, structure, and microhardness of a modified nano-structured carbon layer.

It was established that with laser treatment without melting a radiation power density of  $q < 4 \times 10^4 \text{ W}/\text{cm}^2$  the surface microhardness increases to 950 HV or more, apparently due to forming cementite and eutectic.

During treatment with melting with a power density  $q = 6 \times 10^4 \dots 15 \times 10^4 \text{ W}/\text{cm}^2$  surface hardness comprises 550–800 HV, and within the alloying zone up to 1080 HV due to forming high-carbon martensite, a cellular substructure, and grain refinement. Maximum microhardness applies to a strengthened layer with thickness up to  $70 \mu\text{m}$  with  $q < 4.6 \times 10^4 \text{ W}/\text{cm}^2$ .

A study of electron-beam modification for a steel surface with amorphous nano-structured carbon showed that treatment without melting with  $q = 2 \times 10^4 \text{ W}/\text{cm}^2$  leads to an insignificant increase in surface microhardness, i.e., up to 250 HV, mainly due to forming low-carbon martensite. During treatment with melting at  $q = 3 \times 10^4 - 7 \times 10^4 \text{ W}/\text{cm}^2$  surface microhardness comprises 420 – 600 HV, and within the alloying zone up to 1000 HV. The maximum microhardness is achieved in a strengthened zone with thickness up to  $300 \mu\text{m}$  with  $q < 4.6 \times 10^4 \text{ W}/\text{cm}^2$ .

In studying the effect of production parameters from laser treatment of low-carbon steel (about 0.4% C) with preliminary application to its surface of amorphous nano-structured carbon it has been established that with low radiation power density a specimen surface is subjected to heating without melting and hardness increases, and the surface hardness within a single "spot" varies over a wide range, i.e., from 200 to 950 HV, and in some areas it reaches 1083 HV. This hardness scatter may be explained by nonuniform distribution of energy within a laser beam and a different distance from the area of measurement to the

boundary of the fusion zone with basic metal. In addition, as a rule the maximum hardness is achieved within the center of an action zone and decreases towards its edges. Specimens subjected to laser treatment with a considerable power density, leading to surface melting, also have increased hardness (550 – 800 HV), but more or less uniform distribution both over the surface and through the thickness of the laser action zone.

Metallographic study of a strengthened layer, carried out in transverse microsections at a magnification of  $\times 1000$ , shows that with laser radiation power density up to  $5 \times 10^4 \text{ W/cm}^2$  surface melting does not occur, although within the structure formation of readily melted eutectic and intercrystalline penetration into its depth of more than  $20 \mu\text{m}$  is observed. Eutectic has a droplet shape and is not distributed uniformly either over a specimen surface, or through the thickness of a strengthened layer (Fig. 1a). Eutectic microhardness comprises 1000 – 1800 HV, which is significantly above the microhardness of ferrite, and even above the hardness of cementite. A marked excess of eutectic microhardness compared with that of cementite, is apparently connected with a scale effect, and described in [7, 8]. Coefficients taking account of the scale factor with microhardness measurement with a load of 5 g, are equal to 1.5–1.7, and therefore the hardness values obtained for individual structural components are increased somewhat, which does not change the tendency as a whole.

Treatment of steel with a carbon coating with a laser radiation power density of  $q = 5 \times 10^4 \text{ W/cm}^2$  or

more leads to melting of a specimen surface, and the thickness of a strengthened layer increases from 20 to  $70 \mu\text{m}$  (Fig. 1b–d).

It is seen in Fig. 1d that the structure of a strengthened layer forms uniaxial columnar dendrites, directed perpendicular to the interface between the melting zone and basic metal, which is a consequence of the fast crystallization rate. With an increase in laser radiation power density within the structure there is formation of coarsely acicular martensite, and in surface layers there is formation of intergranular pearlite.

A significant increase in microhardness within fusion zones to 1800 HV (against the microhardness of an original structure of 200 HV) is caused by quenching of liquid phase, as a result of which there is martensite formation; phase  $\alpha \leftrightarrow \gamma$ -recrystallization and phase work hardening causing grain refinement and microstresses within a crystal lattice structure; plastic deformation under action of impact wave and heating action with subsequent recrystallization as a result of which there is an increase dislocation density and crystal lattice micro-distortion, and a cellular structure forms.

It should be noted that within fusion zones the microhardness is not uniformly distributed, since under conditions of fast heating and cooling rates during laser treatment diffusion processes of dissolution and leveling out of the carbon concentration are not completed, which is a reason for forming non-uniform austenite, and consequently non-uniform martensite with respect to carbon content. In addition, close to the interface between the fusion zone and the heat-affected zone (HAZ) as a rule a reduction is observed in microhardness almost to the original value.

The structure of the heat-affected zone, located beneath the fusion zone, is finely acicular martensite with microhardness up to 700 HV, which points indirectly to a high carbon content (up to 0.5–0.8%) within it. The mechanism of martensite formation in the HAZ apparently includes intercrystalline penetration of eutectic, consisting of high-carbon austenite and cementite, dissolution of carbon in  $\text{Fe}_\gamma$ , and subsequent polymorphic transformation. This proposal is confirmed by presence of droplet-like inclusions of eutectic at a distance from the surface up to  $100 \mu\text{m}$  or more (Fig. 1b–d).

In all microphotographs of a strengthened layer obtained with laser treatment in a melting regime, dark inclusions are observed beneath the HAZ, which are cavities formed during

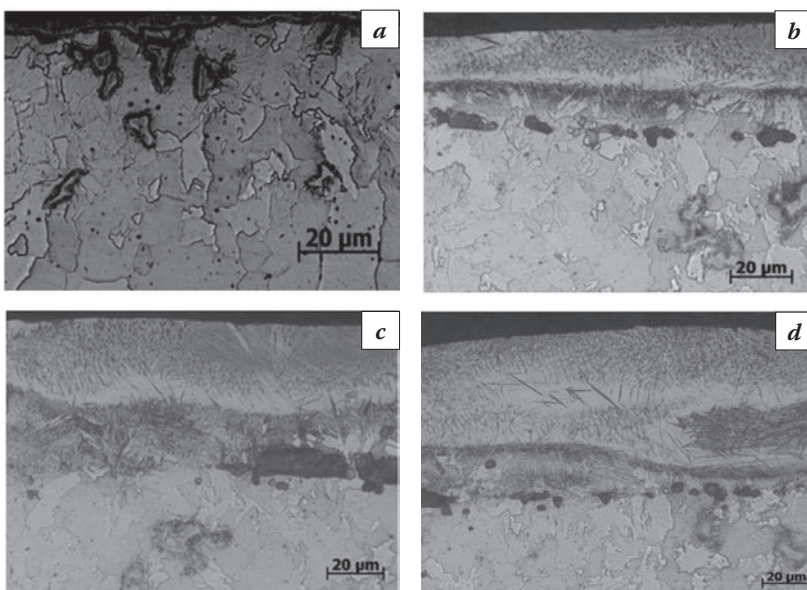


Fig. 1. Low-carbon steel microstructure after laser alloying with amorphous nano-structured carbon with different power density:

$a - q = 3.1 \times 10^4 \text{ W/cm}^2$ ;  $b - q = 4.9 \times 10^4 \text{ W/cm}^2$ ;  
 $c - q = 6.3 \times 10^4 \text{ W/cm}^2$ ;  $d - q = 8.0 \times 10^4 \text{ W/cm}^2$



Fig. 2. Low-carbon steel microstructure after surface modification with amorphous carbon using electron beam heating with different power density:  $a - q = 2.16 \times 10^4 \text{ W/cm}^2$ ;  $b - q = 4.6 \times 10^4 \text{ W/cm}^2$ ;  $c - q = 6.9 \times 10^4 \text{ W/cm}^2$

high-speed heating to a temperature typical for overheating, as a result of which significant tensile stresses arise, and as a consequence breakdown of metal continuity. Presence of these cavities beneath the zone of laser action has also been observed by the authors in [1] during treatment of grey cast iron within which carbon is contained in the form of graphite. However, they explain significant porosity by liberation of gases absorbed by graphite inclusions during cast iron primary crystallization. The gaseous origin of pores in the opinion of the authors is confirmed by their spheroidized shape and smooth internal surface.

A study of the effect of electron beam treatment parameters on formation of a modified layer showed that during treatment with power density up to  $q = 2 \times 10^4 \text{ W/cm}^2$  surface melting does not occur and the level of strengthening is low, i.e., up to 260 HV, mainly due to formation of a cellular structure and an increase in dislocation density (Fig. 2a). With larger values of radiation power a surface melts, and the greater the  $q$ , the modified layer thickness is greater (Fig. 2b), which with  $q = 6.9 \times 10^4 \text{ W/cm}^2$  is 280  $\mu\text{m}$ , and together with a zonal heating effect (HAZ) the strengthened layer thickness achieved is 550–600  $\mu\text{m}$  (Fig. 2c), which is significantly greater than after laser treatment. This is due to the difference in the physical essence of the process: during reaction of a laser beam with a metal almost all of the energy is released at the surface, whereas during reaction of an electron beam with beam electrons penetrate into the depth, commensurate with the thickness of the modified layer, and heating proceeds due to volumetric release of energy.

During steel surface modification using electron beam heating in the fusion zone there is formation of

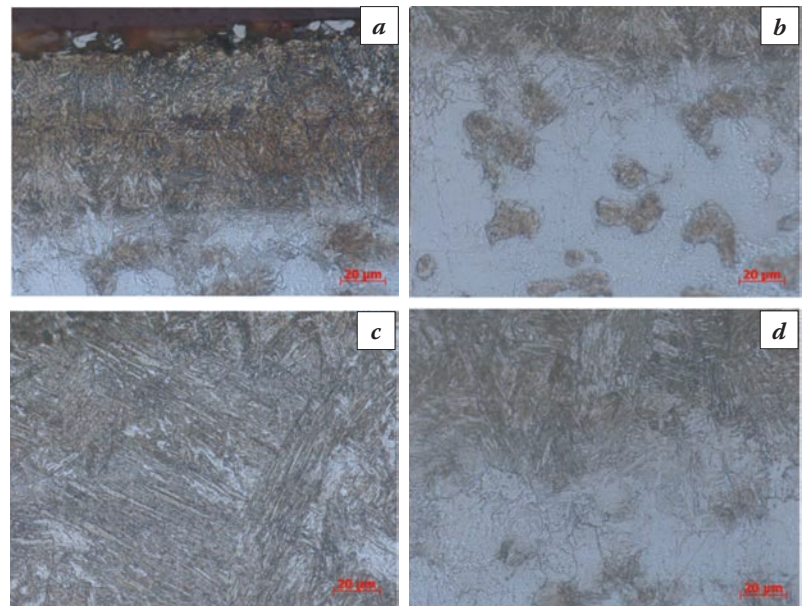


Fig. 3. Low-carbon steel microstructure after surface modification with amorphous carbon using electron beam heating with  $q = 4.6 \times 10^4 \text{ W/cm}^2$  (a, b) and  $q = 6.9 \times 10^4 \text{ W/cm}^2$  (c, d): a, c – fusion zone; b, d – HAZ

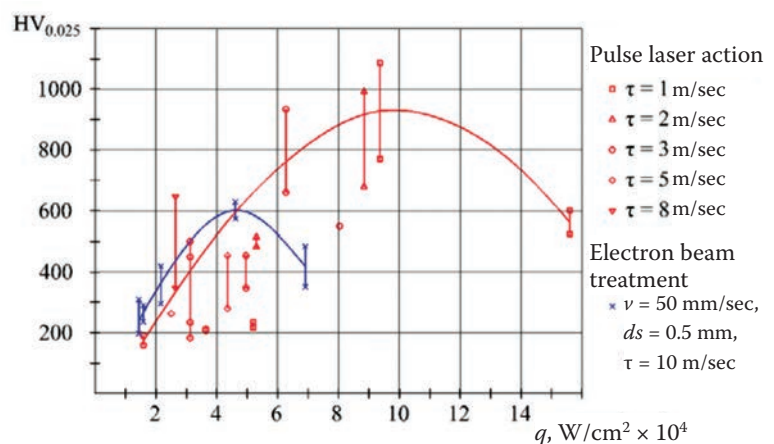


Fig. 4. Effect of CEF power density on steel surface microhardness modified with amorphous nano-structured carbon:

□ – pulse laser action, × – electron beam treatment ( $v = 55 \text{ mm/sec}$ ,  $ds = 0.5 \text{ mm}$ ,  $\tau = 10 \text{ m/sec}$ )

a martensitic structure (Fig. 3a) with microhardness up to 600 HV (Fig. 4), which is somewhat lower than with laser heating. This is connected with the lower carbon concentration dissolved in  $\text{Fe}_\alpha$ , since with an

identical thickness of modifying paste the volume of melting bath with electron beam treatment is greater.

The heat affected zone is a ferrite-pearlite structure within which the amount of pearlitic component is greater than in the original structure (Fig. 3*b* and *d*), which is apparently connected with diffusion of carbon from the base at the austenitizing temperature. Microhardness in the HAZ is higher than that of the basic metal and comprises 300–350 HV, which suggests presence within the structure not only of finely dispersed ferrite-cementite mixture, but lath bainite, formed under conditions of rapid heat removal into the center of a specimen, but at a rate slower than critical.

Therefore, analysis of results of studying the effect of treatment parameters with concentrated streams of energy on formation of a modified layer at a steel surface showed that structure formation during surface modification of nano-structured carbon on the whole is similar to processes occurring with introduction of graphite powder. It has been shown that there are also production regimes for laser and electron-beam treatment that provide a combination of optimum thickness of a strengthened layer with high hardness, and more or less uniform distribution throughout the whole volume of a fusion zone.

## CONCLUSIONS

Comparative analysis of laser and electron-beam action on a steel surface during modification of its with nano-structured carbon showed that with electron-beam treatment and lower value of power density there is formation of a strengthened layer of greater thickness and more uniform microhardness distribution. This is explained by the fact that during reaction of a laser beam with metal almost all of the energy is released at the surface, and with reaction of an electron beam with metal electrons penetrate into some depth and heating proceeds due to volumetric release of energy.

Laser treatment without melting with radiation power density of  $q = 4 \times 10^4 \text{ W/cm}^2$  leads to an increase in steel surface microhardness to 950 HV or more due to forming high-carbon phases such as eutectic and cementite. During treatment with melting with power density  $q = 6 \times 10^4 - 15 \times 10^4 \text{ W/cm}^2$  the

surface hardness comprises 550–800 HV, and within the alloying zone up to 1083 HV due to forming high-carbon martensite, a cellular structure, and grain refinement. The maximum microhardness is achieved in a strengthened zone with thickness up to 70  $\mu\text{m}$  with  $q = 9 \times 10^4 \text{ W/cm}^2$ .

Electron beam modification of a steel surface with amorphous nano-structured carbon without melting with  $q = 2 \times 10^4 \text{ W/cm}^2$  leads to a significant increase in surface microhardness, i.e., up to 250 HV, mainly due to forming low-carbon martensite. During treatment with melting with  $q = 3 \times 10^4 - 7 \times 10^4 \text{ W/cm}^2$  hardness at the surface and within the strengthened zone comprises 420–600 HV. The maximum microhardness is achieved within a strengthened zone with thickness up to 300  $\mu\text{m}$  with  $q = 4.6 \times 10^4 \text{ W/cm}^2$ .

## REFERENCES

1. Rykalin N.N., Uglov A.A., Zuev I.V., Kokora A.N. Laser and Electron-Beam Treatment of Materials: Handbook [in Russian]. Moscow : Mashinostroenie, 1985.
2. Chudina O.V. Surface alloying of iron-carbon alloys with the use of laser heating // *Metallovedenie I Termicheskaya Obrabotka Metallov*. 1994. No. 11. 2–7.
3. Chudina O.V., Brezhnev A.A. Surface alloying of carbon tool steels using laser heating // *Metal Technology*. 2014. No. 2. 19–24.
4. Chudina O.V. Modification of a steel surface using laser heating // *Svaroch. Proizvod*. 2016. No. 3. 24–28.
5. A. Solina, M. De Sanctis, L. Paganini, et al. Origin and development of residual stresses induced by laser surface hardening treatments // *J. Heat Treat*. 1984. 3. 193–194.
6. Bocharov G.S., Eletsii A.V., Zakharenkov A.V. et al. Optimization of strengthening of a steel surface with carbon nanostructures and subsequent treatment with high-energy sources: Proc. XIV Internat. Sci.-Tech. Conf. "Rapidly hardened materials and coatings" [in Russian], MAI. Moscow, 2016. P. 31.
7. Matyunin V.M., Marchenkov A.Yu., Demidov A.N. Study of the influence of a dimensional effect on results of determining hardness at different scale levels // *Tekhnol. Metallov*. 2013. No. 6. 53–54.
8. Atkinson M. Phenomenology of the size effect in hardness tests with a blunt pyramidal indenter // *J. Mater. Sci*. 1998. 33(11). 2937–2947.

# EFFECT OF LASER REMELTING ON SURFACE MICROSTRUCTURE AND CORROSION RESISTANCE OF ULTRA-HIGH SPEED LASER CLADDING COATING

LIU Ming-xia<sup>1a</sup>, CHANG Geng-rong<sup>1</sup>, DUAN Kai Liang<sup>2</sup>, FU Fu-xing<sup>1</sup>, XIE Yan-xiang<sup>1</sup>,  
DAI Jun<sup>1</sup>, YU Li-jun<sup>1</sup>, XU Ke-wei<sup>1,3</sup>

<sup>1</sup>Shaanxi Key Laboratory of Surface Engineering and Remanufacturing, Xi'an University, China

<sup>2</sup>ZKZM Laser Tech. Co., Ltd. Xi'an, China

<sup>3</sup>State Key Laboratory for Mechanical Behavior of Materials, Xi'an Jiaotong University, China

<sup>a</sup> liumingxia1121@163.com

Ni625 coatings were prepared on 2Cr13 stainless steel substrate by ultra-high speed laser cladding (USLC). The effects of the laser remelting (LR) on the microstructure and the corrosion resistance of the coatings were investigated. The micro-morphology and microstructure of the coatings were measured by surface roughness meter, optical microscope (OM), scanning electron microscope (SEM), X-ray diffraction (XRD). The effects of LR on the corrosion resistance of the USLC Ni625 coatings were analyzed by the electrochemical test and the salt spray test. The results show that the surface roughness of the coating decreased significantly from 13.27  $\mu\text{m}$  to 1.76  $\mu\text{m}$  after LR treatment. The microstructures of the cladding layer grew in the form of dendrite and the grains near the surface of the cladding layer was refined by LR. The phases in the cladding coating was mainly the NiCr austenite phase with fcc structure and rarely changed but with the preferential orientation weakened after LR treatment. The self-corrosion potential of the USLC+LR specimen is the lowest of  $-0.554\text{V}$ , which decreased by 0.117V compared with that of the USLC specimen. After salt spray test, the weight loss of the USLC+LR specimen was 94.1% and 66.8% less than that of 2Cr13 substrate and the USLC specimen. The above results exhibit that LR treatment not only could improve the surface quality of high-speed laser cladding coating, but also can increase the corrosion resistance of the coating.

**Keywords:** Ultra-high speed laser cladding (USLC); laser remelting (LR); surface quality; microstructure; corrosion resistance.

## INTRODUCTION

Laser remelting (LR) is a process that uses laser beam to melt material surface without adding any metal elements, so as to improve material surface properties [1]. LR can not only eliminate the original defects such as pore, crack and inclusion, but also improve the hardness, wear resistance and corrosion resistance of the structure obtained by quench recrystallization. This method can be combined with a variety of surface coating technologies, such as High Velocity Oxygen Fuel (HVOF) [2, 3], plasma spraying [4, 5], laser cladding [1], laser additive manufacturing<sup>[6]</sup>, etc. Among them, laser cladding and laser remelting have become one of the hotspots in engineering research because of their easy combination in technology [7–10]. Some researchers also applied laser cladding and remelting to repair turbine blades, and the remelted leading edge displayed promising results [11].

The ultra-high speed laser cladding (USLC) invented in Germany in 2017 has the technical characteristics of low heat input, high processing efficiency,

low dilution rate and small follow-up processing capacity [12]. So, compared with traditional laser cladding technology, USLC could break the efficiency restricting large-scale popularization. At the same time, it could also take the place of electroplating without environmental pollution [13, 14]. However, due to the process characteristics of USLC, the compactness of the coating is not as good as that of traditional laser cladding, so its corrosion resistance needs to be further investigated. Therefore, it is possible to further improve the surface quality of coatings by USLC combined with LR. However, the related research has not yet been reported in the literatures.

In the present paper, 2Cr13 was selected as the substrate and Ni-based alloy coating was prepared by USLC. Subsequently, the morphology and phase change of the coatings before and after LR were studied, and the corrosion resistance of the coatings was compared as well. It might provide experimental basis for the process optimization of such USLC coatings.

## EXPERIMENTAL

USLC and LR experiments with synchronous powder feeding were completed by using ZKZM-4000 fiber laser, as shown in Fig. 1. The cladding substrate material is 2Cr13 steel, and the size of the substrate is 100 mm×100 mm×20 mm. The cladding powder material is Ni625 nickel-based alloy and its particle size is 50~100  $\mu\text{m}$ . The chemical composition is shown in Table 1. Before cladding, Ni625 alloy powder was dried for 2 hours at 200 °C in vacuum to remove moisture. The melting pool was protected by  $\text{N}_2$  during cladding. The process parameters were as follows: laser power of 2KW, lap rate of 80%, powder feeding speed of 26 g/min, scanning speed of 7 m/min, step length of 0.4 mm and protective gas flow of 10 L/min. For comparison, LR treatment was applied on the coating after cladding. The laser power was 1.6KW, and the other process parameters were the same as those of USLC process.

The surface topography of the USLC and USLC+LR specimens before and after laser remelt-

ing was observed by visual measurement. The change of surface roughness was measured by TIME3221 surface roughness tester. HIROX KH-1300 three-dimensional microscope was used to analyze the micro-morphology of the coating along the growth direction. Before observation,  $\text{HCl}:\text{HNO}_3=3:1$  etchant was selected for metallographic sample preparation. The etching time was 5 minutes by using the etching method. Phase analysis of the USLC and USLC+LR specimens was carried out by using 7000S X-ray diffractometer. The X-ray was generated by a Cu target with voltage of 40 kV and current of 40 mA. The diffraction angle ranges from 10° to 90° with the scanning speed of 8°/min. The micro-morphology of the remelted coatings was observed by Nova NanoSEM 450 scanning electron microscopy.

The polarization curves of the substrate, the USLC and USLC+LR specimens were measured by CS350 electrochemical workstation. The electrolyte was 3.5 wt.% NaCl solution, and the experiment was carried out at room temperature. The polarization curves of the specimens were determined by potentiostatic scanning method, and the scanning rate was 1 mV/s. The neutral salt spray test was carried out in SHTH-270 salt spray test chamber for 96 hours. By using 3.5 wt.% neutral NaCl solution, the corrosion resistance of the substrate, the USLC and USLC+LR specimens were tested respectively. The temperature in the salt spray corrosion chamber was maintained at 35 °C.

## RESULTS AND DISCUSSION

Fig. 2 exhibits the macro-morphology of the USLC and USLC+LR specimens. In Fig. 2a, the surface smoothness of the USLC specimen before remelting was obviously, which was improved compared with that of conventional laser cladding<sup>[1]</sup>. Notice that in Fig. 2b, the surface of the remelted cladding layer for the USLC+LR specimen is more compact after LR, which there are no macro cracks, pore and tumour defects.

In order to observe the surface changes of the cladding layer more intuitively before and after remelting, the roughness of the USLC and USLC+LR specimens was measured in parallel cladding direction and vertical cladding direction. The results were shown in Fig. 3a, and the average results were shown in Fig. 3b. The results exhibit that the surface roughness of the coating is 13.27  $\mu\text{m}$  before remelting

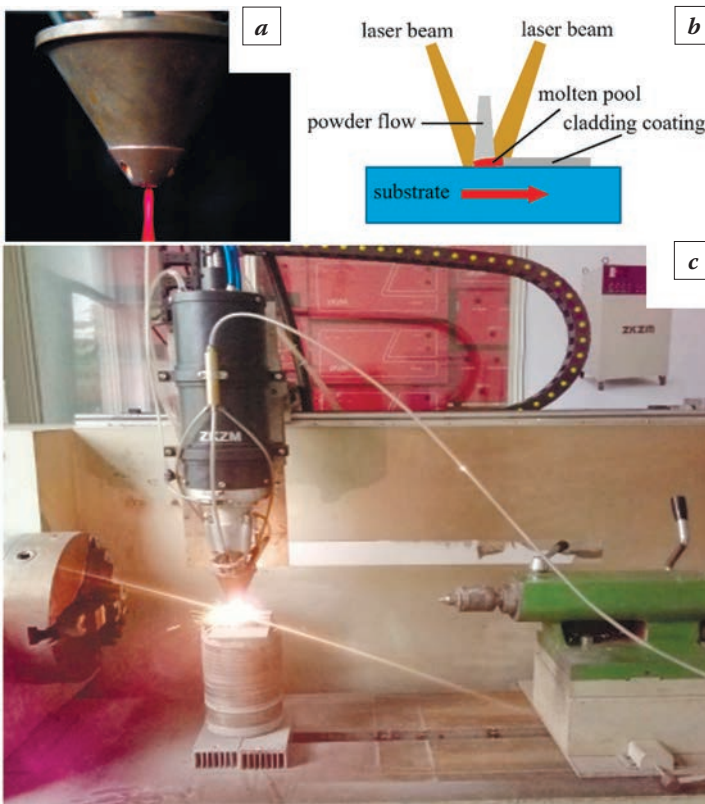


Fig. 1. The laser head (a), sketch of ZKZM-USLC system with center powder feeding (b) and the USLC+LR process (c)

Table 1. Chemical composition of Ni625 alloy powder, wt. %

Element	C	Al	Ti	Fe	Mo	Nb	Cr	Ni
wt. %	0.1	0.16	0.2	3	8.72	3.54	22.69	61.57

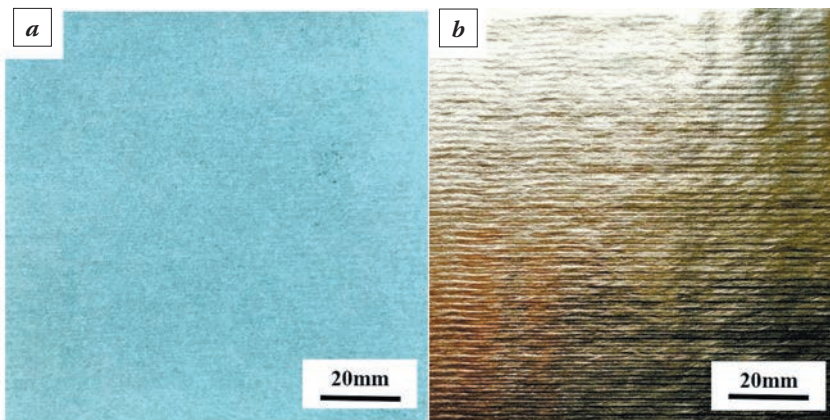


Fig. 2. Macroscopic morphology of (a) the USLC specimen and (b) the USLC+LR specimen

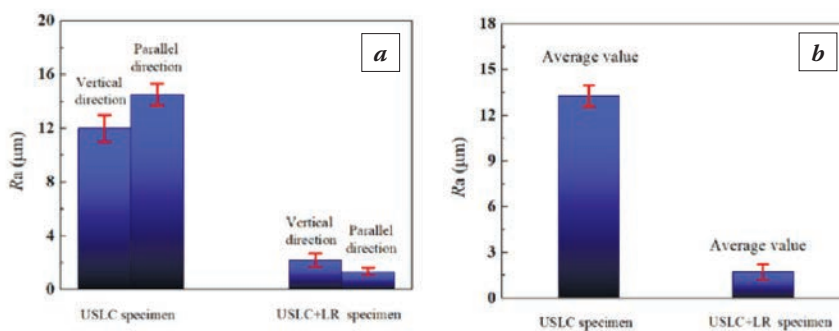


Fig. 3. Surface roughness of (a) the USLC specimen and (b) the USLC+LR specimen

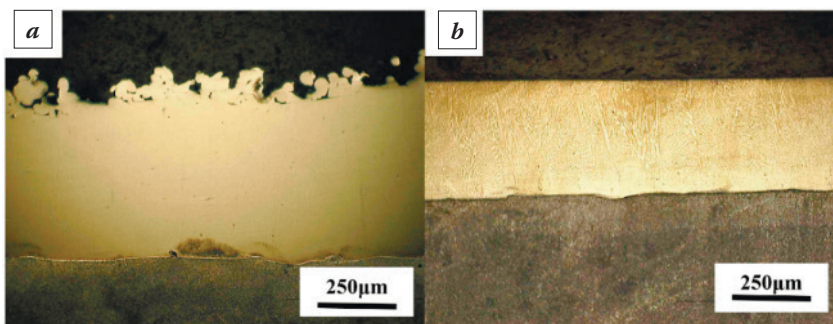


Fig. 4. OM topographic photos of (a) the USLC specimen and (b) the USLC+LR specimen

and  $1.76 \mu\text{m}$  after remelting. It can be found that the roughness after remelting decreases obviously, which indicates that LR induces the surface melting, which would eliminate some impurities and gases, even make the grain refined and the surface smooth. This process enhances the surface quality effectively, and finally achieves the goal of improving the surface smoothness.

In addition, it can be seen from Fig. 3a that the roughness of vertical cladding direction is slightly lower than that of parallel cladding direction for the USLC specimen. By comparison, for the USLC+LR specimen, the roughness of vertical cladding direc-

tion becomes slightly higher. This might be due to the process and path of LR.

Fig. 4 is the cross section morphology of the USLC and USLC+LR specimens. Obviously, the results showed that the surface of the cladding layer becomes smooth and uniform after remelting. Secondly, the thickness of the coating before and after remelting is  $0.5 \text{ mm}$  and  $0.4 \text{ mm}$  respectively. By contrast, the thickness of the coating after remelting decreased, which indicates that the surface of the cladding layer after LR would turn to be more compact.

Fig. 5 is an enlarged view of the microstructure of the USLC and USLC+LR specimens. Fig. 5a, 5c and 5e were the microstructures of the near surface, middle and bottom of the coating before remelting, respectively. It can be clearly seen that dendrites grow in the form of dendrites from the bonding zone to the near surface zone. This is directly due to the process of cladding, in which a small molten pool was formed, and the cooling rate of the molten pool was faster, which made the time of solute diffusion shorter. Therefore, non-equilibrium solidification structure, i.e. dendrite morphology, was formed in the process of rapid solidification [7]. Due to the rapid melting, the high solidification rate and the large temperature gradient, needle-like, strip-like and dendritic morphology

during cladding along the growth direction turn to be different. Fig. 5b, 5d and 5f were the near surface, middle and bottom microstructures of the remelted coatings respectively. It was found that they still grow in the form of dendrites. The difference is that remelting had an effect on the macrostructure and structure of the near surface area of the coatings, and the microstructure was refined after LR. This was because in the process of cooling and solidification, the temperature gradient at the interface of molten pool decreased and the crystallization rate increased. As a result, the dendrites became finer after LR.

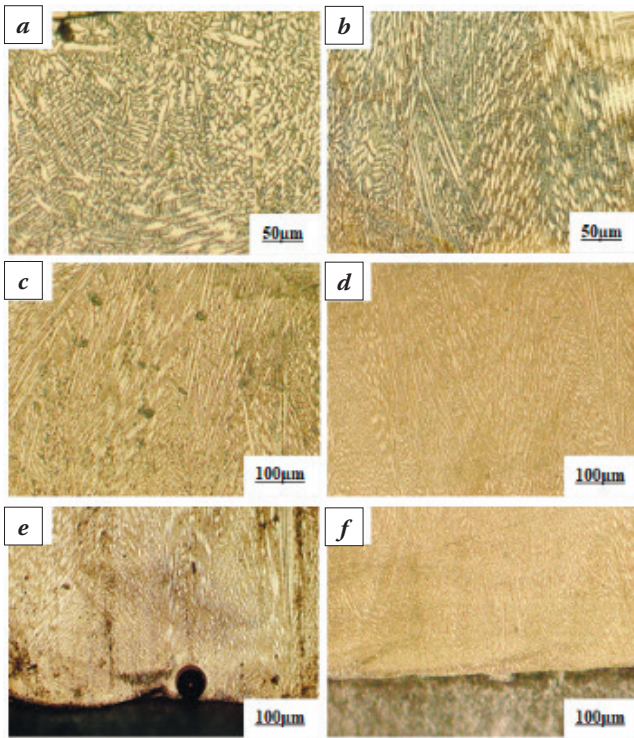


Fig. 5. Microstructure of different sections of (a) the USLC specimen and (b) the USLC+LR specimen: (a) ~ (b) in the top, (c) ~ (d) in the middle, (e) ~ (f) at the bottom

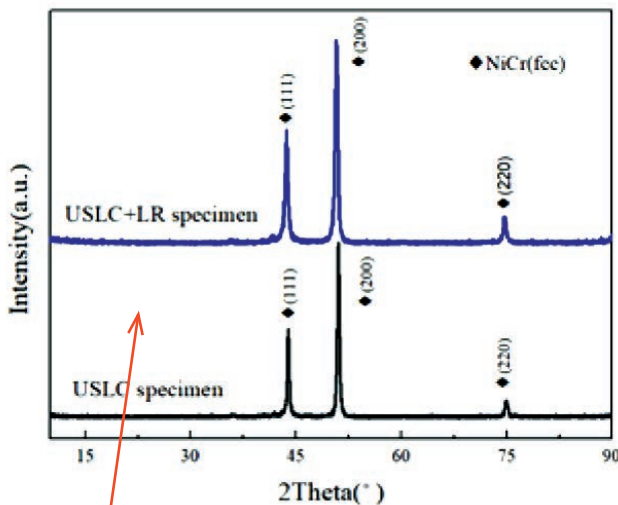


Fig. 6. XRD results of (a) the USLC specimen and (b) the USLC+LR specimen

Fig.6 shows the XRD spectrums of the USLC and USLC+LR specimens. It can be seen that the phases in the coating was mainly the NiCr austenite phase with face-centered cubic structure and rarely changed after remelting. It mainly grows along (111), (200) and (220) directions with the preferred direction of (200). Notice that for the USLC+LR specimen, the preferential orientation tends to be weakened after remelting treatment. The intensity ratio of diffraction peak

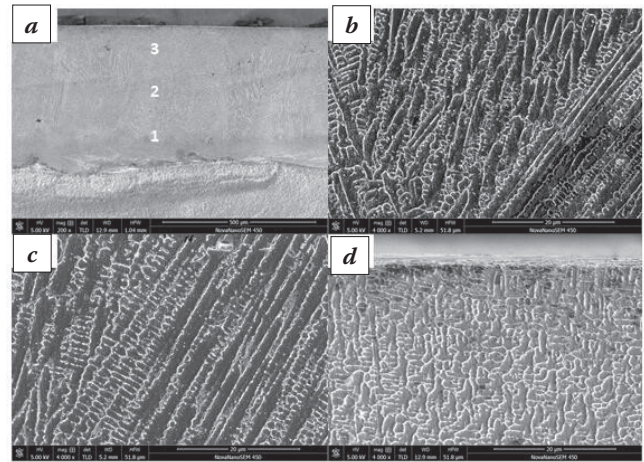


Fig. 7. Microstructure distribution of the USLC+LR coating: a – the whole cladding layer; b – Zone 1; c – Zone 2; d – Zone 3

$I_{(200)}/I_{(111)}$  decreased from 1.96 before remelting to 1.81 after remelting. Cieslak et al. studied the phase transition in the solidification process of Ni625 [15]. It was pointed out that NiCr austenite phase was first precipitated from liquid phase, and Laves phase was precipitated after the reaction reached saturation. However, Laves phase was not found in XRD because of the low NbC content.

In order to further study the structure and morphology of the cross section of the cladding layer, SEM results of the USLC+LR specimen was shown in Fig. 7. Thereinto, Fig. 7a is the macro-morphology of the coating section. Fig. 7b, 7c and 7d are the enlarged microstructures of the bottom, middle and near surface areas of the coating, respectively.

Fig. 7b shows that dendrites grow in the opposite direction of heat flow. This is due to the better thermal conductivity near the junction, which is easy to dissipate heat, leading to rapid cooling of the cladding layer. Meanwhile, because of the fast cooling rate at the bottom, the primary dendrites had relatively shorter growth time. As a result, the primary dendrites exhibit to be slender and the secondary dendrites on the main trunk of primary dendrites turned to be shorter. As shown in Fig. 7c, the slower cooling rate in the middle area resulted in the sufficient time for dendrites to grow. It can be found that the obvious increase of primary dendrite spacing, and the development of secondary dendrites. Fig. 7d is located at the near-surface area. It is noted that the direction of dendrite growth has changed under the influence of SR. The structure of near surface area is turned to be finer dendrites.

Potential polarization curves of the substrate, the USLC and USLC+LR specimens are shown in Fig. 8. It can be seen that the self-corrosion potential  $E_{corr}$

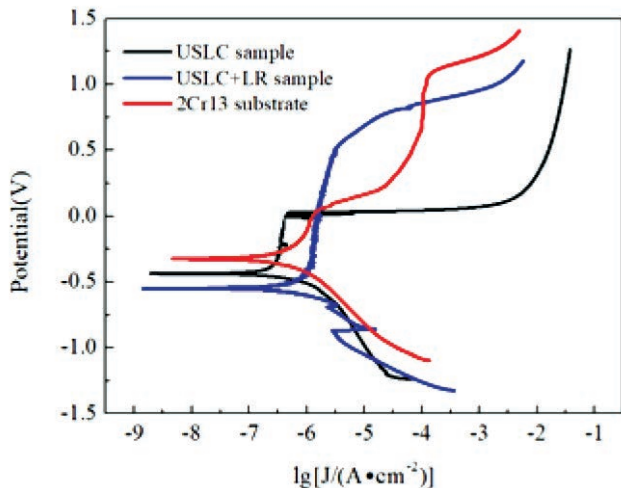


Fig. 8. Polarization curve of electrochemical corrosion

of the USLC+LR specimen is the lowest of  $-0.554\text{V}$ , while that of the 2Cr13 substrate is the highest with  $E_{corr}$  of  $-0.325\text{V}$ . On one hand,  $E_{corr}$  of the USLC specimen decreases by  $0.112\text{V}$  compared with that of the substrate, which demonstrates that the corrosion resistance of Ni625 alloy coating by USLC preparation technology is better than the 2Cr13 substrate. On the other hand,  $E_{corr}$  of the USLC+LR specimen decreases by  $0.117\text{V}$  compared with that of the USLC specimen. The result indicates that the corrosion motive force of the LR coating in 3.5% NaCl solution decreases, and the corrosion resistance of the coating is significantly improved. As shown in Fig. 2b, Fig. 4b and Fig. 7d, after LR surface treatment, the compactness of the coating is greatly improved and the grain microstructure is refined as well. The above structural changes result in the reduction of electrochemical corrosion rate and eventually improve the corrosion resistance of the USLC+LR coating.

The experimental results of salt spray are shown in Fig. 9 and Fig. 10. Fig. 9 is a comparison of corrosion mass loss of the substrate, the USLC and USLC+LR specimens, while Fig. 10 exhibits a comparison of sample morphology before and after salt spray experiments. It can be seen from Fig. 9 that the mass loss per unit area of 2Cr13 substrate is  $2.166\text{ mg}$ , which is higher than that of the USLC and USLC+LR specimens. Specially, the mass loss per unit area of cladding layer is only  $0.127\text{ mg}$  after LR process. It is showed that the weight loss of the USLC+LR specimen was 94.1% and 66.8% less than that of 2Cr13 substrate and the USLC specimen. Meanwhile, as shown in Fig. 10f, there is almost no corrosion products for the USLC+LR specimen. The experimental results demonstrate once again the corrosion resistance of the USLC+LR specimen after laser remelting treatment is the best.

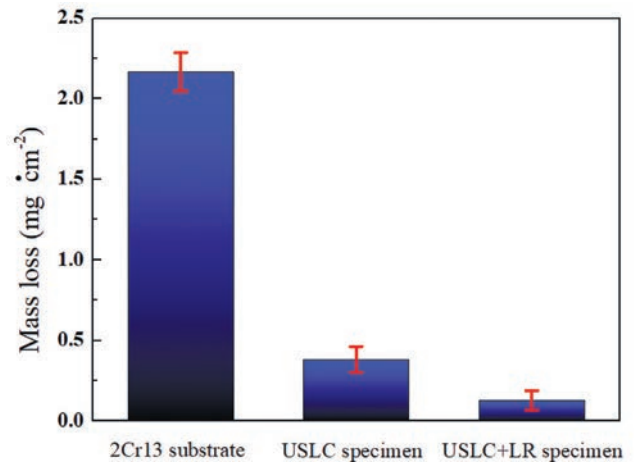


Fig. 9. Mass loss per unit area in salt spray test

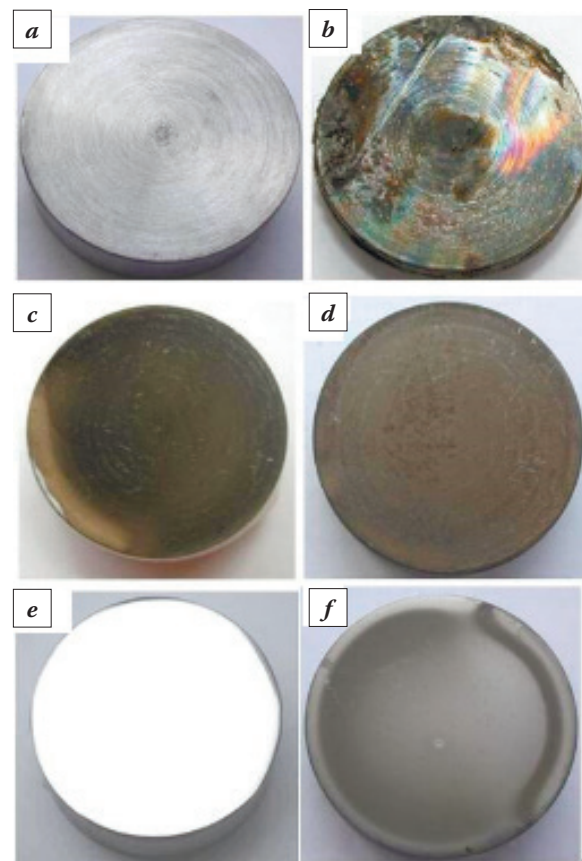


Fig. 10. Photos before and after salt spray test: a~b – 2Cr13 substrate, c~d – the USLC specimen and e~f – the USLC+LR specimen

## CONCLUSION

The effects of LR treatment on surface topography, toughness, microstructure, phases and corrosion resistance of the USLC Ni625 coatings on 2Cr13 steel substrate have been investigated in the present research. The following conclusions can be drawn.

(1) Compared with the 2Cr13 steel substrate, USLC Ni625 coatings with better surface quality could improve the corrosion resistance.

(2) LR treatment can not only significantly reduce the surface roughness of USLC coating and but also effectively improve the surface compactness. The structure of the USLC+LR coating along the growth direction is in the form of dendrite, and the grain microstructure is refined after remelting.

(3) The phases in the cladding coating was mainly the NiCr austenite phase with fcc structure and rarely changed but with the preferential orientation weaken after LR treatment.

(4) The above structural changes result in the reduction of electrochemical corrosion rate and eventually improve the corrosion resistance of the USLC+LR coating.

## ACKNOWLEDGMENTS

The authors would like to acknowledge projects of National Natural Science Foundation of China (51271139, 51471130), Shaanxi Nature Scientific Research Plan (2018JM5105, 2018JQ5173), Shaanxi Education Department Science and Technology Research Plan (18JS096, 18JS099), Xi'an Science and Technology Plan (2019KJWL06).

## REFERENCES

1. **Li Y.J., Dong S.Y., Yan S.X. et al.** Elimination of voids by laser remelting during laser cladding Ni based alloy on gray cast iron // *Opt. Laser Technol.* 2019. 112: 30–38.
2. **Vostřák M., Tesar J., Houdková Š. et al.** Diagnostic of laser remelting of HVOF sprayed Stellite coatings using an infrared camera // *Surf. Coatings Technol.* 2017. 318: 360–364.
3. **Houdková Š., Pala Z., Smazalová E. et al.** Microstructure and sliding wear properties of HVOF sprayed, laser remelted and laser clad Stellite 6 coatings // *Surf. Coatings Technol.* 2017. 318: 129–141.
4. **Yang K., Li J.Q., Wang Q.Y. et al.** Effect of laser remelting on microstructure and wear resistance of plasma sprayed  $\text{Al}_2\text{O}_3$ -40% $\text{TiO}_2$  coating // *Wear.* 2019. 426–427: 314–318.

5. **Yu J.B., Wang Y., Zhou F.F. et al.** Laser remelting of plasma-sprayed nanostructured  $\text{Al}_2\text{O}_3$ -20wt.%  $\text{ZrO}_2$  coatings onto 316L stainless steel // *Appl. Surf. Sci.* 2018. 431: 112–121.

6. **Yang X.S., Liu J.N., Cui X.F. et al.** Effect of remelting on microstructure and magnetic properties of Fe-Co-based alloys produced by laser additive manufacturing // *J. Phys. Chem. Solids.* 2019. 130: 210–216.

7. **Zhou S.F., Xu Y.B., Liao B.Q. et al.** Effect of laser remelting on microstructure and properties of WC reinforced Fe-based amorphous composite coatings by laser cladding // *Opt. Laser Technol.* 2018. 103: 8–16.

8. **Cai Z.B., Cui X.F., Liu Z. et al.** Microstructure and wear resistance of laser clad Ni-Cr-Co-Ti-V high-entropy alloy coating after laser remelting processing // *Opt. Laser Technol.* 2018. 99: 276–281.

9. **Li R.F., Jin Y.J., Li Z.G. et al.** Effect of the remelting scanning speed on the amorphous forming ability of Ni-based alloy using laser cladding plus a laser remelting process // *Surf. Coatings Technol.* 2014. 259: 725–731.

10. **Rahman Rashid R.A., Nazari K.A., Barr C. et al.** Effect of laser reheat post-treatment on the microstructural characteristics of laser-clad ultra-high strength steel // *Surf Coatings Technol.* 2019. 372: 93–102.

11. **Kaierle S., Overmeyer L., Alfred I. et al.** Single-crystal turbine blade tip repair by laser cladding and remelting // *CIRP J. Manu. Sci. Technol.* 2017. 19: 196–199.

12. **Koruba P., Reiner J.** Thermal imaging of laser powder interaction zone in ultra-high speed laser cladding process: 14th Quantitative Infrared Thermography Conference (QIRT). Berlin, Germany, Jun 25–29. 2018.

13. **Schopphoven T., Gasser A., Backes G.** EHLA: Extreme high-speed laser material deposition, economical and effective protection against corrosion and wear // *Laser Technik J.* 2017. 14: 26–29.

14. **Koruba P., Jurewicz P., Reiner J. et al.** Ultra-high speed laser cladding (UHSLC) technology for stellite 6 functional coatings deposition in aviation industry // *Przeglad Spawalnictwa.* 2017. 89: 15–19.

15. **Cieslak M.J., Headley T.J., Romig A.D. et al.** A melting and solidification study of Alloy 625 // *Metallurgical Transactions A.* 1988. 19: 2319–2331.

# EFFECTS OF DIFFERENT TYPES OF DISCHARGE ON THERMO-CHEMICAL PROCESSES OF STRUCTURAL AND TOOL STEELS

A.S. Sergeeva, L.G. Petrova, V.A. Aleksandrov, V.M. Vdovin

Moscow Automobile and Road Construction State Technical University (MADI). Moscow, Russia  
sergeevamadi@yandex.ru

The paper studies the process of gas nitriding of iron and steel in an electric discharge. Data were obtained on the acceleration of the process of saturation with nitrogen compared to traditional furnace nitriding. The rate of formation of both the nitrated layer as a whole and its individual sections increases: the diffusion layer and the nitrides zone. At the same time, the process can efficiently proceed both with and without additional heating of the muffle. As parameters to control the kinetics of growth of the layer, the electric discharge current density and the temperature of heating the muffle are used. The regulatory effect of saturating environment parameters was studied during nitriding in a glow discharge.

**Keywords:** thermo-chemical treatment, nitriding, electric discharge, diffusion layer

## INTRODUCTION

Gas nitriding is one of the most common methods of thermo-chemical treatment (TCT) of metals, it is widely used for surface hardening of machine parts and tools. The disadvantage of the process is a relatively long-time duration of the technological cycle. Therefore, one of the main directions of improving the process of nitriding is the search for intensification possibilities of the process.

It is known that the saturation rate of a metal with nitrogen is influenced by the rates of elementary TCT processes: dissociation of saturating gas molecules with the formation of active atoms (ions) of nitrogen, the delivery of active atoms (ions) to the surface of the processed product, their adsorption on the surface and, finally, the diffusion of active atoms in solid metal. Since diffusion in the solid phase is the limiting stage of the saturation process, most of the known attempts to intensify the nitriding process are reduced to finding ways to accelerate the diffusion of nitrogen in the metal. The effect of heat and other types of energy contributes to the acceleration of physical and chemical processes. The methods for intensifying nitriding using plasma [1], laser radiation [2, 3] and ultrasound [4, 5] have been studied. In addition, the acceleration of the nitriding process can be achieved by composition control of the saturating atmosphere [6, 7], using step and gas-cyclic processes [8, 9], during the formation of catalytic [10, 11] and barrier [12] surface oxide films.

The use of an electric gas discharge of various physical nature is one of the ways to intensify the nitriding process. The intensification degree of saturation depends on external conditions: the type and parameters of the discharge, electrodes and chamber walls, pressure and temperature.

The purpose of this work is a theoretical and experimental research of TCT processes in an electric discharge of various nature, the study of the effect of processing parameters on the structure and kinetic parameters of the diffusion layer.

## THEORETICAL BACKGROUND

Analysis of the processes occurring during the interaction of the metal surface with the saturating gaseous medium at CHT, shows that the role of electrophysical and electrochemical phenomena in them is very large. The course of chemical reactions in the discharge depends on the type of discharge: arcing-type, corona, flare, glow, quiet (silent) discharge.

The effect of accelerating nitriding in an electric discharge is associated with an increase in the reactivity of a gas due to the splitting of molecules into atoms and their ionization. The growth of the diffusion layer is influenced by the number of active atoms (ions) of nitrogen adsorbed directly on the metal surface. The number of active gas particles capable of participating in the reactions increases with the ionization of the gas as a result of electrical discharge.

When conducting nitriding in weak electrostatic fields, as well as during radiation heating, the nitrogen potential of the saturating atmosphere is determined by ammonia anions. When anodic process of saturation intensification contributes the electrostatic attraction of negative ions with a metal surface when a positive potential is applied to the product. The highest intensity of the process corresponds to the field strength necessary for the formation of the maximum number of ions  $\text{NH}_3^-$ . At optimal parameters, the process on the product-anode is accelerated by 1.5...2.5 times compared with the speed of the process during furnace heating.

In strong electric fields, the effect of gas discharges (glow, spark or corona) is accompanied by the formation of positive ammonia or nitrogen ions in the saturating gas, which are attracted by a negatively charged metal surface (cathode process). The part is heated to a given TCT temperature due to the bombardment of the treated surface with ions. The most common method of chemical heat treatment at the cathode process is nitriding in a glow discharge, which occurs 1.5...2.0 times more intense than TCT during radiation heating.

Mechanisms to accelerate processes in an electric discharge are associated with thermal intensification of chemical reactions during heat discharge by a discharge (for example, in an electric arc), with a photochemical effect due to the generation of short-wave radiation (for example, in an electric spark and glow discharge), as well as by the direct action of free electrons on the discharge atoms and molecules of reactants. It is known that during the chemical treatment with the use of an electric discharge, molecules and compounds that are not formed outside the discharge are formed in the gas: "active" hydrogen, nitrogen, oxygen (atomic gases H, N and O), free radicals, diatomic molecules.

The electrical parameters of the discharge have a significant impact on the rate of reactions: one of the factors affecting the reaction rate, its progress and productivity, is the density of the discharge current  $J$ .

The mechanism of intensification of diffusion saturation processes in an electrostatic discharge is associated with the nature of the electric spark, in which energy is released in a short period of time, which sharply increases the temperature of the spark channel, causing optical radiation, the appearance of electric and magnetic fields, ionization processes, etc.

A high degree of the saturating atmosphere ionization, a high concentration of ions, and radiation effects on the surface of the machined parts determine the possibility of the formation of a diffusion layer during CHT in an electric spark discharge with-

out additional heating of the muffle. The process is intensified due to the influence of the electric field both on the processes of the gas phase activation and on the processes of adsorption and diffusion.

## METHODS OF EXPERIMENTAL STUDY

An installation consisting of a muffle (working container), a source of high-voltage voltage, a gas-cylinder station, and systems for controlling electrical and gas-dynamic parameters of the process (Fig. 1) was used to study the process of saturation of iron and steel with nitrogen. Nitriding in an electric field is carried out at atmospheric pressure and the application of voltage to the electrodes: one of the electrodes is the sample being processed, the second is the metal reactor vessel. Studies were carried out on technical iron, steels 40Cr and 38Cr2MoAlV, and on tool steel R18.

Samples of steels prepared for nitriding are connected to the discharge electrode. The furnace is sealed and purged with ammonia for 15...30 minutes, then voltage is applied to the electrodes. At the ignition voltage, a corona (or spark) discharge occurs and impact ionization of the saturating atmosphere occurs. The discharge initiates the dissociation of ammonia, accompanied by the formation of nitrogen-containing ionic complexes that bombard the treated surface.

In contrast to traditional furnace nitriding of TCT in an electric field, it is controlled both by standard technological parameters: the process duration and temperature (in the case of additional heating of the muffle), so and the current strength. At a nitriding temperature of 450...600 °C, when charge carriers arise due to thermal dissociation of the atmosphere, a relatively low voltage of electric current is required to form and maintain a corona or spark discharge. At

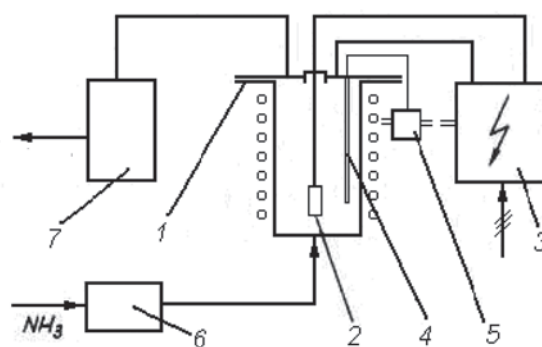


Fig. 1. Schematic diagram of the installation for the implementation of the process of nitriding in an electric field: 1 – muffle; 2 – detail; 3 – control unit; 4 – thermocouple; 5 – muffle heating regulator; 6 – ammonia consumption regulator; 7 – dissociometer

the same time, TCT in an electric field with the formation of a spark discharge can be carried out without heating the working container at the expense of external heat sources (at  $t=20\text{ }^{\circ}\text{C}$ ), but this will require the application of a significantly higher electric voltage at the stage of the onset of the discharge for the initial ionization of the gas in the electric discharge.

To study the possibility of intensifying and controlling the process of nitriding in a glow discharge, investigated the effect of the composition of a saturating medium on the formation of a diffusion layer in steel 38Cr2MoAlV. The nitriding processes were carried out at saturation in the glow discharge plasma, both at the anodic and cathodic processes: in pure ammonia, mixtures of ammonia with propane, with argon, and in nitrogen-hydrogen mixtures with different ratio of components.

## RESULTS AND DISCUSSION

### Influence of nitriding parameters in an electric discharge on the kinetics of the saturation process and hardening of steel.

A significant acceleration of the formation of a diffusion layer in an electrostatic field is experimentally established as compared with traditional nitriding in both steels and technical iron. Thus, when treating steel 38Cr2MoAlV in an electrostatic field at a density of discharge electric current of  $80\text{ }\mu\text{A}/\text{mm}^2$  without additional heating of the muffle for 3 hours, a layer with a depth of 0.30 mm forms, whereas with standard gas nitriding of this steel at  $550\text{ }^{\circ}\text{C}$ , a layer with a depth of 0.55 mm is formed in 30...35 hours. The total layer thickness at a current density of  $80\text{ }\mu\text{A}/\text{mm}^2$  and nitration time of 1 hour is as follows: in technical iron – 0.25 mm, in steel 38Cr2MoAlV – 0.157 mm, in steel R18 – 0.065 mm. With an increase in the nitriding time, the total thickness of the nitrated layer grows according to a parabolic law, which is confirmed by the diffusion control of the process (Fig. 2).

An increase in the current during nitriding accelerates the formation of both the diffusion underlayer and the surface zone of the compounds (Fig. 3). For example, at a current density of  $32\text{ }\mu\text{A}/\text{mm}^2$  (saturation time is 1 h), a nitride zone with a thickness of 2... 3  $\mu\text{m}$  forms in technical

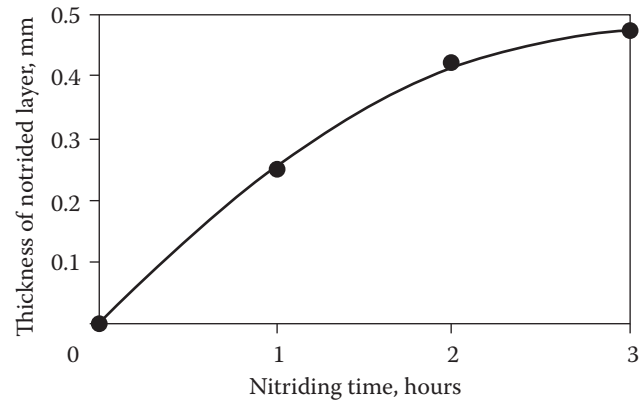


Fig. 2. The effect of the nitriding duration in an electric field on the thickness of the diffusion layer in the technical iron ( $t = 20\text{ }^{\circ}\text{C}$ , current density  $80\text{ }\mu\text{A}/\text{mm}^2$ )

iron; it becomes about  $18\text{ }\mu\text{m}$  at  $64\text{ }\mu\text{A}/\text{mm}^2$ , and 25...30  $\mu\text{m}$  at  $80\text{ }\mu\text{A}/\text{mm}^2$ .

The external heating temperature of the muffle has an anomalous effect on the rate of formation of the diffusion layer. For example, additional heating of the tank from room temperature to  $300\text{ }^{\circ}\text{C}$  increases the growth rate of the layer by two to three times, allowing a current of 50 mA to give a total depth of 0.55 mm for 1h in the technical iron (Fig. 4a). A further increase in temperature does not affect the growth of the diffusion sublayer. The effect of temperature in the muffle on the thickness of the  $\epsilon$ -phase nitride zone is of an extreme nature (Fig. 4b), which reflects changes in the phase composition of this zone.

It is established that the level of surface hardening during nitriding in an electric field varies for different materials. Thus, the surface hardness of technical iron and carbon, and low-alloy structural steels increases slightly. A significant increase in hardness is observed only in alloyed steel (Fig. 5), which is consistent with the general laws of the classical nitriding process. For example, the surface hardness of steel

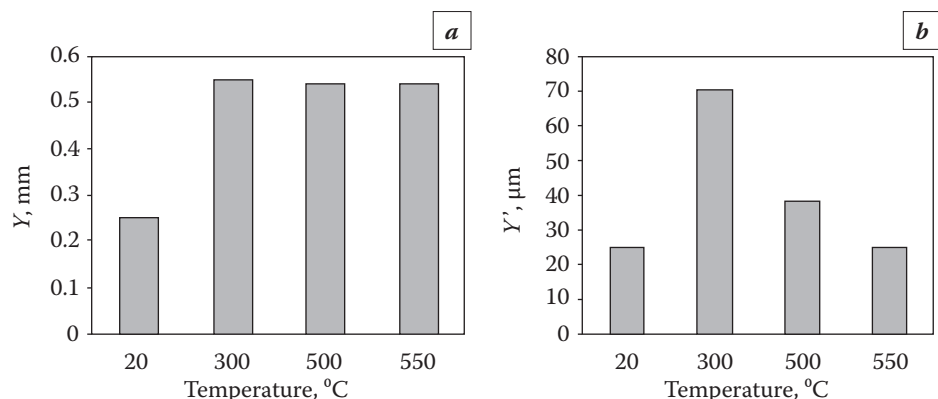


Fig. 3. Effect of current density on the thickness of the diffusion underlayer  $Y$  (a) and the nitride zone  $Y'$  (b) in the technical iron when nitriding in an electric field without heating the muffle ( $20\text{ }^{\circ}\text{C}$ ) and heating the muffle to  $300\text{ }^{\circ}\text{C}$  (nitriding time 1 h)

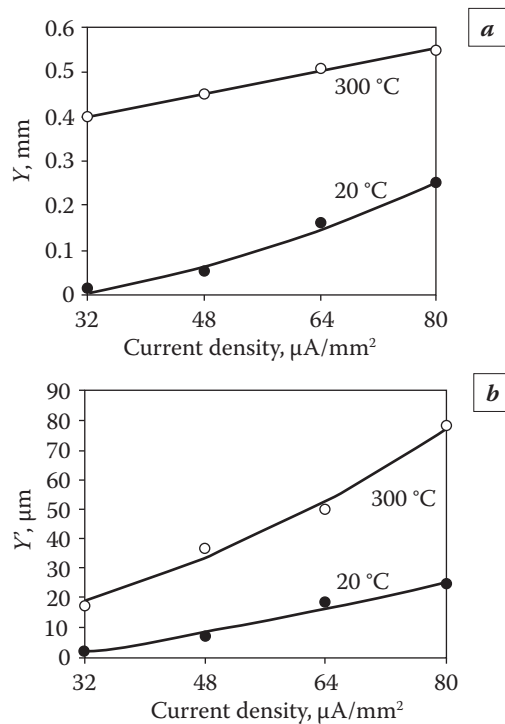


Fig. 4. Effect of muffle preheating temperature on the thickness of the diffusion underlayer  $Y$  (a) and the nitride zone  $Y'$  (b) in technical iron when nitriding in an electric field (nitriding time 1h, current density  $80 \mu\text{A}/\text{mm}^2$ )

38Cr2MoAlV increases to 1050...1150 HV, a similar effect is caused, as a rule, by the formation of nitrides of alloying elements. The hardness of the nitrated surface increases with an increase in the duration of the process, which can be explained by an increase in the volume fraction of hardening nitride phases.

#### The effect of a saturating atmosphere during TCT in a glow discharge on the structure of a diffusion layer.

Analysis of the experimental results shows that when steel is saturated in a glow discharge plasma in the atmospheres under study, qualitatively similar diffusion layers are formed, consisting of the surface zone of the compounds and the zone of internal nitriding. However, the rates of formation of diffusion layers and their phase composition depend on the gas-dynamic parameters of ion nitriding and the composition of the saturating atmosphere.

The maximum growth rate of the nitrated layer, having a multilayer structure, in iron and in the classic nitrated layer corresponds to saturation in the atmosphere of pure ammonia at optimum pressures in the working volume of the container for each processing temperature. In this case, the nitride zone in technical iron is a mixture of nitrides  $\epsilon(\text{Fe}_3\text{N})$  and  $\xi(\text{Fe}_2\text{N})$ , and in steel 38Cr2MoAlV – a homogeneous  $\epsilon$ -phase (Fig. 6). Such a structure is

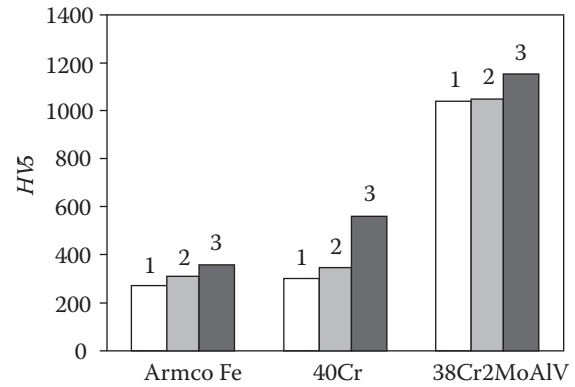


Fig. 5. Surface hardness of technical iron and steel nitrated in an electric field (reactor temperature 20 °C;  $I = 50 \text{ mA}$ , numbers on the diagram – process duration, h)

favorable for products that require corrosion resistance, wear resistance of rubbing surfaces (for example, threaded joints) and resistance under shock loads.

The process of ionic nitriding in ammonia diluted with argon (10% vol. Ar in the mixture), at a temperature of 620 °C, allows for 6 hours to get a solid wear-resistant layer in steel 38Cr2MoAlV, including the nitride zone from doped  $\epsilon$ - and  $\gamma'$ -phases and the eutectoid (Fig. 7).

When nitriding in a carbon-containing glow discharge plasma, from the point of view of the surface characteristics of the diffusion layers, the mixture consisting of 88...92% vol. ammonia and 8...12% vol. propane, which provides the zone of compounds from a mixture of carbonitrides  $\text{Fe}_3(\text{NC})$  and  $\text{Fe}_2(\text{NC})$  in the technical iron and  $\epsilon$ -carbonitride  $\text{Fe}_3(\text{NC})$  in steel 38Cr2MoAlV (at a temperature of 520 °C). An increase in the nitriding temperature to 650 °C leads to the appearance in the zone of compounds of insignificant amounts of carbonitride isomorphous to cementite lattice  $\text{Fe}_3(\text{NC})$ .

Nitriding in a nitrogen-hydrogen atmosphere, obtained by preliminary 100% dissociation of ammonia, makes it possible to form a zone of compounds based on the homogeneous  $\gamma'$ -phase. The thickness of the nitride zone of the  $\gamma'$ -phase with a nitriding time of 1 hour is 5...7  $\mu\text{m}$  and practically does not increase with time, which may be explained by its narrow homogeneity area.



Fig. 6. The microstructure of the diffusion layer in 38Cr2MoAlV steel after nitriding in a glow discharge in pure ammonia at a temperature of 540°C, a pressure of 20 mm Hg, a process time of 16 h



Fig. 7. The microstructure of the diffusion layer in steel 38Cr2MoAlV after nitriding in a glow discharge in a mixture of 90% vol.  $\text{NH}_3$  + 10% vol. Ar at a temperature of 620 °C, a pressure of 20 mm Hg, process time 6 hours

Since the diffusion rate of nitrogen in nitrides is significantly lower than the diffusion mobility of nitrogen in solid solutions, one of the factors intensifying the nitriding processes of steels is the creation of layers based on internal nitriding zones. The process of nitriding is effective, providing regulation of the nitrogen potential of the atmosphere at the level of the maximum solubility of nitrogen in phases with its maximum mobility.

So, when nitriding in ammonium-argon plasma of a glow discharge of 10% vol.  $\text{NH}_3$  + 90% vol. Ar according to the cyclic process mode ( $p = 0.3\text{--}0.6$  mm Hg), a layer of high-nitrogen  $\alpha$ -solid solution is formed without a surface nitride zone, which is 1.5 times as thick as the layer obtained with a similar the cathode process.

## CONCLUSIONS

1. Experimentally shown is the acceleration of the process of diffusion saturation with nitrogen of technical iron and steel when nitriding in an electric field with the formation of a spark discharge compared to classical gas nitriding. It was established that the main parameters regulating the growth of the layer under the conditions of an electric discharge are the electric current density and the temperature of heating of the reaction muffle. By adjusting the temperature, you can achieve the desired ratio of the thickness of the nitride zone and the diffusion underlayer.

2. Unlike a glow discharge, the spark and corona discharges burn steadily at normal pressure, which does not require the use of vacuum systems to maintain and control the gas-dynamic parameters of the discharge and additional sources of radiation heating. In this regard, prospects for the development of electrophysical methods for gas-discharge nitriding, which include processes in an electrostatic and high-frequency field, are opening up. An additional advantage of the nitriding process in an electric discharge is a twofold reduction in gas consumption due to the high degree of ionization of the atmosphere.

## ACKNOWLEDGMENTS

This research is supported by the Russian Science Foundation, project no. 17-19-01473.

## REFERENCES

1. Petrova L.G., Aleksandrov V.A., Demin P.E. Thermochemical treatment of steels in the plasma of a hydrostatic glow-spark discharge // *Metal Science and Heat Treatment*. 2012. Vol. 54, No. 5–6. P. 309–312.
2. Chudina O.V., Petrova L.G., Aleksandrov V.A. et. al. Increase of reliability of loaded machine parts by surface modification using methods of laser treatment // *ARPN Journal of Engineering and Applied Sciences*. 2018. Vol. 13, No. 7. P. 2477–2481.
3. Konoplin A.Yu., Baurova N.I. Hardness of the Near-Weld Zone during Contact Spot Welding of Steels Using an Adhesive-Weld Technology // *Russian Metallurgy*. 2016. No. 13. P. 1308–1311.
4. Prikhod'ko V.M., Aleksandrov V.A., Fatyukhin D.S., Petrova L.G. Effect of ultrasonic cavitation on nitrided steel surface layer condition // *Metal Science and Heat Treatment*. 2015. Vol. 57, No. 5–6. P. 300–303.
5. Fatyukhin D.S., Nigmatzyanov R.I., Luznov J.M. et. al. A study of the influence of cavitation structures on the facial layers of structural materials // *Journal of Industrial Pollution Control*. 2017. Vol. 33, No. 2. P. 1612–1616.
6. Soldatov V.I., Mezhonov A.E., Aleksandrov V.A., Bibikov S.P. Technology and plant for nitriding steels in an atmosphere of ammonia and air // *Metal Science and Heat Treatment*. 1988. Vol. 30, No. 12. P. 911.
7. Aleksandrov V.A., Grachev A.V., Barabanov S.I. Shortening of the process of nitriding of corrosion-resistant steels // *Metal Science and Heat Treatment*. 2011. P. 344–346.
8. Belashova I.S., Petrova L.G., Sergeeva A.S. Intensified saturation of iron with nitrogen by the method of thermogasocyclic nitriding // *Polymer Science. Series D*. 2018. Vol. 11, No. 1. P. 90–95.
9. Belashova I.S., Shashkov A.O. Kinetics of growth of the diffusion layer in nitriding by the thermogasocyclic method // *Metal Science and Heat Treatment*. 2012. Vol. 54, No. 5–6. P. 315–319.
10. Petrova L.G., Aleksandrov V.A., Malakhov A.Y. Control of the structure of diffusion layer in carbon steels under nitriding with preliminary deposition of copper oxide catalytic films // *Metal Science and Heat Treatment*. 2017. P. 180–185.
11. Aleksandrov V.A., Ostaeva G.Y., Papisova A.I. et. al. Synthesis of copper-polymer nanocomposite on steel surface and composite-based catalyst for steel nitriding // *Colloid Journal*. 2015. Vol. 77, No. 5. P. 556–560.
12. Shestopalova L.P. Influence of preliminary oxidation on the subsequent nitriding // *Russian metallurgy (Metally)*. 2016. Vol. 2016, No. 13. P. 1241–1248.

## BENEFITS AND PROPERTIES OF LASER-HARDENING

Němeček Stanislav<sup>1</sup>, Černý Ivo<sup>2</sup>, Kec Jan<sup>2</sup>, Ganev Nikolaj<sup>3</sup>, Čapek Jiří<sup>3</sup>

<sup>1</sup> RAPTECH s.r.o. Zruč-Senec, Czech Republic

<sup>2</sup> SVÚM Praha. Praha, Czech Republic

<sup>3</sup> ČVUT Praha. Praha, Czech Republic

nemecek@raptech.cz

Laser hardening brings a great increase in part life and it is an industry-proven process, typically used for hardening of moulds, gears, shafts etc. It was mainly the recent advancement of diode lasers that turned it into a competitive process. The paper describes the nature of residual stresses, the influence on hardness, tribological lifetime and fatigue properties of such parts. Investigations have to be performed in order to gain a comprehensive knowledge about effects on microstructure, hardness, surface properties of treated materials. This contribution contains results of a partial studies of laser hardening in industrial practice.

**Keywords:** laser; hardening; residual stresses; cracks; tribology.

### INTRODUCTION

Laser hardening offers short processing times and appreciable cost savings, as well as capabilities to accommodate almost any geometry, and control the depths and widths of the treated surfaces. In addition, laser hardened surfaces exhibit additional beneficial properties when compared to conventionally hardened surfaces. These include differences in tribological, fatigue, and corrosion behavior, specifically an improved wear life, fatigue and corrosion resistance [1].

Sheet forming dies for automotive industry may serve as a good example in this context, Fig. 1. The car body consists of about 300 components, which represent a demand for about 750 pairs of press dies (progressive dies, punching and trimming dies). Car manufacturers launch about 120 new car models every

year. Based on that number, the cost estimate for die making is 12 billion euro every year. Laser hardening of rounded and shearing edges may double the number of parts formed. Automotive die materials are ordinary hypoeutectoid tool steels (most frequently 1.2311) and hypereutectoid steels (e.g., 1.2379) but the adoption of laser hardening by car manufacturers also led to creation of several specially developed steels (e.g., Toolox44).

### Differences in surface hardening technologies

In *flame hardening*, the depth of heating is given by the relative speed of the flame movement across the surface. The efficiency of heat transfer to the material is poor and the surrounding surfaces become heated as well. As a result, the dwell time required for austenitizing increases, the grains in the material coarsen, and their boundaries may become burnt. The surface also develops a layer of oxides. In this process, the uniformity and control of temperature are limited and inaccurate. In induction hardening, the heat generated depends on electric resistance and current. The depth of heating is given by the frequency of the power source. The lower the frequency, the shallower is the hardening depth. Even with high-frequency induction heating, however, heating takes several seconds.

In *flame hardening*, as well as in *induction hardening*, the heating stage must be followed by sufficiently rapid cooling (using a water spray or



Fig. 1. Laser hardening of a forming die

polymer solution). There is an ever-present risk that steam and a vapor blanket may form during cooling, which would retard the heat removal rate and prevent the surface from hardening. Similar to the heat-affected zone in weld joints, there is a deep transition zone beneath the hardened layer. This is the zone in which the elevated temperature, though insufficient for hardening, has caused some changes in the matrix of the parent metal. Unfortunately, these changes are typically for the worse. On the other hand, the hardening depth achieved by these methods may be up to 10 mm as opposed to the several tenths of a millimeter that laser hardening produces.

In *laser treatment*, the austenitizing temperature must be achieved in the surface, as with the other techniques. However, thanks to rapid heating rates of thousands of degrees per second, the resulting transitional heat-affected zone is very thin.

The maximum laser hardened depth is approximately 2 mm, depending on the heat conductivity of the material. The hardening depth can be controlled by the speed of the beam movement and by the temperature. To improve control, the process is typically monitored using a pyrometer linked to the laser source and operated by robot. By regulating the power input, this control loop can maintain a fixed surface temperature, thus providing uniform hardness and preventing local melting.

In the heating step, austenitizing temperature, that is, a temperature above  $A_{c3}$ , must be achieved in the surface layer of steel. Rapid heating with a laser beam is one of the factors which minimize the distortion of the part heated. As the material around the laser spot remains cold, it does not expand, and the distortion does not occur. Another difference from the other surface hardening techniques lies in the heat removal mechanism which is based on self-quenching. It involves rates of several thousand  $^{\circ}\text{C}/\text{sec}$ . There is no need for cooling the surface using a liquid supplied from outside because the interior of the part remains cold and absorbs the heat by conduction at a sufficient rate (i.e., cooling by convection). One can therefore assume that phase transformation begins from within the part and the surface is the last to cool down.

Laser beam hardening is much more favorable to the material in terms of crack susceptibility than other techniques. The steep thermal gradient from quenching causes severe (tensile) stresses which lead to surface crack initiation. In laser hardening, however, the cooling process begins by heat removal to the cold interior of the workpiece. The temperatures thus equalize gradually from within the part. This minimizes the resulting stresses and eliminates cracking.

The maximum hardness level achievable in a steel with 0.1 to 0.2 % C is approximately 40 HRC. Surface-hardened steels with 0.4 % C typically have a hardness of 58 to 60 HRC. In hypereutectoid steels, hardness may reach 65 HRC. Pearlitic cast irons may reach hardnesses above 65 HRC, particularly if their surface was melted and solidified as ledeburite. In through-hardened parts, subsequent tempering is used to relieve internal stresses. By contrast, laser hardening is not followed by any heat treatment operation, not even tempering. However, laser hardening of large surfaces creates overlapping zones between adjacent hardening tracks which experience self-tempering. The width of such zones on the surface is approximately 1 mm (depending on the hardening depth and speed). As mentioned above, the decrease in hardness also depends on the carbon content in steel.

## EXPERIMENTS AND RESULTS

Continuous wave laser sources are preferred for laser hardening applications. The most widely used systems rely on diode or fiber lasers. Surfaces of experimental specimens were laser treated using the facilities of the RAPTECH company, 3kW high power diode laser from Laser Line GmbH with a dual-channel pyrometer for temperature measurement. The optical head is installed on FANUC robot Fig. 2.

### Volume changes and tribological behavior after quenching

Transformation hardening is based on changes in crystal lattice, which are accompanied by volume changes. The volume of the resulting martensite is approximately 4% greater than the volume of the parent



Fig. 2. Robotic laser hardening cell – robot and diode laser

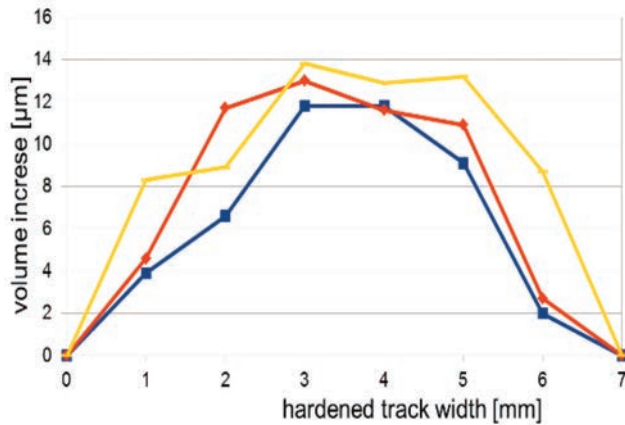


Fig. 3. Volume increase on the cross-section in the hardened layer of C45 material

phase. The increase in volume is also influenced by carbon content and by the thickness of the hardened layer. Fig. 3 shows the depth profile of volume change upon laser hardening up to the depth of 2 mm in C45 steel. In this case, the increase represents 12-14 micrometers, which does not compromise the part's precision and requires no subsequent grinding.

Thanks to the finer resulting microstructure, laser hardening provides better abrasion resistance than hardening by induction. No effect of the tempered overlapping zones has been detected in the tribological characteristics of parts studied to date (Fig. 4).

### Residual Stress and Hardness Depth Profiles

In hardness profile measurement, the maximum hardness is often found not on the surface but in the

depth of several tenths of millimetre below the surface in many materials. This fact has various consequences, such as acceptance inspection disputes in cases where the prescribed hardness "has not been met". Another example is the machining process. Laser-hardened surfaces need no final grinding. This is very beneficial with gear wheels, which are costly to grind. The allowance for grinding (e.g. 0.2 mm for correcting distortion in long parts) may thus contribute to higher final surface hardness. Another factor is the potential surface decarburisation during manufacture of a semi-finished steel product. Differences found in machined components are therefore less dramatic than in the above mentioned case. Considering the known relationship between the carbon content and hardness of material, one can assume, that residual stresses will vary as well. This assumption was confirmed by the present experiment. The surface in the laser track on the specimen of the ČSN 12050 (C45) material was gradually etched away and residual stresses were measured by X-ray diffraction, Fig. 5. Deleterious tensile stress was detected in the surface, which can contribute to crack initiation. At the same time, no more than 0.1 millimetre below the surface, in a depth which was reached by removing the oxidised layer, the stress is zero. With increasing depth, favourable compressive stresses prevail, which tend to inhibit crack propagation. Illustrative evidence is shown in Fig. 5. The soft surface exhibits hardness of 320 HV. Below the surface, hardness increases and peaks at 550 HV in the depth of 0.5 mm, Fig. 6. The same depth is the point where maximum compressive stresses were found.

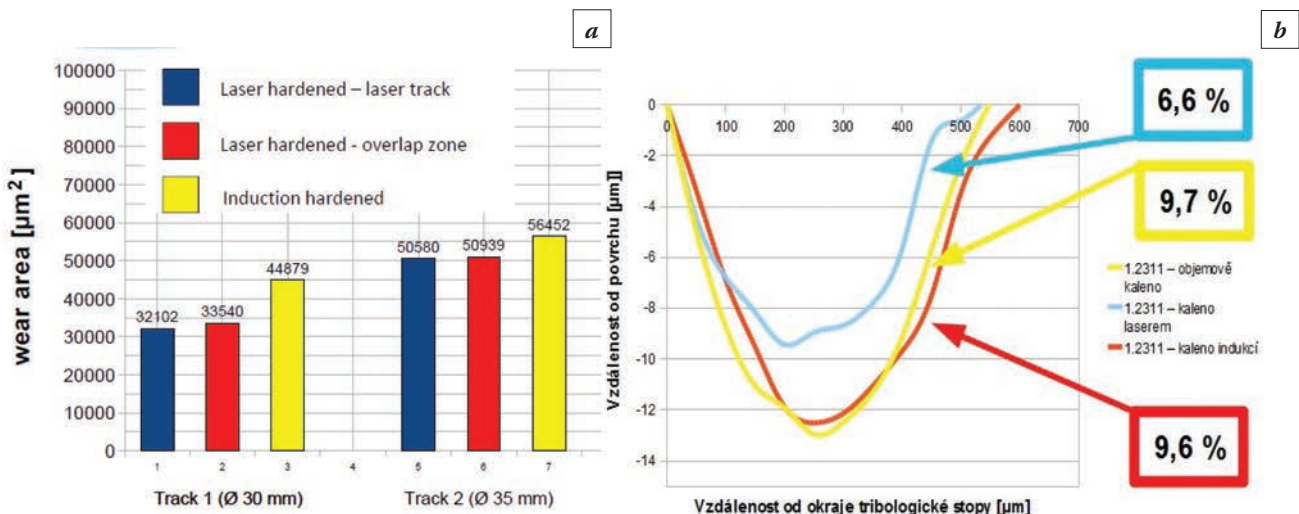


Fig. 4. *a* – results of measurement of wear resistance of 1.2311 steel by pin-on-disc test. The columns compare the data for the centerline of a laser track (blue), for an overlapping zone between laser tracks (red), and for an induction-hardened surface (yellow). *b* – this figure compares wear resistance in 1.2311 steel after various treatments: volume hardening (yellow), induction hardening (red), and laser hardening (blue) [1]

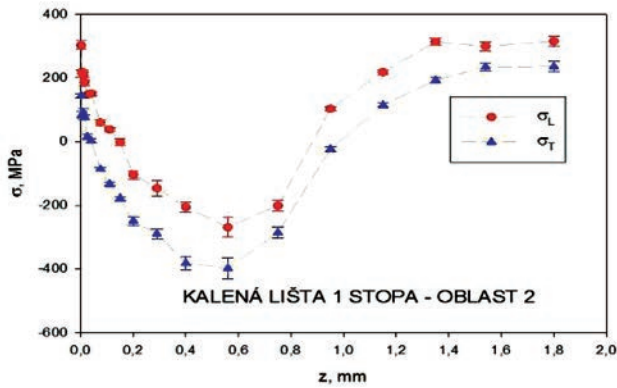


Fig. 5. Residual stress depth profile from the surface through the hardened layer

### Fatigue tests

Reference tests on the base material without laser hardening were performed using specimens of two variants: 42CrMo4 and 42CrMoS4 (the same material with an increased level of sulphur). Hardening depths in K3 and K4 specimens evaluated from macrostructure observation on metallographic sections through the surface ranged between 1.5 and 1.8 mm. The hardening depth determined as the depth where microhardness drops to one half was much less: between 0.5 and 0.8 mm.

The large scatter in data (Fig. 7) is surprising and quite unusual, namely with the 42CrMoS4 material. (The reliability expressed as  $R^2$  is no more than 0.22.) To some extent, it was encountered in the case of the 42CrMo4 material as well: the  $R^2$  is no more than 0.33. Fatigue properties show that the two versions of the material exhibit differences which had not been detected in prior composition analysis, microstructure observation or hardness tests. Scatter was found predominantly in fatigue strength data. Unexpected premature failures occurred in several cases. In this respect, the 42CrMoS4 variant performed more poorly than 42CrMo4. The obvious cause is the large amount of sulphide inclusions.

On the other hand, the results of fatigue tests of specimens hardened at higher beam velocity are very promising. The scatter is very small ( $R^2 = 0.99$ ) and the treated material exhibits clearly higher fatigue strength than the feedstock in initial condition. This surface treatment has virtually eliminated scatter and enhanced the fatigue performance throughout the entire loading range. This effect may be related to the relatively high compressive residual stresses which have been detected by structural X-ray methods at the Faculty of Nuclear Sciences and Physical Engineering of the Czech Technical University (Ganev N. et al). Namely, where fatigue cracks form from sur-

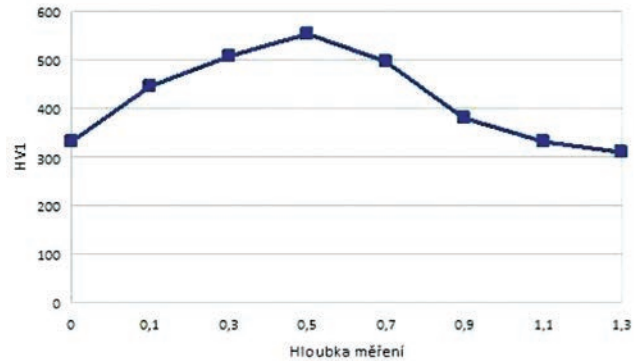


Fig. 6. HV1 hardness depth profile from the surface through the hardened layer

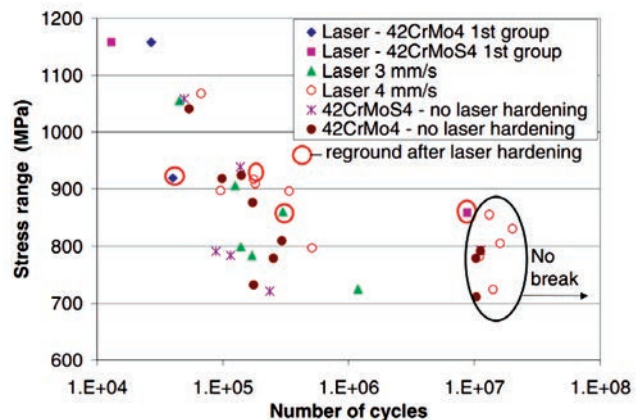


Fig. 7. Fatigue S-N curve for different groups of specimens

face or subsurface microstructural defects, their growth at the short crack stage is impeded or even arrested by the compressive residual stress.

A higher hardening velocity at higher thermal load on the specimen therefore leads to higher residual stresses. Hardening at a velocity of 3 mm/s, which was the lower velocity variant, did not improve fatigue properties and in part led to their deterioration. In this case, too, the longitudinal compressive residual stresses were considerably lower and even negligible.

### ACKNOWLEDGMENT

This paper presents results of the project EUREKA Astracomp E!11711 "Advanced surface and thermal treatments for increasing durability of railway components and tools" funded from the *Ministry of Education, Youth and Sports* of the Czech Republic.

### REFERENCES

1. Fiedler L. Monitoring of Wear and Dynamic Impact Loading of Laser Surface Hardened Steels: Bachelor thesis, University of West Bohemia, 2012.

# CHARACTERIZATION OF $\text{Al}_2\text{O}_3/\text{TiAlN}/\text{TiN}$ MULTILAYER COATINGS PREPARED BY PULSED DC PLASMA-ENHANCED CHEMICAL VAPOR DEPOSITION

Kazuki Kawata, Toru Kidachi

Oriental Engineering Co., Ltd. Research and Development Division. Saitama, Japan

k-kawata@oriental-eg.co.jp

$\text{Al}_2\text{O}_3/\text{TiAlN}/\text{TiN}$  multilayer coatings were deposited onto steel specimens by pulsed dc plasma-enhanced chemical vapor deposition using a mass-production-type facility. Using XPS, we demonstrated that the coatings exhibited a three-layered structure composed of  $\text{Al}_2\text{O}_3/\text{TiAlN}/\text{TiN}$  coatings. The cross section of the upper  $\text{Al}_2\text{O}_3$  coating revealed a dense structure that differed from the columnar structures of the cross sections of the TiN and TiAlN coatings. Analyses by XRD or XPS demonstrated that the upper-layer coating was  $\text{Al}_2\text{O}_3$ . The surface hardness of the  $\text{Al}_2\text{O}_3/\text{TiAlN}/\text{TiN}$  multilayer coatings was 22.0 GPa, which was greater than those of the TiN and CrN coatings prepared by physical vapor deposition. The  $\text{Al}_2\text{O}_3/\text{TiAlN}/\text{TiN}$  multilayer coatings exhibited greater oxidation resistance than the TiN and CrN coatings. Furthermore, compared with the other specimens investigated in this work, the  $\text{Al}_2\text{O}_3/\text{TiAlN}/\text{TiN}$  multilayer coatings exhibited superior soldering and erosion resistance in a molten aluminum die-casting alloy.

**Keywords:** pecvd; aluminum oxide; die-casting; multilayer; duplex process.

## INTRODUCTION

Properties such as good erosion resistance, good soldering resistance, and good thermal fatigue resistance are required in aluminum die-casting dies. To achieve these performance requirements, various surface treatments have been applied to such dies. The physical vapor deposition (PVD) method has been used to deposit films onto die-casting pins and small insert dies because it is a low-temperature processing method. However, it is not suitable for depositing films onto large-scale dies with complicated shapes involving slits or holes because the throwing power of the films tends to be poor. Furthermore, the PVD method tends to generate film defects such as droplets or pinholes and the thermal fatigue resistance of PVD-deposited films is low because no nitrogen diffusion layer is present. In contrast, pulsed dc plasma-enhanced chemical vapor deposition (PECVD) has been widely used to deposit films onto metal dies with complicated geometries, such as aluminum die-casting dies and aluminum extrusion dies, because of its good coating adhesion and good throwing power even at low coating temperatures [1]–[7]. Pulsed dc PECVD enables a duplex process (plasma nitriding (PN) and coating) to be performed in a single cycle within the same plant. Therefore, the process can be used to deposit coatings that satisfy requirements

related to both erosion resistance and heat-checking resistance. In the present study, a duplex process (PN and  $\text{Al}_2\text{O}_3/\text{TiAlN}/\text{TiN}$  multilayer coatings) was used to treat high-speed tool steel (JIS-SKH51) and hot-work tool steel (JIS-SKD61) in a mass-production-type pulsed dc PECVD facility. We compared several properties of specimens prepared using the duplex process with those of nitrided specimens and specimens prepared by PVD.

## EXPERIMENTAL

Plasma diffusion treatment and PECVD coating were performed using a mass-production-type pulsed dc PECVD facility. Figure 1 shows a schematic of the pulsed dc PECVD facility used in the experiments. The facility comprised a reaction chamber, an external heater, a vacuum system, a rotation system for a working table, a bipolar pulsed dc power supply, a gas supply system, and a computer-control system. The effective dimensions of the work pieces treated using this facility were a diameter of 540 mm and a height of 800 mm.

The duplex process was performed on steel substrates in two steps. PN with the formation of only a diffusion layer was followed by the deposition of  $\text{Al}_2\text{O}_3/\text{TiAlN}/\text{TiN}$  multilayer coatings. The diffusion-

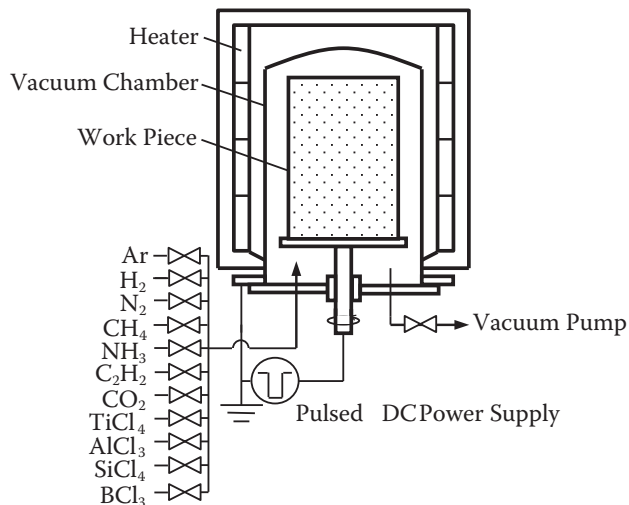


Fig. 1. Schematic of the pulsed dc PECVD facility

layer depth was approximately 75  $\mu\text{m}$ . The duplex process was performed as a continuous process, where the hard coatings were applied one after another immediately after PN in a single plant.

The  $\text{Al}_2\text{O}_3/\text{TiAlN}/\text{TiN}$  multilayer coatings were deposited onto steel substrates at 550  $^\circ\text{C}$  using mixtures of  $\text{TiCl}_4$ ,  $\text{AlCl}_3$ ,  $\text{H}_2$ ,  $\text{N}_2$ ,  $\text{Ar}$ , and  $\text{CO}_2$ . In the duplex process, PN was performed to improve the heat-checking resistance of die-casting dies. The  $\text{Al}_2\text{O}_3/\text{TiAlN}/\text{TiN}$  multilayer coatings were deposited to improve the erosion resistance of the dies. In the multilayer coatings, the lower TiN coating was formed to improve the adhesion between the substrate and the middle TiAlN coating. In the triple-layered coating, the middle TiAlN coating was used to improve the adhesion between the lower TiN coating and the upper  $\text{Al}_2\text{O}_3$  coating. Table 1 shows the PN and pulsed dc PECVD processing conditions.

Table 1. PN and pulsed dc PECVD processing conditions

	PN	TiN	TiAlN	$\text{Al}_2\text{O}_3$
Temperature ( $^\circ\text{C}$ )	550	550	550	550
Duration (h)	1	2	2	2
Pressure (Pa)	100–270	100–270	100–270	100–270
Voltage (V)	450–600	500–700	500–700	500–700
Frequency (kHz)	20–50	20–50	20–50	20–50
Duty cycle (%)	10–60	10–60	10–60	10–60
$\text{H}_2$ (vol%)	1600	2000	2000	2000
$\text{N}_2$ (vol%)	400	500	500	–
$\text{Ar}$ (vol%)	–	100	100	100
$\text{CO}_2$ (vol%)	–	–	–	100
$\text{TiCl}_4$ (vol%)	–	60	10–60	–
$\text{AlCl}_3$ (vol%)	–	–	10–60	60

The specimens were prepared from Japanese Industrial Standards (JIS) SKH51 (high-speed tool steel) and SKD61 (hot-work tool steel). The chemical composition of the SKH51 was 0.89% C, 0.34% Si, 0.31% Mn, 4.16% Cr, 4.85% Mo, 5.88% W, and 1.89% V. The SKH51 specimens were quenched at 1150  $^\circ\text{C}$  and double tempered for 120 min at 550  $^\circ\text{C}$  in a vacuum furnace before the surface treatments were applied. The Rockwell hardness (HRC) of the untreated specimen was 62. The chemical composition of the SKD61 was 0.40% C, 0.94% Si, 0.42% Mn, 5.11% Cr, 1.22% Mo, and 0.81% V. The SKD61 specimens were quenched at 1020  $^\circ\text{C}$  and double tempered for 120 min at 600  $^\circ\text{C}$  in a vacuum furnace before the surface treatments were applied. The Rockwell hardness (HRC) of the untreated specimen was 48. The SKH51 specimens for hardness measurements, structure observations, friction and wear examinations, and compositional analyses were 20 mm in diameter and 5 mm in thickness. The SKD61 specimens for oxidation resistance tests were 20 mm in diameter and 5 mm in thickness, whereas those for soldering tests and erosion tests were 10 mm in diameter and 100 mm in length. The properties of gas-nitriding specimens (compound layer thickness: 8  $\mu\text{m}$ , diffusion layer depth: 0.15 mm), TiN coatings (thickness: 2.5  $\mu\text{m}$ ), and CrN coatings (thickness: 2.2  $\mu\text{m}$ ) prepared by PVD (cathodic vacuum arc deposition) were also evaluated for comparison with those of the  $\text{Al}_2\text{O}_3/\text{TiAlN}/\text{TiN}$  multilayer coatings. The multilayer coatings were analyzed by scanning electron microscopy (SEM), transmission electron microscopy (TEM), electron diffraction (ED), X-ray photoelectron spectroscopy (XPS), and X-ray diffraction (XRD). The hardness

of these coatings was measured using a nanoindenter. The testing conditions were as follows: maximum indentation load, 5 mN; loading time, 10 s; holding time, 1 s; unloading time, 10 s; Berkovich indenter tip. The adhesion of these coatings was evaluated by the Rockwell C test. Oxidation resistance tests were conducted by exposing specimens to air for 60 min at high temperatures. The friction and wear properties were evaluated with a ball-on-disk-type tribometer (CSEM). The testing conditions were as follows: ball, Al (JIS-A1050, diameter, 5.5 mm); load, 1 N; sliding speed, 50 mm/s; sliding distance, 100 m; and no lubricant was used. The erosion resistance of each specimen was investigated by immersing the specimens into a molten aluminum die-casting alloy (JIS-ADC12) at 700  $^\circ\text{C}$ . In the erosion resistance tests, the specimens were immersed in a molten aluminum

alloy for 120 min and then cleaned in a NaOH solution until most of the soldered aluminum alloy was leached from their surfaces. The erosion loss for the specimens was measured with an electric balance. The procedure of immersing the specimens into the molten aluminum alloy was repeated twice; i.e., the immersion was performed intermittently and the specimens were immersed for a total of 360 min. Soldering resistance tests were performed after the specimens had been immersed in the molten aluminum alloy bath at 700 °C for 120 min and subsequently extracted from the bath.

## RESULTS AND DISCUSSION

### Morphology of Cross Sections

Fig. 2 shows a cross-sectional SEM image of the  $\text{Al}_2\text{O}_3/\text{TiAlN}/\text{TiN}$  multilayer coating deposited by pulsed dc PECVD. The cross sections of the TiN and TiAlN coatings prepared by pulsed dc PECVD exhib-

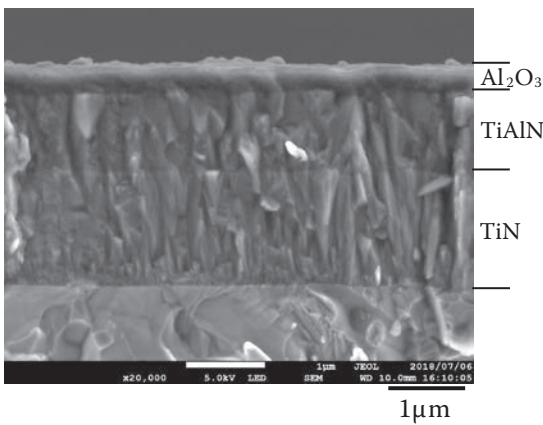


Fig. 2. Cross-sectional SEM image of the  $\text{Al}_2\text{O}_3/\text{TiAlN}/\text{TiN}$  multilayer coating deposited by pulsed dc PECVD

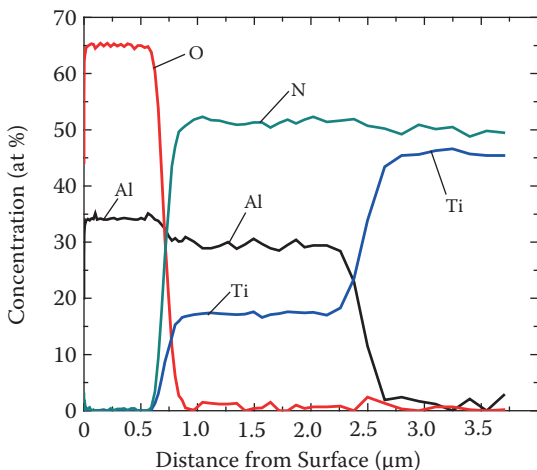


Fig. 3. XPS concentration depth profiles for each element in the  $\text{Al}_2\text{O}_3/\text{TiAlN}/\text{TiN}$  multilayer coating

ited columnar structures. The cross section of the upper  $\text{Al}_2\text{O}_3$  coating in the  $\text{Al}_2\text{O}_3/\text{TiAlN}/\text{TiN}$  multilayer coating exhibited a dense structure. TEM analysis revealed that the upper  $\text{Al}_2\text{O}_3$  coating in the  $\text{Al}_2\text{O}_3/\text{TiAlN}/\text{TiN}$  multilayer coating was composed of fine crystals with a size of 100 nm or less.

### Compositional and Structural Analyses

Fig. 3 shows the XPS concentration depth profiles for each element in the  $\text{Al}_2\text{O}_3/\text{TiAlN}/\text{TiN}$  multilayer coating. On the basis of the concentration distributions of Ti, Al, N, and O, we confirmed that the coating was composed of three layers. Examination of the chemical bonding state of each element in the upper coating by XPS revealed that  $\text{Al}_2\text{O}_3$  was present. Fig. 4 shows the  $\text{Al}2p$  XPS spectra of the upper  $\text{Al}_2\text{O}_3$  coating produced by pulsed dc PECVD. Fig. 5 shows the XRD pattern of the  $\text{Al}_2\text{O}_3/\text{TiAlN}/\text{TiN}$  multilayer coatings. The diffraction peak of the coating

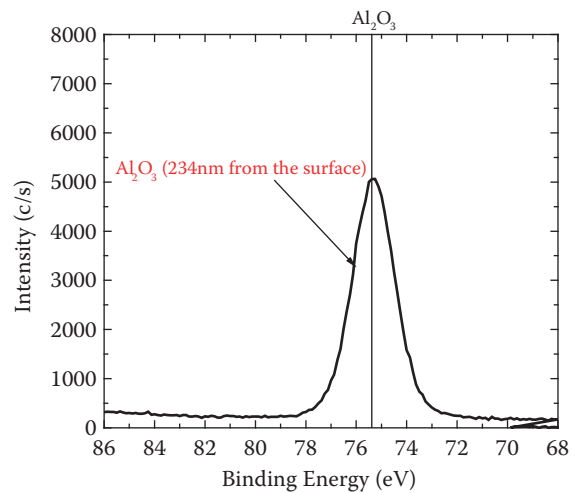


Fig. 4.  $\text{Al}2p$  XPS spectra of the upper  $\text{Al}_2\text{O}_3$  coating produced by pulsed dc PECVD

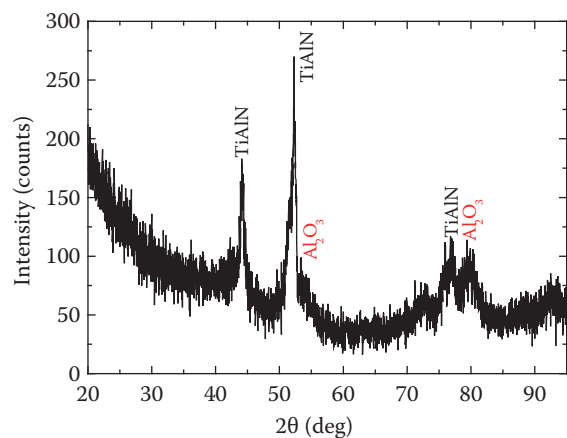


Fig. 5. XRD pattern of the  $\text{Al}_2\text{O}_3/\text{TiAlN}/\text{TiN}$  multilayer coatings (Co-K $\alpha$ , 40 kV, 36 mA, incident angle, 0.3 degree)

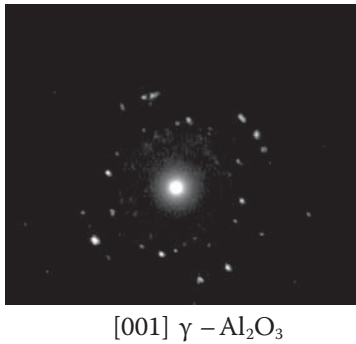


Fig. 6. ED image of the upper  $\text{Al}_2\text{O}_3$  coating

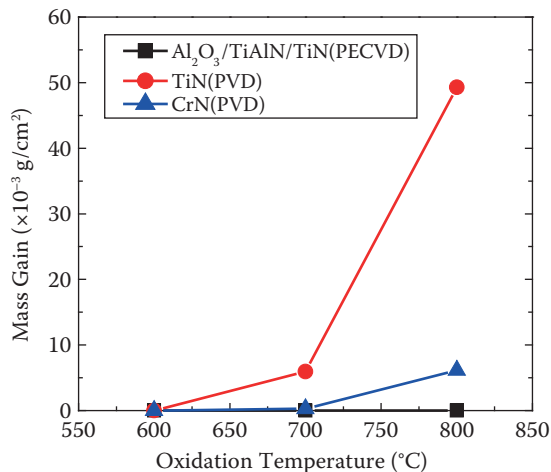


Fig. 7. Relationship between the oxidation temperatures and the mass gain for the  $\text{Al}_2\text{O}_3/\text{TiAlN}/\text{TiN}$  multilayer coating (PECVD), the TiN coatings (PVD), and the CrN coatings (PVD)

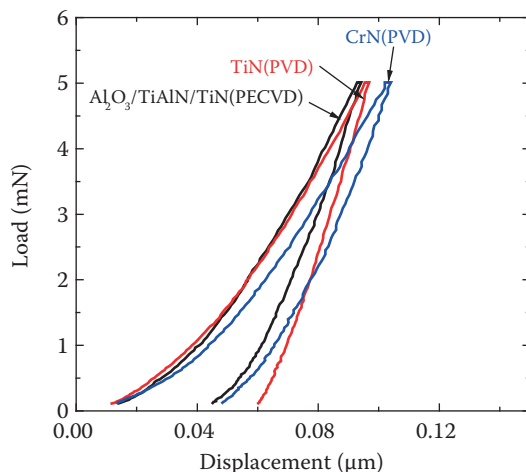


Fig. 8. Load versus displacement curves for the  $\text{Al}_2\text{O}_3/\text{TiAlN}/\text{TiN}$  multilayer coatings (PECVD), the TiN coatings (PVD), and the CrN coatings (PVD) obtained using the nanoindentation method

revealed that aluminum oxide ( $\gamma\text{-Al}_2\text{O}_3$ ) was formed. Fig. 6 shows an ED image of the upper  $\text{Al}_2\text{O}_3$  coating. This image indicates that  $\gamma\text{-Al}_2\text{O}_3$  was formed in the upper coating.

## Oxidation Properties

Fig. 7 shows the relationship between the oxidation temperatures and the mass gain for the  $\text{Al}_2\text{O}_3/\text{TiAlN}/\text{TiN}$  multilayer coatings, the TiN coatings (PVD), and the CrN coatings (PVD). The oxidation start temperature was  $600^\circ\text{C}$  for the TiN coatings and  $700^\circ\text{C}$  for the CrN coatings. Furthermore, the mass gain increased substantially with increasing oxidation temperature. In comparison, the mass gain for the  $\text{Al}_2\text{O}_3/\text{TiAlN}/\text{TiN}$  multilayer coatings was zero at  $800^\circ\text{C}$ . Therefore, the  $\text{Al}_2\text{O}_3/\text{TiAlN}/\text{TiN}$  multilayer coatings exhibited the best oxidation resistance among the investigated specimens.

## Surface Hardness and Adhesion

Fig. 8 shows the load versus displacement curves for the  $\text{Al}_2\text{O}_3/\text{TiAlN}/\text{TiN}$  multilayer coatings obtained using the nanoindentation method. The nanoindentation hardness was 22.0 GPa for the upper  $\text{Al}_2\text{O}_3$  coating in the  $\text{Al}_2\text{O}_3/\text{TiAlN}/\text{TiN}$  multilayer coatings, 20.1 GPa for the TiN coatings (PVD), and 19.2 GPa for the CrN coatings (PVD). Therefore, the surface hardness of the upper  $\text{Al}_2\text{O}_3$  coating in the  $\text{Al}_2\text{O}_3/\text{TiAlN}/\text{TiN}$  multilayer coatings was greater than those of the TiN and CrN coatings. In the Rockwell C adhesion test, delamination of the  $\text{Al}_2\text{O}_3/\text{TiAlN}/\text{TiN}$  multilayer coating in the indentation area was not observed. We considered that the coatings exhibited excellent adhesion, HF1, according to the VDI classification method [8].

## Tribological Properties

Fig. 9 shows the relationship between the friction coefficient and the sliding distance for the  $\text{Al}_2\text{O}_3/\text{TiAlN}/\text{TiN}$  multilayer coatings, the TiN coatings (PVD), and the CrN coatings (PVD). The friction coefficients for a sliding distance of 100 m were approximately 0.47 for the  $\text{Al}_2\text{O}_3/\text{TiAlN}/\text{TiN}$  multilayer coatings, approximately 0.75 for the TiN coatings, and approximately 0.73 for the CrN coatings. Therefore, the  $\text{Al}_2\text{O}_3/\text{TiAlN}/\text{TiN}$  multilayer coatings exhibited the lowest friction coefficient among the investigated specimens. The  $\text{Al}_2\text{O}_3/\text{TiAlN}/\text{TiN}$  multilayer coated disks did not exhibit oxidized adhesive wear due to the friction and wear tests. Moreover, the counterpart ball wear scar for the  $\text{Al}_2\text{O}_3/\text{TiAlN}/\text{TiN}$  multilayer coatings was relatively small compared with those for the other specimens. These results demonstrate that the  $\text{Al}_2\text{O}_3/\text{TiAlN}/\text{TiN}$  mul-

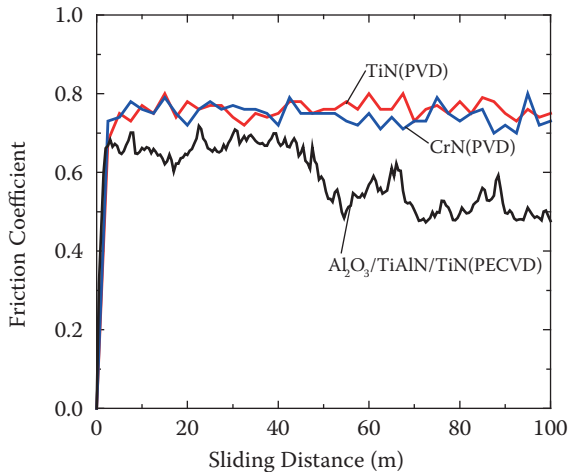


Fig. 9. Relationship between the friction coefficient and the sliding distance for the Al<sub>2</sub>O<sub>3</sub>/TiAlN/TiN multilayer coatings (PECVD), the TiN coatings (PVD), and the CrN coatings (PVD)

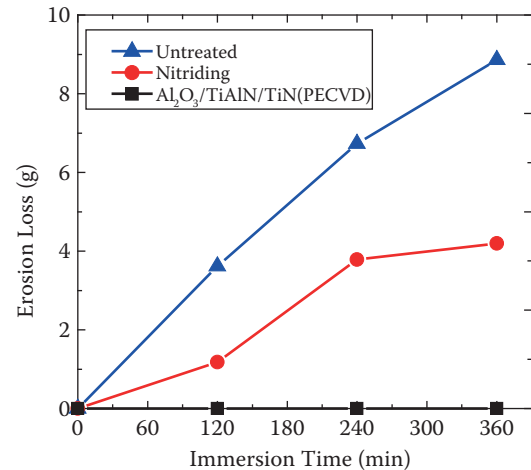


Fig. 10. Relationship between the immersion time and the erosion loss for the an untreated specimen, a nitrided specimen, and specimen with the Al<sub>2</sub>O<sub>3</sub>/TiAlN/TiN multilayer coating

tilayer coatings exhibited excellent tribological characteristics.

### Erosion and Soldering Properties

Fig. 10 shows the relationship between the immersion time and the erosion loss for an untreated specimen, a nitrided specimen, and specimen with the Al<sub>2</sub>O<sub>3</sub>/TiAlN/TiN multilayer coating. The erosion of the untreated specimen and the nitrided specimen increased with increasing immersion time. However, the Al<sub>2</sub>O<sub>3</sub>/TiAlN/TiN coatings exhibited no erosion even after 360 min of immersion. The Al<sub>2</sub>O<sub>3</sub>/TiAlN/TiN multilayer coatings exhibited the best erosion resistance among the investigated specimens. Fig. 11 shows the appearance of the various specimens after they were immersed in molten aluminum alloy for 120 min. The soldering resistance tests using molten aluminum alloy demonstrated that the Al<sub>2</sub>O<sub>3</sub>/TiAlN/TiN multilayer coatings exhibit the best soldering resistance among the investigated specimens.

### APPLICATION

The duplex process (PN and Al<sub>2</sub>O<sub>3</sub>/TiAlN/TiN multilayer coatings prepared by pulsed dc PECVD) has already been applied to aluminum die-casting dies and aluminum extrusion dies. In actual aluminum die-casting dies, the soldering resistance, erosion resistance, and thermal fatigue resistance of coatings prepared using the duplex process have



Fig. 11. Appearance of the various specimens after the soldering resistance tests

been demonstrated to be better than those of coatings prepared using PVD (TiN, CrN, and TiAlN). In addition, for application to aluminum extrusion dies, the process has been effective in improving die life and the finished skin of aluminum products.

### CONCLUSIONS

The following conclusions were drawn from these experiments:

1. The cross section of the upper Al<sub>2</sub>O<sub>3</sub> coating in the Al<sub>2</sub>O<sub>3</sub>/TiAlN/TiN multilayer coating prepared by pulsed dc PECVD exhibited a dense structure.

2. Examination of the chemical bonding state of each element in the upper coating by XPS revealed that  $\text{Al}_2\text{O}_3$  was present.

3. Analyses by XRD and ED demonstrated that aluminum oxide ( $\gamma\text{-Al}_2\text{O}_3$ ) was formed in the upper coating.

4. The oxidation resistance of the  $\text{Al}_2\text{O}_3/\text{TiAlN}/\text{TiN}$  multilayer coatings was better than those of the TiN and CrN coatings by PVD.

5. The  $\text{Al}_2\text{O}_3/\text{TiAlN}/\text{TiN}$  multilayer coatings exhibited good film adhesion.

6. The surface hardness of the upper  $\text{Al}_2\text{O}_3$  coating in the  $\text{Al}_2\text{O}_3/\text{TiAlN}/\text{TiN}$  multilayer coatings was 22.0 GPa, which was greater than those of the TiN and CrN coatings deposited by PVD.

7. The  $\text{Al}_2\text{O}_3/\text{TiAlN}/\text{TiN}$  multilayer coatings exhibited excellent tribological properties.

8. The  $\text{Al}_2\text{O}_3/\text{TiAlN}/\text{TiN}$  multilayer coatings exhibited the best erosion resistance and soldering resistance among the investigated specimens.

9. The duplex process (PN and  $\text{Al}_2\text{O}_3/\text{TiAlN}/\text{TiN}$  multilayer coatings prepared by pulsed dc PECVD) has already been applied to aluminum die-casting dies and aluminum extrusion dies.

coatings deposited by pulsed d.c. plasma-assisted chemical vapour deposition (PACVD) // *Surf. Coatings Technol.* 1998. 108–109: 206–210.

2. **Täschner Ch., Ljungberg B., Endler I., Leonhardt A.** Deposition of hard crystalline  $\text{Al}_2\text{O}_3$  coatings by pulsed d.c. PACVD // *Surf Coatings Technol.* 1999. 116–119: 891–897.

3. **Heim D., Holler F., Mitterer C.** Hard coatings produced by PACVD applied to aluminium die castin // *Surf. Coat. Technol.* 1999. 116–119: 530–536.

4. **Kawata K., Hiroyuki Sugimura, Osamu Takai.** Characterization of (Ti, Al)N films deposited by pulsed d.c. plasma-enhanced chemical vapor deposition // *Thin Solid Films.* 2001. 386: 271–275.

5. **Kawata K., Sugimura H., Takai O.** Characterization of multilayer films of Ti-Al-O-C-N system prepared by pulsed d.c. plasma-enhanced chemical vapor deposition // *Thin Solid Films.* 2001. 390: 64–69.

6. **Kawata K., Sekiya Y., Kidachi T.** Characterization of multilayer coatings of Ti-Al-Si-C-N-O system prepared by pulsed DC plasma-enhanced chemical vapor deposition: Proc. 15th IFHTSE Congress. Vienna, September. 2006. 516–521.

7. **Klimek K.S., Gebauer-Teichmann A., Kaestner P., Rie K.-T.** Duplex-PACVD coating of surfaces for die casting tools // *Surf. Coat. Technol.* 2007. 201: 5628–5632.

8. **Heinke W., Leyland A., Matthews A., Berg G., Friedrich C., Broszeit E.** Evaluation of PVD nitride coatings, using impact, scratch and Rockwell-C adhesion tests // *Thin Solid Films.* 1995. 270: 431–438.

## REFERENCES

1. **Jarms C., Stock H.-R., Mayr P.** Mechanical properties, structure and oxidation behaviour of  $\text{Ti}_{1-x}\text{Al}_x\text{N}$ -hard

# THE FORMATION COMPOSITE COATINGS OF STRUCTURAL STEEL BY THE COPPER-CONTAINING NANOPARTICLES

V.A. Alexandrov, I.Yu. Isayeva, I.V. Odinokova, G.Yu. Ostaeva

Moscow automobile and road construction state technical University (MADI). Moscow, Russia

irina-razumova-xim@yandex.ru

A new method for producing composite coatings for surface hardening of structural steels has been developed. It consists in applying an ultra-fine suspension containing alloying elements and substances necessary for the reactions involved in the formation of solid solution nuclei of alloying elements in the matrix using copper-containing nanoparticles, followed by thermal diffusion saturation (metallization) and nitriding in the plasma of an electric discharge.

**Keywords:** hardness; strength; durability; endurance; nitriding; electric discharge; the copper-containing nanoparticles; nanocomposites; catalysis.

## INTRODUCTION

Currently, the need for new processes for surface hardening, which will reduce the use of expensive alloy steels increases replacing them with more common and cheaper.

In this matter, the urgent task is to develop simple, affordable, economical, environmentally friendly and highly efficient technologies for surface hardening of steels in order to obtain the specified performance properties in specific operating conditions. These technologies will improve the hardness, strength, wear resistance, corrosion resistance, endurance, brittle fracture resistance and other mechanical and operational characteristics of materials and finished products. This article focuses on the combined technological process of surface hardening of structural steels, including thermodiffusion alloying of the surface of the nanodispersed coating in the process of plasma nitriding, using catalysts, including copper-containing nanoparticles, nickel and chromium oxides, as well as the study of the properties and composition of the metallized and nitrided coating.

## EXPERIMENTAL PART

Objects of research – are samples and steel products 25Cr2Ni2MoFe in the state of delivery.

Nitrided products (Fig. 1) and samples with dimensions of  $\varnothing 15 \times 4$  mm in structural States after improvement. The treatment was performed on an

experimental nitriding plant in glow discharge plasma (Fig. 2). The installation includes: 1) a device for supplying electric potential to the processed parts; 2) a system for preparing a saturating environment; 3) a reactor in which the nitriding process takes place; 4) a vacuum pump to create the necessary pressure in the reactor.

The duration of saturation was 1 and 6 hours at a temperature of 575 °C in the atmosphere of a mixture of ammonia, carbon dioxide and water vapor.

Metallographic studies were carried out using a light microscope «AXIOVERT 25CA» with an increase of 500 times. Marble reagent (4 g  $\text{CuSO}_4$  + 20 ml HCl + 20 ml  $\text{H}_2\text{O}$ ) was used to identify the structure.

The surface hardening of steel products includes the following stages:

1. Obtaining of suspension, containing copper nanoparticles, which are a catalyst for the diffusion

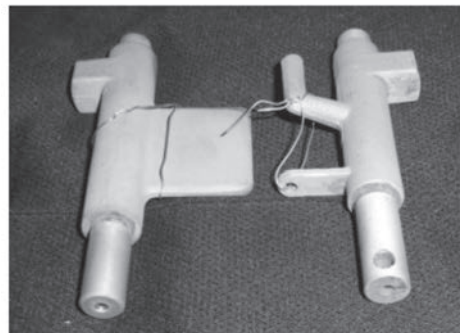


Fig. 1. Products after processing according to the proposed technology



Fig. 2. Scheme of the device for the nitriding process

saturation process, and alloying elements (nickel and chromium oxides).

2. Application of composite film on the surface of the processed products.

3. Carrying out of diffusion saturation in an electric discharge plasma.

At the first stage, an ultradispersed suspension was obtained, which contained the copper nanoparticles and particles of alloying elements (nickel and chromium oxides). Copper-containing nanoparticles were synthesized in an aqueous polymer solution of PVP by reduction of copper ions using TBAB at room temperature [5, 6]. The reaction product is Sol, the dispersed phase of which is actually a nanocomposite comprising nanoparticles and macromolecules.

Sol was combined with components obtained in an electrodeless high-frequency (arc) discharge by evaporation of NiCr10 in an air atmosphere.

At the second stage, the product of 25Cr2Ni-2MoFe steel was maintained in the resulting suspension for 2...3 minutes. It should be noted that the product does not need additional washing. Further, the steel product was dried at room temperature with air flow.

540...650 °C. In this case, the surface layer is saturated with nitrogen to form dispersed nitrides (Cr; Fe; Ni) the alloying elements.

After processing, the structure of the surface layer of the samples was studied, were determined the thickness of the layer, the phase composition, its microhardness and wear resistance.

## RESULTS AND DISCUSSION

It is known that the properties of nanostructured systems, including their activity and selectivity as catalysts of various chemical reactions, depend on the size of nanoparticles.

The formation of transparent stable sols  $\text{Cu}^{1+}$  and  $\text{C}^0$  in the presence of PVP in the first stage and their resistance to aggregation after the addition of  $\text{Ni}^{2+}$ ,  $\text{Cr}^{n+}$  indicates the formation of nanodispersed particles. Fig. 3 depicts the image of the surface structure of the samples after applying the composite film on the processed products

After treatment with only copper sol (Fig. 3a) a copper-containing layer is formed consisting of dis-

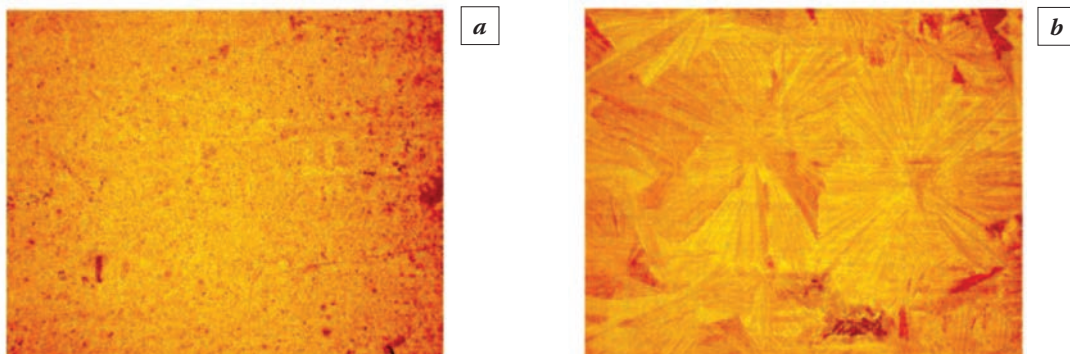


Fig. 3. Surface structure of the sample: *a* – coated with copper-containing nanoparticles; *b* – coated with Cu –  $\text{Cr}^{n+}/\text{Ni}^{2+}$

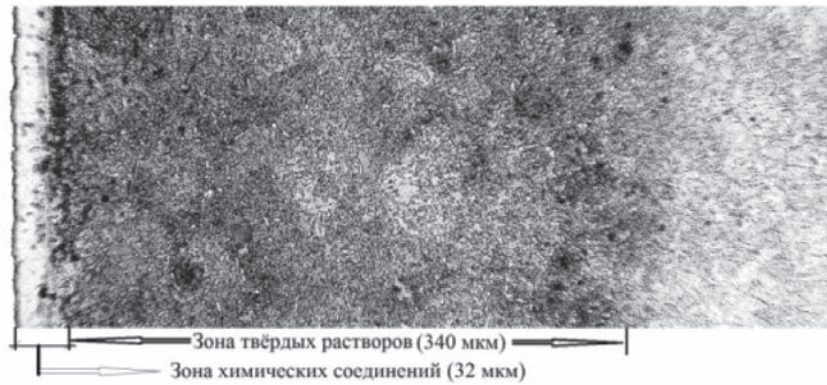


Fig.4. Structure of modified coating

crete particles, spaced at distance from each other. While, after application to the surface of the product suspension containing copper nanoparticles and particles of alloying elements (Fig. 3b) is observed a different structure resulting from the self-organization of these particles.

The activity of the catalyst determines the thickness of the modified layer, formed over the definite time, and also contributes to the intensification of the migration process of alloying elements deep into the product. The copper-containing nanoparticles deposited on the surface as part of the composite coating exhibit the high catalytic activity. This property of copper-containing nanoparticles allows to obtain an additional effect in the reaction of ammonia dissociation with the generation of nitrogen ions and to intensify the process of penetration of nitrogen and alloying elements into steel. The microstructure of the obtained layers is reflected in Fig. 4.

As a result of the studies, was found an increase in the concentration of alloying elements in the surface layer, which led to an increase in the microhardness and thickness of the hardened layer. It follows from this that the proposed method for producing composite coatings, perform in the function both as the catalyst and the carrier of the alloying elements, has a great potential for applying the strengthening structural steels.

Нет источников

## CONCLUSIONS

1. The particularities of the composite coating provide a nanoscale range of copper particles and alloying elements obtained in an electrodeless high-frequency discharge. The subsequent diffusion annealing leads to an increase of the thickness of the hardened layer, and also allows to obtain a transition layer consisting of a zone of solid solutions of nitrides of alloying elements.

2. The studies of the samples showed characteristics corresponding to the characteristics of high-alloyed steels, which proves the effectiveness and prospects of the developed method.

*This work was supported by the Ministry of Education and Science of the Russian Federation (project No. 16.11777.2018/11.12.) within the framework of a design part of the state assignment in the field of scientific research.*

## REFERENCE

1. **Alexandrov V.A.** Obtaining of a multilayer modified coatings on the surface of steel products to enhance operational characteristics // *Hardening technologies and coatings*. 2014. No. 12(120). P. 13–19.
2. **Chudina O.V., Alexandrov V.A., Brezhnev A.A.** Perspective technologies of creating of diffusion coatings on steels with high mechanical characteristics. 2009. No. 46. P. 72–75.
3. **Kusmanov S. A., Dyakov I. G., Naumov A.R.** Electrochemical features of anodic electron-plasma treatment of steels. 2013. No. 5(19). P. 11–15.
4. **Topolyansky P.A., Ermakov S.A., Sosnin N.A., Topolyansky A.P.** Electrochemical features of anode electrolytic and plasma treatment of steels. 2013. No. 4(76). P. 28–38.
5. **Papisov I.M., Isaeva I.Yu., Ostaeva G.Yu., Eliseeva E.A., Papisova A.I., Kozlovskii V.F.** Formation of copper(I) oxide nanoparticles at an early stage of copper sol synthesis in the presence of poly(vinylpyrrolidone) // *Colloid Journal*. 2015. 77(6) : 780–786.
6. **Ostaeva G.Yu., Isaeva I.Yu., Morenko I.V., Eliseeva E.A., Litmanovich A.A.** Synthesis and redox interconversions of copper-containing nanoparticles stabilized by poly(N-vinylpyrrolidone) // *Polymer Science. Ser. B*. 2019. 61(3) : 254–260.

# MICROSTRUCTURE AND CORROSION BEHAVIOR OF DLC FILMS DEPOSITED ON SUS316L AND TITANIUM SUBSTRATE FOR BIPOLAR PLATES

Beibei Han<sup>1</sup>, Dongying Ju<sup>2</sup>, Susumu Sato<sup>3</sup>, Maorong Chai<sup>4</sup>

<sup>1</sup>Department of Electronic Engineering, Graduate School of Engineering, Saitama Institute of Technology.  
Saitama, Japan; hanbei9091@gmail.com

<sup>2</sup>Advanced Science Institute, Saitama Institute of Technology. Saitama, Japan;  
Ningbo Haizhi Institute of Materials Industry innovation. Ningbo, China;  
Hangzhou Dianzi University. Hangzhou, China; dyju@sit.ac.jp

<sup>3</sup> Department of Electronic Engineering, Graduate School of Engineering, Saitama Institute of Technology.  
Saitama, Japan; ssato@sit.ac.jp

<sup>4</sup> Advanced Science Institute, Saitama Institute of Technology. Saitama, Japan;  
State Power Investment Corporation. Beijing, China; mrchai@sit.ac.jp

Metal bipolar plates for the PEMFC offer many advantages over conventional graphitic materials. The amorphous hydrogenated (a-C:H)/diamond-like carbon (DLC) films have been deposited on SUS316L and titanium substrate at different gas flow ratio  $\text{CH}_4/\text{H}_2$  and deposition time using ion beam enhanced deposition (IBED) for bipolar plates to improve conductivity and corrosion behavior in this paper. Surface morphology and microstructure of DLC film-coated SUS316L and titanium were analyzed by SEM, AFM and Raman spectrum. The resistivity and corrosion behavior were investigated and compared between DLC film-coated SUS316L and titanium substrate by four-probe method and ICP. Results show that the minimum Ra of DLC film-coated SUS316L is 3.77, which is smaller than that of titanium, about 5.76. The Raman spectrum of all the samples exhibits the evolution of a DLC film with clearly observed D and G peak located at about 1380 and 1560  $\text{cm}^{-1}$  respectively. It also confirms the  $\text{sp}^3\text{-C}$  content increasing as the deposition time increases for all the samples which results in the lower metal ion dissolution concentration. The minimum resistivity of  $10.76\text{E-}04\Omega\text{-cm}$  for DLC film-coated SUS316L is obtained, which is higher than that of  $6.29\text{E-}04\Omega\text{-cm}$  for DLC film-coated titanium. The metal ion dissolution concentration of DLC film-coated SUS316L deposited at a low C:H ration exhibits a minimum of about 16.60ppm, while DLC film-coated titanium has a lower metal ion dissolution concentration of about 0.34ppm deposited at a high C:H ration. Therefore, the better conductivity and anti-corrosion properties of DLC film-coated titanium make it a good candidate for PEMFC bipolar plates.

**Keywords:** DLC film; microstructure; corrosion behavior; SUS316L; titanium.

## INTRODUCTION

Recently, in the automobile industry, researches on automobiles equipped with a hydrogen fuel cell are underway for the purpose of reducing the emission of greenhouse gases and preventing global warming. As a consequence, much attention has recently been devoted to the development of more efficient and cleaner technologies. Hydrogen fuel cells have attracted attention in the automotive industry because they do not affect the global environment adversely. Fuel cells are environmentally friendly energy generation devices, which convert chemical energy directly into electrical energy with high efficiency and virtual zero-emissions [1]. Among the various fuel cells under development, polymer electrolyte

membrane fuel cells are regarded as one of the most promising power sources for residential and transportation applications due to their high power density, low operating temperature, and rapid start-up [2]. A typical polymer electrolyte membrane fuel cell comprises membrane electrode assemblies (MEAs), gas diffusion layers (GDLs) and bipolar plates. However, there are some problems. For example, among the components of hydrogen fuel cells, bipolar plates are the most bulky and most expensive to manufacture [3]. These plates play multiple roles in the long-term operation of the fuel cell, including feeding the fuel and air to a gas diffusion layer-electrodes assembly, managing heat and water flow, and providing the electrical contact between adjacent cells. Currently, the high cost and the large mass of these components

are considered to be a major barrier to the commercial application of polymer electrolyte membrane fuel cells [4]. Hence, the reduction of the cost, mass, and volume of these bipolar plates is critical to the development of fuel cells. For practical application, bipolar plate materials should possess high corrosion resistance, high electrical conductivity, and low permeability and be economic to manufacture [5, 6]. Traditionally, bipolar plates are made from non-porous graphite, because of its good electronic conductivity and high chemical stability in polymer electrolyte membrane fuel cell environments. However, its low toughness, gas permeability and the difficulties in machining gas flow channels increase fabrication costs and the overall size of a polymer electrolyte membrane fuel cell stack [7, 8]. Instead of this, considerable effort has been made into the development of metal bipolar plates, from materials such as stainless steel and titanium and aluminum alloys [9]. The performance of fuel cells is reduced due to the corrosion behavior because the proton conductivity of the polymeric electrolyte membrane is decreased due to the poison of Fe, Cr, Ni and Ti ions [10]. To overcome these drawbacks, depositing a protective coating on the metallic bipolar plate is necessary by various surface modification techniques. Compared with the CVD techniques, the Ion beam enhanced deposition (IBED) method provided coatings with lower compressive stress.

In this paper, 316L stainless steel and titanium substrates were coated with amorphous hydrogenated carbon (a-C:H) films by Ion beam enhanced deposition (IBED) technique. The characterizations and corrosion behaviors of the DLC coated stainless steel and titanium deposited with different gas ratios  $\text{CH}_4/\text{H}_2$  and deposition times were investigated and evaluated. The chemical bonding structure and composition of the DLC coatings were analyzed. The purpose of this study is to evaluate and compare the anti-corrosion properties of the stainless steel substrate.

## EXPERIMENTAL

### DLC films preparation

The DLC films, formed by hydrogenated amorphous carbon (a-C:H), were deposited onto the stainless steel 316L and titanium substrate using gas  $\text{CH}_4$  and  $\text{H}_2$  by IBED technology. The deposition mechanism is complex. In ion beam deposition process, the hydrocarbon gas is ionized and extracted through a grid by an accelerating voltage. Then the ionized hydrocarbon ions are accelerated to form ion beam. Several reactions, electron-neutral, ion-neutral and

neutral-neutral reactions, are taken place in the plasma. These different species of positive ions, radicals and other hydrocarbon are generated in the reactions. There are several surface processes such as adsorption, desorption, direct incorporation of ions, reemission of H, ion-induced incorporation of neutral radicals, adsorbed layer reactions, surface etching reactions and sputtering in the species deposition of DLC film [11]. The neutral species promote DLC film growth due to the ions mass deposition rate [12]. The most species in plasma and these species that contribute more to DLC growth are  $\text{CH}_5^+$  and  $\text{CH}_3^+$  ions. The schematic diagram of IBED process is shown in Fig. 1. In the IBED process, high-energy ions mix the initial few atomic layers of the coating material into the surface being coated. This forms an alloyed bond layer that promotes coating adhesion and allows coatings to be applied to virtually any substrate material without an intermediate bonding layer. The coating is grown from the alloyed layer and the high-energy ion flux controls the coating's grain structure, density and residual stresses.

The substrates with size of 100 mm (L) × 100 mm (W) × 0.1mm (H) were ultrasonically cleaned in acetone for 15 min to remove the grease contamination from the surface. Prior to the deposition, the chamber was evacuated to a base pressure of  $4 \times 10^{-4}$  Pa for producing plasma discharge. Then the gas  $\text{CH}_4$  and  $\text{H}_2$  mixture were injected into the chamber. The chamber pressure was changed as the gas sent, so the chamber pressure was fixed at  $2 \times 10^{-3}$  Pa through the pressure valve. The gas flow, accelerating current and voltage were fixed at 0.4~0.5 sccm, 2.5 mA and 10kV for all the samples. Finally the DLC coating with high adhesion was created. After processing, the substrate was cooled down to room temperature inside the chamber. Four kinds of films were formed in our study (Table 1).

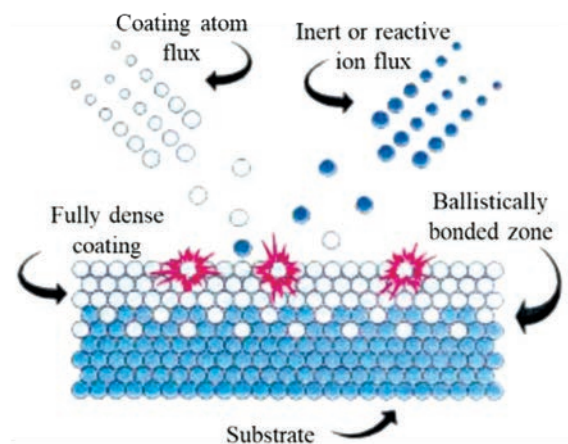


Fig. 1. Schematic diagram of IBED process

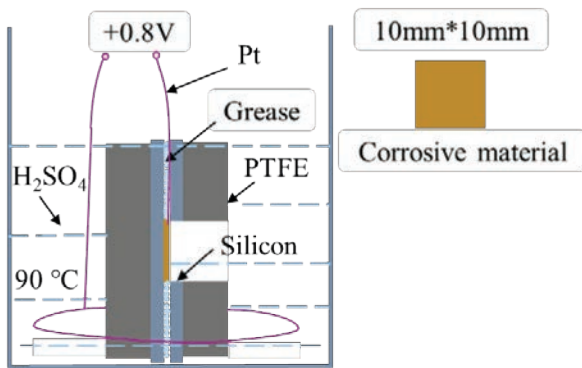


Fig. 2. Schematic diagram of the setup used to simulate the PEMFC condition

Table 1. Parameters for different processing conditions

Substrate	SUS316L			
	Ti			
Gas ratio $\text{CH}_4/\text{H}_2$	1:1		1:0	
Time	6 hrs	12 hrs	6 hrs	12 hrs

### Structural characterization

The surface and cross-sectional morphology of the DLC films were analyzed before and after potentiostatic test using a scanning electron microscopy (HITACHI, TM3000). The surface roughness was evaluated by atomic force microscopy (SPM9500-J3), with a scanning frequency of 2.0 Hz. The bonding state of a-C:H DLC coating was evaluated by a NRS-4100 Raman spectroscopy with a laser wavelength of 532.0 nm, spot size of  $\Phi 34 \mu\text{m}$ , and laser power of 0.03 mW. The electrical resistivity was measured by four-probe method.

### Potentiostatic corrosion test and inductively coupled plasma (ICP) measurements

Anti-corrosion property is an important factor for evaluating the performance of bipolar plates. Fig. 2 displays the schematic diagram of the setup used to simulate the PEMFC environment. The three-electrode system has been referenced in the previous literature. It comprised a DLC-coated substrate as working electrode, a platinum wire as counter electrode, and a saturated calomel electrode (SCE) as the reference electrode. A 0.5 mol/L sulfuric acid corrosion solution was set as the based electrolyte and heated to 90 °C. The potentiostatic test was conducted for 168 h at a potential of 0.8 V to simulate the PEMFC operating conditions. One end of all samples were embedded in epoxy resin with an exposed area

of  $10 \times 10 \text{ mm}^2$ . Meanwhile the surface was connected to the platinum wire by soldering. After test the metal ions in sulfuric acid corrosion solution were detected to evaluate the anti-corrosion property of uncoated and DLC film-coated titanium substrates by inductively coupled plasma (ICPS-7000) atomic emission spectroscopy.

## RESULTS AND DISCUSSION

### Surface topography of the DLC films

The surface topography of uncoated substrates and DLC films are observed by AFM and the results are shown in Fig. 3. The DLC films are observed to be dense and composed of spherical particles with diameters of  $0.2 \sim 1.6 \mu\text{m}$  on the entire titanium surface. The surface of SUS316L becomes smoother than titanium. And the minimum Ra of DLC film-coated SUS316L is 3.77, which is smaller than that of titanium, about 5.76. For SUS316L, the surface morphologies of DLC films deposited at gas ratio  $\text{CH}_4/\text{H}_2=1:1$  show a smoother surface and a smaller granules than that of DLC films at  $\text{CH}_4/\text{H}_2=1:0$ . Titanium has the opposite result. From Fig. 3 the long deposition time is beneficial for the smooth surface morphology with almost no pinholes.

The cross-section morphology images of the DLC film deposited on SUS316L and titanium are presented in Fig. 4. The DLC layer deposited on SUS316L has a maximum thickness of about 569.8 nm from the Fig. 4b. The maximum thickness of DLC film coated titanium is about 587.1 nm from the Fig. 4h. The long processing time are more beneficial for the deposition of DLC films. The C:H ration has a different effect on the deposition of DLC film depending on the metal structure.

The Raman spectroscopy is a non-destructive and routine method for characterizing the bonding structure of carbon films. The wide peak of DLC film is created by overlapping two peaks, G (graphite) peak and D (disorder) peak. The position of G peak and ratio of D peak intensity to G peak intensity (ID/IG) are the important factors which fully depended on the DLC film structure. The Fig. 5 displays the ID/IG and G-peak position of DLC films coated (a) SUS316L and (b) titanium. The change of G peak position toward higher wavenumber indicated that the film's structure was varied from  $\text{sp}^3\text{-C}$  to  $\text{sp}^2\text{-C}$ . A decrease in the ID/IG ratio correspond to a decrease in  $\text{sp}^2/\text{sp}^3$  ratio. The G peak position was shifted from 1558 to  $1570 \text{ cm}^{-1}$  by decreasing the ratio of  $\text{CH}_4$  and the deposited time

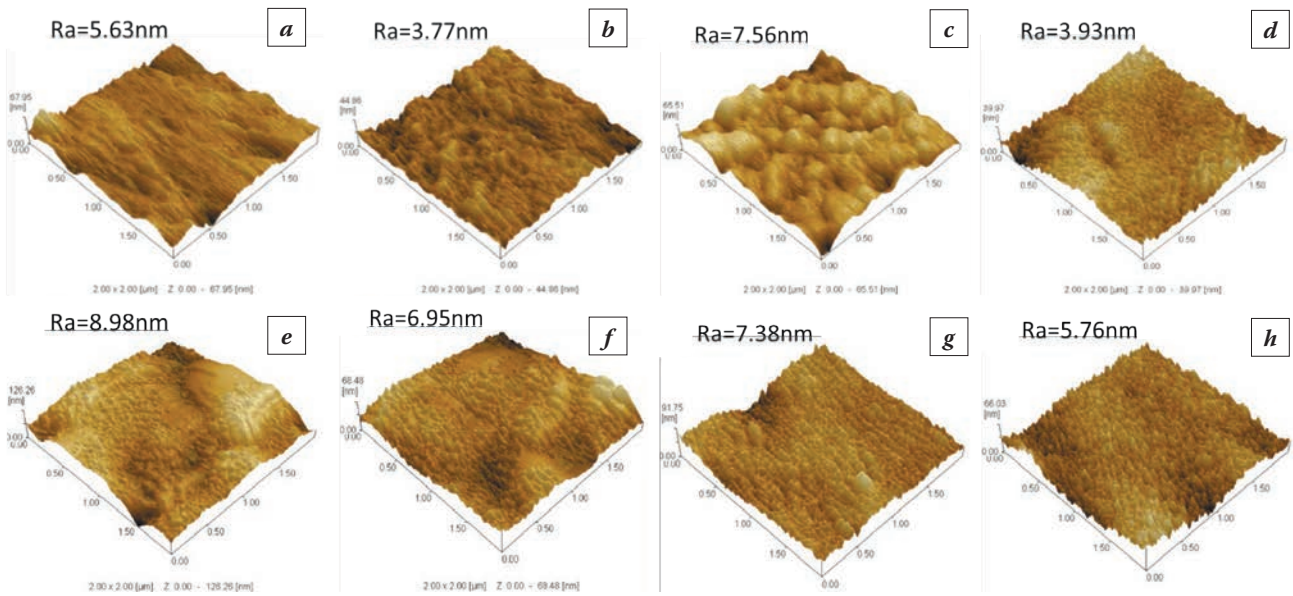


Fig. 3. AFM images of DLC films deposited on SUS316L at (a)  $CH_4/H_2 = 1:1$ , 6 hrs; (b)  $CH_4/H_2 = 1:1$ , 12 hrs; (c)  $CH_4/H_2 = 1:0$ , 6 hrs; (d)  $CH_4/H_2 = 1:0$ , 12 hrs and Ti at (e)  $CH_4/H_2 = 1:1$ , 6 hrs; (f)  $CH_4/H_2 = 1:1$ , 12 hrs; (g)  $CH_4/H_2 = 1:0$ , 6 hrs; (h)  $CH_4/H_2 = 1:0$

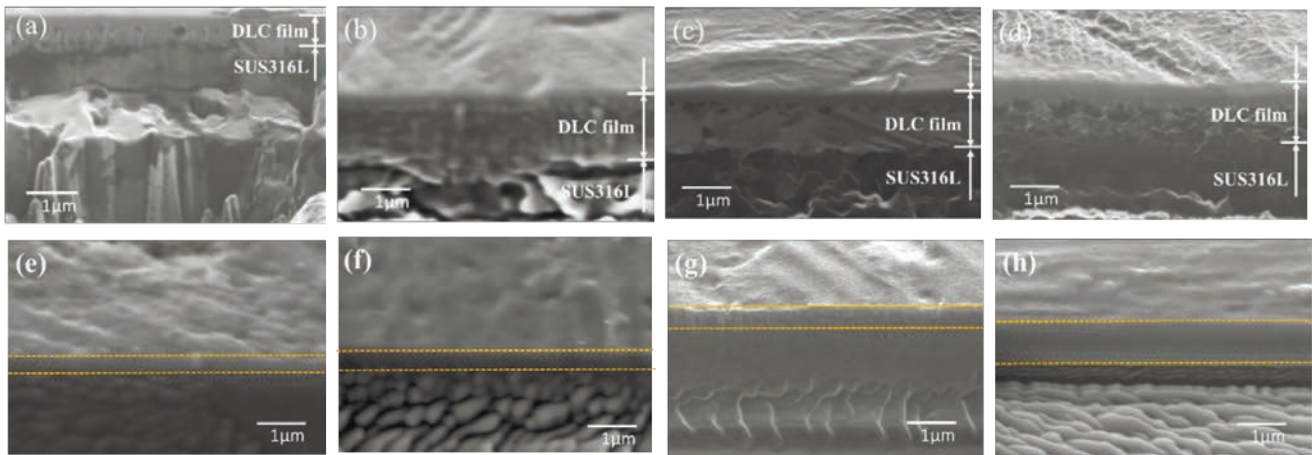


Fig. 4. SEM images of DLC films deposited on SUS316L at (a)  $CH_4/H_2 = 1:1$ , 6 hrs; (b)  $CH_4/H_2 = 1:1$ , 12 hrs; (c)  $CH_4/H_2 = 1:0$ , 6 hrs; (d)  $CH_4/H_2 = 1:0$ , 12 hrs and titanium at (e)  $CH_4/H_2 = 1:1$ , 6 hrs; (f)  $CH_4/H_2 = 1:1$ , 12 hrs; (g)  $CH_4/H_2 = 1:0$ , 6 hrs; (h)  $CH_4/H_2 = 1:0$

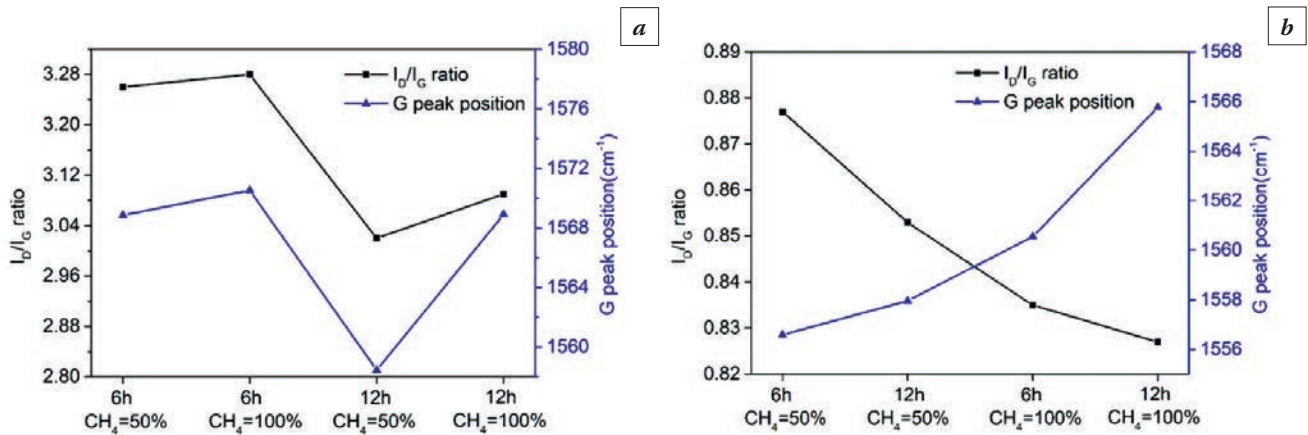


Fig. 5. The  $I_D/I_G$  and G-peak position of DLC films coated (a) SUS316L and (b) titanium

for stainless steel substrate. The  $G$  peak position was shifted from  $1557$  to  $1566\text{ cm}^{-1}$  by increasing the ratio of  $\text{CH}_4$  and the deposited time for titanium substrate. The  $\text{ID/IG}$  ratio of DLC film deposited on stainless steel is reduced to a minimum of  $3.02$  at  $\text{CH}_4/\text{H}_2 = 1:1$ ,  $12$  hrs, whereas titanium is reduced to a minimum of  $0.83$  at  $\text{CH}_4/\text{H}_2 = 1:0$ ,  $12$  hrs. This is consistent with the DLC film thickness.

### Electrical resistivity of the DLC films

The conductivity is the key factor for the metallic bipolar plate of fuel cells. The low resistivity will obtain the high performance. The resistivity of substrates and DLC films measured by four-point method were shown in Fig. 6. The SUS316L substrate had the highest resistivity of  $14.30\text{E-}04\Omega\cdot\text{cm}$ . The DLC films deposited at  $\text{CH}_4/\text{H}_2 = 1:0$ ,  $6$ h showed lower resistivity of about  $10.76\text{E-}04\Omega\cdot\text{cm}$  which is half that of substrate from Fig. 6a. Com-

pared to the uncoated titanium, the electrical resistivity of DLC film-coated titanium substrates decreased obviously, and reached to the minimum of  $6.29\text{E-}04\Omega\cdot\text{cm}$ . It can be seen that the electrical resistivity value decreases as the  $\text{CH}_4$  ratio increases to  $100\%$ . So the titanium coated-DLC film is available for fuel cells.

### Characterization of the DLC films after potentiostatic corrosion test

Fig. 7 displays the typical Raman spectrum of DLC films deposited on SUS316L and titanium after corrosion test. The peaks of SUS316L coated-DLC films at the condition of  $\text{CH}_4/\text{H}_2 = 1:1$ ,  $12$  hrs were more distinct than the DLC films at the condition of gas ratios  $\text{CH}_4/\text{H}_2 = 1:0$  after the corrosion test. The titanium coated-DLC film at  $\text{CH}_4/\text{H}_2 = 1:0$ ,  $12$  hrs has the strongest Raman peak. Therefore, DLC film deposited on titanium has the better anti-corrosion resistance.

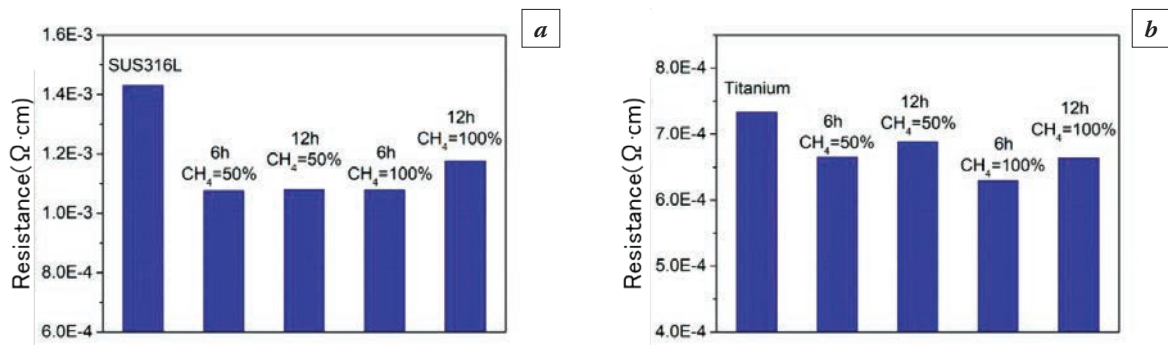


Fig. 6. Resistivity of substrates and DLC films deposited on (a) SUS316L, (b) titanium

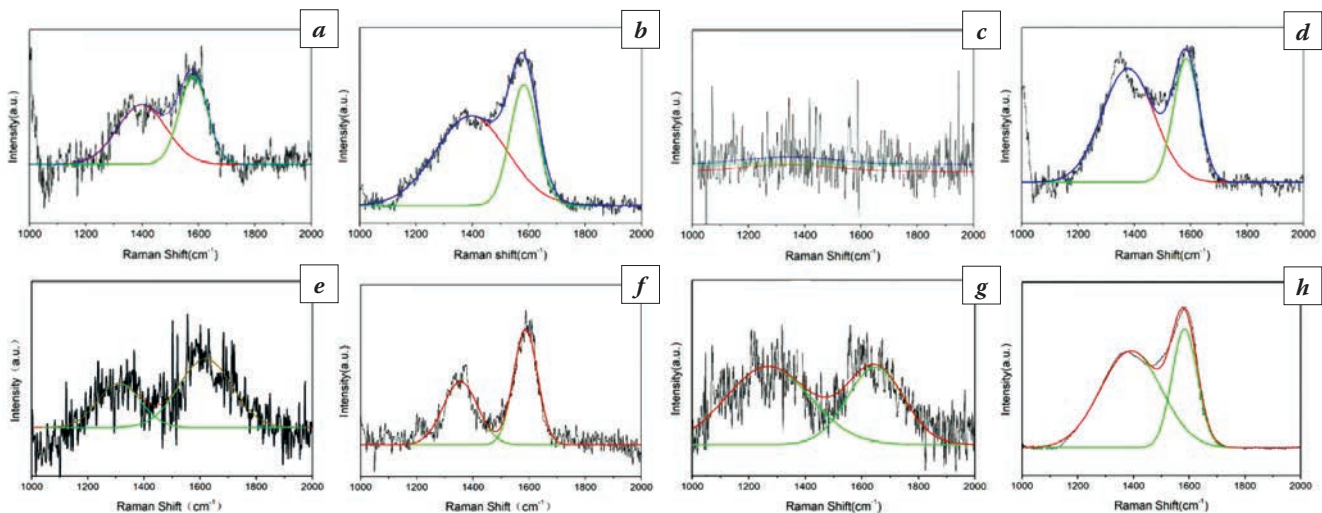


Fig. 7. Raman spectrum of DLC films deposited on SUS316L at (a)  $\text{CH}_4/\text{H}_2 = 1:1$ ,  $6$  hrs; (b)  $\text{CH}_4/\text{H}_2 = 1:1$ ,  $12$  hrs; (c)  $\text{CH}_4/\text{H}_2 = 1:0$ ,  $6$  hrs; (d)  $\text{CH}_4/\text{H}_2 = 1:0$ ,  $12$  hrs and Ti at (e)  $\text{CH}_4/\text{H}_2 = 1:1$ ,  $6$  hrs; (f)  $\text{CH}_4/\text{H}_2 = 1:1$ ,  $12$  hrs; (g)  $\text{CH}_4/\text{H}_2 = 1:0$ ,  $6$  hrs; (h)  $\text{CH}_4/\text{H}_2 = 1:0$  after corrosion test

Table 2. Metal ions concentration (ppm)

	Substrate	DLC film (CH <sub>4</sub> /H <sub>2</sub> = 1:1, 6 hrs)	DLC film (CH <sub>4</sub> /H <sub>2</sub> = 1:1, 12 hrs)	DLC film (CH <sub>4</sub> /H <sub>2</sub> = 1:0, 6 hrs)	DLC film (CH <sub>4</sub> /H <sub>2</sub> = 1:0, 12 hrs)
<b>SUS316L</b>	42.54	33.90	16.60	34.39	19.56
<b>Ti</b>	0.58	0.50	0.43	0.37	0.34

## Inductively coupled plasma (ICP) results

Table 2 displays the metal ions of DLC films-coated stainless steel and titanium. Compared to the concentration of uncoated substrate, the metal ions of DLC films has a significant reduction, indicating that the DLC films play an important role on protecting the substrate. The SUS316L coated-DLC film deposited at the condition of gas ratios CH<sub>4</sub>/H<sub>2</sub> = 1:1 has a lower concentration than that of gas ratios CH<sub>4</sub>/H<sub>2</sub> = 1:0. However the titanium coated-DLC film deposited at CH<sub>4</sub>/H<sub>2</sub> = 1:0 has a lower concentration. The metal ion dissolution concentration of DLC film-coated SUS316L deposited at a low C:H ration exhibits a minimum of about 16.60 ppm, while DLC film-coated titanium has a lower metal ion dissolution concentration of about 0.34 ppm deposited at a high C:H ration. The corrosion behavior is consistent with the cross-section SEM images and Raman spectrum of the DLC films.

## CONCLUSIONS

The DLC films have been deposited on SUS316L and titanium substrate at different gas flow ratio CH<sub>4</sub>/H<sub>2</sub> and deposition time using IBED for bipolar plates to improve conductivity and corrosion behavior in this paper. The minimum Ra of DLC film-coated SUS316L is 3.77, which is smaller than that of titanium, about 5.76. The Raman spectrum of all the samples exhibits the evolution of a DLC film with clearly observed D and G peak located at about 1380 and 1560 cm<sup>-1</sup> respectively. It also confirms the sp<sup>3</sup>-C content increasing as the deposition time increases for all the samples which results in the lower metal ion dissolution concentration. The minimum resistivity of 10.76E-04Ω·cm for DLC film-coated SUS316L is obtained, which is higher than that of 6.29E-04Ω·cm for DLC film-coated titanium. The metal ion dissolution concentration of DLC film-coated SUS316L deposited at a low C:H ration exhibits a minimum of about 16.60 ppm, while DLC film-coated titanium has a lower metal ion dissolution concentration of about 0.34 ppm deposited at a high C:H ration. Therefore, the better conductivity and anti-corrosion properties of DLC film-coated titanium make it a good candidate for PEMFC bipolar plates.

## REFERENCES

1. **Xu J., Huang H.J., Li Z.Y. et al.** Corrosion behavior of a ZrCN coated Ti alloy with potential application as a bipolar plate for proton exchange membrane fuel cell // *J. Alloys Compd.* 2016. 663: 718–730.
2. **Hwang J.J., Chang W.R., Weng F.B. et al.** Development of a small vehicular PEM fuel cell system // *Int. J. Hydrogen Energ.* 2008. 33: 3801–3807.
3. **Tawfik H., Hung Y., Mahajan D.** Metal bipolar plates for PEM fuel cell—A review // *J. Power Sources.* 2007. 163: 755–767.
4. **Shanian A., Savadogo O.** A non-compensatory compromised solution for material selection of bipolar plates for polymer electrolyte membrane fuel cell (PEMFC) using ELECTRE IV // *Electrochim Acta.* 2006. 51: 5307–5315.
5. **Kumagai M., Myung S.T., Kuwata S. et al.** Application of Ni-free high nitrogen stainless steel for bipolar plates of proton exchange membrane fuel cells // *Electrochim Acta.* 2009. 54: 1127–1133.
6. **Fu Y., Lin G.Q., Hou M. et al.** Carbon-based films coated 316L stainless steel as bipolar plate for proton exchange membrane fuel cells // *Int. J. Hydrogen Energy.* 2009. 34: 405–409.
7. **Dhakate S.R., Sharma S., Borah M. et al.** Expanded graphite-based electrically conductive composites as bipolar plate for PEM fuel cell // *Int. J. Hydrogen Energ.* 2008. 33: 7146–7152.
8. **Lee S.K., Kim K.H., Kim Y.T. et al.** Occurrence of Rhizina Root Rot in a Black Pine (*Pinus thunbergii*) Forest Located at the Western Coastal Area in Korea and Its Spreading Patterns // *Res. Plant Dis.* 2005. 11: 208–212.
9. **Mawdsley J.R., Carter J., Wang X.P. et al.** Composite-coated aluminum bipolar plates for PEM fuel cells // *J. Power Sources.* 2013. 231: 106–112.
10. **Dai W., Gao X., Liu J. et al.** Compositionally modulated multilayer diamond-like carbon coatings with AlTiSi multi-doping by reactive high power impulse magnetron sputtering // *Applied Surface Science.* 2017. 425: 855–861.
11. **Joan M.G., Enric B.** Mechanical and Surface Characterization of Diamond-Like Carbon Coatings onto Polymeric Substrate. *arXiv preprint arXiv* 2015. 1509: 08512.
12. **Robertson J.D.** Diamond-like amorphous carbon // *Materials science and engineering: R: Reports.* 2002. 37: 129–281.

Правильно?

# ULTRASONIC SURFACE TREATMENT OF COMPONENTS PRODUCED BY ADDITIVE MANUFACTURING TECHNOLOGIES

S.K. Sundukov, D.S. Fatyukhin, A.A. Volkov

Moscow Automobile and Road Construction State Technical University (MADI). Moscow, Russia  
sergey-lefmo@yandex.ru

Due to a number of factors, certain functional surfaces of a component have poor geometric properties and require additional treatment. The main problem is the finishing of complex internal surfaces, the geometry of which does not allow to apply traditional processing methods. In this paper, it is proposed to use ultrasonic liquid treatment as a finishing treatment. The main advantage of the ultrasonic treatment is the fact that cavitation bubbles spread over the volume being processed are the working bodies. This allows the processing of complex internal surfaces of products obtained by additive technologies. Experimental studies have shown a reduction in altitude roughness parameters up to 3 times. To implement the process of ultrasonic finishing, a coordinate processing unit has been developed, the processing strategy of which is developed according to the original 3D model.

**Keywords:** additive manufacturing technologies; ultrasonic treatment; roughness.

The working principle of additive manufacturing technologies is based on the layer-by-layer production of components using a digital 3D model, which allows to obtain elements of a unique shape. From the point of view of mechanical engineering, the technology of selective laser melting based on the sequential fusion of metal powder layers is of the greatest interest.

Products obtained by the method of selective laser melting have a different state of the surface layer in the perpendicular and parallel directions of the melted powder layer (Fig. 1).

The upper surface is formed by the crystallization of the final layer during the production of the part; the lateral surface is the result of successive melting of the layers of powder, in which each layer is subject-

ed to temperature effects when the next melts, and transitions from layer to layer are visually noticeable on the side surface.

Improving the quality of these surfaces is an important task, especially the lateral surface, since it forms complex-internal channels and cavities of the product obtained by additive technologies. The currently used method of isostatic pressing reduces the porosity of the product, and the method of laser flashing of the surface reduces the roughness only on the outer surfaces [1].

As a finishing method for complex surfaces, it is proposed to use ultrasonic liquid treatment, the main advantage of which is that in this case the working bodies are represented by cavitation bubbles and their clusters distributed in the liquid by acoustic

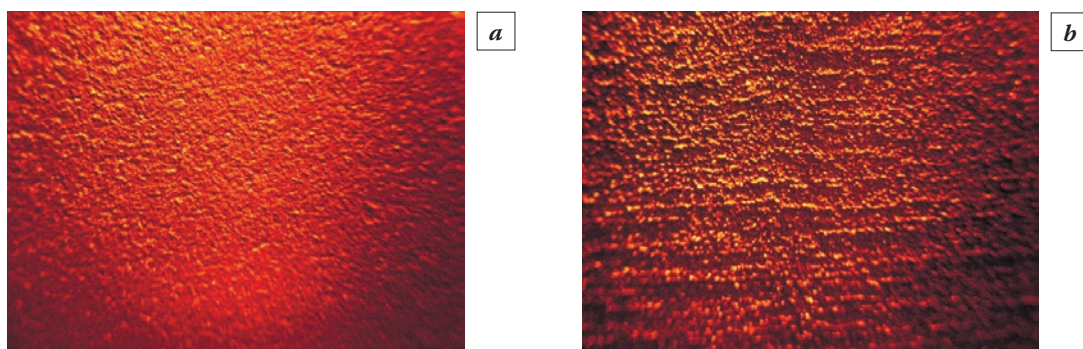


Fig. 1. Photos of the product obtained by the method of selective laser melting:  
*a* – the upper surface; *b* – the side surface

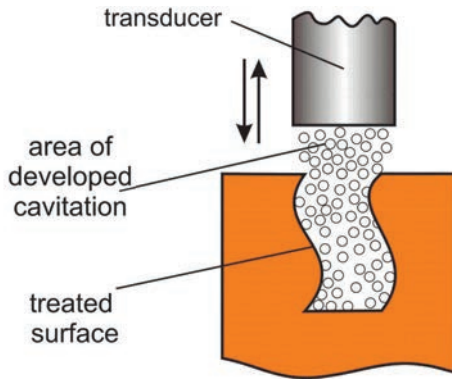


Fig. 2. Processing Scheme

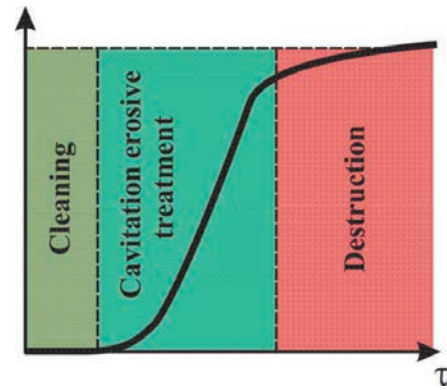


Fig. 3. The stages of the impact of ultrasonic liquid treatment on the surface of products ( $\tau$  – processing time)

flows [2–4]. This allows to process any complex surfaces that are under ultrasonic action (Fig. 2).

Since the efforts created by the working bodies have microscopic values and are repeated with a very high frequency, the nature of the impact on the material is cumulative.

In this regard, the effect of ultrasonic liquid treatment on the surface of products can be divided into 3 stages (Fig. 3)

The first stage, characterized by the absence of a change in the properties of the surface layer, is most suitable for the operation of cleaning parts obtained by additive technologies from residues of unmelted powder. At the second stage, the geometry and properties of the surface begin to change, and this process occurs up to a certain limit - cavitation-erosion treatment. Further, only the destruction of the surface layer is observed [5].

When insoluble abrasive particles are added to the voiced liquid, the nature and degree of impact of ultrasonic treatment on the surface changes. The presence of irregularities in the technological liquid medium leads to a decrease in the cavitation strength of the liquid and to an increase in the number of cavitation centers. The mechanism of action on the surface is based on the micro-cutting action of abrasive particles, which acquire acceleration as a result of the transfer of impulse from shock waves, acoustic micro- and macro-leaks - cavitation abrasive treatment.

Table 1. The effect of ultrasonic treatment on surface roughness

Processing type	Roughness parameters, micron		
	$R_a$	$R_z$	$R_{max}$
Cavitation-erosion treatment	17.9	99.8	295
Cavitation abrasive treatment	7.51	48.2	57.8

Experimental studies on the effect of cavitation and cavitation-abrasive treatment on surface properties were carried out on samples of steel PH-1.

Cavitation treatment during a long time (60 min) does not lead to significant changes in roughness as steels having a ferritic structure are characterized by low cavitation resistance. High roughness leads to unequal distribution of cavitation activity, i.e. working bodies, which are represented by oscillating and collapsing voids, have the most considerable effect in places with greatest surface irregularities [6].

When cavitation abrasive treatment for 2 min there is a significant reduction in roughness. Due to the short processing time and the damping functions of abrasive particles on the surface, no traces of erosion were observed. The change in the layer is due to the fact that the destruction occurs along the protrusions of the surface of the grains. The results are presented in Table 1.

The reduction of roughness parameters has a positive effect on such properties as wear resistance, strength, corrosion resistance and thermal conductivity.

To optimize and improve the efficiency of ultrasonic liquid processing, depending on the complexity of the profile of the product being processed and its size, it is advisable to use various technological equipment, which is based on the principle of geometry management (mainly increase in volume) of the developed cavitation zone.

An effective way to increase the volume of the cavitation treatment zone is to move the oscillatory system along a predetermined path that follows the surface profile of the product. For processing complex-profile products obtained by additive technologies, moving along 3 coordinates is required.

The LEFMO-07 installation implements a scheme of sequential ultrasonic liquid treatment by moving a rod oscillatory system along the surface of the prod-

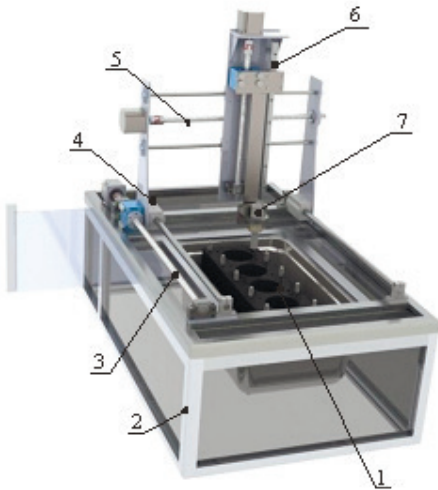


Fig. 4. Installation of coordinate ultrasonic processing:

- 1 – the object of cleaning; 2 – framework of the lower unit of the installation; 3 – framework of the upper unit of the installation; 4 – drive of longitudinal displacement of radiator; 5 – drive of transverse displacement of radiator; 6 – drive of vertical displacement of radiator; 7 – ultrasonic oscillatory system

uct. The displacement strategy is created using the 3-D model obtained in the CAD system at the design stage.

The organization of movement in 3 coordinates is realized by using 3 drives consisting of a stepping motor and a ball screw drive. “LEFMO-07” allows the processing of products of any geometric complexity (Fig. 4).

The advantage of this installation is the ability to produce selective laser melting and post-processing of a product using a single 3D model of the product.

Thus, the use of ultrasonic technologies as a finishing operation of the cycle of additive production will allow to provide the required geometric parameters of complex surfaces, which will expand the possibilities of using additive technologies.

## REFERENCES

1. Nigmatzyanov R.I., Sundukov S.K., Fatyukhin D.S., Grib V.V., Kartsov S.K. Additive manufacturing with ultrasound // Russian Engineering Research. 2017. Vol. 37, No. 12. P. 1070–1073.
2. Livanskiy A.N., Prikhodko V.M., Sundukov S.K., Fatyukhin D.S. Research on the influence of ultrasonic vibrations on paint coating properties // Transactions of Famena. 2016. Vol. 40, No. 1. P. 129–138.
3. Fatyukhin D.S., Nigmatzyanov R.I., Luznov J.M., Sinev A.V., Trifonov O.N. A study of the influence of cavitation structures on the facial layers of structural materials // Journal of Industrial Pollution Control. 2017. 33(2). P. 1612–1616.
4. Kazantsev V.F. Fizicheskaya Osnova Tekhnologicheskikh Primenenij Ul'Trazvuka [Physical Basis of Technological Applications of Ultrasound]. Text. Moscow, MADI. 2008. P. 102.
5. Kazantsev V.F., Kuznetsov S.Y., Sundukov S.K., Fatyukhin D.S., Britvin L.N. Ultrasound treatment of curved contours and complex surfaces // Russian Engineering Research. 2017. Vol. 37, No. 12. P. 1074–1076.
6. Aleksandrov V.A., Sundukov S.K., Fatyukhin D.S., Filatova A.A. Ultrasonic Methods for Improving Object Surface Quality Prepared by Corrosion-Resistant Steel Powder Selective Laser Melting // Metal Science and Heat Treatment. 2018. 60(5–6). P. 381–386.

# THE COMBINATION OF ULTRASONIC HARDENING AND NITRIDING

R.I. Nigmatzianov, S.K. Sundukov, V.A. Perekrestova

Moscow Automobile and Road Construction State Technical University (MADI). Moscow, Russia

lefmo@yandex.ru

The article discusses the application range of ultrasound and methods of chemical-thermal treatment, their various combinations and technologies for the formation of operational properties of the surface layer of machine parts. In recent years, a lot of attention has been paid to the development of surface hardening technologies, as it is the state of the surface layer that outlines the operational properties of machine parts and mechanisms. In order to make steel highly wear-resistant it is necessary to create a certain set of mechanical properties, the first and foremost of which is high hardness. One popular method of steel surface targeted modification is nitriding, which helps to increase the hardness and wear-resistance of a part as a result of nitrogen diffusion at elevated temperatures. The disadvantage of this method is the small thickness of a modified area. In addition, the significant difference between the hardness of the nitrided layer and that of the base material can lead to cracking of the surface layer under local loads. On the other hand, the increase in wear-resistance can be achieved with the use of surface plastic deformation methods. One of the surface plastic deformation (SPD) methods is ultrasonic hardening.

**Keywords:** ultrasonic vibrations; the ultrasonic surface plastic deformation; chemical-heat treatment; nitriding.

## INTRODUCTION

One popular method of steel surface targeted modification is nitriding, which helps to increase the hardness and wear-resistance of a part as a result of nitrogen diffusion at elevated temperatures. The disadvantage of this method is the small thickness of a modified area. In addition, the significant difference between the hardness of the nitrided layer and that of the base material can lead to cracking of the surface layer under local loads. On the other hand, the increase in wear-resistance can be achieved with the use of surface plastic deformation methods. One of the surface plastic deformation (SPD) methods is ultrasonic hardening. The deforming element in this case is a tool of the ultrasonic oscillating system. Ultrasonic hardening helps to obtain a much thicker hardened layer compared to that after nitriding. However, the increase in microhardness is not big. Changes in physical, mechanical and operational properties of materials are the result of totally different processes. Nitriding is the result of iron nitrides and carbonitrides formation, while ultrasonic hardening is the result of plastic deformation. It is obvious that the application of a combined method including nitriding and hardening should give fundamentally new results. The research revealed that the maximum effect concerning both the degree of hardening and the thickness of the hardened layer was achieved with the application of nitriding, followed by ultrasonic hardening (SPD with the use of ultrasonic tool). The obtained results allow us to assert that the complex

ultrasonic treatment and nitriding increase the microhardness of material surface up to 2...2.5 times and harden the surface layer for thickness of up to 350  $\mu\text{m}$ .

## HEADING

The reliability and durability of the performance of its functions by a mechanical engineering product is determined by a number of performance properties of parts and their joints: static and fatigue strength, surface contact static and dynamic strength, corrosion resistance, contact stiffness, tightness, wear resistance, etc. All these performance properties largely depend on the quality of the surface layer of parts. To increase hardness, strength and wear resistance, as well as if you only need to strengthen the surface layer of products, and leave the core viscous (for example, for torsional parts: shafts, spindles, levers, bolts, columns, etc.) is used the nitriding. A significant disadvantage of this method of chemical heat treatment is the considerable duration of the process.

In this regard, of particular interest is the search for new processing technologies that significantly reduce the duration of thermal diffusion processes, as well as improve the quality of the surface layer. This technology is ultrasonic, which allows to intensify various processes, including the chemical-heat treatment (CHT).

Among the methods of surface hardening, the highest density of coatings and best adhesion to the base metal are obtained with thermal diffusion saturation. The stability of the structure and the constancy of the linear dimensions in time with high hardness

and wear resistance can be achieved by nitriding – the process of saturation of the surface with nitrogen.

However, despite the high quality of the thermal diffusion coating, nitriding has significant drawbacks. Perhaps the most important drawback is the long duration of the process at high temperatures. So, to obtain a hardened layer with a depth of 0.5 mm, an exposure of 50–100 hours in a medium of dissociated ammonia at 500 °C is required. Another important disadvantage is the long exposure at high temperatures, which significantly reduces the mechanical properties of the material of the product, which is not always eliminated by subsequent heat treatment. Also, heat treatment of the product at temperatures above phase transformations can degrade the properties of the coating (cracks, oxidation, etc.) appear. In some cases, after heat treatment, the surface geometry changes, which leads to the addition of finishing operations of mechanical treatment to achieve the required accuracy class [1]. Accordingly, the issue of developing new processing technologies capable of ensuring the quality of the surface layer with a shorter process time is relevant. These technologies include ultrasonic technology.

Ultrasonic are elastic mechanical vibrations with a frequency exceeding the threshold of sounds heard by a person in the range from 20 kHz to 1.5–2 MHz. Ultrasonic technologies today are actively used in many areas of society, including in mechanical engineering, with the aim of obtaining new qualitative results. For the intensification of technological processes, oscillations with a frequency of 18–88 kHz are used, higher frequencies are characteristic in the use of various kinds of measurements and in flaw detection.

The use of ultrasound in combination with nitriding gives a number of positive effects. With different sequences and methods of ultrasonic exposure, those or parameters of the surface layer of products are achieved.

It is known that when ultrasonic oscillations are communicated in solids, diffusion processes are accelerated. So, experimentally confirms the effect of ultrasonic vibrations on the process of gas nitriding when ultrasound is supplied to the sample. Increases the hardness of the surface layer and the depth of penetration of nitrogen [2]. With an increase in the duration of the process, the depth of the nitrated layer when exposed to ultrasonic vibrations is in all cases greater than that of the samples without the use of ultrasound, and with a 15-hour process, the difference in the depth of the diffusion layer reaches 120 µm. The studies were carried out on a sample with a diameter of 10 mm and a length of 60 mm, which is approximately equal to the half-wave length with oscillations with a frequency of 29 kHz. Due to

the structural features of ultrasonic generators, large amplitudes of the order of 10–15 µm can be obtained only with magnetostrictive transducers. In addition, at high frequencies there is a significant absorption of ultrasound. There is a relationship between amplitude and intensity of ultrasonic vibrations. The intensity of ultrasound is proportional to the wave resistance of the medium and the squares of the frequency and amplitude of oscillations [3].

During the experiment, one end was screwed into the hole at the end of the waveguide. Nitriding was carried out at a temperature of 500 °C (the temperature of the saturating medium was measured with a thermocouple inserted in a protective case into the furnace space, and the temperature of the sample was thermocouple welded to its surface). Depending on the duration of the process, the surface hardness increase, in all cases a greater hardness was observed in the samples with the superposition of ultrasonic vibrations compared with the samples, without ultrasound. Starting from a 10 hour process, the surface hardness was not much different.

Attention is drawn not only to the study of thermal diffusion saturation in a gaseous medium with the supply of ultrasonic vibrations, but also to ion implantation of nitrogen atoms [4]. As a result of implantation, a nitrated layer is formed on the surface of the samples, which represents the internal nitriding zone, the phase composition of which is determined by the implantation temperature and the method of preliminary surface preparation. With increasing nitriding temperature, the proportion of nitride phases in the surface layer increases, which leads to an increase in hardness and an increase in corrosion resistance. Ultrasonic processing intensifies the process of implantation of nitrogen ions, increasing the depth of the hardened layer due to the formation of a large number of crystal lattice defects and increasing the surface microhardness due to an increase in the share of nitride phases.

New opportunities opened up ultrasound technology for the restoration of aluminum pistons by thermal diffusion saturation methods. The use of ultrasound made it possible to clean the oxide film on the surface of the part, and the imposition of ultrasonic vibrations during the process itself made it possible to accelerate the diffusion process. This effect is explained by the fact that ultrasonic vibrations destroy the oxide film, bring the components of the diffusion mixture closer to the sample surface, which creates favorable conditions for the diffusion of the elements of the saturating medium into the crystal lattice of the sample. For this study, the sample was placed in a rigid mount to the emitter. Regulation of the wavelength of oscillations of the membrane is carried out by selecting the membrane.

Ultrasonic technologies allow not only to reduce the time required for saturation of the surface with nitrogen, but also to improve the quality of the surface layer. Thus, nitriding and the use of ultrasonic surface plastic deformation (USPD) before or after the methods of chemical heat treatment yields qualitatively new results.

Surface roughness is one of the important criteria for assessing the quality of the surface layer, and in many cases the increase in this parameter does not meet the operational requirements. As noted earlier, nitriding leads to a change in surface roughness. In this regard, after thermal diffusion saturation, it is necessary to add operations that provide the necessary surface geometry. At the same time, under the conditions of the same parameters (duration and temperature of the process) this change will be different.

Studies prove [5] that the use of ultrasonic surface-plastic deformation allows to significantly reduce the height of asperities caused by chemical-thermal treatment. The changes in the surface asperities due to plastic deformation within the limits of the Ra measurement range from 6.300 to 0.025  $\mu\text{m}$ . With ultrasonic hardening (SPD with use of ultrasonic tool), periodic contact with the frequency of ultrasonic vibrations occurs between the surface and the instrument. During processing, the tool was pressed against the surface to be machined with a force of 25 N. The frequency of ultrasonic vibrations was 19.7 kHz, and the amplitude was 10–12  $\mu\text{m}$ .

During the experiment, measurements were made of the surface roughness Ra before thermal diffusion saturation and ultrasonic hardening, as well as after saturation of the surface and after the combined treatment. The results of the experiment showed that after applying the method of chemical-heat treatment, the surface roughness increased from 0.4 to 0.9  $\mu\text{m}$ , with a subsequent ultrasonic hardening its decrease to 0.3  $\mu\text{m}$  was observed.

In comparison with nitriding, ultrasonic hardening allows you to get a greater depth of the riveted layer, but the increase in microhardness is not so great. The use of surface-plastic deformation with an ultrasonic instrument without prior nitriding allowed us to obtain the microhardness of the hardened surface layer 329 HV, whereas with a two-stage treatment, as a result of the hardening of the nitrided layer, it increases to 800. Depending on the processing time, the surface microhardness is different, so with the duration deformations with an ultrasonic instrument within 5 s – it increased from 225 HV (after nitriding) to 472 HV, and at 10 s – to 618 HV.

The depth of the hardened layer also increases, which is explained by an increase in the efficiency of transmission of the distribution of shock loads from the ultrasonic instrument due to the high hardness

of the nitrided layer. In this case, the nitrated layer is an intermediate element between the indenter of the ultrasonic instrument and the base metal of the product. The complex effect allowed us to obtain a depth of the hardened layer of 350 microns.

When ultrasonic surface plastic deformation is observed, the formation of structure defects associated with the absorption by dislocations of ultrasonic wave energy is observed. There are different points of view on the effect of preliminary surface plastic deformation on the process of formation of diffusion layers in a metal [6]. One point of view states that preliminary surface plastic deformation hampers diffusion of interstitial atoms. This view is based on the fact that interstitial atoms actively interact with dislocations in the crystal lattice, where dislocations absorb atoms of dissolved elements. From another point of view, the preliminary plastic deformation and the resulting structural defects contribute to a more active diffusion of the substance being introduced.

Thus, we can talk about the prospects of using ultrasonic vibrations for the intensification of thermal diffusion processes, as well as the relevance of the study of new technologies for the complex treatment of the surface layer by ultrasound and nitriding.

## REFERENCES

1. **Britvin L.N., Germanova V.A., Karagodin V.I., Nigmatzyanov R.I., Fatyukhin D.S.** Hardening of the surface layer of machine parts by methods of chemical heat treatment and ultrasonic technologies // *Bulletin of the Moscow Automobile and Road State Technical University (MADI)*. 2017. No. 1 (48). P. 63–67.
2. **Aleksandrov V.A., Kazantsev V.F., Fatyukhin D.S.** Formation of the surface layer by the method of complex ultrasonic treatment and nitriding // *Science-intensive technologies in mechanical engineering*. 2013. No. 3. P. 33–36.
3. **Nigmatzyanov R.I., Morschilov M.V., Perekreстова V.A., Sergeev I.D., Sukhov A.V.** Installation of chemical heat treatment and ultrasonic treatment for hardening the surface layer of steel products // *High technology in mechanical engineering*. 2018. No. 7 (85). P. 17–22.
4. **Britvin L.N., Gaevskii V.V., Germanova V.A., Nigmatzyanov R.I., Prikhod'ko V.M.** Surface modification by combined thermochemical and ultrasound treatment // *Russian Engineering Research*. 2017. Vol. 37, No. 12. P. 1087–1089.
5. **Fatyukhin D.S., Babchenko N.V., Titkov V.D.** Ultrasonic cavitation-abrasive processing // *Science-intensive technologies in mechanical engineering*. 2013. No. 3 P. 23–26.
6. **Prikhod'ko V.M., Aleksandrov V.A., Fatyukhin D.S., Petrova L.G.** Effect of ultrasonic cavitation on nitrided steel surface layer condition // *Metal Science and Heat Treatment*. 2015. Vol. 57. Issue 5-6. P. 300–303.

# RECOGNITION OF SUBFILM CORROSION OF METAL SURFACES OF MACHINES PARTS WITH VARIOUS COATINGS BY INFRARED THERMOGRAPHY

E.A. Kosenko, V.A. Zorin, N.I. Baurova

Moscow Automobile and Road Construction State Technical University (MADI). Moscow, Russia

KosenkoKate@mail.ru

The article describes a method for recognizing of local zone of subfilm corrosion of metal surfaces of machines parts by the method of infrared thermography. The technique and the results of experimental studies on the detection of subfilm corrosion in samples with different paint coatings are presented. A mathematical description of the diagnostic system is presented. The dependence of the diagnostic signal value on the color and thickness of the paint coatings materials is proposed. Recommendations on the application of the described method in assessing the corrosion state of metallic objects are proposed.

**Keywords:** defect; infrared radiation; corrosion; paint coating; thermal field; color.

## INTRODUCTION

Despite modern advances in the development of anti-corrosion tools to protect financial losses from corrosion damage to machines parts and their premature failure, continue to grow. The consequences of a sudden failure of the process equipment, metalworking elements and machines parts can be expressed not only in the form of financial costs to restore their working capacity, but also pose a risk to the environment, people's life and health.

One of the most dangerous types of corrosion destruction is subfilm corrosion. The products of metal corrosion do not reach the surface of the coating at the early stages of its development; therefore, they are hardly noticeable for visual detection. Subfilm corrosion manifests itself in the form of local swelling of the paint coating or in the form of a cobweb-like network of thread that grow rapidly from the center of the hearth. Thread of subfilm corrosion do not cause deep lesions of the metal, but in the center of corrosion the destruction of the material takes place deep into, leading to a through-lesion.

It is possible to minimize the likelihood of risks associated with sudden failures of ground transport and technological machines due to corrosion damage by organizing periodic monitoring of their corrosion state.

The level of corrosion is determined by methods of destructive and non-destructive testing. The methods of destructive control are used, as a rule, after the failure of the technical system to determine the causes of the occurrence of destruction and to

develop measures to prevent its occurrence in the future. To determine the state of the object of control and the possibility of its further operation using methods of non-destructive testing [1–4].

One of the most common methods for assessing the corrosion state of controlled objects is the visual-optical method. This method is based on the study of metal surfaces for the presence of corrosion damage using a magnifying glass and / or optical microscope. The size and nature of corrosion damage is fixed on paper with a soft pencil or by creating an impression on lead or plastic. However, the visual-optical method allows to make a conclusion only about the macrodamages of the test object and does not provide complete information about its corrosion state. A more accurate estimate can be obtained using chemical, electrochemical and physical methods of non-destructive testing. The physical methods used to assess the degree of corrosion damage to the test object include: ultrasonic flaw detection, acoustic emission, radiography, thermography, electrical resistance method, etc.

Due to its informativeness, high performance and safety, non-destructive testing methods are widely used by the method of infrared thermography, based on the difference in thermophysical properties of corrosion-damaged and non-defect areas of the test object [5–6].

Significant difficulties in the implementation of infrared thermography of metal objects are attributed to the high reflectivity of their surfaces. In addition, one of the problems in monitoring objects made from metals that have a high thermal diffusivity is the short lifetime

of temperature signals in corrosion zones, which requires the use of additional means to enhance temperature signal and time of its optimal observation [7–10].

## EXPERIMENTAL RESEARCH TECHNIQUE

The method of active infrared thermography when recognizing corrosion defects can be realized not only on the basis of the difference in thermal and physical properties, but also on the basis of the difference in the absorption and reflection coefficients of infrared radiation by the defect-free and defect-free structures of the test objects.

In order to determine the dependence of the diagnostic signal value, which characterizes the presence of under-film corrosion on the thickness of the paint coating and its color, steel samples of the St3ps GOST 380-2005 grade were prepared; Next, the samples were applied acrylic paintwork of different thickness:

- sample № 1 – the thickness of the paint coating  $h = 9\text{--}10\ \mu\text{m}$ ;
- sample № 2 – the thickness of the paint coating  $h = 14\text{--}16\ \mu\text{m}$ ;
- sample № 3 – the thickness of the paint coating  $h = 23\text{--}25\ \mu\text{m}$ .

To determine the dependence of the diagnostic signal value on the paint coating color, samples with paint coating thickness equal to  $h = 23\text{--}25\ \mu\text{m}$  of different reflectivity of the following colors were prepared:

- sample № 4 – glossy black (paint brand Otrix number 926);
- sample № 5 – matt black (paint brand Kudo KU-1102);
- sample № 6 – white glossy (paint brand Otrix number 927);
- sample № 7 – white matte (Red Fox paint № 1007 (F100));
- sample № 8 – glossy red (paint brand Mobihel Helios № 1015);
- sample № 9 – metallic colors (paint brand Parade R-3012).

Due to the fact that the value of the temperature diagnostic signal for describing the diagnostic system depends on the power of the infrared source, let us represent the test object as system  $A$ , which has  $n$  possible states (states  $A_1, \dots, A_n$ ), and the infrared source as  $B$ , having  $m$  possible states (states  $B_1, \dots, B_m$ ), a diagnostic signal obtained as a result of measurements, can be represented as system  $C$ , which is determined by a combination of states  $A$  and  $B$  ( $C = AB$ ). Then, the value of the diagnostic signal can be represented in the form of a matrix (Table 1):

The presented matrix displays all possible combinations of the colors of the test object with the dif-

Table 1. The matrix of possible states of the diagnostic system

	$B_1$	$B_2$	...	$B_m$
$A_1$	$A_1 B_1$	$A_1 B_2$	...	$A_1 B_m$
$A_2$	$A_2 B_1$	$A_2 B_2$	...	$A_2 B_m$
...	...	...	...	...
$A_n$	$A_n B_1$	$A_n B_2$	...	$A_n B_m$

ferent power levels of the infrared radiation source. At the same time, the implementation of the state of system  $B$  does not affect the probability of the possible state of system  $A$  and vice versa, that is, systems  $A$  and  $B$  are independent. The entropy (degree of uncertainty) of a complex system, a combination of two statistically independent systems  $A$  and  $B$ , is equal to the sum of the entropies of these systems and when combined, the entropy increases or remains the same.

For convenience, we present the combination of  $A$  and  $B$  systems in the form of a generalized system  $D$ .

The probability of a particular state of system  $C$ , having  $k$  possible states (states  $C_1, \dots, C_k$ ) depends on the state in which system  $D$  is located, having  $q$  possible states (states  $D_1, \dots, D_q$ ). Analyzing the change in the surface temperature of the infrared source depending on the color of the test sample (see Table 1), it can be concluded that the reflected heat flow in one way or another, though not to a large extent, affects the infrared source, this means that system  $C$  affects the state of system  $D$ . Then the probability of a possible state of systems  $C$  and  $D$  will be:

$$\sum_{k=1}^r P(D_q / C_k) = 1 [1],$$

where  $P(D_q / C_k)$  is the likelihood of the implementation of the state  $C_k$  at the implementation of the state  $D_q$ .

This equality means that regardless of the implementation of a particular  $D_q$  state, only one of the  $C_k$  states is necessarily implemented. That is, only one of the values of possible diagnostic signals will indicate the presence of a defect in the  $D_q$  system.

The entropy of a complicated system combining two statistically dependent systems  $C$  and  $D$  will be:

$$H(CD) = - \sum_{k=1}^r \sum_{q=1}^s P(C_k) P(D_q / C_k) \times \\ \times [\log P(C_k) + \log P(D_q / C_k)] [2],$$

where  $P(C_k)$  is the likelihood of implementation of the  $C_k$  state.

To evaluate the metal's degree of damage from corrosion, one can use the equations of the catastrophe theory, which allow one to determine the margin of the dimensions of a corrosion defect at a given intensity of its expansion, as well as the most effective

methods for protecting metal products, preventing structural failure and reducing the likelihood of sudden technical system failures.

Samples were exposed to an infrared source. Studies were conducted using a thermal imager according to a one-sided procedure.

## RESULTS AND DISCUSSION

Analysis of the obtained thermograms showed that the thickness of the paintwork practically does not affect the value of the diagnostic signal, and the temperature range corresponding to the subfilm corrosion defect is in the range from 26.2 to 28.5 °C with the temperature of the defect-free surface about 30 °C.

Based on the analysis of histograms of temperature distribution on the sample surface automatically constructed using special software, it is possible to quantify corrosion damage in selected areas of the studied thermograms.

In order to minimize the likelihood of a diagnostic error, are invited to submit the values of the reflected temperature flow from the defects and defects-free in the structural as a coefficient of reflection. The average reflection temperature  $\langle t_{ref} \rangle$  divided by average temperature of the infrared source  $\langle t_s \rangle$  equals coefficient of reflection  $K_{ref}$ .

For inspection objects of different colors, the diagnostic signal from the corrosion damage area is possible according to the value of some indicator  $\delta$ , which is the difference between the conventional unit (100%) and the ratio in percentage terms of the reflection coefficient from the defective surface  $K_{ref}^{def}$  to the reflection coefficient from the defect-free surface  $K_{ref}$ .

The  $\delta$  indicator for each sample has its own value depending on the color (white matte – 1.9; white glossy – 3.6; red – 5.9; black matte – 2.9, black glossy – 3.7; metallic – 10, 9).

In contrast to the thickness of the color paintwork has a significant impact on the value of the diagnostic signal. So, the highest value of the reflection coefficient corresponds to the sample with metallic colored paintwork material, the smallest - to the white matte sample. At the same time, the reflection coefficient of black surfaces is higher than white ones. This is explained by the fact that white surfaces reflect visible light rays well and almost completely absorb infrared.

## CONCLUSION

Obtained in the process of experimental studies of the values of temperature diagnostic signals from corrosion damage corresponding to the specific colors of pain coating engineering products, avoid errors of di-

agnosis and the associated costs of redesigning products, as well as losses caused by the failure of technical system [11]. It should be noted that it is difficult to evaluate this method of the corrosion state of objects with white matte acrylic paint. Therefore, when recognizing subfilm corrosion of such objects, it is advisable to apply alternative physical methods of non-destructive testing (for example, ultrasonic flaw detection).

## REFERENCES

1. **Calabrese L., Brancato V., Paolomba V., Proverbio E.** An experimental study on the corrosion sensitivity of metal alloys for usage in PCM thermal energy storages // *Renewable Energy*. 2019. 138: 1018–1027.
2. **Teixeira A.P., Palencia O.G., Guedes Soares C.** Reliability Analysis of Pipelines With Local Corrosion Defects Under External Pressure // *Journal of Offshore Mechanics and Arctic Engineering* Another reference. 2019. 141(5).
3. **Petrova L.G., Alexandrov V.D., Demin P.E., Kasachev A.V.** Corrosion resistance of parts used for metal structures of bridge structures, and the possibility of improving it by applying zinc-filled coatings // *Bulletin of the Moscow State Automobile and Road Technical University (MADI)*. 2016. 4(47): 49–56.
4. **Petrova L.G., Likhachev T.E., Malakhov A.Yu.** Research complex for monitoring the structural state of structural materials and its use in the analysis of the destruction of steel parts of automobiles // *Bulletin of the Moscow State Automobile and Road Technical University (MADI)*. 2013. 2(33): 11–17.
5. **Zorin V.A., Baurova N.I., Kosenko E.A.** Features of Research on the Thermophysical Properties of Road-Building Materials // *Polymer Science. Series D*. 2018. 11(1): 72–76.
6. **Zorin V.A., Baurova N.I., Kosenko E.A.** Detection of defects in components made of dispersion-filled polymeric materials by the method of infrared thermography // *Polymer Science. Series D*. 2017. 10(3): 241–243.
7. **Moyseychik E.A., Vavilov V.P., Kuimova M.V.** Thermographic Testing of Steel Structures by Using the Phenomenon of Heat Release Caused by Deformation // *Journal of Nondestructive Evaluation Infrared*. 2018. 37(2).
8. **Tabatabaei N.** Applied Sciences (Switzerland) // *Matched-filter thermography*. 2018. 8(4).
9. **Chulkov O.A., Vavilov V.P.** Analysis of the effect of black coating on corrosion detection in aluminum by active infrared thermography // *Bulletin of Siberian science*. 2014. 2: 40–44.
10. **Rudskoy A.I., Kodzhaspirov G.E., Kliber J., Apostolopoulos C.H.** Advanced metallic materials and processes // *Materials Physics and Mechanics*. 2016. 25(1): 1–8.
11. **Kosenko E.A., Zorin V.A., Baurova N.I.** The use of infrared thermography in the recognition of subfilm corrosion // *Corrosion: materials, protection*. 2019. 1: 43–47.

# COMBINED SURFACE MODIFICATION OF STEEL BY ZINC COATING AND NITRIDING

L.G. Petrova, P.E. Demin, A.V. Kosachev, G.Yu. Timofeeva

Moscow Automobile and Road Construction State Technical University (MADI). Moscow, Russia

petrova\_madi@mail.ru

Two methods of combined surface modification of low-carbon steel are studied: 1) application of zinc-filled coatings by painting technique and subsequent gas nitriding; 2) simultaneous thermo-diffusion saturation by zinc and nitrogen. Microstructure and microhardness of steel samples were examined; forming of a transition zone was determined under visually observed surface layer/coating with increased concentrations of Zn and N. Electrochemical corrosion tests have shown that nitriding provides additional protection of zinc-filled coatings; corrosion resistance depends on thickness of a coating, and on the type of a binder (organic or silicate one). Combined saturation by zinc and nitrogen forms diffusion layers with increased wear resistance and reduced friction coefficients together with improved corrosion resistance in salt fog.

**Keywords:** zinc-filled coatings; electrochemical corrosion tests; combined saturation; diffusion layer.

## INTRODUCTION

Corrosion and wear of metal parts and constructions are the main damages limiting their lifetime. Both phenomena are the consequences of metal interaction with external factors, so their appearances depend on composition and structure of metal's surface. Techniques of coatings application and surface modification are widely used for protection as against wear and against corrosion. The problem is that, as a rule, the structure of surface layer increasing wear resistance simultaneously decreases corrosion resistance, and vice versa. Can we receive coatings or layers which influence positively on both wear and corrosion resistance? Some previous results suggest promising solutions on forming of multi-component layers in steels by combined techniques of metallization and nitriding [1–6].

It is known that zinc-based coatings are applied for effective corrosion protection of steel parts and constructions working in corrosive environment of atmosphere, precipitations, humidity, condensed moisture, etc. There are several methods of Zn-based coatings and layers application [7, 8] which can be categorized into two main groups according to the factors of existence or absence of diffusion processes.

The first group includes thermo-diffusion Zn-metallization processes with forming of diffusion layers of gradual structure. Corrosion resistance of such layers is the consequence of protective properties of different Fe-Zn phases. We have supposed that com-

ination of diffusion saturation by zinc with diffusion saturation by nitrogen may influence the structure and phase composition of steel surface layer and may amend wear-corrosion relation.

Processes of application of so called zinc-filled coatings belong to the group of “diffusion-free” processes. Such coatings are applied by painting techniques, for example, by cold Zn-plating, and provide two possible mechanisms of corrosion protection: electrochemical (cathode) mechanism and barrier mechanism of painted films [8]. Protective Zn-filled coatings have a distinct boundary with a steel substrate without enough adhesion. The origin of low adhesion consists in the sharp change of residual stresses at the interface of the coating with metal substrate. To a certain extent, residual stress profile may be described by microhardness gradient in the connection zone. Therefore the control of microhardness gradient across the surface layer may be a tool for prevention of coatings exfoliation. Gradual microhardness profiles are attributes diffusion layers receiving by thermo-chemical treatment (TCT). TCT techniques, such as nitriding, are based on the principles of diffusion saturation; and they form diffusion layers with gradual structural changes. Additionally, nitriding is one of the basic TCT processes for wear resistance increase of different steel parts.

The purpose of the study consists in the investigation of nitriding effect on corrosion and wear resistance of Zn-filled coatings, and in the examination of properties of modified layers received by combined

processes of zinc diffusion metallization with nitriding.

## METHODS OF STUDY

Low-carbon steel 09Mn2Si was used for experimental study. The following specimens of the steel were prepared: 10×10×1 mm for metallographic examinations, 20×40×5 mm for electrochemical tests, and 10×10×10 mm for wear tests. Cylinders samples of 4 mm diameter were used for corrosion tests in a salt fog. All specimens were annealed at 850 °C; the surface was mechanically grinded and degreased.

Two techniques were applied for surface modification of steels:

(1). **Nitriding of zinc-filled coatings.** Zinc-filled coatings were previously applied by cold zinc-plating (painting) technique. Paint mixtures contained fine-dispersed Zn-powder and film-forming substance. Two kinds of film-forming substances were used: organic binder – modified polyurethane, and silicate binder – potassium water glass with the density 1.2 g/cm<sup>3</sup>. Zinc concentration was up to 85 weight % in organic-based mixtures, and up to 75 weight % in silicate-based mixtures. Painted specimens were nitrided in ammonia atmosphere at temperature 540 °C during 24 hours.

(2). **Combined diffusion saturation by zinc and nitrogen.** Specimens were previously covered by slip suspension containing metal zinc powder (25%), quartz sand (70%) as filler, ammonium chloride NH<sub>4</sub>Cl (5%) as a transportation agent, and PVA-glue as a binder. Diffusion saturation was carried out in ammoniac at temperature 600°C during 1–4 hours.

Metallographic examinations of coatings and diffusion layers were made in AXIOVERT 25CA microscope. Auger-spectroscopy (PHI 680) was used for elements concentration analysis. Microhardness tests were carried out by the PMT-3 measurer.

Corrosion tests of specimens were conducted in a salt fog chamber Ascott S120iP in accordance with the ASTM B117-11, and with the GOST 9.401-91 of RF. 5%-solution of sodium chloride (NaCl with pH=6,5) was sprayed inside the chamber by compressed air. Testing temperature was 35 °C, and humidity was 95-100%. Specimens were placed in the chamber below spraying level that excluded direct action of salt solution. Salt fog was condensed at specimens' surface with constant rate; testing time was from 24 to 240 hours. The results of the tests were assessed visually by specific view of corrosion products and by their distribution. Parameters of square of corrosion damage (*S*) after test duration and the time ( $\tau$ ) until so

called "red corrosion" spots appearance were determined and analyzed.

Electrochemical corrosion tests were made according to the method of classical anodic and potentiodynamic (PD) curves tracing in direct and reverse passage (STO 00190242-001-2008 Standard of I.P. Bardin Central Research Institute for Ferrous Metallurgy). 0.5M solution of sulfuric acid H<sub>2</sub>SO<sub>4</sub> was used as test environment. The following parameters of corrosion process were measured: electrochemical potentials of passivation beginning and completion ( $E_p^s$  and  $E_p^e$ ), and passivation interval ( $E_p^e - E_p^s$ ). Additionally parameters of local corrosion evaluation were detected: free corrosion stationary potential  $E_c$  (potential of anodic dissolution beginning), and the maximum value of anodic current density  $i_{max}$ . The higher is the negative value of  $E_c$ , and the lower is the value of  $i_{max}$ , the better corrosion resistance of a tested metal is considered.

Wear tests were carried out by CSMTRB tribometer. Friction coefficients were detected by contact method according to ASTM Standard. Samples were abraded by 3-mm spherical counter-body made of hardened Inox420 steel during their reciprocation. The following test parameters were applied: normal load was 1.5N, maximum linear speed was 6 cm/s; indenter pass amplitude was 6 mm; number of cycles was 4000; the total indenter pass length was 48 m.

Wear parameters ( $W$ , mm<sup>3</sup>/h) were calculated on the basis of tracks volume ( $V$ ) by Tribo4.4U software. Depth and width of tracks were measured by the profilometer "Hommel Tester T8000-RC120-400". Specimens for corrosion and wear tests are marked in the Table 1.

Table 1. Description of specimens for corrosion and wear tests

No.	Description
1	as-received/without treatment
2	nitriding 540 °C/24 h
3	single-layer organic-based Zn-filled coating
4	single-layer silicate-based Zn-filled coating
5	single-layer organic-based Zn-filled coating and nitriding 540 °C/24 h
6	double-layer organic-based Zn-filled coating and nitriding 540 °C/24 h
7	single-layer silicate-based Zn-filled coating and nitriding 540 °C/24 h
8	polyurethane-based hot zinc coating
9	Zn+N diffusion saturation 600 °C/4 h, NH <sub>3</sub>

## RESULTS AND DISCUSSION

### Microstructure of nitrified zinc coatings and layers

After gas nitriding of previously applied zinc-filled coating the film of about 50 microns thickness is observed at the surface having visible boundary with steel substrate. Nitriding activates diffusion processes; this results in the internal sub-layer formation under the coating with increased concentrations of zinc and nitrogen (Fig. 1). This diffusion layer softens the microhardness profile (see curve 1 at Fig. 2). Increased microhardness of the internal part of the layer is the consequence of the solid solution hardening by nitrogen.

Combined process of diffusion saturation of steel by zinc and nitrogen forms modified layer with the thickness up to 100 microns. The layer consists of an external zone of about 30 microns enriched by zinc (up to 80–92% Zn directly at the surface), of a transition zone of 30–40 microns thickness, and of an internal nitriding zone. Due to such structure of the modified layer the microhardness depth profile is gradual (see curve 2 at Fig. 2). Diffusion of nitrogen and zinc occurs at a greater depth than after

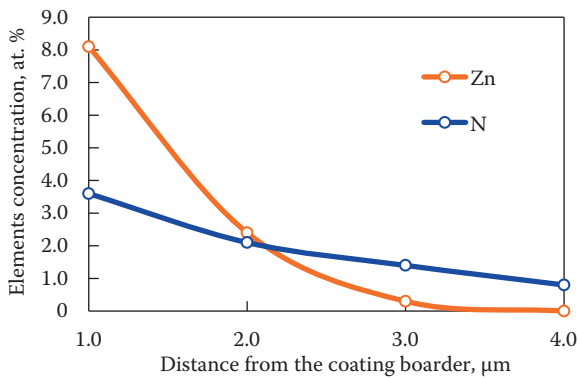


Fig. 1. Zinc and nitrogen concentrations under Zn-filled coating after nitriding

Table 2. Concentrations of elements in transition zone of Zn-N diffusion layer

Depth from the external zone, [microns]	Concentration of elements, [at.%]		
	Fe	N	Zn
5	51.2	10.8	4.5
16	52.5	7.1	0
32	62.9	3.3	0

consequent process (Table 2); and microhardness values are higher.

### Corrosion tests results

It is known that corrosion resistance of zinc coatings depends on the following factors: working temperature, type of corrosive environment (pH parameter), thickness of a coating, zinc concentration in a coating, and a type of a binder (film-former).

Nitriding increases the resistance of zinc-filled coating against electrochemical corrosion (Fig. 3). Increase of  $E_c$  absolute value in 1.5 times and 8...10-fold decrease of  $i_{max}$  value is observed comparing to the parameters for un-nitrified organic-based coating. Minimal current density values are measured for

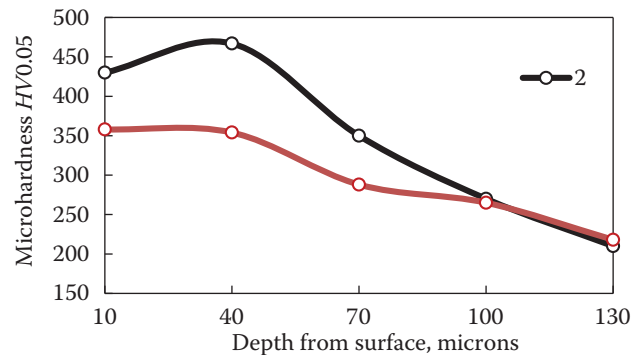


Fig. 2. Microhardness profiles of steel with nitrified zinc-filled coating (1) and with Zn-N diffusion layer (2)

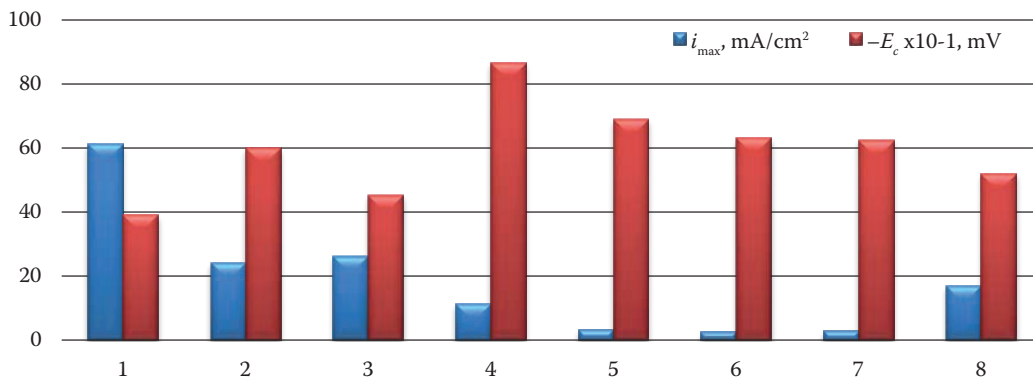


Fig. 3. Corrosion parameters  $E_c$  and  $i_{max}$  for specimens after different treatment modes

nitrided double-layer zinc coating (specimen No. 6). In nitrided silicate-based zinc coating the  $i_{\max}$  value decreases in 4 times; whereas some reduction of  $E_c$  absolute value is observed (specimens No. 4 and No. 7). Corrosion parameters of specimens with nitrided Zn-filled coatings have very similar values independently of the type of a film-former. After the most effective combination of cold zinc plating with nitriding (specimens No. 5, No. 6, and No. 7) 25-fold reduction of the  $i_{\max}$  value is achieved comparing to the value for as-received specimen without treatment, and 6-fold decrease of this parameter is shown comparing to the values for these steel after hot zinc-plating (No. 8).

Comparison of electro-chemical parameters of specimens after different methods of treatment shows that traditional nitriding as well as nitriding of Zn-filled coatings narrows passivation interval of steel in acid environment. While combined diffusion saturation by zinc and nitrogen saves this parameter at the level of untreated steel.

### Wear tests results

Wear tests have shown that nitriding made additionally to Zn-metallization increases wear resistance parameter  $W$  (Table 3). Both processes: nitriding of Zn-filled coatings and combined Zn-N diffusion saturation, result in about similar wear resistance that is 5 times higher comparing to wear parameter of Zn coating without nitriding. But the second process improves time profile of friction coefficient  $\eta$  and decreases  $\eta_{\min}$  and  $\eta_{\max}$  values.

### CONCLUSIONS

Combined diffusion saturation of steel by zinc and nitrogen may be good alternative to zinc-filled coatings for usage in conditions of corrosion and wear. Diffusion layers have proper structure with transition zone/internal nitriding zone of significant thickness. This zone has increased zinc and nitrogen concentration due to the diffusion of the elements under the surface layer. Diffusion layer with transition zone has gradual microhardness profile that decreases residual stress at the boundary with the substrate steel and promote adhesion improvement. Zn+N diffusion layers in low-carbon steel has increased wear resistance and reduced friction coefficients comparing to the parameters of Zn-filled coatings either nitrided or not. Steel with such layers shows significant corro-

Table 3. Wear tests results of steel samples after different treatment modes

No.	Treatment	$\eta_{\min}$	$\eta_{\max}$	V, mm <sup>3</sup>	W, mm <sup>3</sup> /h
4	Zn-filled coating	0.006	0.650	0.330	1.50
7	Nitriding of Zn-filled coating	0.113	0.895	0.056	0.26
9	Zn-N diffusion saturation	0.004	0.320	0.066	0.30

sion resistance increase in salt fog in comparison with un-treated steel. From the other hand, for reasons of maximum improvement of electrochemical corrosion parameters Zn-filled coatings remains more effective.

### ACKNOWLEDGMENTS

*This work was supported by the Russian Science Foundation, project no. 17-19-01473.*

### REFERENCES

1. **Aleksandrov V.A.** Combined TCT process for surface hardening of steels // Metal Science and Heat Treatment. 2010. Vol. 52, No. 5–6. P. 214–218.
2. **Petrova L.G., Aleksandrov V.A., Demin P.E.** Thermo-chemical treatment of steels in plasma of hydrostatic spark discharge // Metal Science and heat treatment of metals. 2012. No. 6. P. 41–46.
3. **Demin P.E., Petrova L.G., Aleksandrov V.A.** Increase of corrosion resistance of steel plugs of the engine by combined aluminum and titanium plating // Hardening technology and coatings. 2013. No. 9. P. 20–33.
4. **Aleksandrov V.A.** Formation of multilayer modified coatings on the surface of steel parts for improvement of performance properties // Hardening technology and coatings. 2014. No. 12. P. 13–19.
5. **Chudina O.V., Petrova L.G., Borovskaya T.M.** Mechanisms of hardening of iron by laser alloying and nitriding // Metal Science and Heat Treatment. 2002. Vol. 44, No. 3–4. P. 154–159.
6. **Petrova L.G., Aleksandrov V.A., Malakhov A.Yu., Zinchenko V.M., Karagodin V.I.** Improvement of Operation Lifetime of Machine Parts with Composite Coatings in Wear Conditions // International Journal of Mechanical Engineering & Technology (IJMET). 2014. Vol. 8, No. 10. P. 855–861.
7. **Subbotina O.Yu., Yaroslavceva O.V.** Features of the application and testing of zinc-rich coatings of various types // Industrial painting. 2007. No. 1. P. 38–44.
8. **Petrova L.G., Demin P.E., Kosachev A.V., Barabanov S.I.** Application of Diffusion Techniques for Formation of Zinc Coatings to Improve Corrosion Resistance of Structural Steels // Polymer Science, Series D. 2017. Vol. 10, No. 2. P. 179–184.

# INFLUENCE OF CONTACT SURFACES ON THE PROPERTIES OF THE TWO-PIVOTAL SYSTEMS

A. Neverov, O. Seliverstova, I. Sergeev

Moscow Automobile & Highway State Technical University (MADI), Moscow, Russia  
neverov\_an@mail.ru

It is carried out theoretical and experimental study of the nonlinear properties of composite pivotal systems with the threaded connection of elements at the low supersonic frequencies in the standing-wave operation. It are obtained expressions for the amplitudes of the highest harmonics, generated by the contact plane. Amplitude of 1-st harmonic, generated by flat dry acoustic contact in the composite pivotal ultrasonic vibratory system, it is proportional to  $n$  degree of the amplitude of the basic driving signal (the fundamental harmonic) and is inversely proportional to  $(n-1)$  to degree of the static force, which tightens the elements of system. It is shown that the acoustic contact in the composite pivotal oscillatory systems with their longitudinal vibrations can be approximated by the concentrated pliability. An experimental study of the threaded connection of waveguides is executed, the satisfactory agreement of theoretical and experimental results is obtained. It is shown theoretically and experimentally that the acoustic contact in the composite pivotal vibratory systems is not linear and can be the source of the higher harmonics.

**Keywords:** surface; rough; bearing curve; pivot; highest harmonics; frequency; contact pliability; effort of the tightening.

## INTRODUCTION

With the calculation of frames the contact between the elements is assumed to be, as a rule, ideal. This assumption, however, can be accepted without the preliminary substantiation only for the permanent connection, when elements are made from one bar of metal. With other methods of connecting in the system appear the parting planes, which can be the sources additional the elastic energy losses [1]. Therefore the concrete calculation of contact conditions of waveguides is necessary with the design of the ultrasonic both measuring [2], and technological equipment [3].

The basic methods of connecting the elements of oscillatory systems are in detail described in [4].

Many publications are devoted to questions of the generation of harmonics by the acoustic contact of rough surfaces (for example, see [5–7]). This contact acoustic nonlinearity on the border of rigid surfaces is considerably more than the nonlinearity, connected with the anharmonicity of intermolecular forces. Therefore it is completely promising for different practical applications, in particular, for control of the natural frequencies of composite vibratory system and of the amplitude of their of vibrations with the resonance, and also for quality control of contact in different technological and monitor arrangements. The studies indicated were conducted in other frequency range in the regime of the traveling wave.

## MODEL OF THE RAPPROCHEMENT OF THE ROUGH SURFACES

Let us examine the dry contact of two flat rough surfaces.

Model “is collected” from the rods of different length, whose distribution is assigned with the aid of the function  $n(\varepsilon)$  – the number of rods, intersected by the section, which corresponds to the relative rapprochement of the surfaces  $\varepsilon$ . It is shown that the contact of two rough surfaces can be described as the contact of the smooth surface of the rough, whose parameters bearing curved  $b$  and  $\nu$  they are determined from the formulas:

$$b = k_{\nu_1,2} b_1 b_2 \frac{(H_{\max_1} + H_{\max_2})^{\nu_{s1} + \nu_{s2}}}{H_{\max_1}^{\nu_1} \cdot H_{\max_2}^{\nu_2}}; \nu = \nu_1 + \nu_2,$$

where  $b_1$ ,  $b_2$ ,  $\nu_1$ ,  $\nu_2$  are the parameters of the bearing curved contact surfaces,  $H_{\max_1}$ ,  $H_{\max_2}$  – are their maximum altitudes of unevennesses,

$k_{\nu_1,2} = \frac{\nu_1 \nu_2}{\nu_1 + \nu_2} \cdot \frac{\Gamma(\nu_{s1}) \Gamma(\nu_{s2})}{\Gamma(\nu_1 + \nu_2)}$ ,  $\Gamma(\nu)$  is the gamma-function.

The model of this rapprochement is given in Fig. 1. Rough surface is simulated by the collection of the uniform rods of different height. This model is physically completely substantiated, since, although the area of the spot of the contact of each separate protrusion increases with the rapprochement of sur-

Правильно?

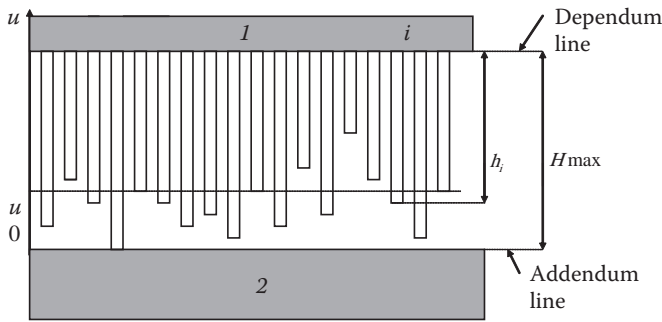


Fig. 1. Pivotal model of the contact

faces, the average area of the spot of contact remains practically constant because into the contact they enter newer and newer protrusions.

Let the smooth surface (lower, marked converges 2) with number with the dependum line of rough surface to the value  $u$  (coordinate  $u = 0$  corresponds to addendum line). it corresponds to addendum line). Dependum line we consider it fixed, her coordinate is always equal  $H_{max}$ . In this case the force, which influences  $i$  the protrusion must be equal

$$F_i = ES_i \frac{h_i + u - H_{max}}{h_i}, \quad (1)$$

where  $E$  is the modulus of elasticity,  $S$  is the sectional area of  $i$ -th protrusion,  $h_i$  is the maximum altitude of the  $i$ -th protrusion of rough surface, which reached smooth.

Expression (1) can be given to the form:

$$F_i = ES_i \frac{x - \varepsilon_i}{1 - \varepsilon_i} \theta(x - \varepsilon_i), \quad (2)$$

where  $x = \frac{u}{H_{max}}$  – the relative rapprochement of

the surfaces,  $\varepsilon_i = 1 - \frac{h_i}{H_{max}}$ ,  $\theta(x - \varepsilon_i)$  – the unit function of Heaviside.

The force, which influences all protrusions of rough surface with its relative rapprochement with the smooth on  $x$ , it will be determined by the summing up of expressions (2) along the entire surface:

$$F(x) = \sum_{i=1}^N ES_i \frac{x - \varepsilon_i}{1 - \varepsilon_i} \theta(x - \varepsilon_i), \quad (3)$$

where  $N$  is the number of protrusions on the contact surface.

Пусть  $n(x)$  is the number of rods, intersected by the section  $u$ . We count the function  $n(x)$  of continuous and monotonic. Then with the displacement of smooth surface on  $dx$  the actual contact area of surfaces increases on

$$dS = S(x)n'(x)dx, \quad (4)$$

where  $S(x) = \sum_{i=1}^{N(x)} S_i$  – the nominal area of the contact,

$n(x)$  – a relative quantity of protrusions, intersected

by the section  $x = \varepsilon$ , function  $n(\varepsilon)$  is the equation of bearing curved rough surface. Substituting sum of (3) by integral, we obtain:

$$F(x) = ES \int_0^x \frac{x - \varepsilon}{1 - \varepsilon} n'(\varepsilon) d\varepsilon. \quad (5)$$

The initial section of bearing curved rough surface can be approximated by the exponential function [8]:

$$n(\varepsilon) = b\varepsilon^\nu, \quad (6)$$

where  $b$  и  $\nu$  – the empirical parameters, obtained by treating the profilograms of the surfaces. Substituting (6) in (5) and representing the denominator of the element of integration in the form of a number, we obtain:

$$F(x) = ESb\nu \sum_{n=0}^{\infty} x^{n+\nu+1} B(n+\nu, 2) = ESb\nu \sum_{n=0}^{\infty} x^{n+\nu+1} \frac{\Gamma(n+\nu) \cdot \Gamma(2)}{\Gamma(n+\nu+2)}, \quad (7)$$

where  $z = \frac{\varepsilon}{x}$ ,  $B(n+\nu, 2)$  is the beta-function,  $\Gamma(n+\nu)$ ,

$\Gamma(2)$ ,  $\Gamma(n+\nu+2)$  – gamma-function from the appropriate arguments.

Using properties of gamma-function and substituting value  $x = \frac{u}{H_{max}}$ , we obtain:

$$F(u) = ESb\nu H_{max}^{-(n+\nu+1)} \sum_{n=0}^{\infty} \frac{u^{n+\nu+1}}{(n+\nu)(n+\nu+1)}. \quad (8)$$

Правильно?

## HARMONIC ACTION ON THE CONTACT

Let us examine the case, when static force  $P$  and law of the vibrations

$$u_{\sim} = u_m \cos \omega t, \quad (9)$$

are assigned, where  $u_{\sim}$  is the current sinusoidal displacement in the contact at the moment of the time  $t$ ,  $u_m$  is the amplitude of vibratory displacement in it,  $\omega$  is the angular vibration frequency.

Then displacement in the contact  $u$  will be the sum of the static displacement  $u_0$  and sinusoidal vibration with the frequency  $\omega$  and the amplitude  $u_m$ . It can be recorded in the form:

$$u = u_0(1 + m \cos \omega t), \quad (10)$$

where  $m = \frac{u_m}{u_0}$ .

We will consider that the contact is not torn up. This is carried out with  $m \leq 1$ .

Force  $F$ , acting in the contact, is also the sum of constant  $F_0$  and variable  $F_m$  of components; moreover variable component is not monochromatic, but it contains as a result of (8) the higher harmonics. Let us try to calculate their amplitudes, for which will substitute (10) in (8) and let us decompose the obtained expression in the Taylor series, who must converge.

$$F(x) = ESb \nu H \max \sum_{n=0}^{\infty} \frac{u_0^{n+\nu+1}}{(n+\nu)(n+\nu+1)} \times \sum_{l=0}^{\infty} \binom{n+\nu+1}{l} (m \cos \omega t)^l, \quad (11)$$

where  $\binom{n+\nu+1}{l}$  are the binomial coefficients.

Being limited in the decomposition (8) by the members of the third order in terms of  $m$ , we obtain:

$$F = F_0 + F_1 \cos \omega t + F_2 \cos 2\omega t + F_3 \cos 3\omega t + \dots, \quad (12)$$

where  $F_0$  – the constant component of force,  $F_l$  – amplitude of the 1-3 harmonics of force, moreover

$$F_0 = ESb \left[ \frac{\varepsilon_0^{\nu+1}}{\nu+1} + \frac{\nu}{4} \varepsilon_0^{\nu-1} \varepsilon_m^2 + \dots \right], \quad (13)$$

$$F_1 = ESb \left[ \varepsilon_0^{\nu} \varepsilon_m + \frac{\nu(\nu-1)}{8} \varepsilon_0^{\nu-2} \varepsilon_m^3 + \dots \right], \quad (14)$$

$$F_2 = ESb \left[ \frac{\nu}{4} \varepsilon_0^{\nu-1} \varepsilon_m^2 + \frac{\nu(\nu-1)(\nu-2)}{64} \varepsilon_0^{\nu-3} \varepsilon_m^4 + \dots \right], \quad (15)$$

$$F_3 = ESb \left[ \frac{\nu(\nu-1)}{24} \varepsilon_0^{\nu-2} \varepsilon_m^3 + \frac{\nu(\nu-1)(\nu-2)(\nu-3)}{384} \varepsilon_0^{\nu-4} \varepsilon_m^5 + \dots \right], \quad (16)$$

We obtain in the first approximation from the expressions (13) and (14):

$$\varepsilon_0 = \left( \frac{P_0(\nu+1)}{ESb} \right)^{\frac{1}{\nu+1}}, \varepsilon_m = \frac{F_1}{ESb} \left( \frac{ESb}{(\nu+1)P_0} \right)^{\frac{\nu}{\nu+1}}. \quad (17)$$

Substituting (17) in the equations (15) and (16), we obtain:

$$F_2 = \frac{\nu}{4(\nu+1)} \frac{F_1}{P} F_1; F_3 = \frac{\nu(\nu-1)}{24(\nu+1)^2} \left( \frac{F_1}{P} \right)^2 F_1;$$

$$F_n = \frac{1}{2^{n-1}(\nu+1)^{n-1} B(n+1, \nu-n)} \left( \frac{F_1}{P_0} \right)^{n-1} F_1. \quad (18)$$

The value of contact pliability is important for calculating the composite vibratory systems. It is possible to determine it from the expression of force for the fundamental harmonic (14);

$$C_1 = \frac{u}{F_1} = \frac{\varepsilon_m H \max}{F_1} \approx \frac{1}{ESb} \left( \frac{ESb}{(\nu+1)P_0} \right)^{\frac{\nu}{\nu+1}} = \left( \frac{ESb}{((\nu+1)P_0)^{\nu}} \right)^{\frac{1}{\nu+1}}. \quad (19)$$

Equivalent pliability, as it follows from (19), it depends on the effort of the tightening of rods. Therefore natural frequencies and amplitudes of the vibrations of composite oscillatory systems on the fundamental harmonic will be also dependent on the conditions of the tightening of their elements.

### EXPERIMENTAL INSTALLATION, THE PROCEDURE OF THE EXPERIMENT

Oscillating the system being investigated (Fig. 2) was two identical package piezo transducers, one transducer was used as source of longitudinal elastic vibrations, and another – as their receiver. The construction of transducers was selected in such a way that they with the calculation could be approximated by the uniform rods. The characteristic impedances of transducers were equal. The natural frequencies of

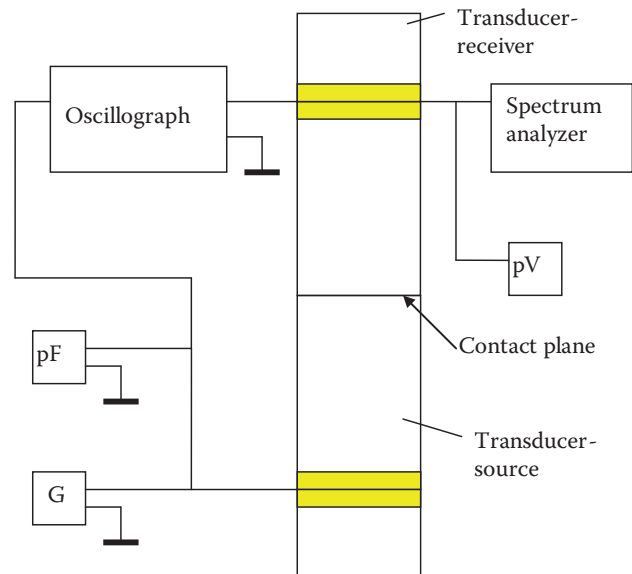


Fig. 2. Schematic diagram of the experimental installation

transducers comprised  $22,60 \pm 0,05$  kHz. For the comparison was investigated the control oscillatory system of the same geometry, as investigated, but without the section of joint, whose frame turned from one bar of the metal.

Transducer – source was attached to the stationary parts of experimental installation in the node of longitudinal displacements. The transducer – receiver was joined to it with the aid of the threaded connection M8'1. The moment of delay was created and was controlled by spring dynamometer on the arm 10 sm. Entire vibratory system was located vertically. Transducer – source was excited by harmonic signal from the ultrasonic generator  $G$ . The frequency of driving signal was determined with the aid of the frequency meter pF. The value of integral output signal was fixed with voltmeter pV. The value of the signal of each separately undertaken harmonic was determined by the spectrum analyzer. The form of input and output signals was controlled on the screen of dual-trace oscillograph.

The breaking in of contact surfaces for the purpose of reaching the equilibrium roughness was conducted prior to the beginning of experiments [8].

With the excitation of the transducer – source by simple harmonic signal the acoustic contact on the border of the transducer – source and transducer – receiver as a result of its nonlinearity generates the signals of the higher harmonics. If the frequency of these harmonics proves to be close to one of the natural frequencies of the system, this harmonic falls into the resonance, its amplitude must be sufficiently great.

## RESULTS OF THE EXPERIMENTS

With a study of the control system of the generation of the higher harmonics it was not discovered.

The experimental dependences of the amplitudes of the first, second and third harmonics of output signal on the effort of tightening the threaded connection of the transducers – source and receiver – and on the amplitude of input signal with the subharmonic excitation are given in Fig. 3a, b, c ( $S$  is the nominal area of the contact of converters).

Should be noted the circumstance that the spread of results in the amplitudes of harmonics with the threaded connection of waveguides is considerably more than with the electromagnetic connection.

In the experiments with the control vibratory system of the generation of the higher harmonics it was not registered, which attests to the fact that the harmonics were generated by contact between the transducers.

The amplitudes of the first  $F_1$  и  $n$ -ing  $F_n$  harmonics and the static effort of the tightening of the rods  $P$  are connected with relationship (18), from where it follows

$$\frac{F_1^n}{F_n} = 2^{n-1}(\nu+1)^{n-1} B(n+1, \nu+n) P^{n-1}.$$

The effort of the tightening  $P$  и turning torque  $M_{kp}$  during assembling of connection are directly proportional, they are connected with known formula N.E. Zhukovskiy [9]:

$$P = M_{kp} \left[ \frac{d_{av}}{2} \operatorname{tg}(\psi + \rho) + f_2 \cdot \frac{1}{3} \frac{d_{in}^3 - d_{out}^3}{d_{in}^2 - d_{out}^2} \right]^{-1},$$

where  $d_{av}$ ,  $d_{in}$  и  $d_{out}$  are average, inside and outer thread diameters respectively,  $\Psi\rho$  is the angle of undercutting the fillets of screw,  $\rho = \operatorname{arctg} f_{\text{TP1}}$  is the angle of friction,  $f_1$  is the coefficient of the friction of the materials, which compose threaded pair,  $f_2$  is the coefficient of friction on the bearing surface.

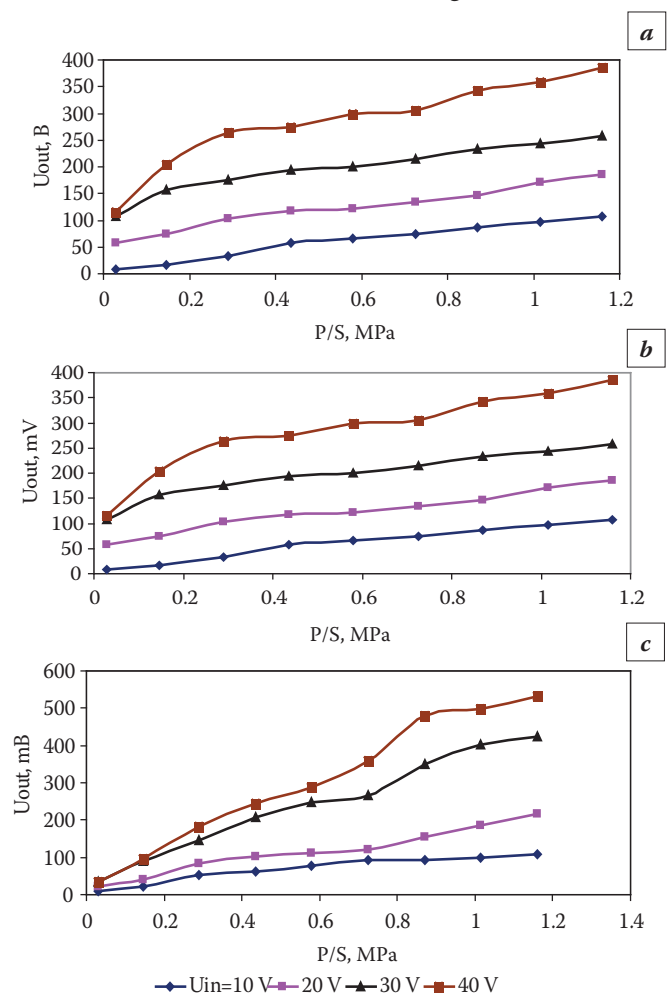


Fig. 3. Dependence of the amplitude of output signal on the effort of the tightening of rods and amplitude of input signal for first (a), the second (b) and the third (c) harmonics;  $S$  – the nominal area of the contact

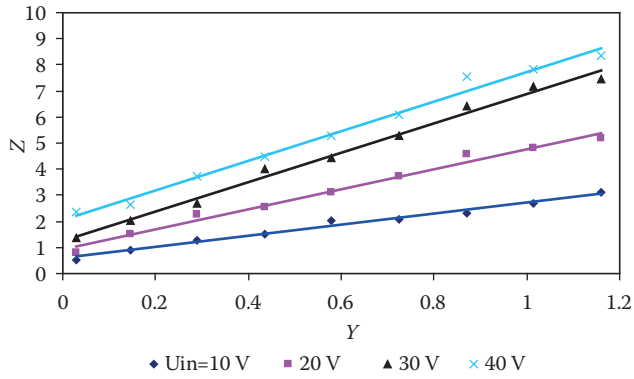


Fig. 4. Dependences  $Z = \frac{U_1^2}{U_3}$  ( $V^2/mV$ )

from  $Y = \frac{P}{S}$  (MPa) for the second harmonic

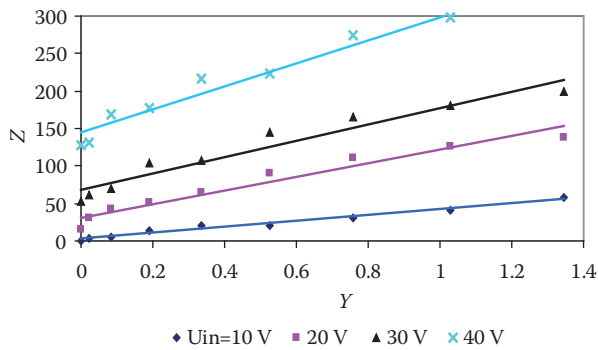


Fig. 5. Dependences  $Z = \frac{U_1^3}{U_3}$  ( $V^3/mV$ )

from  $Y = \left(\frac{P}{S}\right)^2$  (MPa)<sup>2</sup> for the third harmonic

It is obvious that the forces  $F_1$  and  $F_n$  are proportional to the signals of the corresponding harmonics.

In Fig. 4 the dependences are given  $Z = \frac{U_1^2}{U_2}$  ( $V^2/mV$ ) from  $Y = \frac{P}{S}$  (MPa), where  $S$  is the nominal area of the contact, for the second harmonic.

In Fig. 5 the dependences are given  $Z = \frac{U_1^3}{U_3}$  ( $V^3/mV$ ) from  $Y = \left(\frac{P}{S}\right)^2$  (MPa)<sup>2</sup> for the third harmonic.

The carried out constructions show that these dependences are linear with the sufficiently high authenticity ( $R^2 > 0,9$ ).

## RESULTS AND THE CONCLUSIONS

Theoretical studies of the connection of ultrasonic waveguides is executed, it is obtained expression for the amplitudes of higher harmonics and equivalent pliability of the contact.

An experimental study of the threaded connection of ultrasonic waveguides is executed, the satisfactory agreement of the theoretical and experimental results is obtained.

The nonlinearity of acoustic contact in the composite pivotal oscillatory systems with the threaded connection of elements and the possibility of the generation in it of the higher harmonics is experimentally shown.

## REFERENCES

1. **Markov A.I.** Ultrasonic cutting of the hard-to-work materials. M. : Mashinostroenie, 1968 (In Russian).
2. **Kolesnikov A.E.** Ultrasonic measurements. M. : Izdatel'stvo standartov, 1982 (In Russian).
3. **Gladilin A.V.** Inspection of the acoustic contact of piezoelectric ultrasonic transducers with the subject of the study // Issledovano v Rossii. [Internet]. 2000. 3. C. 943.: <http://zhurnal.ape.relarn.ru/articles/2000/65> (In Russian).
4. **Teumin I.I.** Ultrasonic oscillatory systems. M. : Mashgiz, 1959 (In Russian).
5. **Richardson J.M.** Harmonic generation at unbounded interface. I. Planar interface between semi-infinite elastic media // Int. J. Eng. Sci. 1979. Vol. 17, No. 1. P. 73–85.
6. **Buck O., Morris W.L., Richardson J.M.** Acoustic harmonic generation at unbounded interface and fatigue cracks // Appl. Phys. Lett. 1978. Vol. 33, No. 5. P. 371–373.
7. **Solodov I., Döring D., Busse G.** New opportunities for NDT using non-linear interaction of elastic waves with defects / The 10<sup>th</sup> Int. Conf. of the Slovenian Soc. for Non-Destructive Testing. Keynote paper. 16 p.
8. **Kragel'skiy I.A., Dobichin M.N., Kombalov V.A.** Bases of calculations for the friction and the wear. M. : Mashinostroenie, 1977 (In Russian).
9. **Birger I.A., Iosilevich G.B.** Threaded and flange joints. M. : Mashinostroenie, 1990 (In Russian).

## RESEARCH OF SURFACE STRENGTHENED AUTOMOBILE PARTS DURING AUTOMOBILE-TECHNICAL EXPERTISE

A.Yu. Malakhov, T.E. Likhachova, V.A. Perekrestova, A.E. Perekrestov

Moscow Automobile and Road Construction State Technical University (MADI). Moscow, Russia

laromadi@yandex.ru

The article provides examples of research of strengthened surfaces of automobile parts during the automobile-technical expertise at the Institute of automobile-technical expertise of the Moscow Automobile and Road Construction State Technical University (MADI). The authors give the reasons for the failure of parts of modern automobile with a strengthened surface during their work. The article shows examples and causes of destruction of the engine crankshafts, the trailer hitch truck, the clutch support ring and the gear valve mechanism of the engine. These reasons for failure of parts of modern automobile are associated with excessive loads on parts, parts defect in their manufacture or improper assembly (installation).

**Keywords:** the automobile-technical expertise; the strengthened surface; the chemical heat treatment (CTO); the carburizing; the nitriding; the surface hardening with induction heating by high frequency current (HDTV).

### INTRODUCTION

The surface of various parts of modern automobile are subjected to strengthening. Without strengthening the surface of these parts will not be able to work for a long time. For example, the parts of fuel equipment, gear transmission and gearbox, necks crankshafts, cams of the camshafts, the top compression piston rings of the engine, intake, exhaust valve, tie-rod ball and others. In the process of their work in the automobile, they can fail (destruction). The Institute of independent automobile-technical expertise of the Moscow Automobile and Road Construction State Technical University (MADI) is a specially created organization is a specially created organization that has been investigating the causes of failure of parts of modern cars during their operation for more than 20 years. During this time, the Institute of independent automotive expertise has collected a lot of material on various types of technologies used to strengthen the surfaces of parts of modern automobile, as well as possible reasons for their failure (destruction). This article will give examples of studies of only some of the studied at the Institute of independent automotive parts examination of modern cars. This article will give examples of only some of the research conducted at the Institute of independent automotive expertise MADI.

### METHODS OF STUDY

The article gives examples of the study of the causes of failure of the engine crankshafts, trailer hitch truck, clutch support ring and gear valve mechanism of the engine.

The chemical composition of the material of the parts was determined with the use of x-ray fluorescence spectrometer Axios mAX Advanced, production PANalytical (Netherlands) and optical emission spectrometer OBLF QSN 750, production GmbH (Germany).

The surface and core hardness of the parts was determined using a portable dynamic hardness tester NOVOTEST T-UD3, manufactured by NOVOTEST (Russia), stationary hardness tester TK-2M, manufactured by ZIP (Russia) and micro-hardness tester PMT-3M, manufactured by LOMO (Russia).

The microstructure of the material was studied using optical metallographic microscope Neophot-21, manufactured by GmbH (Germany), scanning electron microscope (SEM) JEOL JSM-6480LV, manufactured by JEOL (Japan) and portable digital microscope Levenhuk DTX 500, manufactured by Levenhuk (China).

Chemical heat treatment (CTO) includes thermal and chemical action to change the chemical composition, structure and properties of the surface layer of a metal or alloy. Chemical-thermal treatment is car-

ried out as a result of diffusion saturation of metal or alloy with non-metals (C, N, B, etc.) or metals (Al, Cr, Zn, etc.) at a certain temperature in the active saturating medium [1].

Cementation (carburization) is called CTO, which consists in the diffusion saturation of the surface layer of steel with carbon when heated (more often 900–950 °C) in a carbonaceous medium (carburetor) [1].

Nitriding is CTO, consisting in the diffusion saturation of the surface layer of steel with nitrogen (nitrogen and carbon) when heated in the appropriate medium [1].

The main purpose of surface hardening: increase hardness, wear resistance and endurance limit of the processed product. The core remains viscous and takes the shock loads. In practice, surface hardening with induction heating by high frequency current (HDTV) is more often used. Induction heating occurs due to the thermal action of the current induced in the product placed in an alternating magnetic field [2].

## RESULTS AND DISCUSSION

### Research of the crankshaft № 1

The crankshaft after installation on the engine broke very quickly. The destruction of the crankshaft occurred at one of its connecting rod neck (Fig. 1).

Necks of the crankshaft must be strengthened. Usually, crankshaft necks are strengthened by surface hardening with induction heating with high frequency current (HDTV). Sometimes nitriding of the entire crankshaft is used for strengthening.



Fig. 1. The destruction of the crankshaft № 1

The chemical composition of the material from which the crankshaft №1 is made is presented in Table 1.

The material of the crankshaft № 1 is high-quality medium-carbon steel alloyed with manganese and silicon, with a minimum amount of harmful impurities (phosphorus and sulfur less than 0.025%).

The results of the measurement of the hardness of the surface necks of the crankshaft №1 and its core are shown in Table 2.

The hardness values of the strengthened crankshaft necks after HDTV should be 50...55 HRC. The hardness of the crankshaft № 1 coincides with the hardness of its core and on the average equal to 20 HRC. This means that the necks of crankshaft № 1 have not been strengthened.

The microstructure (ferrite + sorbitol) of the material of the crankshaft neck №1 in its cross section is shown in Fig. 2. The microstructure of the crankshaft neck is the same in cross section and does not change from the core to the surface.

The cause of the destruction of the crankshaft №1 is a defect in its manufacture. Necks of the crankshaft have not been strengthened [3–5].

Table 2. Crankshaft neck hardness and its core hardness (HRC)

Neck number	1	2	3	4	5
Root necks	20	19	20	20	19
Connecting rod necks	19	20	20	19	18
Crankshaft core	20				

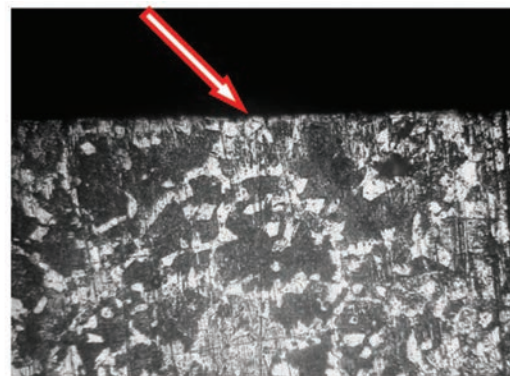


Fig. 2. The microstructure (ferrite + sorbitol) of the material of the crankshaft neck №1 in its cross section. Magnification. × 200

Table 1. The chemical composition of the material of the crankshaft № 1, %

Fe	C	Si	Mn	P	S	Cr	Ni	Cu	Al	Ti	Mo	V
Main element	0.41	0.67	1.45	0.01	0.02	0.24	0.03	0,046	0.014	0.015	0.01	0.15

Table 3. The chemical composition of the material of the crankshaft № 2, %

Fe	C	Si	Mn	P	S	Cr	Ni	Cu	Al	Ti	Mo	V
Main element	0.43	0.25	0.69	0.007	0.015	1.15	0.048	0.05	0.01	0.002	0.37	0.092

### Research of the crankshaft № 2

The broken crankshaft № 2 has longitudinal cracks on the necks (Fig. 3).

The chemical composition of the material from which the crankshaft № 2 is made is presented in Table 3.

The material of the crankshaft №2 is high-quality medium-carbon steel alloyed with manganese and chromium, with a minimum amount of harmful impurities (phosphorus and sulfur less than 0.025%).

The results of the measurement of the hardness of the surface necks of the crankshaft № 2 and its core are shown in Table 4.

The hardness of the crankshaft necks equal to 64 HRC shows that the crankshaft necks have been strengthened.

Table 4. Crankshaft neck hardness and its core hardness (HRC)

Neck number	1	2	3	4	5
Root necks	64	62	64	64	64
Connecting rod necks	63	64	63	63	64
Crankshaft core	22				

The research of the microstructure of the material of the crankshaft neck № 2 over its cross section showed that the crankshaft neck was subjected to quenching with induction heating with high frequency current (HDTV) and then nitriding (Fig. 4).

The cause of the cracks on the crankshaft necks and its breakdown is associated with a violation of the technology of combining hardening with induction heating with high frequency current (HDTV) and nitriding.

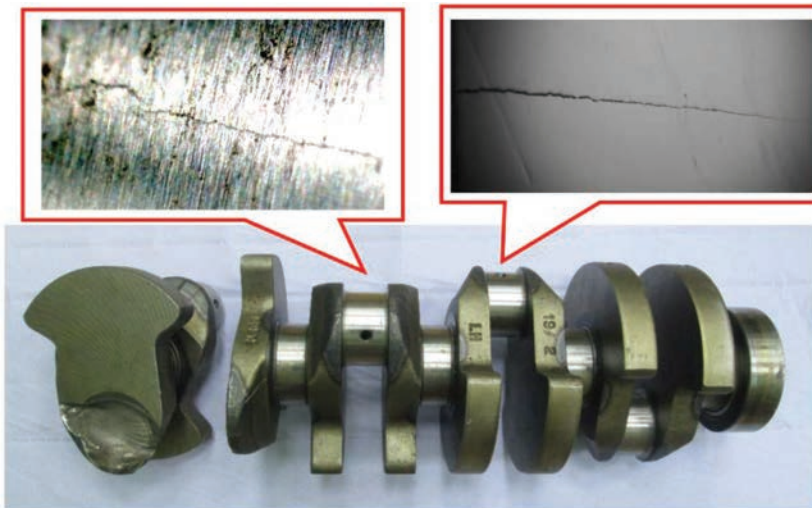


Fig. 3. Longitudinal cracks in the webs of the crankshaft № 2

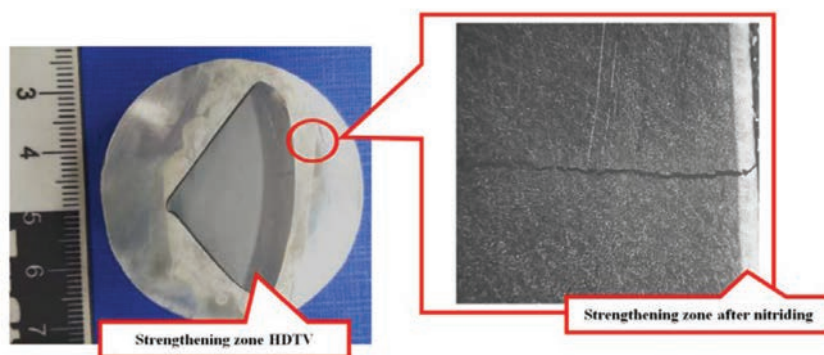


Fig. 4. The research of the microstructure of the material of the crankshaft neck № 2 over its cross section

### Research of the trailer hitch truck

The broken trailer hitch truck is shown in Fig. 5.

The chemical composition of the material from which the trailer hitch truck is made is presented in Table 5.

The material of the trailer hitch truck is high-quality medium-carbon steel alloyed with manganese and chromium, with a minimum amount of harmful impurities (phosphorus and sulfur less than 0.025%).

The results of the measurement of the hardness of the surface trailer hitch truck and its core are shown in Table 6.

The hardness of the surface trailer hitch truck equal to 56 HRC shows that the trailer hitch truck have been strengthened.

The research of the microstructure of the material of the trailer hitch truck hardness over its cross section (Fig. 6) showed that the trailer hitch truck hardness was subjected to quenching with induction heating with high frequency current (HDTV).



Fig. 5. The broken trailer hitch truck

Table 5. The chemical composition of the material of the trailer hitch truck, %

Fe	C	Si	Mn	P	S	Cr	Ni	Cu	Al	Ti	Mo	V
Main element	0.40	0.35	0.85	0.009	0.018	1.08	0.04	0.1	0.05	0.015	0.45	0.065

Table 6. Surface trailer hitch truck hardness and its core hardness (HRC)

Surface trailer hitch truck	56
Trailer hitch truck core	24

The cause of breakdown of the trailer hitch truck is associated with the application of a large load exceeding the strength of the material of the trailer hitch truck.

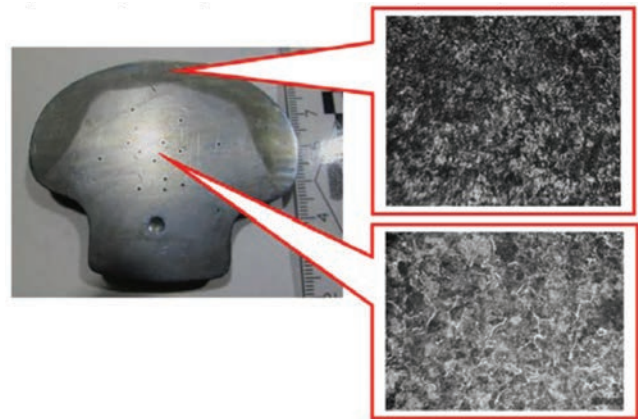


Fig. 6. The research of the microstructure of the material of the trailer hitch truck hardness over its cross section

### Research of the clutch support ring

The broken clutch support ring is shown in Fig. 7.

The chemical composition of the material from which the clutch support ring is made is presented in Table 7. For comparison, Table 7 shows the chemical composition of a similar clutch support ring from another automobile.

As can be seen from Table 7, the material of a clutch support ring is different from the material of a similar clutch support ring from another automobile. The steel from which the similar clutch support ring from another automobile is made has more carbon



Fig. 7. The broken clutch support ring

Table 7. The chemical composition of the material of the broken clutch support ring and similar clutch support ring from another automobile, %

Clutch	The chemical composition, %												
	C	Si	Mn	P	S	Cr	Ni	Mo	Cu	Al	Ti	V	As
Broken clutch support ring	0.065	0.011	0.27	0.011	0.010	0.047	0.036	0.005	0.053	0.046	0.002	0.005	0.008
Similar clutch support ring from another automobile	0.20	0.17	1.19	0.012	0.002	0.92	0.043	0.015	0.040	0.007	0.002	0.005	0.002

Table 8. Surface and core hardness a broken clutch support ring and similar clutch support ring from another automobile (HRC)

Broken clutch support ring		Similar clutch support ring from another automobile	
Surface	Core	Surface	Core
725 HV	127 HV	780 HV	403 HV

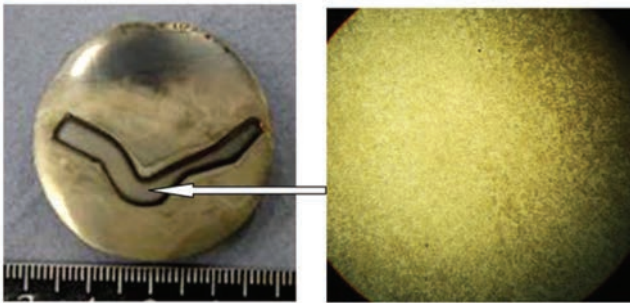


Fig. 8. The microstructure of the broken clutch support ring material

and is alloyed with manganese. This makes this steel more durable.

The results of the measurement of the surface and core hardness are shown in Table 8.

The research of the hardness of the broken clutch support ring showed that the surface of clutch support ring was subjected to cementation (carburization). The core hardness of a broken clutch support ring is much less than the core hardness of a similar clutch support ring from another automobile.

The microstructure of the broken clutch support ring material is shown in Fig. 8. The microstructure consists of almost 100% ferrite.

The reason for the breakdown of the clutch support ring is due to the wrong material for its manufacture. Steel with a very low carbon content was chosen.

### Research of the gear valve mechanism of the engine

The broken gear valve mechanism of the engine is shown in Fig. 9.

The chemical composition of the material from which the gear valve mechanism is made is presented in Table 9.

The gear valve mechanism material is a hard powder alloy based on iron.

The results of the measurement of the surface and core hardness of the gear valve mechanism are shown in Table 10. For comparison, Table 9 shows



Fig. 9. The broken gear valve mechanism of the engine

Table 9. The chemical composition of the material from which the gear valve mechanism is made

Cu	Fe	Cr	Ni	Mn	P	Si	Al	C
%	%	%	%	%	%	%	%	%
2.61	96.42	0.048	0.082	0.162	0.03	0.16	0.11	≈ 1

Table 10. Surface and core hardness a broken gear valve mechanism and similar gear valve mechanism from another automobile (HRC)

Broken gear valve mechanism		Similar gear valve mechanism from another automobile	
Surface	Core	Surface	Core
20...21	20...21	61...62	20...21

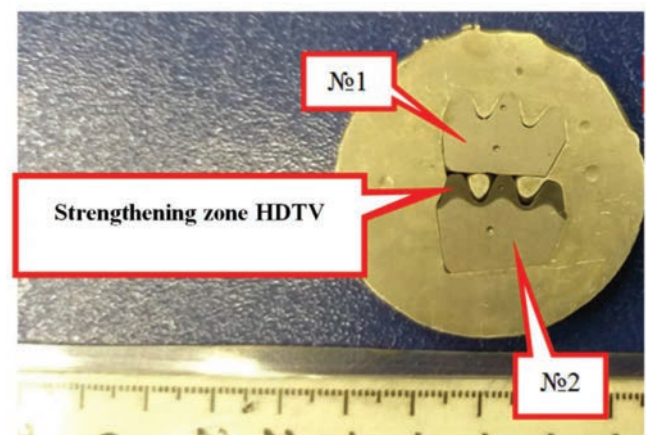


Fig. 10. The microstructure surface of similar gear valve mechanism from another automobile (the sample № 2) and broken gear valve mechanism (the sample № 1)

the chemical composition of a similar gear valve mechanism material from another vehicle.

Measuring the hardness of the broken gear valve mechanism showed that the surface of the gear was not subjected to strengthening. Surface of the similar

gear valve mechanism from another automobile was subjected to quenching with induction heating with high frequency current (HDTV).

The microstructure study confirmed that the surface of similar gear valve mechanism from another automobile (the sample № 2) has a strengthening zone HDTV (Fig. 10). Broken gear valve mechanism (the sample № 1) of the strengthening zone HDTV does not.

The cause of the destruction of the gear valve mechanism is a defect in its manufacture. Surface of the gear valve mechanism have not been strengthened.

## CONCLUSIONS

Given in the article examples of studies of various parts of modern automobile show that the causes of their destruction may be:

- no surface strengthening;
- wrong choice of material for manufacturing;
- a large load exceeding its strength is applied to the automobile parts;

– violation of surface strengthening technology of automobile parts.

## REFERENCES

1. **Lahtin Yu.M.** Chemical heat treatment of metals / Yu.M. Lahtin, B.N. Arzamasov // Textbook for universities. Moscow: Metallurgiya, 1985. 256 p.
2. **Lahtin Yu.M.** Materials Science / Yu.M. Lahtin, B.N. Arzamasov // Study guide for higher technical educational institutions. Moscow: Mashinostroenie, 1990. 528 p.
3. **Malakhov A.Yu.** Diagnostics of the hardened surface of metal products after heat and chemical treatment / Shestopalova L.P., Petrova L.G. // Moscow: Repair, restoration, modernization. 2013. № 2. P. 12–22.
4. **Malakhov A.Yu.** Research complex for monitoring the structural state of structural materials and its use in the analysis of the destruction of steel parts of automobiles / Petrova LG, Lihacheva TE // Moscow: Vestnik MADI, 2013. № 2 (33). P. 11–17.
5. **Malakhov A.Yu.** The use of thin methods of analysis to study the structure of modified layers in steels after heat treatment / Shestopalova L.P., Petrova L.G. // Nelineinyy mir. 2012. № 6. Vol. 10. P. 344–355.

# EFFECT OF FORGING ON CREEP PROPERTIES OF CAST CR BASED STEEL

**Doryun Lee, Dongjun Mun**

POSCO, 6261, Donghaean-ro, Nam-gu. South, Korea  
david2do@posco.com

It is known that high Cr steel is generally excellence on creep characteristics. Therefore, it is widely adopted when it is intended to be used for a long time by various devices of a high temperature annealing furnace. And, it is known that hot forging is also good method for increasing the creep characteristics of steel because of making dense structure. Therefore, in this paper, we conducted the experiment to investigate the creep improvement effect of hot forging of Cr based cast steel. Specifically, we choose KHR20T cast steel (25% Cr based steel alloy) because it is known for excellence in low creep deformation on high temperature. After heating to a specific heat cycle, forging and cooling were performed, and creep tests were performed under high temperature annealing conditions. As a result, it was expected that creep characteristics after hot forging could be improved, but it's not. In this paper, the cause analysis is also included.

**Keywords:** forging; creep; cast; residual stress.

## INTRODUCTION

In general, the annealing furnace should be used for a long time without deformation at high temperature. The creep characteristic is used as the physical parameter that is the basis of deformation judgment in the furnace, and various methods for increasing the creep characteristic are used in the annealing furnace. Basically, it is possible to improve the creep characteristic by cooling [1], and it is also solved by stress reduction by strengthening machinery with the basis of solid mechanics. It can also be solved by using materials with excellent creep property. Case of iron is similar to those described above. Generally, the scattering of the physical properties of steel with rolling process is smaller than cast iron [2–4]. So, we usually use steel with rolling process more than cast iron. However, if a special shape product is needed to be made at low cost, it is made into a cast iron. Even, the dispersion of physical characteristics such as creep becomes larger. In order to overcome this, there have been many researches aiming to reduce the variation or improve the physical characteristics through hot forging [2–5].

In this paper, hot forging, cooling, heating, and creep tests were performed to improve the creep characteristics of cast high Cr – based materials. And the cause of the change were investigated.

## MATERIAL AND EXPERIMENTS

The material used in this study is KHR20T, which is known to have excellent Cr-based creep properties. The chemical composition of this material is as follows.

### Experiment Process

In this study, the experiments were conducted in the same order as in Fig. 1. That is, the same process was performed until air cooling after sand casting. After then creep test were performed with or without hot forging. The purpose of this study is to investigate the effect of hot forging on casted KHR20T material to improve creep performance.

In this process, the target temperature of hot forging was arbitrarily selected at 900 °C and the

Table 1. Chemical Composition of KHR20T

Chemical Composition (%)										
Material	C	Mn	Si	Cr	Ni	Nb	P	S	Ti	Fe
KHR20T	0.432	0.712	1.153	24.15	21.89	0.32	0.025	0.011	–	–

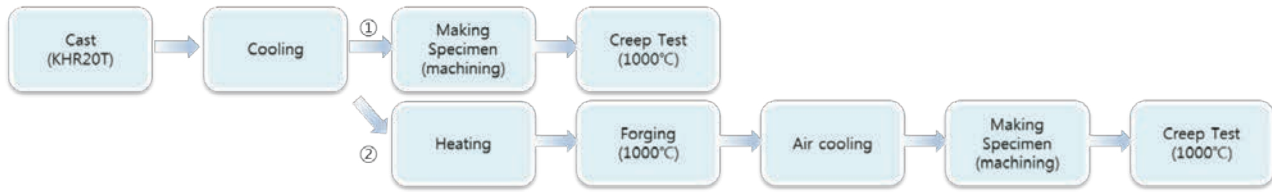
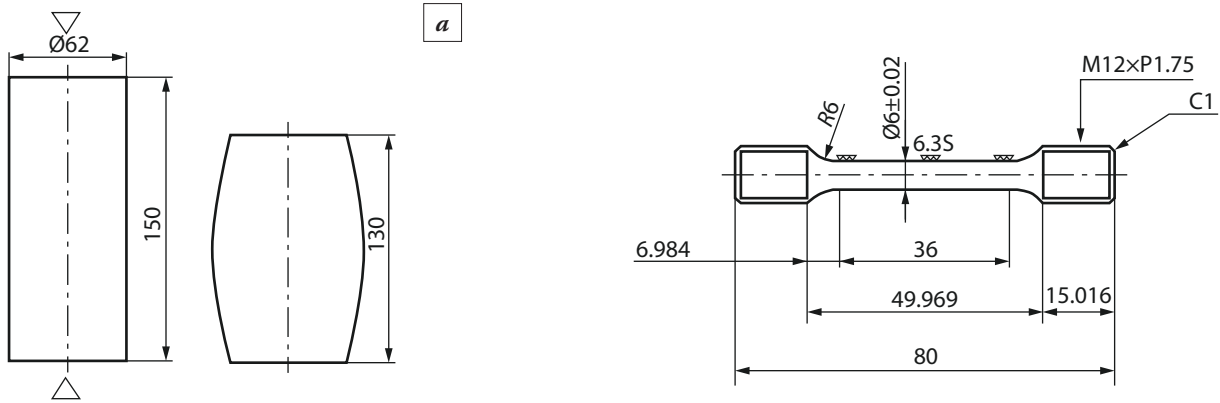


Fig. 1. Process of Experiment

Fig. 2. Shape of Specimens: *a* – Shape of Specimen before and after Forging; *b* – Shape of Final Specimen for Creep test

specimen heated for 2 hours in the annealing furnace. After heating, as shown in Fig. 2*a*, cylindrical specimens were forged at 12% in the longitudinal direction and air-cooled. The temperature and time for forging are shown in Fig. 3. All of the specimens for the creep test were fabricated as shown in Fig. 2*b* at the center of the cylindrical specimen. Creep tests were performed on specimens before and after forging up to 161 hours under the load condition of 20 MPa and 1000 °C temperature condition.

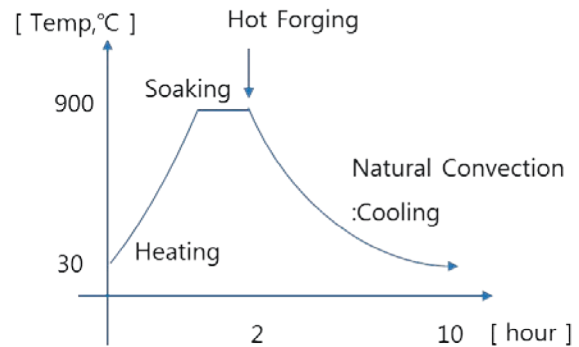


Fig. 3. Forging Process and Pictures

## RESULTS & ANALYSIS

### Creep Test

As a result of creep tests under the same experimental conditions as above, the casting material showed an elongation of less than 0.5% without any problem for 161 hours in only two samples. However, forging materials, all three samples were broken within 24 hours. In other words, under the experimental conditions, the creep performance was decreased due to forging. The detailed results are shown in Fig. 4.

### Residual Stress Analysis

In some of the papers related to forging, residual stress may remain after cooling or heat treatment. And residual stress also may remain in forging itself [6-8]. Since the creep performance may be deteriorated when the residual stress remains in the interior,

it is analyzed based on the simulation whether the internal residual stress is retained in the forging process as compared with the casting material.

First of all, in the case of simulation, the condition is not the same as the actual condition, but the condition is simplified as shown in Fig. 5. It has been performed to analyze how much the residual stress

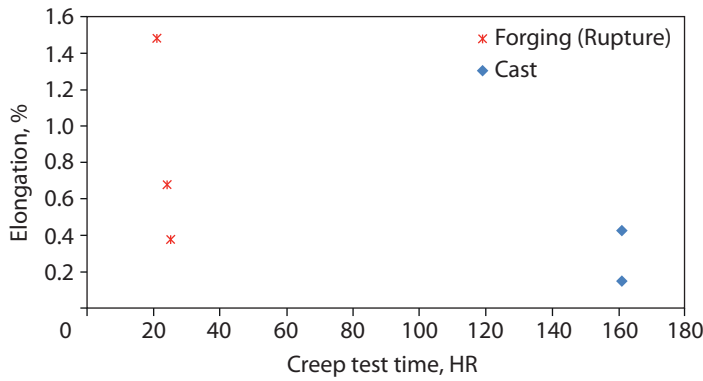


Fig. 4. Creep Test Result

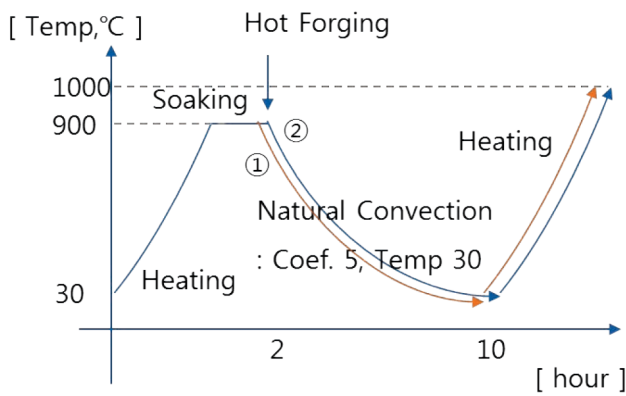


Fig. 5. Simulation Concept

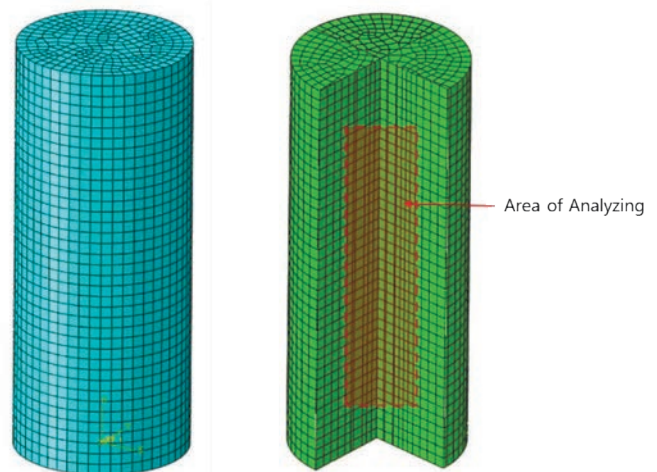


Fig. 6. FEM Modelling and Area of Analyzing

occurs only by hot forging. The specific heat, the thermal conductivity, the thermal expansion coefficient, and the stress-strain curve for each temperature were measured experimentally to proceed the simulation.

Simulation was performed based on FEM. And a commercial software Abaqus 2017 version was used. The modeling shape is shown in Fig. 6, which is the same as the actual specimen shape. In the analysis, it is assumed that the cutting part due to machining is excluded, and it is analyzed based on the data of the center part except for the bottom 10 mm as shown in Fig. 6.

In the analysis of the FEM results, the residual stress in the height direction of the cylindrical specimen, which is considered to affect the creep test, was selected as the analysis parameter. As

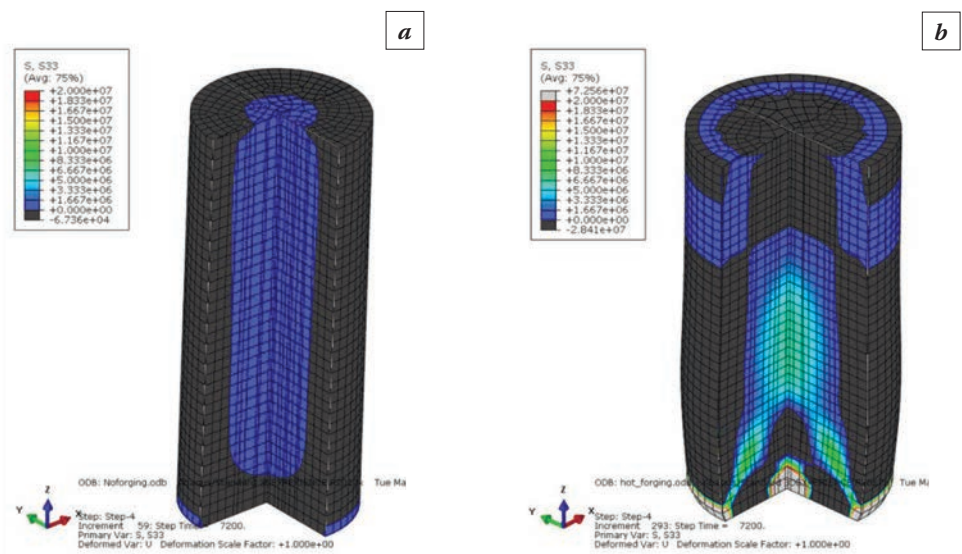


Fig. 7. Stress Result (Z-direction): a – Normal Specimen; b – Forging include Specimen

a result, as shown in Fig. 7 and Fig. 8, it can be seen that the tensile residual stress in the height direction remains less than 1 MPa in the analyzed region. But, The specimens subjected to forging work remained more than 25 MPa. This result can be used as a basis for the forging operation under

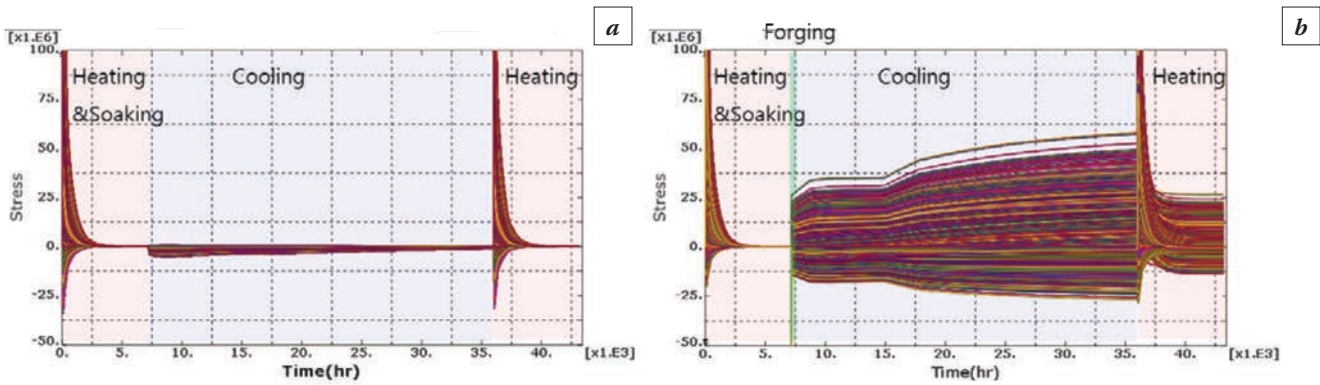


Fig. 8. Stress Result Graph (Z-direction): *a* – Normal Specimen; *b* – Forging include Specimen

the experimental conditions to make the creep performance worse.

In order to verify the validity of the present analysis, the residual stress at the bottom of the forged specimen was measured by the hole-drilling experiment. The center position was machined 0.2 mm to 0 ~ 2mm and analyzed by Uniform Stress method. As a result, we're able to get 60 ~ 99 MPa tensile residual stress data with the radial direction. Comparing with simulation data, it can be considered as valid because we've got approximately 50 MPa tensile residual stress data from FEM analysis.

## CONCLUSION

In this study, hot forging was performed to improve creep performance of KHR20T material, which is known to have excellent creep characteristics and Cr based steel. However, as a result, creep performance with hot forging process deteriorated compared to casting. Based on FEM analysis, it was found that residual stress were caused by unsuitable forging operation. A more optimized forging process may result in dense tissue and decrease creep variation, but further research is needed. As a result, it is difficult to improve the creep performance of this material with this forging process method.

## REFERENCES

1. **Rajendran R.** Creep life prediction of a high strength steel plate // *Materials and Design*. 2008. Vol. 29, No. 2. P. 427–435.
2. **Wei-Di Cao, Xiao-Ping Lu, Jia-Jun Liu.** A Comparative Study of Monotonic Fracture, Environmentally Assisted Fracture and Fatigue Behaviour of Cast and Forged High Strength Steels // *Materials Science and Engineering*. 1984.
3. **Satrio Herbirowo.** Microstructure and mechanical characteristics of hot forged lateritic steels // *MATEC Web of Conferences* 204, 2018.
4. **Uematsu Y.** Effects of HIP and forging on fracture behaviour in cast iron with spheroidal vanadium carbides dispersed within martensitic-matrix microstructure // *Materials Science and Engineering*. 2010. Vol. 527, Is. 10–11. P. 2621–2628.
5. **Morris D.G.** High creep strength, dispersion-strengthened iron aluminide prepared by multidirectional high-strain forging // *Acta Materialia*. 2010. Vol. 58, No. 18. P. 6080–6089.
6. **Bang W., Jung J.Y.** Analysis of Residual Stress Development in Open-Die Forged Axisymmetric Parts Using FEM // *Transactions of Materials Processing*. 2001. Vol. 2001, No. 10. P. 233–235.
7. **Tanner D.A.** Reducing residual stress in 2014 aluminium alloy die forgings // *Materials & Design*. 2008. Vol. 29, Is. 7. P. 1489–1496.
8. **Shiga, Masao.** Improved 12Cr Rotor Forging for Ultra-Super-Critical Steam Turbine // *Journal of the Iron and Steel Institute of Japan*. 1990. Vol. 76, No. 7. P. 1092–1099.

# POSSIBILITY OF NITRIDING TREATMENT OF Si UNDER N<sub>2</sub> ATMOSPHERE PURIFIED BY CaSi<sub>2</sub>

Tsuyoshi Saito, Kento Kurihara, Ryota Gemma

Department of Materials Science, School of Engineering, Tokai University, Kanagawa, Japan  
tsuyoshiSaito\_017@star.tokai-u.jp

In this study, the possibility of nitriding Si (100) substrate via gas phase – solid phase reaction was investigated. Under controlled oxygen partial pressure at laboratory scale, CaSi<sub>2</sub> was employed as an effective trap of impurity gases like oxygen, attempting to initiate nitriding at lower temperatures. The experiments were carried out at different N<sub>2</sub> flow rate, to study possible impact of N<sub>2</sub> flowing rate on nitriding of Si. While flowing N<sub>2</sub> gas throughout the apparatus at different flow rate (60 ml/min. and 180 ml/min.), the Si(100) substrates were heat treated under following conditions; the temperature of the nitrogen purification furnace containing CaSi<sub>2</sub> was kept at 400 °C and the temperature of the nitriding furnace, which is connected right after the purification furnace, was heated to 600 °C. Phase identification, elemental analysis and investigation of the chemical bonding state of the heat treated samples were performed by using XRD, EDX, GI-XRD, and XPS, respectively. The measurement results of XRD, GI-XRD and EDX were independent of the nitrogen gas flow rate. On the other hand, N was detected by XPS measurement in case of the sample treated at lower flow rate (60 ml/min), while the sample treated at higher flow rate (180 ml/min) did not show any sign of nitrogen incorporation. The results obtained here suggests that a Si nitride thin film might be formed under even slower N<sub>2</sub> flow rate.

**Keywords:** nitriding; Si, Si<sub>3</sub>N<sub>4</sub>, CaSi<sub>2</sub>.

## INTRODUCTION

Nitriding treatment is industrially applied as a surface hardening method and is generally used to extend the life of molds<sup>[1]</sup>, transmission gear [2] and cutting tools [3]. Ammonia gas nitriding and plasma nitriding processes are often employed. However, pretreatments are usually necessary and uniform processing is sometimes difficult due to e.g. edge effect. Therefore, if a method for solving such problems can be developed, quality of the nitride industrial products would be improved and the cost would be reduced.

Si<sub>3</sub>N<sub>4</sub> attracts attention as a structural material for high temperature applications due to its good mechanical and thermomechanical properties [4] and thus regarded as a promising tool used in friction stir welding [5] and the material of metal matrix composition [6, 7]. In the industry, sintered bodies of Si<sub>3</sub>N<sub>4</sub> are mainly used as materials for parts such as gas turbines, engines and bearings. Meanwhile, Si<sub>3</sub>N<sub>4</sub> are considered also as an important functional material. Studies have been conducted on the preparation of Si<sub>3</sub>N<sub>4</sub> thin films by plasma chemical vapor deposition [8] and sputtering [9], and they are applied to functional films of large scale integrated circuit [8] and protective films of optical disks [10].

In this study, we investigated the possibility of nitriding Si (100) substrate via gas phase - solid phase reaction under controlled oxygen partial pressure at laboratory scale, with using CaSi<sub>2</sub> as an effective trap of impurity gases like water vapor and oxygen, thereby attempting to initiate nitriding at lower temperatures.

## MATERIALS AND METHODS

Si (100) substrates (15 mm × 15 mm) were cut out from a bare Si (100) substrates and ultrasonically cleaned in acetone for 10 min. and subsequently in ethanol for 10 min. Thereafter, the samples were subjected to nitriding experiment using a set up shown in Fig. 1.

The experimental set up (Fig. 1) in this research consists mainly of a furnace for purification of nitrogen and a furnace for nitriding Si (hereinafter referred to as nitrogen purification furnace and nitriding furnace, respectively). While flowing N<sub>2</sub> gas (purity: 99.99995%) throughout the apparatus, the temperature of the nitrogen purification furnace containing CaSi<sub>2</sub> was heated to 400 °C and the temperature of the nitriding furnace containing Si was heated to 600 °C (When the nitriding furnace was at

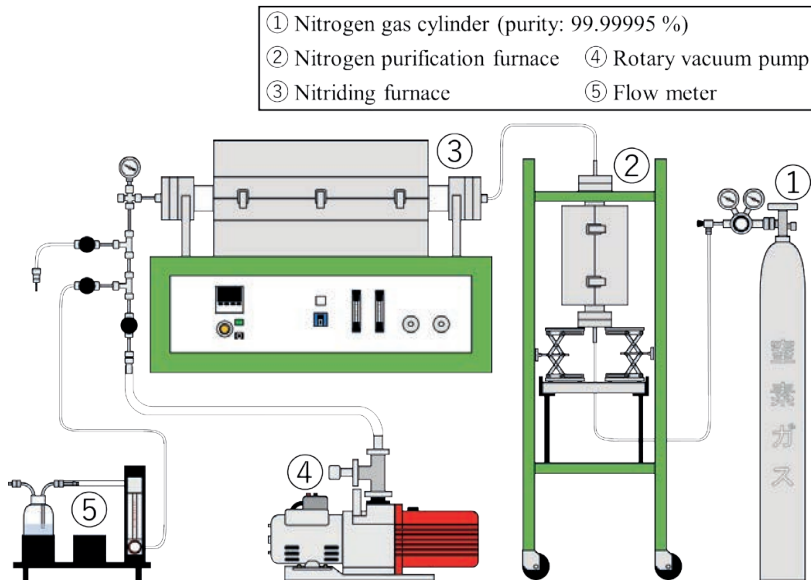


Fig. 1. Schematic diagram of the experimental set up

Table 1. Experimental condition of nitriding

Sample	Sample shape	Sample size	$T_1$ (°C)	$T_2$ (°C)	Retention time, h	Flow rate (ml/min)
Si (100)	plate-like	1.5×1.5	400	600	20	60
Si (100)	plate-like	1.5×1.5	400	600	20	180

200 °C, it was held for 1 hour). After carrying out the nitriding treatment for 20 hours, the samples were furnace-cooled to room temperature.

The experimental conditions of nitriding are summarized in Table 1 ( $T_1$ : maximum retention temperature of nitrogen purification furnace,  $T_2$ : maximum retention temperature of nitriding furnace). In these experiments, the influence of the flow

rate of  $N_2$  gas on the Si substrate was investigated.

Identification of the phase of sample, elemental analysis and investigation of the chemical bonding state were performed by using X-ray Diffraction (XRD, Rigaku, Miniflex600, with  $Cu K\alpha$ ), Energy Dispersive X-ray analysis (EDX, JEOL, JSM-7100F), Grazing Incidence XRD (GI-XRD, PHILIPS, X-pert MRD), and X-ray Photoemission Spectroscopy (XPS, ULVAC-PHI, PHI Quantera 2, with monochromatic  $Al K\alpha$ ) after the nitriding experiment.

## RESULTS AND DISCUSSION

The XRD measurement result of the Si substrate after the nitriding experiment is shown in Fig. 2. As a result of XRD measurement, only the peak of Si (400) was detected independent of the  $N_2$  flow rate. The other peaks found in Fig. 2 are considered as stray X-rays (see the sharpness of these small peaks).

The results of GI-XRD on the Si substrate after the nitriding experiment are shown in Fig. 3. GI-XRD measurement was performed in order to detect surface phase more effectively. However, from the GI-XRD measurement results, a peak of Si (400) was detected and no other phases were clearly found. Furthermore, to the difference of the flow rate was not observed in the diffractograms.

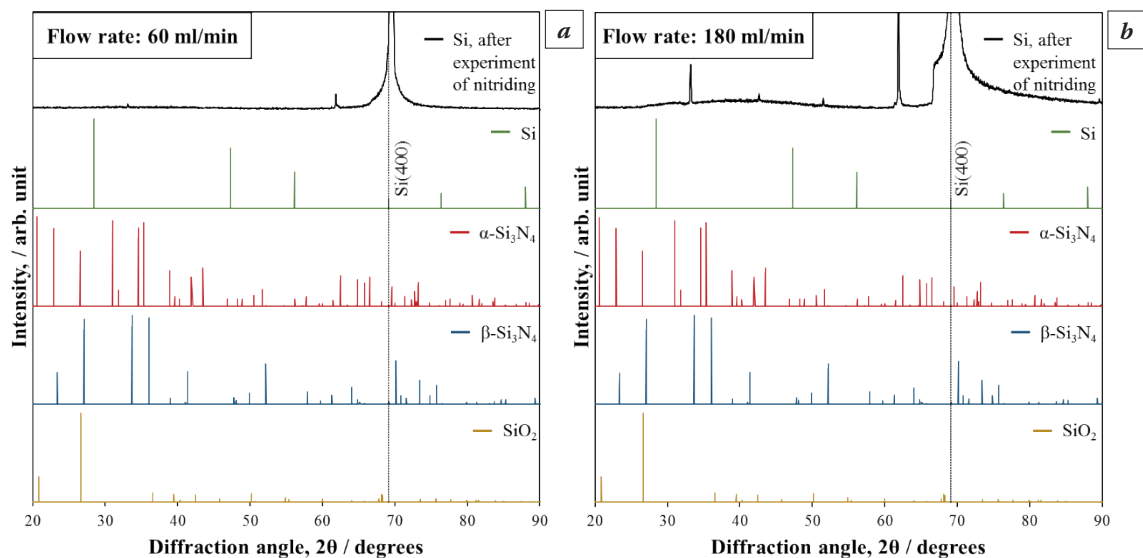


Fig. 2. XRD patterns of Si substrate after the nitriding experiment and each reference profiles of Si [11],  $\alpha$ - $Si_3N_4$  [12],  $\beta$ - $Si_3N_4$  [13] and  $SiO_2$  [14]. *a* – Flow rate: 60 ml/min; *b* – Flow rate: 180 ml/min

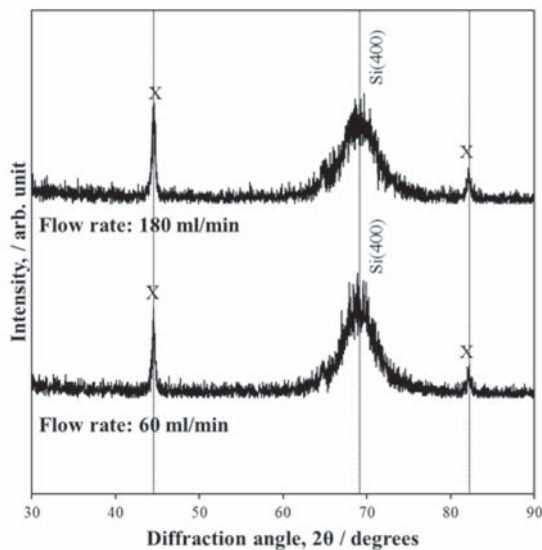


Fig. 3. Comparison of GI-XRD measurement results

The EDX analysis results are shown in Fig. 4. Si, C and O were detected by the EDX analysis. However, N was not detected (see the spectrum in Fig. 4). The impact of  $N_2$  flow rate was not significant, as well as in the XRD and GI-XRD measurement results.

The nitride layer, if any, could be very thin and therefore, the composition and chemical bonding state of elements on the surface of the sample were investigated by XPS. The XPS measurement result of the Si substrate after the experiment of nitriding is shown in Fig. 5. As a result of XPS measurement, a peak indicative of N1s was detected in the sample after the experiment of nitriding performed under lower flow rate of  $N_2$  gas (60 ml/min), while N was not detected on the sample treated at higher flow rate of  $N_2$  gas (180 ml/min).

At lower flow rate, the removal of impurities like  $O_2$  by  $CaSi_2$  could be more effective than the case of

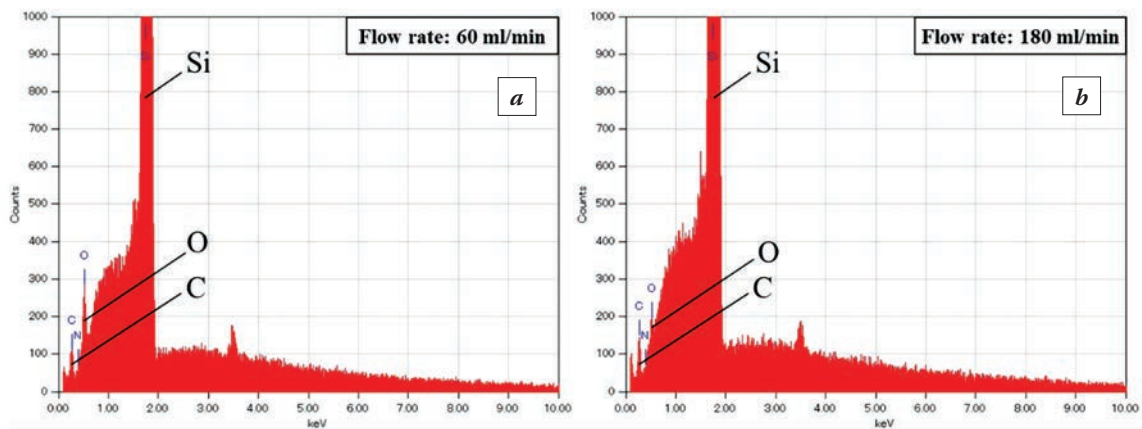


Fig. 4. Comparison of EDX spectra of samples treated at  $N_2$  flow of (a) 60 ml/min, (b) 180 ml/min

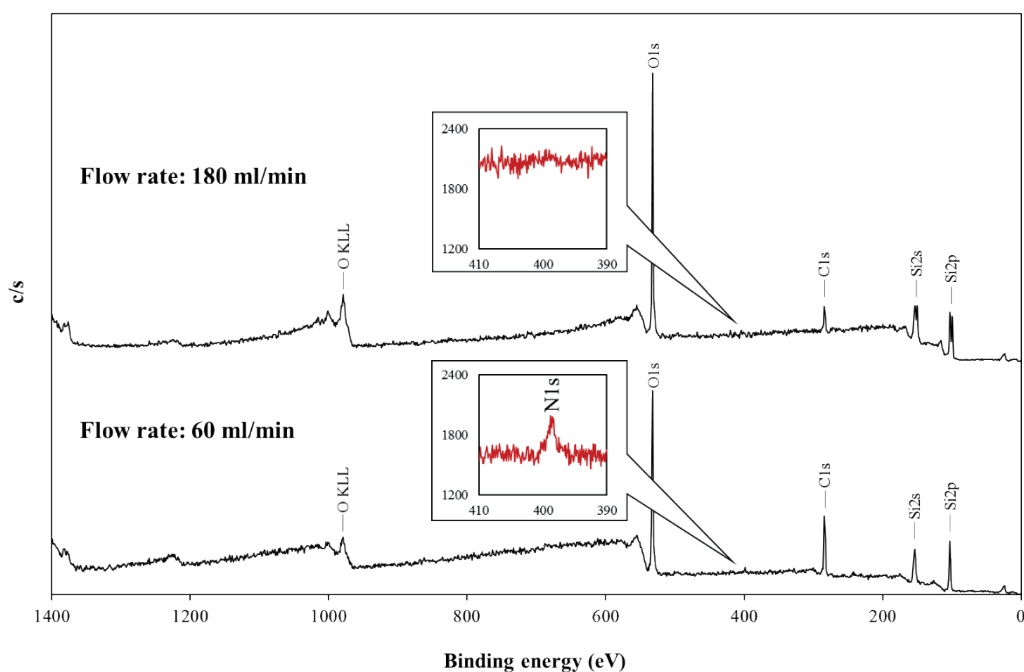


Fig. 5. Comparison XPS spectra. The inset shows the binding energy range comparing N1s peak

higher flow rate and the dissociation of natural oxide layer on the Si (100) surface could have been initiated. This is supported by XPS results obtained in this study.

## CONCLUSION

In this preliminary study, a possibility of surface nitriding of Si (100) was studied. XRD and EDX measurements did not yield clear indication of nitriding. However, XPS analysis of nitride Si (100) treated under low flow rate slightly showed a trend of nitriding, hinting at that even slower flow rate might enhance the expected  $N_2$  purification reaction, thereby initiating the nitriding more effectively.

## ACKNOWLEDGEMENT

Authors would like to thank Mr. Masaki Morikawa at Technology Joint Management Office, Research Promotion Division, Tokai University for his kind help in the XPS measurement.

## REFERENCE

1. **Uehara Naoki, Isokawa Kenji, Sekiya Shigenobu, Kamiya Yukio.** Improvement of Hot-Work Die Life by Low Temperature Gas Carbonitriding Process // DENKI-SEIKO (ELECTRIC FURNACE STEEL). 1977. 48; 4–14.
2. **Umeda Takaaki, Miyabe Kazuo.** Development of Manufacturing Technology for Nitriding Processes Using Nitriding Potential Control // Komatsu technical report. 2014. 60; 17–23.
3. **Takase Takao.** Nitriding of Tool Steel // DENKI-SEIKO (ELECTRIC FURNACE STEEL). 1979. 50; 192–201.
4. **Sasaki Gen, Nakase Hirofumi, Suganuma Katsuaki, Fujita Teruaki, Niihara Koichi.** Mechanical Properties and Microstructure of  $Si_3N_4$  Matrix Composite with Nano-Meter Scale SiC Particles // Journal of the Ceramic Society of Japan. 1992. 100; 536–540.
5. **Young-Gon Kim, In-Ju Kim, Ji-Sun Kim, Jae-Hyun Park.** Mechanical Properties and Tool Life of Friction-Stir-Welded DP590 Using the  $Si_3N_4$  Tool // Materials Transactions. 2014. 55; 1557–1563.
6. **Junichi Hojo, Koji Eto, Motohiro Umezu, Kazushi Kishi, Seiki Umebayashi.** Microstructure and Mechanical Properties of Sintered Bodies of Fine Powders in  $Si_3N_4$ -TiN System // Journal of the Japan Society of Powder and Powder Metallurgy. 1998. 45; 25–30.
7. **Kumar J.Pradeep, Robinson D.S. Smart, Chithirai Pon Selvan.** Experimental Evaluation of Strength and Wear Rate of AA7075/TAC/ $Si_3N_4$ /Ti Nano Hybrid Metal Matrix Composite // International Journal of Mechanical Engineering and Technology. 2018. 9; 1690–1698.
8. **Kobayakawa Mikiko, Tanemura Seita, Niwa Hiroaki, Saitoh Kazuo.** Silicon Nitride Coatings Prepared by Low Pressure Plasma CVD // Journal of the Vacuum Society of Japan. 1988. 31; 167–173.
9. **Shimamoto Naonobu, Hirohata Yuko, Hasiba Masao, Hino Tomoaki, Yamashina Toshiro, Yabe Katsumasa.** Preparation of Silicon Nitride Film by Sputtering Method (II) -Properties of Film Structure // Journal of the Vacuum Society of Japan. 1993. 36; 212–214.
10. **Katsuda Shinichi, Kawanishi Yoshitaka.** Stability on SiN Thin Films Prepared by Reactive Sputtering // Journal of the Ceramic Society of Japan. 1992. 100; 134–137.
11. **Weitzer F., Remschnig K., Schuster J.C., Rogl P.** Phase equilibria and structural chemistry in the ternary systems M-Si-N and M-B-N (M= Al, Cu, Zn, Ag, Cd, In, Sn, Sb, Au, Tl, Pb, Bi) // Journal of Materials Research. 1990. 5; 2152–2159.
12. **Riello Pietro, Canton Patrizia, Fagherazzi G.** Calibration of the Monochromator Bandpass Function for the X-ray Rietveld Analysis // Powder Diffraction. 1997. 12; 160–166.
13. **D du Boulay, Ishizawa Nobuo, Atake T., Streltsov V., Furuya Kenji, Munakata Fumio.** Synchrotron X-ray and ab Initio Studies of Beta- $Si_3N_4$  // Acta Crystallographica Section B Structural Science. 2004. 60; 388–405.
14. **Keith H.D., Wills H.H.** Lattice Spacings in Clear Crystalline Quartz and Their Variability // American Mineralogist. 1955. 40; 530–534.

# HISTORY OF AVIATION BEARING STEELS DEVELOPMENT AND ITS HEAT TREATMENT

T.M. Pugacheva

OJSC «YPC SAMARA» – Samara State Technical University, Samara, Russia  
t.pugacheva15@yandex.ru

With the increase in the aircraft engine power the more stringent requirements for reliability and durability in conditions of constantly increasing speed, temperature and load capacity to the bearings have been applied. This led to the need for continuous improvement of aviation bearing steels in composition, quality and heat treatment technology. The paper presents an overview of the history of the domestic and foreign steels development in combination with its heat treatment starting from volumetric hardened grades of type ShH15, 52100 and heat resistant – 8H4V9F2, VKS241, M50, carburized grades of type 20KH2N4A, M50NiL, nitrided – 32CrMoV13, M50 and ending with subjected to a duplex chemical heat treatment hardened (carburization+nitriding) M50NiL steel.

**Keywords:** aviation bearings; steel; heat treatment; carburization; nitriding; duplex hardening.

## INTRODUCTION

Aviation bearings operate at very high contact stress combined with shock loads, vibrations, exposure to aggressive environments and elevated temperatures. In order to satisfy strict and constantly increasing operational requirements, special steel groups with appropriate heat treatment were developed [1–4]. The following parameters as non-metallic inclusion purity, macrostructure density, as well as carbide and microstructural uniformity are of particular importance for bearing steels. Therefore, the bearing steel melting technology has also constantly being improved. Now, as a rule, additional vacuum remelting or electroslag+vacuum arc remelting have carried out. Until recently, low-alloyed high-carbon (type IX15, 52100) and low-carbon, carburized (type 20X2H4A, M50NiL) steels and heat-resistant steels (like EI347, M50) [1–6, 10, 12] were the most widely used for aviation bearings. (The class of corrosion steels in the article is not considered.)

## MATERIALS AND HEAT TREATMENT TECHNOLOGY OF AVIATION BEARINGS

Since the beginning of the last century, for rolling bearings relatively inexpensive high-carbon chromium steel (~ 1.0% C, ~ 1.5% Cr) has used. To increase mainly hardenability such alloying elements as silicon, manganese

and molybdenum have added. The most common grades are ShH15, ShH15SG and foreign analog – 52100 (Table 1).

To ensure good machinability, as well as to prepare the structure for hardening heat treatment, these steels in the initial state should have a granular (fine-grained) perlite structure with a hardness of HB 179–207 for ShKh15 or HB 179–217 ShH15SG. The structure does not allow large grains and cementite mesh [1, 2, 4, 7]. The required structure is formed by spheroidization annealing with heating to temperatures of 780–800 °C and subsequent slow cooling. The final heat treatment consists of volumetric hardening from temperatures 820–860 °C (the lowest temperatures refer to small sizes details, and the highest-to large ones) in oil with temperature 30–60 °C (large balls-in a soda solution) and the subsequent cooled down to 20–25 °C and low tempering at temperatures of 150–160 °C for ShH15 and 165–180 °C – for ShH15SG. The formed structure of the latent crystalline or small-crystalline martensite with spherical evenly distributed carbide particles and insignificant

Table 1. Chemical composition of high carbon chromium steels

Grade	Element, % mass			
	C	Cr	Mn	Si
ShH15 (GOST 801)	0.9–1.05	1.3–1.65	0.2–0.4	0.17–0.37
ShH15SG (GOST 801)	0.9–1.05	1.3–1.65	0.9–1.2	0.40–0.65
52100 (ASTM A295)	0.8–1.1	1.3–1.6	0.25–0.45	0.15–0.30

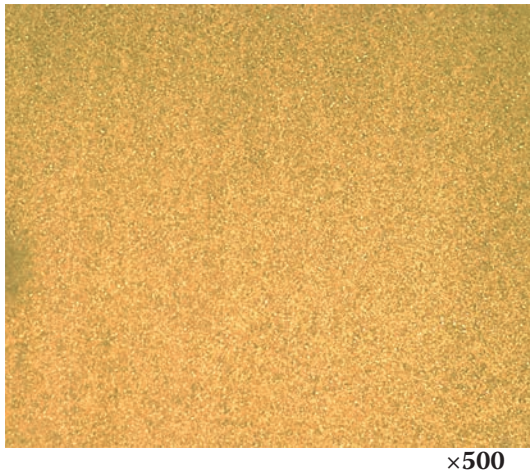


Fig. 1. Microstructure of hardened ShH15 steel

quantity of residual austenite (Fig. 1) should have uniform high hardness 60–65 HRC throughout the bearing part sections. This achieves high contact strength and wear resistance, as well as dimensional stability of parts, which is also important in ensuring the reliability and durability of the bearing. To reduce residual stresses after grinding and finishing additional tempering at temperatures below the main one is carried out.

Possessing high hardness and durability high-carbon chromium steels have low impact viscosity, therefore in dynamic loading conditions bearings other material- case carburized steels was required. These steels have low carbon content (~0.2%) and contain such alloying elements as chromium, manganese, titanium or chromium and nickel, or nickel and molybdenum or only chromium. The chromium-nickel steel of the 20X2N4A grade (abroad use steel 4320, 9310) is the most widespread (Table 2).

To obtain a fine-grained structure and improve machinability cutting normalization at 900–920 °C and tempering at 640–660 °C or only one tempering carry out before the carburization. The formed structure is globular sorbite with hardness not more than HB 241. Hardening heat treatment includes carburization at 930–950 °C (at gas environment) or 1040–1050 °C (at vacuum), high tempering at 600–640 °C during 4–6 hour to reduce the residual austenite amount and subsequent quenching from tem-

peratures of 780–800 °C in oil [7]. The final operation – low tempering at 160–200 °C. The optimum structure of the hardened case is provided at saturation of a surface layer by carbon not more than 0.8–1.0% and is hidden or small-needle martensite (Fig.1). In the hardened case the carbide mesh and large isolated carbides are not allowed. Low-carbon tempered martensite is formed in the core. The surface hardness is 58–62 HRC, core hardness – 35–45 HRC. The grinding stresses take off additional tempering at 120–140 °C. The increased durability of bearings made of case carburized steel in comparison with the first group's steels is largely achieved by forming residual compressive stresses in the hardened surface layer. Optimized residual compressive stresses, on the one hand, lead to lower surface stresses, and on the other hand, prevent cracking.

However, neither high-carbon chromium or low-carbon case carburized steels cannot provide sufficient aviation bearing life of in elevated temperature conditions as they begin to be intensively read out when heated above 200 °C. In this connection, it was required to become with increased heat resistance. At first [2, 5] at us and abroad used high-alloyed high-speed steels R18 and R9 (foreign analogues are T1, M1, M2, M10), and then domestic bearings began to make mainly from tungsten containing 8X4V9F2 steel, and foreign ones – from molybdenum containing non-tungsten M50 steel (Table 3). At present to ensure high metallurgical quality, domestic steel is subjected to electro-slag or/and vacuum-arc melting, and M50 is melted in vacuum induction furnaces fol-



Fig. 2. Microstructure of the hardened case 20H2N4A steel

Table 2. Chemical composition of carburized steels

Grade	Element, % mass					
	C	Si	Mn	Cr	Mo	Ni
20H2N4A (GOST 4543)	0.16–0.22	0.17–0.37	0.3–0.6	1.25–1.65	–	3.25–3.65
4320 (ASTM A837)	0.17–0.22	0.15–0.30	0.45–0.65	0.4–0.6	0.2–0.3	1.65–2.0
AISI 9310	0.08–0.13	0.15–0.30	0.45–0.65	1.00–1.40	0.08–0.15	–

Table 3. Chemical composition of heat-resistant steels

Grade	Element, % mass							
	C	Cr	Mo	W	V	Mn	Si	Ni
8H4V9F2 (TU 14-1-2244)	0.7–0.80	4.0–4.6	0.30	8.5–9.5	1.4–1.7	0.4	0.4	0.35
M50 (AMS 6491)	0.8–0.85	3.75–4.25	4.0–4.50	–	0.9–1.10	0.15–0.35	0.25	–

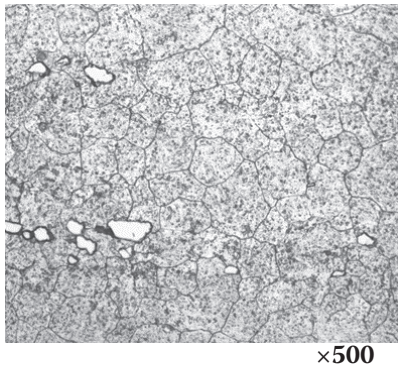


Fig. 3. Grain variety of 8X4V9F2 steel

lowed by single or multiple vacuum-arc remelting (VIM-VAR technology).

Heat treatment of 8X4V9F2 steel at the preliminary stage includes full annealing at 800–860 °C or isothermal annealing with exposure at a temperature of 700–750 °C followed by slow cooling. The resulting structure is fine-grained perlite and excess carbides with a hardness of HB 207–255. The hardening heat treatment consists of heating up to temperatures of 800–830 °C, subsequent heating up to 1200–1240 °C and oil quenching. Then it follows by 2–3-times tempering at temperatures of 565–580 °C with air cooling after each tempering. Instead of continuous cooling with the purpose of warping and residual stresses reduction it is possible to apply step hardening with endurance at 400–600 °C. However, the reduction of cooling rate during quenching weakens the effect of secondary hardening due to the impoverishment of austenite tungsten [8]. 8X4V9F2 steel is characterized by a grain variety – the individual grain growth on a fine-grained background (Fig. 3), which is manifested even with relatively short-term heating and increases with the heating duration. Therefore it is necessary to assign hardening heat temperature for each melting and apply as short as possible endurance. Carrying out of repeated tempering for 8X4V9F2 steel, as well as for other high-speed steels, is associated with necessity to reduce residual austenite quantity to the minimum possible level. The microstructure (Fig. 4) formed after heat treatment should be a small-

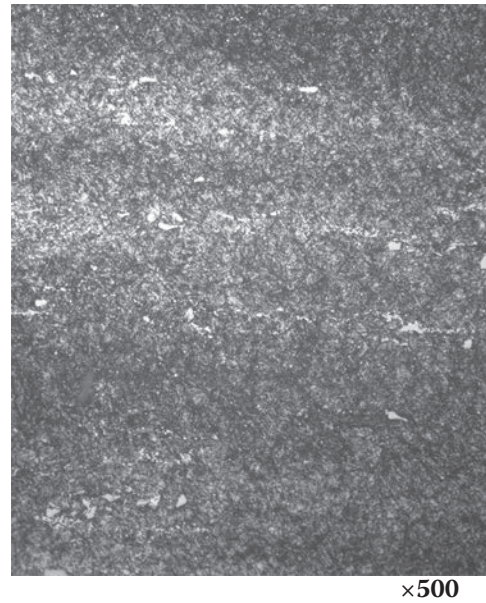


Fig. 4. Microstructure of hardened 8X4V9F2 steel

needle martensitic matrix with carbides and should have a hardness of 60–65 HRC.

The disadvantage of 8H4V9F2 steel is high carbide heterogeneity (Fig. 5), which is extremely unfavorable for bearings due to the chipping of particles during operation. The new heat-resistant volumetric hardened bearing steel 8H5M3VFB (VKS 241) (Table 4) with additives of molybdenum, niobium and tantalum, developed in VIAM [9, 10], contains considerably less quantity of tungsten and more homogeneous distribution of carbides (Fig. 6) comparing to 8H4V9F2 steel. At present, this steel is undergoing experiment-industrial testing.

In foreign practice in addition to the above-mentioned steel grades for high-speed aerospace bearings carburized M50NiL steel [6], which was developed in

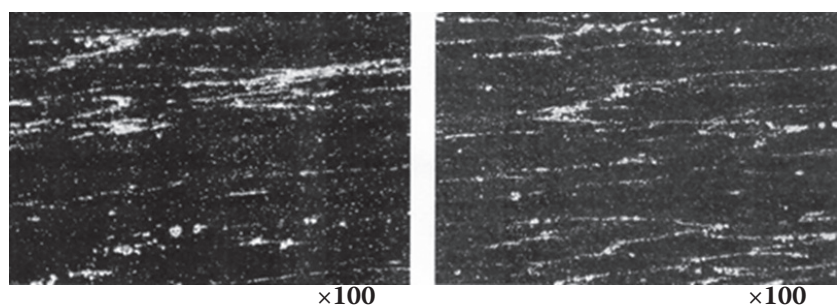


Fig. 5. Carbide heterogeneity of bar Ø85 mm from steel 8H4V9F2-Sh

Table 4. Chemical composition of 8H5M3VFB-VI (VKS241-VI) steel

Element, % mass									
C	Si	Mn	Cr	Ni	Mo	V	W	Nb	Ta
0.80–1.10	0.30–0.50	0.10–0.40	4.50–5.50	0.15–0.40	3.00–3.50	0.50–1.00	1.00–1.50	0.10–0.30	0.05–0.15

Table 5. Chemical composition of M50NiL steel

Element, % mass							
C	Cr	Mo	W	V	Mn	Si	Ni
0.11–0.15	4.00–4.25	4.00–4.50	≤ 0.25	1.13–1.33	0.15–0.35	0.10–0.25	3.20–3.60

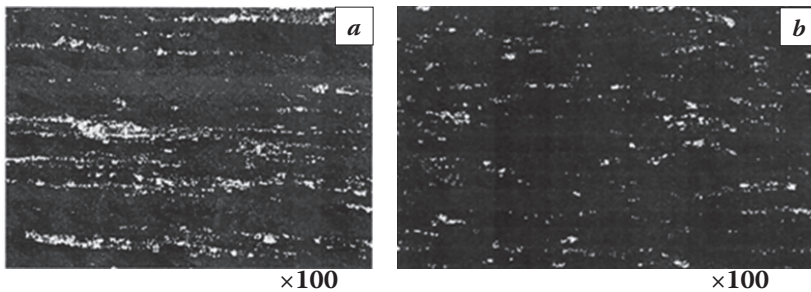
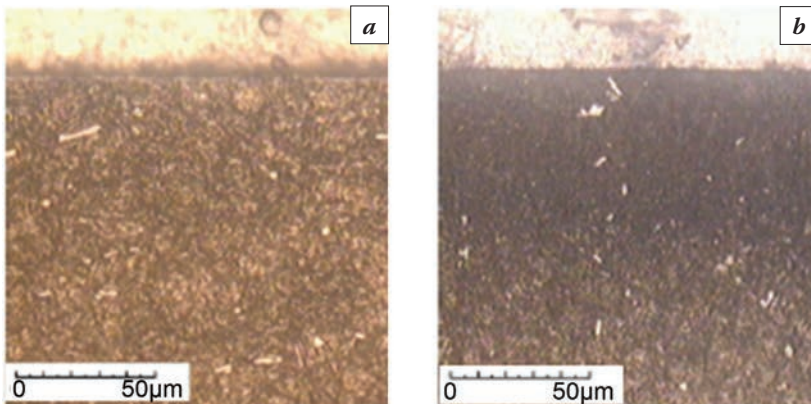
Fig. 6. Carbide heterogeneity of bar  $\varnothing 55$  mm and  $\varnothing 45$  mm from steel 8H5M3VFB-VI (VKS241-VI)

Fig. 7. Microstructure of standard (a) and duplex (b) hardened M50 steel [7]

the 1980, is widely used (Table 5). The composition of M50NiL steel has a lower carbon content compared to M50 and a high nickel content and a little vanadium. With proper carburization and heat treatment, this steel is characterized by high wear and fatigue resistance in combination with high fracture toughness of the core. Formed during heat treatment the significant residual compressive stresses in the case hinder or even stop the cracks growth and that provides an increased bearing life. Present research in the field of heat treatment with the purpose to increase durability and reliability of aerospace bearings working at high temperatures, speeds and loads, is connected with using of ion-plasma nitriding after standard hardening and tempering and with double

processing, combining carburization and nitriding [7, 11].

Nitriding in comparison with the carburization usually provides a higher surface hardness and forms higher residual compressive stresses in the case, which should increase wear resistance in sliding conditions. In addition, since nitriding is carried out at a relatively low temperature (480–550 °C) without subsequent heat treatment, it practically does not cause distortion of size and shape and maintains the state stability in time and at heating. According to [7], hardening consisting of plasma nitriding of standard hardened M50 steel and carburized M50NiL steel, significantly increases the bearing life in conditions of full and boundary lubrication, contaminations and at damage on the working tracks. Microstructure of standard and duplex hardened M50 steel is shown in Fig. 7. Studies have shown that in the same test conditions the shortest service life has M50 steel, the service life of the carburized M50NiL steel about 5 times higher,

even more durability in case of duplex hardening of M50 steel, and none of tested bearings made of duplex hardened M50NiL steel fail until the test was suspended (1500 hours).

In work [11] is shown, that rolling bearing fatigue resistance of nitriding 32CrMoV13 VIM-VAR (AMS 6481) steel (Table 6) is better, than at M50 and M50NiL steel, including at boundary and polluted greasing. After hardening and tempering at 625–650 °C on hardness of 380–420 HV and subsequent nitriding at 525–550 °C on depth of layer 0.55–0.75 mm surface hardness made 730–830 HV<sub>30</sub>, residual compressive stresses at depth of 200–400  $\mu$ k – order-500 MPa. After the nitriding process, the diffusion layer microstructure consists of the tempered

Table 6. Chemical composition of steel 32CrMoV13 (AMS 6481)

Element, % mass					
C	Cr	Mo	V	Mn	Si
0.29–0.36	2.80–3.30	0.70–1.20	0.15–0.35	0.40–0.70	0.10–0.40

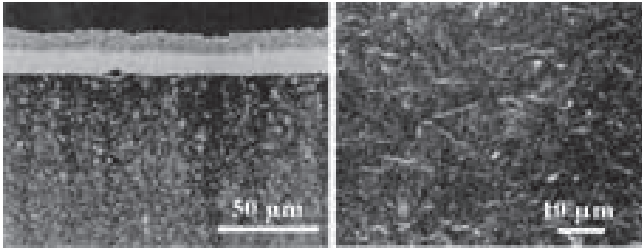


Fig. 8. Microstructure of nitrided 32CrMoV13 steel [11]

martensite, inter and intragranular carbides, except for the sub-surface zone where most of them have disappeared being replaced by smaller nitride or carbonitride precipitates (Fig. 8) A fine nano-metric precipitation of disk-shaped nitrides also occurs inside the needles in the whole diffusion zone.

The application of nitriding process in duplex hardening increases the surface hardness both at room and at elevated temperatures, also forms compressive residual stresses in the case higher than carburization. This provides high wear and fatigue resistance and durability of bearings. However, it should be noted that exceeding the residual stresses of a certain level could lead to an increase in the subsurface stretching greater than after standard heat treatment and could cause shorter bearing life. In addition, it is necessary to ensure absence of the grain boundaries precipitations that reduce the fatigue resistance of nitrided steel.

## CONCLUSION

Thus, over the past hundred years, the development of aviation bearing steels has followed the path of increasing hardness in the working temperature range, while ensuring sufficient core impact toughness and the formation of residual compressive stress optimal level in the subsurface area to compensate operational tensile stresses. First, high-carbon chrome steels, which were exposed to through hardening were used, then low-carbon alloy steels which heat

treatment consisted of carburization, hardening and tempering were added, finally, heat-resistant high-alloy hardened or carburized steels were developed, which in recent years has been subject to duplex hardening: standard heat treatment and nitriding.

## REFERENCES

1. **Voinov S.G., Shalimov A.G.** Ball bearing steel. M.: GNTI, 1962.
2. **Sprishovsky A.I.** Rolling bearings. M.: Mechanical Engineering, 1968.
3. **Conter L.Ya.** Steel for heat-resistant bearings. M.: NIIAVTOPROM, 1978.
4. **Spektor A.G., Zelbeth b. M., Kiselev S.A.** Structure and properties of bearing steels. M.: Metallurgy, 1980.
5. **Franz-J.** An Overview of Performance Characteristics, Experiences and Trends of Aerospace Engine Bearings Technologies. Science Direct [Internet]. Chinese Journal of Aeronautics 20 (2007) 378–384 Available from <https://sciencedirect.com>. Chinese Journal of Aeronautics 20 (2007) 378–384.
6. **Gloeckner P., Rodway C.** The Evolution of Reliability and Efficiency of Aerospace Bearing Systems. Engineering, 9, 962–991 Available from <https://doi.org/10.4236/eng.2017.911058>.
7. **Bashnin Yu.A., Ushakov B.K., Secey A.G.** Heat treatment technology. M.: Metallurgy, 1986.
8. **Geller Yu. A.** Instrumental steel. M.: Metallurgy, 1975.
9. **Gromov V.I., Voznesenskaya N.M., Pokrovskaya N., Tonnysheva O.A.** High-strength structural and corrosion-resistant steel FSUE «VIAM» for aviation engineering // Aviation materials and technologies, 2017. № S. P. 159–174.
10. Materials FSUE «VIAM» for friction knots and special bearings [Internet]. Available from <http://opzt.ru/wp-content/uploads/2018/09/Vopros-5-Gromov-V.I..pdf>.
11. **Girodin D.** Deep Nitrided 32CrMoV13 Steel for Aerospace Bearings Applications [Internet]. NTN Technical Review No. 76. 2008. Available from [https://www.ntnglobal.com/en/products/review/pdf/NTN\\_TR76\\_en\\_p024\\_031.pdf](https://www.ntnglobal.com/en/products/review/pdf/NTN_TR76_en_p024_031.pdf).
12. **Bhadeshia H.K.D.H.** Steels for bearings Progress in Materials Science. Vol. 57, Is. 2. February 2012, P. 268–435 Available from <https://www.sciencedirect.com/science/article/pii/S0079642511000922#>.

## NITRIDING OF STEELS IN ELECTROLYTIC PLASMA: SPECIFICS OF COMBINED PROCESSES

L. G. Petrova, P. E. Demin

Moscow Automobile and Road Construction State Technical University (MADI). Moscow, Russia  
petrova\_madi@mail.ru

The process of hydro-plasma nitriding is presented consisting in surface saturation of steels in low-temperature hydrostatic glow-discharged plasma generated in nitrogen containing liquid electrolyte. The method can be applied for strengthening of small machine parts made of carbon steels or low-alloyed steels for increase of wear and corrosion resistant of items working in corrosive and abrasive conditions (moisture, humor, sand, etc.). Processes of hardening of steels by nitriding in low-temperature electrolyte plasma combined with surface alloying by diffusion metallization by an alloying element (chromium, aluminum, vanadium, titanium, tungsten, cobalt, nickel, molybdenum, and niobium) are discussed.

**Keywords:** thermo-chemical treatment; electrolytic plasma; nitriding; surface strengthening; carbon steels; alloyed steels.

### INTRODUCTION

The main up-to-date trend in thermo-chemical treatment consists in the development of combined processes using several saturating sources and application of high-energy effects such as laser beam or plasma [1–3]. The new technologies of surface strengthening should provide significant increase of mechanical and physic-chemical properties of treating materials to prolong durability and working life of machine parts, from the one side, and to promote energy and resources saving by intensification of processes and economy of expensive components. These tasks are solved by usage of the new method of thermo-chemical treatment in low-temperature plasma generated in liquid electrolyte – Electrolyte Plasma Nitriding (EPN), and of new combined processes of surface alloying on the bases of EP-nitriding.

Electrolyte Plasma Nitriding consists in surface saturation of steels in liquid nitrogen-containing electrolyte (ammonium chloride solution) [4–6]. Treated item or specimen is dipped into this electrolyte in the open container and electric power is supplied. At given values of electrical voltage the electrolyte begins to evaporate actively, vapour cover is formed (so called “steam jacket”) around treating item (cathode) with the thickness of 50...120 microns. Combustion of steam jacket produces low-temperature plasma containing high concentration of active nitrogen atoms (ions) bombarding the sur-

face and penetrating into the metal. Nitrogen ions interact with ions of metal (iron or alloying components of steel) with forming of alloyed solid solution and chemical compounds (nitrides). In plasma the temperature of a specimen and around it increase significantly that cause rapid diffusion of nitrogen in metal with forming of diffusion layer according to the well-known regularities of thermo-chemical treatment. Considerable acceleration of saturation of steels by nitrogen is realized: the full-grown diffusion layer can be formed during 1.5...3 min. Such intensification is stipulated by the following mechanisms: active dissociation process in electrolyte vapour with avalanche-like forming of ions of nitrogen, intensive absorption due to ion bombardment of the surface and high-speed diffusion of nitrogen in metal provided by high temperature of surface layer heated in plasma.

When electric power is switched off the steam jacket has become to be broken and a specimen cool down rapidly as a result of heat exchange with the environment – so something that is like “nitro-quenching” becomes possible.

### METHODS OF STUDY

The treatment by EPN was studied for technical iron, carbon steels with carbon contents from 0.15 to 0.8% and for alloyed steels of pearlitic, martens-

ite and austenitic classes (40Cr, 20Cr13, 40Cr13, 40Cr12Ni8Mn8MoV).

Special laboratory equipment was constructed including open container with device for holding specimen and electrical facilities.

The main technological parameters of the process are: electrical voltage ( $U$ ), intensity of a current ( $I$ ) and the time of saturation (time of feeding the plasma). For stable burning of low-temperature plasma and for exclusion of a regime of arc discharge it is necessary to provide the voltage of  $U = 170...200$  V depending on the size of an item. Intensity of a current is maximal ( $I_{\max} = 1.0...1.5$  A) before the moment of generation of steam jacket, and at the stage of stable plasma burning the value decreases to  $I_{\min} = 0.10...0.12$  A. The time of saturation is 1.5...3 min.

The very specific feature of EPN consists in difficulties in the exact experimental determination of temperature of saturation – the main parameter of thermo-chemical treatment influencing on diffusion processes. The reason is that the temperature of a specimen surface can differ from the temperature of the steam jacket (that can be measured experimentally by different devices). The temperature of specimen surface is calculated on the basis of a model connecting physical parameters of electrodes and electrolyte with the following input parameters of the process: electrical voltage ( $U$ ), radius of an item ( $R$ ) (for symbolically cylindrical specimen) and the depth of its dipping into electrolyte ( $h$ ). The quantitated analysis has shown that the temperature of a surface:

$$T = \frac{2\sqrt{2U^2hk}}{Xd\sqrt{\alpha\lambda R}}, \quad (1)$$

is a function of electrical resistivity of vapor ( $X$ ), thickness of the vapor cover ( $d$ ), coefficient of heat emission of the electrolyte ( $\alpha$ ), heat conduction of metal ( $\lambda$ ), and coefficient of a part of energy coming from the cover to the cathode ( $k$ ).

The calculations have shown that for an item of the given size ( $R$ ) it is possible to find the necessary voltage and the depth of dipping for achieving the required temperature for diffusion.

## RESULTS AND DISCUSSION

### Structure of nitrided layers

In technical iron during 1.5 min of saturation diffusion layer is formed consisting of chemical compounds zone ( $\epsilon$ -phase) with thickness of 30 microns and internal nitriding zone with  $\gamma'$ -phase precipitations with thickness of 150 microns.

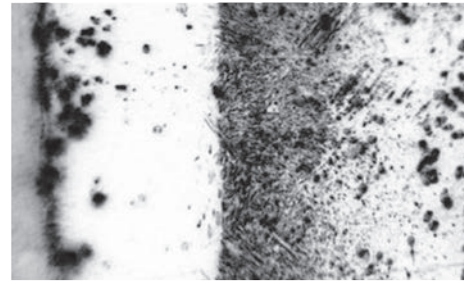


Fig. 1. Micrograph of the 0.8%C carbon steel after EPN,  $\times 200$

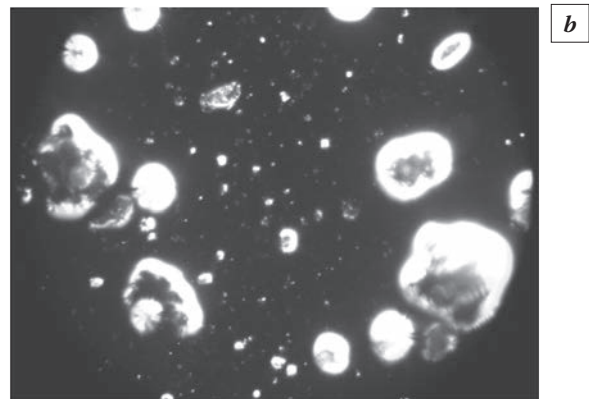
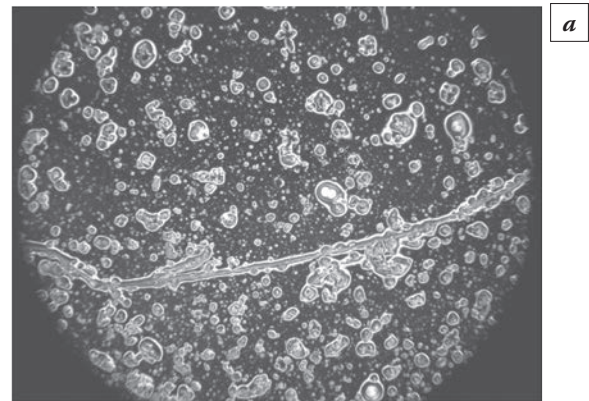


Fig. 2. Chromium carbides and nitrides in 20Cr13 steel after EP-nitriding, HITACHI S-800,  $\times 25000$  (a) and  $\times 100000$  (b)

For carbon and alloyed steels significant differences were detected. For example, in the steel with 0.8% of carbon the structure is: the upper dense layer of  $\epsilon$ -nitride (20...30 microns) and the inner zone of nitrogen-enriched martensite (20 microns) as a result of "nitro-quenching" (Fig. 1).

In chromium steel 20Cr13 the thickness of nitrides layer is 15 microns; internal nitriding zone has the thickness up to 100 microns and contains dispersed precipitations of nitrides and carbides of chromium, and nitrides particles are significantly more fine than carbides (Fig. 2).

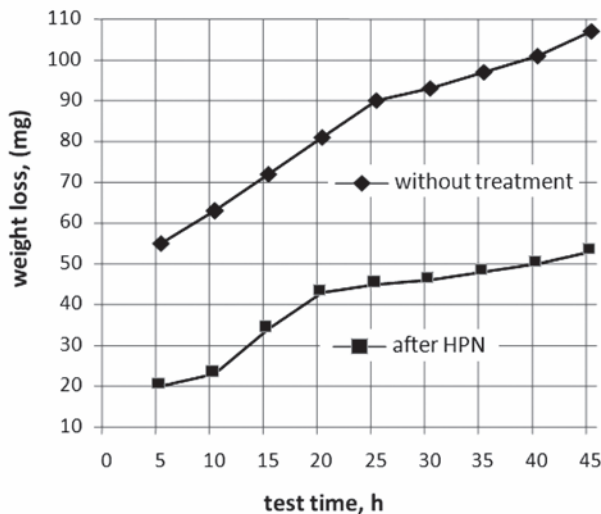


Fig. 3. Wear resistance of samples of 20Cr13 steel after EPN comparing with non-treated samples (standard wear tests of weight loss)

### Mechanical properties of EPN-treated steels

Mechanical tests of different steels after EP-nitriding have shown significant increase of micro-hardness of their surface layer (till 13000...16000 MPa depending on a steel). Wear resistance of high-chromium steels increases in 3 times comparing with the characteristics of non-treated steel (Fig. 3). In nitrided chromium-nickel steels increase of wear resistance is observed together with the high level of corrosion resistance.

Surface strengthening of carbon steels is caused by forming of nitrogen-containing martensite as the result of nitro-quenching, and of hardening of alloyed steels due to precipitation of dispersed special nitrides in internal nitriding zones.

### Specifics of combined processes of EPN with metallization

The process consists in combination of EPN of carbon steels with their surface alloying by diffusion metallization from plasters containing powders of

Table 1. Thickness of modified layer on steel 40 (y) and its micro-hardness ( $H_{100}$ ) after metallization of different elements combined with EPN

Metal	W	V	Mo	Ti	Co	Nb	Cr	Al
y, microns	40	80	90	65	85	60	70	150
$H_{100}$ , MPa	7700	6400	16000	5300	3500	7300	4400	15000

metals (W, V, Cr, Co, Ti, Nb, Mo, Al). For diffusion of metals higher temperatures are required comparing with the temperatures of nitriding. The temperature can be raised by decrease of heat conductivity of the electrolyte that can be made by increase of its density by adding of graphite. Besides, graphite having the high electrical conductivity gives the possibility of increase of the intensity of a current.

The parameters of a process are: electrical voltage – 35...40 V, intensity of a current – 13...15 A. The composition of a plaster is: 50% of graphite, 30% of metal powder, 20%  $NH_4Cl$ , organic binder. Plaster is covering on a surface of a specimen by thin layer (2 mm), and then it's treated by EPN in electrolyte of ammonium chloride with addition of powder of graphite.

Ions of nitrogen and chlorine in plasma generated as from electrolyte and from plaster provide complex saturation both by nitrogen and alloying metal transporting by chlorine ions to the surface of metal. After 3 min of saturation rapid cooling of a specimen in electrolyte is occurs that causes quenching of high-alloyed surface with forming of martensite.

As a result of combined treatment in nitrogen-containing plasma with addition of graphite saturation of carbon steels is occurs by one of the metals (W, V, Cr, Nb, Ti, Mo, Al), nitrogen and carbon with forming of complex alloyed diffusion layers with thickness of 40...150 microns depending on the type of the alloying element (Table 1). In modified layer there are nitrides, carbides (or carbo-nitrides) of iron and alloying elements, and in several cases intermetallides:  $Fe_xMe_y + Me_x(C,N) + \alpha(Me,N)$  (Table 2). In general this treatment can be classified as metallizing-carburizing-nitriding. After surface alloying by strong nitride forming elements mainly nitrides are formed such as titanium nitrides that is confirmed by increase of concentration of nitrogen and titanium

Table 2. Phase composition of diffusion layers in 0.4%C steel after metallization by different elements combined with EPN

Alloying element	Phase composition
W	$\alpha(W,N) + W_2N + \gamma' - Fe_4(N,C)$
V	$\alpha(V,N) + V(N,C)$
Mo	$\alpha(Mo,N) + Mo_2N + Fe_7Mo_6 + \gamma' - Fe_4(N,C)$
Nb	$\alpha(Nb,N) + Nb(N,C)$
Cr	$Cr_2O_3 + \alpha(Cr,N) + CrN + Cr_2N + \gamma' - Fe_4(N,C)$
Ti	$\alpha(Ti,N) + Ti(N,C) + Fe_2Ti$

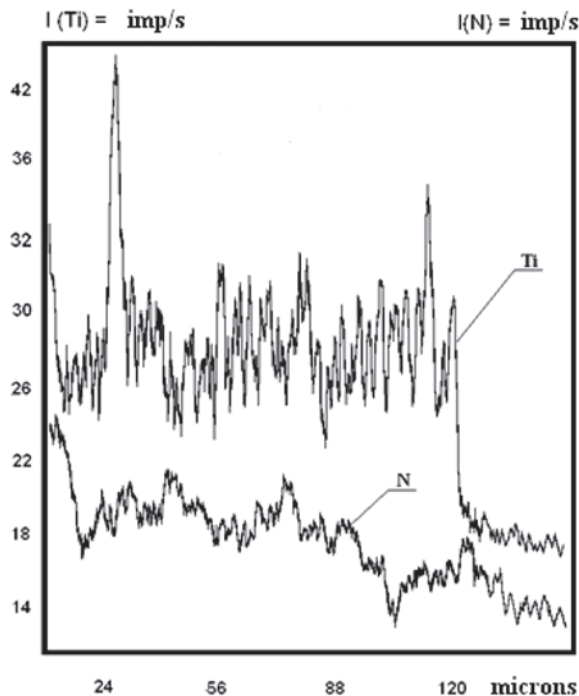


Fig. 4. Concentration profiles of titanium and nitrogen in the diffusion layer of 0.4%C steel after combined "titanizing-nitriding"



Fig. 5. Microstructure of modified layer 0.4%C in steel after "aluminizing-nitriding", x200

in the diffusion layer (Fig. 4). Thus, classic internal nitriding zone of 2-nd type (according to Lakhtin's classification [3]) is formed.

The structure of modified layer of carbon steels after metallization by aluminum combined with EPN has their specifics (Fig. 5). At the surface thin film of aluminum oxide  $Al_2O_3$  is formed with thickness of about 25 microns, under the film transitional diffusion layer is observed (70 microns) with heightened concentration of Al, C and N and precipitates of alloyed by aluminum  $\gamma'$ -nitrides. In deeper layers very typical hypereutectoid structure is found with the boundary net of carbides with martensite needles inside. The total thickness of the diffusion layer is about 150 microns. Modified surface alloyed lay-

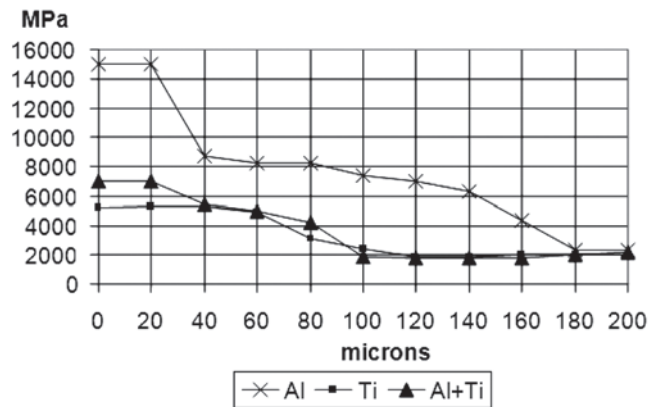


Fig. 6. Micro-hardness profiles of surface layer of 0.4%C steel after different variants of metallization combined with EPN

ers have high micro-hardness (Table 1). The level of strengthening is a function of volume fraction of dispersed nitrides (carbo-nitrides) of alloying elements and their dimensional parameters. This depends on thermodynamic activity of a metal to form nitrides (carbides) from the one side, and on concentration of a metal and nitrogen in solid solution, from the other.

The micro-hardness profiles correspond to the specifics of phase composition of diffusion layer. For example, in "aluminized-nitrided" layer the maximal micro-hardness (15000 MPa) is directly near the surface in the layer of aluminum oxide forming, then the hardness decreases to 8000 MPa in transitional zone and to 2000 MPa in the core (Fig. 6). In this case sharp gradient of hardness can lead to the brittleness of a layer. More even distribution of micro-hardness can be achieved by combined metallization by aluminum and titanium (Fig. 6). In this case corrosion resisting properties providing by "aluminizing-nitriding" can be kept.

The tests have shown that the characteristics of mechanical properties of carbon steels after combined treatment are much higher comparing with traditional methods of their strengthening. The hardness of surface alloyed layer is in 4.7...5.7 times higher than the hardness of steels without treatment, and in 1.4...3 times higher than the hardness providing by traditional nitriding processes.

The working time of machine parts of agricultural and road machines, oil-and-gas industrial equipment treated by EPN-technology, in operation in conditions of wear, corrosion and dynamic loadings increases in 3...7.5 times.

## CONCLUSIONS

Nitriding of steels in low-temperature electrolytic plasma (EP-nitriding) allows to intensify significantly the process of nitriding: time of diffusion saturation is 1.5...3 min comparing with several hours of classical nitriding.

EP-nitriding provides surface strengthening of carbon steels by nitro-hardening with formation of nitrogen-enriched martensite, and of alloyed steel due to precipitation of dispersed nitrides of alloying elements in the internal nitriding zone.

Combined processes of EP-nitriding with diffusion metallization by nitride-forming elements provide forming of high alloyed dispersion hardening surface layer in carbon steels with high characteristics of hardness, wear and corrosion resistance.

## ACKNOWLEDGMENTS

This work was supported by the Russian Science Foundation, project no. 17-19-01473.

## REFERENCES

1. **Aleksandrov V.A.** Combined TCT Process for Surface Hardening of Steels // *Metal Science and Heat Treatment*. 2010. Vol. 52, No. 5–6. P. 214–218.
2. **Chudina O.V., Brezhnev A.A.** Surface Alloying of Carbon Tool Steels Using Laser Heating // *Russian metallurgy (Metally)*. 2015. Vol. 2015, No. 13. P. 1090–1093.
3. **Chudina O.V., Petrova L.G., Aleksandrov V.A. et. al.** Increase of reliability of loaded machine parts by surface modification using methods of laser treatment // *ARP Journal of Engineering and Applied Sciences*. 2018. Vol. 13, No. 7. P. 2477–2481.
4. **Slovetskiy D.I.** Mechanisms of plasma-electrolytic heating of metals // *Thermal Physics of High Temperatures*. 1986. 24(2): 353–356.
5. **Belashova I.S., Petrova L.G., Aleksandrov V.A. et.al.** Improving the Properties of Low-Alloy and Carbon Steel Tools by Cyclic Nitriding // *Russian Engineering Research*. 2018. Vol. 38, No. 1. P. 53–56.
6. **Petrova L.G., Aleksandrov V.A., Demin P.E.** Thermochemical treatment of steels in plasma of hydrostatic spark discharge // *Metal Science and heat treatment*. 2012. No. 6. P. 41–46.
7. **Petrova L.G., Demin P.E., Kosachev A.V., Barabanov S.I.** Application of Diffusion Techniques for Formation of Zinc Coatings to Improve Corrosion Resistance of Structural Steels *Polymer Science, Series D*. 2017. Vol. 10, No. 2. P. 179–184.
8. **Demin P.E., Petrova L.G., Aleksandrov V.A.** Increase of corrosion resistance of steel plugs of the engine by combined aluminum and titanium plating // *Hardening technology and coatings*. 2013. No. 9. P. 20–33.

# THE NEW TECHNOLOGY OF STRENGTHENING THE LARGE-SCALE STAMP WORKING SURFACES FOR SHEET STEEL PRODUCTS THROUGH HARD CHROME PLATING

A.A. Chervyakov, A.V. Chikurov, A.K. Tikhonov

OOO "PCG" Russia

pcg.office@mail.ru; chikurov\_a@mail.ru; AK.Tihonov@vaz.ru

The new technology of solid chrome plating of cast-iron large-size dies, which allows solving the problems of modern body building, is considered.

**Keywords:** stamp-size; punch; matrix clamp; chrome plating; cast-iron.

Hard chrome plating is one of the most common methods of galvanic hardening of working surfaces in the world, and is used for:

- protection against wear of the base material and protection from sticking to the surface of contacting materials,
- to increase the hardness and wear resistance of various measuring and cutting tools, rubbing parts of instruments and machines.

Chrome plating allows you to significantly increase the useful life of critical parts of the equipment and thereby save on repairs, in comparison with other methods of surface hardening.

Chrome plating is best for large-sized products, such as:

- press molds for manufacturing of plastic and rubber products;
- deep drawn stamps for manufacturing of sheet steel products [1–4].

There are many methods of hard chrome plating, but the following methods are widely used [1]:

- high-speed chrome plating in the electrolyte duct (used for chrome plating of internal and external surfaces of products having a simple configuration);
- chrome plating by immersing the product in a chrome electrolyte bath.

**Main properties of chromium-plated surfaces are:**

- low coefficient of friction (a pair of chrome-cast iron 0.06–0.08) [3];
- high microhardness (coatings can reach values up to 1200 HV) [2];
- low adhesion to other materials [4];

– high heat resistance and good chemical resistance provide chrome-plated parts with a high resource in any operating conditions.

Chrome plating of the working surfaces of the stamp allows you to:

- to increase the service life of die tooling, due to the wear of the chrome plating, and not the wear of the base metal;
- significantly reduce the amount of lubricants used;
- reduce the cost of service stamps associated with downtime stamping line for cleaning [1–3].

Various brands of cast irons are used for the production of deep drawing dies. Until recently, in the manufacture of parts of press dies (clamp, punch, die), as a rule, gray cast iron of HF and HRTD brands was used [5]. The hardness of such cast iron does not exceed 300 HB [6]. The perlite-ferritic microstructure of such lamellar graphite cast irons is shown in Fig. 1.



Fig. 1. Gray cast iron of HRTD

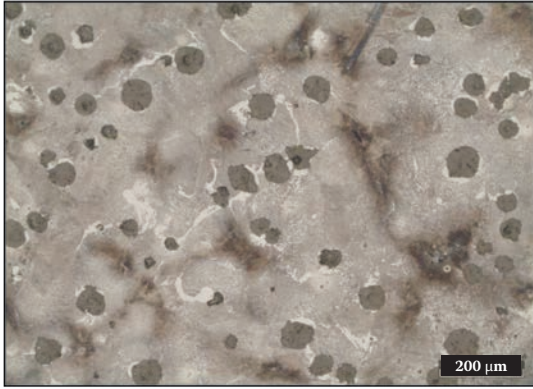


Fig. 2. High strength cast iron K5CD800i

Recently, various types of high-strength cast irons have become widespread in the world for casting die parts. Their use can significantly reduce the weight of parts stamps and increase their strength and durability. The hardness of such cast irons is about 400 HB and higher [7]. The perlitic-ferritic microstructure of such nodular cast irons is shown in Fig. 2.

The cost of gray and high-strength cast iron differs by about 2 times.

The quality of stamped parts largely depends on the state of the working surfaces of cast iron stamps. When reusable and permanent use of the stamp, due to the impact of friction that occurs between the die tooling and the part, deformation, destruction, abrasion, change and wear of the working surfaces occurs, which leads to defects in the parts.

Therefore, the surfaces of parts of die tooling have to be periodically repaired.

The use of hot-dip galvanized steel in the automotive industry has led to a new problem in stamping.

The presence of zinc coating on the surface of the stamped part has a significant impact on the coefficient of friction in the zone of contact of the workpiece with the equipment and on the conditions of plastic deformation of the metal in the process of molding and drawing. The surface layer of the coating tends to peel in the conditions of plastic deformation of the base metal and contact action from the tool. That is, in the process of stamping, delaminated particles of zinc coating and other contaminants of the parts being stamped “weld” to the surface of the stamp, and gradually accumulating, they begin to deform and damage the surface of the parts being stamped leaving defects. That leads to the forced frequent stops of the stamping line for manual cleaning of the working surfaces of the die tooling.

## Technology «PCG»

After many years of research, we, together with AVTOVAZ, created a domestic innovative technology for local chrome plating of large deep drawing dies, which eliminates or reduces the problems associated with the classical chrome plating technology, namely [11]:

- all the processes of preparation and application of the coating take place in one local bath with a working volume from 0.5 to 1 m<sup>3</sup>;

- technology has a closed cycle with minimal discharges of pollutants;

- the proposed technology does not involve the use of load-lifting mechanisms for moving large-sized parts in the coating process, which prevents the risk of a part weighing up to 20 tons falling into a bath with chrome-plating electrolyte. The part is moved by crane only to install it on the cart and to send it to the customer;

- in case of possible spillage of the solution, there is a hermetic emergency bath with a capacity of up to 1 m<sup>3</sup>, which prevents the pouring of aggressive solutions throughout the workshop;

- the bath moves on the trolley;

- the process bath is fed from 1.2 m<sup>3</sup> baths for preparatory solutions and 3 m<sup>3</sup> baths for chromium plating electrolyte, which leads to a significant reduction in material costs.

We have done a great deal of research on samples of various grades of cast irons and developed a chromium plating technology that guarantees high adhesion of chromium to the base material and patents of the Russian Federation are received [9, 10].

An installation for the development of chrome plating technology for large-sized automotive dies was developed and created and patents of the Russian Federation are received [8]. As a prototype, a large forming stamp of AVTOVAZ was used on the detail “Rear wheel arch of VAZ-2108 a/m”.

The economic justification of the new technology of chromium-plating of large-sized car dies can be verified, using the example of the AVTOVAZ stamp on the floor of the “Sidewall of the body” of the VAZ-1118 vehicle, from steel – HZ 01YuT.

The working surfaces of the parts of the HRTD gray cast iron punch were coated with a hard chrome coating with a thickness of 20–40 μm with a microhardness of 700–1000 HV.

The use of this stamp in the production of AVTOVAZ, strengthened by our technology showed, that the number of cycles to the surface repair of dies has increased from 5.000 to 500.000 die forgings.

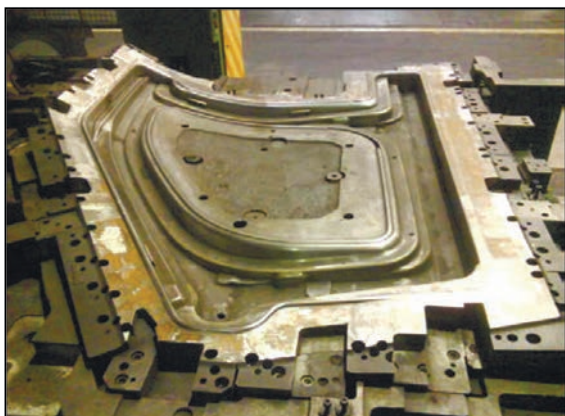


Fig. 3. Before chrome plating



Fig. 4. After chrome plating



Fig. 5. Matrix



Fig. 6. Punch



Fig. 7. The detail of the mold  $\Phi$  2.8 m

Fig. 3 at the top left shows the details of this stamp before chrome plating, Fig. 4 – after chrome plating.

Comparative characteristics of classical and PCH technology are given in the Table.

The table shows, that the environmental load on the environment by the technology «PCG» is reduced by an order of magnitude, in comparison with the traditional chrome plating technology Fig. 5–9 shows samples of equipment that was chromium-plated in PCG LLC.

**Comparative table**

The requirements for the conduct of the process	Traditional technology	Technology PCG LLC.
Volume of working baths, m <sup>3</sup>	30–50	3–5
The power of the heating elements, кВт	400–700	45
The use of lifting equipment in the process	Beam crane 20 tons or more	no
Insulation non-chrome surfaces	yeah	no
The entrainment of electrolyte of chromium plating with every detail, liter	50	<u>5</u>
Contamination of the electrolyte degreasing and chrome plating	yeah	no
The capacity of treatment facilities subject to the emergency discharge of chromium wastewater, m <sup>3</sup>	more than 50	Enough 5
Resistance of die tooling, cycle	Less than 100 000	More than 500 000

Перевод



Fig. 8. Matrix



Fig. 9. Matrix



RENAULT

CHANGEMENTS DE VIE  
CHANGEMENTS L'AUTOMOBILE

DREAM / DIMat / Service 68140 / TCR LAB 0 60  
Technocentre – 1, Avenue du Golf  
78288 Guyancourt Cedex

**NOTE TECHNIQUE N° 68140-2012-16192**

<b>DE LA PART DE :</b>	Jean-Marie MALHAIRE	68140
<b>TÉL :</b>	+33 (0) 1 76 85 08 57	
<b>FAX :</b>	+33 (0) 1 76 89 13 06	
<b>E-MAIL :</b>	jean-marie.malhaire@renault.com	
<b>Pour action :</b>	Bruno TRADOTTI	65307
<b>Copie :</b>	Christian GRENTE	68140
	Corinne DAVID	68140
	Marc CAPPELAERE	65307
	Patrice BELLARD	65307

Guyancourt, le 13/11/2012

**Thème : Chromage dur électrolytique sur outillage de presse RUSSIE**

**Objectif : Conformité épaisseur et dureté.**

**Attente : Prise en compte des résultats.**

**RESUME – CONCLUSION :**

Un outillage de presse, revêtu de Chrome dur électrolytique, a été confié à la DIMat, afin de déterminer l'épaisseur et la dureté du revêtement appliqué.

Les analyses réalisées conduisent aux conclusions suivantes :

- L'épaisseur du revêtement est de **32 µm**, conforme aux préconisations de la norme EM24.15.150B (épaisseur préconisée de 10 à 30 µm sur zones travaillantes, une épaisseur de 10 µm doit être assurée quelque soit la zone considérée).
- La dureté Hv0,05 est de **1045,5 Hv + /- 64,1 Hv**, conforme aux préconisations de la norme EM24.15.150/B (le dépôt obtenu a une dureté de l'ordre de 800 à 1000 HV).

Jean-Marie MALHAIRE  
*Original signé*  
*Transmis par courrier électronique*

Marie-Thérèse VACHER  
*Original signé*

Pour toutes réclamations ou suggestions, veuillez utiliser cette adresse mail to : [Reclamations.DIMat@renault.com](mailto:Reclamations.DIMat@renault.com)

PROPRIETE RENAULT CONFIDENTIEL

C

Fig. 10

Fig. 10 on the right shows the protocol-conclusion of the laboratory f. Renault on the quality of chrome plating applied to the cast-iron sample in PCG LLC.

## REFERENCES

1. **Solodkova L.N., Kudryavtsev V.N.** Electrochemical chromium plating.// Appendix to the journal «ELECTROPLATING AND SURFACE TREATMENT». Moscow, Globe. 2007. P. 191.
2. **Melnikov P.C.** Reference book on electroplating in mechanical engineering // Engineering Moscow. 1979. P. 296.
3. **Lobanov C.A.** Practical electroplating tips Engineering. Leningr. department, 1989. P. 248
4. **Algin F.F., Belenky M.A., Gaul I.E. et al.** Electroplating // Reference book Moscow, Metallurgy, 1987. P. 736.
5. CTP 37.101.0028-2001 Foundry goods. General specifications // Enterprise standard. Tolyatti, OJSC «AVTOVAZ», 2001. P. 25.
6. **GOST 1412–85** Cast iron with lamellar graphite casting. Brand.
7. **GOST 7293–85** Nodular cast iron for castings. Brand.
8. Utility model patent №93806 Russian Federation 21.12.2009 year, Device for local application of galvanic coatings on the outer surfaces of large products; patentee of JSC «Volga electroplating Center».
9. Pat. for invention № 2430197 Russian Federation or 21.12.2009, Method of local chrome plating of large-size products; patentee of JSC «Volga electroplating Center».
10. Pat. for invention № 2603935 Russian Federation or 04.06.2015, Method of nonporous solid chrome plating of cast iron and steel parts; patentee of JSC «Volga electroplating Center».
11. The Journal «Metallurgy Of Machinery Building». 2016. № 2. P. 25–29.

*Авторы, название?*

# THE PRINCIPLES OF CREATING NEW ECONOMICALLY ALLOYED FERRITIC STEELS WITH A UNIQUE COMPLEX OF DIFFICULT TO COMBINE PROPERTIES

A.I. Zaitsev<sup>1,2</sup>, A.V. Koldaev<sup>1</sup>, A.B. Stepanov<sup>1</sup>, N.A. Arutyunyan<sup>1,2</sup>, S.F. Dunaev<sup>2</sup>

<sup>1</sup>I.P. Bardin Central Research Institute of Ferrous Metallurgy (TsNIIchermet). Moscow, Russia

<sup>2</sup>Chemical Faculty, Lomonosov Moscow State University. Moscow, Russia

koldaevanton@gmail.com, aizaitsev1@yandex.ru

The basis for the creation of a new generation of economically alloyed steels, strengthened by obtaining a dispersed ferritic structure and a bulk system of nanoscale phase precipitates and their production technology was developed. It is shown that such steels, for the first time, have a unique complex of high hard-to-combine strength, yieldability, formability, fatigue and corrosion resistance and other service properties. It was shown, that Ti -microalloying system, including in conjunction with Mo, has the advantages compared with a more complex system of alloying with V, Nb, Ti, Mo due to the peculiarities of the kinetics of the carbide formation, carbonitride precipitates of microalloying elements.

**Keywords:** sparingly alloyed ferritic steels; dispersed microstructure; nanoscale phase precipitates; interphase precipitates; kinetics; strength; yieldability; formability; fatigue resistance; corrosion resistance; production technology.

Based on the results of the analysis of the mechanisms used to form the structure and properties of existing high-strength automotive steels, the impossibility of simultaneously obtaining of high difficult to combine strength, yieldability, formability, fatigue and corrosion resistance and other service properties was shown. The use of traditional hardening mechanisms (grain-boundary, solid-solution, dispersion hardening) in the development of the most common low-alloy high-strength automotive steels leads to a significant reduction in yieldability, corrosion resistance and other characteristics of the product. In order to overcome this negative phenomenon, progressive automotive steels have been developed, which are strengthened by the presence of solid (firm) structural components. Due to the significant difference in hardness, strength of structural components, and the metal matrix, it is not possible to achieve high values of the hole expansion ratio, formability and corrosion resistance. Thus, for all common types of high-strength automotive steel the problem of simultaneous achievement of high performance of these properties is not solved.

The most promising direction in it is the development of a new generation of steels, which are strengthened by a dispersed ferritic structure and a bulk system of nanoscale phase precipitates. The design of such steels can be based on the Ti micro-

alloying system, including in conjunction with Mo or more complex systems (V, Nb, Ti, Mo in general). However, progress in this direction is constrained by the lack of reliable data and adequate models of the formation kinetics for the different types of carbide, carbonitride precipitates, as well as their influence on the structure and properties of steel. Therefore, the principles of new ferritic steels creating, despite their high importance, are established mainly by trials and errors (1-3), and the achievable set of properties apparently has not been found out.

For a reasonable choice of the composition and parameters of the metal working a study of the carbide (carbonitride) formation kinetics was conducted, first of all, for the most important components – niobium and titanium. In the case of Nb, it was carried out on low-carbon low-alloy steel of model chemical composition (wt. %): C – 0.11, Mn – 1.72, Nb – 0.05 with and without deformation (4). It was found that without deformation the precipitation of niobium carbonitride has significant kinetic limitations. Even with a significant degree of supersaturation and cooling (more than 300 °C) of the solid solution it takes a significant time – not less than 20–40 minutes to form any significant amount of precipitates of this phase. After deformation at isothermal exposure at 900 °C, the formation of Nb(C,N) is significantly accelerated: it begins at an exposure of about 10 s and finishes within 250–300 s, which is a long period

of time for the commonly used in practice modes of temperature and deformation treatment of steel. This suggests in support of the conclusion that in the process of hot rolling of steel, the Nb(C,N) and other phases formation, as a rule, is not fully concluded, and finishes, for example, in the subsequent heat treatment of rolled products.

This fact is confirmed by the results of the study of low-carbon V, Nb micro alloyed steel with model composition (wt. %): C – 0.06, Mn – 0.59, Cr – 0.63, V – 0.051, Nb – 0.031. It was found that the decrease in the finish temperature of rolling from 890–905 to 820–830 °C leads to a decrease in the size of the ferrite grain according to GOST 5639 from 8–9 to 10–11, an increase in the yield strength from 440–450 to 480–490 MPa, with close values of time resistance, high elongation (28–30%) and toughness (300–400 J/cm<sup>2</sup>). This is due to the formation of a greater number of Nb(C,N) secretions in austenite during hot rolling that inhibit the recrystallization of austenite and lead to the refinement of grain.

The second key mechanism of hardening of the steel is associated with the formation of interfacial (at the front of the phase transformation of steel) precipitates of size 2–6 nm, and the distance between the layers 20–50 nm, as a consequence of stabilizing austenite effect of chromium. Despite the presence of interphase carbide, carbonitride niobium and/or vanadium precipitates, the most preferred for hardening, the obtained strength characteristics of the rolled products are lower than the values corresponding to the strength classes of 550, 600 MPa, which may be result of the relatively low manganese and micro-alloying elements content. An additional negative factor is associated with the partial expenditure of carbonitride-forming elements on the formation of less effective austenitic precipitates.

In order to clarify the above-mentioned circumstances, a study of 8 steels, the composition of which is closer to the XPF steel composition produced by TATA steel (UK, Netherlands) (3) with different contents (wt. %): V 0.05–0.20, Nb 0.010–0.110, Ti 0.07–0.17, in the absence and in the presence of 0.19–0.20 Mo. It was found that the rolling product obtained by the mode: the finish temperature of rolling 900 ± 15 °C, the cooling rate of 10–15 °C/s to the temperature of coiling 650 °C from steels of all compositions, except one, meet the requirements for rolling strength categories 550 and 600 MPa. Outlier steel structure is characterized at the same time by the low content of Nb and Ti (0.030 and 0.078 wt.% respectively), the absence of micro-alloying Mo, rather high nitrogen content, reducing the

potential of positive effect of titanium and niobium. The results of the study by transmission electron microscopy showed that the structure in all cases is represented mainly by block and polygonal ferrite at different ratios of their volume content. Niobium micro-alloyed steels contain austenite and interphase precipitates and vanadium micro-alloyed steels – interphase and ferritic precipitates. As in the previously studied micro-alloyed niobium steel, the forming austenitic precipitates are responsible for the implementation of the grain boundary hardening mechanism, and interphase and possibly ferritic precipitates are responsible for the dispersion hardening. This method of achieving a given structural state and properties is close to the existing approach in the case of traditional low-carbon low-alloy high-strength automotive steels. The formation of a certain volume fraction of austenitic precipitates of relatively large sizes significantly reduces the potential of the micro-alloying elements for the formation of more efficient interfacial and ferritic precipitates of small sizes. This leads to a certain reduction in the resulting set of properties of rolled products. In addition, to obtain the strength properties of rolled products that meet the requirements for strength classes 550, 600 MPa, as shown by the results of the V, Nb and Ti concentration must be at a relatively high level – about 0.2, 0.1 and 0.1 wt.%, respectively. In addition, Mo micro-alloying stimulate an increase in the rate of nucleation and a decrease in the rate of growth of carbide, carbonitride micro-alloying elements, which helps to reduce their size and, as a result, increase the strength of the rolled products. The need to provide such a large content of expensive micro-alloying elements is associated with significant costs. These circumstances reduce the technical and economic efficiency of the V, Nb, Ti, Mo micro-alloyed ferritic steels production.

Fundamentally different picture takes place in the system of Ti micro-alloying ferritic steels, including in conjunction with Mo. The study of the formation of all possible phase precipitates types for two model steels of compositions (wt.%): C – 0.070, 0.063; Mn – 1.64, 1.61; Ti – 0.090, 0.096; Mo – 0.22, 0.21; N – 0.009, 0.003 was conducted. The possibility of complex FCC carbide  $Ti_xMo_yC_z$  forming was established. The proportion of molybdenum in its composition increases, and at temperatures of  $\gamma \rightarrow \alpha$  transformation of steel corresponds to the  $Ti_{0.43}Mo_{0.08}S_{0.49}$ . Almost pure TiC is formed in the hot rolling temperature range. The formation of its nanoscale precipitates is much slower than for Nb(C,N). At 900 °C it begins only after 100–200 s and finishes after more than 1000 s. The precipitates formation is significant-

ly accelerated with a concentration increase of titanium in the solid solution, nevertheless remains at a significantly lower level compared to Nb(C,N). As a result, the formation of austenitic precipitates during the temperature-deformation treatment of steel, practically, does not take place.

Hardening of steel occurs due to the formation of a dispersed ferritic microstructure of a certain morphology and a system of interfacial and/or ferritic precipitates. The level of strength properties of rolled products from the studied steels, especially the second composition, meets the requirements for the strength class of 600 MPa and even for some modes of temperature-deformation processing of the metal significantly exceeds them. When using high temperatures of the finish of rolling and coiling ( $T_{fr} = 900\text{ °C}$  and  $T_c = 620\text{ °C}$ ), most of the steel precipitates are the most effective interfacial, and the rolled product has the highest mechanical properties. Increasing the strength of steel also contributes to the increase in the cooling rate of the strip after rolling from 8–11 °C/s to 23–28 °C/s, which determines the morphological characteristics of the resulting ferrite. To achieve the maximum performance of the complex properties the composition and processing parameters of steel should be selected so as to simultaneously ensure the formation of a dispersed ferritic structure of a certain morphology and system of interphase carbide (carbo-nitride) precipitates.

To solve this problem, as well as to determine the role of Mo in the system of Ti – Mo microalloying steel studied 4 compounds with different content of Ti – 0,045–0,170 wt.% with and without Mo (0.21 wt.%) at a carbon content of 0.08 wt.%. It is found that at relatively low cooling rates of 10–15 °C/s, little dislocation polygonal ferrite and more effective interfacial carbide nanosized precipitates are formed, which, in addition to strength, stimulate an increase in yieldability, formability and other properties of the rolled products. Increasing the cooling rate to 30°C/s leads to the formation of high dislocation block (acicular) ferrite and ferrite precipitates. Their contribution to hardening is slightly less than interfacial, however, the contribution of grain refinement and dislocations to strength characteristics is greater. Therefore, the combination of extreme effect of all hardening mechanisms in the steel, of course, will significantly increase its strength characteristics up to 1000–1200 MPa. This can be achieved by optimizing the chemical composition, the temperature of the finish of rolling, coiling, the cooling rate after rolling. The optimum temperature of the finish of rolling – 900 °C, the temperature of coiling – 650 °C. The rolling product obtained by this

mode meets the requirements for the strength class 600 MPa with a large margin.

The obtained results of structural studies indicate that the carbon concentration in the studied steels is excessively high, which leads to the formation of per-lite colonies, cementite in some steels. To achieve a unique complex of high difficult to combine service properties of the developed ferritic steels the reducing of carbon concentration to the level of 0.04–0.06 wt. % is advisable. The presence of Mo in the steel significantly accelerates the nucleation and, on the contrary, reduces the growth rate of carbide precipitates. The concentration of titanium is a key factor, and its increase causes a favorable increase in the amount of carbide precipitates. It is found that the contribution to the hardening of steel due to the formation of phase precipitates can reach significant values – more than 300 MPa.

The influence of the cooling rate from the finish temperature of rolling to the temperature of coiling in the range of 5–20 °C/s was established. It was found that the increase in the cooling rate of the rolled steel after the completion of rolling to the temperature of the coiling for all studied steels leads to an increase in the yield point. At the same time, the breaking point is not regular. Thus, by controlling this parameter, it is possible to effectively change both the values of the yield and tensile strength and their ratio.

Thus, the design principle of Ti micro-alloyed, including with Mo, ferritic steels significantly differs from existing approaches and can provide a complex of difficult to combine high strength, yieldability, fatigue and corrosion resistance, and other service properties, which is not previously achievable. As the results of the study show, the recommended concentration of Ti and Mo in steel is at the level of 0.1 and 0.2 wt. %, which is necessary to obtain rolled products with strength classes 550, 600 MPa %, respectively. And it depends on the content of nitrogen and sulfur, since the determining factor is the concentration of Ti in solid solution after it was fixated in the nitride, sulfide, carbosulfide. Therefore, high strength properties can be obtained at a lower titanium content. This is confirmed by the results of the study of steel model composition (wt. %); C – 0.052; Mn – 1.51; Ti – 0.12; Mo – 0.17; N – 0.003. The most favorable fine-grained ferritic microstructure and high mechanical properties are attained upon increasing the temperature of finish of rolling to 890 °C, the coiling temperature – 650 °C. This is in good agreement with those obtained above, the optimal values of temperature of finish of rolling is 900 °C, the coiling temperature 650 °C. The resulting complex of strength

properties in all studied modes of treatment significantly exceeds the requirements of a strength class 600 MPa, which indicates the possibility of titanium amount reducing. Manganese content should be limited to 1.5 wt. %.

Direct experimental evidence of the simultaneous high dislocation acicular ferrite structure and interphase carbide precipitates formation possibility obtained. This makes it possible to achieve a complex of extremely high strength up to 1000–1200 MPa, yieldability, formability, fatigue and corrosion resistance, operational reliability and other service properties, while reducing costs, metal consumption.

*The study was carried out by a grant from the Russian Science Foundation. (project No. 18-19-00639) in FSUE I.P. Bardin Central Research Institute for Ferrous Metallurgy.*

## REFERENCES

1. **Funakawa Y., Shiozaki T., Tomita K., Yamamoto T., Maeda E.** Development of high strength hot-rolled sheet steel consisting of ferrite and nanometer-sized carbides // ISIJ Int. 2004. Vol. 44. P. 1945–1951.
2. **Seto K., Funakawa Y., Kaneko S.** Hot rolling high strength steels for suspension and chassis parts “NANO-HITEN” and “BTH steels” // JFE Technical report. 2007. No. 10. P. 19–25.
3. **Rijkenberg A., Blowey A., Bellina P., Wooffindin C.** Advanced High Stretch-Flange Formability Steels for Chassis & Suspension Applications // SCT2014 (4th International Conference on Steels in Cars and Trucks), 15–19 June 2014, Braunschweig, Germany.
4. **Koldaev A.V., D'yakonov D.L., Zaitsev A.I., Arutyunyan N.A.** Kinetics of the formation of nanosize niobium carbonitride precipitates in low-alloy structural steels // Metallurgist. 2017. Vol. 60, No. 9. P. 1032–1037.

# MEASUREMENT OF COOLING CURVES AND VISUALIZATION OF BOILING PHENOMENON ON CYLINDER PROBE

Hideo Kanamori<sup>1</sup>, Tsuyoshi Sugimoto<sup>3</sup>, Riki Homma<sup>4</sup>, Msayuki Kato<sup>4</sup>, Dong-Ying Ju<sup>2</sup>

<sup>1</sup> Graduate School of Saitama Institute of Technology. Saitama, Japan

<sup>2</sup> Advanced Science Institute, Saitama Institute of Technology. Saitama, Japan

<sup>3</sup> Nissan Motor Co., Ltd. Kanagawa, Japan; and Department of Engineering, Saitama Institute of Technology. Saitama, Japan

<sup>4</sup> Lubricants Research Laboratory of Idemitsu Kosan Co.,Ltd. Chiba, Japan

dyju@sit.ac.jp

In this paper, two cylindrical specimens (rod probe) made of silver and SUS 303 were used. The specimen was immersed in a quenching oil (Dafne Bright Quench) at a temperature of 60 °C. The flow rate was 0.13 to the specimen through a pipe provided in the lower part of the specimen. At a flow rate of 26,39 mm / s for injection (forced convection). Thermocouples were used to measure the cooling zone of the interior and surface of the specimen, while high-speed cameras and PIV visualization techniques were used to observe and measure the flow field around the specimen. By observing the forced convection effect produced by the jet flow, it was found that the nucleation boiling phase of the sample surface changed as the jet velocity changed, but the temperature at which the film boiling rupture (specific temperature) was constant.

**Keywords:** rod probe; cooling curves; identification; heat transfer coefficients; inverse method; quenching.

## INTRODUCTION

Two systems with temperature differences of several hundred degrees different by several tens of mass make contact, and the liquid system on the low temperature side with large mass changes or less in temperature during cooling, the solid on the high temperature side with small mass from 850 °C In the cooling process where it is cooled to 200 °C or less, the liquid has a boiling behavior of [1, 2], and in the case of steel on the solid side, stress / strain accompanied by structural transformation, thermal contraction, expansion, etc. The behavior of the cooling process proceeds while affecting each other [3, 4]. The whole change becomes a combination of them, and the prediction is a very difficult problem. In addition, the residual of the steam film in quenching causes unexpected uneven cooling and causes the generation of troublesome heat treatment distortion.

In order to solve this problem, it is specific to the liquid obtained by measuring the surface temperature of the surface of the test piece when the silver rod probe specified by JIS K 2242 heat treatment oil cooling performance test method is cooled by the heat treatment liquid A cooling curve can be obtained that shows the process of cooling by film boiling, nucleate boiling, and convective heat transfer. Using the analytical solution

of the heat transfer equation of a cylinder from this cooling curve, identify the heat transfer coefficient which is different for each temperature on the side of the cylinder (inversely depending on temperature) and analyze the heat transfer as the boundary value of finite element method, so that heat treatment simulation became possible [4–7].

In this paper, we heat the cylindrical test bar of austenitic stainless steel (SUS 303) and the silver cylindrical test bar to a temperature of 850 °C, then put the test bar into the cooling oil and measure the cooling curve of the test bar. In order to evaluate the difference between the shape of the vapor film on the surface of the silver test bar and the SUS304 test bar and the characteristic temperature of the vapor film during the quenching, this paper uses the PIV visualization technology of the high-speed camera to measure the flow field changes around the test bar to verify The relationship between the characteristic temperature and the coolant flow rate. At the same time, the difference in characteristic temperature and heat transfer coefficient between the silver test bar and the stainless steel test bar was also confirmed. In this paper, we used an austenitic SUS 303 steel similar to steel with no structural transformation, and measured the difference in the characteristic temperature at which the vapor film collapses. In addition,



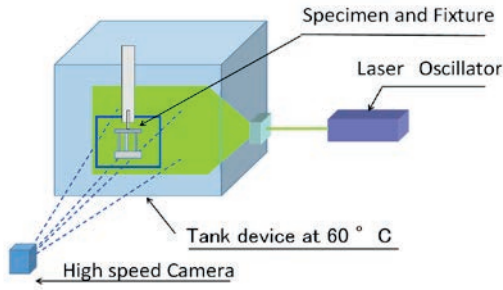


Fig. 2. Schematic diagram of visualization device

Table 1. Properties of Coolant

Quenching oil : Daphne Bright Quench				
Temperature, °C	Density, g/m <sup>3</sup>	Viscosity, mm <sup>2</sup> /sec	Conductivity, W/m·K	Specific Heat, J/g·K
60	834.9	14.94	0.1315	2.03
70	828.7	11.20	0.1307	2.07
80	822.5	8.667	0.1300	2.11

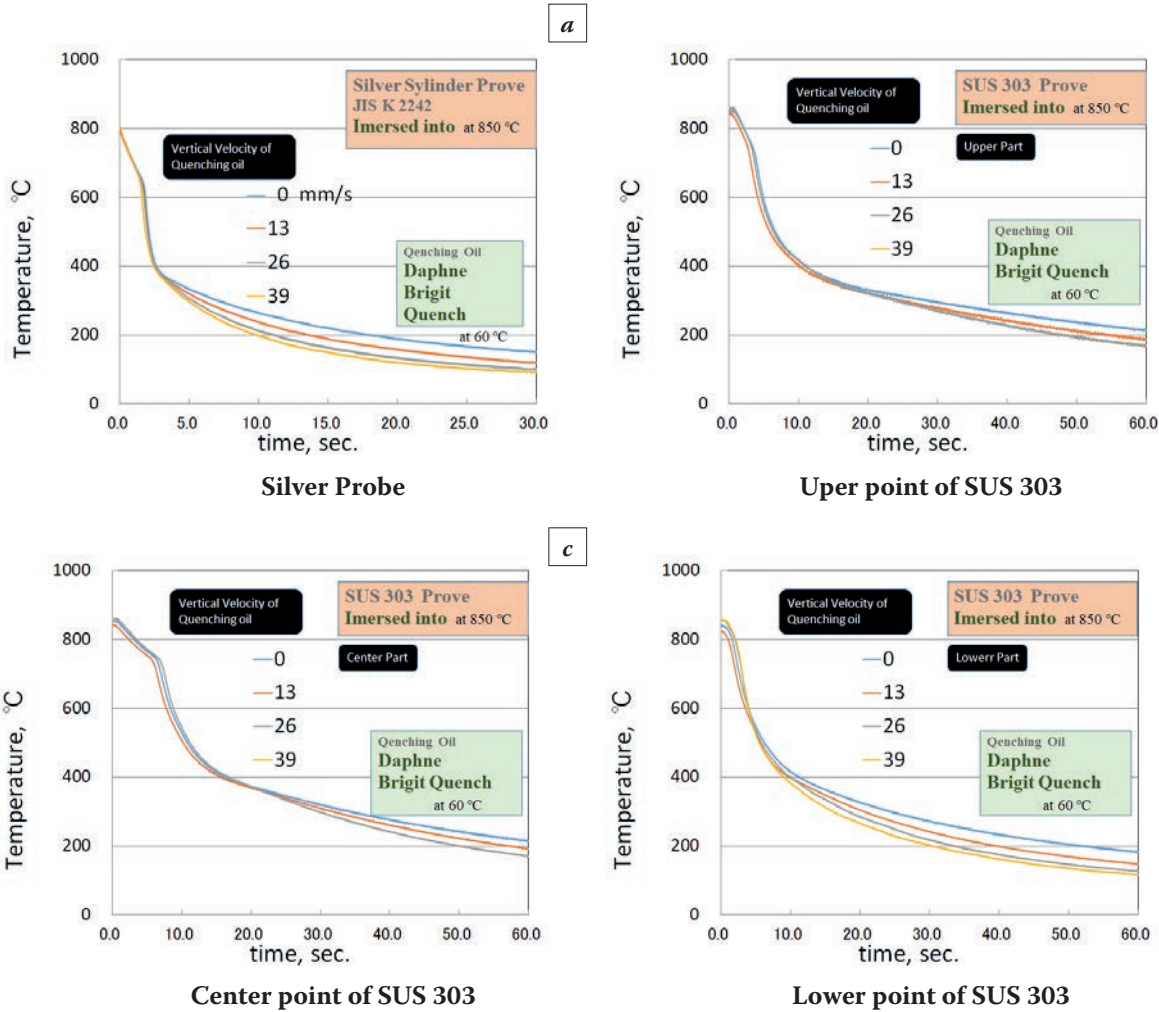


Fig. 3. Measured Cooling Curves Temperature measured just below the surface

“FLOgraph-PIV” software made by Photron Co., Ltd. from the image obtained from the high-speed camera.

## RESULTS AND DISCUSSION

### Cooling curves

The cooling curve measurement result of the sample coolant is shown in Fig. 3. In the silver probe and center part of SUS 303 specimen, that was measured temperature at center of cylinder, it could be

observed clearly the film boiling stage, but in upper and lower part, it can not be observed film boiling stage clearly. Therefore, the specific temperature that was collapsed boiling film was observed clearly in silver probe and center part of SUS 303 cylinder specimen. And in side surface of cylinder, the specific temperature was constant for velocity of coolant. It was observed the specific temperature of silver was 638 °C, SUS 303 was 730 °C higher than 100 degree. Influence of velocity of coolant appeared below 400 °C, that was convection stage. Therefore cooling

speed was increased depend on velocity of coolant in convection stage, in shown Fig. 3.

**Results of visualization**

Fig. 4a shows the cooling curves at positions of the upper, center and lower point on the side of the

SUS303 rod probe. Fig. 4b shows an image taken with a high speed camera. Fig. 4(c) shows the vector value of flow field analyzed using the PIV visualization technique. It can be seen from Fig. 4a that the flow field around the test bar varies greatly at different times when it is cooled. Before 1.56 seconds, the vapor film in the middle of the side of the rod probe was basically formed, which belongs to the film boil-

Cooling Time, s	Cooling Curves	Picture, 1/240 s Temperature, °C	PIV Analysis
0.24	<p>SUS 303 Prove Imersed into at 850 °C 0 mm/s Center Part Upper Part Lower Part Quenching Oil Daphne Bright Quench at 60 °C 0.24 s</p>	<p>850.1 852.3 839.0</p>	
1.56	<p>SUS 303 Prove Imersed into at 850 °C 0 mm/s Center Part Upper Part Lower Part Quenching Oil Daphne Bright Quench at 60 °C 1.56 s</p>	<p>820.6 834.6 803.3</p>	
4.15	<p>SUS 303 Prove Imersed into at 850 °C 0 mm/s Center Part Upper Part Lower Part Quenching Oil Daphne Bright Quench at 60 °C 4.15 s</p>	<p>676.2 778.7 587.1</p>	
6.48	<p>SUS 303 Prove Imersed into at 850 °C 0 mm/s Center Part Upper Part Lower Part Quenching Oil Daphne Bright Quench at 60 °C 6.48 s</p>	<p>505.2 736.6 493.5</p>	
	<b>a) Cooling curves on upper, center and lower part of cylinder probe</b>	<b>b) Image taken by a high speed camera</b>	<b>c) Vector results by PIV analysis</b>

Fig. 4. Images and results of PIV analysis

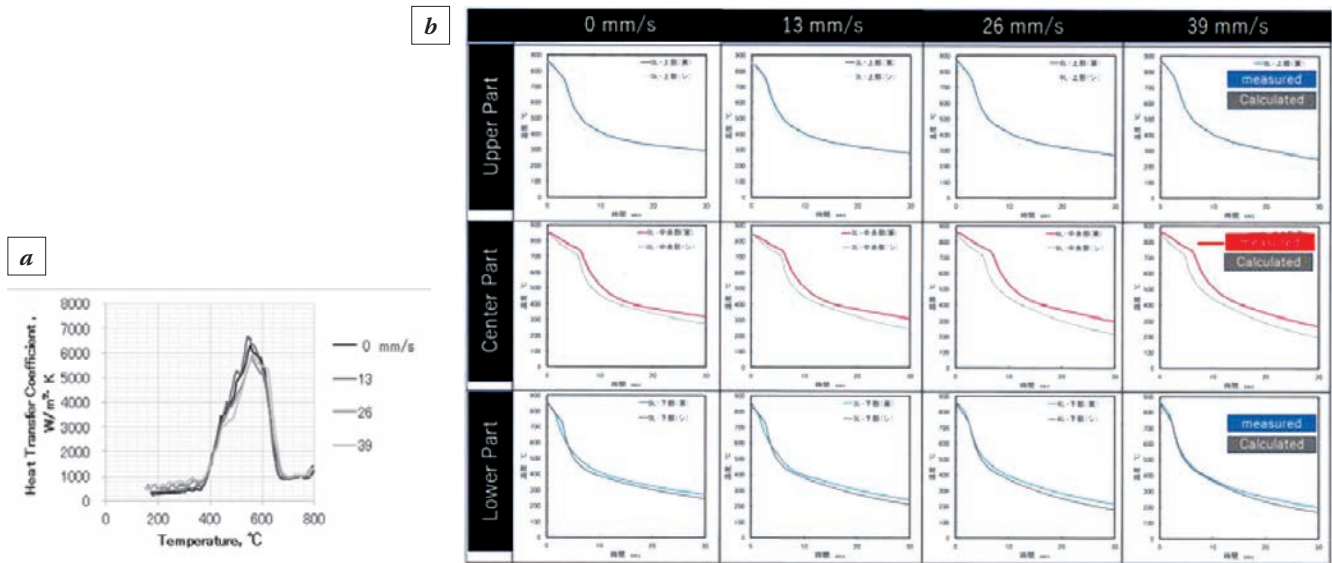


Fig. 5. Comparison of simulation results for each point cooling curves of SUS 303 and measured data

ing stage. At 6.48 seconds, the vapor film on the side of the began to peel off, which was in the nuclear boiling stage. However, there was no film boiling on the upper and lower sides of the rod probe, and there was no obvious vapor film on the surface. Therefore, it can also be seen from the cooling curve that there is a characteristic temperature in the center of the side of the rod probe, but there is no characteristic temperature in the upper and lower portions of the side of the rod probe.

## SIMULATION RESULTS heat tranecer coefficient

Heat trancelefer coefficient identified from cooling curve of silver cylinder JIS K 2242 in Fig. 5a. Cooling curves calculated from two-dimensional thermal conduction analysis of SUS 303 material by inputting it to the CAE heat treatment simulation code DEFORM HT and the result compared with the cooling curve measurement value in Fig. 5b. the calculated cooling curve matched the measured value, validity of experiment, identification analysis and calculation was confirmed acknowledgment. So that, these system can use quenching simulation for analysis or prediction.

## CONCLUSIONS

1) Connect the thermocouple to the center of the side of the SUS 303 cylindrical test bar and the inside of the test bar at 5 mm inward to measure the cooling curve. The cooling curves of the three positions were

compared with those measured at the center of the silver test bar. The characteristic temperature of the SUS 303 test bar was found to be about 730 °C, which is higher than the characteristic temperature of the silver test bar.

2) Even if the flow rate of the coolant becomes 0, 13, 26 and 39 mm / s, the characteristic temperature shows a constant value in the range of  $\pm 10$  °C.

3) No vapor film formation was observed at the upper and lower ends of the SUS 303 test bar, even if the flow rate was increased.

4) The high-speed camera captures the cooling state, the vapor film cools, and repeatedly expands and contracts at the center. The results obtained correspond to the cooling curve.

5) From the cooling curve of the silver test bar, a vapor film was observed on the side of the test bar. The cooling speed of the silver test bar is more than doubled compared to the SUS 303 test bar. The characteristic temperature of the test silver sample was 638 °C, and the result of the flow rate was not obtained within the range of  $\pm 10$  °C.

6) Using the cooling curve of the silver test bar, the heat transfer coefficient was calculated by inverse solution method, and the obtained heat transfer coefficient was brought into the heat treatment simulation program to re-simulate the cooling curve of the SUS 303 test bar. It is found that the heat transfer coefficient of the silver test bar is relatively large, which is not suitable for the heat treatment simulation of the SUS 303 test bar. This shows that although the commonly used silver test bars have certain effects on the evaluation of the cooling performance of the heat treatment coolant, there are still problems to be solved for accurately calculating the heat transfer co-

efficient of the steel surface and the deformation of the accurately simulated parts.

### ACKNOWLEDGMENT

This work was supported by High-Tech Research Center in Saitama Institute of Technology in Japan. The authors also thank Mr. Masami Yamanaka and Mr. Katsumi Ichitani, IDEMITSU KOSAN Co., Ltd., for useful advice on experimental method.

### REFERENCES

1. **Tagaya M., Tamura I.** Research of Quenching Liquid // NIPPON KINZOKU GAKKI-SI. Vol. 15–16. 1951–1952. Report1-4.
2. **Dhir V.K.** Investigation of Mechanisms Associated with Nucleate Boiling Under Microgravity Conditions // Proceedings of the Third Microgravity Fluid Physics Conference. NASA CP–3338. 1996. P. 153–158.
3. **Inoue T., Nagaki S., Kishino T., Monkawa M.** // Ing. Arch. 1981. 50-5. P. 315–327.
4. **Inoue T., Ju D.Y., Arimoto K.** // Proc. 1st int. Conf. Quenching and Control of Distorsion. 1992. P. 205–212.
5. **Mukai R., Ju D.Y.** Simulation of carburizing-quenching of a cylinder. Effect of carbon content on residual stresses and distortion // Journal de Physique IV (proceedings). 2004. P. 489–497, DOI: 10.1051/jp4:2004120056.
6. **Ju D.Y., Zhang W. M., Zhang Y.** Modeling and experimental verification of martensitic transformation plastic behavior in carbon steel for quenching process // Materials Science and Engineering A. 2006. Vol. 438, No. 440. P. 246–250, DOI: 10.1016/j.msea.2006.01.125.
7. **Hideo Kanamori, Tatsuo Inoue etc.** Identification of Heat Transfer Coefficient of Quenching Media // Netsushori. 1996. 36(6). 390–395.

## HEAT TREATMENT OF FASTENERS AT AO BELEBEEVSKY PLANT “AVTONORMAL”

Нет  
аннотации

A.A. Sorokin

AO Belebевsky plant “Avtonormal”. Belebey, Russia  
asorokin@belzan.ru

????????

**Keywords:** fasteners; annealing; hardening; ferrite-martensite steels; cold-heading; hardenability.

The most important components of the manufacturing process of cold-headed fasteners with subsequent quenching are the requirements for the steel grade used and preparation process for forging. Together with branch institutes and metallurgical plants of Russia a number of research works were carried out in the facilities of AO BelZAN. As a result the following information was obtained:

1. The most mass product for cold-headed fasteners is economically alloyed boron-containing steel. Quenching into oil (as compared to quenching into water) boron-containing steels allows obtaining stable mechanical properties of finished products, while the viscosity characteristics are increased by 15–20%. At the same time, the best combination of strength and plastic properties is provided at steel hardening into oil starting from 950 °C. With subsequent tempering at 550 °C.

2. Studies on the production of carbon, economically alloyed steels made it possible to obtain the following information: a reduced disposition for austenite grain growth of 20G2R, 30G1R (23MnB4, 30MnB) steels in the temperature range of 950–1000 °C was revealed, which allows temperature rise of quenching to 980–1000 °C, which means subsequent increase of hardenability of boron-containing steel. It was also noted that an increase in the carbon content from 0.12 to 0.35% in boron-containing steels contributes to an increase in their tendency to austenite grain growth by 10–15%.

3. Carbon steels have a significant tendency for austenite grain growth in the entire austenitization temperature range of 850 + 1200 °C, and, as in the case of economically alloyed steels, increasing their

carbon content from 0.10 to 0.20% increases their tendency to austenite grain growth by 5÷10%.

4. The tendency of the studied steels to structural heredity was revealed in the range of annealing temperatures used at present. Therefore, to ensure a homogeneous fine structure of economically alloyed boron-containing steels 20G2R, 30G1R and alloyed steel 38CrMnNiMo (SAE 8640) with the initial large grain, additional austenitization is necessary at a temperature of 830–850 °C (for steel 20G2R, 30G1R) and 850–870 °C (for steel 38CrMnNiMo). For carbon steels 10 and 20 with initially coarse austenite grains, additional austenitization is not required since phase recrystallization occurs at traditionally used spheroidizing annealing temperatures.

5. Laboratory studies have shown that economically alloyed boron-containing steel 20G2R, 30G1R and alloyed steel 38CrMnNiMo with larger austenitic grains have lower characteristics of technological plasticity and higher values of strength characteristics (when reducing the grain size from 65 to 20 microns, technological plasticity increases by 8–12%). This is due to the fact that the used annealing modes are insufficient for atomization of austenitic structure (demonstration of structural heredity). Therefore, it is necessary to choose modes for double annealing of steels supplied with initially large austenitic grain, including annealing or normalization from a temperature of 900–910 °C (which will contribute to the atomizing of austenite structure) with subsequent annealing, carried out according to the traditional technology.

6. It is shown that increase in cooling rate from 0.1 to 1 °C/min practically does not affect the degree

of spheroidizing of perlite (cementite) in economically alloyed boron-containing steels 20G2R, 30G1R and only an increase in cooling rate to 5 °C/sec leads to a significant decrease in the degree of spheroidization (up to 40%). Unlike boron-containing steels, steel 38CrMnNiMo has maximum degree of spheroidization (~ 84%), at furnace cooling rates in the range of air cooling temperatures this steel practically does not spheroidize.

7. On the basis of the studies obtained and data received from previous studies, the structures of the investigated boron-containing, alloyed and carbon steels should be separated according to the level of hardenability and technological plasticity during cold heading of high-strength fasteners:

- For economically alloyed boron-containing steels 12G1R, 20G2R, 30G1R, alloyed steel 38CrMnNiMo as well as low-carbon steels 10 and 20 with initially fine structure ( $D^r < 30 \mu\text{m}$ ) of both spheroidized and lamellar perlite does not show a significant difference in the performance patterns of each steel studied, regardless of the structural state (lamellar or spheroidized perlite).

- At austenitic grain size of  $30 < D^r < 50 \mu\text{m}$  (for economically alloyed boron-containing steels 12G1R, 20G2R, 30G1R and low-carbon steels 10 and 20) and at  $20 < D^r < 40 \mu\text{m}$  (steel 38CrMnNiMo), the hardenability characteristics of lamellar structures are 20–30% higher, while technological plasticity is 15–20% lower compared to steel with a spheroidized structure.

- For economically alloyed boron-containing steels 20G1R, 30G1R, alloyed steel 38CrMnNiMo, and also low-carbon steels 10 and 20 with the initially coarse-grained structure ( $D^r > 50 \mu\text{m}$ ), lamellar structures in steels for cold-heading are not allowed.

- Dilatometric studies of economically alloyed boron-containing steels showed that for 30G1R steel the critical quenching rate (in the temperature range of 700–800 °C) per bainite-martensite structure is 10 °C/sec (which is ensured when quenching into water a steel billet corresponding to the average level of alloying of the grade, 54 mm in diameter and when quenched in oil, 38 mm in diameter). For the 20G2R steel, the critical rate is already 52 °C/sec (which is ensured when quenching into water a steel billet corresponding to the average level of alloying of the

grade, 39 mm in diameter and when quenched in oil, 24 mm in diameter).

Development work on cold forging of stud parts from steels with a two-phase ferrite-martensite structure allows us to conclude that under the conditions of AO BelZAN, it is possible not only to manufacture 8.8 property class parts without subsequent quenching, but also to produce rolled steel with ferrite-martensite structure.

## REFERENCES

1. **Lyakishev N.P., PlinerYu.L., Lappo S.I.**, Boron-containing steels and alloys. M. : Metallurgia, 1986. 192 p.
2. **Zolotareva E.N., Klyachko M.A., Feldman B.L.** Selection of the optimal composition of boron-containing steels for the production of high-strength fasteners using cold-heading method / Materials of the seminar “Prospects for the production of precise blanks and parts by the method of volumetric deformation. M. : MDTPD, 1990.
3. **Zolotareva E.N., Klyachko M.A.**, Choice of the composition of low-alloyed boron-containing steels for cold-heading / Materials of the seminar “Prospects for the production of precise blanks and parts by the method of volume deformation”. M. : MDTPD, 1990.
4. **Mamoria A., Tamura E., Hori A.** Influence of quenching conditions on the processing temperature on the mechanical properties of steel // Tetsu to hagane. 1975. Vol. 61, No. 4. P. 298.
5. **Otida E.** Study of the hardenability of boron-containing steel during quenching with forging heating by neutron diffraction // Tetsu to hagane. 1982. Vol. 68, No. 12, P. 1280.
6. **Ueno Ito K.** Effect of austenitization temperature and cooling rate in the austenitic phase on the hardenability of boron-containing steel // Tetsu to hagane. 1988. Vol. 74, No. 12. P. 2337–2344.
7. **Ueno Ito K.** Optimal conditions for obtaining the maximum effect of hardenability at introduction of boron // Tetsu to hagane. 1988. Vol. 74, No. 5. P. 910–917.
8. **Akmatsu N.** Features of heat treatment of boron-containing steel and its use in mechanical structures // Tetsu to hagane. 1983. Vol. 69, No. 13. P. 1317.
9. **Shiga T.** Hardenability of steel in the process of direct quenching and distribution of boron // Tetsu to hagane. 1984. Vol. 70, No. 13. P. 1388.

## CONTROL OF THE STRUCTURE AND PROPERTIES OF COLD ROLLED STEEL OF TWO-PHASE FERRITE AND MARTENSITIC STEEL (OF DFMS TYPE) SUBJECTED TO CONTINUOUS ANNEALING

I.G. Rodionova<sup>1</sup>, O.N. Baklanova<sup>1</sup>, A.A. Pavlov<sup>1</sup>, N.A. Karamysheva<sup>1</sup>, A.S. Melnichenko<sup>2</sup>,  
S.V. Denisov<sup>3</sup>, V.E. Telegin<sup>3</sup>, S.G. Andreev<sup>3</sup>, A.V. Mastyaev<sup>3</sup>

<sup>1</sup>I.P. Bardin Central Research Institute of Ferrous Metallurgy (TsNIIChermet). Moscow, Russia

<sup>2</sup>National University of Science and Technology «MISiS». Moscow, Russia

<sup>3</sup>PAO «Magnitogorsk Iron and Steel Works». Magnitogorsk, Chelyabinsk region, Russia

igrodi@mail.ru

Using the methods of statistical analysis to assess the influence of the chemical composition and technological parameters on the properties of cold-rolled DFMS or DP steels after processing in a continuous annealing unit (CAU) or the continuous hot-dip galvanizing unit (CHDGU), key technological parameters have been identified, optimizing of which allow improving the complex of mechanical characteristics. The formulated hypotheses about the mechanisms of influence of technological parameters on the processes occurring at different stages of the production of cold-rolled steel have been tested experimentally.

**Keywords:** dual-phase ferritic martensitic steels; DPFMS steels; high-strength steels; cold-rolled steels; thermal treatment; continuous annealing unit; the continuous hot-dip galvanizing unit; technological parameters; mechanical properties; statistical analysis.

Two-phase ferritic and martensitic steels (DFMS or DP) are the most popular group of progressive high-strength steels used for the manufacture of various high-loaded car parts. These steels are characterized by high strength, good ductility, low ratio of yield strength to ultimate resistance, high index of strain hardening and VN-effect. Currently, rolled products from cold-rolled uncoated and galvanized DFMS are produced in the range of strength classes ranging from 450 to 980 MPa.

Experience in the production of such steels shows that there is often instability of the obtained values of strength characteristics within one strength class despite the compliance of rolled properties with the requirements of international standards. In addition, it is important to increase the plasticity of steels, which is at the lower level of requirements in most cases. The complex of DFMS properties is formed on the basis of traditional mechanisms of hardening (grain boundary, solid, dispersion), but the ratio of the structural components formed in the final product – ferrite and martensite, their specific properties and characteristics prevails. Each technological conversion of production has an impact on the formation of the structure and properties of rolled products made of DFMS.

Thanks to the methods of data arrays statistical analysis we determine key technological parameters

influencing the properties of DFMS strength class of 600 MPa and 780 MPa. The analysis performed made it possible to formulate recommendations on the optimal hot rolling and annealing modes both in the continuous annealing unit (CAU) and in the continuous hot-dip galvanizing unit (CHDGU) in order to obtain the required set of properties, as well as to identify reserves for increasing the strength and plasticity of the DFMS of a certain strength class by controlling the technological parameters.

On the basis of thermodynamic calculations of temperature conditions for the existence of equilibrium fractions of the main (structural) and excess phases, as well as recommendations on the results of statistical analysis, a program was developed and laboratory simulation of annealing of DFMS of 600 MPa and 780 MPa strength classes for both CAU and CHDGU modes was carried out. Table 1 shows the chemical composition of the steels involved in the process of laboratory modeling. The rolled samples have been treated on GLEEBL 3500 laboratory complex allowing the combination of continuous processing thermal cycle of the sample loading force exerted upon the strip during its passage through the continuous units.

Fig. 1 shows the dependence of the strength characteristics of the model samples of rolled strength class 600 from the annealing temperature during

Table 1. Chemical composition of steel of 600 MPa and 780 MPa classes for laboratory modeling

Strength class	C	Si	Mn	S	P	Cr	Ni	Cu	Al	N	Nb	Mo
600 MPa	0.08	0.04	1.45	0.007	0.01	0.29	0.02	0.03	0.039	0.007	0.019	0.208
780 MPa	0.09	0.07	1.91	0.005	0.011	0.31	0.02	0.03	0.046	0.007	0.025	0.10

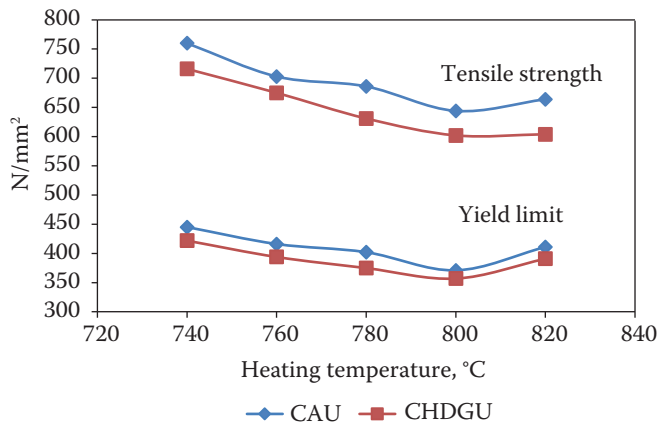


Fig. 1. Dependence of strength characteristics of model steel samples of class 600 on heating temperature and strip speed during processing by CHDGU mode

processing according to the CAU and CHDGU modes.

It is clear that a decrease in the annealing temperature leads to an increase in strength characteristics. After processing by the CAU mode, the level of

strength characteristics is higher than by the CHDGU mode, which is probably due to a significantly lower end temperature of accelerated cooling (275 °C instead of 470 °C). As shown by the study of the microstructure of steel, at heating temperatures of 740–780 °C it consists of ferrite and martensite (Fig. 2*a, b*). As the annealing temperature increases to 800 °C, the proportion of «spots» of martensite significantly decreases; in the structure one may witness the release of cementite near the «spots» in large numbers; this is the result of the decay of weakly stable austenite sites formed at heightened annealing temperatures (see Fig. 2*b, d*). This change in structure is true for both the CHDGU regime (Fig. 2) and the CAU regime (Fig. 3). The difference is that the proportion of sites of the austenite decayed by the bainite mechanism after processing under the CAU regime at high heating temperatures is significantly less, and the degree of martensite decay during the low-temperature overcooling is not high. This was confirmed by the results of the study on a transmission electron microscope. Besides, it should be noted more dispersed

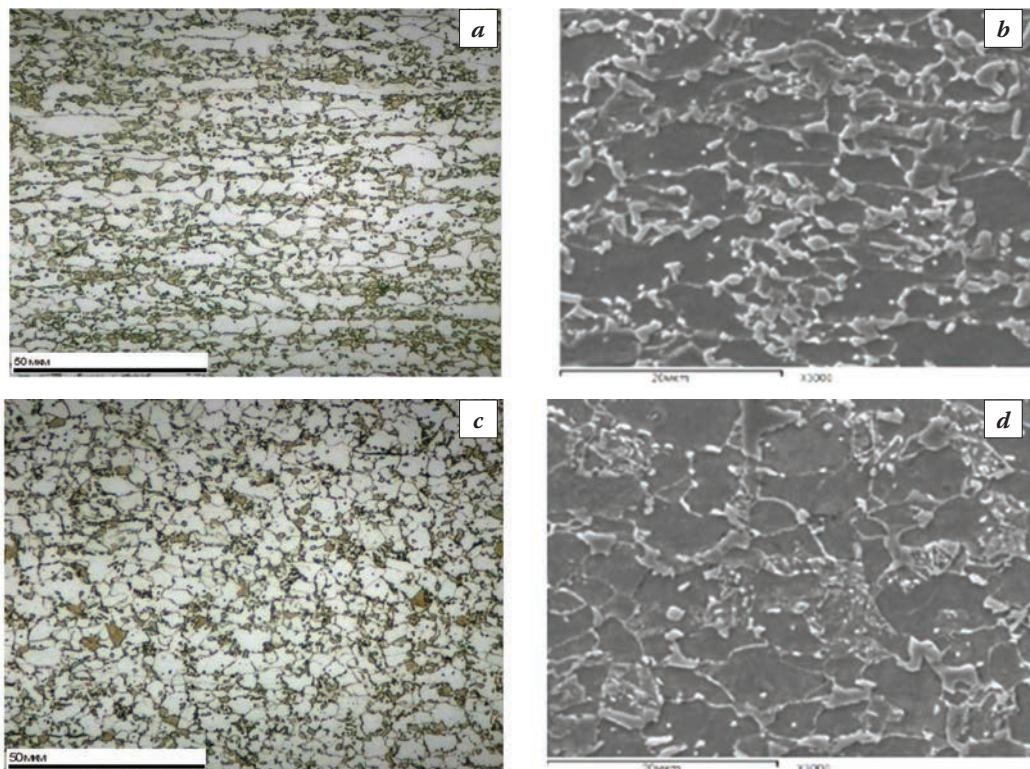


Fig. 2. Microstructure of class 600 steel after modeling annealing according to the CHDGU mode: *a, b* – annealing temperature 740 °C; *c, d* – annealing temperature 800 °C

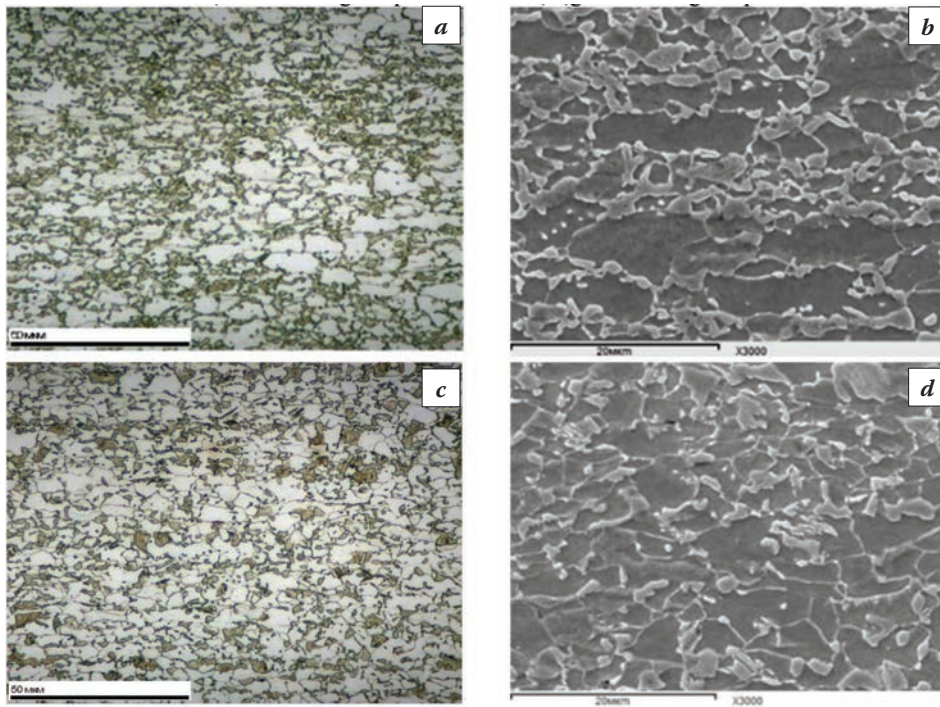


Fig. 3. Microstructure of class 600 steel after modeling annealing according to the CAU mode: *a, b* – annealing temperature 740 °C; *c, d* – annealing temperature 800 °C

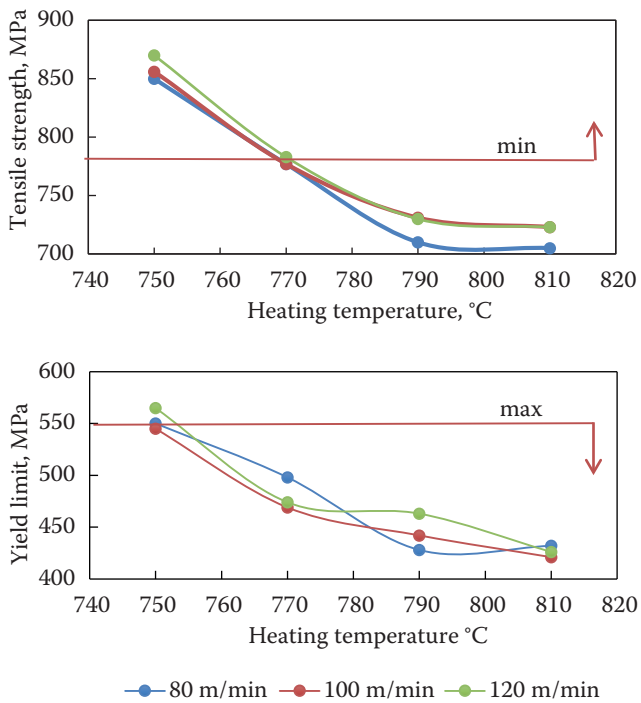


Fig. 4. Steel strength characteristics change depending on heating temperature and strip speed

size of martensitic grains after processing under the CHDGU regime with respect to more short-term stay of the metal in the heating zones and exposure when processing in this mode.

On steel with strength level of 780 MPa (the steel composition see Table 1) the influence of process-

ing parameters on the properties of steel was carried out in the simulation of the CHDGU mode. When processing of samples, three speed modes were used. Fig. 4 shows the obtained dependences of the strength characteristics of the annealing temperature and the speed of the strip showing that at the heating temperature range 750–770 °C the strength characteristics of the steel meet the requirements for 780 class steel. The temperature range 750–790 °C poses the highest rate of drop in the values of strength characteristics. With increasing temperature the plasticity of steel increases monotonically.

According to the microstructure analysis the difference in the structural state of the steel after its annealing at the temperatures of 750, 770 and 790 °C is as follows. Fig. 5a shows that after annealing at a temperature of 750 °C, the recrystallization of ferrite has not yet fully occurred, the grains retain an elongated shape, some have a characteristic blockage. Martensite grains are combined into compact groups, the size of martensite grains ranges from 1 μm to 3 μm. As the annealing temperature increases, the shape of the ferritic grains changes and acquire limits close to the polyhedral type (Fig. 5b, c). After annealing at a temperature of 770 °C, the martensite spots are more evenly distributed in the ferritic matrix, while their size has not changed significantly, but the volume fraction of martensite has slightly decreased. Annealing at a temperature of 790 °C led to a further decrease in the volume fraction of martensite due to

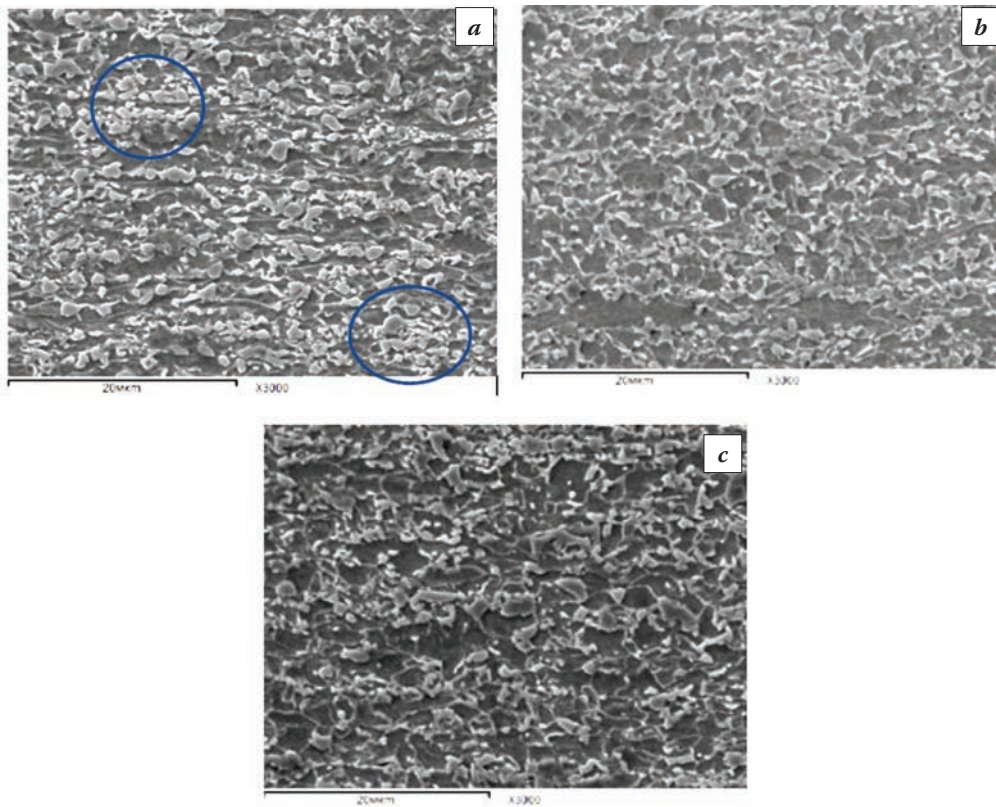


Fig. 5. Microstructure of steel of 780 MPa class after heating temperatures of 750 °C (*a*), 770 °C (*b*) and 790 °C (*c*) (strip speed is 120 m/min)

the formation of a new ferrite, while the size of martensite spots increased slightly. Due to the fact that the formation of a new ferrite during the austenite breakage is accompanied by the enrichment of the remaining volume of austenite with carbon, which significantly increases its stability, respectively, and the resulting martensite is also characterized by a more stable state.

The laboratory simulation of processing according to CAU and CHDGU modes on samples of carbonated rolled two-phase ferritic and martensitic steels of 600 and 780 MPa classes showed the ability to control the formation of the structure to ensure the required level of properties of the rolling stock, as well as to assess the possibility to improve the complex of mechanical and technological characteristics.

# INVESTIGATION OF THE STEEL STRUCTURE 15Kh11MF-Sh DEPENDING IN THE THERMO-DEFORMATION PARAMETERS OF TREATMENT, INVESTIGATION OF THE CHARACTERISTICS OF LARGE-SIZED STAMPED BLANKS OF TURBINE BLADES

M.O. Smirnov<sup>1</sup>, T.A. Chizhik<sup>1</sup>, I.N. Tsybulina<sup>1</sup>, A.M. Zolotov<sup>2</sup>

<sup>1</sup>PJSC «Power machines». Saint-Petersburg, Russia

<sup>2</sup>Peter the Great St. Petersburg Polytechnic University, Saint-Petersburg, Russia

Smirnov\_MO@power-m.ru; Chizhik\_TA@power-m.ru; Tsybulina\_IN@power-m.ru; prf\_zam@mail.ru

One of the priority directions of development of the Russian energy industry is the creation of a half-speed steam turbine for nuclear power plants. A feature of such a turbine is a significant increase in weight and size characteristics of the main components compared with the full-speed turbine. For the working blades of the last stage of the rotor of the low pressure cylinder, steel 15Kh11MF-Sh is used. To date, the stamped blanks of turbine blades of steel 15Kh11MF-Sh had a maximum length of 1.3 m, in the case of a half-speed turbine, the stamping length is more than 2 m. An increase in the dimensions of the working blades leads to an increase in the existing working loads, which requires the provision of a set of service properties in the volume of large workpieces.

This research investigated the effect of thermal deformation parameters of stamping and subsequent heat treatment on the structure and properties of steel 15Kh11MF-Sh. Investigation of the actual metal structure of blade forgings from steel 15H11MF-Sh was carried out. The results of mathematical and physical modeling of metal deformation processes are compared, and mechanical properties of the blades are obtained.

**Keywords:** plastic deformation; martensitic steel; turbine blade; heat treatment; microstructure.

## INTRODUCTION

The blades of the last stages of the low-pressure cylinder of the steam turbine are highly loaded parts, the material of which has high requirements for operational reliability. One of the main conditions is the stability of the mechanical characteristics throughout the cross section, which is determined by the uniformity of the structure obtained in a stamped blank.

In this investigation, a stamped blank of a turbine blade made of steel 15Kh11MF-Sh is considered. The initial blank for stamping has a length of more than 2 meters. Such dimensions are extreme in the manufacture of parts on existing equipment – steam-air die-forging hammer with a mass of falling parts of 25 t. The technology developed earlier implies 4 stamping junctions (heating and deformation), which are necessary for the final forming of a stamped blank [1]. In the final stages, when the blade projection area increases, the rigidity of the stamping process approaches the limit level and the forging height deformation during one heating (9–12 hammer blows) becomes 6–7 mm. Stagnant zones of plastic deformation and a high gradient of temperature fields are

formed, which may adversely affect the final structure of the blade metal and its properties [2].

Deformations of 5–15% may be critical, with them possibly an intensive increase in grain size, for this reason, when developing technology, investigation is needed to determine the effect of thermal deformation parameters on the microstructure of steel 15Kh11MF-Sh [3, 4]. It was decided to fix such changes using compression tests at various temperatures and upsetting rations, followed by heat treatment according to the blade manufacturing cycle [5–7]. Such tests are usually carried out to construct third kind recrystallization curves, which make it possible to predict the formation of a microstructure in finished products [8–13].

The aim of this work is to study the microstructure of steel 15Kh11MF-Sh with various thermal deformation parameters of the process of stamping large-sized blanks of turbine blades.

## MATERIAL AND EXPERIMENTAL METHOUDS

Prior to testing for compression, the quenching temperature of steel 15Kh11MF-Sh was investigat-

ed. The temperature was selected on samples from blanks for stamping in the laboratory by experienced quenching at temperatures of 990; 1005; 1020; 1035; 1050; 1065 °C. According to the analysis of the microstructure, the quenching temperature was chosen – 1020 °C, tempering was carried out at 680 °C. The mechanical properties of the metal correspond to the strength category KP70 required by construction.

For compression tests, the Gleeble-3800 Pocket Jaw module was used. The test temperatures and the degree of deformation of the samples during compression tests were chosen on the basis of the overlap condition of the possible ranges of variation of the thermal and deformation parameters of the process of stamping turbine blades on the hammer during the last transition. Samples selected from forgings for stamping, sample drawing and testing scheme are shown in Fig. 1. The chemical composition of the investigated melting is presented in Table 1.

In the work carried out earlier, the dependences of the strain resistance were obtained, which are necessary for mathematical modeling, with a strain degree of 0,8, various strain rates of 0,1; 1; 10; 20; 33 s<sup>-1</sup> and temperatures of 800, 930, 980, 1030, 1080, 1130, 1180 C. Compression tests was performed to the logarithmic true deformation.

When conducting tests for the study of thermal deformation parameters at  $T = 1180; 1130; 1080; 1030; 980; 930$  °C, the samples were heated at a rate of  $v_{\text{heat}} = 5$  °C/s to  $t_{\text{heat}} = 1180$  и 1160 °C, kept at this temperature  $\tau = 60$  s for homogenization of the composition. Next, the samples were cooled at a rate of 3 °C/s to the test temperature, after which a compression test was performed with a true strain of 0,05; 0,1; 0,2; 0,6 at the strain rate of 1 s<sup>-1</sup>. The cooling of the samples to room temperature took place in the specimen grips.

The microstructure was analyzed using a Carl Zeiss optical microscope and a Thixomet image analyzer in the middle of the working part of samples. Macrotemplates for the manufacture of thin sections were cut from the working part of the sample by the method of electro-erosion cutting along the direction of deformation. Heat treatment of half of the deformed specimens was carried out according to the selected heat treatment mode. Analysis of the grain was carried out by comparison with standard grain grading scales, GOST 5639.

Table 1. Chemical composition of the investigated steel

Chemical elements content, %									
C	Si	Mn	Cr	Mo	V	Ni	S	P	Cu
0.14	0.42	0.39	10.2	0.63	0.26	0.27	0.006	0.013	0.14

## RESULTS

Analysis of the results in the investigation of rheological properties showed a logical increase in the strain resistance with decreasing test temperature. The type of the dependence of stress on the degree of deformation remained unchanged in all cases, a continuous increase in flow stresses at all strain rates is observed. At all temperatures, except for 800 °C, the stress decreases at a strain rate of 0,1 s<sup>-1</sup>, which is due to the suppression of recrystallization processes at high strain rates. This decrease is also observed at a speed of 1 s<sup>-1</sup> at a processing temperature of 1180 °C (Fig. 2).

Proceeding from the obtained dependences of the flow stress on the degree of true deformation, one can say that the development of dynamic recrystal-

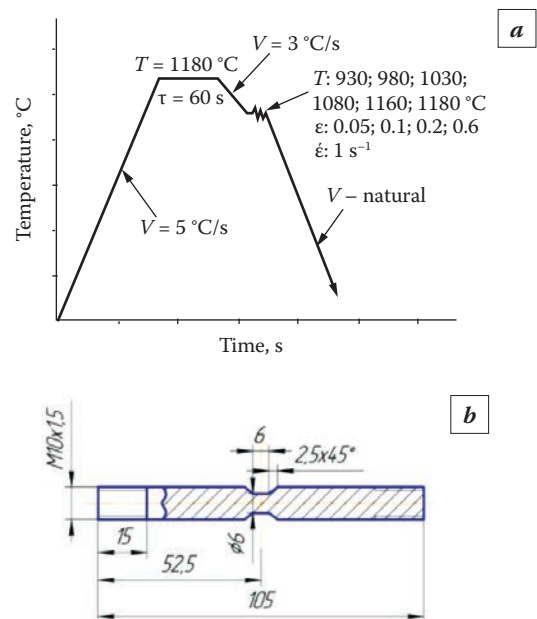


Fig. 1. Scheme of the experiment steel 15Kh11MF-Sh for the study of thermal deformation parameters (a) and the sketch of the sample for testing (b)

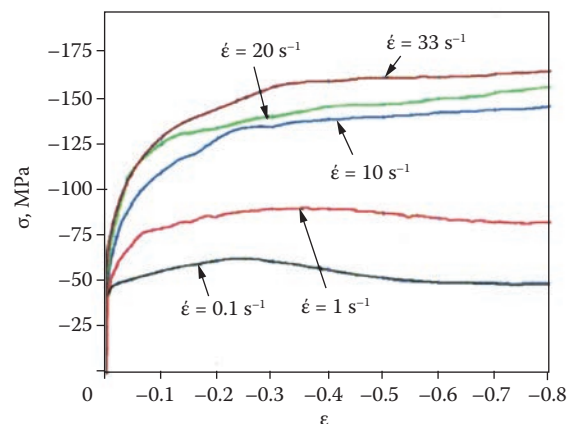


Fig. 2. Strain resistance at a processing temperature of 1180 °C

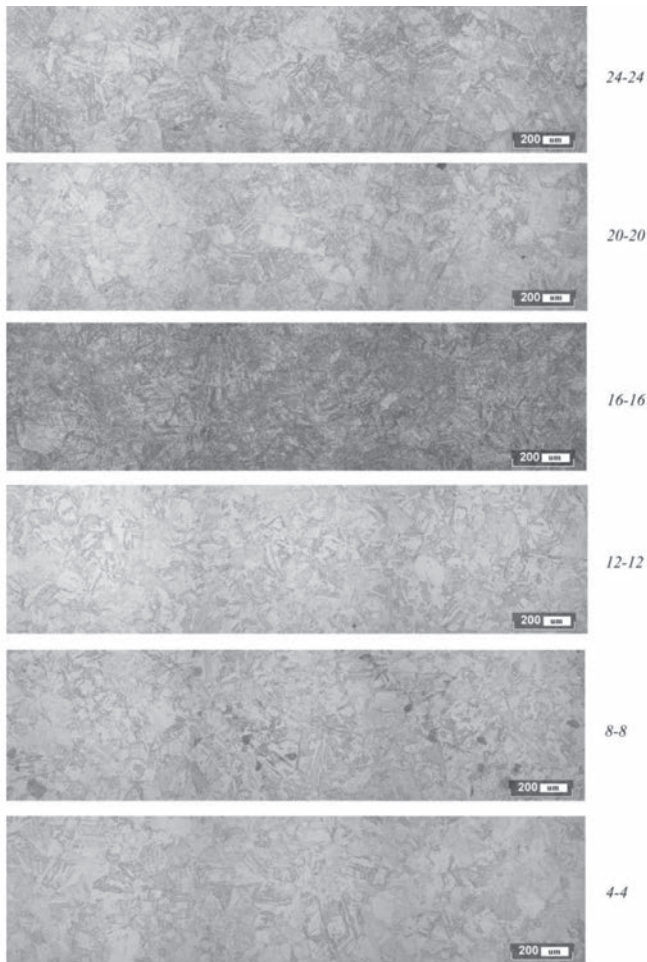


Fig. 3. The microstructure of the samples that have undergone heat treatment after deformation (numbering according to Table 2),  $\times 200$

lization at processing temperatures was not detected, which is confirmed by similar investigations of the dependencies of the deformation resistance of high-chromium steels [14–16].

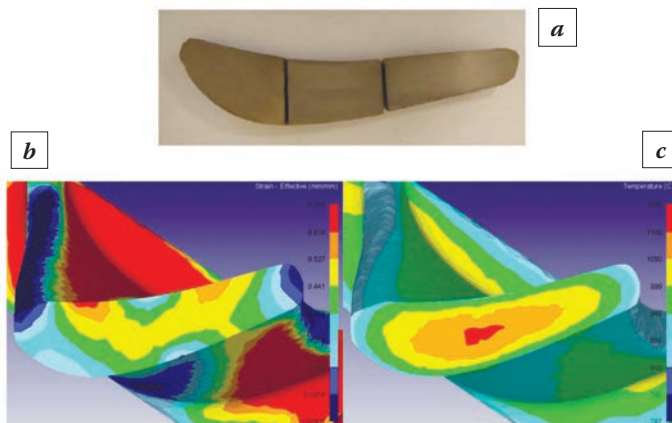


Fig. 4. Templet from an airfoil of stamped billet of a turbine blade (a), distribution of strain intensity (b) and temperature (c) in this section

The microstructure of the metal of the deformed and heat-treated samples for the investigation of thermal deformation parameters is martensite, the character of the grains is equiaxial. The grain size for all deformation parameters is uniform, with a predominance of grains of 5 grade, in certain operation modes there is a presence of grains of 4 grade. The microstructure of the metal of the deformed samples with the maximum degree of deformation and different temperatures, after carrying out heat treatment, is shown in Fig. 3.

The deformation parameters (temperature and degree of deformation), the grain grade and the average grain size of the deformed samples are shown in Table 2. The parameters of the metal microstructure of the deformed samples are also presented without heat treatment.

An analysis of the grain size carried out on the metal of the deformed specimens without subsequent heat treatment did not reveal significant differences compared with the heat-treated metal after deformation, which is probably based on high cooling rates of the thin section of the sample.

There are no critical deformation zones. Grinding the grain size with increasing degree of deformation is not observed at any compression temperature. Increasing the degree of deformation at processing temperatures of 930, 980, 1180 °C actually does not affect the behavior of the structure of the material. At temperatures of 1080, 1130 and 1180 °C, starting from a degree of deformation of 0,1 and 0,2, lath martensite prevails, and at a deformation of 0,6, the presence of retained ferrite is noticeable. In the case of a treatment temperature of 980 °C, the release of globular carbides  $Me_{23}C_6$  is noticeable along the large-angle boundaries of the original austenitic grains, at the boundaries of martensitic rails, and at low degrees of strain, carbides are located along the body of a martensite grain [17].

According to the results of mathematical modeling of stamping process and analysis of compression tests samples, the microstructure of the finished blade was evaluated prior to launch into production. The parallel solution of these problems led to the conclusion about the possibility of using technology with small deformations on the latest stamping transitions.

After manufacturing an pilot batch of stamped blanks, an investigation of the microstructure in stagnant zones of plastic deformation, concentrated in the areas adjacent to the suction side, pressure side, and the leading and trailing edges was conducted. The zone was determined based on the results of mathematical modeling of the stamping process, the maximum temperature and strain gradients at the moment after the end of the deformation process at the fourth stamping transition were selected (Fig. 4).

Table 2. Staging and investigation results

Summary investigation table						
№	Designation of samples that passed heat treatment after deformation	Temperature, °C /upsetting ratio	Grain grade (GOST 5639 scale)		The average grain size (GOST 5639), $\mu\text{m}$	
			After heat treatment 1020 °C, 2 hours, cooling in water	Without heat treatment	After heat treatment 1020 °C, 2 hours, cooling in water	Without heat treatment
1	1-1	930/0.05	5	5	62	62
2	2-2	930/0.1	5-4	5-4	62-88	62-88
3	3-3	930/0,2	5-4	5-4	62-88	62-88
4	4-4	930/0.6	5-4	5-4	62-88	62-88
5	5-5	980/0.05	5	5	62	62
6	6-6	980/0.1	5	5	62	62
7	7-7	980/0.2	5-4	5	62-88	62
8	8-8	980/0.6	5	5-4	62	62-88
9	9-9	1030/0.05	5-4	5-4	62-88	62-88
10	10-10	1030/0.1	5	5	62	62
11	11-11	1030/0.2	4	4	88	88
12	12-12	1030/0.6	4-5	4-5	88-62	88-62
13	13-13	1080/0.05	4-5	5-4	88-62	62-88
14	14-14	1080/0.1	5	5	62	62
15	15-15	1080/0.2	5-4	5-4	62-88	62-88
16	16-16	1080/0.6	5	–	62	–
17	17-17	1130/0.05	5	5-4	62	62-88
18	18-18	1130/0.1	5	5-4	62	62-88
19	19-19	1130/0.2	5	5	62	62
20	20-20	1130/0.6	5	5	62	62
21	21-21	1180/0.05	5	5	62	62
22	22-22	1180/0.1	5	5	62	62
23	23-23	1180/0.2	5-6	5	62-44	62
24	24-24	1180/0.6	5	5	62	62

Table 3. The results of mechanical testing of stamped blanks with a minimum (min) and maximum (max) surface hardness

Mechanical properties									
Direction and location of sample clipping	Workpiece hardness	$\sigma_{0,2}$ , MPa	$\sigma$ , MPa	$\delta$ , %	$\Psi$ , %	KV, J	KCU, J/cm <sup>2</sup>	% ductile constituent	HB, impact samples
Longitudinal, airfoil part	max	759	879	19	59	29,28,31	68,53	29,32	269
	min	718	836	17	61	40,42,42	88,78	36,34	255
Longitudinal, fillet transition	max	731	869	18	59	26,31,30	59,65	26,22	269
	min	723	846	17	60	32,30,37	73,63	25,22	255
Longitudinal, blade root	max	743	865	17	59	29,28,28	60,60	26,25	269
	min	724	844	19	61	34,34,32	68,75	29,31	255
Transverse, blade root	max	748	872	21	59	28,31,25	60,55	25,22	262
	min	727	851	18	61	30,28,28	58,63	27,31	255
Average value for stamped blank	max	745	871	18,8	59	28,7	60	25,9	267,3
	min	723	844	17,8	60,8	34,1	70,8	29,4	255

The result of the analysis shows the coincidence of the obtained microstructure in a stamped blank with a microstructure after simulating hot deformation.

The microstructure in the studied areas of the blade corresponds to modes 16-16 and 20-20. This is due to the fact that the main deformation takes place

on the first blows of the hammer, at the moment when the workpiece has not yet had time to cool due to contact heat exchange.

After manufacturing an pilot batch of stamped blanks of turbine blades, a comprehensive investigation of the mechanical properties and microstructure was carried out.

Significant changes in the mechanical properties and microstructure, depending on the zone of cutting samples from stamped blanks were not found.

It is quite evident that accurate repetitions of the stress-strain state during mathematical, physical modeling and process of production cannot be achieved, however, the results of the analysis of microstructure and stable of mechanical properties show the adequacy of the application of this methodology to the steel in question. Steel type 15Kh11MF-Sh showed good processability and hardenability in the manufacture of large-sized turbine blades.

## CONCLUSIONS

The heat treatment condition of stamped blanks of blades has been determined. Compression tests have been carried out for various tremor-deformation parameters of the stamping process, with and without subsequent heat treatment. On the basis of the completed investigations, it was concluded that the degree of deformation does not significantly affect the microstructure of a stamped blank of a turbine blade made of steel 15Kh11MF-Sh. Stagnant zones of plastic deformation do not lead to grain growth, and the developed stamping technology, including four heating with no significant deformation at the final transition, is accepted in production.

The results of investigation of the mechanical properties and the microstructure of the material of blanks that have undergone experimental stamping confirm that the production of large-sized turbine blades from steel 15Kh11MF-Sh produces the same structure and approximately equal level of mechanical characteristics over the cross section of the stamped blank.

## REFERENCES

1. **Smirnov M.O., Chizhik T.A., Zolotov A.M., Mishin V.V., Shishov I.A.** Primenenie matematicheskogo modelirovanija dlja izgotovlenija krupnogabaritnyh shtampovok turbinnih lopatok iz zharoprochnoj stali // Tjzheloe mashinostroenie. 2018. № 4. S. 29–33.
2. **Gorelik S.S., Dobatkin S.V., Kaputkina L.M.** Rekristallizacija metallov i splavov. M. : MISIS, 2005. 432 s.

3. **Kodzhaspirov G.E., Rudskoj A.I., Rybin V.V.** Fizicheskie osnovy i resursosberegajushhie tehnologii izgotovlenija izdelij plasticheskim deformirovaniem. SPb. : Nauka, 2006. 350 s.

4. **Fei Chen, Facai Ren, Jun Chen, Zhenshan Cui, Hengan Ou.** Microstructural modeling and numerical simulation of multi-physical fields for martensitic stainless steel during hot forging process of turbine blade // International Journal of Advanced Manufacturing Technology. 2015. 82(1-4). P. 85–98.

5. **Nikol'skij L.A., Figlin S.Z., Bojcov V.V. et. al.** Gorjachaja shtampovka i pressovanie titanovyh splavov. M. : Mashinostroenie, 1975. 285 s.

6. **Zolotov A.M., Chizhik T.A., Smirnov M.O.** Postroenie diagramm rekristallizacii tret'ego roda titanovogo splava VT6 // Nauchno-tehnicheskie vedomosti SPbPU. Estestvennye i inzhenernye nauki. 2017, T. 23, № 4. 118–126 s.

7. **Grigor'ev A.K., Kodzhaspirov G.E., Rybin V.V., Rubcov A.S.** Struktura i svojstva dvuhfaznoj nerzhavjushhej stali posle V.T.M.O. // Izv. Vuzov. Chernaja metallurgija. 1977. № 6. S. 124–128.

8. **Rogel'berg I.L., Shpichineckij E.S.** Diagrammy rekristallizacii metallov i splavov. M. : Metallurgizdat, 1950. 280 s.

9. **Biront V.S.** Teorija termicheskoj obrabotki metallov. Otzhig: Ucheb. Posobie / SFU: ICMiZ. Krasnojarsk. 2007. 234 s.

10. **Bernshtejn M.L., Rahshtadt A.G.** Metallovedenie i termicheskaja obrabotka stali. Tom 2. Osnovy termicheskoj obrabotki. M. : Metallurgija, 1983. 368 s.

11. **Grigor'ev A.K., Kodzhaspirov G.E.** Issledovanie razuprochnenija stali pri proktke v rezhimah V.T.M.O. // Izv. Vuzov. Chernaja metallurgija. 1978. № 8. S. 102-105.

12. **Kodzhaspirov G.E., Kamelin E.I.** Issledovanie dinamicheskoi rekristallizacii vysokoprochnoj nizkolegirovannoj stali s primeneniem fizicheskogo modelirovanija. // Materials Physics and Mechanics. 2016. 27. P. 215–222.

13. **Lanskaja K.A.** Vysokohromistye zharoprochnye stali. M. : Metallurgija, 1976. 216 s.

14. **Lozhnikov Ju.I.** Gorjachaja deformacija struktura i svojstva azotosoderzhashhij stalej razlichnogo naznachenija: avtoref. dis. kand. tehn. nauk: 05.16.01. Moskva, 2004. 25 s.

15. **Smirnov M.A., Pyshmincev I.Ju., Laev K.A., Ahmed'janov A.M.** Vlijanie vysokotemperaturnoj termomehanicheskoj obrabotki na svojstva vysokohromistoj stali // Vestnik JuUrGU, Serija «Metallurgija». 2012. № 39. S. 85–88.

16. Diagrammy gorjachej deformacii, struktura i svojstva stalej: sprav. / pod red. M.L. Bernshtejna. M. : Metallurgija, 1989. 544 s.

17. **Roncerja L.M., Vebera S., Theisena V.** Nucleation and precipitation kinetics of M23C6 and M2N in an Fe–Mn–Cr–C–N austenitic matrix and their relationship with the sensitization phenomenon // Acta Materialia. 2011. Vol. 59. P. 6275–6286.

# FRACTURE TOUGHNESS AND FRACTURE MICRORELIEF OF STAINLESS STEEL WITH ULTRAFINE-GRAINED STRUCTURE

E.N. Beletskiy, M.R. Tyutin, L.R. Botvina, U.S. Perminova

A.A. Baikov Institute of Metallurgy and Materials Science of the Russian Academy of Sciences. Moscow, Russia  
enbel@mail.ru

Currently, more and more attention is paid to the ultrafine-grained (UFG) materials, because their mechanical and physical properties are significantly different from the materials in the initial state. One of the effective methods of obtaining ultra-fine grained structure is severe plastic deformation, in which the material is exposed to large shear deformations at high pressure and low homologous temperature. It is known that after such processing of steels of various classes there is a significant improvement in the strength and service properties while maintaining satisfactory plasticity. The most well-known methods of severe plastic deformation are equal-channel angular pressing (ECAP) and torsion under hydrostatic pressure (THP).

The purpose of this work was to assess the effect of ECAP on fracture toughness, as well as to study the fracture mechanism by studying the fracture microrelief of steel with the coarse- and ultrafine-grained structure using optical and scanning microscopy. Austenitic Cr-Ni-Ti stainless steel in different processing conditions was studied.

**Keywords:** fracture toughness; shear lips; zone of stable growth of crack; severe plastic deformation (SPD); equal-channel angular pressing (ECAP).

The assessment of the fracture toughness of samples with a UFG structure is complicated by the technological difficulties of producing billet of the required size for the manufacture of standard samples used to determine the fracture toughness. It is well known [1] that it is difficult to maintain the correctness of the applicability of the approaches of linear fracture mechanics on small-sized samples. In this regard, it is necessary to develop a methodology for assessing the fracture toughness of small-sized samples. It is necessary to conduct additional studies to assess the mechanical characteristics and study the fracture mechanism of the sample of different orientation with respect to the loading direction.

The investigated steel in the coarse-grained condition was studied after hot rolling and quenching at

1050 °C for 1 hour with water cooling. For ECAP billets were used with a diameter of 20 mm and a length of 90 mm. The ECAP was carried out under the following modes: 4 passes at 20 °C, 6 passes at 200 °C and 6 passes at 400 °C using a matrix with channels intersecting at 120° along the Bc route, that is, after each pass, the billet was rotated 90° [2–5].

To assess the fracture toughness according to the method described in ASTM E399, we used compact disk specimens with dimensions of  $\varnothing 20 \times 6$  mm,  $\varnothing 20 \times 3$  mm (Fig. 1a). A preliminary fatigue crack at the notch tip was created with a decreasing stress intensity factor in order to prevent the formation of plastic deformation zone at the crack tip, affecting the fracture toughness value. The crack opening gage was mounted on the stem of the Nano Plug'n'Play fa-

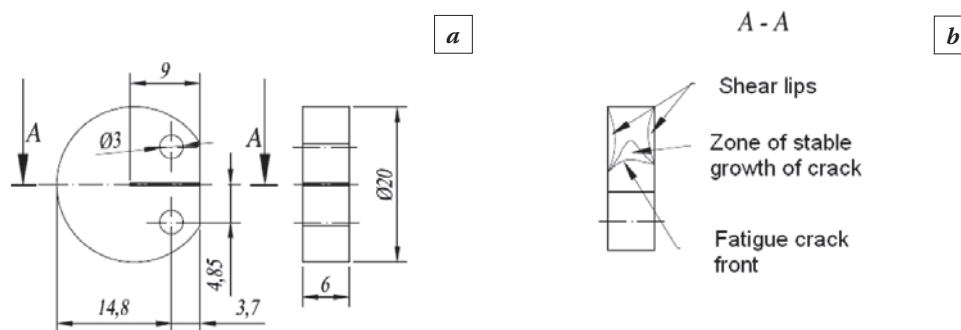


Fig. 1. General view of sample (Disk shaped ASTM E399): *a* – specimen geometry, *b* – scheme of the fracture specimen

Table 1. Properties of the austenitic Cr-Ni-Ti stainless steel in different processing conditions

State	$\sigma_{YS}$ , MPa	$\sigma_{UTS}$ , MPa	$D$ , nm	$K_Q$ , MPa $\cdot\sqrt{m}$	$S_{STAB}$	$S_{SL}$
Quenching at 1050 °C	313	605	25000	22.4	0.066	0.373
ECAP 20 °C (4 passes)	1228	1173	430	66.1	0.111	0.241
ECAP 400 °C (6 passes)	940	1009	200	65	0.145	0.211
ECAP 200 °C (6 passes)	1038	1047	100	68	0.156	0.159

tigue machine (maximum load 15 kN) manufactured by BiSS P.Ltd. In the process of testing, the compliance of the loading device was taken into account by subtracting its values obtained on similar samples without notch.

As a result of the tests, the fracture toughness of Cr-Ni-Ti steel in the initial state after quenching, as well as after equal-channel angular pressing (ECAP) at different temperatures and different number of passes was evaluated. Macro- and microrelief of fracture were studied, the length and area of the zones of stable growth of cracks and shear lips were estimated. It was found that the condition of the plane stress state, which is necessary for determining the  $K_{IC}$ , was not fulfilled; therefore, the calculated value of stress intensity factor  $K_Q$  was estimated.

Table 1 presents the mechanical properties of the material  $\sigma_{YS}$ ,  $\sigma_{UTS}$ , subgrain structure size  $D$  obtained in [2–5], as well as the values of the fracture toughness  $K_Q$ , area of stable growth of crack  $S_{STAB}$  and shear lips area  $S_{SL}$  (Fig. 1b). The zone sizes were normalized to the working area of the sample, because the thickness of the samples differed from each other.

It is established that with the decrease in grain size to a subgrain size of 430 nm, the strength characteristics and fracture toughness of the steel under study sharply increases ( $\approx 33\%$  of the initial state). However, further reduction in the size of structural elements does not lead to a significant increase in this value (Fig. 2c). Analysis of the results of quantitative fractography showed a similar dependence of the fracture toughness value on the stable crack growth area  $S_{STAB}$  (Fig. 2a) and on the shear lips area (Fig. 2b). Thus, it can be concluded that the increased fracture toughness of samples with a UFG structure is associated with a longer stage of stable crack growth compared with samples in the quenching state. The reduction in the area of the shear lips is connected with a decrease in the plasticity of the material as a result of ECAP.

As can be seen in the Fig. 3, the fracture relief in the zones of stable and accelerated crack growth has a viscous character both for the samples in the quenched and sub microcrystalline state. Staged change in the microrelief of the fracture was re-

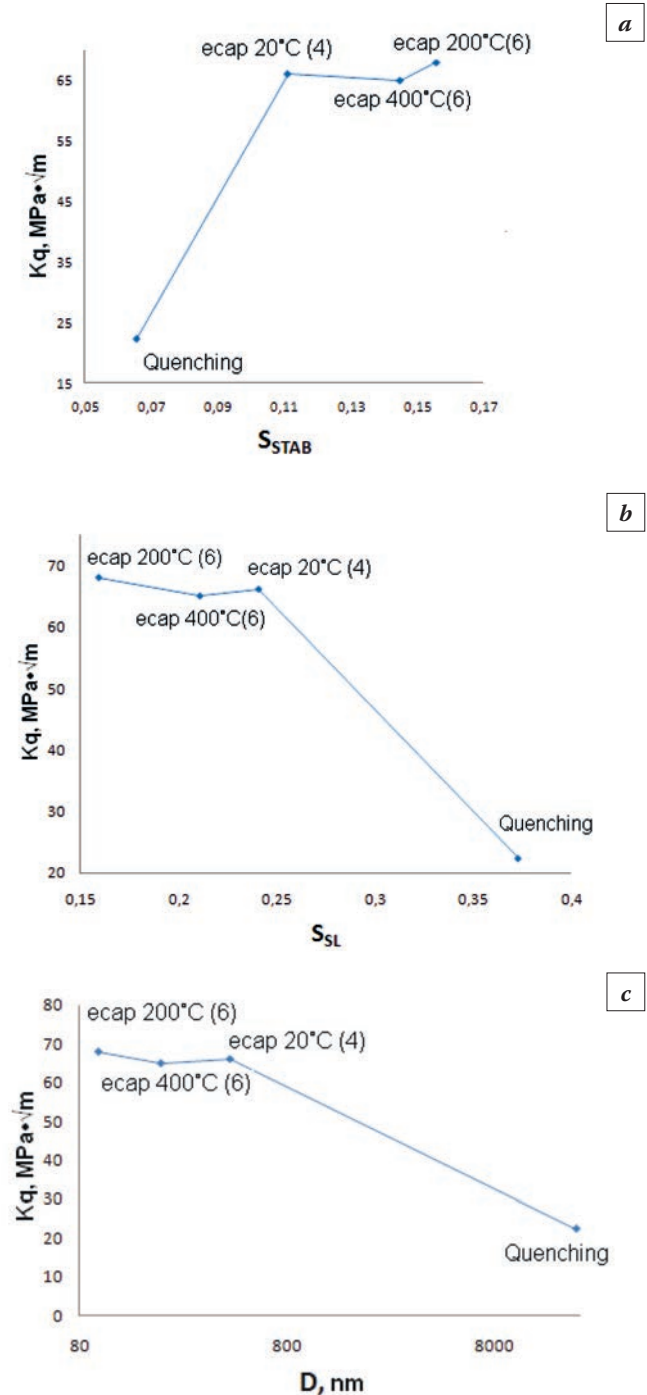


Fig. 2. Dependencies of fracture toughness  $K_Q$  on the area of stable crack growth  $S_{STAB}$  (a),  $K_Q$  on the shear lips area  $S_{SL}$  (b),  $K_Q$  on the subgrain structure size  $D$  (c)

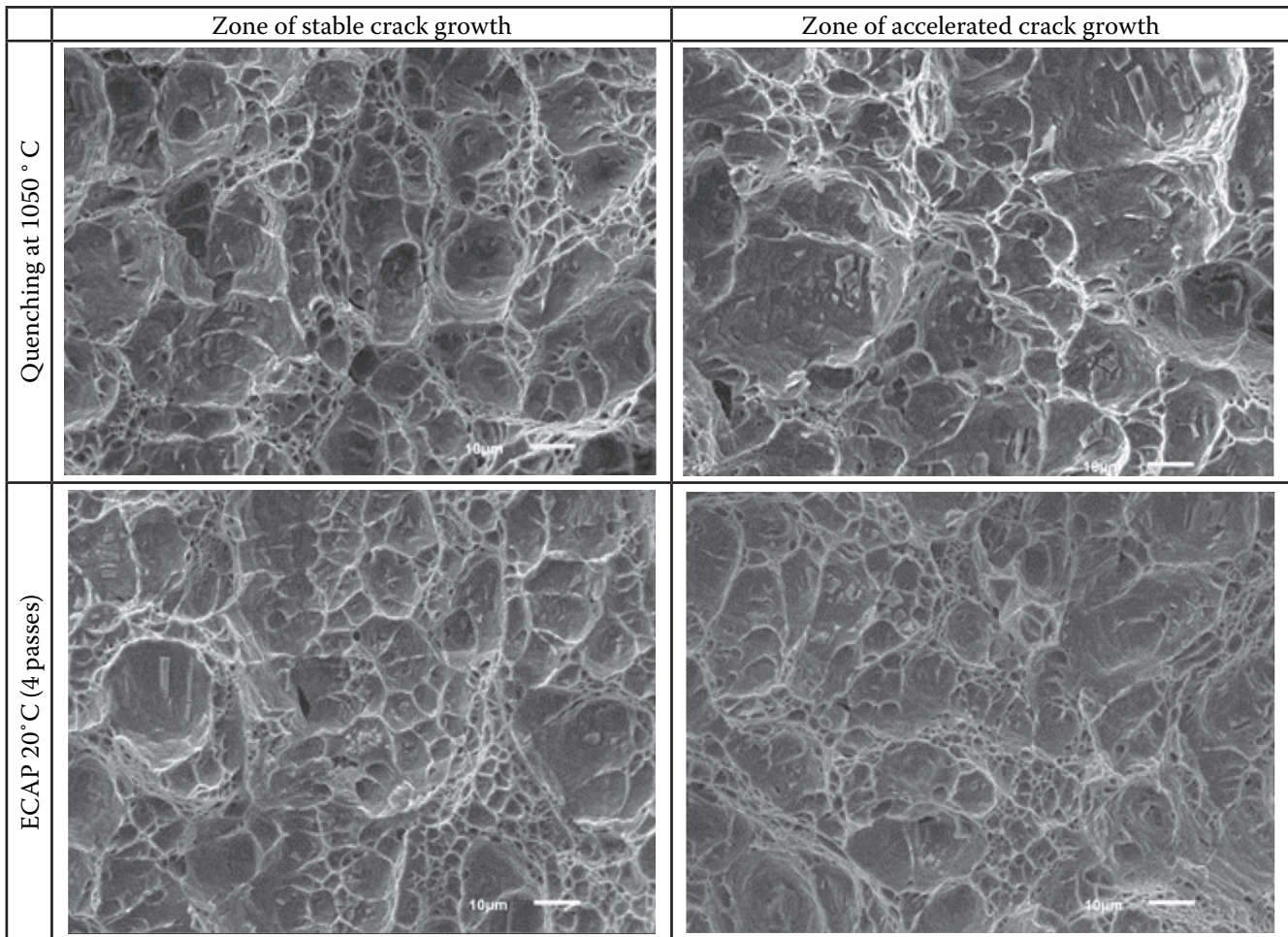


Fig. 3. Microrelief of fractured surfaces

vealed. In the region of stable crack growth, equiaxial dimples are predominantly observed. In the zone of accelerated crack growth, the dimples become elongated, which indicates the appearance of shear stress component. With a decrease in the size of the subgrain structure, the proportion of small dimples grows.

The work was supported by the Fundamental Research Program 37 P of the Presidium of the Russian Academy of Sciences.

## REFERENCES

1. Pineau A., Benzerga A.A., Pardoën T. Failure of metals III: Fracture and fatigue of nanostructured metallic materials // *Acta Materialia*. 2016. Vol. 107. P. 508–544.
2. Dobatkin S.V., Skrotzki W., Rybalchenko O.V., Terent'ev V.F., Belyakov A.N., Prosvirnin D.V., Raab G.I., Zolotarev E.V. Structural changes in metastable austenitic steel during equal channel angular pressing and subsequent cyclic deformation // *Materials Science & Engineering A*. 2018. Vol. 723. P. 141–147.
3. Dobatkin S.V., Terent'ev V.F., Skrotzki W., Rybalchenko O.V., Pankova M.N., Prosvirnin D.V., Zolotarev E.V. Structure and Fatigue Properties of 08Kh18N10T Steel after Equal\_Channel Angular Pressing and Heating // *Russian Metallurgy (Metally)*. 2012. Vol. 2012. P. 954–962.
4. Dobatkin S. V., Rybal'chenko O. V., Kliauga A., Tokar' A. A. Effect of shear strain on the structure and properties of chromium-nickel corrosion-resistant steels // *Metal Science and Heat Treatment*. 2015. Vol. 57. P. 44–51.
5. Rybal'chenko O.V., Prosvirnin D.V., Tokar A.A., Levin V.P., Tyutin M.R., Raab G.I., Botvina L.R., Dobatkin S.V. Effect of ECAP on structural, mechanical and functional characteristics of the austenitic Cr-Ni-Ti steels // *Journal of Physics*, 2018, Conf. Series 1134, doi:10.1088/1742-6596/1134/1/012049.

# INFLUENCE OF THERMO TREATMENT ON THE DISLOCATION SUBSTRUCTURE AND PHOTOCATALYTIC PROPERTIES OF ZNO

I.M. Sosnin<sup>1</sup>, A.A. Vikarchuk<sup>1</sup>, A.E. Romanov<sup>2</sup>

<sup>1</sup>Togliatti State University, Togliatti, Russia

<sup>2</sup>University ITMO, St. Petersburg, Russia

sim.nanosci@gmail.com

---

Properties of functional materials are greatly dependent on their defect structure. Thermo treatment is one of the most effective approaches of control of defect substructure of crystal materials. In the case of semiconductors defect state influences on the band structure and their functional properties. Photocatalysis is one of the most promising ways of using semiconductors, which is widely applied among methods of purification of wastewater against toxic organic pollution. The main advantage of photocatalysis along with other advanced oxidation processes is the possibility of using solar light as a source of energy for degradation of organic substances, that allows to decrease treatment cost. In the present work we show that thermo treatment of ZnO nano- and microparticles influences the photocatalytic activity due to the ordering of dislocation structure. Powder of ZnO had been fabricated by hydrothermal method. Next it was annealed at 650 °C during 3 hours with slow cooling occurring with the furnace. Obtained samples show high photocatalytic activity under UV light and under visible (wavelength 410 nm).

**Keywords:** zinc oxide; annealing; dislocation substructure; band structure.

---

## INTRODUCTION

Zinc oxide (ZnO) is one of the most popular semiconductor materials. It is widespread in many industrial branches, such as a fabrication of gas sensor [1], ultraviolet detectors [2], solar cells [3], photocatalysis [4] and other. Photocatalysis permits to initiate the chemical degradation of toxic organic substances in the presence of semiconductor under light irradiation. Such a technique is used for purification of wastewater. If photon energy is higher than band gap of semiconductor, chemical degradation takes place. Most of commercially used photocatalytic active materials (TiO<sub>2</sub>, ZnO, SnO<sub>2</sub>, WO<sub>3</sub>) have high band gap (3,4 eV and more), which corresponds to ultraviolet irradiation with length of wave 360 nm and smaller. Creation of photocatalysts, active under solar irradiation allows to decrease cost of water purification. Variation of chemical composition of semiconductor usually allow to change band structure and increase the photocatalytic activity. Doping of ZnO with cobalt, cadmium, iron allows to modify band structure but is very dangerous in view of high toxic properties of these metals. Another way of enhancing of light spectrum to visible range, which could activate the photocatalytic degradation is modification of defect structure, such examples are shown in patents. There are a lot of kinds of defects in ZnO influencing on the photocatalytic

properties. For example, oxygen vacancies [5] and zinc interstitial [6]. At the surface is created sub-bandgap with lower width due non-stoichiometry. Defects of crystal lattice also may play negative role, paper it is shown reducing of photocatalytic activity after milling of ZnO nanoparticles due formation of zinc vacancies, which are the recombination centers of electrons and holes. Annealing of ZnO at different temperatures allows to increase activity due diffusion of oxygen vacancies from the depth of the crystal to the surface. Further augmentation of annealing temperature promotes relaxation of oxygen vacancies and decreasing of photocatalytic activity. Different authors show various value of the most appropriate of annealing temperature of ZnO: 250 °C, 350 °C, 400 °C and other. In the present work we show that dislocation structure appreciably influences the photocatalytic activity too. We prepared zinc oxide by hydrothermal method and then annealed in the range of temperatures from 200 to 1000 °C. Width of bandgap and microstrain in obtained samples have been slightly changed. Samples annealed at 1000 °C showed the smallest dislocation density, but they displayed activity lower than initial samples. Samples annealed at 650 °C performed maximum activity under UV and visible light. X-ray diffraction showed that dislocation structure is significantly changed: it transformed from chaotic to ordered.

## EXPERIMENTAL

### Fabrication of ZnO samples

Samples of photocatalysts have been synthesized by our original method, based on hydrothermal process [7]. Zinc chloride dissolved in solution of ethylene glycol and water have been treated with alkaline at constant stirring and heating at 70 °C for 2 hours. ZnO particles formed as a result of interaction between zinc chloride and alkaline. Formed ZnO powder have been separated from solution by centrifugation and washed with distilled water several times against byproducts. Next resulting powder had been dried at 105 °C and divided on four parts. Each part had been annealed at different temperature: from 200 to 1000 °C for 3 hours. Samples was slowly cooled together with furnace.

### Description of ZnO samples

ZnO particles had plate-like shape with plate thickness 20–50 nm, in other two dimensions their size reaches 500 nm (Fig. 1a). X-ray diffraction

(XRD) analysis of the initial sample proved that it is ZnO with wurtzite crystal structure (zincite), space group P63mc. Ratio of lattice constants was  $c/a = 1.602$ . Full width at half maximum (FWHM) of XRD peaks of annealed at 650 °C ZnO samples is proportional to the tangent of the angle  $2\theta$ , this behavior can be attributed to the presence of ordered dislocation substructure; such type of substructure order was confirmed with Williamson-Hall (W-H) plot. Substructure of ZnO was changed from chaotic to ordered.

### Photocatalytic tests

The photocatalytic activity of obtained ZnO particles was analyzed under visible light (wavelength 410 nm) and ultraviolet lamp (wavelength 365 nm) radiation. Particles (1 g/l) were dispersed by using ultrasonic device in aqueous solution of phenol (1 mg/l). Then resulting suspension was stirred at 500 rpm during the photocatalytic experiment. Phenol concentration was measured with spectrofluorophotometer Shimadzu RF-6000 (Shimadzu, Japan). Fig. 2 shows the results of photocatalytic tests. Annealed samples displayed activity higher than initial, moreover in the presence of annealed sample phenol had been degraded under visible light (Fig. 2b).

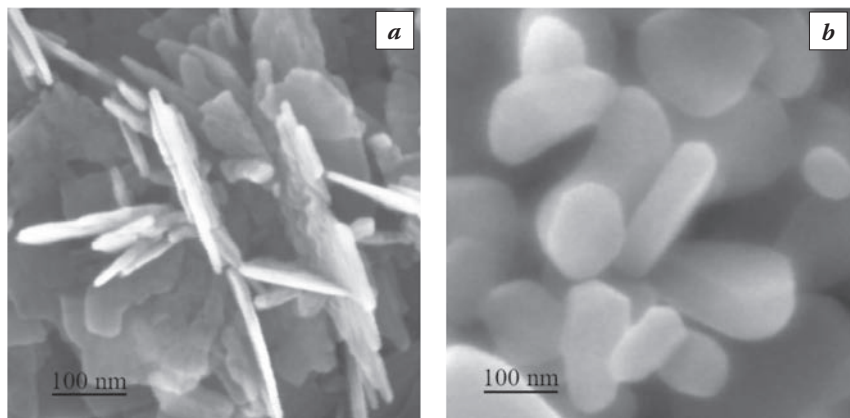


Fig. 1. SEM images of ZnO samples (a) until and annealing (b) after annealing at 650 °C

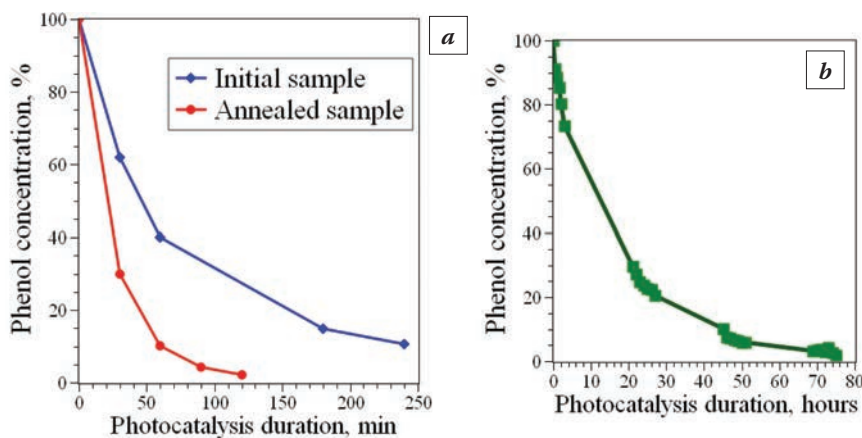


Fig. 2. Results of photocatalytic tests of obtained ZnO particles (a) under UV light, (b) under visible light

## DISCUSSION

In the present work we show that thermo treatment of ZnO influence the photocatalytic activity of them. Powder of nano- and microparticles was fabricated by hydrothermal method. Next it was annealed at 650 °C during 3 hours with slow cooling occurred with the furnace. Obtained samples show high photocatalytic activity under UV light and under visible (wavelength 410 nm). We think that there are two reasons of such activity of ZnO samples. The reason of rising of activity is ordering of dislocation structure with increasing of regions of coherent scattering. At this case density of linear dislocation increases and band

structure changes. Additional levels appear inside the bandgap due to which the photocatalytic activity of the material increases.

*This work was supported by the grant of the Ministry of Education and Science of the Russian Federation, State Task 16.2314.2017/4.6.*

## REFERENCES

1. **Spencer M.** Gas sensing applications of 1D-nanostructured zinc oxide: Insights from density functional theory calculations // *Progress in Materials Science*. 2012. 57 (3): 437–486.
2. **Wang Y. et al.** A Self-Powered Fast-Response Ultraviolet Detector of p–n Homojunction Assembled from Two ZnO-Based Nanowires // *Nano-Micro Lett.* 2016. 1(11): 1–7.
3. **Hossain M.F., Zhang Z.H., Takahashi T.** Novel micro-ring structured ZnO photoelectrode for dye-sensitized solar cell // *Nano-Micro Letters*. 2010. 2 (1): 53–55.
4. **Wang J., Liu P., Fu X., Li Z., Han W., Wang X.** Relationship between Oxygen Defects and the Photocatalytic Property of ZnO Nanocrystals in Nafion Membranes // *Langmuir*. 2009. 25 (2): 1218–1223.
5. **Al-Sabahi J., Bora T., Al-Abri M., Dutta J.** Controlled Defects of Zinc Oxide Nanorods for Efficient Visible Light Photocatalytic Degradation of Phenol // *Materials*. 2016. 9 (4): 238. doi:10.3390/ma9040238.
6. **Warule S.S., Chaudhari N.S., Kale B.B., More M.A.** Novel sonochemical assisted hydrothermal approach towards the controllable synthesis of ZnO nanorods, nanocups and nanoneedles and their photocatalytic study // *CrystEngComm*. 2009. 11 (12): 2776.
7. **Sosnin I.M., Vickarchuk A.A., Malkin V.S., Belko V.L.** Approach of fabrication of photocatalyst based on zinc oxide. 2018. Rus. pat. RU 2678983.

# ULTRASONIC TREATMENT OF ALUMINUM ALLOYS IN THE TECHNOLOGY OF CASTING PRODUCTS WITH ENHANCED RESOURCE CHARACTERISTICS

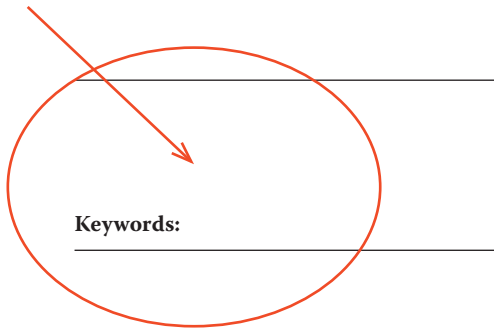
A.U. Petrov<sup>1</sup>, A.E. Shestovskikh<sup>1</sup>, V.N. Timofeev<sup>1</sup>, V.I. Luzgin<sup>2</sup>,  
A.S. Koptyakov<sup>2</sup>, I.V. Kostin<sup>3</sup>, S.G. Bocvar<sup>3</sup>

<sup>1</sup>RELTEC Ltd. Ekaterinburg, Russia

<sup>2</sup>Ural Federal University. Ekaterinburg, Russia

<sup>3</sup>RUSAL ETC LLC. Russia

Нет аннотации и  
ключевых слов



Keywords:

Application of a powerful ultrasonic treatment of the melt on the stage of technological metallurgy processing is increasingly being used through the last decade. Ultrasonic treatment of metal melts allows simultaneous realization of a number of technological processes, such as grain cleaning (grinding), segregation and degassing control (reduction), which gives a certain universality and effectiveness of this method when solving the problem of improving the quality of foundry products.

Ultrasonic treatment of aluminum melts is the most effective, cheap and environmentally friendly mean of degassing dissolved hydrogen in Al–Si cast alloys. Hydrogen dissolved in an aluminum melt can reach  $6.5 \times 10^{-6}$  m<sup>3</sup>/kg in a liquid state at a temperature above melting point and drops at a temperature slightly below melting point  $3.4 \times 10^{-9}$  m<sup>3</sup>/kg. During the solidification, this difference causes redundancy of precipitated hydrogen, which leads to its zoning between solid dendrites and the formation of porosity. Gas and shrinkage porosity dramatically reduces the mechanical properties of products, reduces flaw resistance, and impairs ductility and endurance [1].

Natural degassing of liquid aluminum takes fairly long time (up to 1 hour), the hydrogen content is reduced to  $(1-2) \cdot 10^{-6}$  m<sup>3</sup>/kg. Such a long process of degassing is unacceptable in foundry production. Application of a short-term ultrasonic treatment of

the aluminum melt (up to 2 min) allows to reduce the hydrogen content to  $(0.7-0.8) \cdot 10^{-6}$  m<sup>3</sup>/kg, which is acceptable for industrial application of this method [1].

High intensity of the melt degassing in aluminum alloys is achieved by high-energy ultrasonic treatment, when developed cavitation takes place. Cavitation in a liquid metal can be initiated by introducing a certain level of acoustic energy. The threshold of cavitation in typical aluminum melts is from 0.55 to 0.85 MPa, which is achieved at a radiation intensity of 10 W/cm<sup>2</sup> [2].

Currently, the following variants of technological processes have been applied (Fig. 1) using ultrasonic effects on low-melting-point fusible metal and their alloys:

- ultrasonic degassing in a limited volume of melt with periodic or continuous feeding of the melt;
- ultrasonic treatment of the melt during crystallization by the method of continuous casting of ingots or the exact casting of shaped castings [3].

One of the promising directions in solving the problem of improving the performance of aluminum alloys is the application of ultrasound to obtain a molten dispersion-strengthened composite materials and alloyed alloys [4].

To implement the above ultrasound technologies, the research and development enterprise RELTEC

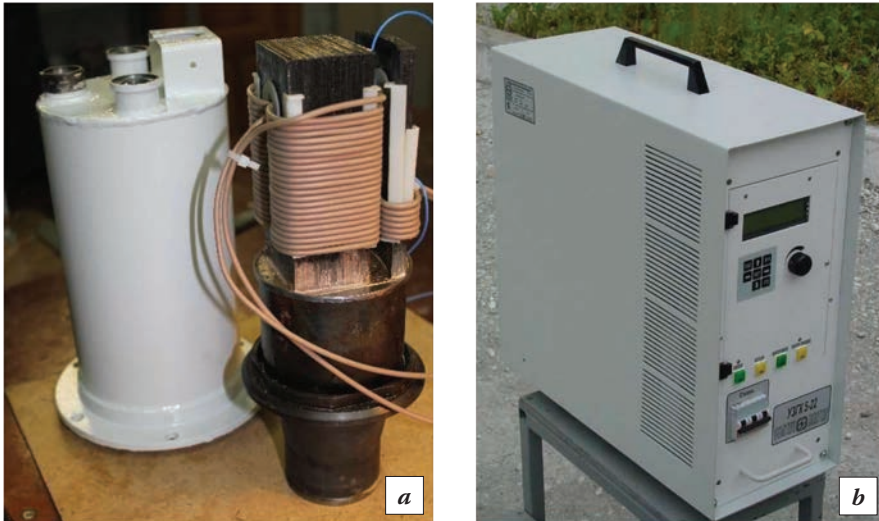


Fig. 1. Ultrasonic treatment equipment: *a* – magnetostrictive transducer with feedback; *b* – ultrasonic electric generator

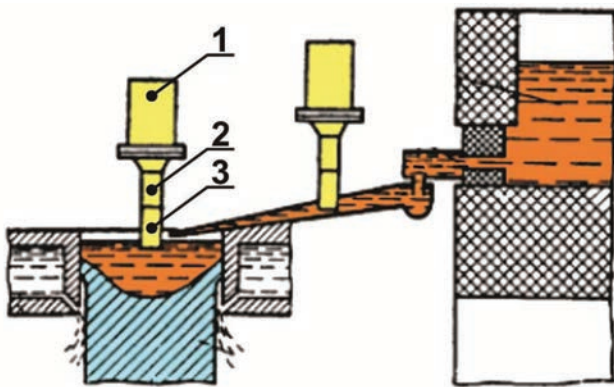


Fig. 2. Technological line: 1 – magnetostrictive transducer with acoustic feedback MST-4-18FB (MST-15A-18 analog); 2 – high-quality sonotrode; 3 – niobium (titanium) emitter [2]

has developed and successfully implements abroad (Great Britain, the Netherlands, India, South Korea, Spain) equipment for the ultrasonic treatment of aluminum and magnesium melts (Fig. 1). In the Russian Federation, this equipment was used and tested in 2017 at the RUSAL ETC LLC enterprise.

This ultrasonic equipment is part of the technological line for the preparation of aluminum and magnesium melts and casting into molds (Fig. 2).

The device for ultrasonic treatment of aluminum and magnesium melts includes an ultrasonic electric generator (USG), a magnetostrictive transducer (MST), an immersion radiating sonotrode (emitter), a control and stabilization system of oscillations of the emitter (CS).

The best technological effect is achieved when the generator-transformer-sonotrode system is op-

erated near their electrical and mechanical resonance. The reconciliation of the MST and the transducer must ensure an efficient transfer of mechanical vibrations through the contact area with the liquid metal. For transferring ultrasonic vibrations to a liquid metal, the sonotrode must be made of a material resistant to aluminum and magnesium melts. The most resistant to such influences are niobium alloys. The modulus of normal elasticity of niobium, unlike almost all high-temperature metals and alloys (titanium, molybdenum, tungsten, etc.), does not

change in the temperature range of 20 – 1200 °C. For all other high-temperature materials, it monotonously decreases upon heating. The thermal stability of the elastic characteristics of niobium and its alloys led to the preservation of acoustic properties when working in a liquid metal [2].

A number of ultrasonic technologies require regulation and stabilization of acoustic power introduced into the substance being processed. When processing molten metals, the maximum possible acoustic energy is required, which must be introduced into the melt in order to reduce the processing time, thereby increasing the productivity of the installation. Acoustic energy is characterized by the intensity of ultrasonic vibrations, which is determined by the expression:

$$I = \frac{1}{2} A^2 \omega^2 c \rho \left[ \frac{W}{m^2} \right], \quad (1)$$

where:  $A$  – medium particles oscillation amplitude (shift amplitude stabilization of sonotrode end);  $\omega$  – rate of phase change;  $c$  – sound speed in substance;  $\rho$  – density.

According to the mathematical expression, it follows that by changing or stabilizing the amplitude of the displacement of the end of the emitter, it is possible to adjust or stabilize the intensity of the acoustic energy introduced into the melt.

To regulate and stabilize the acoustic energy of the ultrasonic device, developed by the RELTEC Co., the dependence between acoustic energy (magnitude) and shift amplitude of sonotrode end is used. The installation control system monitors the displacement amplitude using a feedback acoustic sensor installed in the MST-4-18FB.



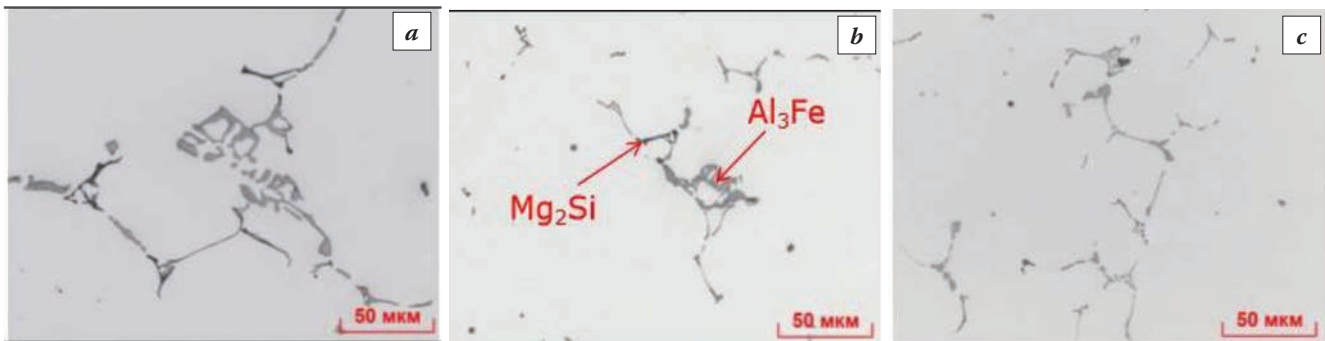
Fig. 3. Computer rack

Table 1. The chemical composition of alloy 5052

Alloy grade	Components, %							
	Mg	Fe	Si	Cr	Ti	B	Mn	Al
5052	2.37	0.24	0.12	0.18	0.017	0.0006	0.012	basis

Table 2. Effect of melt processing technology on the phase structure of Al<sub>3</sub>Fe and Mg<sub>2</sub>Si

Melt processing technology	Quantitative characteristics of phases			
	Linear phase size, D <sub>cp</sub> , μm (D <sub>min</sub> -D <sub>max</sub> )		Volume fraction of phases in the structure, %	
	Al <sub>3</sub> Fe	Mg <sub>2</sub> Si	Al <sub>3</sub> Fe	Mg <sub>2</sub> Si
no UST	40.6 (12.9–78.9)	35.1 (12.9–77.4)	2.0	0.38
1.5 kW UST	36.0 (12.6–70.8)	28.8 (14.9–70.1)	1.9	0.30
3 kW UST	31.1 (13.2–62.1)	30.8 (17.6–48.7)	2.3	0.33

Fig. 4. The structure of Al<sub>3</sub>Fe and Mg<sub>2</sub>Si phases without UST (a) and with UST (b, c): 1.5 kW – b, 3.0 kW – c

The control system is assembled in a computer rack (Fig. 3) and is executed on the basis of an industrial controller. On the front panel there is a computer monitor screen, through which interface of information-control system (operator panel) is implemented. Software, executed on the basis of industrial controller, forms the required structure of the control system (CS) rack. The software has three-level structure, the lower level is the USG software, at the middle level, all levels of software are interfacing, at the top level, a man-machine interface for monitoring and controlling is provided.

The software performs the following functions:

- implementation of the screen interface;
- organizing the archiving of the parameters of the current process, storing the archive, organizing access to any selected archive.
- control of the process parameters and maintaining the amplitude of the emitter vibration and the power of the ICP set by the operator;

The research of the equipment developed by RELTEC was carried out in pilot industrial conditions at the place of the company RUSAL during the semi-continuous casting of large-size aluminum alloy ingots 5052. The influence of the cavitation effect on the grinding of iron-containing components and Mg<sub>2</sub>Si phases was determined. The chemical composition of the alloy is given in Table 1.

Casting was carried out in water-cooled molds of 600 × 1630 mm cross-section by standard technology. Ultrasonic treatment was carried out in the melt flow up to the crystallization at 700–720 °C and 17.4 kHz, 1.5 or 3.0 kW. Ingots structure was studied on etched sections. Results of the study are presented in Table 2 and Fig. 4.

Volume fraction of phases in microstructure does not differ significantly from processing technology, whereas their linear dimensions have a number of significant differences. So, average phase size of Al<sub>3</sub>Fe due to ultrasonic treatment is reduced by 25%,

and  $Mg_2Si$  by 10%. And such a grinding of the average size occurs as a result of a significant reduction in the number of phases is larger than 50–60  $\mu m$ . Maximum phase value of  $Al_3Fe$  is crushed from 79 to 62  $\mu m$ , and  $Mg_2Si$  from 77 to 49  $\mu m$ , i.e. the more power and ultrasound amplitude, the better cavitation effect on the melt flow during casting of large aluminum alloy ingots.

Device for ultrasonic treatment of aluminum and magnesium alloys, developed by the RELTEC company, can be easily adapted for existing or developing lines, which are designed for preparation of, aluminum and magnesium melts and casting technologies, for high-quality products with increased resource characteristics. The high efficiency of the technological process of degassing or doping the melt with nanodispersed intermetallic materials is achieved by the controllability of the ultrasonic treatment with a constant control of the energy transferred to the

melt and the oscillations of the immersed radiating sonotrode. Significant reduction in the time of ultrasonic treatment of the metal melt makes this method most economically viable and environmentally friendly.

## REFERENCES

1. **Alba-Baena N., Eskin D.** Kinetic of ultrasonic degassing of aluminum alloys // *Light Metals 2013* / ed. by B. A. Sadler. Hoboken, 2013. P. 957–962.
2. **Eskin G.I.** Ultrasonic treatment of molten aluminum. 2nd ed. revised and enlarged. M.: Metallurgy, 1988. 232 p.
3. **Agranat B.A. and others.** Ultrasonic technology. M.: Metallurgy, 1974. 503 p.
4. **Abramov O.V., Prihodko V.M.** Powerful ultrasound in metallurgy and engineering. M.: Yanus-K, 2006. 688 p.

Правильно?

## PROPERTIES OF THE QUENCHANTS MEASURED WITH LIŠČIĆ/QRC AND ISO 9950 OR ASTM D6200 PROBES

**Božidar Matijević**

University of Zagreb, Faculty of Mechanical Engineering and Naval Architecture. Zagreb, Croatia

bozidar.matijevic@fsb.hr

For evaluation of quenchants under real industrial conditions, the new Liščić/QRC probe is designed. The Liščić/QRC is special upon design, because it is instrumented with 3 thermo-couples on the same radius of the cross-section at the middle of the probe length. The outer thermo-couple measures the temperature at 1 mm below surface, the second one at 4.5 mm below surface, and the third one at the centre of the probe. The working principle of the probe is the measurement of the dynamics of heat extraction which is best represented by the change of temperature gradients. Second type of probe developed to evaluate the cooling properties of relatively small samples of a quenchant used in this paper is standard ASTM D6200 probe, which consists from cylindrical test specimen having one thermocouple at its geometrical centre. Comparative testing was recently performed with the Liščić/QRC probe and standard probe with one vegetable oil (Palm Oil) and a commercially available mineral oil (Kalenol 32). The work was performed at the Quenching Research Centre (QRC) of the Faculty for Mechanical Engineering, University of Zagreb, Croatia. The results of this paper showed distinctive differences in the quenching behaviour of these two quenchant media.

**Keywords:** quenching intensity; Liscic/QRC probe; standard ISO 9950 probe; Palm Oil; mineral oil.

### SCOPE AND RESULTS

The Cooling characteristics of a liquid quenchant are usually determined by cooling curve analysis using a laboratory test such as ISO 9950, Industrial Quenching Oils, Determination of Cooling Characteristics, or ASTM D6200, Standard Test Method for Determination of Cooling Characteristics of Quench Oils by Cooling Curve Analysis, which utilize a small cylindrical test probe that is 12.5 mm in diameter by 60 mm length with one thermocouple (TC) at its geometrical centre [1, 2]. These tests are invaluable for characterization and selection of a relatively small volume ( $\leq 2$  L) of a quenching fluid or for regular monitoring of a quenching bath under laboratory testing. However, the use of such small test probes is of limited value for the measurement and recording of the real quenching intensity while quenching actual components, which are typically much larger under workshop conditions. The Liscic/QRC probe (QRC – Quenching Research Centre) was designed to measure and record the cooling intensity of all types of liquid quenchants using different quenching techniques including immersion quenching, intensive quenching, delayed quenching, martempering, and austempering to characterize the quenching processes in industrial practice and to compare their quenching intensity

[3]. The probe is a solid cylinder 50 mm in diameter and 200 mm in length, constructed of Inconel 600, a nickel-chromium austenitic alloy, which during heating and cooling does not undergo structural transformation and is oxidation resistant. The ratio between length and diameter ( $L/D = 4$ ) assures that heat dissipation through both ends of the probe is negligible so that in the cross-section at the half point along the length of the probe where the TCs are positioned, only radial heat flow exists. This is a prerequisite for one-dimensional (1-D) heat transfer calculations. Because of the cylindrical shape of the probe, it is applicable for heat transfer calculations of axially symmetric workpieces with diameters between 20 and 100 mm. By placing the outer TC (the measured data of which are used as input for heat transfer calculations) at 1 mm below the surface, minimum damping effect of transient surface temperature is assured. Also, the lagging effect (because of thermal diffusivity) is minimized due to the short distance to the surface. The response time (which depends on the outer diameter of the TC) is relatively short because the diameter of the TC at 1 mm below the surface is only 1 mm. Comparative testing was recently performed with the standard probe and the Liscic/QRC probe with one vegetable oil (Palm Oil) and a commercially available conventional mineral oil (Kalenol 32) [4–7]. Summary of

physical properties of palm oil and mineral oil is as follows:

Property	Palm Oil	Mineral Oil	Test Method
Viscosity, 40 °C, mm <sup>2</sup> /s	40.39	32	ISO 3104
Viscosity, 100 °C, mm <sup>2</sup> /s	8.53	5.4	ISO 3104
Viscosity Index	136	100	ISO 2909
Density 15/20 °C, g/mL	0.9151	0.863	ASTM D4052
Open Cup Flash Point, °C	326	225	ISO 2592
Pour Point, °C	-6	-15	ISO 3016
Acid Number, mg KOH/g	0.18	0	ISO 6618
Saponification Number, mg KOH/g	197.3	0	ISO 6293

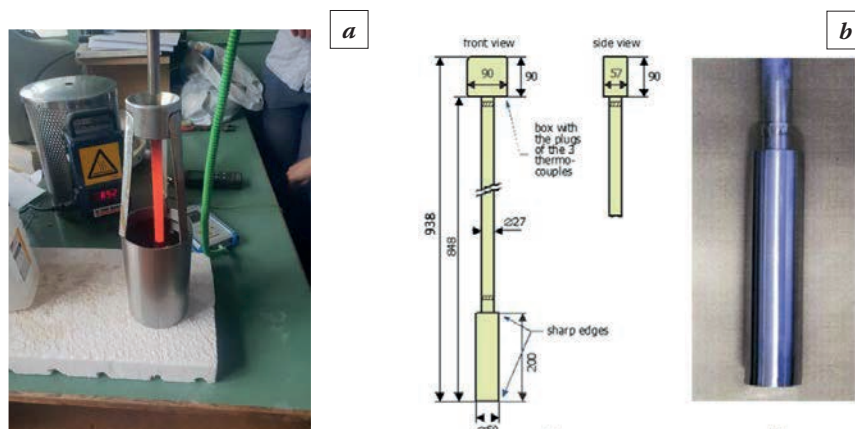
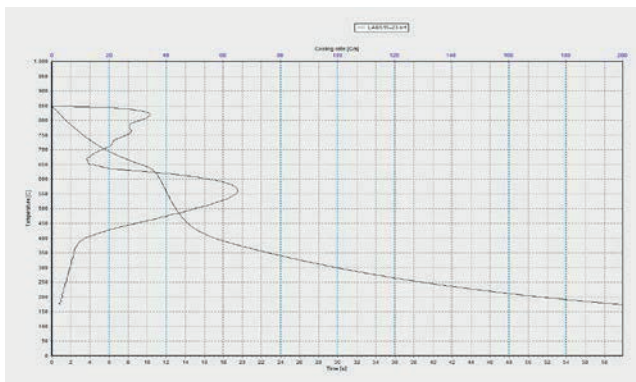


Fig. 1. A laboratory ISO 9950 small cylindrical test with probe of 12.5 mm (a) and Drawing of the Liscic/ QRC probe with the handle and photo of the Liscic/QRC probe (b)

### CONCLUSION

The cooling curve data for the palm oil shows it cools more quickly than the mineral oil, but it would be of additional interest to understand how quickly relative to other quenchants well known to exhibit faster cooling than mineral oil. The comparison of the cooling curves for palm oil and the mineral oil clearly show that palm oil does not exhibit film boiling. The Liscic/QRC probe can be used also by engineers to investigate deeply and widely mentioned self-regulated thermal phenomenon during quenching in water and water salt solutions which is the basis for performing austempering processes in cold liquids. The series of experiments described here provides clear evidence that testing the quenching intensity of liquid quenchants by the Liscic/QRC probe under industrial conditions, in this case relatively large section sizes and quenchant volumes, will provide information not as readily attainable when using small laboratory probes.



Curve name:	LAB515-23.ivf	CR300 [C/s]:	6.39
Date:		CR550 [C/s]:	64.48
CRmax [C/s]:	65.12	Time to 600 C [s]:	11.34
T(CRmax) [C]:	557.79	Time to 400 C [s]:	17.09
t(CRmax) [s]:	12.02	Time to 200 C [s]:	51.39
Tvp [C]:	645.4	Theta 1 [C]:	644.35
Tcp [C]:	333.73	Theta 2 [C]:	421.71

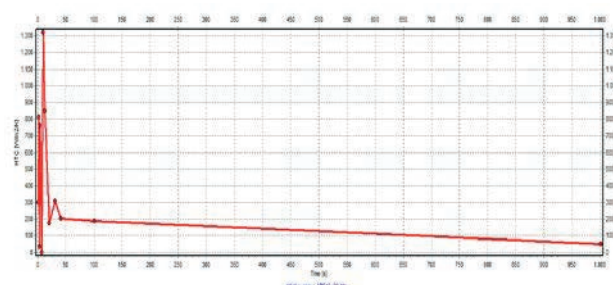
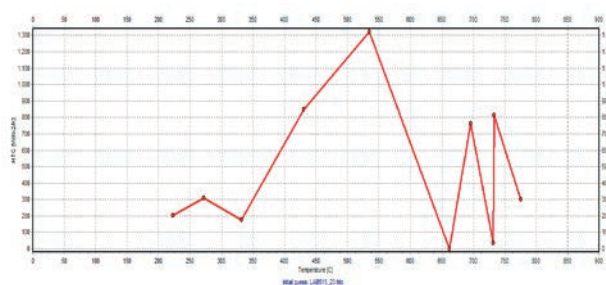


Fig. 2. Cooling time-temperature curves, characteristic parameters,  $HTC \alpha = f(T)$  and  $HTC \alpha = f(t)$  of mineral oil KALENOL 32 at 23 °C without agitation determined using ISO 9950 small cylindrical test

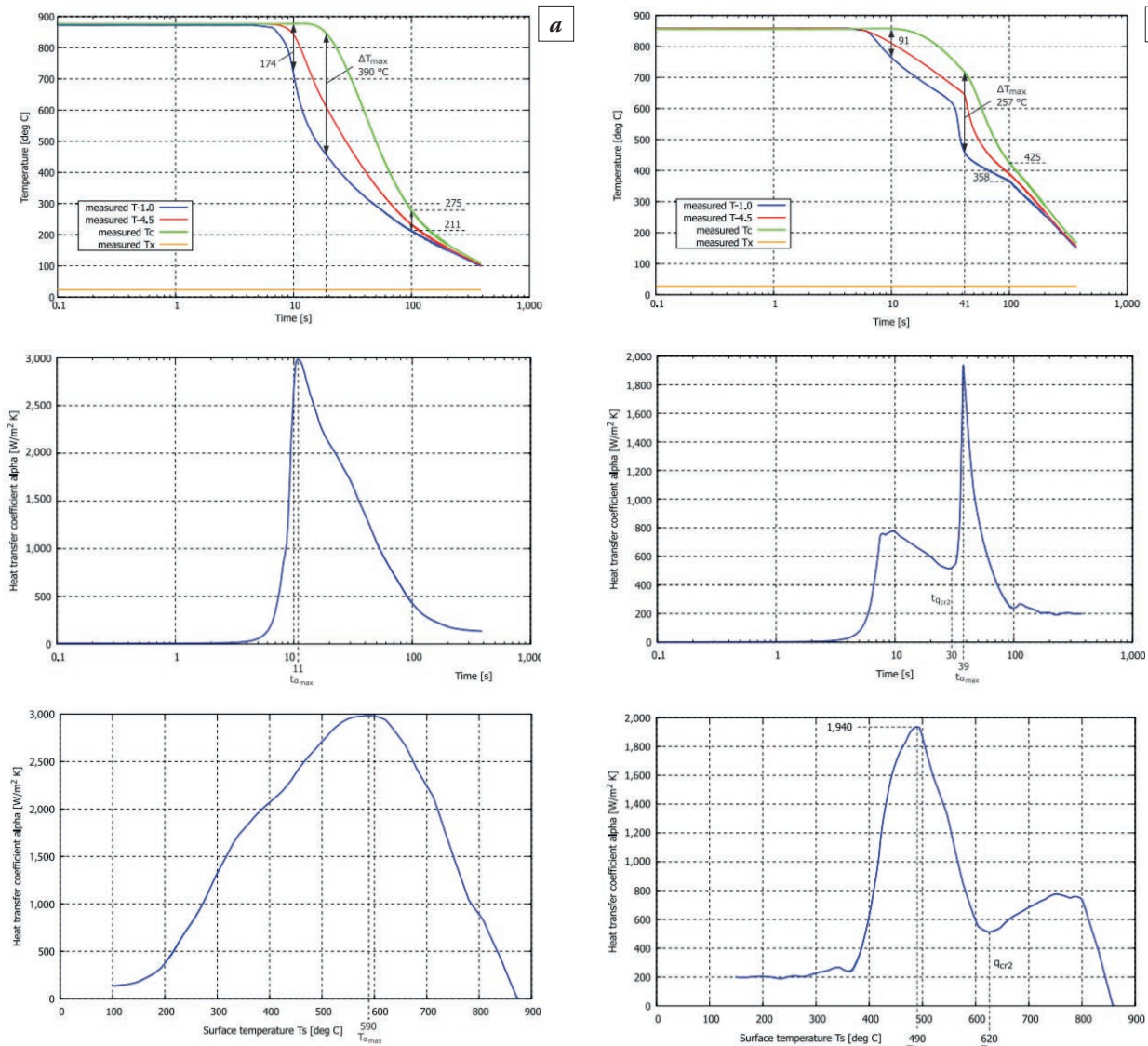


Fig. 3. Cooling time-temperature curves, HTC  $\alpha = f(t)$  and HTC  $\alpha = f(T_s)$  of palm oil at 23 °C without agitation (a) and Cooling time-temperature curves, HTC  $\alpha = f(t)$  and HTC  $\alpha = f(T_s)$  of mineral oil KALENOL 32 at 23 °C without agitation

## REFERENCES

1. ISO 9950:1995: Industrial quenching oils – Determination of cooling characteristics – Nickel-alloy probe test method; [www.iso.org/standard/17848.html](http://www.iso.org/standard/17848.html)
2. ASTM D6200-01: Standard Test Method for Determination of Cooling Characteristics of Quench Oils by Cooling Curve Analysis, ASTM International, West Conshohocken, PA, 2001; [www.astm.org](http://www.astm.org).
3. Liščić B., Filetin T. Measurement and Recording of Quenching Intensity in Workshop Conditions Based on Temperature Gradients // Materials Performance and Characterization. 2016. Vol. 5, No. 1. P. 209–226; <https://doi.org/10.1520/MPC20160007>.
4. Simencio Otero R.L., Canale L.C., Totten G.E. Use of Vegetable Oils and Animal Oils as Steel Quen-

chants: A Historical Review—1850-2010 // J. ASTM Int. 2011. Vol. 9, No. 1. P. 1–38; <https://doi.org/10.1520/JAI103534>.

5. Kobasko N., Liščić B. Eureka: Engineering Materials and Design, November 2017, 48–53; doi: 10.21303/2461-4262.2017.00495.

6. Liščić B. Measurement and Recording of Quenching Intensity in Workshop Conditions Based on Temperature Gradients // Materials Performance and Characterization. 2016. 5 (1). 209–226; doi: 10.1520/mpc20160007.

7. Matijević B., Canale F.B., Liščić B., Totten G.E. Using Thermal Gradient Measurements to Compare Bath Temperature and Agitation Effects on the Quenching Performance of Palm Oil, Canola Oil and a Conventional Petroleum Oil // Materials Performance and Characterization. 2019. 1, 8. 223–248; doi:10.1520/MPC20180135.